Chemistry of Iridium(III) based 'Aggregation Induced Emission' Active Complexes: Applications in Sensing and Bioimaging

THESIS

Submitted in partial fulfillment of the requirements for the degree

of

DOCTOR OF PHILOSOPHY

by

Parvej Alam

Under the supervision of

Prof. Inamur Rahaman Laskar

BIRLA INSTITUTE OF TECHNOLOGY AND SCIENCE

PILANI (RAJASTHAN) INDIA

2016

BIRLA INSTITUTE OF TECHNOLOGY AND SCIENCE
PILANI (RAJASTHAN)

CERTIFICATE

This is to certify that the thesis entitled **Chemistry of Iridium(III) based 'Aggregation Induced Emission' Active Complexes: Applications in Sensing and Bioimaging** submitted by **Mr. Parvej Alam** ID No **2011PHXF017P** for the award of Ph. D. Degree of the Institute embodies the original work done by him under my supervision.

Signature in full of the Supervisor

Dr. Inamur Rahaman Laskar
Designation: Associate Professor

Date:

Dedicated to

My beloved Ammi and

Abbu

Acknowledgement

I take this opportunity to put my gratitude and thanks on record to all those who were of great help and support to me in their own special ways during the journey of my doctoral studies.

Firstly, I would like to thank my supervisor, Professor Inamur Rahaman Laskar, who gave me the opportunity to join his group in the BITS Pilani, and directed me through nearly five years of thesis work. His supportive discussions and enthusiasm for chemistry always replenished my energy to work. His inspiring hard work and constant motivation have helped me to understand better and remain optimistic during the course of my study. His forensic scrutiny of my technical writing has been invaluable.

I am immensely thankful to the Vice-Chancellor, Directors, Deputy Directors and Deans of Birla Institute of Technology and Science (BITS) Pilani for providing me the opportunity to pursue my doctoral studies by providing necessary facilities and financial support.

My whole-hearted gratitude to Prof. Sanjay Kumar Verma, Dean, Academic Research Division (ARD), BITS Pilani, Pilani Campus and Prof. Ram Kinkar Roy (earlier DRC Convener) and Prof. Ajay Kumar Sah, (present DRC Convener), Departmental Research Committee (DRC), Department of Chemistry, BITS Pilani, Pilani Campus for his official support and encouragement. I owe my sincere thanks Dr. Hemanth Jadav, Dr. Navin Singh, nucleus members of ARD, other members of DRC, Department of Chemistry, BITS Pilani, Pilani Campus for their cooperation and constant support. I, overwhelmingly acknowledge the office staff of ARD, whose secretarial assistance helped me in submitting the various evaluation documents in time.

I am grateful to the members of my Doctoral Advisory Committee, Prof. Subit Kumar Saha and Dr. Surojit Pande for their great cooperation in refining my thesis. I am thankful to Prof. Saumi Ray and Dr. Bibhas Ranjan Sarkar for their kind support.

I am thankful to my research collaborators, Dr. Angshuman Roy Choudhury, IISER Mohali for Single X-Ray, NMR, HRMS facility and valuable suggestions. I would like to thank Prof. Nikhil Ranjan Jana (IACS, Kolkata), Dr. Rajdeep Choudhury (BITS Pilani) and Prof. Jitendra Panwar (BITS Pilani) for biological studies.

Also, I am thankful to Dr. Pere Alemany (University at de Barcelona, Spain), Dr. Shamik Chakraborty (BITS Pilani, Pilani Campus) and Dr. Debashree Bandyopadhyay (BITS Pilani, Hyderabad Campus) for validating some of the experimental data through computational calculations.

I am grateful to Dr Ashish Gupta, Samtel centre for Display Technologies IIT Kanpur for solid state quantum yield calculations.

I am thankful to all the respectable faculty members and office staffs of the Department of Chemistry, BITS Pilani for their generous help and support along with fruitful discussions during the different stages of my doctoral study. Thanks are also to all the office staff of the other Departments for their help during my work. My sincere thanks to the Librarians (previous Dr. M. Ishwara Bhatt and current Mr. Giridhar Kunkur), BITS Pilani and other staff of library for their support and help rendered while utilizing the library facilities.

My sincere thanks to Dr. Mirnmoyee Basu, Dr. Manoj Muthyala, Dr. Amit Tiwari, Mr. Sonu, Dr. Sandeep Tripathi, Mr. Narendra Mishra, Mr. Anand Gupta, Mr. Arun, Abdul Shakoor, Nisar Mir, Mr. Ganesh, Sunita Poonia, Sunita Chaudhury, Sushila, Roshan Nazir and Noorullah Baig for chemistry discussions. Thanks to my group members Mr. Saleem Pasha, and Mr. Vishal Kachawal with whom I have worked. I extend my heartfelt thanks to my friends Mr. Ravi Pratap Singh, Dr. Bhupendra Mishra, Dr. Amrith, Mr. Mukund, Ms. Menakshi, Ms. Santosh, Nitesh, Mr. Emil, Mr. Prasant, Mr. Arpit, Mrs. Prameela Jha, Mrs. Pushp Lata, Dr. Navin Jain, Mr. Gagandeep Singh, Jharna pala, Amar Chaudhury, Monika Poonia, Surendra Pratap, Tej Verma, Pramod Saini and Mr. Phool Hasan.

I would like to thank my parents Manir Alam and Jainab Khatoon, who always pushed me to succeed over the years. Their vision, ethical principles, moral support, endless patience and eternal inspiration, to face any situation in life have guided to the successful completion of this work. You sacrificed a lot for my education and I truly do appreciate it. I would also like to acknowledge my brother Mr. Israfil Alam, my sister Jaitoon Nisha and my sweet niece Maham, Anas and nephew Asad for their love and support.

Finally, I want to acknowledge DST and BITS Pilani for financially support in the form of Project Fellow during my research tenure.

Parvej Alam

Abstract

The thesis entitled "Chemistry of Iridium(III) based 'Aggregation Induced Emission' Active Complexes: Applications in Sensing and Bioimaging " deals with the synthesis of new iridium(III) based metal complexes which exhibited a unique 'Aggregation induced emission (AIE)' property, structurally characterized and studied their luminescent properties. The synthesized complexes were used in different applications such as sensing and bioimaging. The thesis is divided in seven chapters.

The first chapter of the thesis describes a literature overview about the fundamentals of fluorescence, various types of transitions such as MLCT, LLCT etc, different approaches of synthetic techniques of luminescent iridium(III) complexes and their many applications. Additionally, the chapter describes the history of AIE property and their probable mechanistic pathways. The general features of AIE active iridium(III) complexes are described in this chapter. The background of bioimaging and sensoric applications of luminescent materials have been described in this chapter. The details about iridium(III) complexes used in bioimaging and sensoric applications are also given.

The second chapter of the thesis describes the materials and instruments are used to furnish the whole thesis work.

The third chapter of the thesis describes a convenient route to synthesis of a series of monocyclometalated iridium(III) complexes which involves in two steps. Initially, an intermediate, $[IrHCl[(o\text{-}C_6H_3X)P(Ar)_x\text{-}(PAr_xR_y)_2]$ [A (**j, k, l, m**)], six-coordinated iridium(III) complex involving a 4-membered chelate was isolated. Then, it was transformed into a monocyclometalated iridium(III) complex, $[(C\text{^}N)Ir(PAr_{x-1}R_y)_2(Cl(H)]$ (**1-13**), through replacement of the 4-membered chelates with 5-membered cyclometalates. The intermediates and the complexes were structurally characterized by FTIR, ^{1}H, ^{13}C and ^{31}P NMR spectroscopic techniques. Octahedral coordination for iridium(III) in **2, 8, 9** and **13** was established by single crystal X-ray diffraction study. Experiments on photophysical properties and quantum chemical calculations reveal a mixed LC/MLCT/LLCT nature for the lowest excited states – all these complexes that emit bright light in the solid state. Fine tuning of the emission wavelength throughout the visible range was achieved through suitable combinations of chromophoric cyclometalates and non-chromophoric aryl phosphine ligands. More interestingly, all studied complexes were found to exhibit AIE activity. Two of these AIE active materials **6** and **13** were found to have high sensitivity for the detection of picric acid (PA). Additionally, **6** was used as a potential non-toxic bioimaging probe.

The fourth chapter of the thesis describes the syntheses of mono cyclometalated diamine iridium(III) complexes. The chapter consists of two parts.

In part A, two AIE active iridium(III)-diimine complexes [mono(1,10-phenanthroline)bis(tri-phenylphosphine)(di-hydrido)iridium(III)hexafluorophosphate (**3**) and mono(1,10 phenanthrolin)bis(triphenylphosphine)(hydrido)(chloro)iridium(III)hexafluorophosphate (**4**)] were synthesized from a single specified reaction. Ground and excited state electronic properties of these complexes were investigated using density functional theory (DFT) and time-dependent DFT (TDDFT). Molecular orbitals were also exploited to compute ground state dipole moments. The solid thin-films of **3** and **4** exhibited the solvent polarity dependent vapour-responsive emission properties (vapoluminescence). In part B, two new mono cyclometalated iridium(III) complexes [$Ir(PPh_3)_2$(bpy-H)(Cl)(H), (bpy-H = κ^2N,C-2,2′-bipyridine) or Ir(bipy-H), "rollover" complex] and [$Ir(PPh_3)_2$(bipy)$(H)_2$]A, (bipy = 2,2′-bipyridine; A = counterions) with remarkable AIE were synthesized from a single specified reaction. The emission color from bluish green to yellowish-orange after repeated protonation and deprotonation of [Ir(bipy-H)] is highly reversible in nature. [Ir(bipy-H)] is sensitive toward pK_a of the acid. The tuning of photophysical property has been demonstrated with respect to pK_a of the acids. However, [$Ir(PPh_3)_2$(bipy)$(H)_2$]A exhibited counterion dependent tuning of emission wavelength. [Ir(bipy)]Cl exhibited a dual property *i.e.*, mechanochromism and vapochromism and its causes were rationalized. DFT based calculations were performed to investigate in detail the electronic properties of these compounds in the solid state. The emission properties of the two crystals, [Ir(bipy)]A (A=Cl, PF_6) were extensively discussed by analyzing the crystal packing, the frontier molecular orbitals and the calculation of the nature of the low-lying excited states. The restriction of internal rotation of the phenyl rings in the phosphine ligands due to intermolecular interactions was suggested as the most plausible origin of the AIE effect in these crystals.

The fifth chapter of the thesis describes the syntheses of new AIE based iridium(III) complexes [$Ir(PPh_3)_2$(C^N)(Cl)(H)], (where C^N= Schiff bases) by using Schiff bases. These complexes showed a drastic reversible color contrast in presence of acid-base. Out of four, one donor-accepter (D-A) system was found as TICT probe which was further utilized for CO_2 detection.

The sixth chapter was divided into two parts, the part A describes the syntheses of a series of iridium(III) complexes with the help of microwave (MW) reactor. In part B, an 'Aggregation InducedEmission (AIE)' active blue emitting bis cyclometalated iridium(III)complexes with app -ended diphosphine ligands[$Ir(F_2ppy)_2$L1/L2)2(Cl)] (F_2ppy=2-2′,4′difluoro) phenylpyridine; L1

=1,2 bis (diphenylphosphino)ethane; L2= bis(diphenylphosphino)propane) was realized on a suitable route. The free phosphorous donor atom present on the appended diphosphine was shown to provide selective binding to the Hg^{2+} ions. The selective binding ability of the probe molecule towards Hg^{2+} ions resulted in a detectable signal due to complete quenching of their AIE property. The quenching effect of the probe molecule was explored and found that the resultant of the degradation of the probe iridium(III) complex triggered by the presence of Hg^{2+} ions due to an interplay of a soft-soft interaction between the free phosphorous atom of probe molecule with Hg^{2+} ions. These complexes were modelled to obtain deeper understanding of excited state properties and the results were tentatively correlated with the experimental data.

The seventh chapter consists of synthesis of a greenish-blue emissive bis-cyclometalated iridium(III) complex with octahedral geometry using convenient route where a bulky substituted ligand, N1-tritylethane-1,2-diamine ligand (trityl- based rotating unit) (L) was coordinated to iridium(III) in non-chelating mode, [$Ir(F_2ppy)_2(L1)(Cl)$], [F_2ppy=2-(2′,4′difluoro)phenylpyridine ; L1 = N_1-tritylethane-1, 2-diamine]. The purpose to introduce rotor in **1** was anticipated to initiate in AIE activity into it. The presence of secondary amine in ligand led the complex in sensing acids. The mechanism of this change in **1** under acidic medium was explored. A bright yellow emissive complex was formed on exposing **1** towards hydroxide ion which was isolated, characterized and identified as a new ‘Aggregation Induced Enhanced Emission’ (AIEE) active complex. The detection limit of hydroxide ion was determined to 126 nM. Ground and excited state properties of **1** was investigated using DFT and TD-DFT based calculations and several important aspects of the experimental facts were validated.

List of abbreviations and symbols

Abbreviation/Symbol	Description
α	Alpha
Å	Angstrom
a	Ongsager cavity radius
ACN	Acetonitrile
n-BuLi	*n*-Butyl lithium
β	Beta
Bu	Butyl
Calcd.	Calculated
COD	1,5- cyclooctadiene
^{13}C	Carbon-13
Conc	Concentration
^{0}C	Degree centigrade
c	velocity of light
δ	Delta
$CDCl_3$	Deuterated chloroform
cd	candela
d	Doublet
dd	Doublet of doublet
DCM	Dichloromethane
DMF	*N*,*N*-Dimethylformamide
DMSO-d_6	Deuterated dimethylsulfoxide
DFT	Density Functional Theory
EI	Electron ionization

ESI	Electron spray ionization
EtOAc	Ethyl acetate
Equiv	Equivalent
e.g.	exempli gratia
Ɛ	dielectric constant
ε	molar extinction coefficient
ξ	spin–orbit coupling constant
Δf	solvatochromic shift
^{19}F	Fluorine -19
f_w	Water fractions
f_H	Hexane fractions
G	Gram
h	Hours
HRMS	High resolution mass spectra
IR	Infrared
Ir	Iridium
IC_{50}	half maximal inhibitory concentration
ILCT	Intraligand charge transfer
Hz	Hertz
J	Coupling constant
Kcal	Kilocalories
K_{sv}	Stern–Volmer quenching constant
LLCT	Ligand -to- ligand charge transfer
LMCT	Ligand -to- metal charge transfer
λ	Wavelength

k_T	Rate of energy transfer
lm	lumens
MS	Mass spectrometry
M.p.	Melting point
m	Multiplet
mg	Milligram
MHz	Mega hertz
MLCT	Metal -to- Ligand charge transfer
min	Minutes
mL	Milliliter
µM	Micro molar
M	Molar
mmol	Millimole
MW	Microwave
$\bar{\upsilon}$	Wave number
µ	dipole moment
N_2	Nitrogen gas
η_{ex}	external quantum efficiency
NMR	Nuclear magnetic resonance
nm	Nano molar
nm	nanometer
Os	Osmium
PEG	Polyethylene glycol
Pt	platinum
^{31}P	Phosphorous-31

ϕ	Quantum efficiency
ppm	Parts per million
%	Percentage
rt	Room temperature
R_0	Förstor distance
s	Singlet
σ	standard deviation
t	Triplet
TFA	Trifluoroacetic acid
THF	Tetrahydrofuran
TLC	Thin layer chromatography
THT	Tetrahydrothiophene
TMS	Tetramethylsilane
OTf	Triflouromethanesulfonate
δ	Parts per million
μL	Microliter
μM	Micromolar
v	Volume
W	Watt

Table of Contents

List of Tables

List of Figures

List of Schemes

Chapter I

Introduction

1.1 Introduction

Luminescence (Latin: Lumen = light) is the emission of light by a substance not resulting from heat; it is thus a form of cold body radiation, it can be caused by chemical reaction [1]. It can be many types such as fluorescence, chemiluminescence, bioluminescence, phosphorescence etc. Luminescent materials such as fluorophors or phosphors are materials that emit light (infrared to ultraviolet) under external energy excitation [2-16] [17]. The incident energy, in the form of high energy electron, photons, or electric field, can then be re-emitted in the form of electromagnetic radiation.

The discovery of light is a greatest achievement of mankind, without light the imagination of live is impossible. Unfortunately many poor regions of this world are still struggling with the problem of light, surviving by daily light-dark cycle. In fact, there is no human activity after sunset. The first discovery of light has been done in Stone Age, by rubbing stones. After this, in year 19^{th} century the world started the animal or vegetal origin, such as whale oil or beeswax as a source of light. In 1879, the great scientist Thomas Edison discovered a bulb with carbon filament which became a milestone of modern lighting. The bulb with carbon filament able to convert just 0.2 % of the electricity in to light, but it was more than 20 times higher as compare to a candle. After this invention, the lighting device underwent many substantial change in terms of efficiency and cost effectiveness from decades to decades *e.g.* the tungsten lamp (1906), the sodium vapor lamp (1930s), fluorescent tubes (1940s), the halogen lamp, (1960s), compact fluorescence lamp (1980s), white LED (1996) and finally OLED (1999). Finally they are being replaced by more energy efficient, more compact and more environment friendly technology [18, 19]. The technologies of 21^{st} century are completely based on solid-state luminescent materials. Discovery of solid state smart luminescent materials is a hot topic in today's research. Smart Luminescent Materials describes a wide range of materials that are of current interest including organic light emitting materials, inorganic light emitting diode materials, biomaterials, sensoricmaterials, nanomaterials etc. In addition, both the physics and the material aspects of the field of solid-state luminescence are emerging field of research.

1.1.1 Fluorescence and Phosphorescence phenomena

Photoluminescence are the generation of a visible light from excited molecules after light absorption. These processes are divided into two classes: fluorescent and phosphorescent. When a molecule was absorbed suitable quanta of light, it moved to the vibration levels of one of its electrically excited state known as Frank-Condon excited (FCE) state. The transition of time from ground state to one of the excited state was so short (10^{-15}s) for the significant displacement of nuclei. After excitation, the number of possible ways was possible to reach the ground state and that can be explained based Jablonski diagram (Figure 1.1) [20].

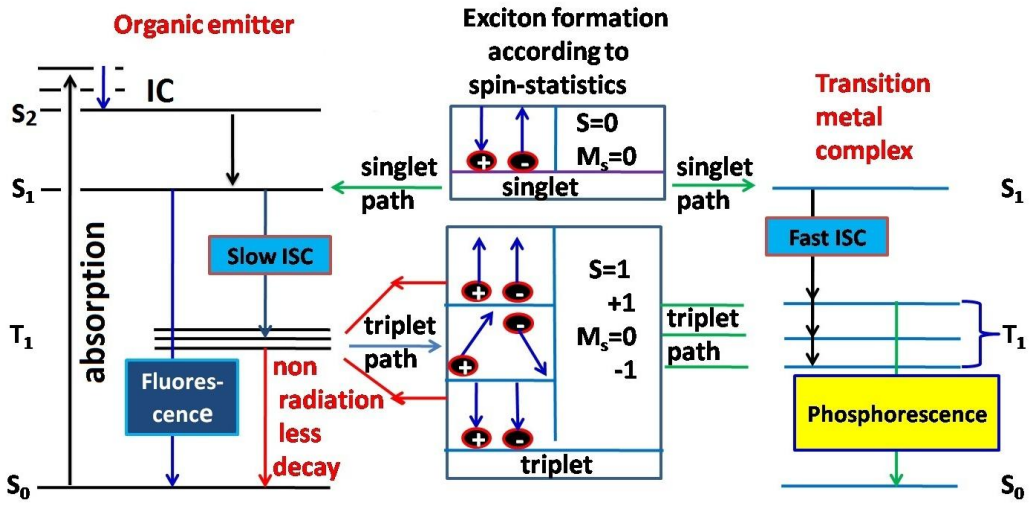

Figure 1.1 Jablonski Diagram for Fluorescence and Phosphorescence.

Fluorescence, a quantum mechanically allowed transition from lowest singlet excited state to ground state within nanosecond time scale where the total spin quantum number S = 0. Conversely, the phosphorescence is a quantum mechanically forbidden transition resulted from triplet excited state to ground state within lifetimes in the microsecond to second regime where the total spin quantum number S = 1.

In Figure 1.1, where S_0 represents the ground singlet electronic state, S_1 represent the first excited singlet electronic state (left) and T_1 represents the first electronic triplet

state (right) where the energy of the triplet state is lower than the energy of the corresponding singlet state.

1.1.1.1 Vibrational Relaxation

During the electronic excitation, a molecule may move to the several vibrational levels and a rapid energy transfer occurs because of collision of molecules with the excited species and solvent. The life time of the vibrational excited molecule ($<10^{-12}$s) is shorter than the lifetime of the electronically excited state that's why the fluorescence originated from the transition from lowest vibrational level of the first excited singlet electronic state to the ground state [21].

1.1.1.2 Internal Conversion (IC)

The Internal conversion (IC) is interelectronic state process where the molecule jumped from higher electronic state to lower electronic state without any emission of radiation. It was happened within the same multiplicity states *e.g.* singlet-to-singlet or triplet-to-triplet states. The probability of internal conversion will be more if the two vibrational energy levels were close enough and they can overlap easily. Moreover, the internal conversion can be occurring between S_0 and S_1 but the gap between S_0 and S_1 should be very less. These type of transitions usually happened for aliphatic compounds where the deactivation rate is too fast that molecule does not have time to fluoresce.

1.1.1.3 Intersystem Crossing (ISC)

A spin crossover between electronic states of different multiplicity - singlet state to a triplet state (S_1 to T_1) is known as Intersystem crossing (ISC). The intersystem crossing process is more facile in presence of heavy atoms *e.g*. Ir(III), Pt(II), Os(IV), iodine (I) or bromine (Br) etc. The presence of heavy atom will increase the probability of spin and orbital interaction *i.e*. spin orbital coupling (SOC) [22-25] and facilitate the intersystem crossing (ISC) process.

1.1.2 Fluorescence Quenching

The decrease in the fluorescence intensity in presence of some external molecule is termed as quenching. It is basically two types; dynamic or collisional quenching and static quenching (Figure 1.2).

1.1.2.1 Dynamic or collisional quenching

A dynamic quenching occurs when the excited state molecule collides with an atom or molecule which may facilitate the non-radiative transition to the ground state. It is a nonradiative energy transfer between the excited state molecule and the quencher (Q). The most favourable condition for dynamic quenching is to use the higher concentration of fluorophore and quencher which will increase the probability of quenching. The life time as well as quantum efficiency will reduce in this process.

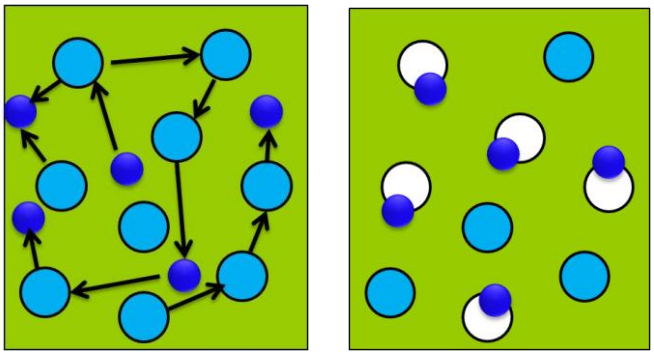

(a) (b)

Figure 1.2 Graphical representation of (a) dynamic and (b) static quenching.

1.1.2.2 Static quenching

In this process fluorophore forms a stable ground state complex (dark complex) with another molecule (quencher) which can lead fluorescence quenching. The life time will not be affected in case of static quenching.

1.1.2.3 Stern-Volmer equation

The decrease in the fluorescence intensity is described by well known Stern-Volmer equation. The ratio of F_0 and F vs concentration of the quencher [Q] obeys the linear relationship. In case of dynamic quenching the question is as follows:

$$F_0/F = 1 + K_{sv}[Q] = 1 + k_q\tau_0[Q]$$

Where F_0 and F are the fluorescence intensities observed in the absence and presence of quencher, respectively, K_{sv} is Stern-Volmer quenching constant, k_q is the bimolecular quenching constant, τ_0 is the unquenched lifetime, and [Q] is the quencher concentration. K_{sv} is indicated the sensitivity of the fluorescence molecule to a quencher. The higher value of K_{sv} indicates the maximum quenching in the system [26-28].

1.2 Resonance Energy Transfer

It is an excited state process where the emission spectrum of a fluorophore (donor) is overlapped with the absorption spectra of another molecule (accepter).

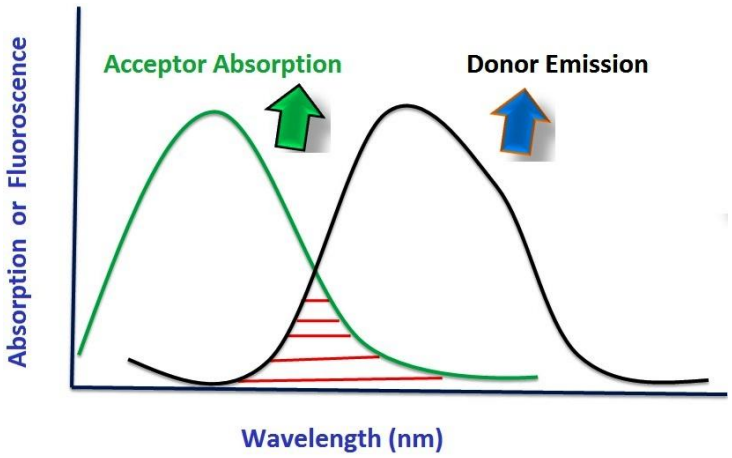

Figure 1.3 Schematic representation of Resonance Energy Transfer.

The essential criterion for Resonance Energy Transfer (RET) [29-32] sometimes called Förstor Resonance Energy Transfer (FRET) is the shorter distance (10 Å -100 Å) between donor and acceptor molecules which facilitate the long-range dipole-dipole interaction [33-37]. The extent of spectral overlap between emission spectra of donor and

absorption spectra of acceptor molecule is the criteria for FRET. It is a non-radiative process (Figure 1.3).

The spectral overlap is described in terms of the Förstor distance (R_0) and the rate of energy transfer k_T (r) is expressed by following equation.

$$k_T (r) = 1/ \tau_D (R_0/r)^6$$

where r is the distance between the donor (D) and acceptor (A) and τ_D is the life time of the donor in the absence of energy transfer.

1.2.1 Effect of solvent on electronic transitions

The emission and absorption spectra are highly affected by nature of solvents. Many sensitive probe molecules were used in labeling of proteins and the lipids in analytical methods because the solute (probe) solute (probe) and solute (probe) -solvent interactions mostly influence the emission and absorption spectra. These interactions will provide valuable information regarding the activities and function of the system. In 1968, Baylis and Johnson observed that the absorption bands are shifted to shorter wavelength in presence of nonpolar solvents (low dielectric constant) while the same bands are shifted to longer wavelength in presence of polar solvents (higher dielectric constant) [38, 39]. After several studies by many research groups (Caldwell and Gagewski, 1971 [40], Leonard et al., 1978 [41]; Richard), the absorption shift towards shorter wavelength is termed as blue shift while the absorption towards higher wavelength is term as red shift. In 1952, McConnell proposed that the blue shifted or red shifted absorption may arise because of n→π* or π→π* transition, respectively [42]. The effect of solvents over spectral properties of solute molecule can be broadly divided into two parts.

1.2.1.1 General solvent interactions

These interactions can be explained based on refractive index (n) and dielectric constant (D) of the solvents and can be divided into following types [43]

1. Dipole-Dipole interactions
2. Dipole- Induced Dipole interactions

3. Induced Dipole- Induced Dipole interactions

1.2.1.2 Specific interaction

These interactions are mainly involving hydrogen bond interaction and complex formation. These interactions are stronger than the non specific interaction and affect abruptly the emission and absorption spectra. According to the Franck−Condon principle, because electron transitions are very fast (10^{-15} s) as compared to nuclear motions, nuclei do not move during the excitation (Figure 1.4) [44, 45].

At the Franck−Condon excited state (FCES), the solute molecule is surrounded by a solvent cage where the solvent molecules possess same orientation like ground state. The molecules from FCES relaxed vibrationally to lowest vibrational level of first excited state within a short period of time ~10^{-13} s.

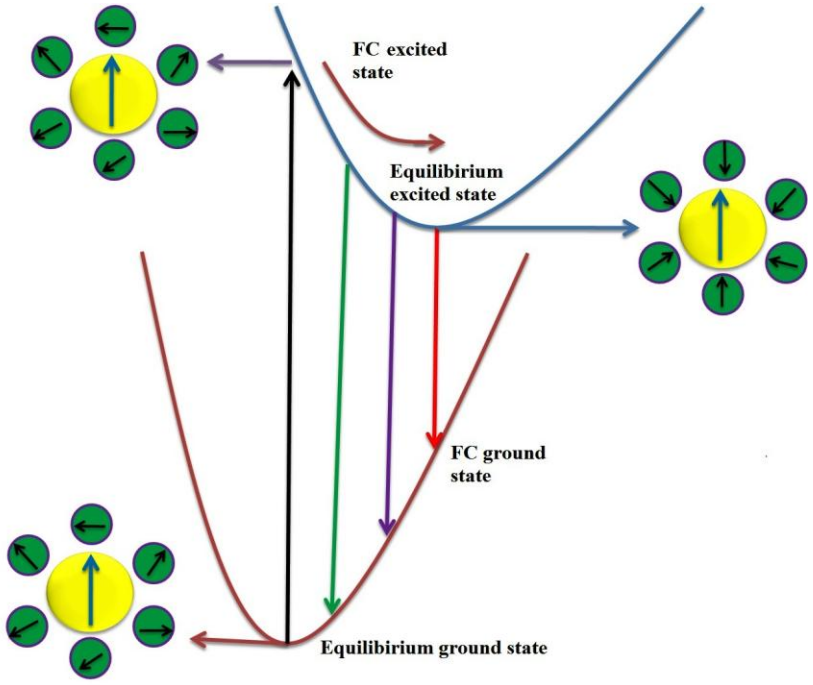

Figure 1.4 Schematic representations of Franck−Condon electronic states; the effects of the electronic and orientation reaction fields on the energy of a dipole in a dielectric medium. The smaller circles represent the solvent molecules and their dipole moments.

In this new environment, the solvent molecules are reoriented around the fluorophore because the energy level differences between the ground and excited states in the fluorophore produce a change in the molecular dipole moment. The process of reorientation of solvent molecules towards fluorophore is known as solvent relaxation [46].

The effect of solvents on fluorescence spectra has been studied by several scientific groups. Pringsheim and Fröster studied the effect of solvents over aromatic compounds [47, 48]. The effect of hydrogen bonding on electronic transitions was well studied by Mataga and Tsumo [49, 50].

The solvatochromic effect (effect of solvent over emission and absorption spectra) was further studied by Lippert, McRae and Suppan. After further modification by Oshika, Lippert and Magata et al. were derived the first equation by considering the change in dipole moment after excitation. In 1955, Lippert and Magata et al. derived a formula which was widely used by scientific groups to analyse the solvatochromic effect using following equation [30, 35, 43, 45, 46].

$$\left(\overline{\nu_{ab}} - \overline{\nu_{fl}}\right) = \left[\frac{2\left(\mu_e-\mu_g\right)^2}{hca^3}\right] \Delta f + \text{constant}$$

$$\text{where} \quad \Delta f = \frac{(\varepsilon-1)}{(2\varepsilon+1)} - \frac{(n^2-1)}{(2n^2+1)}$$

Ɛ is dielectric constant of particular solvent, n is refractive index of a particular solvent, h is Planck's constant, c is the velocity of light, 'a' is the Ongsager cavity radius and μ_g and μ_e are the ground state and excited state dipole moment of the fluorophore, respectively Δf is the solvent polarity parameters, $\Delta\nu = \nu_{abs} - \nu_{em}$ is the solvatochromic shift (in cm^{-1}) between the maxima of absorption and fluorescence emission [$\nu_{abs} = 1/\lambda_{abs(max)}$, $\nu_{em} = 1/\lambda_{em(max)}$].

Scientists worldwide have focused on the development of phosphorescence materials over fluorescence. Fluorescence is allowed transition, which results bright

emission at room temperature. These fluorescence molecules can utilize only 25% of total excitons that means 75% triplet excitons remains unutilized. The way to utilize unused triplet excitons is to employ heavy metals (Ir/Pt/Os etc).

1.3 History and Synthesis of iridium complex

According to crystal field theory for an octahedral geometry, the d –orbital of iridium(III) metal is splitted into two sets of degenerate orbitals, t_{2g} and e_g, separated by an energy gap (Δ_o) where, t_{2g} is fully occupied and e_g is unoccupied orbital. The magnitude of energy difference between t_{2g} and e_g orbital is mostly depends on the field strength of the ligands (strong field or weak field), the oxidation state of the metal (M^+, M^{2+}, M^{3+} etc.) and the size of the orbitals (3d, 4d and 5d). The complexes with iridium(III) metal ion exhibited the large Δ_o because the size of its 5d orbitals and high oxidation state of iridium(III). Additionally, the Δ_o is dependent upon the strength of the coordinated ligand. In case of luminescent iridium(III) complexes, the light absorption is associated with different electronic transition from singlet ground state to singlet excited state which may be ligand centred (^{1}LC), metal-centred (^{1}MC), ligand to metal transition (^{1}LMCT) and in case of C^N cyclometalated ligand, the strong σ-donor and covalent character of the iridium carbon bond (Ir–C) facilitate metal-to-ligand charge transfer (^{1}MLCT). Moreover, emission of iridium(III) complexes always come from triplet state ^{3}MLCT or ^{3}LC because its strong spin–orbit coupling (SOC) constant. The iridium possesses the largest spin–orbit coupling constant (ξ = 3909 cm $^{-1}$) is quite higher compare to other transition metal Fe (ξ = 431 cm^{-1}), Ru (ξ = 1042 cm^{-1}) and Os (ξ =3381 cm^{-1}), respectively) (Figure 1.5) [51-55].

The strong SOC facilitates the intersystem crossing (ISC) by which the singlet-state manifold (S_n) is converted into triplet state manifold (T_n). Thus, the iridium(III) complexes have been popular as triplet harvesting materials.

In early 1970s, $[Ir(bipy)_3](NO_3)_3$ and $Ir(bipy)_3](ClO_4)_3$ were the first *tris*-2,2'-bipyridyl complexes of iridium(III) reported by Flynn and Demas [56]. The coordination mode of bipyridine in these complexes was observed in bidentated fashion. Along with this monodentate and bridging co-ordinations are also known $[(bpy)_2\ IrCl_n\ (H_2O)_{(2-n)}]^{3-n}$ [57]. In the same year, a iridium(III) bridge complexes has been synthesized successfully using benzo[h]quinoline (bq) ligand with general formula $[(bq)_2\ Ir(\mu\text{-}Cl)]_2$. The synthesis of bridge iridium(III) complexes were a breakthrough for the syntheses of luminescent iridium(III) complexes. This complex was the first example of heteroleptic iridium complexes where cyclometalation occurred via C-H activation of aromatic ring, $[(C\text{^}N)_4\ Ir_2(\mu\text{-}Cl)_2]$ (**1**) (where C^N= bq). However, iridium(III) possesses a wide range of complexes with different coordination mode *e.g.* mono-, bis- and tris-cyclometallated species (**2-6**) (Scheme 1.1) [58, 59].

The development of efficient triplet harvesting iridium(III) complexes has been come up as an important research topic in modern research. Many tris-cyclometallated $[Ir(C\text{^}N)_3]$ (**5-6**) or neutral bis-cyclometallated derivatives with ancillary ligands, [where C^N= 2 -phenyl pyridine, F_2ppy=2-(2′,4′-difluoro) phenyl pyridine and ancillary ligands (L^X= acac, picolinate etc.)] (**4**) was observed as efficient emitters that resulted upto 100% internal quantum efficiency. These materials are highly desirable for organic light emitting diodes, bioimaging and sensors.

Synthesis of bis and tris iridium(III) complex (Scheme 1.1) by Mark Thompson et al. was a breakthrough in the field of OLED materials [60][24]. The reaction of $[(C\text{^}N)_4\ Ir_2(\mu\text{-}Cl)_4]$ with neutral ancillary ligands (N^N) in low boiling solvent was resulted an ionic bis cyclometaletated complex $[Ir(C\text{^}N)_2(N\text{^}N)]^+$ where N^N = 2, 2'-bipyridines, 1,10 phenanthrolines, etc.[(routes i, ii and iv); (Scheme 1.1)] (**3**). The reaction of a L^X type of ligand can split iridium bridge in presence of base (Na_2CO_3, K_2CO_3 etc) and resulted a neutral bis cyclometaletated complex $[Ir(C\text{^}N)_2(L\text{^}X)]$ (where L^X = acac, picolinate etc). Syntheses of tris cyclometalated complex can be achieved by three routes [(Scheme 1.1); (iii, iv and v)]. In route (iii), the reaction of $[(C\text{^}N)_4Ir_2(\mu\text{-}Cl)_2]$ with cyclometalated (C^N) ligand produced meridional (*mer*) and facial (*fac*) isomers in good yield. In route (iv), the bis cyclometaled complex with acetylacetone (acac) a

"labile" ancillary ligand produced tris-cyclometalated complex (*fac* or *mer*) in presence of cyclometalated (C^N) ligand. However, a direct approach where $IrCl_3$ or $Ir(acac)_3$ can be used to get the tris cyclometalated complex (*fac* or *mer*) *i.e.* shown in route (v). In presence of heat or light, the kinetically stable *mer* tris complex can be easily converted into *fac* tris complex.

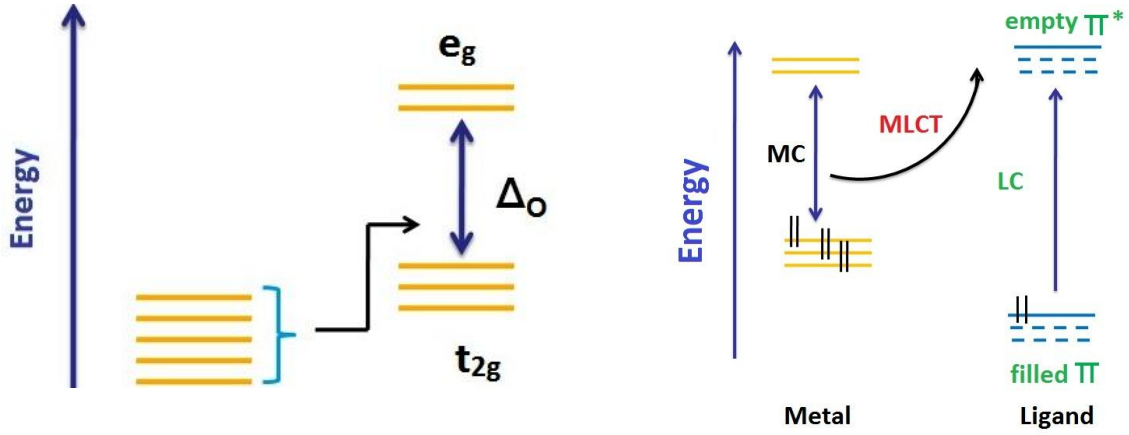

(a) (b)

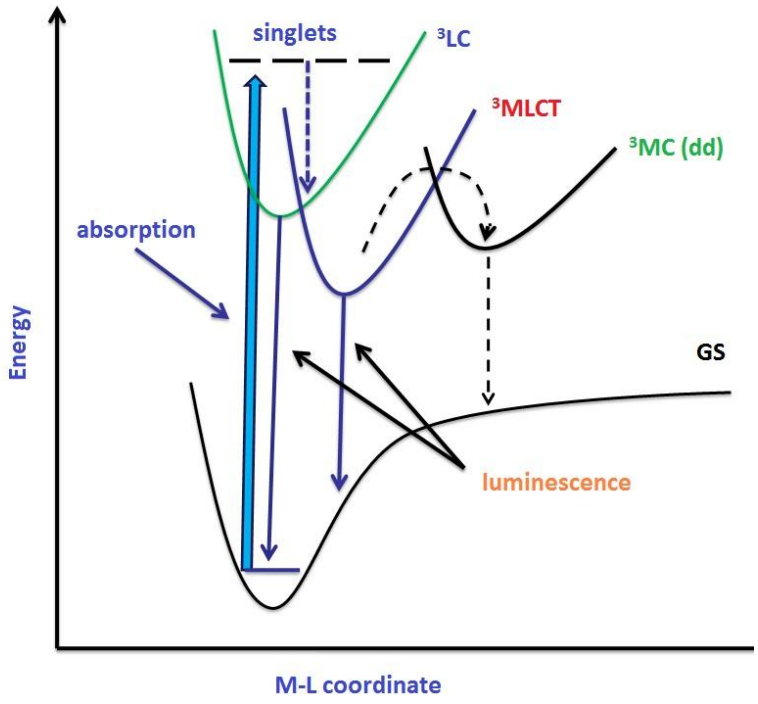

(c)

Figure 1.5 (a) Schematic representation of Crystal field splitting d orbitals in octahedral field; (b) orbital description of MC, MLCT, and LC transitions; (c) electronic transitions involving MC, MLCT, and LC excited states; the MC levels are not emissive.

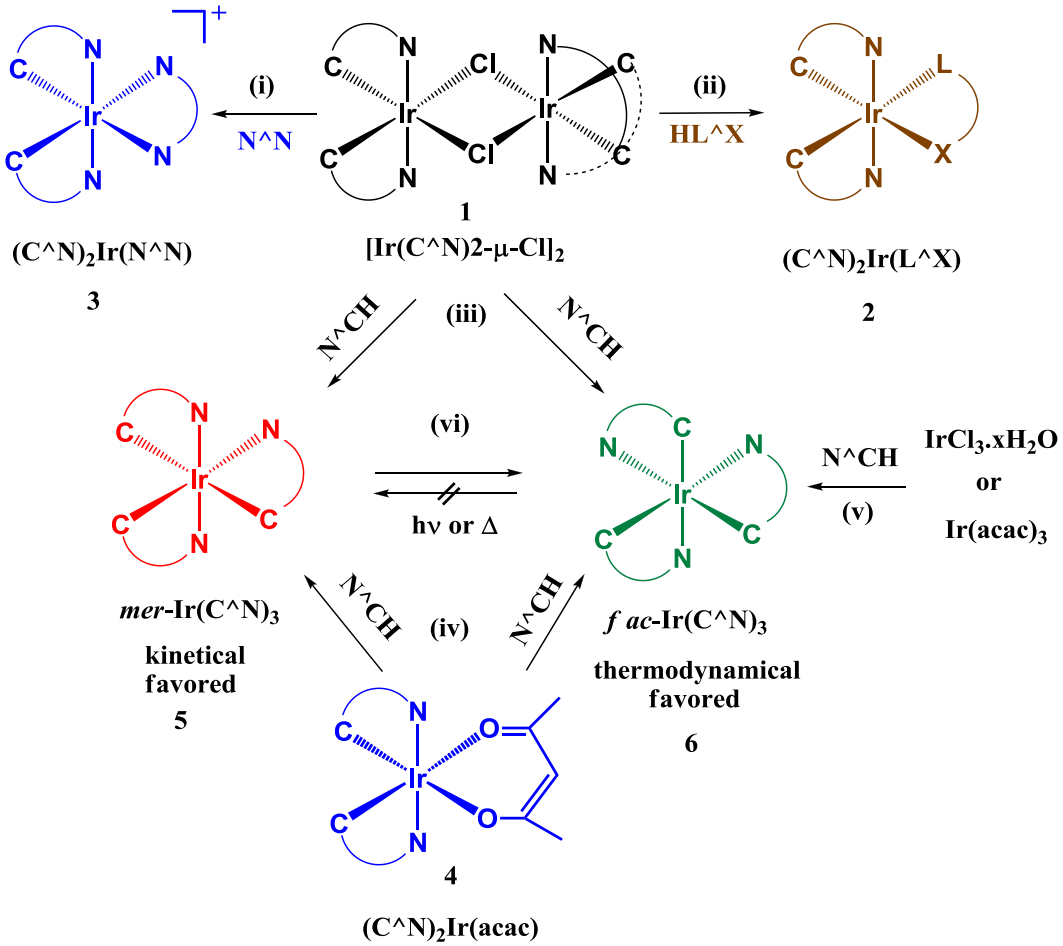

Scheme 1.1 General Syntheses of different iridium(III) complexes.

1.3.1 Homoleptic and Heteroleptic complexes

The octahedral complexes are formed with iridium(III) through coordination of three identical chelated bidentate ligands is known as homoleptic complex. The homoleptic iridium(III) complexes can be two types: (i) facial and (ii) meridional. In facial isomer, the three carbons or three nitrogens are in the same plane while in case of meridional these atoms are not found in the same plane. The facial geometry is more favourable more stable and shows higher quantum efficiency as compare to meridional counterpart.

The iridium(III) complex with two types of ligands is known as heteroleptic complex *e.g.* $[Ir(ppy)_2(pic)]$, this complex having two types of ligand (i) 2-phenyl

pyridine and (ii) picolinic acid. The presence of two different ligands in the octahedral complex resulted several structural isomers (Figure 1.6) [61].

1.3.2 Syntheses of tris iridium(III) complex

A controlled synthesis of *fac* and *mer* isomers in a good yield was reported by Mark Thomson and co workers [62][58]. The reaction temperature (>200 °C) preferably producing the *fac* isomer while at low temperatures (<150 °C) the meridional isomer was isolated [62]. The meridional isomers can be converted into facial isomer at higher temperature indicated that the meridonoal isomer is a kinetically controlled product and facial is thermodynamically controlled product. Akira Tsuboyama et al. synthesized a series of red emitting *fac*-Ir(C^N)$_3$ complexes using Ir(acac)$_3$ and glycerol in 6h (Scheme 1.2) [62]. These complexes were successfully utilized in OLED application and one of the complex Ir(1-phenylisoquinolinato)$_3$ exhibited an excellent external quantum efficiency i.e., η_{ex}= 10.3% and power efficiency 8.0 lm/W at 100 cd/m^2) [63-65].

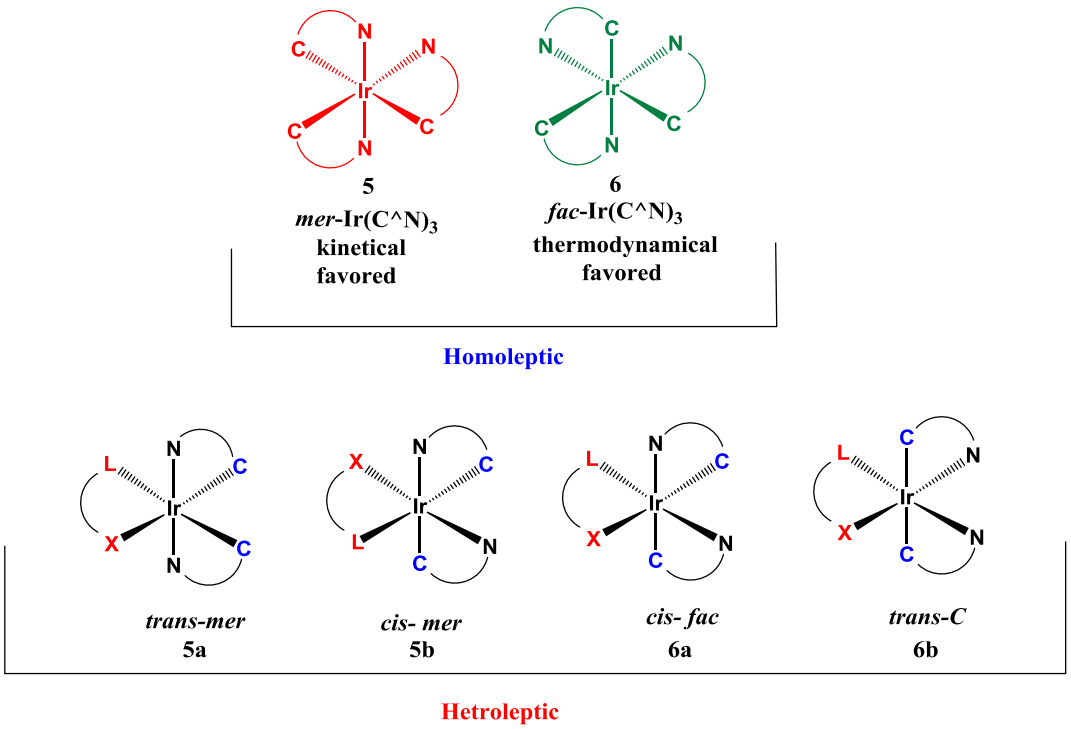

Figure 1.6 Structures of meridional and facial isomers.

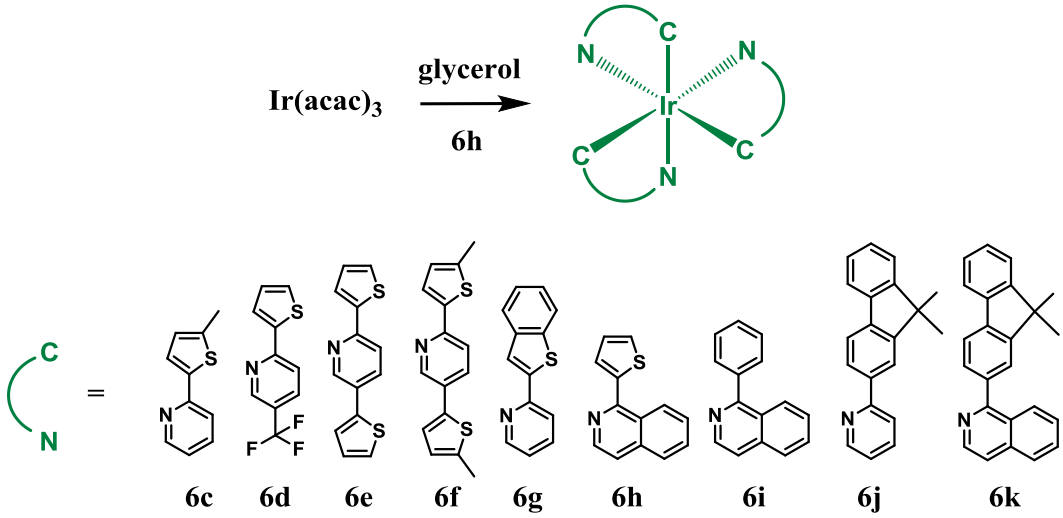

Scheme 1.2 Syntheses of different facial iridium(III) complexes.

Luisa De Cola and co workers synthesized a *mer*-[Ir(dfptrBz)$_3$] by using iridium(III) bridge complex, [Ir$_2$(dfptrBz)$_4$Cl$_2$], AgOTf and dfptrBn in acetone solvent at 50 ^{0}C. Further, the *mer*-[Ir(dfptrBz)$_3$] was successfully converted into *fac*-[Ir(dfptrBz)$_3$] by photoisomerization using a Lot-Oriel 200 W high-pressure mercury lamp equipped with a 280−400 nm dichroic mirror (Scheme 1.3) [66].

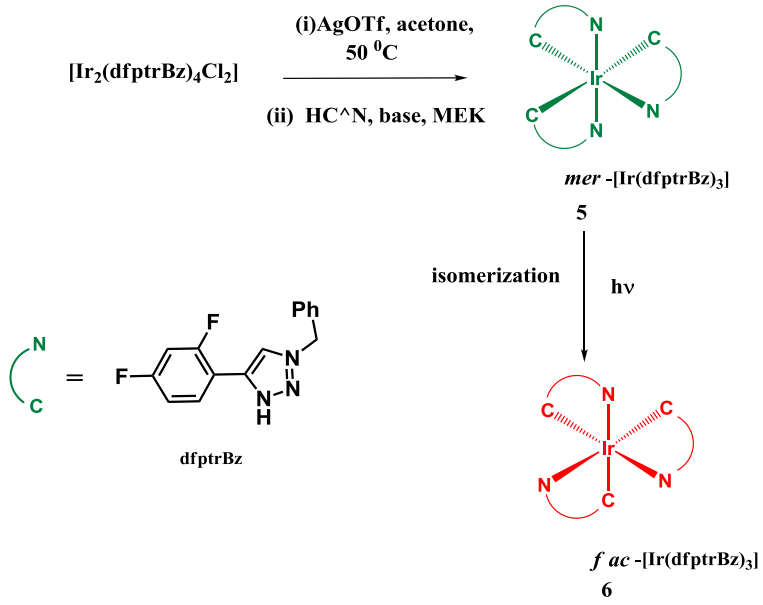

Scheme 1.3 Synthesis of *fac* and *mer* isomers using AgOTf.

1.3.3 Syntheses of bis iridium(III) complex using $[(C\hat{}N)_4\ Ir_2(\mu\text{-}Cl)_2]$ as a precursor

The intriguing property of iridium(III) complexes in color tuning (blue to red), thermal stability and high quantum efficiency at room temperature made them important in various applications. Till date only two types of iridium(III) complexes *i.e.*, bis and tris received the attention in different applications [67, 68].

According to Mark Thomson et al., the neutral bis-cyclometallated acetoacetonate (**7**) and picolinate complexes can be achieved simply by mixing the iridium bridge complex with ancillary ligands (acac or picolinate) with a acid scavenger (Na_2CO_3 or K_2CO_3) and high boiling solvents *e.g.* 2-ethoxyethanol at 140 ^{0}C (Scheme 1.4) [60][24]. The whole reaction mixture was refluxed for 8-15h, resulted a desired complex in good yields and purity. Furthermore, a bis-cyclometallated iridium(III) acetoacetonate (**8**) was synthesized by Tsuzuki et al. in a shorter time (2-6 h) [69] [70, 71].

A further modification was done by De Rosa et al. where silver triflate was used to break the iridium bridge complex in acetone in presence of triethyl amine.

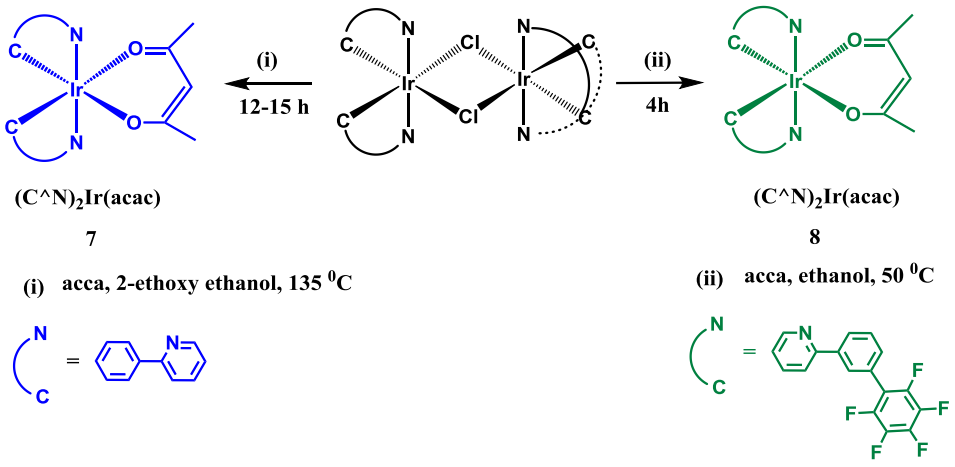

Scheme 1.4 Syntheses of bis iridium(III) complex using iridium di-bridge complex.

1.3.4 Syntheses of bis iridium(III) complex using uncommon precursor

E. Baranoff et al. synthesized a series of heteroleptic complex using two different cyclometalated ligand (2-phenyl pyridine=ppy and 2-(2,4-difluorophenyl)pyridine= F_2ppy) and acetyl acetone as ancillary ligand (**9-16**). The syntheses was achieved by

$[Ir_2(COD)_2Cl_2]$ (COD=1,5-cyclooctadiene) precursor (Scheme 1.5) [72, 73]. The reaction was carried out in presence of non alcoholic solvent decaline at heating condition.

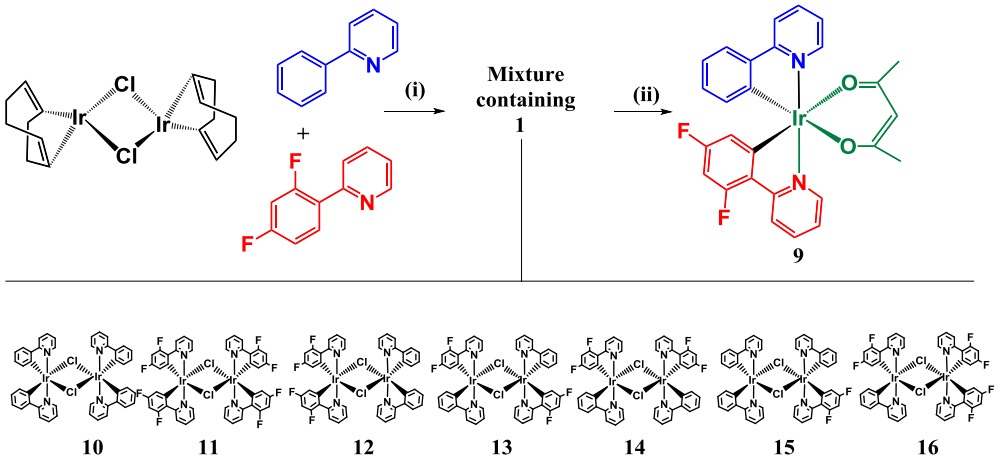

Scheme 1.5 Syntheses of iridium complex using $[Ir_2(COD)_2Cl_2]$ precursor.

Y. K. Kim and co workers synthesized blue emitting complexes (**17-18**) (Scheme 1.6) by $[Ir(COD)_2Cl]_2$, PPh_3 and ppyH in 2-ethoxyethanol. Further, the Cl ligand was successfully substituted by acetonitrile using Ag(OTf), giving a ionic complex $[Ir(PPh_3)_2(ppy)H(ACN)]^+$. This ionic complex was also achieved by a unique precursor; $[Ir(PPh_3)_2(ACN)_2\,H_2]^+$ [74].

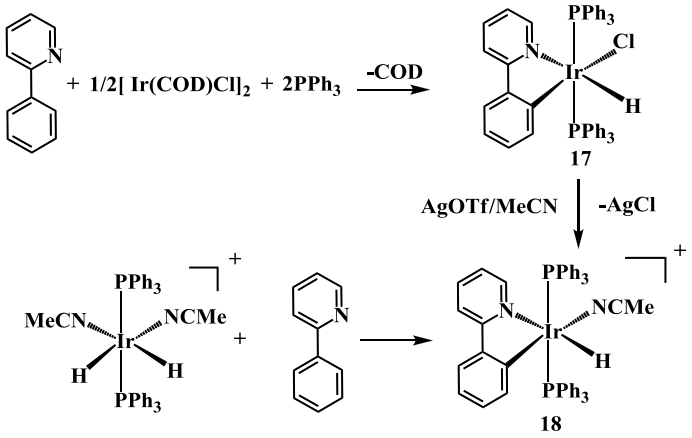

Scheme 1.6 Syntheses of mono cyclometalated iridium(III) complex.

Many research groups were used [$IrCl_3.(THT)_3$] precursor for syntheses of emissive iridium(III) complexes [53, 75, 76]. Chiu et al. synthesized a blue emitting iridium complex using $Ir(THT)_3Cl_3$ (THT = tetrahydrothiophene) as precursor.

J.-Y. Hung et al. synthesized blue emitting iridium complexes using $Ir(THT)_3Cl_3$, benzyldiphenylphosphine and 5-pyridyl-3-trifluoromethyl-1H-pyrazole derivatives using decalin as solvent and whole reaction mixture was reflux for 24h (**19-21**) [77]. Using same protocol P.-T Chau and co workers were isolated three blue emitting isomeric complexes (**22-24**). A similar type of complex was isolated by same group by changing benzyldiphenylphosphine (bdpH) by phenyl diphenylphosphinite (pdpitH) (**25**) [78, 79]. In further modification diphenylphosphinite (pdpitH) was replaced by triphenylphosphite pheny (**26**) (Scheme 1.7) [80].

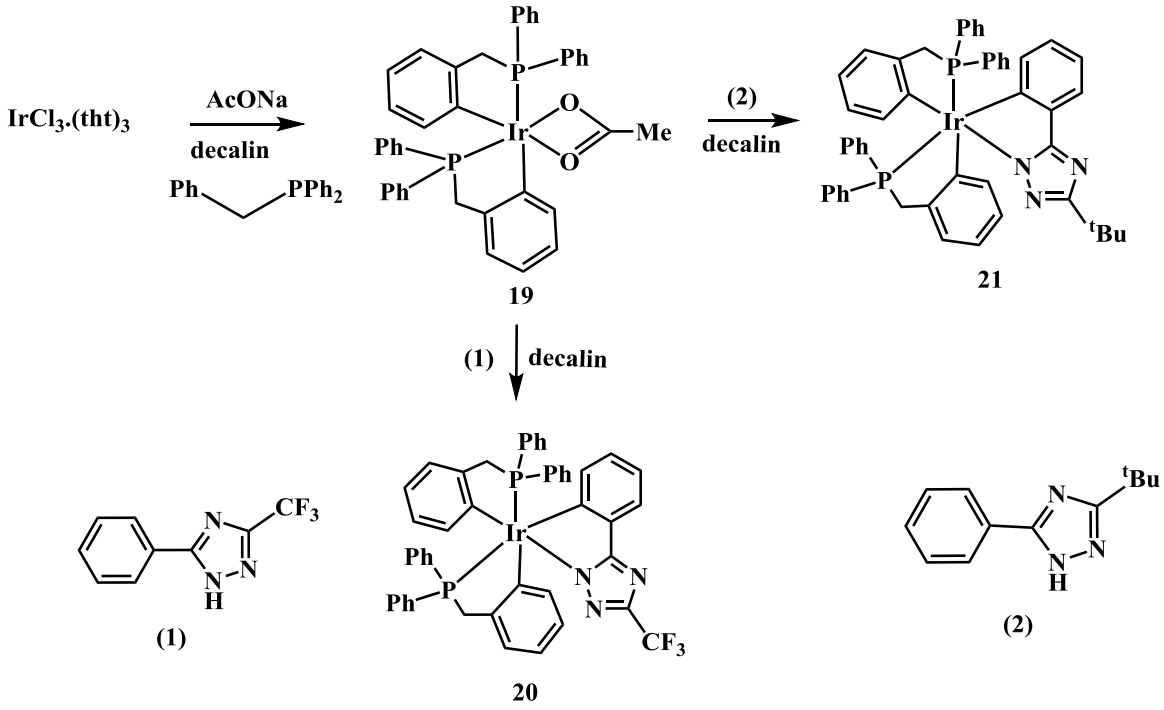

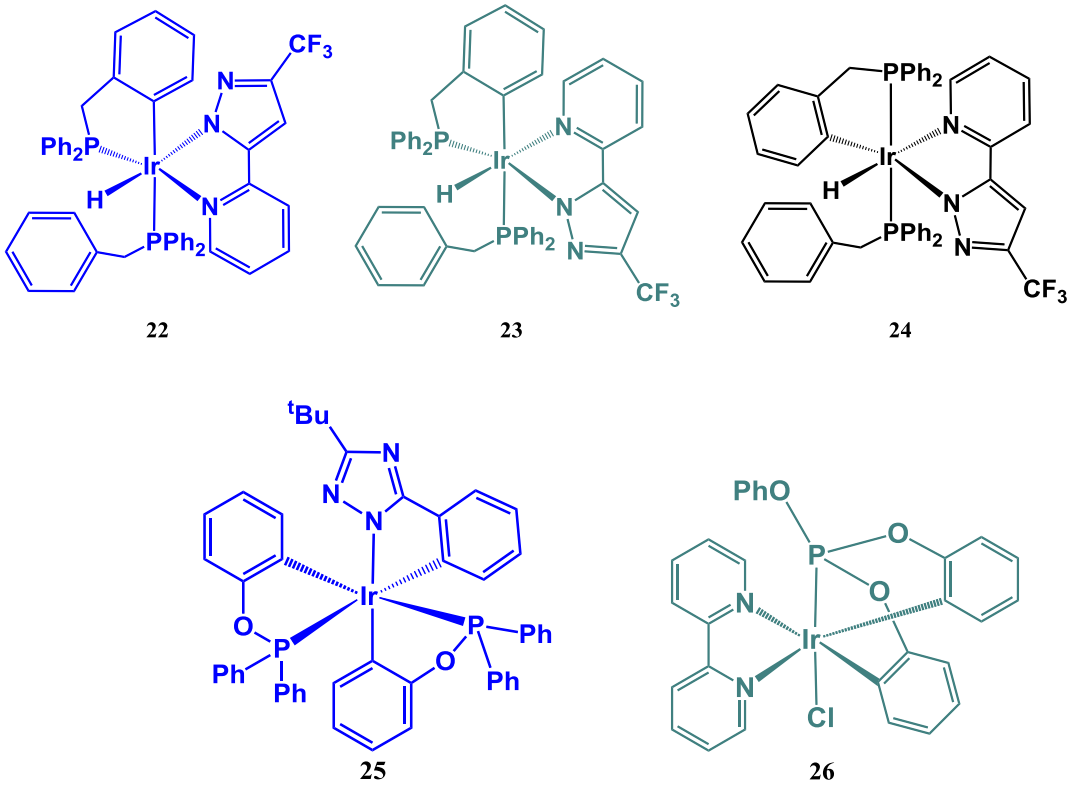

Scheme 1.7 Syntheses of blue emitting iridium(III) complexes.

1.4 Aggregation Induced Emission (AIE)

The current interest from academia and industry is driven to the study and development of strong emitting solid state materials. The solid state materials are a promising candidate for fascinating application like organic light-emitting diodes (OLEDs) [81-91], organic solar cells (OSCs) [92-105], bioimaging [19, 106-120], chemosensors [121-135] for detection of microenvironmental changes and as dynamic functional materials. These luminescent materials mostly contain planar π-conjugated aromatic rings, which will increase the possibility of molecular aggregate to form excimers and exciplexes [136-139]. The close interaction between these planer aromatic rings because of excimers or exciplexes will lead to luminescence quenching and known as 'aggregation-caused quenching (ACQ)' effect. In ACQ, the molecules are strong emissive in the solution state but non emissive or less emissive in the aggregated or solid state. This notorious ACQ is a thorny obstacle which limits for the applications of

luminescent materials in solid state application. To overcome this problem, several strategies are developed such as, the introduction of branched chains, bulky cyclics, spiro kinks, or dendritic wedges are supposed to prevent the close intermolecular interactions between luminophores. However, these approaches are found to less effective to solve this ACQ problem, additionally, introduced new problems. In 2001, Tang and co workers synthesized an interesting 1-Methyl-1, 2, 3, 4, 5-pentaphenylsilole (**27**) molecule which was hardly emissive in common organic solvents but highly emissive in aggregated or solid state [140]. This phenomenon is attributed to the cure of ACQ called 'aggregation-induced emission (AIE)' [140-171]. Motivated by the demands and the fascinating application prospects, the last decade is devoted for development of new organic molecules with AIE property.

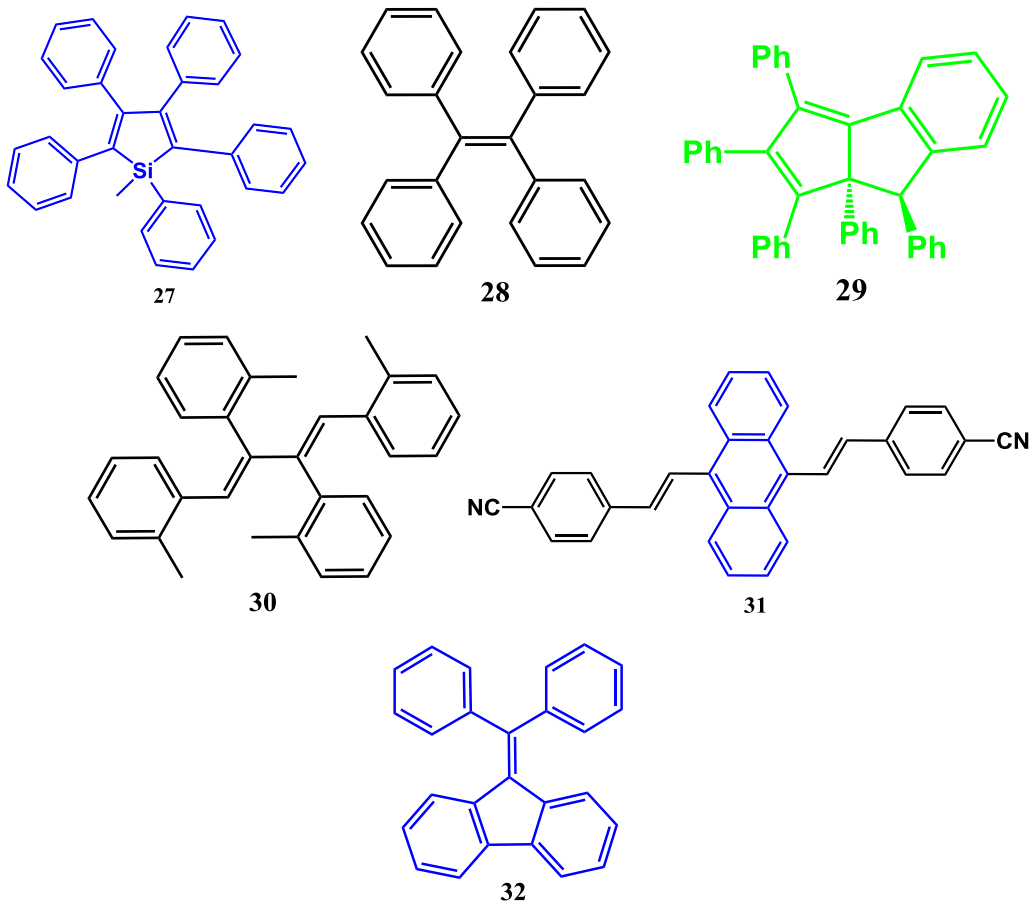

27 28 29 30 31 32

Figure 1.7 Structures of different AIE compounds.

As a result, tetraphenylethenes (**28**), 8,8a-dihydrocyclopenta[a]-indenes (**29**), 1, 4-distyrylbenzenes (**30**), 9,10-distyryl-anthracenes (**31**) and fulvenes (**32**) are used as core and potential molecules for AIE property [160].

For more diversity in the photophysical property, the use of heteroatom in the AIE framework became a fashion. Many heteroatom-containing AIE molecules like tetraphenylthiophene derivatives, dithiole nitrofluorene derivatives and indolo[3,2-b]carbazole derivatives were synthesized by many research groups (Figure 1.7).

However, there has a challenge to explore the mechanism of AIE molecules to the scientific community. The mostly investigated mechanism to explain the AIE property is restricted intramolecular motion (RIM). The RIM mechanism is mainly includes rotations and vibrations of the molecules. The restriction of intramolecular rotation (RIR) of rotor leads to block non-radiative decay and favouring the radiative channels that results enhanced emission. Additionally, RIM mechanism is supported by some controlled experiments like lowering the temperature, increasing viscosity and dispersing molecules in a rigid polymer matrix. In these experiments, the molecular motion and vibration, apart from RIM, restriction of intramolecular charge transfer (ICT), twisted intramolecular charge transfer (TICT), E-Z isomerisation (EZI), formation of J-aggregates formation (JAF), intramolecular planarization, dual mode of assembly, inhibition of photoisomerization, photocyclization and excited-state intramolecular proton transfer (ESIPT) have also been used to explain the AIE property but in a limited manner [143, 166, 172-174].

Few AIE mechanisms are explained as follows:

1.4.1 Restricted Intramolecular Motion (RIM)

Theoretically any molecule can undergo active intramolecular rotation as well as vibration (*e.g.*, bending, stretching, twisting and shearing). These two major processes can lead to energy consumption. The photophysical study of hexaphenyl silole (HPS) by Tang and co workers concluded that the six phenyl rings can be rotated in solution state by which the new nonradiative channels will be opened up and hence the emission intensity being quenched [163]. However, the dynamic rotation of these rings can block

in aggregate or solid state and result a tremendous bright emission. A similar property is obtained in case of tetraphenyl ethylene (TPE) molecule and it is explained based on above hypotheses [175-177]. To prove the restriction of intramolecular rotation, several controlled experiments are performed. The photophysical property of these two molecules (HPS and TPE) are recorded in viscous medium using poly ethylene glycol (PEG) or glycerol where the emission intensity is intensified by increasing concentration of viscous solvents. Hence, the existence of dynamic rotation is restricted in viscous solvents and it supports the restriction of intramolecular rotation (RIR) in the system. However, the restriction in intramolecular motion can be generated by lowering the temperature or putting higher pressure which can also support the RIR mechanism [144, 178-187].

Till date, the RIR is the maximum studied mechanism for AIE process but few other examples such as 10,10′,11,11′-tetrahydro-5,5′-bidibenzo annulenylidene (THBA) also exhibited AIE property without rotary group [173, 188].

The close inspection of THBA revealed the connected two groups are highly flexible and bendable in nature. In solution state, THBA can go in dynamic mode of vibrations or bending which lead to nonradiative decay and the emission intensity get quenched. After aggregate formation, the dynamic vibrations become restricted because of physical constraint associated with the space limitation and generate the AIE property in THBA.

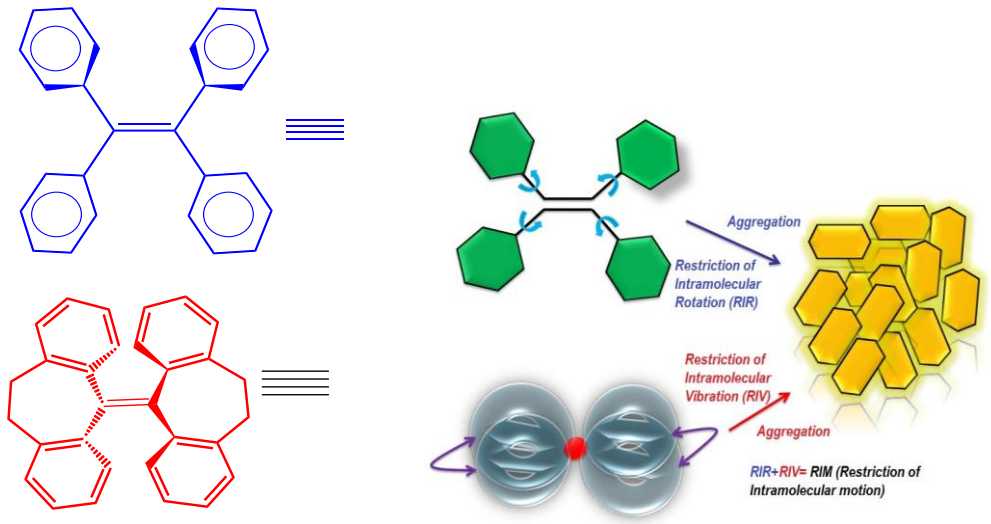

Figure 1.8 Mechanistic pathways for RIM.

From above examples one can conclude that the RIR and RIV are the plausible mechanism for AIE system. By mixing these two processes together (RIR+ RIV), it gives a general picture that the restricted intramolecular motion (RIM) is considered the most studied mechanism for maximum AIE systems (Figure 1.8) [152, 189-198].

1.4.2 J-Aggregate formation (JAF)

More than 76 years ago, Jelley and Scheibe et al. recorded an absorption spectra of pseudoisocyanine chloride (1,1'-diethyl-2,2'-cyanine chloride, PIC chloride) (**33**) [199] which exhibited an unusual behaviour; the absorption maxima was shifted to lower energy region at λ_{max}= 571 nm ($\bar{\upsilon}$=17500 cm^{-1}) with increasing water and the band become more intense and sharp at maximum concentration of water in comparison to absorption in pure ethanol (Figure 1.9) [200].

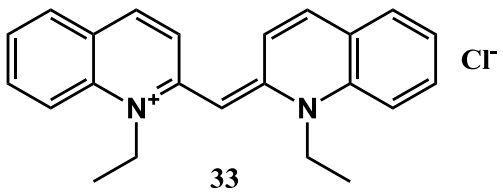

33

Figure 1.9 Structure of 1,1'-diethyl-2,2'-cyanine chloride.

According to encyclopedic definition: "A J-aggregates (a supramolecular self-organization) are the aggregates which results the red shift in absorption band (a bathochromic shift) with increasing sharpness (higher absorption coefficient) under the influence of a solvent or additive or concentration." The dye can be characterized further by a small Stokes shift with a narrow band. The term "J" in J-aggregate is stand for Jelley in accord with the name of their inventor. However, the aggregates with absorption bands shifted to shorter wavelength (hypsochromically shifted) with respect to the monomer absorbance band, in contrast, are called H-aggregates (H-denotes hypsochromic) which results in most cases low or no fluorescence (Figure 1.10).

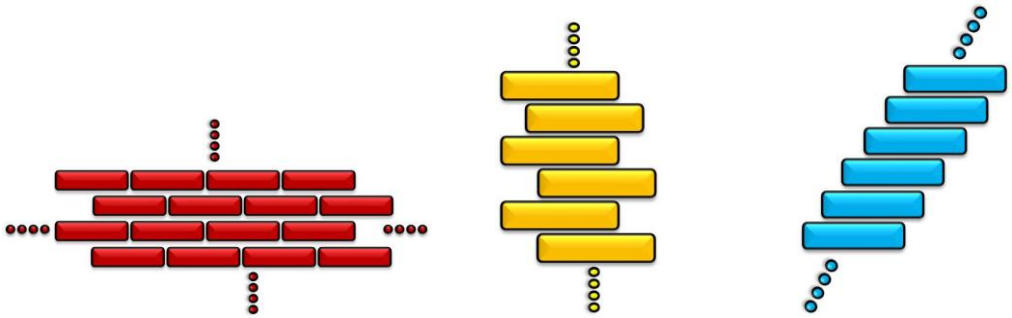

(a) (b) (c)

Figure 1.10 Schematic representations of the possible rearrangements of dye molecules in J-type aggregates, (a) Brickwork arrangement, (b) ladder arrangement, and (c) staircase arrangement.

In few reports, the formation of J- type aggregate leads to red shifted emission with PL intensity enhancement indicating the presence of aggregation induced emission effect. According to the definition of J-type aggregates, the monomer emission need not to be non emissive and it is not compulsory to be AIE active, the other mechanism may play an essential role *e.g.* (Z)-2,3-bis(4'-methyl-[1,1'-biphenyl]-4-yl)acrylonitrile (**34**) (Figure 1.11) [201].

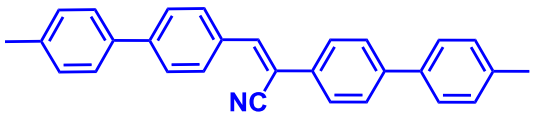

34

Figure 1.11 Structure of (Z)-2,3-bis(4'-methyl-[1,1'-biphenyl]-4-yl)acrylonitrile.

The aggregate formation is not dependent on polar or nonpolar luminogen, the aggregate may arrange themselves in ordered or random fashion, the photophysical property may change accordingly (blue or red shifted, big or small Stokes shift). As per definition, the J-aggregates may form with a luminophores having D-A types of sub groups. The packing of J type aggregates are highly organized and the types of aggregate pack themselves in highly ordered fashion. The presence of several short contacts in the crystal packing lead to restriction of intramolecular motion (RIM) and produced the AIE

property in the system [201, 202]. Most importantly, if the molecules have rigid and planer structure may not be produced AIE activity due to strong π–π stacking interactions but AIE property can be easily achieved with conformationally flexible and structurally twisted molecules [143, 203].

1.4.3 Intramolecular charge transfer (ICT) and Twisted Intramolecular charge transfer (TICT)

Intramolecular charge transfer is a most frequently encountered photochemical primary processes in the chemistry of excited states. In general, upon photo-excitation, an electronic charge transfer occurs from donor to acceptor molecule in a D-A system [where electron donor (D) and electron acceptor (A)] should connected by a π-conjugated bridge). In such intramolecular processes of a conjugated system with donor and acceptor subunits, the reaction product is usually called charge-transfer (CT) state, or an intramolecular CT state (ICT) [204-206]. The photo-excitation leads to the electron distribution or charge separation in ground and excited states which results the neutral and the zwitterionic resonance structures, respectively because of the most of the ICT molecules are displayed the positive solvatochromism.

In case of maximum charge transfer the charge separation will be more and may results two things.

(a) A strong interaction may take place between charge-transfer excited state dipole and solvent dipoles which leads to fluorescence quenching.

(b) A rotation of single bond takes place in the excited state which result an entirely charge-separated state, which is called twisted intramolecular charge transfer (TICT) state.

In 1973, Rotkiewicz, Grellmann and Grabowski found that the emission of 4-(N,N-dimethylamino)benzonitrile (DMABN) was red shifted with increasing solvent polarity [207, 208]. According to them, the DMABN took a planar conformation in the locally excited (LE) or Franck-Condon state. In non polar solvent, the equilibrium of excited state luminogen and solvent molecules retain the planar conformation which resulted in the sharp emission because of more conjugation. However, in the polar medium, the luminogen is not in equilibrium with the surrounding solvent molecules. The

intramolecular rotation brings the luminogen from the LE state to the TICT state [209-212], which results in a total charge separation between the D and A units where the NMe_2 group is possibly perpendicular to the aromatic ring. This entirely charge-separated state is called twisted intramolecular charge transfer (TICT) which is stabilized by the solvating effect of the polar solvent (Figure 1.12).

In 2012, Tang and co workers synthesised a TICT probe molecule with donor-acceptor group (**35**) *i.e.* 2-(2,6-bis(4-(diphenylamino)styryl)-4H-pyran-4-ylidene) malononitrile (TPA-DCM) (Figure 1.13) [213]. The compound is formed a planar conformation in an apolar solvent and showed a strong emission in short wavelength region from LE state. With increasing polarity, the conformation of TPA-DCM became partially twisted and the charges got partially separated. As a result, the increasing polarity is facilitated the LE-to-TICT transitions which lead to the less instance red shifted emission.

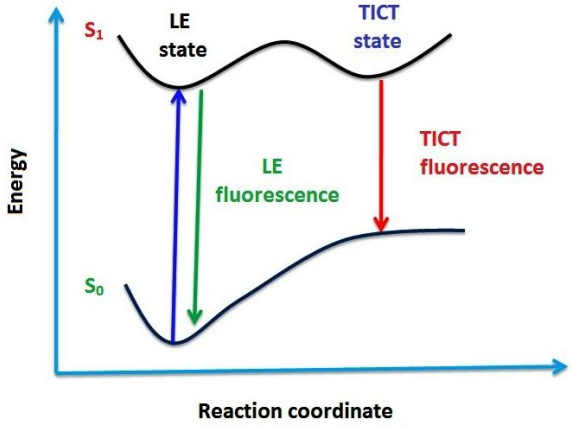

Figure 1.12 Schematic representations of LE and TICT states.

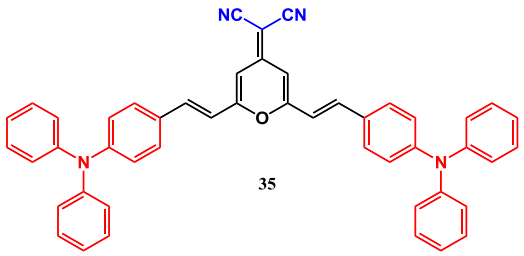

35

.

Figure 1.13 Structure of 2-(2,6-bis((E)-4-(diphenylamino)styryl)-4H-pyran-4-ylidene)malononitrile.

It is assumed that TPA-DCM, D-A system can adopt a twisted conformation in polar medium which results a less electronic conjugation in the system. Hence, the emission intensity of TPA-DCM is quenched due to elevation in HOMO level and a fast intramolecular motion of rotor groups. However, in presence of water (or non solvents) the local environment became less polar and the molecules are adopted less twisted conformation in their aggregated state [173, 214, 215]. Thus, the emission spectra got intensified with blue shifted emission as a result of RIM and TICT-to-LE transition [216-221].

1.4.4 Excited State Intramolecular Proton Transfer (ESIPT)

The excited state intramolecular proton transfer (ESIPT) is a fundamental and most studied process in chemistry and biology. It is an extremely fast (10^{-12}-10^{-15} s) process which is mediated by intramolecular H-bonding. ESIPT is very informative in case of acid-base neutralization and enzymatic reactions (Figure 1.14).

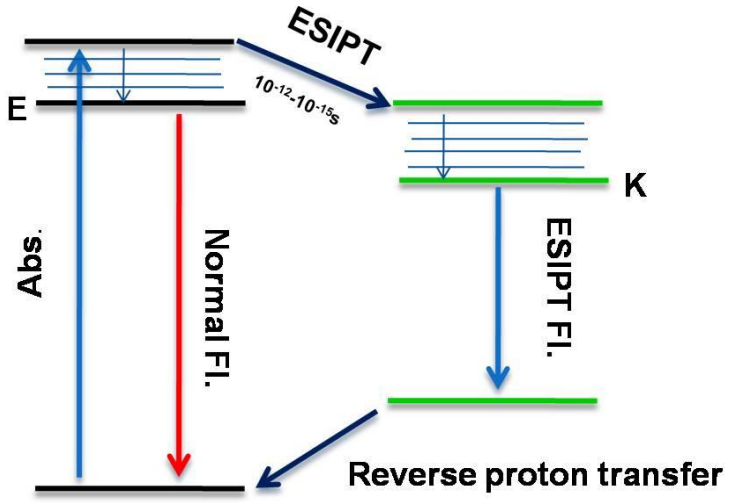

Figure 1.14 Schematic representation of ESIPT.

The ESIPT molecules are well known for uniquely large Stokes' shifted fluorescence emission (6500-12500 cm^{-1}) which may tune the visible region [222-224].

ESIPT is also considered as one of the mechanism for AIE property. Few ESIPT dyes are exhibited enhanced emission after addition of water [222, 225-228]. In 2014, R. Wei et al. synthesized (2-hydroxy-4-methoxyphenyl)(phenyl)-methanone azine (**36**) which is found to exhibit AIE property (Figure 1.15) [229]. The hydroxyl group is forming a six-membered intramolecular hydrogen bonding with azine nitrogen, this strong hydrogen bonding is found to facilitate the ESIPT process in the system. However, the gradual addition of water content resulted the enhancement in emission intensity showing the AIE characteristic. The compound is found non emissive in the solution state because of the multi rotors (C–C and N–N single bonds) and large flexibility. The AIE property in the compound is originated after formation of close aggregates, consequently the molecular motion is suppressed which blocked nonradiative decay channels and enhanced the emission in aggregated state.

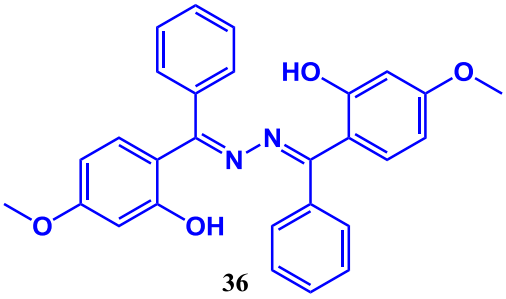

36

Figure 1.15 Structure of (2-hydroxy-4-methoxyphenyl)(phenyl)-methanone azine.

After a successful era of organic AIE molecules, the d-block AIE complex (Au, Ir, Pt, Os, Pd, Zn, Cu, Re, Rh) along with p-block AIE complex (B, In,Te) are not much explored [230-268]. The p and d block luminescence complexes are distinguished for their long luminescence lifetimes (100 ns to ms), large stokes shift (hundreds of nm), high quantum yields in the visible region and straightforward synthetic routes. The extraordinary photophycical behaviour of these complexes are attributed to different charge transfer ^{3}MLCT, ^{3}LLCT, ^{3}LMCT, ^{3}ILCT and strong π-π^* transitions which made them potential candidate for real world applications [269-271].

1.4.5 Aggregation induced emission of iridium(III) complexes

In 2008, group of Chunhui Huang synthesized three iridium(III) complexes. Out of them, two complexes $Ir(ppy)_2(DBM)$ and $Ir(ppy)_2(SB)$ exhibited aggregation-induced phosphorescent emission (AIPE) (where ppy = 2-phenylpyridine, DBM = 1,3-diphenyl-1,3-propanedione, acac = acetylacetonate and SB = 2-(naphthalen-1-yliminomethyl)-phenol).

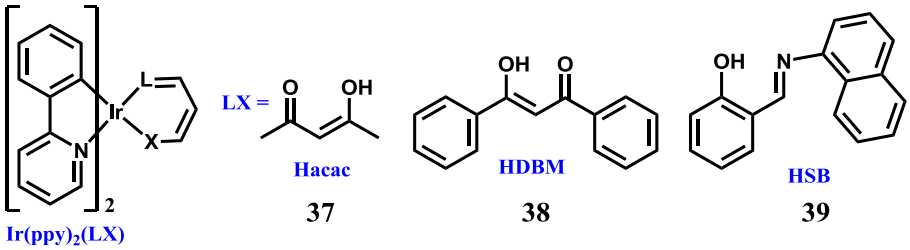

Figure 1.16 Chemical Structures of complexes **37-39**.

The two complexes $Ir(ppy)_2(DBM)$ (**38**) and $Ir(ppy)_2(SB)$ (**39**) did not show any emission in solution state while the $Ir(ppy)_2(acac)$ (**37**) exhibited a strong emission in solution state (Figure 1.16). The solid state quantum yield was found to be 7.6 and 7.9%, respectively for $Ir(ppy)_2$ (DBM) and $Ir(ppy)_2$ (SB). The AIEP property of these complexes was investigated in H_2O/CH_3CN mixture where $Ir(ppy)_2(SB)$ showed an enhanced emission at f_w=40% [272].

The author tried to explain AIE property with the help of crystal data and DFT calculation. The crystal data of complexes reveals the strong π-π interaction between adjacent pyridyl rings of ppy ligands with a face-to-face separation of 3.37 Å in $Ir(ppy)_2(DBM)$ while 3.36 Å in $Ir(ppy)_2(SB)$. The strong π-π interaction elongates the overall degree of π-conjugation and reduces the energy level of π^*_{ppy}, as compared with that in solution. In solid state, a new state metal-to-ligand–ligand charge-transfer transition (MLLCT) was generated which reduced ppy ligands participation in excited state of $Ir(ppy)_2(DBM)$. As a consequence, the ppy interactions was resulted a new MLLCT based emission.

In the same year, Soo Young Park and co workers proposed a mechanistic origin of AIE which was restricted intramolecular motion rather than the intermolecular excimer formation. The chemical structures of the studied complexes contained cyclometalating ligands [2-(2,4-difluoro-phenyl)pyridine (dfppy; **40** and **41**) and 2-phenylpyridine (ppy; **42** and **43**)] and imine-based ancillary ligands [2-(phenyliminomethyl) phenol (pip, **40** and **42**) and 2-((fluoranthen-3-ylimino)methyl) phenol (fip, **41** and **43**)] (Figure 1.17). These complexes were exhibited non luminescence behaviour in solution while a strong emission was observed on thin film. In addition, the complexes showed high quantum efficiency in solid state as compared to their solution ($\phi_{solid}/\phi_{solid}$) > 10^2. The strong emission of the complexes was attributed to special molecular arrangements like J^5-or cross-stacking.

In order to determine this fact, a comparison between absorption spectra of thin and solution was done which showed almost virtually identical spectra. This fact revealed the ground state interaction such as J- or cross-aggregation was not responsible for the observed enhanced phosphorescence in the solid state (EPSS) behavior. According to the author, the more convincing evidence for the origin of the EPSS was the frozen solution of $CHCl_3$ which showed a bright yellow emission and became non-luminescence at RT. A sudden decrease in emission intensity was observed near the melting point of the $CHCl_3$ solvent. A rotation around the N–aryl ring bond of the ancillary ligands could be possible which originated the non emissive character in the system.

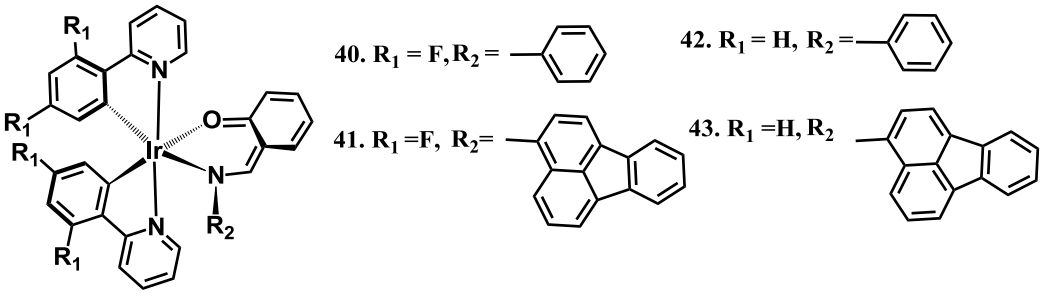

Figure 1.17 Chemical Structures of complexes **40-43.**

This fact was further explained based on DFT calculation which revealed that the thermally activated bond rotation may perturb the nature of the phosphorescent state. In the final remark the author claimed that the emission enhancement was resulted due to restricted intramolecular motion in the ancillary ligand [273].

According to Chunhui Huang and co workers the enhanced phosphorescence emission in the solid state (EPESS) of **44-46** was attributed to π–π stacking of adjacent pyridyl rings of ppy ligands and not due to intramolecular rotational motion. The three ligands L1, L2 and L3 with different degrees of restricted intramolecular rotational motion were introduced into the complexes $Ir(ppy)_2(L1)$ (**44**), $Ir(ppy)_2(L2)$ (**45**) and $Ir(ppy)_2(L3)$ (**46**) (Figure 1.18).

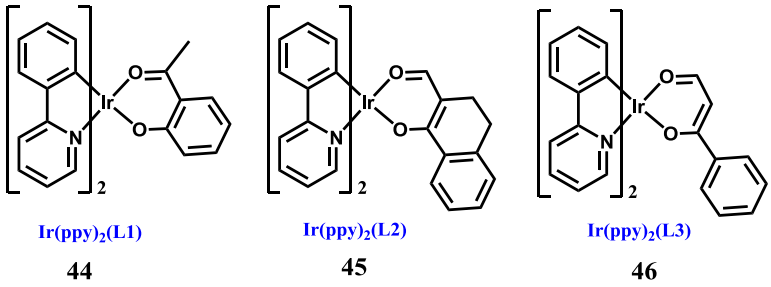

Figure 1.18 Chemical Structures of complexes **44-46.**

These three complexes exhibited very weak emission in solution state while bright emission in solid state. These complexes were termed as EPESS complexes [274].

Youngkyu Do and co workers were reported design and syntheses of iridium(III), iridium(III)/iridium(III) homodinuclear and iridium(III)/platinum(II) heterodinuclear AIE active complexes.

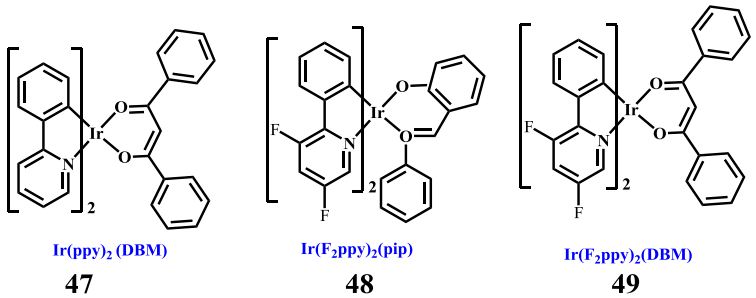

Figure 1.19 Chemical Structures of complexes **47-49**.

In their first report, they were synthesised a polymorphism-induced dual phosphorescent emission $Ir(ppyF_2)_2(DBM)$ (**47**) complex. The solid state exhibited a bright emission in comparison to weak emission observed in solution state (**48-49**) (Figure 1.19) [275]. However, the novel iridium(III)/iridium(III) and iridium(III)/platinum(II)dinuclear complexes, (**50**) and (**51**) showed AIE property. The crystal packing of iridium(III)/platinum(II) complex showed that metal-centered moiety forms effective π–π interactions in the crystal, where the chromophoric F_2ppy ligands got stacked with Ir-centered moieties in adjacent molecules.

In case of Complex **51**, the distance between two adjacent F_2ppy stacking was found ~3.4 Å which was more enough for strong stacking. Interestingly, there was no effective Pt-Pt distance observed (6.575 Å in Pt(A)L⋯Pt(B)L and 4.299 Å in Pt(B)-(ppy)⋯Pt(C)(ppy)]. Based on these strong π–π interactions, newly generated ^{3}M(LL)CT state was proposed to the origin of AIE property in the system (Figure 1.20) [276].

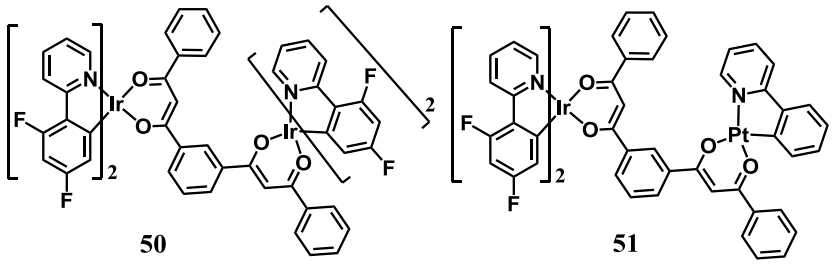

Figure 1.20 Chemical Structures of complexes **50-51.**

An extensive work has been done by Yi Liao and co workers for syntheses and design of different types of AIE materials.

In 2011, three cationic iridium(III) complexes $[Ir(ppy)_2(L2)]PF_6$, $[Ir(ppy)_2(L1)]PF_6$ and $[Ir(oxd)(L2)]PF_6$ (**52-54**) (where ppy= 2-phenyl pyridine oxd= 2,5-diphenyl-3,4-oxadiazole) were strategically deigned and synthesised followed by investigation of AIE property was carried out. The cause of AIE was found to be restricted intramolecular rotation (RIR) [277].

In 2012, two more similar types of complexes were reported keeping the same framework. In this report, the author synthesized 3,8-bis(3',6'-di-tert-butyl-6-(3,6-di-tert-

butyl-9H-carbazol-9-yl)-3,9'-bi(9H-carbazol)-9-yl)-1,10-phenanthroline in place of 4,7-bis(3',6'-di-tert-butyl-6-(3,6-di-tert-butyl-9Hcarbazol-9-yl)-3,9'-bi(9H-carbazol)-9-yl)-1,10-phenanthroline) (**55**-**56**) [278]. This modification was justified in terms of increasing the PLQY and the butterfly-like structure could lead to a decrease in photochemical degradation and increased hydrolytic stability. The presence of rotary groups in the complex were originated the AIE property by blocking the non radiative transition. The AIE complex (**56**) was successfully used in the imaging of SM-7721 cell lines. Further a stepwise modification in the electron donating ability of ancillary was done to investigate the AIE property in the complexes (**57**-**59**). The complexes **57**-**59,** were found to be non–emissive in solution state because of ILCT. These two complexes (**57**-**58**) were exhibited AIE property (Figure 1.21) [279].

A piezochromic aggregation induced emission (PAIE) complex $Ir[(dfppz)_2(L)]PF_6$ (**60**) with 1-(2,4-difluorophenyl)-1H-pyrazole (dfppz) and a dendritic ligand (L) was synthesized by Zhong-Min Su and co workers in 2012. The complex showed non-emissive behaviour in common organic solvents but strong emissive in solid state. Based on DFT calculation, the authors claimed that the weak emission in the solution state was originated because of intramolecular rotation of the dendritic ancillary ligands (Figure 1.22) [280].

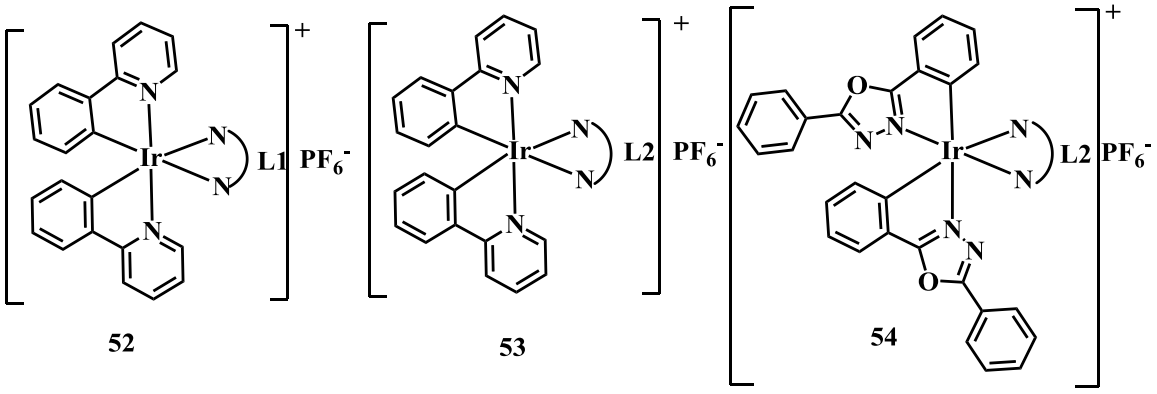

52 **53** **54**

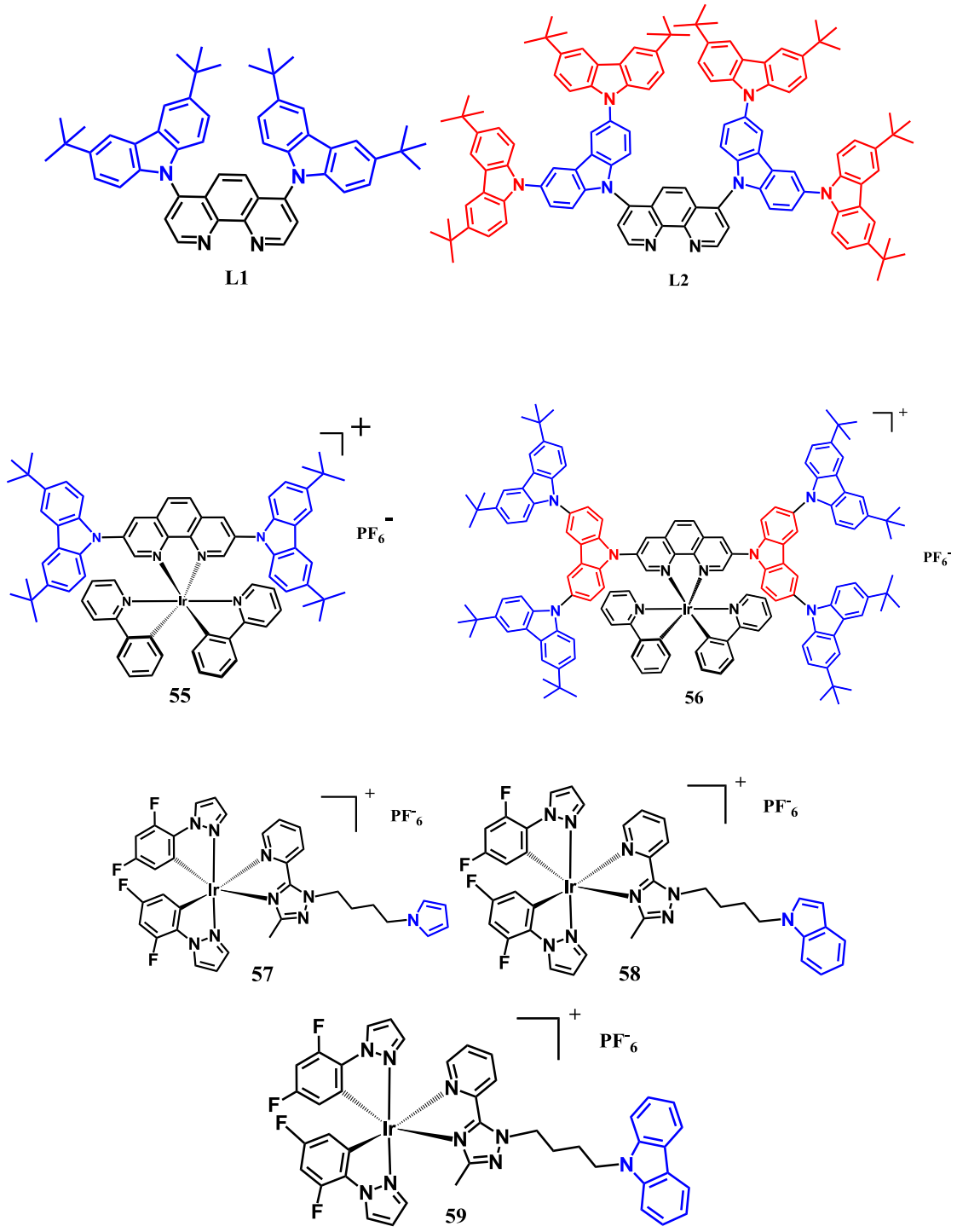

Figure 1.21 Chemical Structures of complexes **52-59**.

By inspired from previous work, Zhong-Min Su and co workers, synthesized three multifunctional cationic iridium(III)-based materials with aggregation-

induced emission (AIE) and piezochromic luminescence (PCL) (**60**) behaviour in a controlled manner. In this reports author was kept the same cyclometalated ligands with ancillary ligand with different substitution (**61**-**63**). The strategic design of the ligands was resulted controlled properties such as PCL behaviour (**61**), an AIE material (**62**), and a PAIE (PCL and AIE behaviour) material (**63**). The author utilized the AIE property of complex **63** as an explosive sensing (picric acid). The static quenching constant (K_{sv}) was found to be 72000 $Lmol^{-1}$(Figure 1.22).

Recently, same group was synthesised two new iridium(III) complexes (**64**-**65**) for selective detection of nitro explosive. The quenching constant K_{sv} was evaluated with the help of Stern–Volmer (SV) plot. The K_{sv} was found to be 52800 M^{-1}. The selective detection of PA by **64** was explained based on energy transfer (ET) mechanism while the other nitro sensing by **65** explained based on photo induced electron transfer (PET) mechanism (Figure 1.22) [278, 280-282].

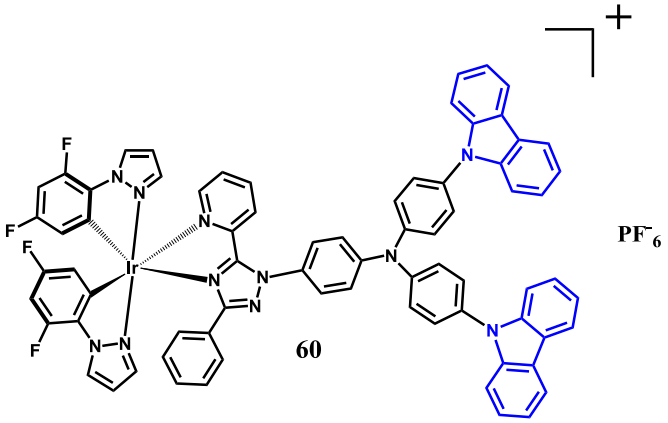

60

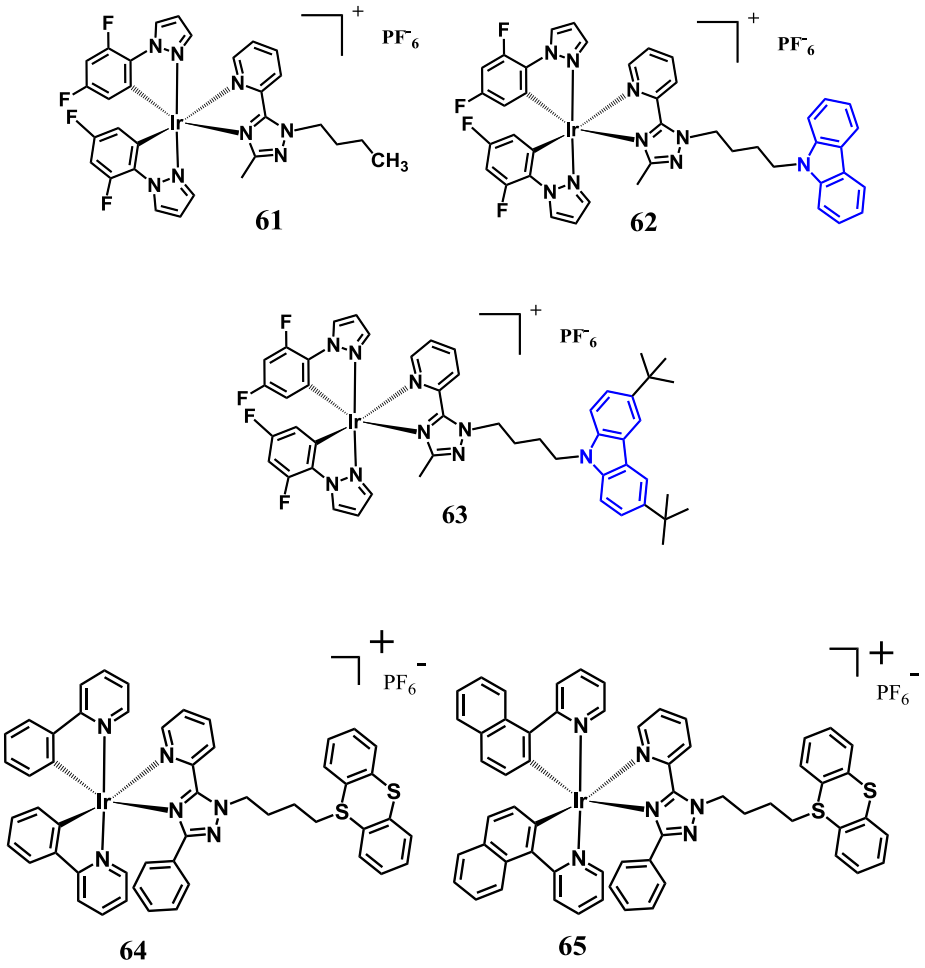

Figure 1.22 Chemical Structures of complexes **60-65**.

In 2011, Fuyou Li and co workers synthesized two iridium(III) complexes having β-diketonate ligands with different degrees of conjugation, 1-phenyl-3-methyl-4-benzoyl-5-pyrazolone (HL1) (**66**) and 1-phenyl-3-methyl-4-phenylacetyl-5-pyrazolone (HL2) (**67**) and 2- phenyl pyridine as chromophoric ligand (**66-67**). Complex **66** was found to AIE nature while complex **67** showed moderate emission in both solid and solution state. A water-dispersible polymer nanoparticle by emulsion polymerization was synthesized by using complex **66**. These $Ir(ppy)_2(L1)$-PNPs used for cytoplasm staining over the nucleus and membrane which was further confirmed by Z-scan confocal microscopy and quantization analysis of the luminescence intensity (Figure 1.23) [283].

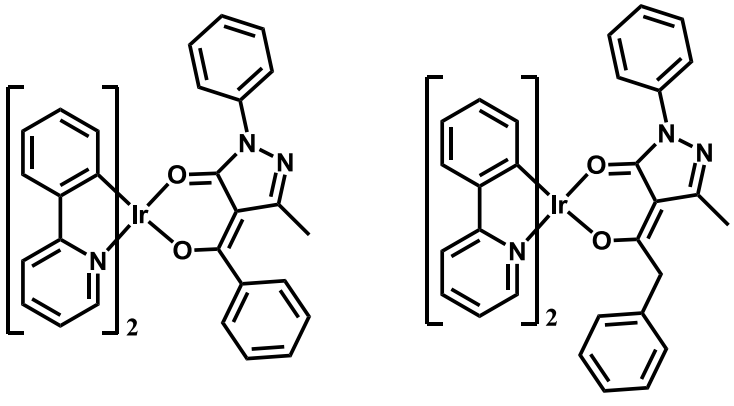

$Ir(ppy)_2(L1)$ **66**

$Ir(ppy)_2(L2)$ **67**

Figure 1.23 Chemical Structures of complexes **66-67**.

In 2014, M. L. P. Reddy and co workers synthesised an iridium(III) bis(2-(2,4-difluorophenyl)pyridinato-N,C2') (2-(2-pyridyl)benzimidazolato-N,N'),[FIrPyBiz] (**68**). This complex was successfully used for detection of TNT in the vapour phase, solid phase, and aqueous media. The detection of TNT was carried out using 70% water-acetone mixture. The detection limit for TNT was found to be 9.08 mg mL^{-1}. The quenching constant was evaluated to be 74 160 L mol^{-1} using SV plot. The author explained the PET as a proposed mechanism for sensing of TNT (Figure 1.24) [284].

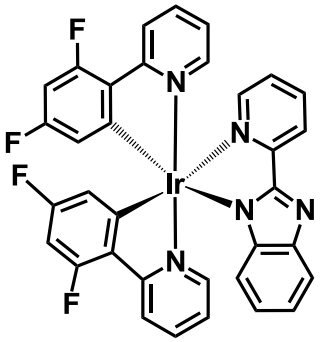

68

Figure 1.24 Chemical Structures of complexes **68**.

M. R. Bryce and co workers reported two new ionic dinuclear iridium(III) schiff base complexes. These complexes, **69** and **70** exhibited AIE property with 37.7 and 26.4 % of absolute quantum efficiency in thin film, respectively. The AIE property of the complexes was investigated by using water-CH_3CN. The aggregate formation at higher water fraction contained more close packed system which experienced the π–π stacking interactions. The restricted intramolecular relaxation in the solid state leads to the observed AIE property (Figure 1.25) [285, 286].

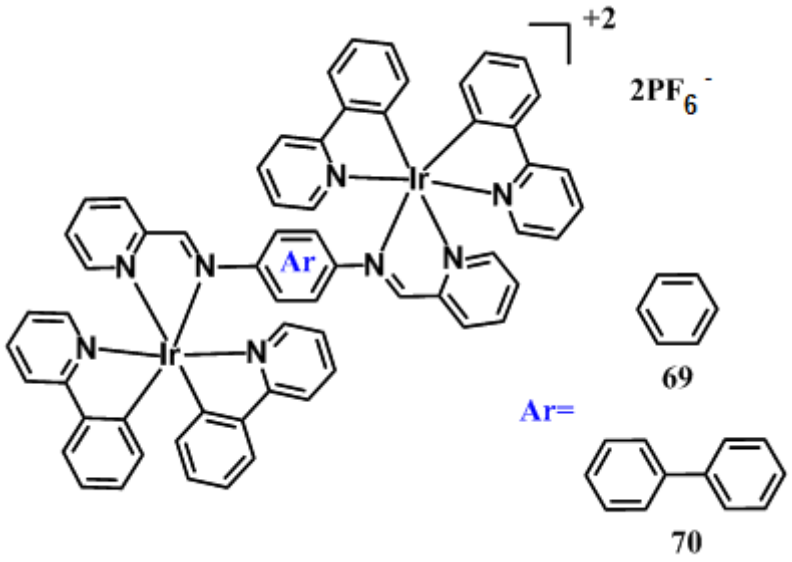

Figure 1.25 Chemical Structures of complexes, **69-70**.

Hui Chao and co workers was synthesized a novel iridium(III) complex $[Ir(btp)_2(PhenSe)]^+$ (**71**, where btp=2-(2-pyridyl)benzothiophene and PhenSe = 1,10-phenanthrolineselenazole) [287]. The complex exhibited a very bright emission in solid state as compare to its solution state. The absolute quantum efficiency of the complex **71** was found to be 21% which was almost >100 times higher than its solution efficiency. Further, the complex was used as a phosphorescent agent for mitochondrial imaging and tracking (Figure 1.26).

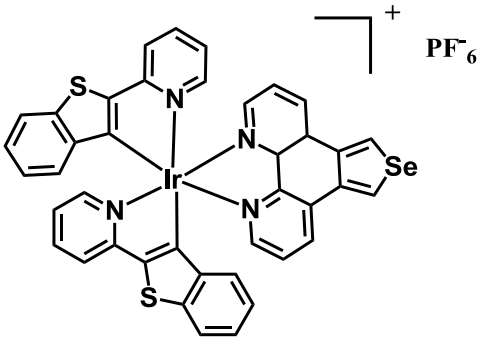

71

Figure 1.26 Chemical Structures of complexes **71**.

Zhong-Ning Chen and co workers synthesised two cationic cyclometallated iridium(III) complexes (**72-73**) with 2,2'-bipyridine-acylhydrazone where ppy used as a chromophoric ligand **(**Figure 1.27**)** [288]. These complexes showed very weak emission in common organic solvents in the concentration range 20 μM-20 mM while solid state exhibited a strong red emission at λ= 643 nm. According to the author, the restriction of C=N conformation rotation was responsible for such remarkable AIE property. The DFT calculation supported the fact; in solution state, the rapid rotation isomerisation of C=N was lead to non-radiative relaxation pathway while in solid state the C=N isomerization highly suppressed due to formation of aggregate or conformational constraint. Furthermore, the complex **72** showed 35 times higher PL intensity after addition of 100 μM Cu^{+2} to its 10 μM solution, making the complex as a potential switch-on phosphorescent sensor for Cu^{+2}.

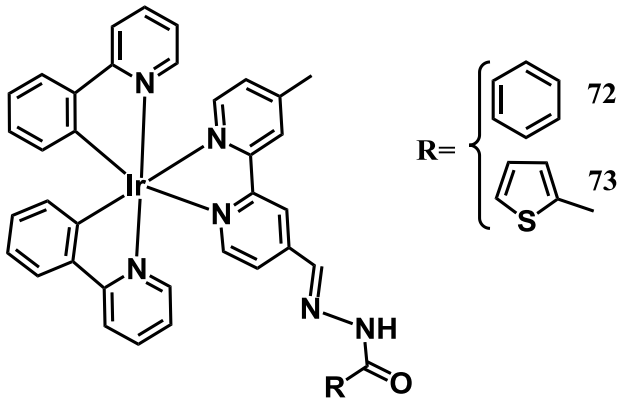

Figure 1.27 Chemical Structures of complexes **72-73**.

1.5 Applications of iridium(III) complexes

The enhancement of more chemical technologies for life science and pathology are compulsory to determine the problems which cannot be solved by conformist medical methods [289-295]. One of the most suitable and successful way to study the details in a cell is by fluorescent bioimaging with fluorescent dyes as labels because fluorescence bioimaging offers an exceptional and attractive approach for visualizing morphological details with sub cellular resolution that cannot be resolved by ultrasound or magnetic resonance imaging (MRI) [296, 297]. Most of the fluorescent probes used are still organic fluorophores, having some limitations such as easy photobleaching, small stokes shifts and difficulty to filter the auto fluorescence of certain organisms [298-300]. On the contrary, phosphorescent transition-metal complexes having metal-to-ligand-charge transfer (MLCT) luminescence exhibitted not only larger stokes shifts but also much longer lifetimes as well as higher stability, making them better candidates as bioimaging probes [19, 24, 111, 113, 115, 119, 270, 301-313]. However, most of these probes suffer a common problem. If the fluorophore concentration is too high, fluorescent probes tend to form aggregates, causing aggregation-caused quenching (ACQ), which reduces fluorescence intensity. It can be tackled by AIE active probes.

1.5.1 Bioimaging by iridium(III) complexes

In 2008, Williams et al. reported the first example of time-resolved imaging based on phosphorescent heavy-metal complexes as luminescent probes [310]; a platinum(II) complex (**74**) which was successfully stained the CHO cell lines and overcome the problem of short-lived background fluorescence (Figure 1.28).

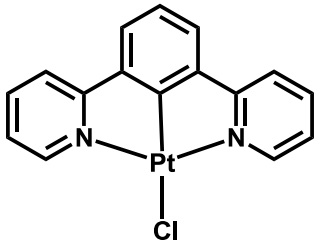

74

Figure 1.28 Chemical Structures of complex **74**.

After theses impressive results, the heavy metal complexes were recognised as potential candidate for bioimaging. Many other heavy metal complexes were synthesized and used for bioimaging [114, 310].

M. Yu and co workers in 2008 synthesized a series of iridium(III) polypyridine complexes (**75-79**) (Figure 1.29) which displayed large stokes shift and long-lived emission in visible region [314]. These complexes were displayed greatly reduced photobleaching as compared with the prominent fluorescent organic dye DAPI (DAPI = 4'6-diamidino-2-phenylindole). The emission property of these complexes were tuned from green to red by simple ligand modification and successfully used for cytoplasm staining [114, 315]. However, many iridium(III) complexes were successfully synthesized and fascinatingly used for specific staining for different cellular compartments.

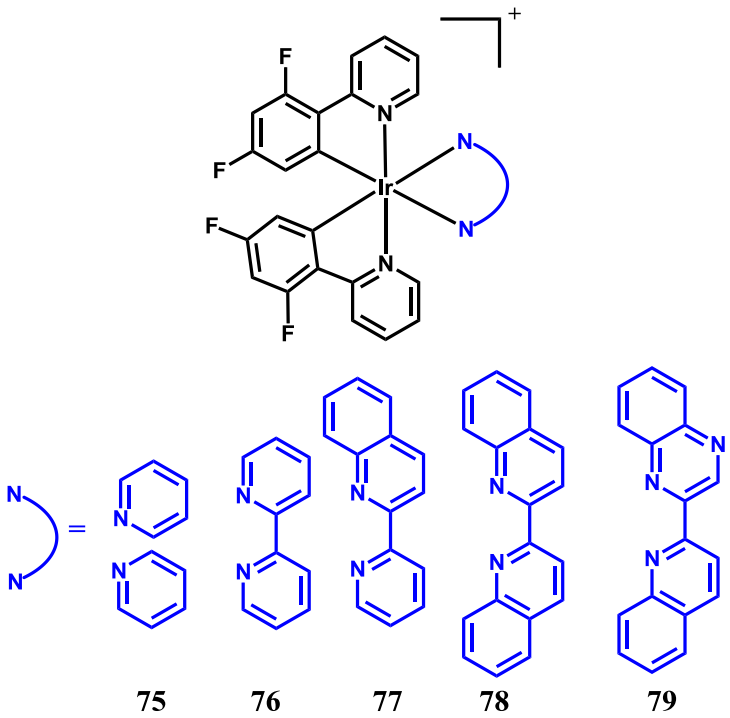

Figure 1.29 Chemical Structures of complex **75-79**.

Zhao et al. synthesized poly (styrene) (PS) nanoparticles and incorporated with iridium(III) complex [283] and similar types of approach was followed by C-W Lai et al.,

where the core cell nanoparticles of supra magnetic Fe_3O_4 was used for imaging [316, 317]. These two complexes (**80-81**) were successfully utilized for cytoplasm staining (Figure 1.30). Two ethylene diamine based iridium(III) cyclometalated complexes were synthesized by C Li et al. and found a successful probe molecule for staining of mitochondria (**82-83**) (Figure 1.31) [61, 318, 319].

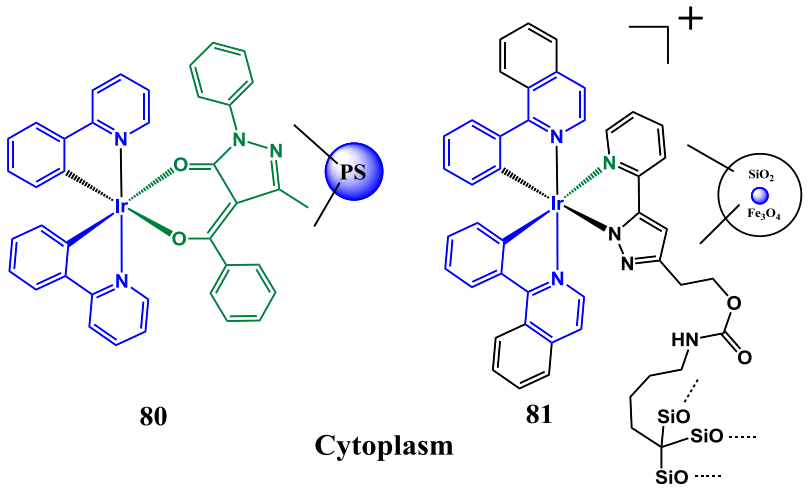

Figure 1.30 Chemical Structures of complex **80-81**.

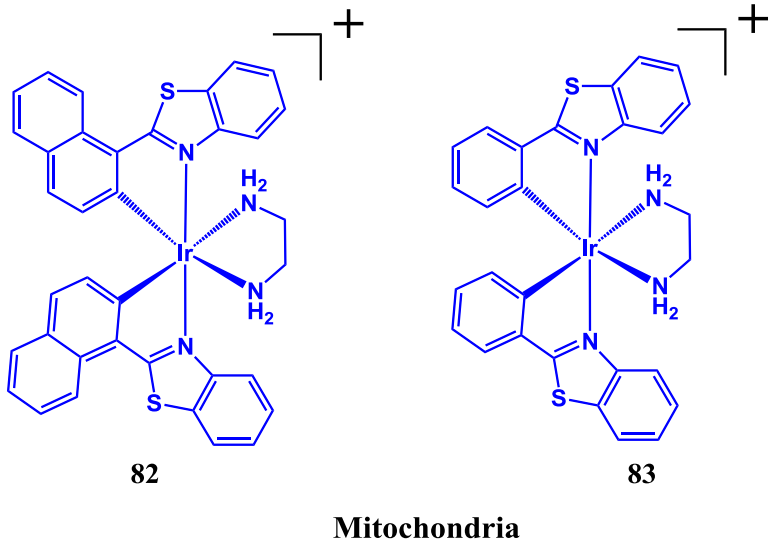

Figure 1.31 Chemical Structures of complex **82-83**.

Many other iridium(III) complexes were synthesized strategically by increasing the high liphophilic character which may help to stain the hydrophobic mitochondria.

The binding tendency of planer dipyridoquinoxaline (**84-85**) with double-stranded DNA and hydrophobic nucleolar proteins favoured the nucleoli staining (Figure 1.32) [320]. The complex with poly ethyleneimine (PEI) [318], (**86**) was found very specific towards selective staining of plasma membranes (Figure 1.33)**.** The solveto complex of iridium(III) such as $[Ir(C\hat{}N)_2(ACN)_2]$ and $[Ir(C\hat{}N)_2(DMSO)_2]$ were found non emissive in their solution state. After incubation, the labile solvent molecules were replaced by biomalecules of nucleus (histidine containing proteins) and resulted a strong emission from nucleus region [321-323].

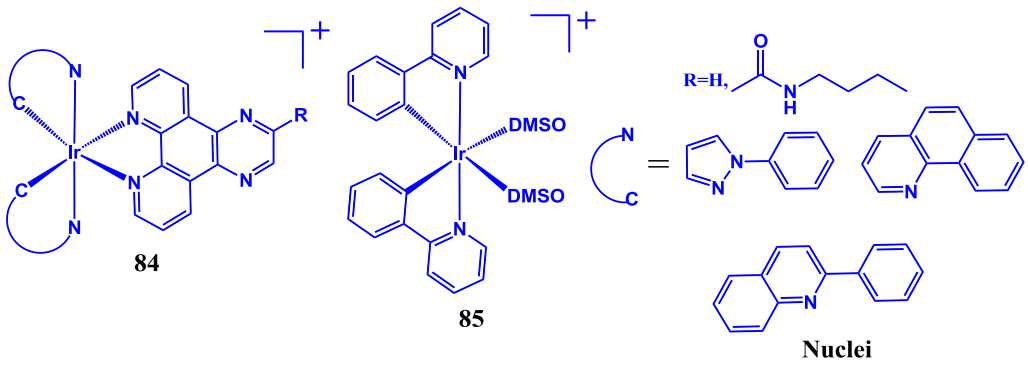

Figure 1.32 Chemical Structures of complex **84-85**.

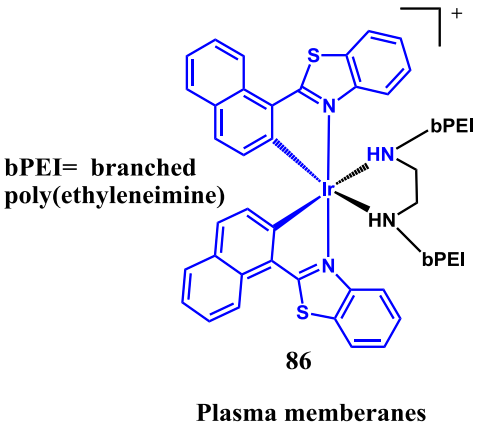

Figure 1.33 Chemical Structures of complex **86**.

1.5.2 Sensing application and iridium(III) complexes

The sensing of different anions and cations has been taken a serious attention by scientific society over last 50 years [324-337]. These ions play an important role in wide range of industrial, chemical and most importantly for biological processes. Many ions were proved themselves as lethal weapon for human health as well for environmental concern such as Hg^{+2}, Cd^{+2}, As^{+2}, Pd^{+2}, CN^{-}, SCN^{-} and many more [61, 110, 127, 129, 133, 135, 166, 338-341].

The addition of analytes (cations or anions) to the probe molecules, results a drastic change in one or more properties of the system, such as emission, absorption, or redox potential characteristics are known as chemosensor. Among many detection techniques, fluorescence detection is considered as most promising tool for sensing applications because of high sensitivity, easy visualization and short response time. A chemosensor generally consist of two units *i.e.* (a) acceptor unit and (b) signaling unit [342, 343]. After selective binding of analyte to the receptor, the signaling unit indicates the effective changes in the optical (turn-on, turn-off or ratiometric change in emission property) properties (Figure 1.34).

The heavy-metal based complexes with phosphorescent emission were considered as a superior sensor over fluorescence counter part because of long lived life time, higher efficiency [342].

In the recent trend the use of phosphorescent heavy-metal complexes [such as Pt(II), Ru(II), Re(I), Ir(III), Cu(I), Au(I)- and Os(II)-based complexes] [129, 342, 343] as chemosensors has been attracted a great attention of researchers. Among these heavy metals iridium(III) luminescent complexes were recognized as a potential probe for sensing application. Till date many iridium(III) based complexes were successfully used for detection of various analytes [344-350].

1.5.2.1 Small ions sensing luminescent materials

M.-L. Ho et al. designed an iridium(III) complex (**87**) with an aza-crown receptor in the pyridyl pyrazolate ligand which was found to very sensitive for Ca^{2+} ions (Figure 1.35) [351].

In 2007, Q. Zhao et al. synthesized a imidazolyl based iridium(III) complex (**88**) where the NH group in imidazole was utilized as a binding site for anions [352]. The addition of F^- and H^+ produced drastic changes in the UV-Vis absorption and emission spectra.

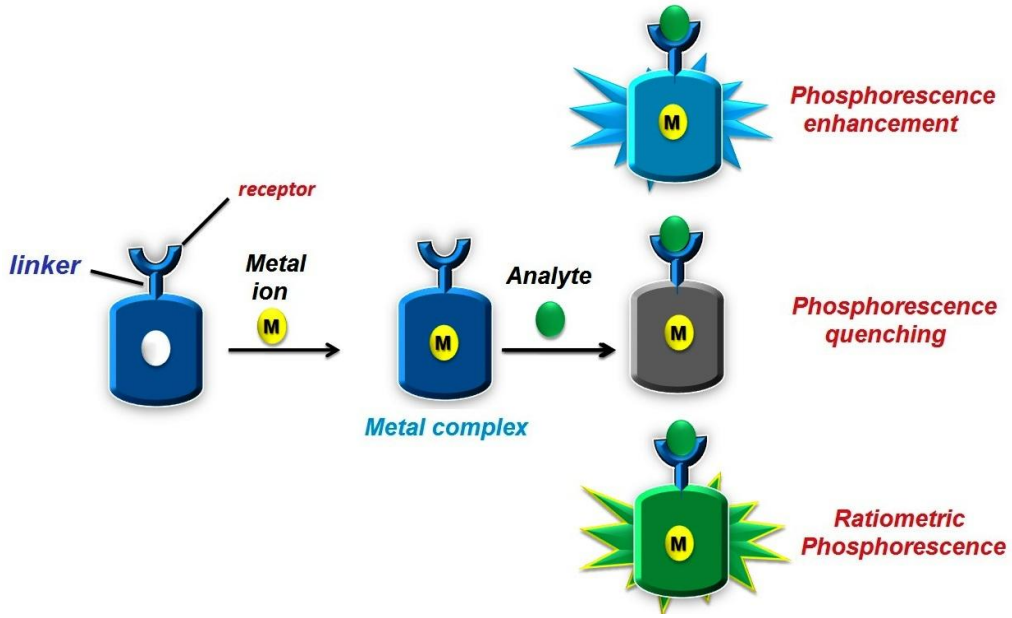

Figure 1.34 A schematic representation of "Receptor signaling unit approach'' for designing phosphorescent chemosensors and possible varying phosphorescence signal responses.

The emission color of the complex was completely quenched after deprotonation which may ascribe photoinduced electron transfer process (PET) (Figure 1.35). An aza-dioxa-dithia crown ether based phosphorescence chemosensor (**89**) was developed by M. Schmittel et al. based on ''receptor–conjugated signaling unit approach'' which was acting as a sensitive luminescence enhancement chemosensor for Ag^+ in aqueous solution. The addition of Ag^+ into the system resulted a red shifted emission with maximum PL enhancement [353] (Figure 1.35).

In a recent literature survey, several reports, [338, 349, 354-361] the detection of mercury ions was carried out taking advantage of the photophysical properties of emissive cyclometalated iridium(III) complexes.

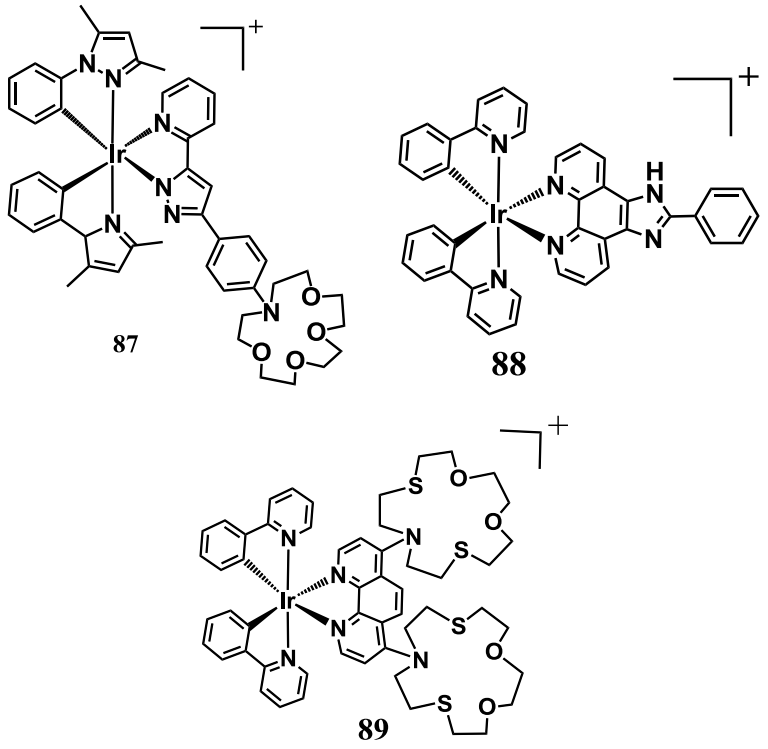

Figure 1.35 Chemical Structures of complex **87-89**.

In most of the cases, a sulphur atom was strategically incorporated into the complex framework to exploit the preferential binding according to Pearson's soft acid - soft base interactions [362] of sulphur with the soft acid mercuric ion. This phenomenon has been exemplified with systems such as $Ir(btp)_2(acac)$ (**90**) [349] (btp = 2-(benzo[b]thiophen-2-yl)pyridine, acacH= acetyl acetone), $Ir(thq)_2(acac)$ (**91**) [354] (thq=2-(thiophen-2-yl)quinoline). The soft-soft interaction also leads to a protection –de-protection mechanism in $[Ir(pba)_2(bipy)PF_6]$ (**92**) [358] (Hpba = 4-(Pyridin-2-yl)benzaldehyde; bipy= 2,2′-bipyridine) or to the Hg^{+2}-induced decomposition observed for $Ir(thq)_2(dbm)$ (**93**) [356] (thq= 2-(thiophen-2-yl)quinoline, dbm= 1,3-diphenylpropane-1,3-dione), $Ir(TBT)_2(acac)$ (**94**) [359] (TBT=2-thiophen-2-yl-benzothiazole), [Ir(ppa)(dmppa) $(Ph_2PS)_2N$] (**95**) [360] (ppa=4-phenylphthalazin-1-ol), (dmppa=1-phenoxy-4 phenylphthalazine)$Ph_2PS)_2N$=bis(diphenylthiophosphoryl)amide), $[Ir(bt)_2(acac)]$ (**96**) [355] (Hbt = 2-phenylben zothiazole), and $[Ir(ppy)_2(PBT)]$ (**97**) (PBT= 2-phenylbenzo[d]thiazole). Hui Zeng et al. reported recently the use of

$[Ir(pbi)_2(acac)]$ (**98**) [363] (pbi= 1,2-diphenyl-1H-benzo[d] imidazole) as a first example of a sulphur free iridium(III) complex used as a highly selective phosphorescent chemosensor for mercuric ions (Figure 1.36).

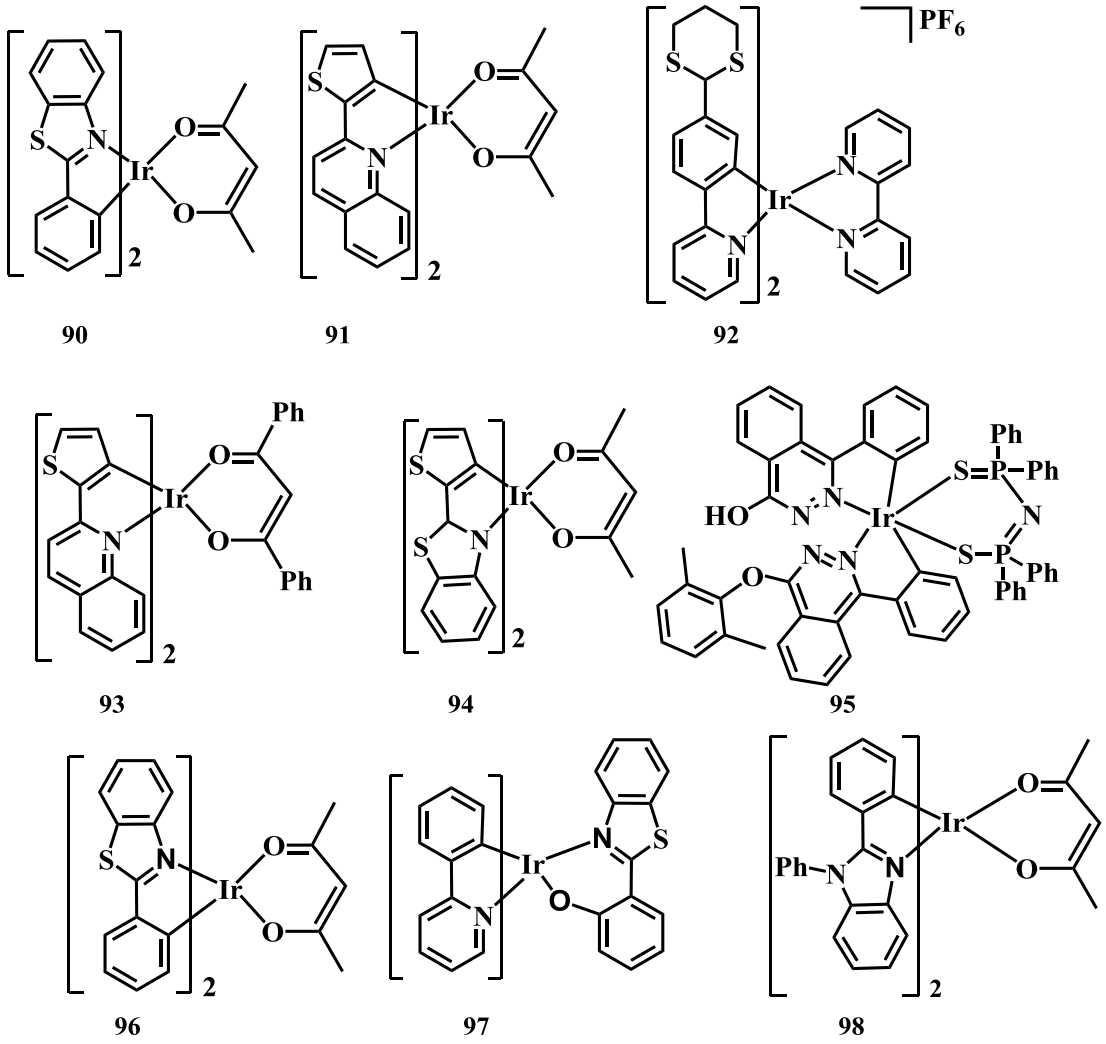

Figure 1.36 Chemical Structures of complex **90-98**.

1.5.2.2 Vapor-responsive luminescent materials

Recently, the smart solid state luminescent materials which are responsive to external stimuli such as shearing, grinding, rubbing, solvent exposure, temperature etc have been received a considerable attention in both scientific and applied research aspects [364]. These types of materials can change their emission color with the effect of external

stimuli which triggers the change in weak molecular interactions such as π-π stacking, hydrogen bonding etc [365-371]. There have an immense potentiality of these smart materials in various applications such as optical data recorders, mechanical sensors, security paper, deformation detectors and storage devices etc [172, 372-378]. The materials which can change their luminescent property in presence of volatile organic complexes (VOCs) are known as vapoluminescent materials [379]. There are many reports of organometallic and coordination complexes of Ru [380], Sn [381], Pt/ Pd [345, 379, 382-384], Cu [385, 386], Zn[387], Au [388], Ag [389], Re/Co [390] which were used in vapor-responsive luminescent materials (**99-106**) (Figure 1.37).

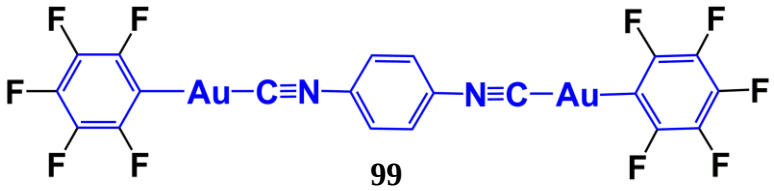

99

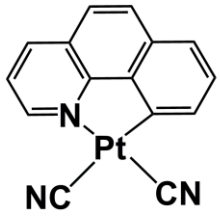

100

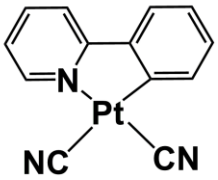

101

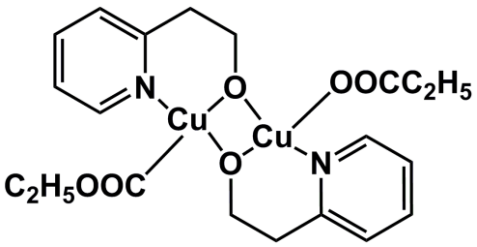

102

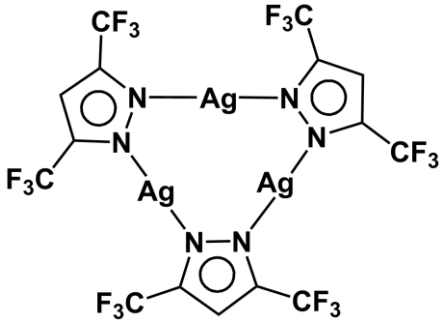

103

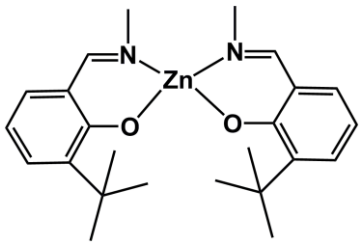

104

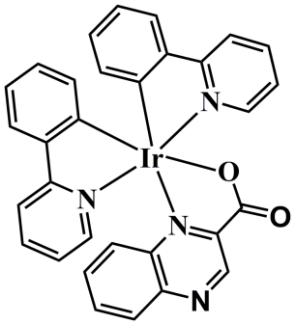

105

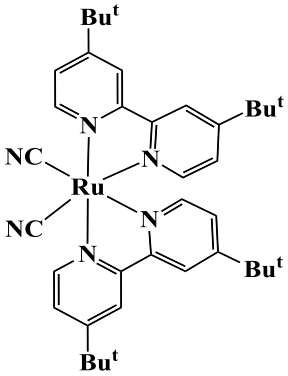

106

Figure 1.37 Complexes (**99-106)** with VOCs property.

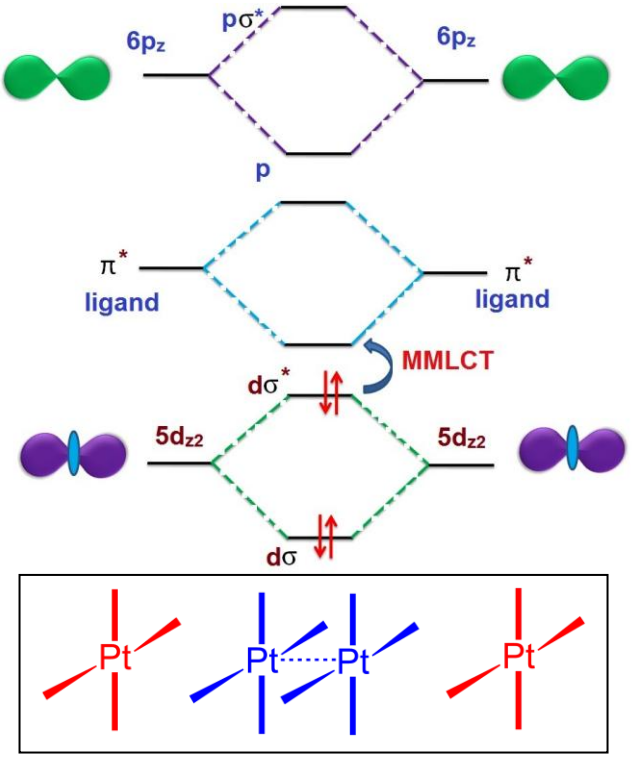

Figure 1.38 Molecular energy diagram of Pt-Pt interaction (formation of MMLCT state).

However, the effect of VOCs may disturb the close lying metal- metal interaction (metallic interaction) or π- π interactions which generally lead to formation of metal/metal-to-ligand charge transfer (MMLCT) state which are completely different

from ordinary metal-to-ligand charge transfer (MLCT) transitions (Figure 1.38) [236, 391-395].

All of them were used as vapor-responsive luminescent materials. However, the most extensive studies were carried out with platinum(II) and gold(I). Metallophilic interactions between Pt(II) /or Au(I) was either disrupted or enhanced upon interactions with VOCs, thereby alter the gap between highest occupied molecular orbital (HOMO) and lowest unoccupied molecular orbital (LUMO), thus, leading to distinct changes in emission or absorption spectra.

In comparison with other luminescent metallic complexes, several distinct advantages were observed with cyclometalated iridium(III) complexes such as, superior quantum efficiencies, easy tunability of light emission wavelength, higher thermal and electrochemical stability, straight forward synthetic routes etc as compared to the other analogues [24]. Notwithstanding the report of emitting iridium(III) complexes as vapoluminescent materials are very limited [396].

1.6 Scope of the present work

The thesis is segregated into seven chapters including a brief introduction to iridium(III) chemistry, aggregation induced emission (AIE) and its role in different applications such as sensing and bioimaging. The first chapter introduces fundamentals of fluorescence, history of luminescent iridium(III) complexes and their various applications. The chapter describes the history of 'aggregation induced emission (AIE)' active iridium complexes and their applications.

The second chapter of thesis provides the details of the materials and instruments used for carrying out the whole experiments throughout Ph.D work.

The third chapter discloses a simple one pot synthetic protocol for the syntheses of the series of AIE active iridium(III) complexes. A fine tuning of emission color (blue to red) was achieved easily in a common octahedral framework. One of the AIE active complexes, $[Ir(ppy)(PPh_3)_2(H)Cl)]$ was encapsulated inside block copolymer micelles which not only inhibited the macroscopic precipitation of the aggregated complex (size <

200 nm), but also transformed these into water soluble particles that exhibited a strong emission. These colloidal luminescent particles were tested for the use as a potential non-toxic bio-imaging probe. The complexes [Ir(ppy)(PPh_3)$_2$(H)Cl)] and [Ir(o-CHOppy)(PPh_3)$_2$(H)Cl)] were proved to be very sensitive and selective for the detection of picric acid (PA). The detection limit of PA was determined to 65 nM and 264 nM using the complexes [Ir(ppy)(PPh_3)$_2$(H)Cl)] and [Ir(o-CHOppy)(PPh_3)$_2$(H)Cl)], respectively.

The fourth chapter of thesis describes syntheses of new AIE active iridium(III) complexes using diimine ligands (2, 2′ -bipyridine and 1, 10-phenanthroline) as chromophoric ligands. The chapter is divided in two parts. In part A, two 1,10 phenanthroline based iridium complexes [mono(1,10 phenanthroline)bis(tri-phenylphosphine)(di-hydrido)iridium(III) hexafluorophosphate(**3**) and mono (1,10phenanthroline) bis(triphenylphoshpine(choloro) iridium(III) hexafluorophosphate (**4**)] were synthesized. The solid thin-films of **3** and **4** exhibited vapoluminescent properties depending on the polarity of the solvents. Rationale for different emission behavior in solid state was thoroughly investigated. Packing diagrams supported the accommodation of small organic solvent molecules inside the crystal lattices. Part B, describes the synthesis of two different varieties of iridium(III) complexes (N^N and C^N coordination) by using chelate 2, 2′- bipyridine ligand. The complex formed with the unusual C^N coordination mode of 2, 2′- bipyridine ligand to iridium(III) was known as rollover complex, [Ir(bipy-H)] (**5**). The emission color changes from bluish-green to yellowish-orange and *vice-versa* after repeated protonation and deprotonation of [Ir(bipy-H)], respectively which invariably supports of its reversibility. The tuning of emission property of [Ir(bipy-H)] was demonstrated with respect to pK_a of different acids. Based on DFT calculations, it was shown the change in electron affinity of pyridinyl ring was responsible for all these processes. The normal (N, N)-bipy chelated coordinating complex [Ir(bipy)]A (**6**) was found to change its emission color with varying the counteranions, [A = Cl^-, BF_4^-, PF_6^-, $N(CN)_2^-$]. [Ir(bipy)]Cl exhibited a dual property mechanofluorochromism and vapofluorochromism and the origin of causes was rationalized.

The fifth chapter of thesis described the syntheses of four iridium(III) complexes which

were readily obtained from the reaction of iridium chloride, triphenyl phosphine and schiff base ligands. The formation of these complexes showed good examples of luminescent iridium(III) complex which were formed through iridium(III) mediated activation of the acyclic imine C-H. Theses complexes showed a reversible emission color change in presence of acid and base, respectively. A noble iridium(III) complex with donor acceptor system was investigated as TICT probe molecule and successfully utilized as CO_2 detection.

The sixth chapter of thesis describes syntheses of bis new AIE active iridium(III) complexes using different phosphines ancillary ligands (P^P) such as Bis(diphenylphosphino)ethane (dppe), 1,2-Bis(diphenylphosphino)ethylene (dppel), 1,3-Bis(diphenylphosphino)propane (dppp) and 1,2-Bis(diphenylphosphino)ethane (dppe). The chapter is divided into two parts – in part A, greenish-blue light emitting $[Ir(ppy)_2(dppel)]$ (**9**), $[Ir(ppy)_2(dppp)]$ (**10**) and $[Ir(ppy)_2(dppe)]$ (**11**) [ppy, 2-phenylpyridine; dppel, 1,2-Bis(diphenylphosphino)ethylene; dppp, 1,3-Bis(diphenylphosphino)propane were synthesized using $[(ppy)_2Ir(\mu\text{-}Cl)_2Ir(ppy)_2]$ (**8**) in very short time with the help of MW reactor. In part B, using $[(F_2ppy)_2Ir(\mu\text{-}Cl)_2Ir(F_2ppy)_2]$ as starting material, the ancillary ligands and dppe and dppp resulted a mono phosphine coordinated bis iridium(III) complex where the one phosphorous of the ligand was kept as pendant. Furthermore, the free phosphorous was utilized for the selective and sensitive detection of Hg^{+2}.

The seventh chapter described the synthesis of a greenish blue emissive *bis*-cyclometalated iridium(III) complex with octahedral geometry where a bulky substituted ligand, N^1-tritylethane-1,2-diamine ligand (trityl- based rotating unit) (L_1) was coordinated to iridium(III) in non-chelating mode, $[Ir(F_2ppy)_2(L_1)(Cl)]$, [F_2ppy=2-(2′, 4′-difluoro)phenylpyridine; L_1 = N^1-tritylethane-1, 2-diamine]. The presence of secondary amine in L_1 has attributed to **1** in sensing acids. It also senses the presence of OH^-. The complex isolated after addition of OH^- was found to be aggregation induced enhanced emission (AIEE) active. Ground and excited state properties of **1** was investigated using DFT and TD-DFT based calculations.

1.7 References

[1] G. Drummen, Molecules, 17 (2012) 14067.

[2] S. Wang, L. Ge, X. Song, J. Yu, S. Ge, J. Huang, F. Zeng, Biosens. Bioelectron., 31 (2012) 212-218.

[3] J. Yu, L. Ge, J. Huang, S. Wang, S. Ge, Lab on a Chip, 11 (2011) 1286-1291.

[4] L. Matisová-Rychlá, V. Bukovský, J. Rychlý, M. Pleteníková, Macromol. Symp., 247 (2007) 340-349.

[5] L. Zhang, F. Xu, Z. Chen, X. Zhu, W. Min, J. Phys. Chem. Lett., 4 (2013) 3897-3902.

[6] B.R. Branchini, T.L. Southworth, D.M. Fontaine, A.L. Davis, C.E. Behney, M.H. Murtiashaw, Biochem., 53 (2014) 6287-6289.

[7] M. Adamczyk, J.A. Moore, K. Shreder, Org. Lett., 3 (2001) 1797-1800.

[8] B.R. Branchini, M.H. Murtiashaw, R.A. Magyar, N.C. Portier, M.C. Ruggiero, J.G. Stroh, J. Am. Chem. Soc., 124 (2002) 2112-2113.

[9] S.K. Cushing, M. Li, F. Huang, N. Wu, ACS Nano, 8 (2014) 1002-1013.

[10] H. Mishra, C.D. Geddes, J. Phys. Chem. C, 118 (2014) 28791-28796.

[11] E.S. Shibu, K. Ono, S. Sugino, A. Nishioka, A. Yasuda, Y. Shigeri, S.-i. Wakida, M. Sawada, V. Biju, ACS Nano, 7 (2013) 9851-9859.

[12] A. Pfister, G. Zhang, J. Zareno, A.F. Horwitz, C.L. Fraser, ACS Nano, 2 (2008) 1252-1258.

[13] F.B. Bramwell, M.L. Spinner, J. Chem. Edu., 54 (1977) 167.

[14] T. Zhou, N. Wang, C. Li, H. Yuan, D. Xiao, Anal. Chem., 82 (2010) 1705-1711.

[15] Y. Zhang, K. Aslan, M.J.R. Previte, S.N. Malyn, C.D. Geddes, J. Phys. Chem. B, 110 (2006) 25108-25114.

[16] D.A. Hartzler, D.M. Niedzwiedzki, D.A. Bryant, R.E. Blankenship, Y. Pushkar, S. Savikhin, J. Phys. Chem. B, 118 (2014) 7221-7232.

[17] H. Shi, Z. An, P.-Z. Li, J. Yin, G. Xing, T. He, H. Chen, J. Wang, H. Sun, W. Huang, Y. Zhao, Cryst. Growth Des., 16 (2016) 808–813.

[18] P. Salam, SID, 32 67-69 (2001).

[19] R.D. Costa, E. Ortí, H.J. Bolink, F. Monti, G. Accorsi, N. Armaroli, Angew. Chem., Int. Ed., 51 (2012) 8178-8211.

[20] D. Frackowiak, J. Photochem. Photobiol. B: Biology, 2 (1988) 399.

[21] S.L. Tesar, V.M. Kasyanenko, I.V. Rubtsov, G.I. Rubtsov, A.L. Burin, J. Phys. Chem. A, 117 (2013) 315-323.

[22] M. Kasha, J. Chem.Phys., 20 (1952) 71-74.

[23] M. Karplus, J. Chem.l Phys., 30 (1959) 11-15.

[24] S. Lamansky, P. Djurovich, D. Murphy, F. Abdel-Razzaq, H.-E. Lee, C. Adachi, P.E. Burrows, S.R. Forrest, M.E. Thompson, J. Am. Chem. Soc., 123 (2001) 4304-4312.

[25] M.G. Colombo, T.C. Brunold, T. Riedener, H.U. Guedel, M. Fortsch, H.-B. Buergi, Inorg. Chem., 33 (1994) 545-550.

[26] A. Nitzan, J. Jortner, J. Kommandeur, E. Drent, Chem. Phys. Lett., 9 (1971) 273-278.

[27] T.D. Gauthier, E.C. Shane, W.F. Guerin, W.R. Seitz, C.L. Grant, Environ.Sci. Tech., 20 (1986) 1162-1166.

[28] H. Boaz, G.K. Rollefson, J. Am. Chem. Soc., 72 (1950) 3435-3443.

[29] E. Matayoshi, G. Wang, G. Krafft, J. Erickson, Science, 247 (1990) 954-958.

[30] J.R. Lakowicz, Y. Shen, S. D'Auria, J. Malicka, J. Fang, Z. Gryczynski, I. Gryczynski, Anal. Biochem., 301 (2002) 261-277.

[31] S. Jang, Y.-C. Cheng, D.R. Reichman, J.D. Eaves, J. Chem. Phys., 129 (2008) 101104.

[32] S. Guo, L. Ma, J. Zhao, B. Kucukoz, A. Karatay, M. Hayvali, H.G. Yaglioglu, A. Elmali, Chem. Sci., 5 (2014) 489-500.

[33] A.A. Deniz, M. Dahan, J.R. Grunwell, T. Ha, A.E. Faulhaber, D.S. Chemla, S. Weiss, P.G. Schultz, Proc. Natl. Acad. Sci., 96 (1999) 3670-3675.

[34] A.R. Clapp, I.L. Medintz, H. Mattoussi, Chem.Phys.Chem., 7 (2006) 47-57.

[35] J. Zhang, Y. Fu, J.R. Lakowicz, J. Phys. Chem. C, 111 (2007) 50-56.

[36] S. Jang, M.D. Newton, R.J. Silbey, Phys.Rev.Lett., 92 (2004) 218301.

[37] K. Kedziora, K. Jalink, Fluorescence Resonance Energy Transfer Microscopy (FRET), in: P.J. Verveer (Ed.) Advanced Fluorescence Microscopy, Springer New York, 2015, pp. 67-82.

[38] N.S. Bayliss, G. Wills-Johnson, Spectrochimica Acta Part A: Molecular Spectroscopy, 24 (1968) 551-561.

[39] N.S. Bayliss, G. Wills-Johnson, Spectrochimica Acta Part A: Molecular Spectroscopy, 24 (1968) 563-573.

[40] R.A. Caldwell, R.P. Gajewski, J. Am. Chem. Soc., 93 (1971) 532-534.

[41] L.J. Andrews, A. Deroulede, H. Linschitz, J. Phys. Chem., 82 (1978) 2304-2309.

[42] H. McConnell, J.Chem.Phys., 20 (1952) 700-704.

[43] J.R. Lakowicz, Principles of fluorescence spectroscopy, Springer Science & Business Media, 2013.

[44] N.S. Bayliss, E.G. McRae, J. Phys. Chem., 58 (1954) 1002-1006.

[45] J.R. Lakowicz, Instrumentation for fluorescence spectroscopy, in: Principles of fluorescence spectroscopy, Springer, 1999, pp. 25-61.

[46] J.R. Lakowicz, Introduction to fluorescence, in: Principles of fluorescence spectroscopy, Springer, 1999, pp. 1-23.

[47] P. Pringsheim, Rev. Mod. Phys., 14 (1942) 132.

[48] B. Valeur, M.N. Berberan-Santos, Molecular fluorescence: principles and applications, John Wiley & Sons, 2012.

[49] N. Mataga, Bull. Chem. Soc. Jpn., 40 (1967) 1350-1354.

[50] N. Mataga, K. Ezumi, Bull. Chem. Soc. Jpn., 40 (1967) 1350-1354.

[51] N. Zhao, Y.-H. Wu, H.-M. Wen, X. Zhang, Z.-N. Chen, Organometallics, 28 (2009) 5603-5611.

[52] F. Zhang, D. Ma, L. Duan, J. Qiao, G. Dong, L. Wang, Y. Qiu, Inorg. Chem., 53 (2014) 6596-6606.

[53] C.-F. Chang, Y.-M. Cheng, Y. Chi, Y.-C. Chiu, C.-C. Lin, G.-H. Lee, P.-T. Chou, C.-C. Chen, C.-H. Chang, C.-C. Wu, Angew. Chem., Int. Ed., 47 (2008) 4542-4545.

[54] H. Yersin, Highly efficient OLEDs with phosphorescent materials, John Wiley & Sons, 2008.

[55] D.M. Roundhill, Photochemistry and photophysics of metal complexes, Springer Science & Business Media, 2013.

[56] C.M. Flynn, J.N. Demas, J. Am. Chem. Soc., 96 (1974) 1959-1960.

[57] R.J. Watts, J.S. Harrington, J. Van Houten, J. Am. Chem. Soc., 99 (1977) 2179-2187.

[58] A.J. Lees, Chem. Rev., 87 (1987) 711-743.

[59] L. Flamigni, A. Barbieri, C. Sabatini, B. Ventura, F. Barigelletti, Photochemistry and photophysics of coordination compounds: iridium, in: Photochemistry and Photophysics of Coordination Compounds II, Springer, 2007, pp. 143-203.

[60] S. Lamansky, P. Djurovich, D. Murphy, F. Abdel-Razzaq, R. Kwong, I. Tsyba, M. Bortz, B. Mui, R. Bau, M.E. Thompson, Inorg. Chem., 40 (2001) 1704-1711.

[61] Y. You, W. Nam, Chem. Soc. Rev., 41 (2012) 7061-7084.

[62] A.B. Tamayo, B.D. Alleyne, P.I. Djurovich, S. Lamansky, I. Tsyba, N.N. Ho, R. Bau, M.E. Thompson, J. Am. Chem. Soc., 125 (2003) 7377-7387.

[63] R.M. Edkins, A. Wriglesworth, K. Fucke, S.L. Bettington, A. Beeby, Dalton Trans., 40 (2011) 9672-9678.

[64] S.J. Lee, K.-M. Park, K. Yang, Y. Kang, Inorg. Chem., 48 (2009) 1030-1037.

[65] K.A. King, P.J. Spellane, R.J. Watts, J. Am. Chem. Soc., 107 (1985) 1431-1432.

[66] J.M. Fernández-Hernández, J.I. Beltrán, V. Lemaur, M.-D. Gálvez-López, C.-H. Chien, F. Polo, E. Orselli, R. Fröhlich, J. Cornil, L. De Cola, Inorg. Chem., 52 (2013) 1812-1824.

[67] E. Baranoff, S. Fantacci, F. De Angelis, X. Zhang, R. Scopelliti, M. Grätzel, M.K. Nazeeruddin, Inorg. Chem., 50 (2011) 451-462.

[68] N.M. Shavaleev, F. Monti, R.D. Costa, R. Scopelliti, H.J. Bolink, E. Ortí, G. Accorsi, N. Armaroli, E. Baranoff, M. Grätzel, M.K. Nazeeruddin, Inorg. Chem., 51 (2012) 2263-2271.

[69] E. Baranoff, S. Suàrez, P. Bugnon, C. Barolo, R. Buscaino, R. Scopelliti, L. Zuppiroli, M. Graetzel, M.K. Nazeeruddin, Inorg. Chem., 47 (2008) 6575-6577.

[70] T. Toshimitsu, S. Nobuhiko, S. Toshiyasu, T. Shizuo, Jpn. J. Appl. Phy., 44 (2005) 4151.

[71] T. Tsuzuki, N. Shirasawa, T. Suzuki, S. Tokito, Adv. Mater., 15 (2003) 1455-1458.

[72] E. Baranoff, B.F.E. Curchod, F. Monti, F. Steimer, G. Accorsi, I. Tavernelli, U. Rothlisberger, R. Scopelliti, M. Grätzel, M.K. Nazeeruddin, Inorg. Chem., 51 (2012) 799-811.

[73] E. Baranoff, B.F.E. Curchod, J. Frey, R. Scopelliti, F. Kessler, I. Tavernelli, U. Rothlisberger, M. Grätzel, M.K. Nazeeruddin, Inorg. Chem., 51 (2012) 215-224.

[74] M.-S. Eum, C.S. Chin, S.y. Kim, C. Kim, S.K. Kang, N.H. Hur, J.H. Seo, G.Y. Kim, Y.K. Kim, Inorg. Chem., 47 (2008) 6289-6295.

[75] C.-H. Lin, Y.-Y. Chang, J.-Y. Hung, C.-Y. Lin, Y. Chi, M.-W. Chung, C.-L. Lin, P.-T. Chou, G.-H. Lee, C.-H. Chang, W.-C. Lin, Angew. Chem. Int. Ed., 123 (2011) 3240-3244.

[76] C.-H. Lin, C.-Y. Lin, J.-Y. Hung, Y.-Y. Chang, Y. Chi, M.-W. Chung, Y.-C. Chang, C. Liu, H.-A. Pan, G.-H. Lee, P.-T. Chou, Inorg. Chem., 51 (2012) 1785-1795.

[77] Y.-C. Chiu, C.-H. Lin, J.-Y. Hung, Y. Chi, Y.-M. Cheng, K.-W. Wang, M.-W. Chung, G.-H. Lee, P.-T. Chou, Inorg. Chem., 48 (2009) 8164-8172.

[78] C.-H. Lin, Y.-C. Chiu, Y. Chi, Y.-T. Tao, L.-S. Liao, M.-R. Tseng, G.-H. Lee, Organometallics, 31 (2012) 4349-4355.

[79] J.-Y. Hung, C.-H. Lin, Y. Chi, M.-W. Chung, Y.-J. Chen, G.-H. Lee, P.-T. Chou, C.-C. Chen, C.-C. Wu, J. Mater. Chem., 20 (2010) 7682-7693.

[80] C.-H. Lin, J.-L. Liao, Y.-S. Wu, K.-Y. Liao, Y. Chi, C.-L. Chen, G.-H. Lee, P.-T. Chou, Dalton Trans., 44 (2015) 8406-8418.

[81] K.M.-C. Wong, M.M.-Y. Chan, V.W.-W. Yam, Adv. Mater., 26 (2014) 5558-5568.

[82] G. Li, T. Fleetham, E. Turner, X.-C. Hang, J. Li, Adv.Opt. Mater., 3 (2015) 390-397.

[83] H.-F. Xiang, S.-C. Chan, K.K.-Y. Wu, C.-M. Che, P.T. Lai, Chem. Commun., (2005) 1408-1410.

[84] C.-H. Yang, M. Mauro, F. Polo, S. Watanabe, I. Muenster, R. Fröhlich, L. De Cola, Chem. Mater., 24 (2012) 3684-3695.

[85] J.A. Gareth Williams, S. Develay, D.L. Rochester, L. Murphy, Coord. Chem. Rev., 252 (2008) 2596-2611.

[86] B. Ma, P.I. Djurovich, M.E. Thompson, Coord. Chem. Rev., 249 (2005) 1501-1510.

[87] D. Kourkoulos, C. Karakus, D. Hertel, R. Alle, S. Schmeding, J. Hummel, N. Risch, E. Holder, K. Meerholz, Dalton Trans., 42 (2013) 13612-13621.

[88] F. Kessler, Y. Watanabe, H. Sasabe, H. Katagiri, M.K. Nazeeruddin, M. Gratzel, J. Kido, J. Mater. Chem. C, 1 (2013) 1070-1075.

[89] H.-Y. Li, L. Zhou, M.-Y. Teng, Q.-L. Xu, C. Lin, Y.-X. Zheng, J.-L. Zuo, H.-J. Zhang, X.-Z. You, J. Mater. Chem. C, 1 (2013) 560-565.

[90] J. Zhuang, W. Li, W. Su, Y. Liu, Q. Shen, L. Liao, M. Zhou, Org. Electron., 14 (2013) 2596-2601.

[91] W.-Y. Wong, Z. He, S.-K. So, K.-L. Tong, Z. Lin, Organometallics, 24 (2005) 4079-4082.

[92] X. Li, W.C.H. Choy, L. Huo, F. Xie, W.E.I. Sha, B. Ding, X. Guo, Y. Li, J. Hou, J. You, Y. Yang, Adv. Mater., 24 (2012) 3046-3052.

[93] Y. Lin, Y. Wang, J. Wang, J. Hou, Y. Li, D. Zhu, X. Zhan, Adv. Mater., 26 (2014) 5224-5224.

[94] Y. Liu, C. Mu, K. Jiang, J. Zhao, Y. Li, L. Zhang, Z. Li, J.Y.L. Lai, H. Hu, T. Ma, R. Hu, D. Yu, X. Huang, B.Z. Tang, H. Yan, Adv. Mater., 27 (2015) 1015-1020.

[95] H. Shang, H. Fan, Y. Liu, W. Hu, Y. Li, X. Zhan, Adv. Mater., 23 (2011) 1554-1557.

[96] Y. Zang, C.-Z. Li, C.-C. Chueh, S.T. Williams, W. Jiang, Z.-H. Wang, J.-S. Yu, A.K.Y. Jen, Adv. Mater., 26 (2014) 5708-5714.

[97] Y. Lin, P. Cheng, Y. Li, X. Zhan, Chem. Commun., 48 (2012) 4773-4775.

[98] H.N. Tsao, J. Burschka, C. Yi, F. Kessler, M.K. Nazeeruddin, M. Gratzel, Energy & Environmental Science, 4 (2011) 4921-4924.

[99] J. Zhao, Y. Li, H. Lin, Y. Liu, K. Jiang, C. Mu, T. Ma, J.Y. Lin Lai, H. Hu, D. Yu, H. Yan, Energy Environ. Sci., 8 (2015) 520-525.

[100] K. Forberich, F. Guo, C. Bronnbauer, C.J. Brabec, Energy Technology, (2015).

[101] Y. Jiang, C. Cabanetos, M. Allain, P. Liu, J. Roncali, J. Mater. Chem. C, 3 (2015) 5145-5151.

[102] I. Jeon, K. Cui, T. Chiba, A. Anisimov, A.G. Nasibulin, E.I. Kauppinen, S. Maruyama, Y. Matsuo, J. Am. Chem. Soc., 137 (2015) 7982-7985.

[103] J. Zhou, X. Wan, Y. Liu, Y. Zuo, Z. Li, G. He, G. Long, W. Ni, C. Li, X. Su, Y. Chen, J. Am. Chem. Soc., 134 (2012) 16345-16351.

[104] S. Ahmad, T. Bessho, F. Kessler, E. Baranoff, J. Frey, C. Yi, M. Gratzel, M.K. Nazeeruddin, Phys. Chem. Chem. Phys., 14 (2012) 10631-10639.

[105] S.M. Feldt, P.W. Lohse, F. Kessler, M.K. Nazeeruddin, M. Gratzel, G. Boschloo, A. Hagfeldt, Phys. Chem. Chem. Phys., 15 (2013) 7087-7097.

[106] Q. Zhao, Y. Liu, Y. Cao, W. Lv, Q. Yu, S. Liu, X. Liu, M. Shi, W. Huang, Adv. Opt. Mater., 3 (2015) 233-240.

[107] W. Lv, T. Yang, Q. Yu, Q. Zhao, K.Y. Zhang, H. Liang, S. Liu, F. Li, W. Huang, Adv. Sci., (2015) 1-9.

[108] D.-L. Ma, H.-Z. He, K.-H. Leung, D.S.-H. Chan, C.-H. Leung, Angew. Chem., Int. Ed., 52 (2013) 7666-7682.

[109] H.-Y. Shiu, H.-C. Chong, Y.-C. Leung, T. Zou, C.-M. Che, Chem. Commun., 50 (2014) 4375-4378.

[110] Q. Zhao, X. Zhou, T. Cao, K.Y. Zhang, L. Yang, S. Liu, H. Liang, H. Yang, F. Li, W. Huang, Chem. Sci., 6 (2015) 1825-1831.

[111] Q. Zhao, C. Huang, F. Li, Chem. Soc. Rev., 40 (2011) 2508-2524.

[112] X.-H. Yang, S. Li, Z.-S. Tang, X.-D. Yu, T. Huang, Y. Gao, Chin. Chem. Lett., 26 (2015) 129-132.

[113] E. Baggaley, J.A. Weinstein, J.A.G. Williams, Coord. Chem. Rev., 256 (2012) 1762-1785.

[114] Y. You, Curr. Opin. Chem. Biol., 17 (2013) 699-707.

[115] K.K.-W. Lo, A.W.-T. Choi, W.H.-T. Law, Dalton Trans., 41 (2012) 6021-6047.

[116] S. Marpu, P.K. Upadhyay, D.T. Nguyen, I.W.H. Oswald, R.K. Arvapally, R.A. Petros, Z. Hu, M.A. Omary, J. Phys. Chem. C, 119 (2015) 12551-12561.

[117] K. Zhang, S. Liu, Q. Zhao, F. Li, W. Huang, Phosphorescent Iridium(III) Complexes for Bioimaging, in: K.K.-W. Lo (Ed.) Luminescent and Photoactive Transition Metal Complexes as Biomolecular Probes and Cellular Reagents, Springer Berlin Heidelberg, 2015, pp. 131-180.

[118] S. Liu, W. Qiao, G. Cao, Y. Chen, Y. Ma, Y. Huang, X. Liu, W. Xu, Q. Zhao, W. Huang, Macromol. Rapid Commun., 34 (2013) 81-86.

[119] J. Chan, S.C. Dodani, C.J. Chang, Nat. Chem., 4 (2012) 973-984.

[120] V.M. Manikandamathavan, N. Duraipandy, M.S. Kiran, V.G. Vaidyanathan, B.U. Nair, RSC Adv., 5 (2015) 24877-24885.

[121] Z. Hai, Y. Bao, Q. Miao, X. Yi, G. Liang, Anal. Chem., 87 (2015) 2678-2684.

[122] L. Cao, R. Zhang, W. Zhang, Z. Du, C. Liu, Z. Ye, B. Song, J. Yuan, Biomaterials, 68 (2015) 21-31.

[123] H.S. Jung, X. Chen, J.S. Kim, J. Yoon, Chem. Soc. Rev., 42 (2013) 6019-6031.

[124] S. Lee, K.K.Y. Yuen, K.A. Jolliffe, J. Yoon, Chem. Soc. Rev., 44 (2015) 1749-1762.

[125] J.F. Zhang, Y. Zhou, J. Yoon, J.S. Kim, Chem. Soc. Rev., 40 (2011) 3416-3429.

[126] Y. Zhou, J. Yoon, Chem. Soc. Rev., 41 (2012) 52-67.

[127] K.-C. Chang, S.-S. Sun, M.O. Odago, A.J. Lees, Coord. Chem. Rev., 284 (2015) 111-123.

[128] M. Formica, V. Fusi, L. Giorgi, M. Micheloni, Coord. Chem. Rev., 256 (2012) 170-192.

[129] D.-L. Ma, V.P.-Y. Ma, D.S.-H. Chan, K.-H. Leung, H.-Z. He, C.-H. Leung, Coord. Chem. Rev., 256 (2012) 3087-3113.

[130] D.W. Boyce, D.J. Salmon, W.B. Tolman, Inorg. Chem., 53 (2014) 5788-5796.

[131] Y. Jeong, J. Yoon, Inorg. Chim. Acta, 381 (2012) 2-14.

[132] M.G. Mohamed, R.-C. Lin, J.-H. Tu, F.-H. Lu, J.-L. Hong, K.-U. Jeong, C.-F. Wang, S.-W. Kuo, RSC Adv., 5 (2015) 65635-65645.

[133] G. Ambrosi, E. Borgogelli, M. Formica, V. Fusi, L. Giorgi, M. Micheloni, E. Rampazzo, M. Sgarzi, N. Zaccheroni, L. Prodi, Sens. Actuators, B, 207, Part B (2015) 1035-1044.

[134] V.K. Gupta, S.K. Shoora, L.K. Kumawat, A.K. Jain, Sens. Actuators, B, 209 (2015) 15-24.

[135] S. Kim, M.S. Eom, S. Yoo, M.S. Han, Tetrahedron Lett., 56 (2015) 5030-5033.

[136] S.A. Jenekhe, J.A. Osaheni, Science, 265 (1994) 765-768.

[137] M.A. Rawashdeh-Omary, M.A. Omary, H.H. Patterson, J.P. Fackler, J. Am. Chem. Soc., 123 (2001) 11237-11247.

[138] C.N. Pettijohn, E.B. Jochnowitz, B. Chuong, J.K. Nagle, A. Vogler, Coord. Chem. Rev., 171 (1998) 85-92.

[139] H. Tachikawa, A.J. Bard, Chem. Phys. Lett., 26 (1974) 568-573.

[140] J. Luo, Z. Xie, J.W.Y. Lam, L. Cheng, H. Chen, C. Qiu, H.S. Kwok, X. Zhan, Y. Liu, D. Zhu, B.Z. Tang, Chem. Commun., (2001) 1740-1741.

[141] Y. Hong, J.W.Y. Lam, B.Z. Tang, Chem. Commun., (2009) 4332-4353.

[142] Y. Jiang, Y. Wang, J. Hua, J. Tang, B. Li, S. Qian, H. Tian, Chem. Commun., 46 (2010) 4689-4691.

[143] Y. Hong, J.W.Y. Lam, B.Z. Tang, Chem. Soc. Rev., 40 (2011) 5361-5388.

[144] J. Wang, J. Mei, W. Yuan, P. Lu, A. Qin, J. Sun, Y. Ma, B.Z. Tang, J. Mater. Chem., 21 (2011) 4056-4059.

[145] Q. Wu, Q. Peng, Y. Niu, X. Gao, Z. Shuai, J. Phys. Chem. A, 116 (2012) 3881-3888.

[146] T. Zhang, Y. Jiang, Y. Niu, D. Wang, Q. Peng, Z. Shuai, J. Phys. Chem. A, 118 (2014) 9094-9104.

[147] N. Zhao, J.W.Y. Lam, H.H.Y. Sung, H.M. Su, I.D. Williams, K.S. Wong, B.Z. Tang, Chem. Eur. J., 20 (2014) 133-138.

[148] B. Chen, X. Sun, R.E. Evans, R. Zhou, J.N. Demas, C.O. Trindle, G. Zhang, J. Phys. Chem. A, 119 (2015) 8854-8859.

[149] H. Wang, Y. Liang, H. Xie, H. Lu, S. Zhao, S. Feng, J. Mater. Chem. C, (2016).

[150] C. Xia, Y. Qian, New J. Chem., 40 (2016) 144-150.

[151] D. Wu, L. Shao, Y. Li, Q. Hu, F. Huang, G. Yu, G. Tang, Chem. Commun., 52 (2016) 541-544.

[152] Y. Yuan, S. Xu, C.-J. Zhang, R. Zhang, B. Liu, J. Mater. Chem. B, 4 (2016) 169-176.

[153] T. Butler, W.A. Morris, J. Samonina-Kosicka, C.L. Fraser, ACS Appl. Mater. Interfaces, (2016).

[154] B. Li, X. Wang, X. Shen, W. Zhu, L. Xu, X. Zhou, J. Colloid Interface Sci., 467 (2016) 90-96.

[155] M.-M. Xue, Y.-M. Xie, L.-S. Cui, X.-Y. Liu, X.-D. Yuan, Y.-X. Li, Z.-Q. Jiang, L.-S. Liao, Chem. Eur. J., 22 (2016) 916-924.

[156] H. Lu, Y. Zheng, X. Zhao, L. Wang, S. Ma, X. Han, B. Xu, W. Tian, H. Gao, Angew. Chem. Ed. Int., 128 (2016) 163-167.

[157] H. Zhang, H. Li, J. Wang, J. Sun, A. Qin, B.Z. Tang, J. Mater. Chem. C, 3 (2015) 5162-5166.

[158] X. Dong, F. Hu, Z. Liu, G. Zhang, D. Zhang, Chem. Commun., 51 (2015) 3892-3895.

[159] Q. Ye, S. Chen, D. Zhu, X. Lu, Q. Lu, J. Mater. Chem. B, 3 (2015) 3091-3097.

[160] J. Mei, N.L.C. Leung, R.T.K. Kwok, J.W.Y. Lam, B.Z. Tang, Chem. Rev., 115 (2015) 11718-11940.

[161] Q. Lu, X. Li, J. Li, Z. Yang, B. Xu, Z. Chi, J. Xu, Y. Zhang, J. Mater. Chem. C, 3 (2015) 1225-1234.

[162] A. Ghosh, A. Sengupta, A. Chattopadhyay, D. Das, Chem. Commun., 51 (2015) 11455-11458.

[163] Z. Zhao, B. He, B.Z. Tang, Chem. Sci., 6 (2015) 5347-5365.

[164] Y. Yuan, C.-J. Zhang, M. Gao, R. Zhang, B.Z. Tang, B. Liu, Angew. Chem., Int. Ed., 54 (2015) 1780-1786.

[165] D. Zhao, F. Fan, J. Cheng, Y. Zhang, K.S. Wong, V.G. Chigrinov, H.S. Kwok, L. Guo, B.Z. Tang, Adv. Opt. Mater., 3 (2015) 199-202.

[166] R.T.K. Kwok, C.W.T. Leung, J.W.Y. Lam, B.Z. Tang, Chem. Soc. Rev., 44 (2015) 4228-4238.

[167] M. Wang, G. Zhang, D. Zhang, D. Zhu, B.Z. Tang, J. Mater. Chem., 20 (2010) 1858-1867.

[168] Z. Chen, J. Liang, X. Han, J. Yin, G.-A. Yu, S.H. Liu, Dyes Pigm., 112 (2015) 59-66.

[169] Z. He, L. Shan, J. Mei, H. Wang, J.W.Y. Lam, H.H.Y. Sung, I.D. Williams, X. Gu, Q. Miao, B.Z. Tang, Chem. Sci., 6 (2015) 3538-3543.

[170] C. Botta, S. Benedini, L. Carlucci, A. Forni, D. Marinotto, A. Nitti, D. Pasini, S. Righetto, E. Cariati, J. Mater. Chem. C, (2016) (DOI: 10.1039/c5tc03352).

[171] X. Yang, X. Chen, X. Lu, C. Yan, Y. Xu, X. Hang, J. Qu, R. Liu, J. Mater. Chem. C, 4 (2016) 383-390.

[172] Z. Ning, Z. Chen, Q. Zhang, Y. Yan, S. Qian, Y. Cao, H. Tian, Adv. Funct. Mater., 17 (2007) 3799-3807.

[173] J. Mei, Y. Hong, J.W.Y. Lam, A. Qin, Y. Tang, B.Z. Tang, Adv. Mater., 26 (2014) 5429-5479.

[174] Z. Chi, X. Zhang, B. Xu, X. Zhou, C. Ma, Y. Zhang, S. Liu, J. Xu, Chem. Soc. Rev., 41 (2012) 3878-3896.

[175] H. Tong, Y. Hong, Y. Dong, Hau, J.W.Y. Lam, Z. Li, Z. Guo, Z. Guo, B.Z. Tang, Chem. Commun., (2006) 3705-3707.

[176] N.B. Shustova, B.D. McCarthy, M. Dincă, J. Am. Chem. Soc., 133 (2011) 20126-20129.

[177] X. Zhang, Z. Chi, H. Li, B. Xu, X. Li, W. Zhou, S. Liu, Y. Zhang, J. Xu, Chem. Asian J., 6 (2011) 808-811.

[178] J. Shi, N. Chang, C. Li, J. Mei, C. Deng, X. Luo, Z. Liu, Z. Bo, Y.Q. Dong, B.Z. Tang, Chem. Commun., 48 (2012) 10675-10677.

[179] T. Han, X. Feng, B. Tong, J. Shi, L. Chen, J. Zhi, Y. Dong, Chem. Commun., 48 (2012) 416-418.

[180] A. Qin, J.W.Y. Lam, B.Z. Tang, Prog. Poly. Sci., 37 (2012) 182-209.

[181] B. Wang, Y. Wang, J. Hua, Y. Jiang, J. Huang, S. Qian, H. Tian, Chem. Eur. J., 17 (2011) 2647-2655.

[182] Z. Zhao, J. W. Y. Lam, B. Zhong Tang, Curr. Org. Chem., 14 (2010) 2109-2132.

[183] K. Li, W. Qin, D. Ding, N. Tomczak, J. Geng, R. Liu, J. Liu, X. Zhang, H. Liu, B. Liu, B.Z. Tang, Sci. Rep., 3 (2013) 1150.

[184] Y. Hong, L. Meng, S. Chen, C.W.T. Leung, L.-T. Da, M. Faisal, D.-A. Silva, J. Liu, J.W.Y. Lam, X. Huang, B.Z. Tang, J. Am. Chem. Soc., 134 (2012) 1680-1689.

[185] H. Shi, R.T.K. Kwok, J. Liu, B. Xing, B.Z. Tang, B. Liu, J. Am. Chem. Soc., 134 (2012) 17972-17981.

[186] W.Z. Yuan, Y. Gong, S. Chen, X.Y. Shen, J.W.Y. Lam, P. Lu, Y. Lu, Z. Wang, R. Hu, N. Xie, H.S. Kwok, Y. Zhang, J.Z. Sun, B.Z. Tang, Chem. Mater., 24 (2012) 1518-1528.

[187] P. Lu, J.W.Y. Lam, J. Liu, C.K.W. Jim, W. Yuan, N. Xie, Y. Zhong, Q. Hu, K.S. Wong, K.K.L. Cheuk, B.Z. Tang, Macromol. Rapid Commun., 31 (2010) 834-839.

[188] H. Wang, E. Zhao, J.W.Y. Lam, B.Z. Tang, Mater. Today, 18 (2015) 365-377.

[189] Y. Ren, J.W.Y. Lam, Y. Dong, B.Z. Tang, K.S. Wong, J. Phys. Chem. B, 109 (2005) 1135-1140.

[190] J. He, B. Xu, F. Chen, H. Xia, K. Li, L. Ye, W. Tian, J. Phys. Chem. C, 113 (2009) 9892-9899.

[191] Y. Li, F. Li, H. Zhang, Z. Xie, W. Xie, H. Xu, B. Li, F. Shen, L. Ye, M. Hanif, D. Ma, Y. Ma, Chem. Commun., (2007) 231-233.

[192] Y. Ren, Y. Dong, J.W.Y. Lam, B.Z. Tang, K.S. Wong, Chem. Phys. Lett., 402 (2005) 468-473.

[193] G. Liang, J.W.Y. Lam, W. Qin, J. Li, N. Xie, B.Z. Tang, Chem. Commun., 50 (2014) 1725-1727.

[194] B.-R. Gao, H.-Y. Wang, Y.-W. Hao, L.-M. Fu, H.-H. Fang, Y. Jiang, L. Wang, Q.-D. Chen, H. Xia, L.-Y. Pan, Y.-G. Ma, H.-B. Sun, J. Phys. Chem. B, 114 (2010) 128-134.

[195] J. Chen, C.C.W. Law, J.W.Y. Lam, Y. Dong, S.M.F. Lo, I.D. Williams, D. Zhu, B.Z. Tang, Chem. Mater., 15 (2003) 1535-1546.

[196] T. Li, S. He, J. Qu, H. Wu, S. Wu, Z. Zhao, A. Qin, R. Hu, B.Z. Tang, J. Mater. Chem. C, (2016).

[197] Z. Yang, W. Qin, N.L.C. Leung, M. Arseneault, J.W.Y. Lam, G. Liang, H.H.Y. Sung, I.D. Williams, B.Z. Tang, J. Mater. Chem. C, 4 (2016) 99-107.

[198] S. Gan, W. Luo, B. He, L. Chen, H. Nie, R. Hu, A. Qin, Z. Zhao, B.Z. Tang, J. Mater. Chem. C, (2016) (DOI: 10.1039/C5TC03588K).

[199] G. Scheibe, Kolloid-Zeitschrift, 82 1-14.

[200] F. Würthner, T.E. Kaiser, C.R. Saha-Möller, Angew. Chem., Int. Ed., 50 (2011) 3376-3410.

[201] S. Choi, J. Bouffard, Y. Kim, Chem. Sci., 5 (2014) 751-755.

[202] G. Sun, Y. Zhao, W. Liang, J. Chem. Theory Comput., 11 (2015) 2257-2267.

[203] J. Liu, J.W.Y. Lam, B.Z. Tang, J. Inorg. Organomet. Polym., 19 (2009) 249-285.

[204] Q. Zhang, H. Kuwabara, W.J. Potscavage, S. Huang, Y. Hatae, T. Shibata, C. Adachi, J. Am. Chem. Soc., 136 (2014) 18070-18081.

[205] A. Coskun, E. Deniz, E.U. Akkaya, Org. Lett., 7 (2005) 5187-5189.

[206] Z. Xu, Y. Xiao, X. Qian, J. Cui, D. Cui, Org. Lett., 7 (2005) 889-892.

[207] D. Majumdar, R. Sen, K. Bhattacharyya, S.P. Bhattacharyya, J. Photochem. Photobiol A: Chemistry, 73 (1993) 177-178.

.

[208] K. Rotkiewicz, K.H. Grellmann, Z.R. Grabowski, Chem. Phys. Lett., 19 (1973) 315-318.

[209] W. Rettig, J. Phys. Chem., 86 (1982) 1970-1976.

[210] P. Mazumdar, D. Das, G.P. Sahoo, G. Salgado-Moran, A. Misra, Phys. Chem. Chem. Phys., 17 (2015) 3343-3354.

[211] B. Chen, X. Sun, X. Li, H. Ågren, Y. Xie, Sens. Actuators, B, 199 (2014) 93-100.

[212] J. Catalán, C. Díaz, V. López, P. Pérez, R.M. Claramunt, Eur. J. Org. Chem., 1998 (1998) 1697-1704.

[213] W. Qin, D. Ding, J. Liu, W.Z. Yuan, Y. Hu, B. Liu, B.Z. Tang, Adv. Funct. Mater., 22 (2012) 771-779.

[214] W. Dong, J. Pina, Y. Pan, E. Preis, J.S. Seixas de Melo, U. Scherf, Polymer, 76 (2015) 173-181.

[215] A. Rananaware, D.D. La, S.V. Bhosale, RSC Adv., 5 (2015) 63130-63134.

[216] W. Rettig, Angew.Chem. Int.Ed., 25 (1986) 971-988.

[217] W. Rettig, M. Zander, Chem. Phys. Lett., 87 (1982) 229-234.

[218] W. Rettig, J. Mol. Struct., 84 (1982) 303-327.

[219] Z.R. Grabowski, K. Rotkiewicz, A. Siemiarczuk, J. Lumin., 18–19, Part 1 (1979) 420-424.

[220] N. Barooah, J. Mohanty, H. Pal, A.C. Bhasikuttan, Org. Biomol. Chem., 10 (2012) 5055-5062.

[221] P. Mahato, S. Saha, A. Das, J. Phys. Chem. C, 116 (2012) 17448-17457.

[222] D.P. Murale, H. Kim, W.S. Choi, D.G. Churchill, Org. Lett., 15 (2013) 3946-3949.

[223] V.S. Padalkar, S. Seki, Chem. Soc. Rev., 45 (2016) 169-202.

[224] J.E. Kwon, S.Y. Park, Adv. Mater., 23 (2011) 3615-3642.

[225] Y. Shigemitsu, T. Mutai, H. Houjou, K. Araki, J. Phys. Chem. A, 116 (2012) 12041-12048.

[226] T. Mutai, H. Shono, Y. Shigemitsu, K. Araki, Cryst.Eng.Comm., 16 (2014) 3890-3895.

[227] T. Mutai, H. Sawatani, T. Shida, H. Shono, K. Araki, J. Org. Chem., 78 (2013) 2482-2489.

[228] R. Hu, S. Li, Y. Zeng, J. Chen, S. Wang, Y. Li, G. Yang, Phys. Chem. Chem. Phys., 13 (2011) 2044-2051.

[229] R. Wei, P. Song, A. Tong, J. Phys. Chem. C, 117 (2013) 3467-3474.

[230] H. Honda, J. Kuwabara, T. Kanbara, J. Organomet. Chem., 772–773 (2014) 139-142.

[231] H. Honda, Y. Ogawa, J. Kuwabara, T. Kanbara, Eur. J. Inorg. Chem., 2014 (2014) 1865-1869.

[232] S. Liu, H. Sun, Y. Ma, S. Ye, X. Liu, X. Zhou, X. Mou, L. Wang, Q. Zhao, W. Huang, J. Mater. Chem., 22 (2012) 22167-22173.

[233] S. Yu-Lut Leung, V. Wing-Wah Yam, Chem. Sci., 4 (2013) 4228-4234.

[234] N. Komiya, M. Okada, K. Fukumoto, D. Jomori, T. Naota, J. Am. Chem. Soc., 133 (2011) 6493-6496.

[235] C.A. Strassert, C.-H. Chien, M.D. Galvez Lopez, D. Kourkoulos, D. Hertel, K. Meerholz, L. De Cola, Angew. Chem., Int. Ed., 50 (2011) 946-950.

[236] V.W.-W. Yam, K.M.-C. Wong, N. Zhu, J. Am. Chem. Soc., 124 (2002) 6506-6507.

[237] Y. Kubota, K. Kasatani, H. Takai, K. Funabiki, M. Matsui, Dalton Trans., 44 (2015) 3326-3341.

[238] S. Zhang, Y. Wang, F. Meng, C. Dai, Y. Cheng, C. Zhu, Chem. Commun., 51 (2015) 9014-9017.

[239] Q. Liu, X. Wang, H. Yan, Y. Wu, Z. Li, S. Gong, P. Liu, Z. Liu, J. Mater. Chem. C, 3 (2015) 2953-2959.

[240] X. Wang, Y. Wu, Q. Liu, Z. Li, H. Yan, C. Ji, J. Duan, Z. Liu, Chem. Commun., 51 (2015) 784-787.

[241] Y. Fu, F. Qiu, F. Zhang, Y. Mai, Y. Wang, S. Fu, R. Tang, X. Zhuang, X. Feng, Chem. Commun., 51 (2015) 5298-5301.

[242] R.S. Singh, R.K. Gupta, R.P. Paitandi, M. Dubey, G. Sharma, B. Koch, D.S. Pandey, Chem. Commun., 51 (2015) 9125-9128.

[243] W. Yan, G. Long, X. Yang, Y. Chen, New J. Chem., 38 (2014) 6088-6094.

[244] R. Hu, C.F.A. Gomez-Duran, J.W.Y. Lam, J.L. Belmonte-Vazquez, C. Deng, S. Chen, R. Ye, E. Pena-Cabrera, Y. Zhong, K.S. Wong, B.Z. Tang, Chem. Commun., 48 (2012) 10099-10101.

[245] R. Hu, E. Lager, A. Aguilar-Aguilar, J. Liu, J.W. Lam, H.H. Sung, I.D. Williams, Y. Zhong, K.S. Wong, E. Pena-Cabrera, J. Phys. Chem. C, 113 (2009) 15845-15853.

[246] G. He, B.D. Wiltshire, P. Choi, A. Savin, S. Sun, A. Mohammadpour, M.J. Ferguson, R. McDonald, S. Farsinezhad, A. Brown, Chem. Commun., 51 (2015) 5444-5447.

[247] X. Du, R. Fan, X. Wang, L. Qiang, P. Wang, S. Gao, H. Zhang, Y. Yang, Y. Wang, Cryst. Growth Des., 15 (2015) 2402-2412.

[248] M.A. Baldo, D.F. O'Brien, Y. You, A. Shoustikov, S. Sibley, M.E. Thompson, S.R. Forrest, Nature, 395 (1998) 151-154.

[249] J. Kuwabara, Y. Ogawa, A. Taketoshi, T. Kanbara, J. Organomet. Chem., 696 (2011) 1289-1293.

[250] R. Liu, M.-M. Huang, X.-X. Yao, H.-H. Li, F.-L. Yang, X.-L. Li, Inorg. Chim. Acta, 434 (2015) 172-180.

[251] X.-L. Xin, M. Chen, Y.-b. Ai, F.-l. Yang, X.-L. Li, F. Li, Inorg. Chem., 53 (2014) 2922-2931.

[252] Y. Chen, W.-C. Xu, J.-F. Kou, B.-L. Yu, X.-H. Wei, H. Chao, L.-N. Ji, Inorg. Chem. Commun., 13 (2010) 1140-1143.

[253] V. Sathish, A. Ramdass, Z.-Z. Lu, M. Velayudham, P. Thanasekaran, K.-L. Lu, S. Rajagopal, J. Phys. Chem. B, 117 (2013) 14358-14366.

[254] S. Ali Ezadyar, A.S. Kumbhar, A.A. Kumbhar, A. Khan, Polyhedron, 36 (2012) 45-55.

[255] E.Q. Procopio, M. Mauro, M. Panigati, D. Donghi, P. Mercandelli, A. Sironi, G. D'ALFONSO, L. De Cola, J. Am. Chem. Soc., 132 (2010) 14397-14399.

[256] B. Manimaran, P. Thanasekaran, T. Rajendran, R.-J. Lin, I.-J. Chang, G.-H. Lee, S.-M. Peng, S. Rajagopal, K.-L. Lu, Inorg. Chem., 41 (2002) 5323-5325.

[257] D.A. Evans, L.M. Lee, I. Vargas-Baca, A.H. Cowley, Dalton Trans., 44 (2015) 11984-11996.

[258] D.A. Evans, L.M. Lee, I. Vargas-Baca, A.H. Cowley, Organometallics, 34 (2015) 2422-2428.

[259] G. Zhang, Q. Chen, Y. Zhang, L. Kong, X. Tao, H. Lu, Y. Tian, J. Yang, Inorg. Chem. Commun., 46 (2014) 85-88.

[260] Y.-Z. Xie, G.-G. Shan, P. Li, Z.-Y. Zhou, Z.-M. Su, Dyes Pigm., 96 (2013) 467-474.

[261] B. Xu, Z. Chi, X. Zhang, H. Li, C. Chen, S. Liu, Y. Zhang, J. Xu, Chem. Commun., 47 (2011) 11080-11082.

[262] K. Fujisawa, S. Yamada, Y. Yanagi, Y. Yoshioka, A. Kiyohara, O. Tsutsumi, Sci. Rep., 5 (2015) 7934.

[263] Z. Chen, X. Han, J. Zhang, D. Wu, G.-A. Yu, J. Yin, S.H. Liu, RSC Adv., 5 (2015) 15341-15349.

[264] Z. Chen, J. Zhang, M. Song, J. Yin, G.-A. Yu, S.H. Liu, Chem. Commun., 51 (2015) 326-329.

[265] Z. Chen, D. Wu, X. Han, J. Liang, J. Yin, G.-A. Yu, S.H. Liu, Chem. Commun., 50 (2014) 11033-11035.

[266] J. Liang, Z. Chen, L. Xu, J. Wang, J. Yin, G.-A. Yu, Z.-N. Chen, S.H. Liu, J. Mater. Chem. C, 2 (2014) 2243-2250.

[267] J. Liang, Z. Chen, J. Yin, G.-A. Yu, S.H. Liu, Chem. Commun., 49 (2013) 3567-3569.

[268] Z. Luo, X. Yuan, Y. Yu, Q. Zhang, D.T. Leong, J.Y. Lee, J. Xie, J. Am. Chem. Soc., 134 (2012) 16662-16670.

[269] V. Sathish, A. Ramdass, P. Thanasekaran, K.-L. Lu, S. Rajagopal, J. Photochem. Photobiol., C, 23 (2015) 25-44.

[270] V.W.-W. Yam, K.M.-C. Wong, Chem. Commun., 47 (2011) 11579-11592.

[271] M. Panigati, M. Mauro, D. Donghi, P. Mercandelli, P. Mussini, L. De Cola, G. D'Alfonso, Coord. Chem. Rev., 256 (2012) 1621-1643.

[272] Q. Zhao, L. Li, F. Li, M. Yu, Z. Liu, T. Yi, C. Huang, Chem. Commun., (2008) 685-687.

[273] Y. You, H.S. Huh, K.S. Kim, S.W. Lee, D. Kim, S.Y. Park, Chem. Commun., (2008) 3998-4000.

[274] K. Huang, H. Wu, M. Shi, F. Li, T. Yi, C. Huang, Chem. Commun., (2009) 1243-1245.

[275] C.H. Shin, J.O. Huh, M.H. Lee, Y. Do, Dalton Trans., (2009) 6476-6479.

[276] C.H. Shin, J.O. Huh, S.J. Baek, S.K. Kim, M.H. Lee, Y. Do, Eur. J. Inorg. Chem., 2010 (2010) 3642-3651.

[277] G.-G. Shan, D.-X. Zhu, H.-B. Li, P. Li, Z.-M. Su, Y. Liao, Dalton Trans., 40 (2011) 2947-2953.

[278] G.-G. Shan, L.-Y. Zhang, H.-B. Li, S. Wang, D.-X. Zhu, P. Li, C.-G. Wang, Z.-M. Su, Y. Liao, Dalton Trans., 41 (2012) 523-530.

[279] Y. Wu, H.-Z. Sun, H.-T. Cao, H.-B. Li, G.-G. Shan, Y.-A. Duan, Y. Geng, Z.-M. Su, Y. Liao, Chem. Commun., 50 (2014) 10986-10989.

[280] G.-G. Shan, H.-B. Li, J.-S. Qin, D.-X. Zhu, Y. Liao, Z.-M. Su, Dalton Trans., 41 (2012) 9590-9593.

[281] X.-G. Hou, Y. Wu, H.-T. Cao, H.-Z. Sun, H.-B. Li, G.-G. Shan, Z.-M. Su, Chem. Commun., 50 (2014) 6031-6034.

[282] G.-G. Shan, H.-B. Li, H.-Z. Sun, D.-X. Zhu, H.-T. Cao, Z.-M. Su, J. Mater. Chem. C, 1 (2013) 1440-1449.

[283] H. Wu, T. Yang, Q. Zhao, J. Zhou, C. Li, F. Li, Dalton Trans., 40 (2011) 1969-1976.

[284] K.S. Bejoymohandas, T.M. George, S. Bhattacharya, S. Natarajan, M.L.P. Reddy, J. Mater. Chem. C, 2 (2014) 515-523.

[285] G. Li, W. Guan, S. Du, D. Zhu, G. Shan, X. Zhu, L. Yan, Z. Su, M.R. Bryce, A.P. Monkman, Chem. Commun., 51 (2015) 16924-16927.

[286] G. Li, X. Ren, G. Shan, W. Che, D. Zhu, L. Yan, Z. Su, M.R. Bryce, Chem. Commun., 51 (2015) 13036-13039.

[287] Y. Chen, L. Qiao, B. Yu, G. Li, C. Liu, L. Ji, H. Chao, Chem. Commun., 49 (2013) 11095-11097.

[288] N. Zhao, Y.-H. Wu, J. Luo, L.-X. Shi, Z.-N. Chen, Analyst, 138 (2013) 894-900.

[289] J.R. Lakowicz, Anal. Biochem. 298 (2001) 1-24.

[290] F. Tam, G.P. Goodrich, B.R. Johnson, N.J. Halas, Nano Letters, 7 (2007) 496-501.

[291] M. Iosin, P. Baldeck, S. Astilean, Nuclear Instruments and Methods in Physics Research Section B: Beam Interactions with Materials and Atoms, 267 (2009) 403-405.

[292] J.S. Becker, M. Zoriy, A. Matusch, B. Wu, D. Salber, C. Palm, J.S. Becker, Mass Spectrom. Rev., 29 (2010) 156-175.

[293] F. Zhang, G.B. Braun, Y. Shi, Y. Zhang, X. Sun, N.O. Reich, D. Zhao, G. Stucky, J. Am. Chem. Soc., 132 (2010) 2850-2851.

[294] Q. Liu, Y. Sun, T. Yang, W. Feng, C. Li, F. Li, J. Am. Chem. Soc., 133 (2011) 17122-17125.

[295] L. Raszeja, A. Maghnouj, S. Hahn, N. Metzler-Nolte, Chem. Bio. Chem, 12 (2011) 371-376.

[296] J. Rao, A. Dragulescu-Andrasi, H. Yao, Curr. Opin. Biotechnol., 18 (2007) 17-25.

[297] C.P. Montgomery, B.S. Murray, E.J. New, R. Pal, D. Parker, Acc. Chem. Res., 42 (2009) 925-937.

[298] K. Aslan, I. Gryczynski, J. Malicka, E. Matveeva, J.R. Lakowicz, C.D. Geddes, Curr. Opin. Biotechnol., 16 (2005) 55-62.

[299] O. Stranik, H.M. McEvoy, C. McDonagh, B.D. MacCraith, Sens. Actuators, B, 107 (2005) 148-153.

[300] M. Fernandez-Suarez, A.Y. Ting, Nat. Rev. Mol. Cell. Biol., 9 (2008) 929-943.

[301] Y. Chen, R. Guan, C. Zhang, J. Huang, L. Ji, H. Chao, Coord. Chem. Rev., 310 (2016) 16-40.

[302] J. Liu, Y. Liu, Q. Liu, C. Li, L. Sun, F. Li, J. Am. Chem. Soc., 133 (2011) 15276-15279.

[303] J.A.G. Williams, Chem. Soc. Rev., 38 (2009) 1783-1801.

[304] U. Schatzschneider, Inorg. Chim. Acta, 374 (2011) 19-23.

[305] Q. Liu, J. Peng, L. Sun, F. Li, ACS Nano, 5 (2011) 8040-8048.

[306] U. Schatzschneider, Chem. Eur. J., 13 (2007) 380-395.

[307] F. Bellia, D. La Mendola, C. Pedone, E. Rizzarelli, M. Saviano, G. Vecchio, Chem. Soc. Rev., 38 (2009) 2756-2781.

[308] Z. Qin, J.A. Caruso, B. Lai, A. Matusch, J.S. Becker, Metallomics, 3 (2011) 28-37.

[309] P.-T. Chou, Y. Chi, Chem. Eur. J., 13 (2007) 380-395.

[310] S.W. Botchway, M. Charnley, J. W. Haycock, A.W. Parker, D.L. Rochester, J.A. Weinstein, J.A.G. Williams, Proc. Natl. Acad. Sci., 105 (2008) 16071-16076.

[311] W. Tan, Q. Zhang, J. Zhang, H. Tian, Org. Lett., 11 (2009) 161-164.

[312] D. Li, X. Tian, A. Wang, L. Guan, J. Zheng, F. Li, S. Li, H. Zhou, J. Wu, Y. Tian, Chem. Sci., (2016).

[313] H. Kobayashi, M. Ogawa, R. Alford, P.L. Choyke, Y. Urano, Chem. Rev., 110 (2010) 2620-2640.

[314] M. Yu, Q. Zhao, L. Shi, F. Li, Z. Zhou, H. Yang, T. Yi, C. Huang, Chem. Commun., (2008) 2115-2117.

[315] K.K.-W. Lo, K.Y. Zhang, RSC Adv., 2 (2012) 12069-12083.

[316] Z. Zhou, D. Li, H. Yang, Y. Zhu, S. Yang, Dalton Trans., 40 (2011) 11941-11944.

[317] C.-W. Lai, Y.-H. Wang, C.-H. Lai, M.-J. Yang, C.-Y. Chen, P.-T. Chou, C.-S. Chan, Y. Chi, Y.-C. Chen, J.-K. Hsiao, Small, 4 (2008) 218-224.

[318] S.P.-Y. Li, T.S.-M. Tang, K.S.-M. Yiu, K.K.-W. Lo, Chem. Eur. J., 18 (2012) 13342-13354.

[319] V. Fernandez-Moreira, F.L. Thorp-Greenwood, M.P. Coogan, Chem. Commun., 46 (2010) 186-202.

[320] K.Y. Zhang, S.P.-Y. Li, N. Zhu, I.W.-S. Or, M.S.-H. Cheung, Y.-W. Lam, K.K.-W. Lo, Inorg. Chem., 49 (2010) 2530-2540.

[321] K.K.-W. Lo, S.-K. Leung, C.-Y. Pan, Inorg. Chim. Acta, 380 (2012) 343-349.

[322] P.-K. Lee, H.-W. Liu, S.-M. Yiu, M.-W. Louie, K.K.-W. Lo, Dalton Trans., 40 (2011) 2180-2189.

[323] C. Li, M. Yu, Y. Sun, Y. Wu, C. Huang, F. Li, J. Am. Chem. Soc., 133 (2011) 11231-11239.

[324] T.S. Snowden, E.V. Anslyn, Curr. Opin. Chem. Biol., 3 (1999) 740-746.

[325] J.-S. Wu, W.-M. Liu, X.-Q. Zhuang, F. Wang, P.-F. Wang, S.-L. Tao, X.-H. Zhang, S.-K. Wu, S.-T. Lee, Org. Lett., 9 (2007) 33-36.

[326] M.H. Lee, J.S. Kim, J.L. Sessler, Chem. Soc. Rev., 44 (2015) 4185-4191.

[327] H. Zhu, J. Fan, B. Wang, X. Peng, Chem. Soc. Rev., 44 (2015) 4337-4366.

[328] Y. Ding, Y. Tang, W. Zhu, Y. Xie, Chem. Soc. Rev., 44 (2015) 1101-1112.

[329] Z. Zhang, D.S. Kim, C.-Y. Lin, H. Zhang, A.D. Lammer, V.M. Lynch, I. Popov, O.Š. Miljanić, E.V. Anslyn, J.L. Sessler, J. Am. Chem. Soc., 137 (2015) 7769-7774.

[330] M. Lee, S. Jo, D. Lee, Z. Xu, J. Yoon, Dyes Pigm., 120 (2015) 288-292.

[331] A. Bettoschi, A. Bencini, D. Berti, C. Caltagirone, L. Conti, D. Demurtas, C. Giorgi, F. Isaia, V. Lippolis, M. Mamusa, S. Murgia, RSC Adv., 5 (2015) 37385-37391.

[332] V.K. Gupta, N. Mergu, L.K. Kumawat, A.K. Singh, Talanta, 144 (2015) 80-89.

[333] S. Prabhu, S. Saravanamoorthy, M. Ashok, S. Velmathi, J. Lumin., 132 (2012) 979-986.

[334] S. Aoki, D. Kagata, M. Shiro, K. Takeda, E. Kimura, J. Am. Chem. Soc., 126 (2004) 13377-13390.

[335] Y.-K. Yang, K.-J. Yook, J. Tae, J. Am. Chem. Soc., 127 (2005) 16760-16761.

[336] A.W. Czarnik, Acc. Chem. Res., 27 (1994) 302-308.

[337] H.N. Kim, M.H. Lee, H.J. Kim, J.S. Kim, J. Yoon, Chem. Soc. Rev., 37 (2008) 1465-1472.

[338] C. Wang, K.M.-C. Wong, Inorg. Chem., 50 (2011) 5333-5335.

[339] V. Guerchais, J.-L. Fillaut, Coord. Chem. Rev., 255 (2011) 2448-2457.

[340] Z. Zhang, S. Lu, C. Sha, D. Xu, Sens. Actuators, B, 208 (2015) 258-266.

[341] Y. Long, J. Zhou, M.-P. Yang, B.-Q. Yang, Chin. Chem. Lett.

[342] Q. Zhao, F. Li, C. Huang, Chem. Soc. Rev., 39 (2010) 3007-3030.

[343] N.K. Hien, N.C. Bao, N.T. Ai Nhung, N.T. Trung, P.C. Nam, T. Duong, J.S. Kim, D.T. Quang, Dyes Pigm., 116 (2015) 89-96.

[344] M. Wang, K.-H. Leung, S. Lin, D.S.-H. Chan, D.W.J. Kwong, C.-H. Leung, D.-L. Ma, Sci. Rep., 4 (2014) 6794.

[345] N. Zhao, Y.-H. Wu, L.-X. Shi, Q.-P. Lin, Z.-N. Chen, Dalton Trans., 39 (2010) 8288-8295.

[346] H. Chen, Q. Zhao, Y. Wu, F. Li, H. Yang, T. Yi, C. Huang, Inorg. Chem., 46 (2007) 11075-11081.

[347] L. Xiong, Q. Zhao, H. Chen, Y. Wu, Z. Dong, Z. Zhou, F. Li, Inorg. Chem., 49 (2010) 6402-6408.

[348] Q. Zhao, F. Li, S. Liu, M. Yu, Z. Liu, T. Yi, C. Huang, Inorg. Chem., 47 (2008) 9256-9264.

[349] Q. Zhao, T. Cao, F. Li, X. Li, H. Jing, T. Yi, C. Huang, Organometallics, 26 (2007) 2077-2081.

[350] M.-L. Ho, Y.-M. Cheng, L.-C. Wu, P.-T. Chou, G.-H. Lee, F.-C. Hsu, Y. Chi, Polyhedron, 26 (2007) 4886-4892.

[351] M.-L. Ho, F.-M. Hwang, P.-N. Chen, Y.-H. Hu, Y.-M. Cheng, K.-S. Chen, G.-H. Lee, Y. Chi, P.-T. Chou, Organic & Biomolecular Chemistry, 4 (2006) 98-103.

[352] Q. Zhao, S. Liu, M. Shi, F. Li, H. Jing, T. Yi, C. Huang, Organometallics, 26 (2007) 5922-5930.

[353] M. Schmittel, H. Lin, Inorg. Chem., 46 (2007) 9139-9145.

[354] Q. Zhao, S. Liu, F. Li, T. Yi, C. Huang, Dalton Trans., (2008) 3836-3840.

[355] Y. Wu, H. Jing, Z. Dong, Q. Zhao, H. Wu, F. Li, Inorg. Chem., 50 (2011) 7412-7420.

[356] H.-F. Shi, S.-J. Liu, H.-B. Sun, W.-J. Xu, Z.-F. An, J. Chen, S. Sun, X.-M. Lu, Q. Zhao, W. Huang, Chem. Eur. J., 16 (2010) 12158-12167.

[357] H. Yang, J. Qian, L. Li, Z. Zhou, D. Li, H. Wu, S. Yang, Inorg. Chim. Acta, 363 (2010) 1755-1759.

[358] F. Lu, M. Yamamura, T. Nabeshima, Dalton Trans., 42 (2013) 12093-12100.

[359] F. Yan, Q. Mei, L. Wang, B. Tong, Z. Xu, J. Weng, L. Wang, W. Huang, Inorganic Chemistry Communications, 22 (2012) 178-181.

[360] B. Tong, Y. Zhang, Z. Han, D. Chen, Q.-F. Zhang, Inorg. Chem.Commun., 28 (2013) 31-36.

[361] Y. Liu, M. Li, Q. Zhao, H. Wu, K. Huang, F. Li, Inorg. Chem., 50 (2011) 5969-5977.

[362] R.G. Pearson, J. Am. Chem. Soc., 85 (1963) 3533-3539.

[363] H. Zeng, F. Yu, J. Dai, H. Sun, Z. Lu, M. Li, Q. Jiang, Y. Huang, Dalton Trans., 41 (2012) 4878-4883.

[364] X. Zhang, Z. Chi, Y. Zhang, S. Liu, J. Xu, J. Mater. Chem. C, 1 (2013) 3376-3390.

[365] X. Luo, J. Li, C. Li, L. Heng, Y.Q. Dong, Z. Liu, Z. Bo, B.Z. Tang, Adv. Mater., 23 (2011) 3261-3265.

[366] J. Ni, X. Zhang, N. Qiu, Y.-H. Wu, L.-Y. Zhang, J. Zhang, Z.-N. Chen, Inorg. Chem., 50 (2011) 9090-9096.

[367] X. Zhang, J.-Y. Wang, J. Ni, L.-Y. Zhang, Z.-N. Chen, Inorg. Chem., 51 (2012) 5569-5579.

[368] G.-G. Shan, H.-B. Li, D.-X. Zhu, Z.-M. Su, Y. Liao, J. Mater. Chem., 22 (2012) 12736-12744.

[369] Y. Sagara, T. Mutai, I. Yoshikawa, K. Araki, J. Am. Chem. Soc., 129 (2007) 1520-1521.

[370] J. Kunzelman, M. Kinami, B.R. Crenshaw, J.D. Protasiewicz, C. Weder, Adv. Mater., 20 (2008) 119-122.

[371] Y. Sagara, T. Kato, Angew. Chem., Int. Ed., 47 (2008) 5175-5178.

[372] M. Irie, T. Fukaminato, T. Sasaki, N. Tamai, T. Kawai, Nature, 420 (2002) 759-760.

[373] A. Kishimura, T. Yamashita, K. Yamaguchi, T. Aida, Nat. Mater., 4 (2005) 546-549.

[374] T. Mutai, H. Satou, K. Araki, Nat. Mater., 4 (2005) 685-687.

[375] Y. Sagara, T. Kato, Nat. Chem., 1 (2009) 605-610.

[376] X. Hou, C. Ke, C.J. Bruns, P. R. McGonigal, R.B. Pettman, J. F. Stoddart, Nat. Commun., 6 (2015).

[377] S. Yagai, S. Okamura, Y. Nakano, M. Yamauchi, K. Kishikawa, T. Karatsu, A. Kitamura, A. Ueno, D. Kuzuhara, H. Yamada, T. Seki, H. Ito, Nat. Commun., 5 (2014).

[378] M. Kinami, B.R. Crenshaw, C. Weder, Chem. Mater., 18 (2006) 946-955.

[379] X. Zhang, B. Li, Z.-H. Chen, Z.-N. Chen, J. Mater. Chem., 22 (2012) 11427-11441.

[380] T. Abe, K. Shinozaki, Inorg. Chem., 44 (2005) 849-851.

[381] E.A. Baldauff, J.M. Buriak, Chem. Commun., (2004) 2028-2029.

[382] J. Ni, L.-Y. Zhang, H.-M. Wen, Z.-N. Chen, Chem. Commun., (2009) 3801-3803.

[383] J. Ni, Y.-H. Wu, X. Zhang, B. Li, L.-Y. Zhang, Z.-N. Chen, Inorg. Chem., 48 (2009) 10202-10210.

[384] Z.M. Hudson, C. Sun, K.J. Harris, B.E.G. Lucier, R.W. Schurko, S. Wang, Inorg. Chem., 50 (2011) 3447-3457.

[385] L. Flamigni, A. Barbieri, C. Sabatini, B. Ventura, F. Barigelletti, Photochemistry and Photophysics of Coordination Compounds: Iridium, in: V. Balzani, S. Campagna (Eds.) Photochemistry and Photophysics of Coordination Compounds II, Springer Berlin Heidelberg, 2007, pp. 143-203.

[386] L. Maini, D. Braga, P.P. Mazzeo, B. Ventura, Dalton Trans., 41 (2012) 531-539.

[387] S. Mizukami, H. Houjou, K. Sugaya, E. Koyama, H. Tokuhisa, T. Sasaki, M. Kanesato, Chem. Mater., 17 (2005) 50-56.

[388] E.J. Fernández, J.M. López-de-Luzuriaga, M. Monge, M. Montiel, M.E. Olmos, J. Pérez, A. Laguna, F. Mendizabal, A.A. Mohamed, J.P. Fackler, Inorg. Chem., 43 (2004) 3573-3581.

[389] M.A. Rawashdeh-Omary, M.D. Rashdan, S. Dharanipathi, O. Elbjeirami, P. Ramesh, H.V.R. Dias, Chem. Commun., 47 (2011) 1160-1162.

[390] L.G. Beauvais, M.P. Shores, J.R. Long, J. Am. Chem. Soc., 122 (2000) 2763-2772.

[391] S. Cho, M.W. Mara, X. Wang, J.V. Lockard, A.A. Rachford, F.N. Castellano, L.X. Chen, J. Phys. Chem. A, 115 (2011) 3990-3996.

[392] S.-W. Lai, H.-W. Lam, W. Lu, K.-K. Cheung, C.-M. Che, Organometallics, 21 (2002) 226-234.

[393] Z. Abedin-Siddique, T. Ohno, K. Nozaki, T. Tsubomura, Inorg. Chem., 43 (2004) 663-673.

[394] J.N. Demas, B.A. DeGraff, Anal. Chem., 63 (1991) 829A-837A.

[395] S. Huang, B. Yang, J. Zhong, H. Zhang, Synthetic Metals, 205 (2015) 222-227.

[396] Z. Liu, Z. Bian, J. Bian, Z. Li, D. Nie, C. Huang, Inorg. Chem., 47 (2008) 8025-8030.

2.1 Materials

2.1.1 Used Reagents

Iridium(III) chloride hydrate, 2-phenyl pyridine, 2-chloro pyridine, 2-bromo pyridine, 2,4-difluoroboronic acid, Dibenzo[f,h]quinoline, benzo[h]quinoline, benzaldehyde, Sodium carbonate, triphenylamine, tris(4-(trifluoromethyl)phenyl)phosphine, methyldiphenylphosphine, dimethylphenylphosphine, palladium(0)tetrakistriphenylphosphine, triphenylphosphine, picolinic acid, acetylacetone, 1,2-Bis(diphenylphosphino)ethane, *cis*-1,2-Bis(diphenylphosphino)ethylene, 1,10-phenanthroline, Bis(diphenylphosphino)propane, potassiumhexafluorophosphates, pyridin-2-amine, pyrimidin-2-amine, 5 methylpyridin-2-amine, benzaldehyde, triphenylamine, 2,2'-bipyridine Phosphorous oxychlorid, sodium borohydride, potassium hexafluorophosphate, sodium dicyanamide, 4-(2-pyridyl)benzaldehyde, triphenylphosphine and 2-ethoxyethanol were purchased from Sigma Aldrich Chemical Company.

Trifluoroacetic acid, acetic acid, hydrochloric acid, trifluoro methane sulphonic acid and triethylamine were procured from Merck Company.

The UV-Vis grade solvents (DCM, hexane, ethylacetate, toluene, 1, 4-dioxane, chloroform, acetone and acetinitrile all the names of the solvents) were procured from Merck Company.

2-(naphthalen-2-yl) pyridine and 2-(naphthalen-5-yl) pyridine were synthesized by following the literature [1], PEG(1000)-b-PLA(5000) diblock polymer (MW 6000) was purchased from Polysciences Inc., 2-(2,4-Difluorophenyl) pyridine (F_2ppy) and $[Ir(F_2ppy)_2Cl]_2$ bridge complex were prepared according to a reported procedure [2].

Benzoic acid, 3,5 dinitro toluene, 1,3 dintro benzene, 2,5 dintro phenol, 2,4,6-trinitrophenol and metal nitrate salts were procured from Merck Company.

NaOH, Triethyl amine, Trifluoro acetic acid and Acetic Buffer solutions (pH 1-pH 14) have been prepared by using KCl-HCl, KH_2PO_4-HCl, KH_2PO_4-NaOH and NaOH. For selectivity of anions, different metal salts ($Na_2S_2O_3$, KI, KBr, KF, KCl, $NaNO_3$ etc) were procured from SD fine.

2.2 Methods

2.2.1 Fabrication of thin-film on thin glass substrate for photoluminescence (PL) measurement

The 10^{-3}M solution of irdium complex in THF were prepared. 2-3 drops of the solution were placed on thin glass substrate (2x2cm^2) and the solvent was allowed to evaporate slowly.

2.2.2 Sample preparation to investigate the aggregation induced emission (AIE) property

The concentration of the each complexes were prepared in the range of 10^{-5} -10^{-6} M. The different samples (0-95%) were prepared by addition of different volume fractions of two solvents *e.g.* conc. of 0% water: 10^{-6}M of complex in 1ml THF (rest is 9 mL THF); conc. of 30% water: 10^{-6}M of complex in 1ml (rest is 6 ml THF and 3 ml of Water), conc. of 60% water: 10^{-6}M of complex in 1ml (rest is 3 ml THF and 6 ml water), conc. of 90% water: 10^{-6}M of complex in 1ml (rest is 9 ml of water).

2.2.3 Fluorescence quantum yield calculations

The fluorescence quantum yield (ϕ) of the compounds were calculated with reference to quinine sulphate [3] (ϕ = 0.55) in 0.1N H_2SO_4, the commonly used fluorescence standard. Fluorescence spectra were recorded for solutions of absorbance less than 0.1 at the excitation wavelength. Generally, the longest wavelength band maximum was chosen for excitation. In case of a system with an isosbestic point in the absorption spectra, the excitation was carried out at isosbestic wavelength. Quantum yield of the samples were calculated using the Equation 2.1.

$$\phi_{unknown} = \phi_{standard} \times \frac{F_{unknown}}{F_{standard}} \times \frac{A_{standard}}{A_{unknown}} \qquad (2.1)$$

ϕ is fluorescence quantum yield,

F is area under the curve of corrected fluorescence spectra,

A is absorbance at excitation wavelength.

2.2.4 Luminescence quenching titration study in THF: Water medium

Luminescence quenching titration studies in THF: Water (1:9, v/v) were carried out with gradual increasing PA concentration (5μM, 10 μM and so on) in a micro quartz cuvette keeping the total volume 1.5 mL. For each addition, at least three fluorescence spectrums were recorded at 298K to obtain concordant value. The λ_{ex} was chosen 385 nm and 400 nm for **6** and **13**, respectively with 3 nm slit width.

2.2.5 Experimental procedure for detection limit calculations

To determine the Signal/Noise ratio, the emission intensity of both complexes in THF : Water (1:9, v/v) without PA was measured by 10 times and the standard deviation of blank measurements was determined.

The detection limit is then calculated with the following equation.

Detection limit = 3σ/m; where σ is the standard deviation of blank measurements, m is the slope between the plot of PL intensity versus sample concentration [4-7].

2.3 Instrumentation

2.3.1 UV-Visible spectrophotometer

Absorption spectroscopy is the most widely used spectroscopic tools which provide useful information about the sample under studied. It refers to spectroscopic tool that measures the absorption of radiation, as a function of frequency or wavelength, due to its interaction with a sample. The environmental effects alter the relative energy of ground and excited states, and this alteration causes spectral shifts. The absorbance (A) of an absorber (concentration C) having a molar extinction coefficient ε_λ at wavelength λ is given by the Equation 2.2.

$$A = log\left(\frac{I_0}{I}\right) = \varepsilon_\lambda Cl \qquad (2.2)$$

where A is absorbance (optical density), I_0 and I represent the intensity of the incident and transmitted light, respectively, C is the concentration of the light absorbing species and l is the path length of the light absorbing medium. A matched pair of 1 cm quartz cuvettes (Hellma, 1 cm light path, capacity 3.5 ml, Model: 100-QS) was used for absorption measurements.

UV-Vis absorbance spectra were recorded using a Simadzu Spectrophotometer (model UV-1800 and 2550).

2.3.2 Steady-state spectrofluorimeter

Fluorescence measurements were performed using a Horiba Jobin Yvon Fluoromax-4 scanning spectrofluorimeter and Simadzu (A40195003382SA). The spectrofluorimeter irradiates a sample with excitation light and measures the fluorescence emitted from the irradiated sample to perform a qualitative or quantitative analysis. The block diagram of the instrument is shown in Figure 2.1. The brief description of its components is given below:

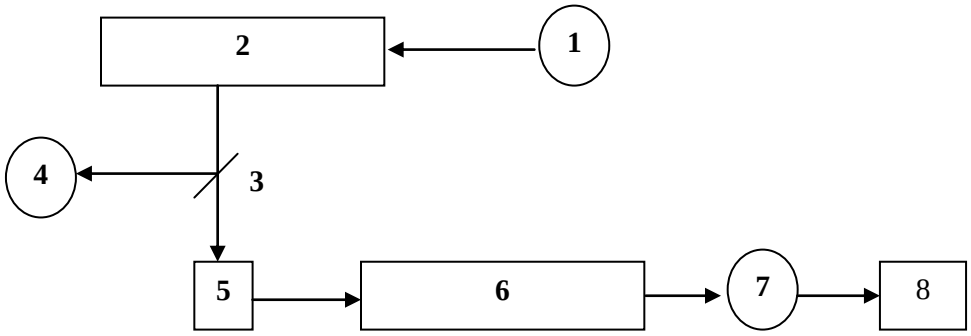

(1) 1905-OFR 150-W Xenon Lamp (2) Excitation monochromator (3) Beam splitter
(4) Monitor side photomultiplier tube (5) Cell holder (6) Emission monochromator
(7) Fluorescence side photomultiplier tube (8) Recorder

Figure Error! No text of specified style in document**..1** Block diagram of a steady-state spectrofluorimeter.

This instrument is equipped with the light source of 1905-OFR 150-W Xenon lamp. The lamp housing is provided with ozone self-decomposition. This instrument contains Czerny-Turner monochromators for excitation and emission. The important part of monochromator is a reflection grating. A grating disperses the incident light by means of its vertical grooves. The gratings in this instrument contain 1200 grooves mm^{-1}, and are blazed at 330 nm (excitation) and 500 nm (emission). Blazing is etching the grooves at a particular angle, to optimize the grating's

reflectivity in a particular spectral region. This instrument uses a direct drive for each grating, to scan the spectrum at up to 200 nm s^{-1}, with accuracy better than 0.5 nm, and repeatability of 0.3 nm. The scan range of this instrument is 240-850 nm. The cell holder holds a cell filled with sample.

The emission monochromator selectively receives fluorescence emitted from the sample and the photomultiplier tube (PMT) measures the intensity of the fluorescence. The monochromator has a diffraction grating whose size is the same as that of the excitation monochromator to collect the greatest possible amount of light.

The detector in this system consists of photomultiplier tube for both photometry and monitor sides. Generally, the Xenon lamps used on spectrofluorimeter are characterized by very high emission intensity and an uninterrupted radiation spectrum. However, their tendency to unstable light emission will result in greater signal noise if no countermeasure is incorporated. In addition, the non-uniformity in the radiation spectrum of the Xenon lamp and in the spectral sensitivity characteristics of the photomultiplier tube (these criteria are generally called instrument functions) causes distortion in the spectrum. To overcome these factors, the photomultiplier tube monitors a portion of excitation light and feeds the resultant signal back to the photomultiplier tube for fluorescence scanning. This scheme is called the light-source compensation system. The slits widths are adjustable from the computer in units of bandpass or millimeters. This preserves maximum resolution and instant reproducibility. The steady-state fluorescence anisotropy measurements were performed with the same steady-state spectrofluorimeter fitted with a polarizer attachment (105UV polarizers), manufactured by POLACOAT Co., USA. The measurement was obtained by placing one polarizer on each of excitation and emission sides. The sample was taken in a Quartz cuvette (Hellma, 1 cm light path, capacity 3.5 ml, Model: 101-QS) with four walls transparent to measure the excitation and emission spectra.

2.3.3 Other instruments

Cyclic voltammetry (CV) measurements were recorded on a Potentiostat/Galvanostate Model 263 A. The platinum, glassy carbon and Ag/AgCl electrodes were used as counter, working and reference electrodes, respectively and the scan rate was maintained to 50 mVs^{-1}.

The complexes were dissolved in acetonitrile (10 mL) and 0.1 M lithium perchlorate ($LiClO_4$) (100 Mg) was added to the solution (used as the supporting electrolyte). The whole experiment was conducted under inert atmosphere.

The dynamic light scattering (DLS) measurements of the aggregates of complexes were carried out in Zeta Sizer, model Nano ZS (ZEN 3600, Malvern Instruments, UK). Samples were filtered prior to the measurements with 0.22-µM filter (Durapore, PVDF). The wavelength of the laser light was 6328 Å, and the scattering angle was 173^o. At least five set of measurements were carried out for each sample at ambient conditions. The scattering intensity signal of the sample is passed to a digital signal processing board called a correlator, which compares the scattering intensity at successive time intervals to derive the rate at which the intensity is varying. This correlator information is then passed to a computer and the data was analyzed with the Zetasizer software to derive size information.

The size and shape of the nanoparticles were measured by scanning electron microscopy (SEM) using a JEOL JSM-6700F FESEM instrument.

TEM images were obtained using a JEOL-2100F TEM at MNIT Jaipur. Samples were prepared by placing 3-4 drops of the appropriate nanoparticle solution on a 300-mesh, carbon-coated Cu grid (EM sciences) and allowing the liquid to evaporate in air. The particle size distribution was based on 50 randomly selected particles. EDS analysis was carried out with the same instrument for TEM and a selected area was used for analysis.

The FT-IR spectra were recorded in ABB Boman MB 3000 instrument, FTIR Simadzu (IR prestige-21) and Perkin Elmer Spectrum 100. The complexes were mixed with dry potassium bromide (KBr) powder and pellets were prepared. The pellets have been used to record FT-IR.

^1H NMR, ^{13}C NMR, ^{19}F and ^{31}P NMR spectra were recorded in a 400 MHz Brucker spectrometer using $CDCl_3$ as solvent and tetramethylsilane (TMS, $\delta = 0$ ppm for ^1H and ^{13}C NMR), Trifluoro acetic acid (CF_3COOH, $\delta = 0$ ppm for ^{19}F NMR) and phosphoric acid (H_3PO_4, $\delta = 0$ ppm for ^{31}P NMR) as internal standard.with a 400 MHz Brucker spectrometer instrument at IISER Mohali and BITS Pilani, Pilani campus.

The photoluminescence (PL) spectra were recorded on a spectrofluoro photometer flouromax-4 (0406C-0809) and

High-resolution MS (HRMS) were carried out with a (TOF MS ES^+ 1.38 eV) VG Analytical (70-S) spectrometer and Q-Tof micro mass spectrometer instrument at IISER Mohali

Time correlated single photon counting (TCSPC) spectra of the iridium complex in THF was obtained through exciting the sample with a picosecond diode laser (IBH Nanoled) using a Horiba Jobin Yvon IBH Fluorocube apparatus (IACS, Kolkata) and Spectrofluorometer FLS920-s Edinburgh (AIRF, JNU, New Delhi).

The solid state quantum yield of the thin film sample was measured using a calibrated integrating sphere in a Gemini Spectrophotometer (model Gemini 180) at IIT Kanpur and PTI QuantaMaster ^{TM} 400 in IACS Kolkata.

Luminescence images of HeLa cells and photostability of the aggregated iridium complex in water and encapsulated in PEG-PLA nanoparticles were performed by drop casting the sample solution on a glass slide and images were captured using an Olympus IX 81 microscope provided with a digital camera.

Microwave reactions were carried out in a CEM Discover (mode l908010). All the reactions were performed under nitrogen atmosphere and the progress of the reaction was monitored using thin-layer chromatography (TLC) plates (pre-coated with 0.20 mm silica gel).

Single crystal X-ray diffraction data for the compounds **1** and **2** were recorded on Bruker AXS KAPPA APEX-II CCD and Rigaku Mercury375/M CD (XtaLAB mini) diffractometer respectively by using graphite Monochromated Mo – K_α radiation at 100.0(1) K by using Oxford cryosystem. The data sets collected Bruker AXS KAPPA APEX-II Kappa were collected using Bruker APEX-II suit, data reduction and integration were performed by SAINT V7.685A12 (Bruker AXS, 2009) and absorption corrections and scaling was done using SADABS V2008/112 (Bruker AXS). The data sets, which were collected on XtaLAB mini diffractometer, were processed with Rigaku Crystal Clear suite 2.0. The crystal structures were solved by using SHELXS2013 and were refined using SHELXL2013 available within Olex2. All the hydrogen atoms have been geometrically fixed and refined using the riding model except the hydride anion, co-ordinating with Ir, which has been located from the difference Fourier map and were refined isotropically. All the diagrams have been generated using Mercury 3.1.1. Geometric calculations have been done using PARST and PLATON. Powder X-ray diffraction (PXRD) were measured by using Rigaku miniflex II desktop X-ray diffractometer.

2.4 References

[1] C. Xu, Z.-Q. Wang, X.-M. Dong, X.-Q. Hao, X.-M. Zhao, B.-M. Ji, M.-P. Song, Inorg. Chim. Acta, 373 (2011) 306-310.

[2] A.F. Rausch, M.E. Thompson, H. Yersin, Inorg. Chem., 48 (2009) 1928-1937.

[3] G.G. Guilbault, Practical fluorescence, Marcel Dekker Inc., New York, 1973.

[4] M.-H. Yang, P. Thirupathi, K.-H. Lee, Org. Lett., 13 (2011) 5028-5031.

[5] D. En, Y. Guo, B.-T. Chen, B. Dong, M.-J. Peng, RSC Adv., 4 (2014) 248-253.

[6] L.N. Neupane, J.M. Kim, C.R. Lohani, K.-H. Lee, J. Mater. Chem., 22 (2012) 4003-4008.

[7] S. Kaur, V. Bhalla, V. Vij, M. Kumar, J. Mater. Chem. C, 2 (2014) 3936-3941.

Chapter III

Syntheses of 'Aggregation Induced Emission 'Active Cyclometalated Iridium(III) Complexes and the Tuning of their Emission Wavelength in a Common Framework: Micellar Encapsulated Probe in Cellular Imaging and sensitive explosive detection

3.1 Introduction

After successful achievement in field of 'Aggregation Induced Emission (AIE)' active organic molecules (which are basically fluorescent in nature), the AIE property has been attempted to introduced into cyclometalated complexes of iridium(III), a well-known and efficient class of triplet emitting materials, for obtaining better quantum efficiency and their applicability in various solid state applications [1-14]. In most of these cases, the AIE property arises due to large amplitude conformational changes of some part of the molecule that are hindered when other molecules become closer in the solid or aggregated state [15-19]. For the development of new applications, it would be extremely interesting to design a particular AIE active system where fine tuning of the emission wavelength could become possible. With this idea in mind, we have chosen a six coordinated iridium(III) system where two different functionalities, chromophoric cyclometalated ligands and more or less freely rotating non-planar triaryl phosphines, were connected to a single iridium(III) centre. The rotating unit are expected to show restricted intramolecular rotation (RIR) [20] in the solid state, triggering AIE activity in these compounds. On systematic variation of the cyclometalated ligand, tuning of the emission wavelength throughout the visible range becomes possible. This chapter presents a series of cyclometalated iridium(III) complexes (**1-13**) have been synthesized that emit light throughout the visible range and, more interestingly, all these complexes have been found to be AIE active.

These metal complexes are soluble in organic solvents but insoluble in water and if water is added to their solution they start aggregating along with the appearance of highly intense emission [21]. However, poor water solubility and macroscopic aggregate formation in presence of water limits their practical application. For example, water soluble materials are necessary for biological labeling applications and in vitro / in vivo imaging application require good colloidal stability of the material under physicological condition along with size preferably < 200 nm [22, 23]. Here, a simple technique has been employed for transferring these insoluble materials into water and used them as a bio-imaging probe.

Today's society has a great threat from explosives through terrorist activities. The convenient way to detect such explosive materials poses a great challenge to the scientists to save human life and environments. The nitro aromatics like trinitrotoluene (TNT), 2,4-dinitro phenol (2,4 DNP), picric acid (PA) etc. are well known explosive

materials which are normally employed as tools in terrorist activities [24-30]. In addition, PA is known as a notorious environmental polluting agent [31]. Many detection techniques like Raman spectroscopy, cyclic voltammetry, gas chromatography, mass spectrometry, ion mobility spectrometry, electrochemical sensing, photoluminescence (PL) spectroscopy and many more have been used to detect such kind of explosives [32-37]. Among these reported techniques, PL based technique offers better sensitivity, shorter response time and economically viable [38-41].

Similar electron affinity [42] of nitro aromatics appeals the scientific community to develop materials for highly sensitive and selective detection. As nitro aromatics by nature are electron deficient species, PL sensors developed with metal complexes / organic molecules worked on the principle of photo-induced electron transfer (PET) from donor to electron poor nitro aromatics (acceptor molecule) and subsequently, results a PL quenching [43-46]. Thus, the linkage of electron rich moiety with the donor will facilitate the electron transfer to the acceptor molecule. Apart from being Lewis acidic electron acceptor nature, nitro phenolic aromatics (picric acid) functions as Bronsted acidic proton donor. In such cases, the PL signal could be observed on shifting of maximum emission wavelength which was attributed to the supramolecular stacked nature of the ion pairs [45].

Till date, very few reports are found with AIE active iridium(III) mediated complexes in detection of explosive materials. X.-G. Hou *et al* reported a maximum Stern–Volmer constant (K_{sv}), 5.28 x 10^4 M^{-1} for selective sensing of picric acid with iridium(III) complex while other two reports [43, 44, 46] on iridium(III) are having K_{sv} values 7.42 x 10^4 M^{-1} and 3.56 x 10^3 M^{-1}, respectively for 2,4,6-trinitrotoluene (TNT) detection. These reports encourage the scientists to selective and sensitive detection of the explosive materials.

3.2 Results and Discussion

3.2.1 Syntheses and Characterization

All monocyclometalated iridium(III) complexes (**1-13**) have been synthesized by a one-pot synthetic route involving two steps. Initially an intermediate, [IrHCl(o-C_6H_3X)$P(Ar)_{x-1}R_y(PAr_xR_y)_2$] [**A (j, k, l** and **m**)] (Scheme 3.1) was isolated in which a six fold coordination environment on iridium(III) involving a 4-membered chelate was formed. It was observed that the time required to obtain the intermediates when using

trifluoro methyl phosphine (**j**) or dimethyl phenyl phosphine (**l**) were relatively longer (~7h) than for the other two intermediates with triphenyl phosphine or diphenyl methyl phosphine (~4h). The presence of Ir-H in the intermediates **A** is supported by the observation of a stretching frequency in the region~2187-2252 cm^{-1} recorded by FTIR and by the appearance of high-field lines in the ^{1}H NMR spectra (proton NMR peak). Although the hydroxylic solvent, 2-ethoxyethanol seems at a first sight to be the most plausible source of hydrogen linked to iridium(III), the same intermediate (**A**) was formed when the reaction was carried out in a non-hydroxylic solvent (1,4-dioxane). The measured ratios of the integrated areas of the high-field lines (for hydride linked to iridium) *vs* aromatic proton resonances were 1 to 50 ± 5 **(j-m)**. Calculated for a mono hydride, 1 to 44, showing that one hydrogen atom was abstracted from the ligand. The only reasonable source for the hydrogen atom which migrates to the iridium(III) centre is the ortho hydrogen adjacent to phosphorous, resulting in a six fold coordination of iridium(III) with a strained 4-membered chelate ring. The yellow intermediate, **j** was transformed into a dark solid at ~212°C [47]. It was characterized by elemental analysis, ^{1}H, ^{13}C and ^{31}PNMR spectra which corresponds to the structure of **j** to $[Ir(PPh_3)_2(P\hat{}C)(Cl)(H)]$ [47].The observed FTIR-band at ~2187 cm^{-1} is assigned to $\nu_{(Ir-H)}$ [47, 48] .

The 'δ' value was found at -19.31 in ^{1}H NMR spectrum further supporting the existence of Ir-H bond in **j** [47, 48]. In **j**, the chemical shift value and the coupling constant, (J_{P-H} = 14.0) suggest that the hydride is coordinated as *cis* to all the P containing ligands present in **j** [47].

^{1}HNMR spectrum shows that there are six groups of protons distinctly observed as multiplets in the aromatic region and their integration values correspond to the total forty four aromatic protons in **j**. ^{31}P NMR spectrum showed three chemical shifts with δ -2.41, -7.54 and -9.54 can be related to three inequivalent phosphorous atoms present in **j**. The ESI-HRMS spectra of **j** was recorded which showed three major fragments at m/z 1015.2635, 753.1603 and 456.1485 these can be attributed to $[Ir(PPh_3)_2(o\text{-}C_6H_4PPh_2)(H)(Cl)+H]^+$, $[Ir(PPh_3)_2(H)Cl]^+$ and $[Ir(PPh_3)(H)+H]^+$, respectively.

The 4-membered chelate ring is present in **j** which suggests a non-isolable $[Ir(PPh_3)_3]$ unit may be preformed to **j.** This unit subsequently changes to **j** through the insertion of iridium into a C-H bond on one of the phenyl units of triphenylphosphines, forming an octahedral complex with new Ir-C and Ir-H σ bonds.

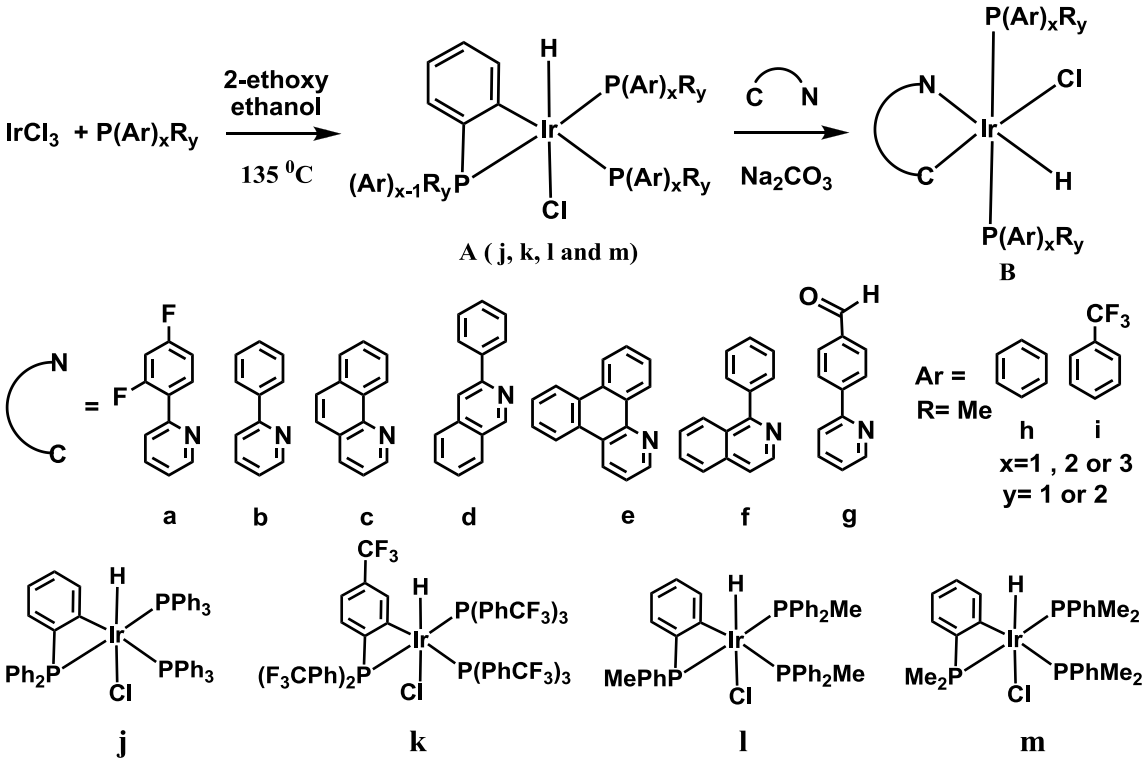

Com.	C^N	Ar	x	y	Com.	C^N	Ar	x	y	Com.	C^N	Ar	x
1	a	i	3	0	**5**	b	i	3	0	**9**	c	h	3
2	a	h	3	0	**6**	b	h	3	0	**10**	d	h	3
3	a	h	2	1	**7**	b	h	2	1	**11**	e	h	3
4	a	h	1	2	**8**	b	h	1	2	**12**	f	h	3
										13	g	h	3

Scheme 3.1 The synthetic route for the monocycometalated iridium(III) complexes B (**1-13**) via intermediates **A (j, k, l** and **m) .**

In the second step, the 4-membered chelate ring in the intermediates (**j-m**) is replaced by the stable 5-membered cyclometalates to form six-coordinated monocyclometalated iridium(III) complexes (B, **1-13**) (Scheme 3.1). The yield of the product has been improved in the range of 10-15%, on carrying out the process in

presence of 3-4 equivalents of sodium carbonate, which is acting as an acid scavenger [49, 50]. The observed chemical shift (δ) in the range of (-15)-(-19) and their low coupling constants (J_{P-H}, 16.0-18.5) (Table 3.1), support the existence of hydride bonded to iridium(III) and *cis* configuration with respect to phosphorous coordinated species (PAr_3) in the complex molecule, respectively. The structure of the complexes **2**, **8**, **9** and **13** is established by X-ray single crystal analyses at 100K. Due to the poor X-ray scattering factor of the hydride ion, in **2**, **8**, **9** and **13** one coordination site around Ir appears to be empty although this position is certainly occupied by the hydride ion as supported by the IR and ^{1}H NMR spectra. The ORTEP diagram (Figure 3.1) shows an octahedral geometry for the coordination environment around the iridium(III) centre for **2**, **8**, **9** and **13**.

Table 3.1 The IR, ^{1}H NMR (for hydride only) and ^{31}P NMR support the presence of a Ir-H bond and phosphorous coordination, respectively for **1-13**

Complex	IR $\nu_{(Ir-H)}$	^{1}H NMR (hydride) ppm	^{31}P NMR ppm
1	2152	-16.73(J=16.8Hz)	8.85
2	2152	-16.76(J=16.8Hz)	7.78
3	2152	-16.71(J=16.8Hz)	-5.05
4	2106	-16.87(J=16.8Hz)	-25.62
5	2144	-16.72(J=16.8Hz)	10.17
6	2090	-16.71(J=16.8Hz)	9.25
7	2113	-16.74(J=16.8Hz)	-4.57
8	2098	-16.88(J=16.8Hz)	-25.45
9	2129	-16.80(J=16.8Hz)	10.58
10	2167	-16.30(J=16.8Hz)	6.56
11	2113	-16.49(J=16.8Hz)	7.79
12	2129	-16.93(J=16.8Hz)	10.17
13	2140	-16.76(J=16.9Hz)	7.93

All optimized structures are very close to the X-ray geometries. Remarkably, the main difference between crystallographic coordinates and geometries obtained from quantum chemical calculations are found in the disposition of the phenyl rings in the phosphine ligands, which can be explained considering the expected greater molecular flexibility of these ligands in solution (Figure 3.2).

3.3 X-ray single crystal analyses

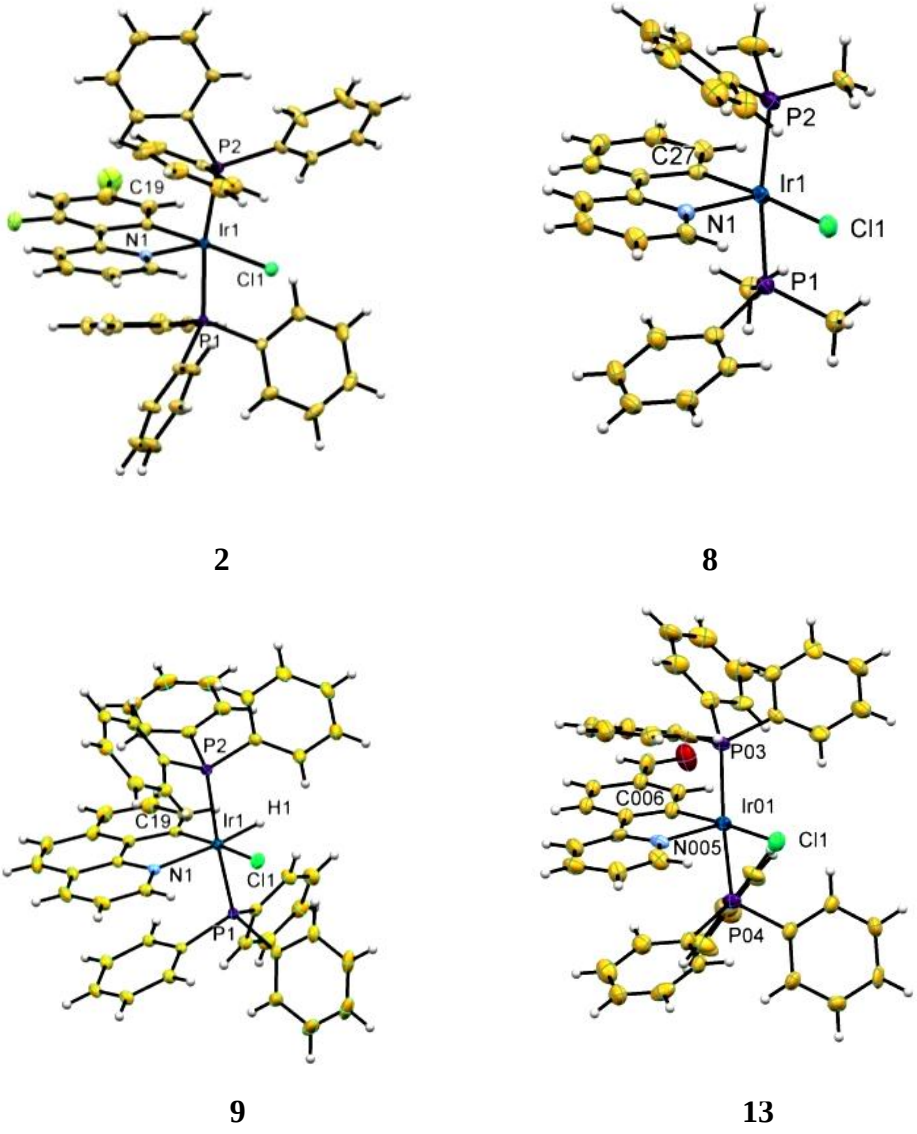

Figure 3.1 ORTEP diagram for complexes, **2, 8, 9** and **13** showing the octahedral geometry at the Ir site (in **2**, **8**, and **13** the hydride coordination to iridium(III) centre couldn't be detected).

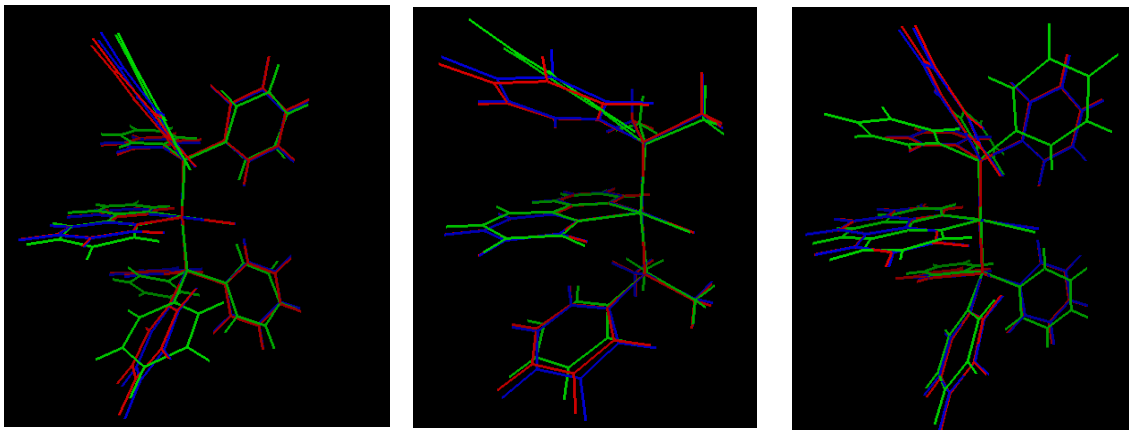

Figure 3.2 Geometry comparison between the X-ray crystal (green), and the ground state (blue) and lowest triplet (red) optimized geometries in DCM solution of complexes **2**, **8** and **9**.

3.4 Photophysical property study

The solution UV-Vis absorption spectra (DCM, 10^{-5}M) show intense bands below 350 nm for the complexes, **1-13** (Figure 3.3) which can be assigned to ligand centered (LC), $^{1}\pi$-π^* transitions [51, 52]. These absorption bands are followed by weaker bands in the range of ~350-450 nm. In this range, two well-resolved broad peaks are observed for **1-9** [inset of (Figure 3.3)] whereas a single broad peak is obtained for **10-13**.

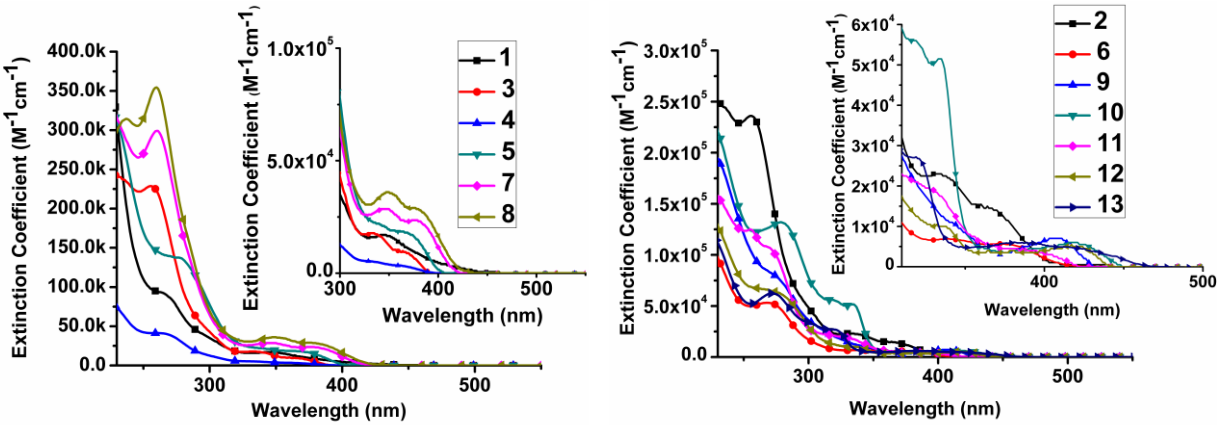

(a) (b)

Figure 3.3 (a, b): Solution UV-Vis absorbance spectra (10^{-5}M, DCM) of the complexes, **1-13** [short range spectrum are shown in inset (360-460 nm)].

Based on the shape, band position and their intensities [Table 3.2], these bands can be assigned to MLCT transitions. Electronic structure calculations of complexes **2**, **6** and **8-12** indicate that the four highest occupied molecular orbitals (HOMOs) correspond to different antibonding combinations between the t_{2g} (d_{xy}, d_{xz} and d_{yz}) orbitals of iridium 'p' orbitals of chlorine and π contributions from the non-pyridine rings of the cyclometalated ligand, while the two lowest unoccupied orbitals (LUMO and LUMO+1) correspond to π* orbitals of the cyclometalated ligand (Figure 3.4). There is almost no participation of the phosphine ligands in these frontier orbitals. Our TDDFT computations suggest that the highest wavelength, weak bands correspond to spin-forbidden transitions to low-lying triplet states resulting from HOMO and HOMO-3 to LUMO electronic excitations (Table 3.3). In all studied complexes, the lowest energy spin-allowed absorption band corresponds to the promotion of an electron from the HOMO to the LUMO, and presents an important MLCT and LLCT, *i.e.* p(Cl) →π*, character (Figure 3.4).

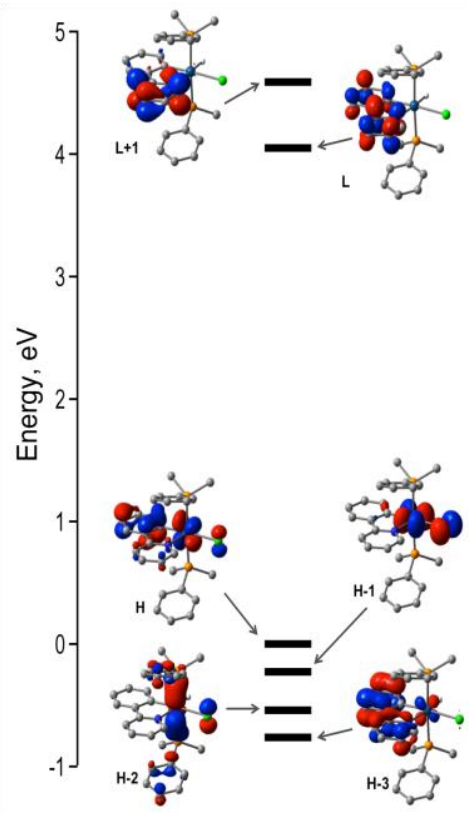

Figure 3.4 Molecular orbital energy diagram (in eV) with respect to the HOMO energy of the frontier molecular orbitals of **8**. H and L stand for HOMO and LUMO, respectively.

Complexes **6** and **8** only differ in the phosphine ligand and, as a result, their transition energies to S_1 are almost identical. On the other hand, fluorine substitution in **2** destabilizes the π*-type LUMO, resulting in a ~0.1 eV increase of the excitation energy. Alternatively, modification of the degree of conjugation in the cyclometalating ligands in **9**, **10**, **11** and **12** can be used to tune the $S_0 \rightarrow S_1$ transition energy almost at will. Overall, computed transition frequencies to the low-lying states of the complexes are in very good agreement with experimental absorption peaks in dichloromethane solution (Figure 3.3).

The emission spectrum of complexes, **1-10** and **13** shows a structured emission (Figure 3.6). Further, these complexes are insensitive to solvatochromic effects *i.e.*, the emission spectra remain practically unchanged irrespective of the polarity of the solvent. These facts suggest that the lowest excited states of **1-10** are of predominantly LC character along with a lesser contribution from MLCT states. This behaviour is also nicely captured by electronic structure calculations. The comparative analysis between the S_1 and T_1 wave functions shows a much lower weight of the HOMO-to-LUMO (MLCT) for the latter (Table 3.3). In particular, the lowest triplet wave function has an important participation of the HOMO-3, largely located on the cyclometalled ligand (Figure 3.5), hence increasing the LC nature of the triplet. The emission color of the complexes has been tuned throughout the visible range by changes in the cyclometalated ligands / or combinations of cyclometalated and phosphine ligands (Figure 3.6).

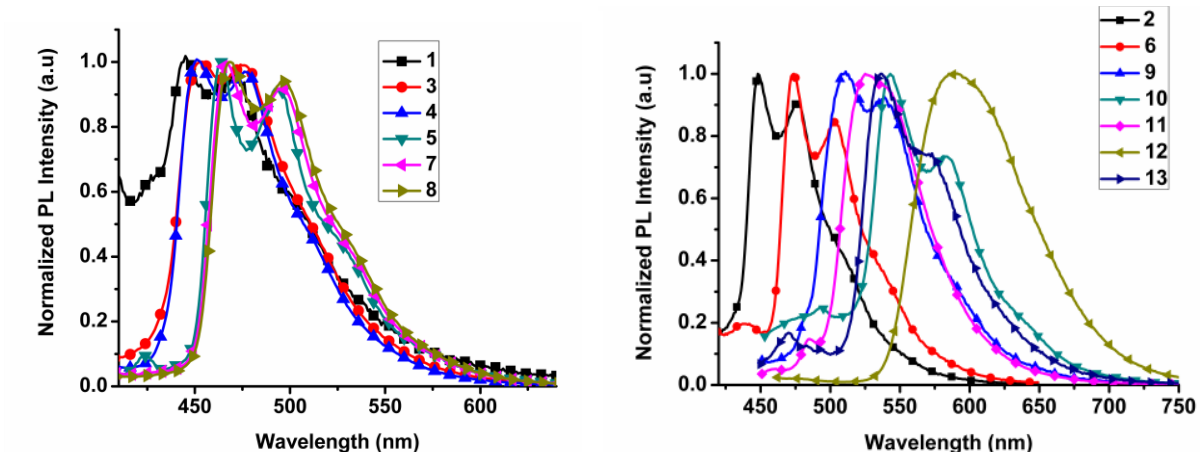

(a) (b)

Figure 3.5 (a, b) Solution state photoluminescence emission spectra for complexes **1-13** showing the tuning of emission wavelengths.

The relative differences in the emission wavelengths for the studied complexes are well recovered by computational results (Table 3.4).

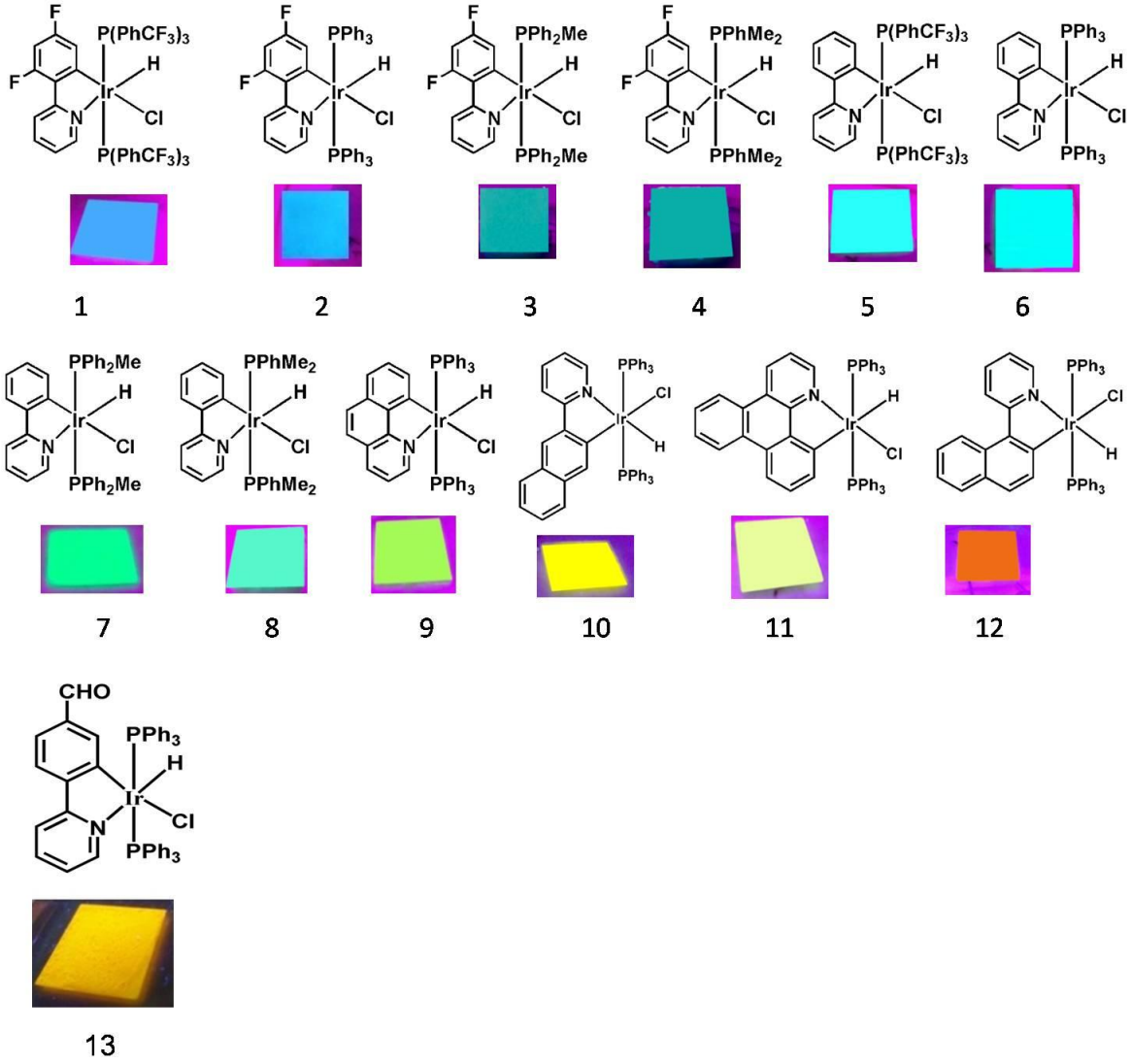

Figure 3.6 Tuning of emission color in solid state throughout the visible range with variation of the cyclometalated and the phosphine ligands.

It is to be noted that a sharp change of color is observed with the variation of the cyclometalated ligands, whereas a minor effect is reflected for changes in the phosphine ligands (Figure 3.6 & 3.7), which is in line with the low electron population on the phosphine ligands for the frontier molecular orbitals (FMO figure should be given) involved in the electron transition (Figure 3.4). Inclusion of a trifluoro methyl substituent in triphenyl phosphine (**1** vs **2**; **5** vs **6**) has a negligible influence in the

emission wavelength (Figure 3.7). Similarly, the complexes with methyl or dimethyl substituted tri phenyl phosphine (**3** vs **4**; **7** vs **8**) show only minor variations in the emission wavelength (Figure 3.7).

There is, however a noticeable difference in color comparing complexes **1** and **2** with **3** and **4** (a similar change is observed when comparing **5** and **6** with **7** and **8**, (Figure 3.6) where the phenyl groups from phosphine are replaced by one or two methyl groups.

In these cases, it is evident that the phosphorous atom coordinating to iridium(III) affects its d-orbitals when the electron accepting phenyl substituents are replaced by methyl groups in the triphenylphosphine ligands.

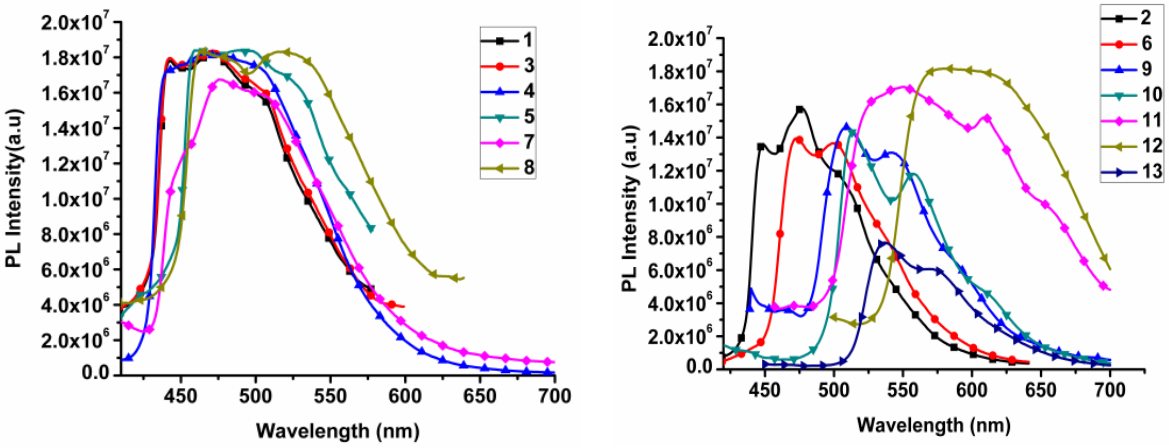

(a) (b)

Figure 3.7 (a, b) Solid state photoluminescence emission spectra for complexes **1-13** showing the tuning of emission wavelengths.

Table 3.2 UV-Vis absorbance [extinction coefficient ($M^{-1}cm^{-1}$) in parenthesis, in Dichlorometahne and [c] =10^{-6} M] and maximum emission wavelengths for the complexes **1-13.**

Complex	UV-Vis absorbance (nm) (ε x 10^4) (M^{-1} cm^{-1})	PL (nm)	
		Solid	Solution
1	268 (9.00), 350(1.60), 430(0.15)	441 (sh), 472, 506 (sh)	445,471
2	255 (23.50) 338 (2.30), 369 (1.50), 430(0.05)	448 (sh), 476, 507 (sh)	451,476
3	255 (2.80), 339 (1.70), 367 (1.00), 419 (0.02)	443 (sh), 478, 507 (sh)	453,475
4	262 (4.10), 337 (0.51), 369 (0.33) 419 (0.05)	481	448,476
5	275 (13.10), 371 (1.70), 430(0.05)	460 (sh), 493, 529 (sh)	463,494
6	269 (5.30), 343 (0.65), 381 (0.51),445 (0.02)	473,498	468,499
7	260 (29.45), 347 (2.87), 385 (2.30), 430 (0.02)	473 (sh), 501	467,497
8	259 (35.20), 349 (3.60), 384 (2.70), 430 (0.02)	475, 507	468,497
9	276 (7.60), 407 (0.71), 451(0.04)	508, 544	512,548
10	280 (13.00), 319 (5.50), 336 (5.10), 424 (0.59)	513, 558	543,585
11	254(12.30), 267(10.70), 331(1.86), 400 (0.27)	548, 610 (sh)	524
12	275(6.7), 336(0.96), 423 (0.40)	593	589
13	272 (6.20), 322(2.70), 405(0.54)	534, 573	535, 575

Table 3.3. Comparison between experimental absorption maxima λ_{exp} and computed transition energies λ_{calc} (in nm) and orbital composition (%) of the lowest excited singlet and triplet states for complexes **2**, **6** and **8-12**.

Complex	state	λ_{exp}	λ_{calc}	H→L	H-n→L[a]
2	T1	430	433	56	25
	S1	369	360	97	
6	T1	445	451	68	19
	S1	381	372	97	21
8	T1	430	445	68	
	S1	384	368	97	
9	T1		494	47	13
	S1	407	400	94	
10	T1		553	63	16
	S1	424	418	94	
11	T1		465	28	17
	S1	400	393	95	
12	T1		567	84	
	S1	423	419	84	

[a]Contribution from H-n with $1 \leq n \leq 3$).

Table 3.4 Comparison between experimental and calculated emission wavelengths of complexes **2**, **6**, **8**, **9**, **10** and **12** in DCM solution. Computed values obtained at the B3LYP/6-31+G(d)/LANL2DZ level (IEF-PCM).

λ_{em} / nm	**2**	**6**	**8**	**9**	**10**	**12**
calculated	537	563	558	636	714	773
Exp	451, 476	468, 499	468, 497	512, 548	543, 585	589

3.5 Aggregation induced emission (AIE)

The photoluminescence (PL) intensity of all these complexes in dichloromethane was found to be very weak as compared to their respective solids / aggregated forms (Figure 3.8). The quantum efficiencies in solution of the complexes have been measured and the observed values are in the range, 0.01-0.89 (for **1-10** measured with respect to quinine sulphate in 0.1M sulphuric acid, quantum yield (QEY) = 0.55, Table 3.5) and 0.012, 0.087 and 0.04 for complexes **11**, **12** and **13** respectively (with respect to coumarin 153 dissolved in degassed ethanol, QEY = 0.38, Table 3.5). The least solution efficiency was observed in **1** (0.011%) while the maximum efficiency in **2** (0.89%). The absolute solid state QE has been measured for all the complexes. The maximum QE was observed for **2** (54.83%), while the minimum observed for **1** (5.41%). The ratio of QE_{solid} / QE_{sol} (ϕ_{solid}/ϕ_{sol}) has been found maximum for **3** (7.34×10^2) and minimum for the case of **2** (0.46×10^2) showing the remarkable AIE property of the complexes [53].

Several experiments have been carried out in order to investigate the cause of the strong solid state emission behaviour exhibited by complexes **1-13**. PL was measured for a series of solutions with different water-THF ratios, in which water content was gradually varied in the range of 0-90% for **1-13** (Figure 3.9).

The PL was found to increase drastically with increasing proportion of water in a water-THF solution while in case of, **13** the PL intensity was decreased at f_w=90% compare to f_w=90% (Figure 3.9c). Since water is a poor solvent for all these complexes, the molecules gets aggregated with increasing concentration of water.

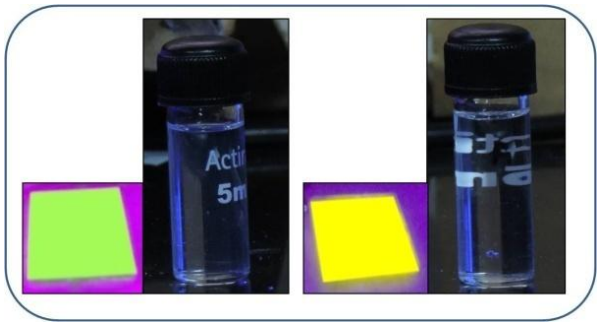

Figure 3.8 The relative luminescence intensity of solid thin film vs. solution for complexes **9** (left) and **10 (**right) under UV lamp (λ_{max} = 365nm). (These are chosen as two representative cases of all the reported complexes).

In another experiment, the gradual increase of the emission intensity is observed with increasing the concentration of polyethylene glycol, a viscous solvent, in a solution of each of the complexes **1-13** dissolved in THF (Figure 3.10). This fact suggests that the hindrance of the rotationally active part with increasing viscosity of the solution may be responsible for the increase of luminescence intensity in aggregated samples. Micrometer size non-uniform aggregated particles have been observed in the SEM image for complex **6** in 90% water-THF solutions. Thus, this experiment indicates that all these complexes are AIE active.

Finally, the AIE effect for complex **6** (as a representative of all other complexes) was studied by the time-resolved photoluminescence technique In THF, the molecules decay bi exponentially (95% molecules decay with life time 2.17 ns and the rest decay with lifetime 43.39 ns).

Solution QE (ϕ_{sol}) for **1-10** has been measured with respect to quinine sulfate (in 0.1M H_2SO_4, QE=0.55, excitation,470nm-480nm); and QE (ϕ_{sol}) for **11-13** has been with respect to coumarin 153 (in degassed ethanol, QE=0.38, excitation, 400-420nm), Solid state phosphorescence QE (ϕ_{solid}) has been recorded using integrating sphere.

With addition of water (30%) into THF, excited molecules decay through three different relaxation pathways (13% and 10% molecules decay with life times of 2 ns and 5.59 ns, respectively, but 77% of the molecules decay through a slow channel with a life time ~484 ns).

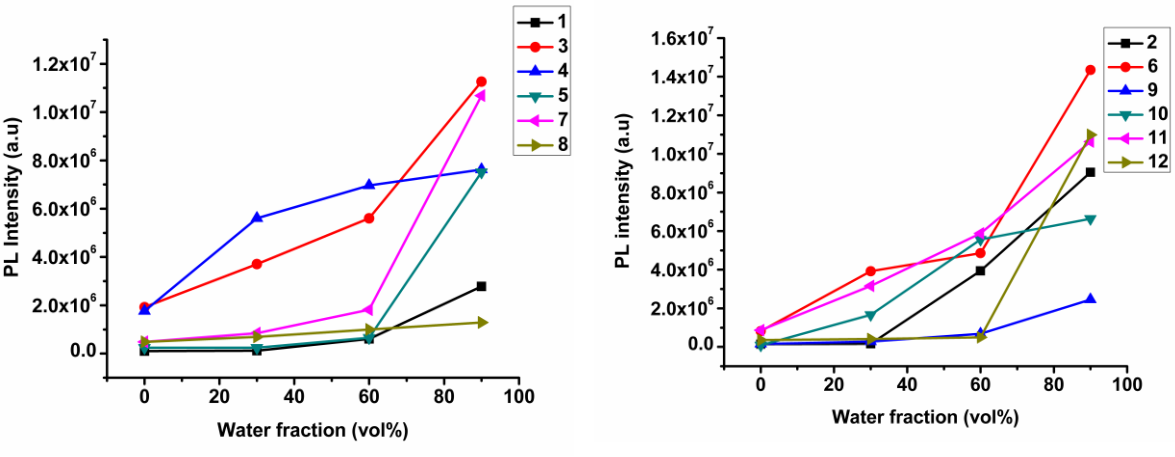

(a) (b)

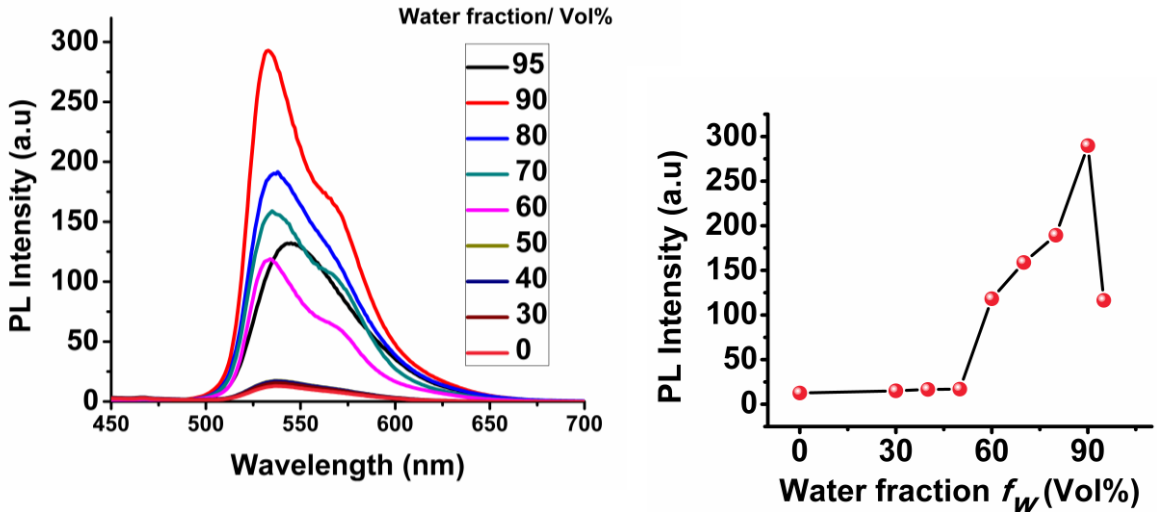

(c) (d)

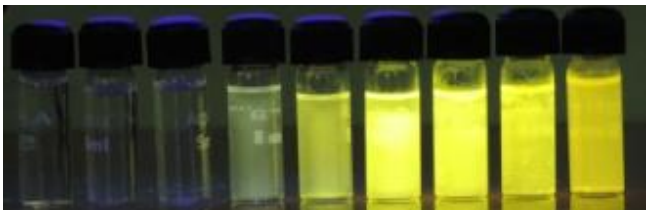

(e)

Figure 3.9 (a, b) Change in PL intensity of complexes **1-12** with changing the water; (c) change in PL intensity after addition of different water fraction for complex **13**; (d) intensity plot of intensity (I) values of **13** versus the compositions of the aqueous mixtures; concentration: 1 x 10^{-5} M; (e) Image of complex **13** in different water-THF mixture (taken under 365 nm UV lamp).

Table 3.5 Solid state quantum efficiency (ϕ_{solid}) and solution state quantum efficiency (ϕ_{sol}) for **1-13**

complex	ϕ^{a}_{sol}	ϕ^{b}_{solid}	complex	ϕ^{a}_{sol}	ϕ^{b}_{sod}
1	0.011	5.41	**7**	0.015	9.46
2	0.890	41.43	**8**	0.048	7.28
3	0.014	10.65	**9**	0.044	9.14
4	0.127	10.95	**10**	0.114	26.4
5	0.014	5.77	**11**	0.012	7.99
6	0.688	54.83	**12**	0.087	11.42
			13	0.04	22.60

With further addition of water molecules (60%) in THF, the decay via the slowest channel is more populated (from 77% to 91%) and the life time increases to ~642 ns. In 90% water, the life time for the slowest component rises to ~4.6 μs, without any noticeable change in population (60%).

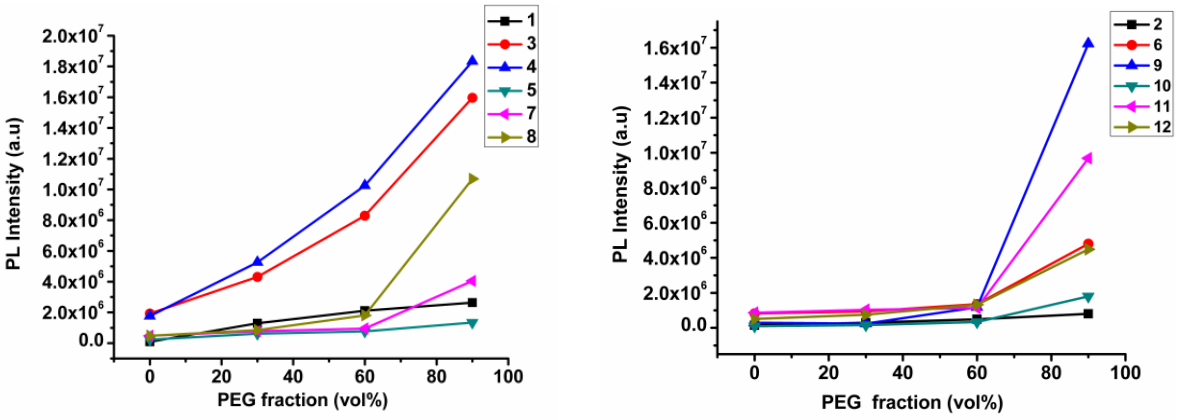

(a) (b)

Figure 3.10 Variation of PL intensity of complexes **1-12** with changing the PEG fraction.

It has been observed that the lifetime for the new relaxation pathway is steadily rising (with population, too) when the concentration of water molecules is increased. This fact leads us to propose that restricted intramolecular rotation (RIR) can affect drastically the radiative/nonradiative recombination processes in the excited states.

The packing diagrams for complexes **2**, **8**, **9** and **13** shows that there are several intermolecular interactions (C−H···π types) where phenyl rings in the triphenyl phosphine units are involved (Figure 3.11).

Thus, the internal rotation of these rings is severely restricted in the crystals. This fact is also consistent with the geometry optimizations using quantum chemical calculations that show that in solution the minimum energy disposition of those phenyl rings is markedly different to that adopted in the crystal structure (Figure 3.1).

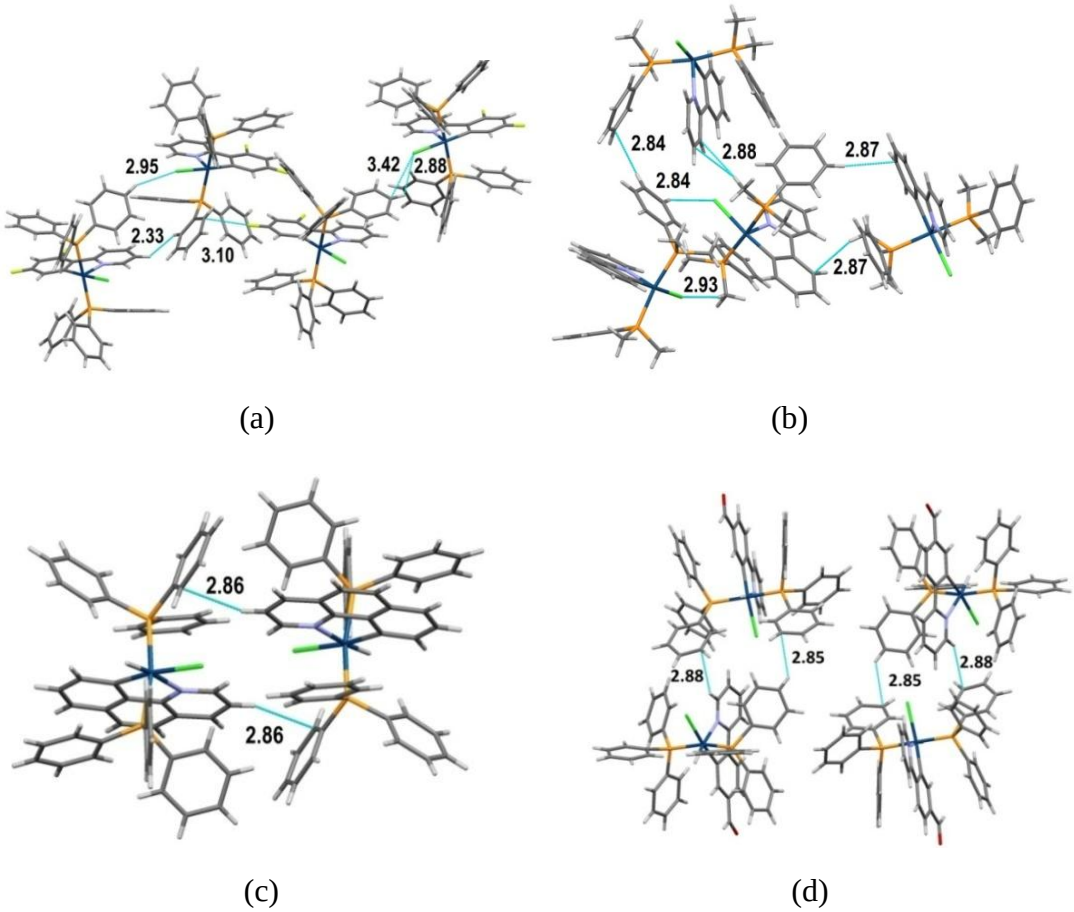

(a) (b)

(c) (d)

Figure 3.11 Packing diagram for **2** (a), **8** (b) and **9** (c); in **2** the unit cell contains four molecules; in **8** the unit cell contains four molecules ; in **9** the unit cell contains two molecules; in **13** the unit cell contains four molecules (the green dotted lines denote the shortest contacts).

This hindered rotation of the phenyl rotors in the crystal state is suggested to block the non-radiative decay channels while simultaneously opening the radiative pathways. As a result, the solid state emission efficiency for all these complexes is predicted to improve significantly, as observed experimentally.

3.6 Applications of AIE

3.6.1 Application in cell imaging

As an illustration of possible applications for these new AIE active complexes, we have employed them in the design of a non-toxic bioimaging probe. Since these complexes are soluble in tetrahydrofuran and dichloromethane but insoluble in water, a polyethylene glycol-polylactic acid (PEG-PLA) based biodegradable polymer has been selected that is known to self-assemble in water and produce a micellar structure with hydrophobic PLA inside and hydrophilic PEG outside [54] in which the AIE active iridium(III) complexes can be encapsulated. In our experiment, complex **6** has been used for bioimaging as probe molecule. Micellar encapsulation of AIE active iridium complexes involves solubilization of a mixture of PEG-PLA and the iridium complex in the organic solvent followed by injection of this mixture in water under vigorous stirring conditions to favour self-assembly of PEG-PLA into micelles that incorporate the iridium complex in its aggregated form (Scheme 3.2).

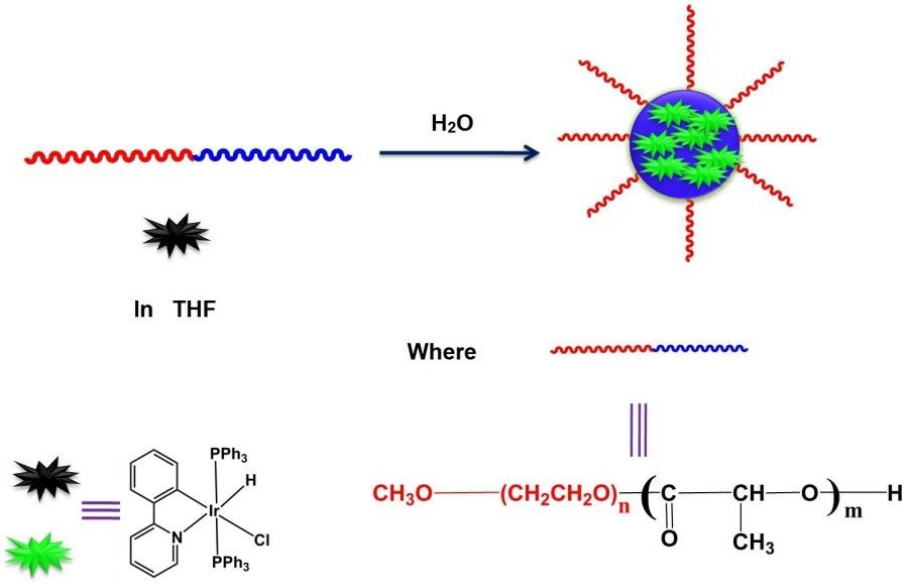

Scheme 3.2 Schematic representation of the synthesis of luminescent iridium complex encapsulated PEG-PLA nanoparticles.

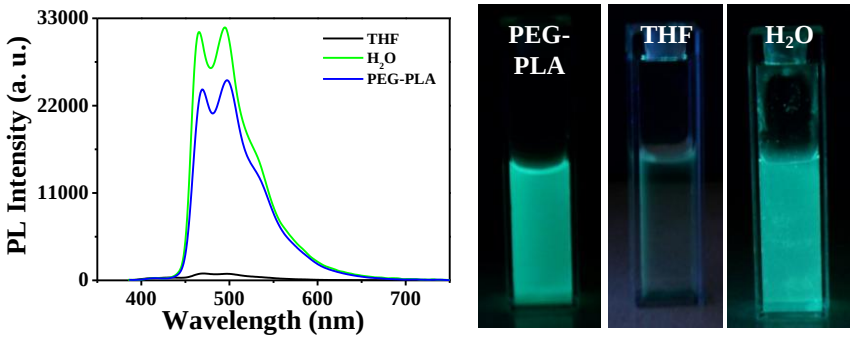

Figure 3.12 Photoluminescence spectra (left) and digital image (right) of iridium complex **6** in Tetrahydrofuran (THF), water and in aqueous medium.

The PL properties of **6** dissolved in THF, in its aggregated form in water and in a PEG-PLA colloidal solution after encapsulation in PEG-PLA micellar nanoparticles are shown in Figure 3.12.

The iridium complex in THF shows a weak green emission under 365 nm excitation with the maximum emission at 470 nm and 495 nm. The aggregated iridium complex in water and encapsulated in PEG-PLA micellar nanoparticles shows strong green emission under excitation at 365 nm with two emission maxima at (465 nm, 495 nm) and (470 nm, 495 nm), respectively. The observation of a similar strong green emission in water and PEG-PLA micelles indicates that the iridium complex is in its aggregated form inside the PEG-PLA micelles.

Aggregation and particle formation of the iridium complex in water is also confirmed from dynamic light scattering (DLS) and scanning electron microscope (SEM) measurements as shown in Figure 3.13. The hydrodynamic diameter of the particles of aggregated complex as determined by DLS ranges from 200 nm to 900 nm. The SEM image shows that the particles of aggregated complex in water have diameter ranging from 50 to 400 nm with a spherical shape (Figure 3.13). These results confirm that the iridium complex aggregates in water to give micron size particles with a wide size distribution (Figure 3.13). In contrast, the hydrodynamic size of PEG-PLA nanoparticles and iridium complex encapsulated PEG-PLA nanoparticles are 35-150 nm and 65-220 nm, respectively (Figure 3.13).

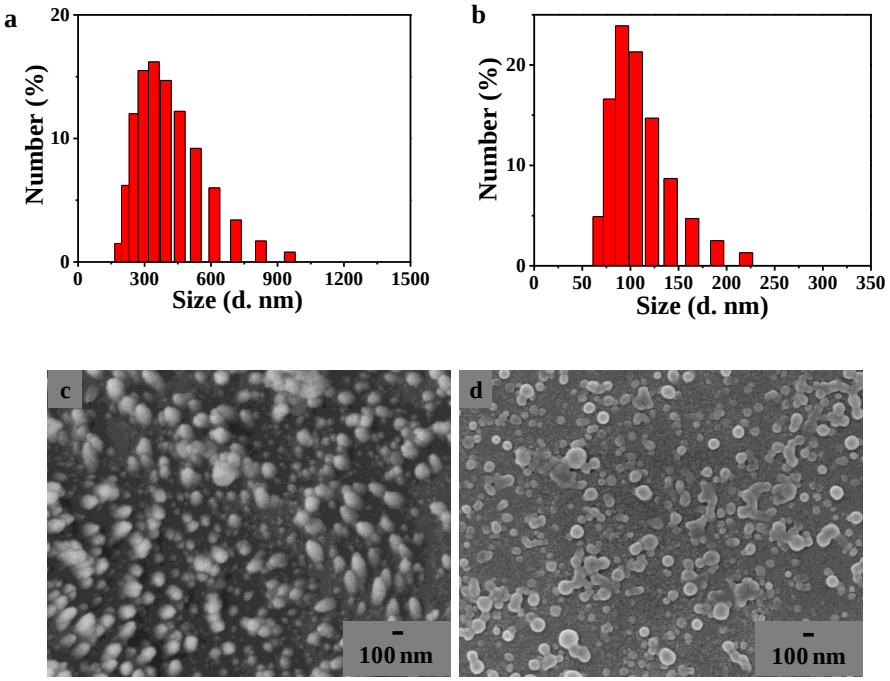

Figure 3.13 DLS histogram (a, b) and SEM image (c, d) of aggregated iridium complex (**6**) in water (a, c) and PEG-PLA particles encapsulated with iridium complex (b, d). Note the comparative smaller size and narrow size distribution of PEG-PLA particles.

A SEM study also confirms that the iridium complex encapsulated PEG-PLA nanoparticles are spherical in shape with radii in the range 40-150 nm (Figure 3.13). These results confirm that PEG-PLA particles containing the complex in its aggregated form are smaller than the particles of pure aggregated iridium complex in water with a relatively narrow size distribution for the encapsulated particles. The size of the micelle is found to increase by about 30 to 70 nm after the encapsulation of iridium complex takes place.

The presence of iridium complex inside the PEG-PLA particles is confirmed from IR spectroscopy. The FTIR spectrum for the isolated iridium complex shows that the major characteristic peaks arise at 2092 cm^{-1} for Ir-H stretching and 3046 cm^{-1} for aromatic C-H stretching. The spectrum for PEG-PLA nanoparticles shows peaks at 2955-2850, 1752 and 1180 cm^{-1} which are characteristic of C-H stretching, C=O stretching and C-O stretching, respectively [55]. In the spectra for PEG-PLA particles including iridium complex vibrational peaks at 2085 cm^{-1} and 3046 cm^{-1}corresponding to the iridium complex and those corresponding to the PEG-PLA are both present (Figure 3.14).

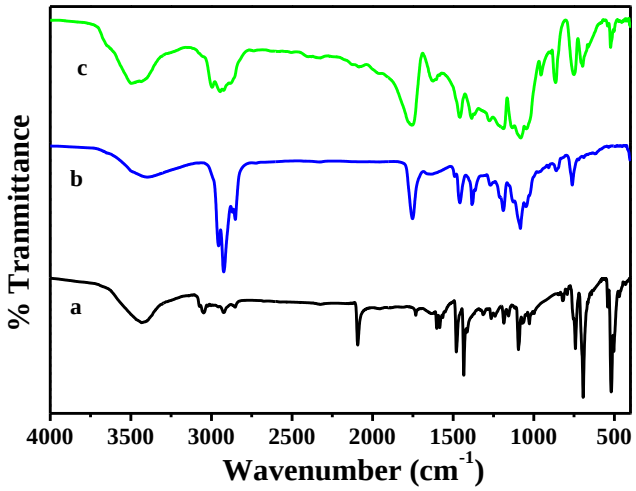

Figure 3.14 FTIR spectra of (a) iridium complex **6**, (b) PEG-PLA nanoparticles and (c) iridium complex **6** encapsulated PEG-PLA nanoparticles.

A PL decay study shows that the lifetime of iridium complex in THF, water and PEG-PLA is 5.1 ns, 6.3 μs and 19.8 μs, respectively (Figure 3.15). Magnitudes of the same order for the lifetimes of the aggregated iridium complex in water and inside the PEG-PLA micelles demonstrate that in both cases the emitting molecules are found in similar micro environments which are notably different from those in THF solutions [56].

The stability of the emission of the aggregated iridium complex under continuous UV irradiation has been tested finding that the iridium complex is stable under UV irradiation for more than a minute. This result suggests that the emission of PEG-PLA particles containing the iridium complex is stable under imaging conditions and can be thus used as imaging probes.

Micelles of PEG-PLA encapsulated AIE active iridium complex have been used as in vitro cellular imaging probes for biomedical applications. For this purpose HeLa cells have been incubated with luminescent PEG-PLA particles and then labelling has been observed under a fluorescence microscope. The results show that the cells become green luminescent under UV excitation as shown in Figure 3.16, suggesting that the particles can be used to label them.

As shown in Figure 3.16, by varying the incubation time, it's difficult to understand whether particles enter into the cytoplasm even after an 8 hours exposure. So, we have performed a series of fluorescence images at different Z planes with

particle labeled of HeLa cells, demonstrating that the particles are located in cytoplasm along with at cell surface (Figure 3.17).

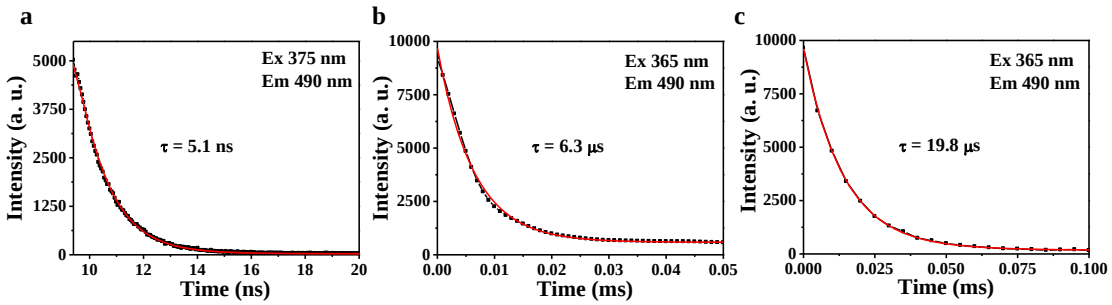

Figure 3.15 Luminescent lifetime decay curve of (a) iridium complex in THF (b) aggregated iridium complex in water and (c) iridium complex encapsulated PEG-PLA nanoparticles. Black and red lines correspond to experimental and fitted data respectively.

Interestingly, particles of iridium complex aggregated in water do not label the cells even after a long incubation time.

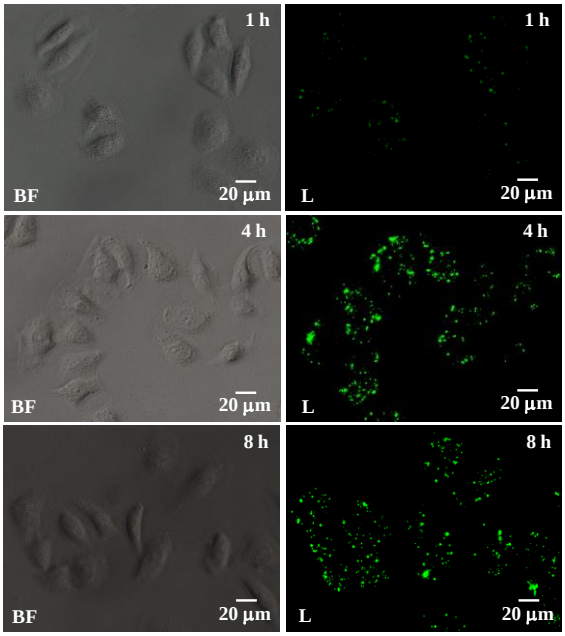

Figure 3.16 Bright field (BF) and luminescence (L) image of HeLa cells labeled with iridium complex (**6**) encapsulated PEG-PLA particles. Cells are incubated with particles for 1, 4 and 8 h and then washed cells are imaged under microscope.

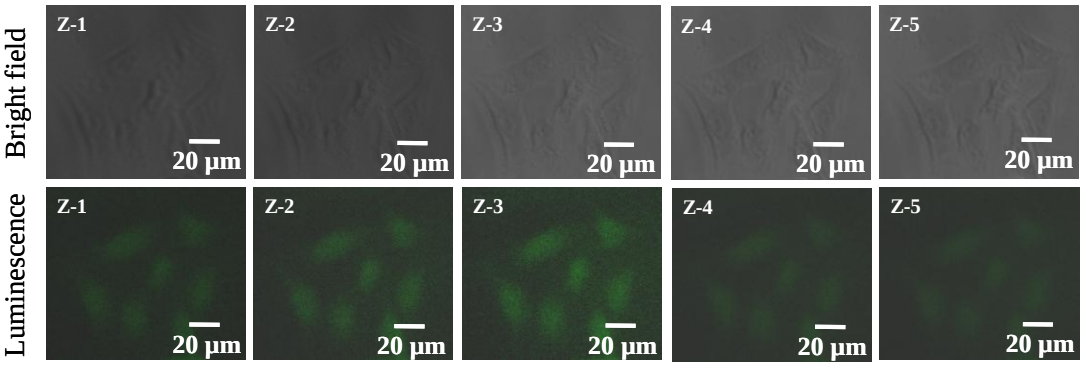

Figure 3.17 A series of images of particle labeled HeLa cells using at different Z planes from top to bottom with consecutive Z-axis slices of 3.42 µm each, demonstrating that the particles are located both in cytoplasm and at cell surface.

This result suggests that successful labeling by photoluminescent PEG-PLA particles is possibly due to their smaller size combined with the lipophilic property of PEG-PLA that leads to a strong interaction of the particles with the cell membrane. Encapsulated PEG-PLA nanoparticles were mixed with Dulbecco's modifed eagle medium (DMEM) with 10% fetal bovine serum (FBS) to check their stability.

The observed digital images of these particles in cell culture medium indicate that there has no significant precipitation till 7 days which ensures colloidal stability of iridium(III) complex **(6)** encapsulated PEG-PLA particles in cell culture media.

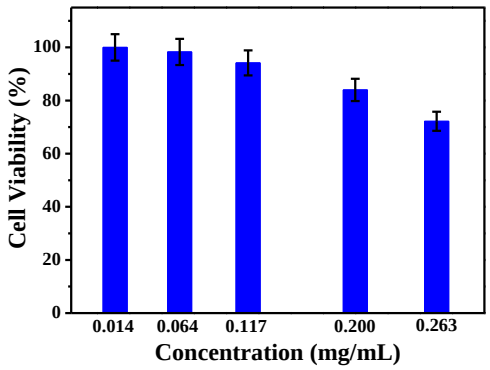

Figure 3.18 Viability of HeLa cells in presence of iridium complex (**6**) encapsulated PEG-PLA nanoparticles. Cells are incubated in presence of different concentrations of iridium complex encapsulated PEG-PLA nanoparticles for 24 hours. (The final concentration of iridium complex encapsulated PEG-PLA nanoparticles used for imaging is 0.117 mg/mL).

The cytotoxicity of the iridium(III) complex **(6)** has been investigated by the conventional MTT assay. HeLa cells are incubated with various amounts of photoluminescent PEG-PLA particles for 24 hrs and cell viability has been estimated. Result shows that cells survival is >80% in all the tested concentrations (Figure 3.18). This result suggests that photoluminescent PEG-PLA particles have low toxicity and can be used as cell imaging probes under in vitro conditions.

3.6.2 Application in Explosive sensing

With considering the advantage of strong AIE property of these complexes, we carried out the detection of different nitro aromatic along with few non-nitro aromatic compounds such as picric acid (PA), 2,4-dinitro phenol (2,4 DNP), 3,5-dinitro toluene (3,5 DNT), 1,3 dinitro benzene (1,3 DNB), nitro toluene (NT), benzoic acid (BA) and toluene (T) (benzoic acid and toluene are non-explosive). It was observed that the **13** resulted phosphorescent quenching after treatment of these nitro compounds (*vide infra*) with the phosphorescent complexes, separately.

The maximum PL quenching was observed with PA where the detection limit was reached up to 264 nM (~98% quenching observed with 5 equivalents PA) (Figure 3.19). On the other hand, **6** showed much better result in detection of PA where the detection limit was reached to 65 nM (~ 99% quenching observed with 5 equivalents PA) (Figure 3.20).

These results inspired us to check the sensitivity of PA with using both the complexes. The PL titration experiment of both the complexes was performed with increasing concentration of PA which shows a drastic drop in PL intensity in both cases. The Stern-Volmer (S-V) plot for both the complexes was non linear in nature and showing curves bending upward (Figure 3.21 & 3.22). Thus, such a nature of S-V plot indicates the operation of static and dynamic quenching processes which demonstrate the quenching become more efficient with increasing concentration of PA. The quenching constants for both 6 and 13 have been calculated and found to $1.90 \times 10^5\ M^{-1}$ and $1.00 \times 10^5\ M^{-1}$, respectively, which is much higher than the reported iridium(III) complexes.

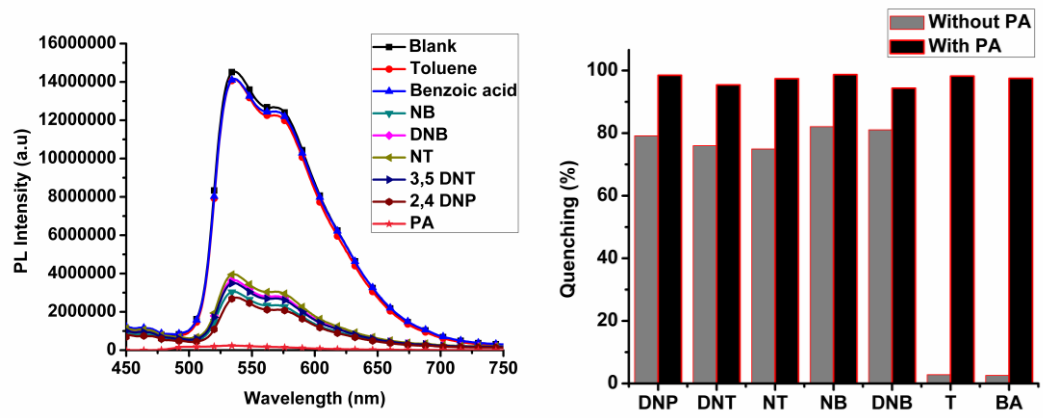

(a) (b)

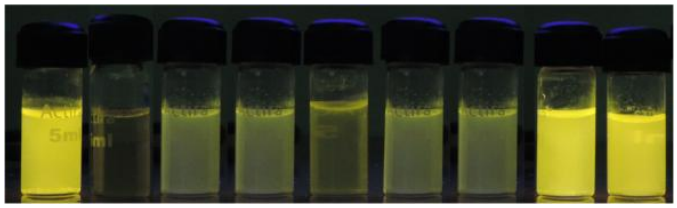

(c)

Figure 3.19 (a) PL spectra of **13** with c =10^{-5} molL^{-1} at f_w = 90 % (in water/THF) upon the addition of 5 equivalents of different nitro based explosive /non explosive compounds (toluene, benzoic acid); (b) Column diagrams of the relative PL intensity of **13** with different explosive / non explosive compounds, at 535 nm. Grey bars represent the addition of various explosive / non explosive compounds to the complex **13** and black bars represents the subsequent addition of PA (5 equivalents) to the above solutions [**13** + explosive /non explosive compounds + PA]; (c) Image of **13** when dispersed at f_w = 90% with c = 10^{-5} molL^{-1}, with adding 5 equivalents of explosive / non explosive compounds, respectively; From left to right: (i) blank; (ii) PA; (iii) 3,5-DNT; (iv) NT; (v) 2,4-DNP; (vi) 1,3-DNB; (vii) NB; (viii) T; (ix) BA (under 356 nm UV lamp).

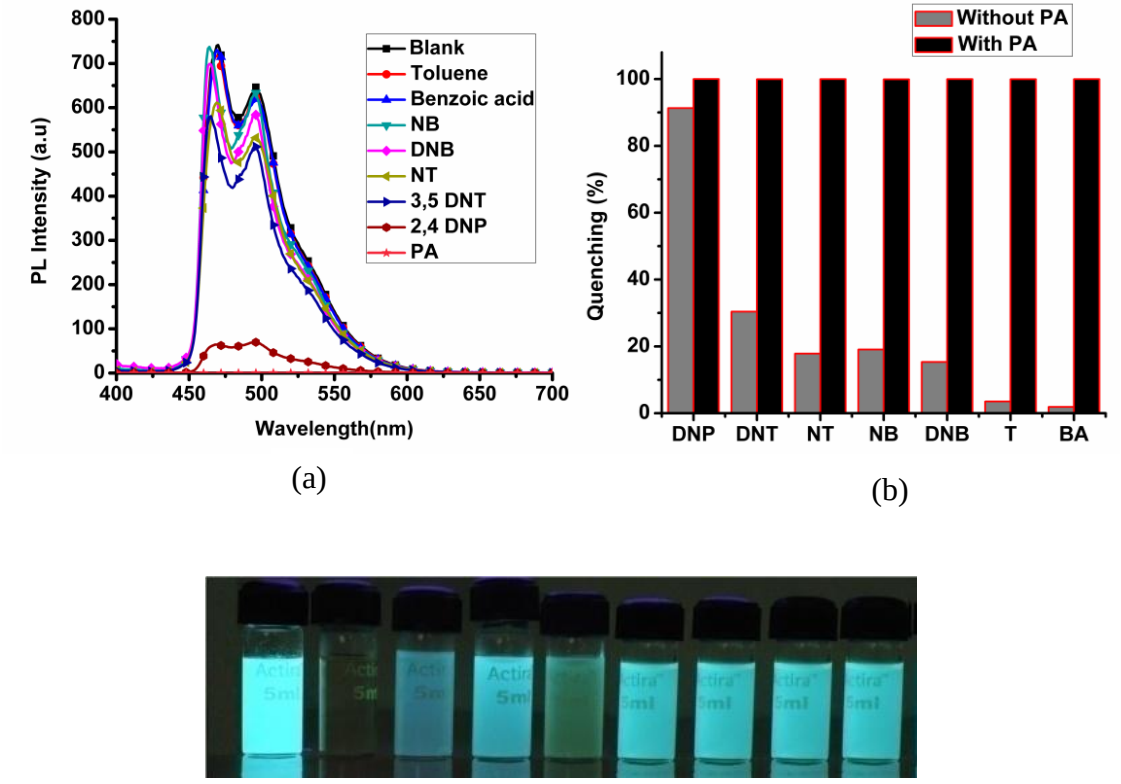

(a) (b)

(c)

Figure 3.20 (a) PL spectra of **6** with c =10^{-5} molL^{-1} at f_w = 90 % (in water/THF) upon the addition of 5 equivalents of different explosive /non explosive compounds; (b) Column diagrams of the relative PL intensity of **6** with different explosive /non explosive compounds, at 470 nm. Grey bars represent the addition of various explosive /non explosive compounds to the **6** and black bars represents the subsequent addition of PA (5 equivalents) to the above solutions [**6** + explosive /non explosive compounds + PA]; (c) Image of **6** when dispersed at f_w = 90% with c = 10^{-5} molL^{-1}, with addition of 5 equivalents of each explosive /non explosive compounds , respectively; from left to right: (i) blank; (ii) PA; (iii) 3,5-DNT; (iv) NT; (v) 2,4-DNP; (vi) 1,3-DNB; (vii) NB; (viii) T; (ix) BA.

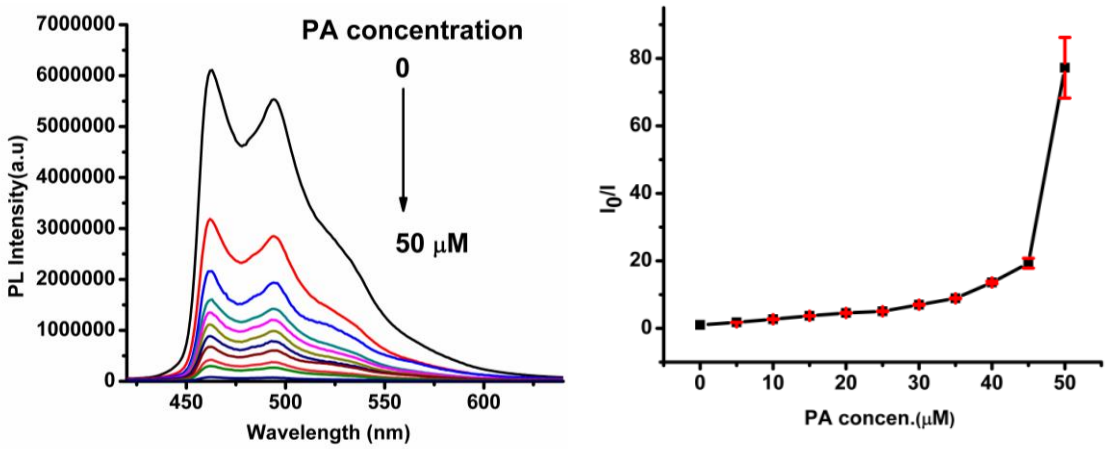

(a) (b)

Figure 3.21 PL spectra of **6** in THF–water (v/v = 1: 9) with different amounts of PA. (b) Corresponding to Stern–Volmer plots of PA.

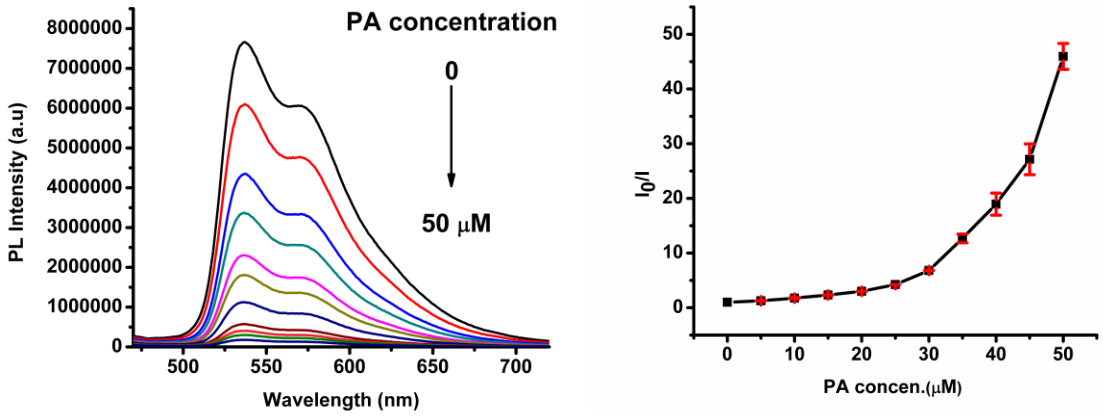

(a) (b)

Figure 3.22 PL spectra of **13** in THF–water (v/v = 1: 9) with different amounts of PA. (b) Corresponding to Stern–Volmer plots of PA.

The HOMO and LUMO level of both the complexes were determined by cyclovoltametric measurements and band edge absorptions. The observed HOMO and LUMO energy levels are−5.47 eV and −2.48 eV for **6**, −5.58 eV and −2.89 eV for **13**, respectively (Figure 3.23). The quenching and selective detection of PA by **6** may be demonstrated either by PET or energy transfer (ET) [57] mechanism because these two mechanisms lead to quenching in the system.

The energy transfer phenomenon may occur if the emission spectra of phosphors overlap with absorption band of the analytes while the quenching caused PET is limited to the phosphors that has a direct interaction with the analytes.

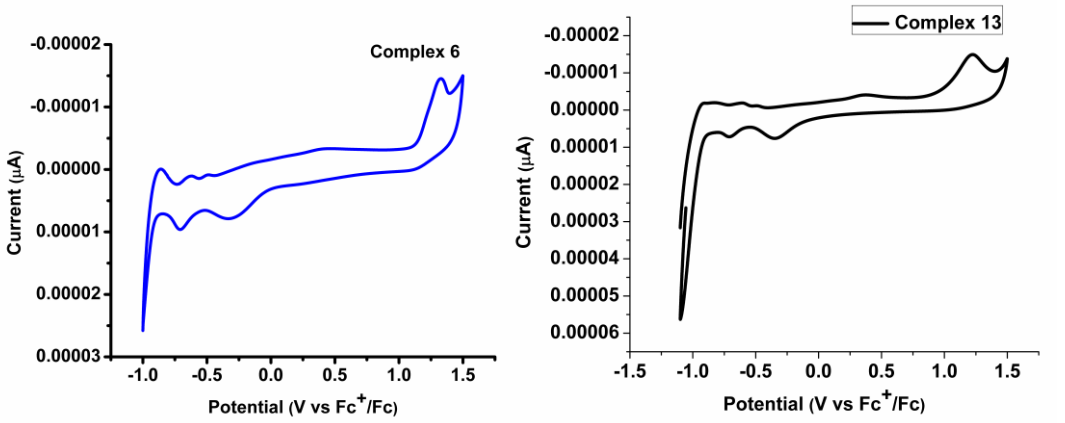

(a) (b)

Figure 3.23 Cyclic voltammogram of **6** (a) and of **13** (b) respectively, recorded in CH_3CN (ACN) at a scan rate of 0.05 V s^{-1}.

The mechanism of quenching for **13** was investigated. The nitro based explosives are highly electron deficient in nature because of the presence of strong electron withdrawing nitro functionality. The lowest unoccupied molecular orbital (LUMO) of nitro compounds were found to be lower in energy with respect to LUMO of **13**. The photo-induced electron transfer (PET) [58-60] is possible from LUMO of 13 to LUMO of NAs (nitro aromatics) [PA=−3.70 eV; DNT=−3.30 eV; NB=−3.35 eV], which resulted the PL (Figure 3.24).

The ET mechanism may be one of the possible mechanisms for enhancing the detection sensitivity as well as selectivity. The absorbance spectra of nitro aromatics have been recorded in two systems, one is in THF and another is in THF-water mixture (1:9, v/v) (Figure 3.25& 3.26).The absorbance spectra of 2,4-DNP and PA show drastic change in THF-water medium in comparison to pure THF medium.

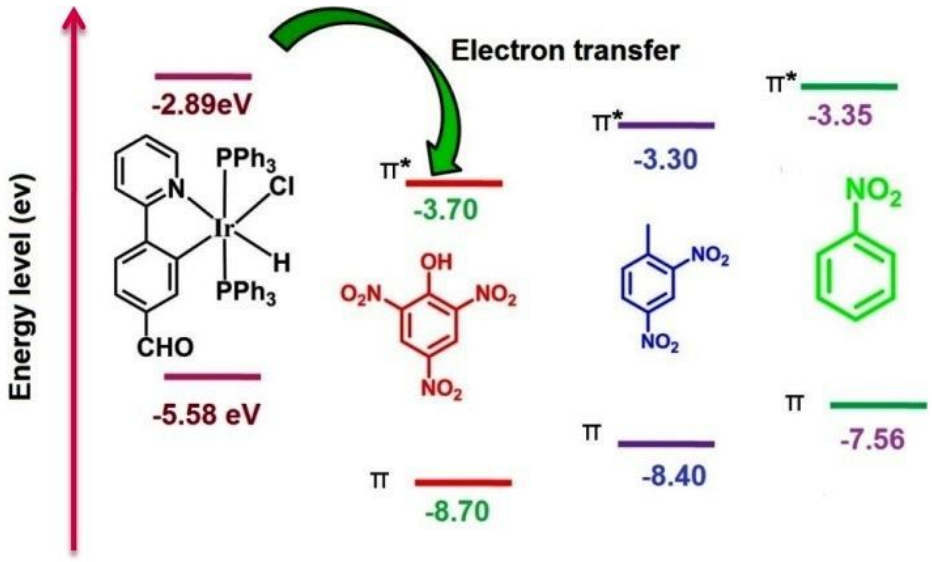

Figure 3.24 Electron transfer mechanism for quenching.

The solution color becomes yellow in THF-water mixture which shows colorless in THF solution. Further, the absorption spectrum in THF-water system is red shifted with respect to the absorption spectrum in pure THF system. This change indicates the acidic nature of 2,4-DNP (pK_a = 4.10) and PA (pK_a = 0.40) in THF-water system [61]. PA can more easily dissociate in THF-water medium as compared to 2,4-DNP which is reflected from the lowing in pK_a value. This fact results relatively a larger extent of overlapping of absorption spectra of PA with the emission spectrum of **6** (Figure 3.25 b).

This larger extent of overlapping is undoubtedly responsible for efficient energy transfer which results quenching of light emission. In case of **13**, there was no overlapping observed between emission spectra of **13** and absorbance spectra of nitro aromatics under experiments (Figure 3.26 b).

The filter paper was soaked with the complex solutions (in DCM) shows clearly noticeable the quenching of emission color (Figure 3.27 & 3.28 λ_{exc} ~365nm).

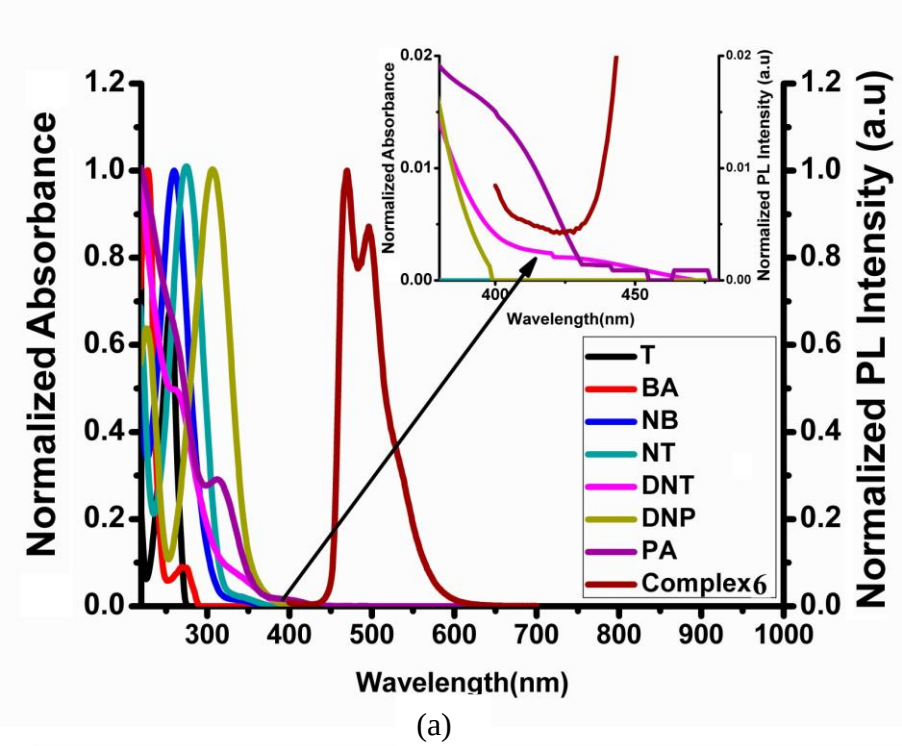

(a)

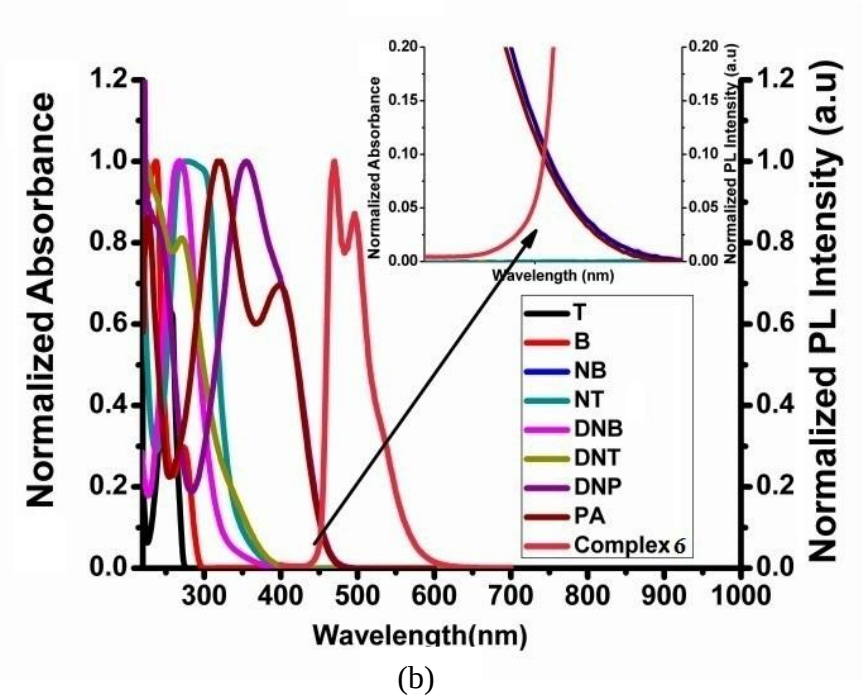

(b)

Figure 3.25 (a) Absorption spectra of different aromatic compounds and emission spectra of 6 in THF. The spectral overlap between the emission of **6** and the absorption of aromatic compounds was shown in inset. (b) Absorption spectra of different aromatic nito and non-nitro compounds and emission spectra of **6** in THF–water (v/v = 1: 9) mixtures. Inset: The spectral overlap between the emission of **6** and the absorption of 6, 4 DNP and PA.

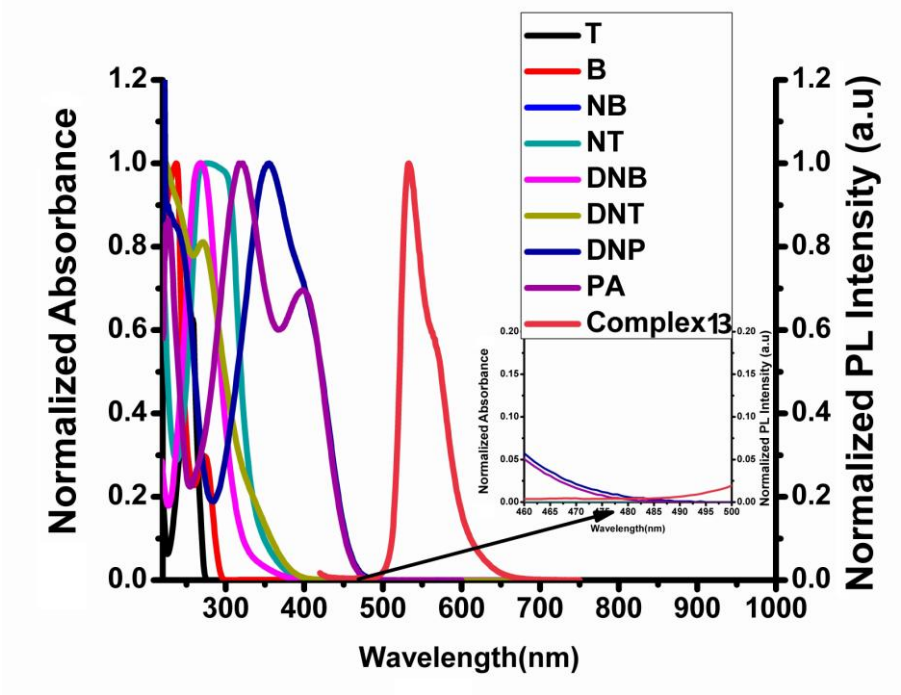

(a)

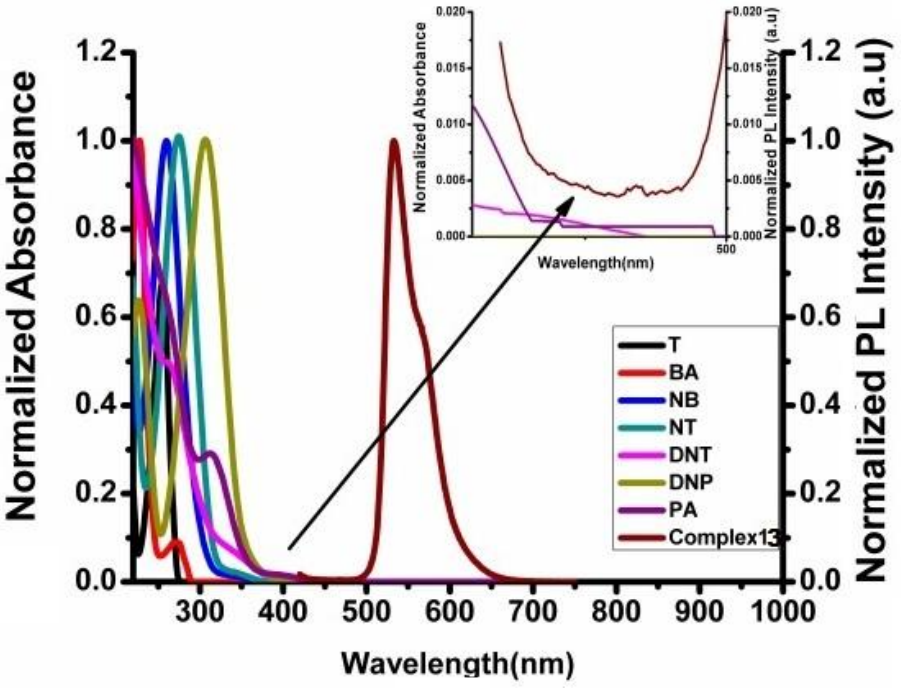

(b)

Figure 3.26 (a) Absorption spectra of different aromatic compounds and emission spectra of 13 in THF. The spectral overlap between the emission of **13** and the absorption of aromatic compounds was shown in inset. (b) Absorption spectra of different aromatic nito and non-nitro compounds and emission spectra of **13** in THF–water (v/v = 1: 9) mixtures. Inset: The spectral overlap between the emission of **13** and the absorption of 2, 4 DNP and PA.

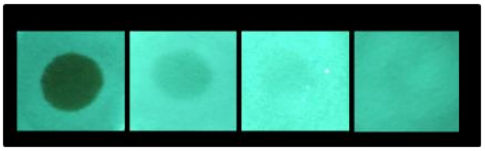

(a) (b) (c) (d)

Figure 3.27 Luminescent photographs of paper plates impregnated by **6** against different concentrations of PA: (a) 10^{-3}, (b) 10^{-6}, (c) 10^{-9}, (d) 10^{-12}.

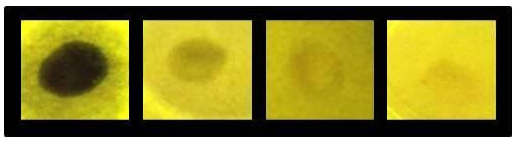

(a) (b) (c) (d)

Figure 3.28 Luminescent photographs of paper plates impregnated by **13** against different concentrations of PA (in M) (a) 10^{-3} (b) 10^{-6}; (c) 10^{-9} (d) 10^{-12}.

3.7 Experimental Section

General Syntheses of Complexes: To a stirred solution of $IrCl_3 \cdot 3H_2O$ (0.5025 mmol) in 2-ethoxyethanol (6 mL), substituted phosphines [triphenyl phosphine, tris(4-(tri fluoro methyl) phenyl) phosphine, methyl diphenyl phosphine and dimethyl (phenyl) phosphine] (1.507 mmol) were added and the reaction mixture refluxed at 130°C for 4-7h. Then, 2-phenyl pyridine derivatives [2,4difluorophenylpyridine, 2-phenylpyridine, benzo [h]quinoline, Dibenzo[f,h]quinoline, 2-(naphthalen-2-yl) pyridine, and 2-(naphthalen-5-yl)pyridine, 4-(2-pyridyl)benzaldehyde] (1.252 mmol) were added to the reaction mixture which was further refluxed for 3-12h. The reaction mass was brought to room temperature. The resulting solid mass was triturated and washed with hexane followed by ethanol for several times to obtain a solid (31-70%) of **1-13** that was purified through recrystallization from a mixture of DCM and hexane (1:1). X-ray quality single crystals for complexes, **2**, **8**, **9 and 13** were collected from the solution.

All synthesized compounds were well characterized by IR, ^{1}H,^{13}C, ^{31}P NMR and HRMS and IR spectral data.

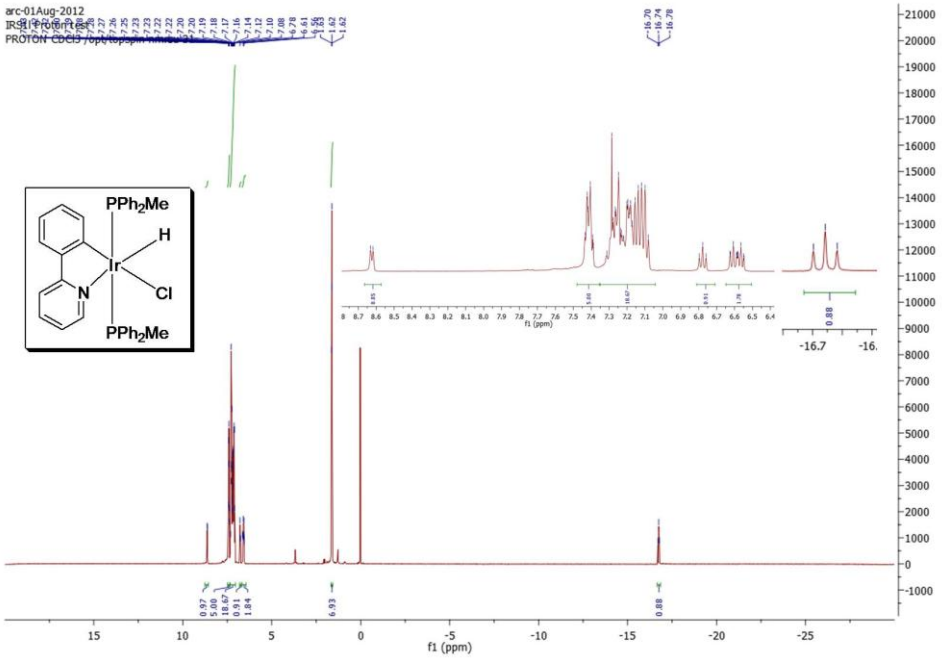

Figure 3.29 ^{1}H NMR spectra of complex **7** recorded in $CDCl_3$.

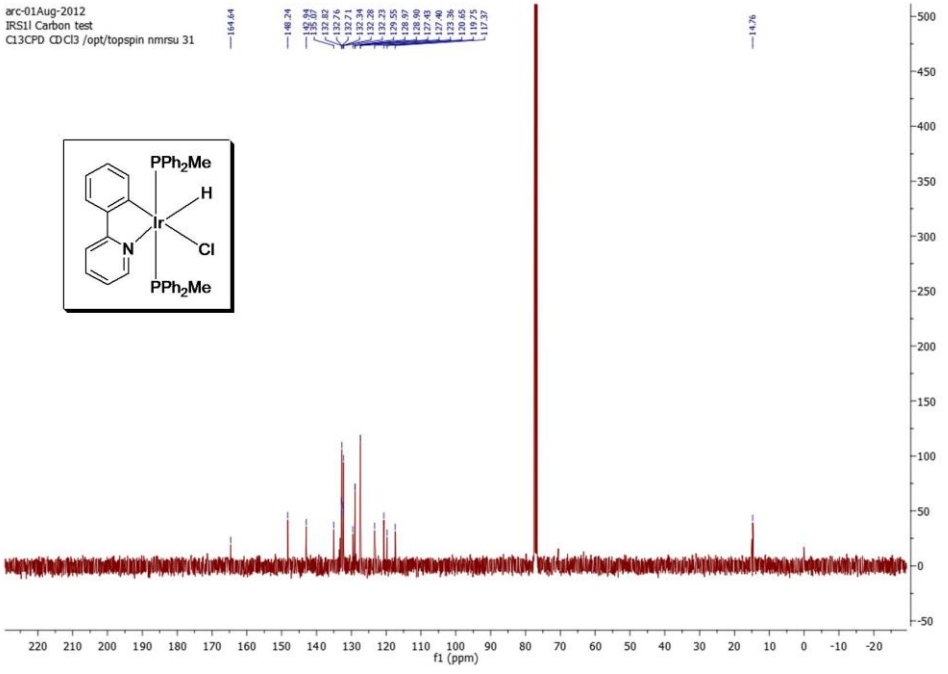

Figure 3.30 ^{13}C NMR spectra of complex **7** recorded in $CDCl_3$.

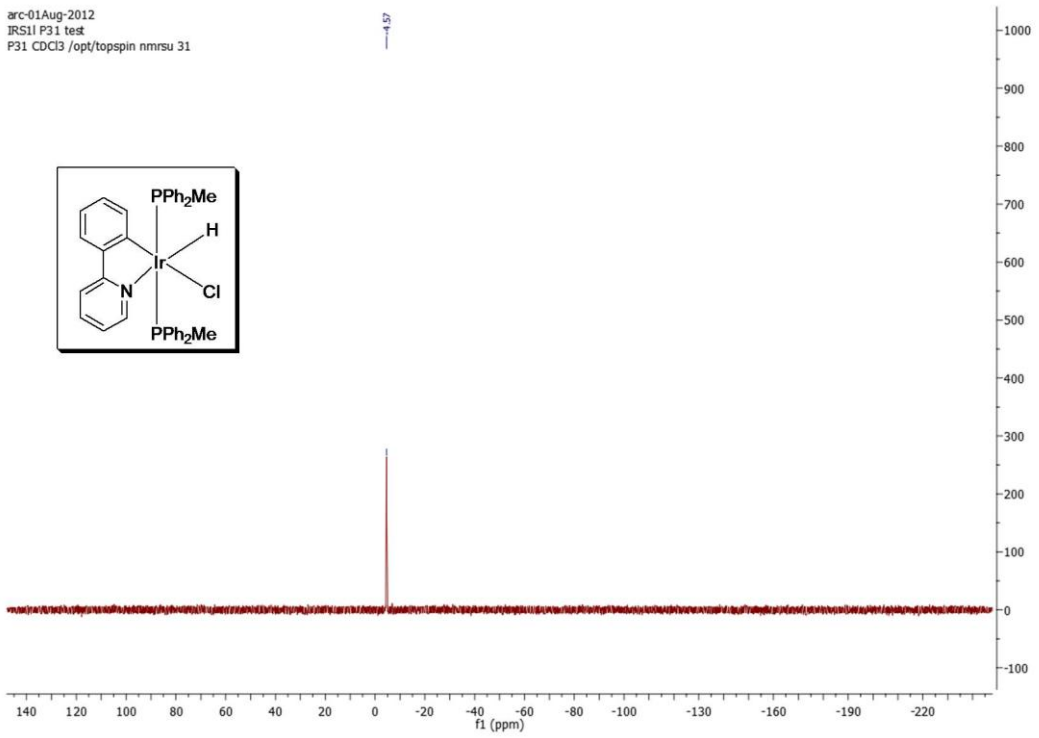

Figure 3.31 ^{31}PNMR spectra of complex 7 recorded in $CDCl_3$.

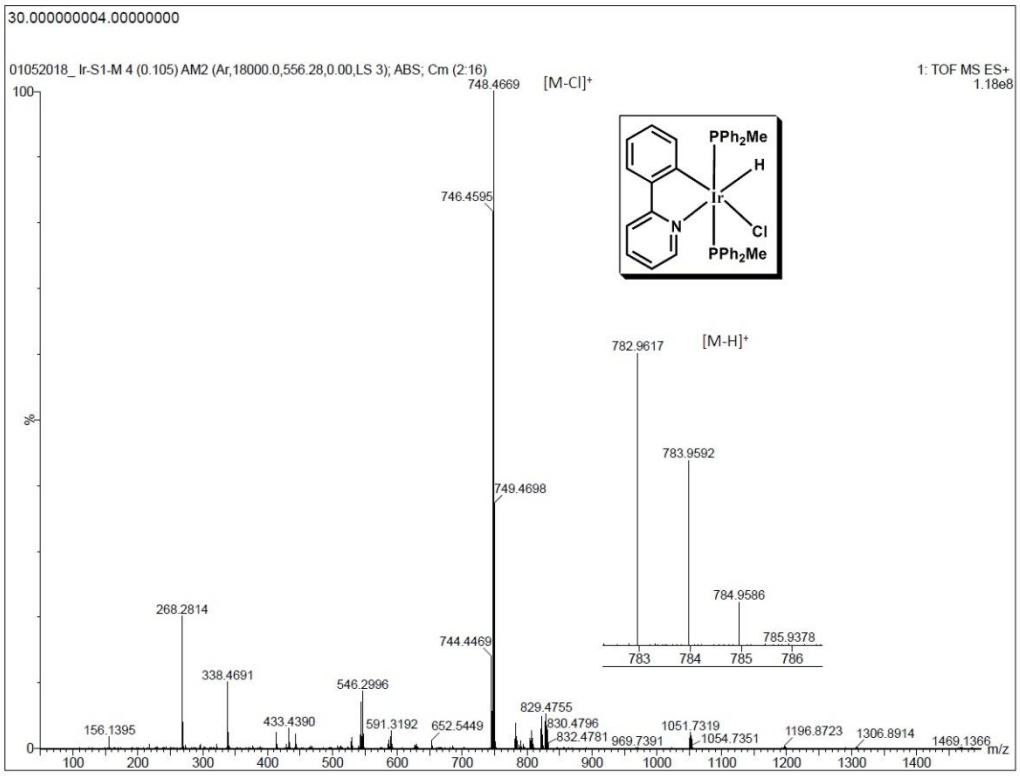

Figure 3.31 HRMS spectra of complex **7**.

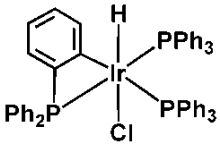

^{1}HNMR (400 MHz, $CDCl_3$) δ 7.57 (dd, J = 14.0, 7.5 Hz, 1H), 7.45 –7.37 (m, 9H) 7.24 – 7.19 (m, 5H), 7.08 (dt, J = 17.0,8.1 Hz, 12H), 6.99 (t, J = 7.5 Hz, 12H), 6.82 – 6.75 (m, 4H), -19.27 (dt, J = 29.2, 8.5 Hz, 1H); ^{13}C NMR (101 MHz, $CDCl_3$) δ 207.00, 206.95, 135.30, 135.20, 135.10, 135.05, 135.00, 132.67, 132.40, 132.16,132.13,132.06,131.96,129.56, 129.19, 128.57, 128.45, 127.16, 127.11, 127.06, 127.01, 126.90, 30.94; ^{31}P NMR (162 MHz, $CDCl_3$) δ 2.41, 7.54, 9.54 for **A (j)**.IR (KBr, cm^{-1}): 2187 (m, ν_{Ir-H}) for **A (j)**.

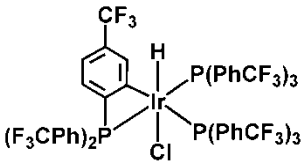

^{1}H NMR (400 MHz, $CDCl_3$) δ 8.11 (dd, J = 13.4, 5.4 Hz, 1H), 7.92 – 7.71 (m, 12H), 7.71 – 7.37 (m, 19H), 7.26 (d, J = 3.1 Hz, 1H), -21.58 (m, 1H).^{13}C NMR (101 MHz, $CDCl_3$) δ 136.42, 134.74, 132.55, 132.44, 125.88, 125.55, 125.03, 124.73.^{31}P NMR (162 MHz, $CDCl_3$) δ 26.39, 4.86, 24.04 for **A(k)**. IR (KBr, cm^{-1}): 2251 (m, ν_{Ir-H}) for **A (k)**.

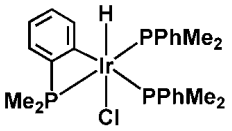

^{1}H NMR (400 MHz, $CDCl_3$) δ 8.13 – 8.02 (m, 1H), 7.61 (dt, J = 8.2, 4.9 Hz, 8H), 7.50 (d, J = 6.7 Hz, 2H), 7.43 – 7.26 (m, 10H), 7.26 – 7.09 (m, 13H), 7.07 – 6.90 (m, 9H), 6.74 (td, J = 7.9, 2.1 Hz, 1H), 2.34 (t, J = 4.1 Hz, 3H), 2.15 (t, J = 4.1 Hz, 6H), -19.40 (dt, J = 17.1, 9.9 Hz, 1H).^{13}C NMR (101 MHz, $CDCl_3$) δ 135.04, 134.68, 134.48, 133.33, 133.29, 133.25, 132.23, 132.15, 131.91, 131.48, 131.22, 130.96, 130.22, 129.53, 129.43, 129.41, 128.93, 128.53, 127.99, 127.86, 127.76, 127.62, 127.48, 127.43, 127.38, 15.86, 15.65, 15.44, 11.75, 11.65, 11.55. ^{31}P NMR (162 MHz, $CDCl_3$) δ -12.28, -40.59, -54.45 for **A (l)**. IR (KBr, cm^{-1}): 2152 (m, ν_{Ir-H}) **A (l)**.

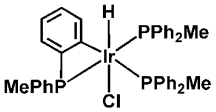

^{1}H NMR (400 MHz, $CDCl_3$) δ 7.55 (dt, J = 7.9, 4.8 Hz, 5H), 7.35 (t, J = 7.3 Hz, 3H), 7.31 – 7.12 (m, 8H), 6.95 (td, J = 7.9, 2.5 Hz, 2 2H), 1.92 (t, J = 4.3 Hz, 15H). ^{13}C NMR (101 MHz, $CDCl_3$) δ 136.23, 135.99, 130.58, 130.54, 130.50, 129.47, 129.39, 128.97, 128.54, 128.49, 128.45, 128.31, 128.21, 13.62, 13.20, 11.08, 10.88, 10.68. ^{31}P NMR (162 MHz, $CDCl_3$) δ -40.60, -49.93 for **A (m)**. IR (KBr, cm^{-1}): 2139 (m, ν_{Ir-H}) for **A (m)**.

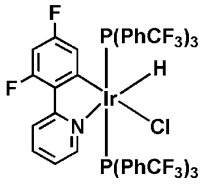

^{1}H NMR (400 MHz, $CDCl_3$) δ 8.76 (d, J = 5.4 Hz, 1H), 7.90 (d, J = 9.6 Hz, 1H), 7.75 – 7.39 (m, 25H), 6.74 (t, J = 6.5 Hz, 1H), 6.24- 6.02 (m, 1H), 5.75 (d, J = 8.8 Hz, 1H), -16.73 (t, J = 16.6 Hz, 1H). ^{13}C NMR (101 MHz, $CDCl_3$) δ 149.09, 137.28, 134.03, 133.97, 133.91, 133.80, 133.53, 132.69, 132.36, 132.04, 131.71, 127.55, 126.36, 124.80, 124.76, 122.48, 122.10, 121.41. ^{31}P NMR (162 MHz, $CDCl_3$) δ 8.85 for **1**. IR (KBr, cm^{-1}): 2152 (m, ν_{Ir-H}), ESI-HRMS. calculated: ($[M-Cl]^+$), m/z 1316.1242 and ($[M-H+Li]^+$): m/z 1357.1012, found: ($[M-Cl]^+$), m/z 1316.1243 ($[M-H+Li]^+$), m/z 1357.1494 for **1**

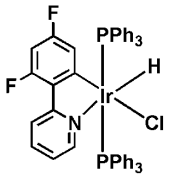

^{1}H NMR (400 MHz, $CDCl_3$) 8.9 (d, 1H), 7.8 (d, J =10.8,1H), 7.5-7.1 (m, 31H), 6.6 (t, 1H), 6.0 (t, 1H), 5.7 (d,J=13.6,1H); ^{13}C NMR (101 MHz, $CDCl_3$) δ 149.90, 136.06, 134.02, 133.97, 133.92, 131.53, 131.27, 131.01, 129.26, 127.41, 127.36, 127.31, 126.55, 121.63, 121.46, 120.66; ^{31}P NMR (162 MHz, $CDCl_3$) δ 7.78 IR (KBr, cm^{-1}): 2152 (m, ν_{Ir-H}), ESI-HRMS. Calculated: ($[M-H]^+$), m/z 942.1609 and ($[M-Cl]^+$): m/z 908.1999, found: ($[M-H]^+$), m/z 942.1600 ($[M-Cl]^+$), m/z 908.1995 for **2** .

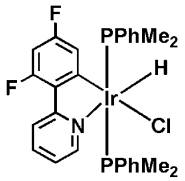

^{1}H NMR (400 MHz, $CDCl_3$) δ 8.82 (d, J = 5.3 Hz, 1H), 7.65 (d, J = 8.4 Hz, 1H), 7.61 – 7.48 (m, 4H), 7.41 (t, J = 7.6 Hz,1H), 7.35 – 7.13 (m, 10H), 7.09 – 7.01 (m, 6H), 6.84 (d, J = 9.1 Hz, 1H), 6.73 (t, J = 6.4 Hz, 1H), 6.22 – 6.05 (m, 1H), 1.71 (t, J = 3.5 Hz, 6H), -16.71 (t, J = 15.5 Hz, 1H). ^{13}C NMR (101 MHz, $CDCl_3$) δ 148.31, 135.91,132.72, 132.66, 132.60, 132.49, 132.39, 132.22, 132.11, 132.06, 132.00, 129.49, 129.05, 127.77, 127.72, 127.67, 127.47, 127.42, 127.37, 122.08, 121.87, 120.84, 95.69, 14.13, 13.94, 13.76. ^{31}P NMR (162 MHz, $CDCl_3$) δ -5.05 for **3**. IR (KBr, cm^{-1}): 2152 (m, ν_{Ir-H}), ESI-HRMS. calculated: ($[M+Na]^+$): m/z 842.2687 and ($[M-HCl+2Na]^+$) m/z 828.7975,found: ($[M+Na]^+$), m/z 842.3762 and ($[M-HCl+2Na]^+$), m/z 828.9851 for **3**.

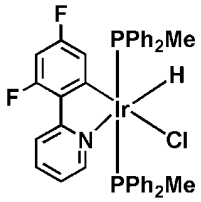

^{1}H NMR (400 MHz, $CDCl_3$) δ 8.85 (d, J = 5.4 Hz, 1H), 7.63(d, J = 8.4 Hz, 1H), 7.56 (m, 1H), 7.35 (t, J =7.4Hz, 1H), 7.26 –7.12 (m, 1H), 7.05 (t, J = 7.3 Hz, 1H), 7.00 – 6.84 (m, 5H), 6.74 (m, 4H), 6.38 – 6.24 (m, 1H), 1.74 (t, J = 3.7 Hz, 6H), 1.62 (t, J =

3.7 Hz, 6H), -17.87 (t, J = 18.1 Hz, 1H).^{13}C NMR (101 MHz, $CDCl_3$) δ 147.63, 135.73, 133.69, 129.47, 128.73, 128.68, 128.64, 128.49, 128.27, 127.39, 127.35, 127.30, 121.97, 120.72, 14.79, 14.59, 14.39, 12.68, 12.49, 12.30. , ^{31}P NMR (162 MHz, $CDCl_3$) δ -25.62 for **4**.IR (KBr, cm^{-1}): 2106 (m, ν_{Ir-H}), ESI-HRMS calculated: ($[M-H]^+$), m/z 694.0983 and ($[M+K]^+$): m/z 734.0698 found: ($[M-H]^+$), m/z 694.0977 ($[M+K]^+$), m/z 734.0695 for **4**.

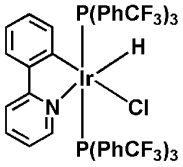

^{1}H NMR (400 MHz, $CDCl_3$) δ 8.73 (d, J = 5.5 Hz, 1H),7.49 (m, 26H), 7.24 (d, J = 7.0 Hz, 1H), 6.74 – 6.59 (m, 2H), 6.27 (d, J =7.7 Hz, 1H), 6.09 – 5.98 (m, 1H), 16.72 (t, J = 16.8 Hz, 1H).^{13}C NMR (101 MHz, $CDCl_3$) δ 165.21, 149.06, 142.87, 141.95, 136.51, 134.23, 134.05, 134.00, 133.94, 131.96, 131.63, 124.91, 124.64, 124.60, 122.20, 121.21, 118.23. ^{31}P NMR (162 MHz, $CDCl_3$) δ 10.17 for **5**. IR (KBr, cm-1): 2144 (m, ν_{Ir-H}),), ESI-HRMS calculated: ($[M-Cl]^+$): m/z 1280.1430, ($[M-H]^+$): m/z 1314.1040, ($[M-H+Li]^+$), m/z 1321.1200 and , found: ($[M-Cl]^+$): m/z 1280.1439, ($[M-H]^+$): m/z 1314.1030, ($[M-H+Li]^+$), m/z 1321.1687 for **5** .

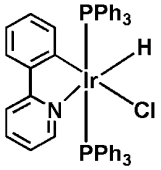

^{1}HNMR (400 MHz, $CDCl_3$) 8.9 (d, J = 5.32,1H), 7.65 (d, J =8.32,1H), 7.5 (t, J=8,1H), 7.4 (d, J = 7.96,1H), 7.2-7.1 (m, 30H), 6.8 (t,J=7.6, ,1H), 6.5 (t, J = 7.16,1H), 6.2 (d, J =7.64,1H), 5.8 (t, J = 7.2,1H); ^{13}C NMR (101 MHz, $CDCl_3$) δ 166.31, 149.61, 143.46, 135.28, 134.10, 134.05, 133.99, 132.03, 131.77, 131.51, 130.04, 128.88, 127.26, 127.21, 127.16, 122.36, 120.43, 119.21, 117.00; ^{31}PNMR (162 MHz, $CDCl_3$) δ 9.25 for **6**. IR (KBr, cm^{-1}): 2098 (m, ν_{Ir-H}), ESI-HRMS calculated: ($[M-H]^+$): m/z 906.1797, ($[M-Cl]^+$): m/z 872.2187, found: ($[M-H]^+$): m/z 906.1766, ($[M-Cl]^+$): m/z 872.2165 for **6** .

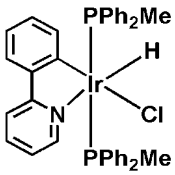

^{1}H NMR (400 MHz, $CDCl_3$) δ 8.62 (d, J = 5.4 Hz, 1H), 7.41 (m, 5H), 7.35 – 7.00 (m, 19H), 6.78 (t, J = 7.4 Hz, 1H), 6.64 – 6.49 (m, 2H), 1.65 – 1.59 (m, 6H), -16.74 (t J =15.9 Hz, 1H). ^{13}C NMR (101 MHz, $CDCl_3$) δ 164.64, 148.24, 142.94, 135.07, 132.82, 132.76,132.71, 132.34, 132.28, 132.23, 129.55, 128.97, 128.90, 127.43, 127.40, 123.36, 120.65, 119.75, 117.37, 14.76., ^{31}P NMR (162 MHz, $CDCl_3$) δ -4.57 for **7**. IR (KBr, cm^{-1}): 2113 (m, ν_{Ir-H}), ESI-HRMS calculated: ($[M]^+$): m/z 783.1562, ($[M-Cl]^+$): m/z 748.1874, found: ($[M]^+$): m/z 782.9617,

([M-Cl]$^+$): m/z 748.4669 for **7**.

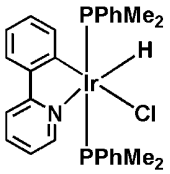

^{1}H NMR (400 MHz, $CDCl_3$) δ 8.76 (d, J = 5.5 Hz, 1H), 7.48 (d, J = 7.5 Hz, 1H), 7.32 – 7.16 (m, 3H), 7.00 (t, J = 7.3 Hz, 2H), 6.90 (t, J = 7.6 Hz, 5H), 6.81 (t, J = 7.3 Hz,1H), 6.76 – 6.70 (m, 4H), 6.63 (t, J = 6.1 Hz, 1H), 1.79 (t, J = 3.6 Hz, 6H), 1.53 (t, J = 3.6 Hz, 6H), -17.88 (t, J = 18.4 Hz, 1H).^{13}C NMR (101 MHz, $CDCl_3$) δ 164.57, 147.59, 142.78, 134.99, 134.34, 129.70, 128.92, 128.88, 128.83, 127.90, 127.21, 127.17, 127.13, 123.25, 120.55, 119.74, 117.37, 14.77, 14.58, 14.38, 13.34, 13.15, 12.96. ^{31}P NMR (162 MHz, $CDCl_3$) δ -25.45 for **8**. IR (KBr, cm^{-1}): 2098 (m, ν_{Ir-H}), ESI-HRMS calculated: ([M-H]$^+$): m/z 658.1171, ([M-Cl]$^+$): m/z 624.1561, found: ([M-H]$^+$): m/z 658.0774, ([M-Cl]$^+$): m/z 624.1204 for **8.**

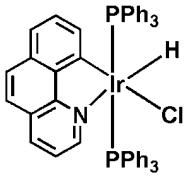

^{1}H NMR (400 MHz, $CDCl_3$) δ 9.13 (d, J = 5.1 Hz 1H), 7.77 (d, J =7.6 Hz, 1H), 7.54 (d, J = 8.7 Hz, 2H), 7.36 – 7.20 (m, 15H), 7.18– 7.07 (m, 8H), 7.03 –6.92 (m, 9H), 6.68 (d, J = 7.3 Hz, 1H), 6.46(t, J = 7.6 Hz, 1H), -16.80 (t, J = 16.3 Hz, 1H). ^{13}C NMR (101 MHz, $CDCl_3$) δ 154.91, 148.39, 140.42, 134.13, 133.86, 133.80, 133.75, 131.69, 131.43, 131.17, 129.46, 128.84, 128.51, 127.13, 127.08, 127.04, 125.75, 122.67, 119.86, 117.58. ^{31}P NMR (162 MHz, $CDCl_3$) δ 10.58 for **9**. IR (KBr, cm^{-1}): 2129 (m, ν_{Ir-H}), ESI-HRMS calculated: ([M-H]$^+$): m/z 930.1797, ([M-Cl]$^+$): m/z 896.2187, found: ([M-H]$^+$): m/z 930.1777, ([M-Cl]$^+$): m/z 896.2217 for **9**.

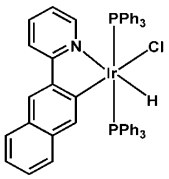

^{1}H NMR (400 MHz, $CDCl_3$) δ 9.20 (d, J = 5.1 Hz, 1H), 8.58 (d, J =7.6 Hz, 1H), 8.47 (t, J = 7.0 Hz, 2H), 7.78 (d, J = 8.0 Hz, 1H), 7.67(m, 2H), 7.36 – 7.20 (m, 13H), 7.12 (t, J = 7.3 Hz, 6H), 7.07 – 6.94 (m,12H), 6.65 (d, J = 7.4 Hz, 1H), 6.44 (t, J = 7.7 Hz, 1H), -16.49 (t, J = 16.4 Hz, 1H). ^{13}C NMR (101 MHz, $CDCl_3$) δ 155.93, 148.89, 141.45, 133.94, 133.88, 133.83, 131.71, 131.45, 131.28, 131.19, 130.30, 129.97, 129.39, 128.86, 128.04, 127.71, 127.17, 127.13, 127.08, 126.46, 124.15, 123.58, 122.99, 120.17, 112.72 for **10**. ^{31}P NMR (162 MHz, $CDCl_3$) δ 7.93. IR (KBr, cm^{-1}): 2113 (m, ν_{Ir-H}), ESI-HRMS calculated: ([M-H]$^+$): m/z 956.1954, ([M-Cl]$^+$): m/z 922.2342, found: ([M-H]$^+$): m/z 956.1945, ([M-Cl]$^+$): m/z 922.2349 for **10** .

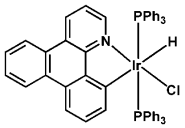

^{1}H NMR (400 MHz, $CDCl_3$) δ 9.17 (d, J = 5.4 Hz, 1H), 8.21 (d, J = 8.6 Hz, 1H), 7.98 (d = 8.1 Hz, 1H), 7.74 –7.63 (m, 1H), 7.49 (m, 2H), 7.44 – 7.30 (m, 11H), 7.28 – 6.96 (m,19H), 6.92 (m, 1H), 6.62 (m, 1H), 6.50 (d, J = 8.4 Hz, 1H), 6.24 (d, J = 8.4 Hz, 1H), - 16.30 (t, J = 16.7 Hz, 1H). ^{13}C NMR (101 MHz, $CDCl_3$) δ 165.90, 150.46, 142.03,135.02, 134.55, 134.55, 134.16, 134.11, 134.11, 134.05, 132.08, 131.77, 131.77, 131.46,130.89, 130.19, 129.02, 128.97, 128.68, 127.23, 127.23, 127.18, 125.19, 121.86, 121.83, 121.48, 119.49., ^{31}P NMR (162 MHz, $CDCl_3$) δ 6.56 for **11**. IR (KBr, cm^{-1}): 2167 (m, ν_{Ir-H}), HRMS-ESI calculated: ($[M-H]^+$): m/z 980.1954, ($[M-Cl]^+$): m/z 946.2343, found: ($[M-H]^+$): m/z 980.1937, ($[M-Cl]^+$): m/z 946.2334 for **11** .

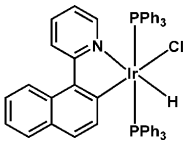

^{1}H NMR (400 MHz, $CDCl_3$) δ 9.08 (d, J = 5.5 Hz, 1H), 7.73 (s, 1H), 7.60 (t, J = 16.4, 7.9 Hz, 2H), 7.45 – 7.39 (m, 2H), 7.38 – 7.30 (m, 11H), 7.26 – 7.18 (m, 1H), 7.17 – 7.05 (m, 8H), 7.05 – 6.86 (m, 11H), 6.72 (t, J = 10.3, 4.2 Hz, 2H), 6.64 (s, 1H), -16.93 (t, J = 16.7 Hz, 1H). ^{13}C NMR (101 MHz, $CDCl_3$) δ 164.68, 160.17, 149.93, 135.31, 134.07, 134.02, 133.96, 131.70, 131.43, 131.18, 128.93, 127.72, 127.38, 127.15, 127.10, 127.05, 125.98, 124.74, 122.41, 121.33, 121.03, 117.88. ^{31}P NMR (162 MHz, $CDCl_3$) δ 10.17 for **12**. IR (KBr, cm^{-1}): 2129 (m, ν_{Ir-H}), calculated: ($[M-Cl]^+$): m/z 922.2342, found: ($[M-H]^+$): m/z ($[M-Cl]^+$): m/z 922.2385 for **12**.

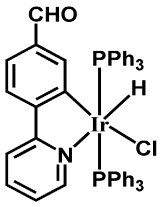

^{1}H NMR (400 MHz, $CDCl_3$) δ 9.15 (d, *J* = 5.5 Hz, 1H), 8.9 (s,1H), 7.56 (d, *J* = 8.0 Hz, 1H), 7.49 – 7.30 (m, 15H), 7.15(m, 18H), 6.81 (t, *J* = 6.0 Hz, 1H), 6.47 (s, 1H). δ 16.76 (t, *J* = 16.9 Hz, 1H); ^{13}C NMR (101 MHz, $CDCl_3$) δ 193.22, 150.69, 133.99, 133.99,133.94, 133.88, 133.88, 131.86, 131.59, 131.31, 129.16, 129.16, 127.43,127.38, 127.38,127.33, 122.47, 121.40, 118.70, 117.65; ^{31}P NMR (162 MHz, $CDCl_3$) δ 7.93; ESI-HRMS calculated: ($[M-Cl]^+$): m/z, 900.2136, found: ($[M-Cl]^+$): m/z, 900.3271, yellow solid; Yield, 68.00 % for **13**.

3.8 Conclusions

The one-pot synthetic route of mono cyclometalated iridium(III) complexes, **1-13** those are strongly emissive in the solid state has been generalized. Tuning of the emission color has been accomplished throughout the visible range through systematic changes in the chromophoric ligands. Quantum chemistry calculations at the DFT and TD-DFT level have been used to explore the intricacies of the electronic nature of the ground and low-lying excited states involved in UV-Vis absorption and photoemission processes confirming the experimental observations. Computed relative transition energies are in good agreement to measured absorption and emission peaks. Investigations were carried out to explore both the nature of the emitting states and the AIE activity for all these complexes. The dual functionalities exhibited by a common iridium(III) framework through proper selection and placement of the chromophoric (cyclometalating) and rotating entity (triarylphosphine) into the iridium(III) coordination sphere provide these molecules with interesting photophysical properties that can be exploited to obtain new cell imaging probes. To illustrate this possibility, the AIE active iridium(III) complex, **6** was successfully encapsulated inside the hydrophobic core of PEG-PLA nanoparticles *via* the simple oil-in-water based emulsion-evaporation method. Aggregation of iridium(III) complex molecules in the hydrophobic core of the PEG-PLA particles leads to an important increase of their emission intensity. The colloidal form of these luminescent PEG-PLA particles has been shown to behave as a potential cell imaging probe. Additionally **6** and **13** have been successfully employed for sensitive and selective detection of nitro-explosives and the Stern–Volmer quenching constant for both the complexes (K_{sv} =1.90 x 10^5 M^{-1} and 1.00 x 10^5 M^{-1} for 6 and 1**3**, respectively) and detection limit for PA is observed to 65 nM and 264 nM for the complexes **6** and **13**, respectively. The experimental observations support that both electron and energy transfer quenching mechanisms are responsible for the selective detection of PA by **6**. Filter paper based an easy way of detection of PA, a portable technique was developed.

3.9 References

[1] V.K. Gupta, S.K. Shoora, L.K. Kumawat, A.K. Jain, Sens. Actuators, B, 209 (2015) 15-24.

[2] Z. Hai, Y. Bao, Q. Miao, X. Yi, G. Liang, Anal. Chem., 87 (2015) 2678-2684.

[3] S. Kim, M.S. Eom, S. Yoo, M.S. Han, Tetrahedron Lett., 56 (2015) 5030-5033.

[4] S. Lee, K.K.Y. Yuen, K.A. Jolliffe, J. Yoon, Chem. Soc. Rev., 44 (2015) 1749-1762.

[5] M.G. Mohamed, R.-C. Lin, J.-H. Tu, F.-H. Lu, J.-L. Hong, K.-U. Jeong, C.-F. Wang, S.-W. Kuo, RSC Adv., 5 (2015) 65635-65645.

[6] S. Marpu, P.K. Upadhyay, D.T. Nguyen, I.W.H. Oswald, R.K. Arvapally, R.A. Petros, Z. Hu, M.A. Omary, J. Phys. Chem. C, 119 (2015) 12551-12561.

[7] X.-H. Yang, S. Li, Z.-S. Tang, X.-D. Yu, T. Huang, Y. Gao, Chin. Chem. Lett., 26 (2015) 129-132.

[8] K. Zhang, S. Liu, Q. Zhao, F. Li, W. Huang, Phosphorescent Iridium(III) Complexes for Bioimaging, in: K.K.-W. Lo (Ed.) Luminescent and Photoactive Transition Metal Complexes as Biomolecular Probes and Cellular Reagents, Springer Berlin Heidelberg, 2015, pp. 131-180.

[9] Q. Zhao, Y. Liu, Y. Cao, W. Lv, Q. Yu, S. Liu, X. Liu, M. Shi, W. Huang, Advanced Optical Materials, 3 (2015) 233-240.

[10] Q. Zhao, X. Zhou, T. Cao, K.Y. Zhang, L. Yang, S. Liu, H. Liang, H. Yang, F. Li, W. Huang, Chem. Sci., 6 (2015) 1825-1831.

[11] H.-Y. Li, L. Zhou, M.-Y. Teng, Q.-L. Xu, C. Lin, Y.-X. Zheng, J.-L. Zuo, H.-J. Zhang, X.-Z. You, J. Mater. Chem. C, 1 (2013) 560-565.

[12] J. Zhuang, W. Li, W. Su, Y. Liu, Q. Shen, L. Liao, M. Zhou, Org. Electron., 14 (2013) 2596-2601.

[13] K.M.-C. Wong, M.M.-Y. Chan, V.W.-W. Yam, Adv. Mater., 26 (2014) 5558-5568.

[14] G. Li, T. Fleetham, E. Turner, X.-C. Hang, J. Li, Adv. Opt. Mater., 3 (2015) 390-397.

[15] W. Dong, J. Pina, Y. Pan, E. Preis, J.S. Seixas de Melo, U. Scherf, Polymer, 76 (2015) 173-181.

[16] K. Garg, E. Ganapathi, P. Rajakannu, M. Ravikanth, Phys. Chem. Chem. Phys., 17 (2015) 19465-19473.

[17] Z. He, L. Shan, J. Mei, H. Wang, J.W.Y. Lam, H.H.Y. Sung, I.D. Williams, X. Gu, Q. Miao, B.Z. Tang, Chem. Sci., 6 (2015) 3538-3543.

[18] T.T. Tasso, T. Furuyama, N. Kobayashi, Chem. Eur. J., 21 (2015) 4817-4824.

[19] W. Xi, Y. Zhang, B. Chen, X. Gan, M. Fang, J. Zheng, J. Wu, Y. Tian, F. Hao, H. Zhou, Dyes Pigm., 122 (2015) 31-39.

[20] N.L.C. Leung, N. Xie, W. Yuan, Y. Liu, Q. Wu, Q. Peng, Q. Miao, J.W.Y. Lam, B.Z. Tang, Chem. Eur. J., 20 (2014) 15349-15353.

[21] W. Qin, D. Ding, J. Liu, W.Z. Yuan, Y. Hu, B. Liu, B.Z. Tang, Adv.Funct. Mater., 22 (2012) 771-779.

[22] D. Wang, J. Qian, S. He, J.S. Park, K.-S. Lee, S. Han, Y. Mu, Biomaterials, 32 (2011) 5880-5888.

[23] L.-Q. Xiong, Z.-G. Chen, M.-X. Yu, F.-Y. Li, C. Liu, C.-H. Huang, Biomaterials, 30 (2009) 5592-5600.

[24] Y. Salinas, R. Martinez-Manez, M.D. Marcos, F. Sancenon, A.M. Costero, M. Parra, S. Gil, Chem. Soc. Rev., 41 (2012) 1261-1296.

[25] K.K. Kartha, S.S. Babu, S. Srinivasan, A. Ajayaghosh, J. Am. Chem. Soc., 134 (2012) 4834-4841.

[26] D.C. Apodaca, R.B. Pernites, F.R. Del Mundo, R.C. Advincula, Langmuir, 27 (2011) 6768-6779.

[27] M. Kumar, V. Vij, V. Bhalla, Langmuir, 28 (2012) 12417-12421.

[28] L. Senesac, T.G. Thundat, Mater. Today, 11 (2008) 28-36.

[29] C.Y.K. Chan, J.W.Y. Lam, C. Deng, X. Chen, K.S. Wong, B.Z. Tang, Macromolecules, 48 (2015) 1038-1047.

[30] Z. Hu, B.J. Deibert, J. Li, Chem. Soc. Rev., 43 (2014) 5815-5840.

[31] R.L. Woodfin, Explosives Definitions, in: Trace Chemical Sensing of Explosives, John Wiley & Sons, Inc., 2006, pp. 331-332.

[32] I.A. Popov, H. Chen, O.N. Kharybin, E.N. Nikolaev, R.G. Cooks, Chem. Commun., (2005) 1953-1955.

[33] S.J. Toal, W.C. Trogler, J. Mater. Chem., 16 (2006) 2871-2883.

[34] Q. Zhang, D. Zhang, Y. Lu, Y. Yao, S. Li, Q. Liu, Biosens. Bioelect., 68 (2015) 494-499.

[35] Y. Li, W. Zhang, Z. Sun, T. Sun, Z. Xie, Y. Huang, X. Jing, Eur. Poly. J., 63 (2015) 149-155.

[36] R. González-Méndez, D.F. Reich, S.J. Mullock, C.A. Corlett, C.A. Mayhew, I. J. Mass Spect., 385 (2015) 13-18.

[37] H.-J. Jiang, J.-L. Zhang, Q.-W. Zhang, S.-H. Ye, Synthetic Metals, 201 (2015) 30-42.

[38] Y. Bai, G.-j. He, Y.-g. Zhao, C.-y. Duan, D.-b. Dang, Q.-j. Meng, Chem. Commun., (2006) 1530-1532.

[39] M. Meaney, V. McGuffin, Anal Bioanal Chem, 391 (2008) 2557-2576.

[40] T.K. Kim, J.H. Lee, D. Moon, H.R. Moon, Inorg. Chem., 52 (2013) 589-595.

[41] L. Li, S. Zhang, L. Xu, L. Han, Z.-N. Chen, J. Luo, Inorg. Chem., 52 (2013) 12323-12325.

[42] A. Saxena, M. Fujiki, R. Rai, G. Kwak, Chem. Mater., 17 (2005) 2181-2185.

[43] X.-G. Hou, Y. Wu, H.-T. Cao, H.-Z. Sun, H.-B. Li, G.-G. Shan, Z.-M. Su, Chem. Commun., 50 (2014) 6031-6034.

[44] K.S. Bejoymohandas, T.M. George, S. Bhattacharya, S. Natarajan, M.L.P. Reddy, J. Mater. Chem. C, 2 (2014) 515-523.

[45] M. Obulichetty, D. Saravanabharathi, Spectrochim. Acta Part A: Molecular and Biomolecular Spectroscopy, 118 (2014) 861-866.

[46] T. Fei, K. Jiang, T. Zhang, Sens. Actuators, B, 199 (2014) 148-153.

[47] M.A. Bennett, D.L. Milner, J. Am. Chem. Soc., 91 (1969) 6983-6994.

[48] H.D. Kaesz, R.B. Saillant, Chem. Rev., 72 (1972) 231-281.

[49] C.-H. Yang, S.-W. Li, Y. Chi, Y.-M. Cheng, Y.-S. Yeh, P.-T. Chou, G.-H. Lee, C.-H. Wang, C.-F. Shu, Inorg. Chem., 44 (2005) 7770-7780.

[50] C.-H. Chang, C.-L. Ho, Y.-S. Chang, I.C. Lien, C.-H. Lin, Y.-W. Yang, J.-L. Liao, Y. Chi, J. Mater. Chem. C, 1 (2013) 2639-2647.

[51] I.R. Laskar, S.-F. Hsu, T.-M. Chen, Polyhedron, 24 (2005) 189-200.

[52] S. Lamansky, P. Djurovich, D. Murphy, F. Abdel-Razzaq, R. Kwong, I. Tsyba, M. Bortz, B. Mui, R. Bau, M.E. Thompson, Inorg. Chem., 40 (2001) 1704-1711.

[53] Y. Ren, J.W.Y. Lam, Y. Dong, B.Z. Tang, K.S. Wong, J. Phys. Chem. B, 109 (2005) 1135-1140.

[54] Q. Wang, Y. Bao, J. Ahire, Y. Chao, Adv. Healthcare Mater., 2 (2013) 459-466.

[55] A.M. Talarico, M. Ghedini, C.O. Rossi, E.I. Szerb, Soft Matter, 8 (2012) 11661-11669.

[56] N.R. Jana, Phys. Chem. Chem. Phys., 13 (2011) 385-396.

[57] J. Wang, J. Mei, W. Yuan, P. Lu, A. Qin, J. Sun, Y. Ma, B.Z. Tang, J. Mater. Chem., 21 (2011) 4056-4059.

[58] V. Bhalla, A. Gupta, M. Kumar, Org. Lett., 14 (2012) 3112-3115.

[59] B. Roy, A.K. Bar, B. Gole, P.S. Mukherjee, J. Org. Chem., 78 (2013) 1306-1310.

[60] V. Bhalla, A. Gupta, M. Kumar, D.S.S. Rao, S.K. Prasad, ACS Appl. Mater. Interfaces, 5 (2013) 672-679.

[61] N. Dey, S.K. Samanta, S. Bhattacharya, ACS Appl. Mater. Interfaces, 5 (2013) 8394-8400.

Chapter IV

Aggregation Induced Emission Active Mono Diimine Iridium(III) Complexes and their Applications in Sensing and Mechanofluorochromism

4.1 Introduction

In last 40 years, the photochemistry of inorganic complexes has been flourished exceptionally. In the era of 1970s the concept of 'solar' photochemistry came in to picture [1-4]. The scientific community had started to study the rich excited state properties where the bipyridine complex of Ruthenium $[Ru(bpy)_3]^{+2}$ an electron transfer reagents [5], was declared as champion. After this successful study, many scientific research groups tried to explore the excited state properties of different metals like Os(II), Ir(III), Pt(II), Pd(II), Re(I) and Cu(I). Among them, the iridium(III) metal has the capability to form a wide range of complexes *e.g.* mono-, bis- and tris-cyclometallated complexes [6-8].

In 1990, Brewer et al. reported the syntheses of a series of iridium(III) complexes, cis-$[IrL_2Cl_2]^+$ (**1**) (where, L = bidentate chelate) by slightly modified procedure. The mixture of $IrCl_3.3H_2O$ and 2 equivalents of L were refluxed for 2 h in EtOH-H_2O mixture resulted 20-70% yield, depending on the nature of L (Figure 4.1.1) [9].

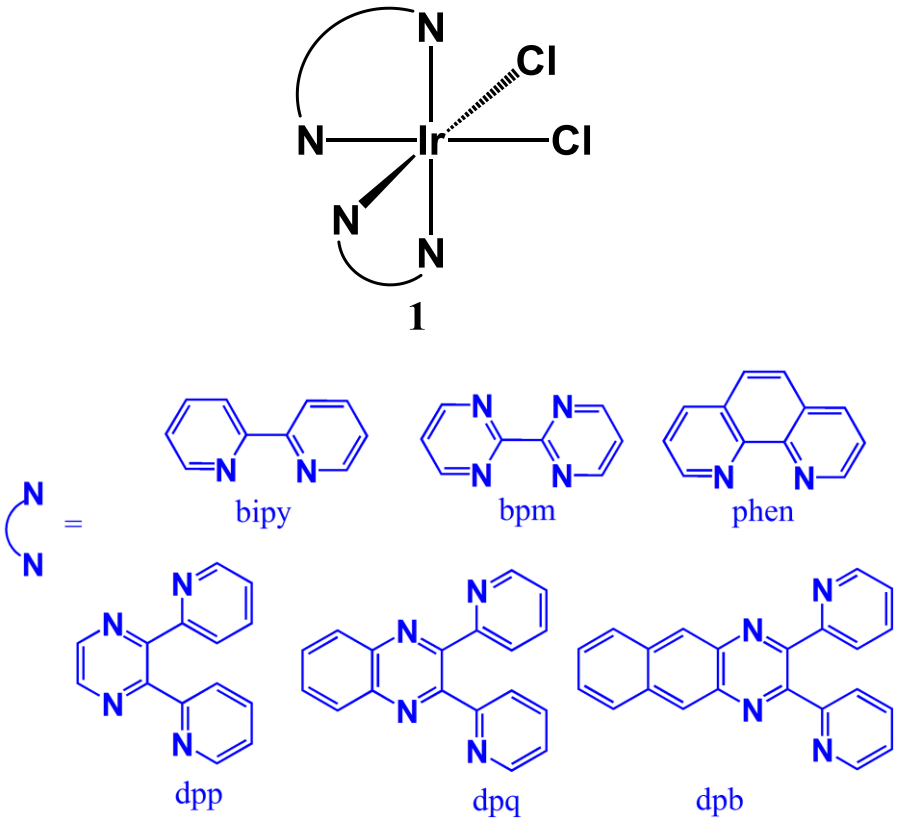

Figure 4.1.1 Structures of diamine ligands used in syntheses of iridium(III) complex formation.

4.1.1 Use of 1, 10 phenanthroline in iridium(III) complexes

1,10 phenanthroline has been widely used as chelating ligand in coordination/organometallic chemistry. It has been extensively used with many metals like Fe, Co, and Ni. In 1963, B.Chiswell and S. E. Livingstone synthesized the first iridium(III) complex using 1,10 phenanthroline as chelateing ligand [10, 11]. They have synthesized three types of iridium(III) complexes (**2a**) tris-chelated, $[Ir(phen)_3]X_3.nH_2O$ (X = C1, Br, I, ClO_4,) (**2b**) bis-chelated, $[Ir(phen)_2X_2]X.nH_2O$ (X = CI, Br); (**2c**) those containing a bis-chelated cation and a mono-chelated anion, $[Ir(phen)_2X_2]$ $.[Ir(phen)X_4].nH_2O$ (X = CI, Br, I).

After successful utilization of neutral luminescent iridium(III) complexes in organic light emitting diodes (OLEDs), the scientific community developed new ionic transition-metal complexes (iTMCs). The iTMCs can facilitate the charge transport across the thin film and avail the need for electron and hole-injection layers because they contains the mobile counterions [12]. Several iTMCs have been synthesized using iridium metal but 1,10 phenanthroline used as a supporting ligand (Figure 4.1.2). A. Valore and co-workers synthesized a series of iTMCs where they have used 1,10 phenanthroline and substituted 1,10 phenanothroline as supporting ligands (**2d**) (Figure 4.1.2) [13, 14].

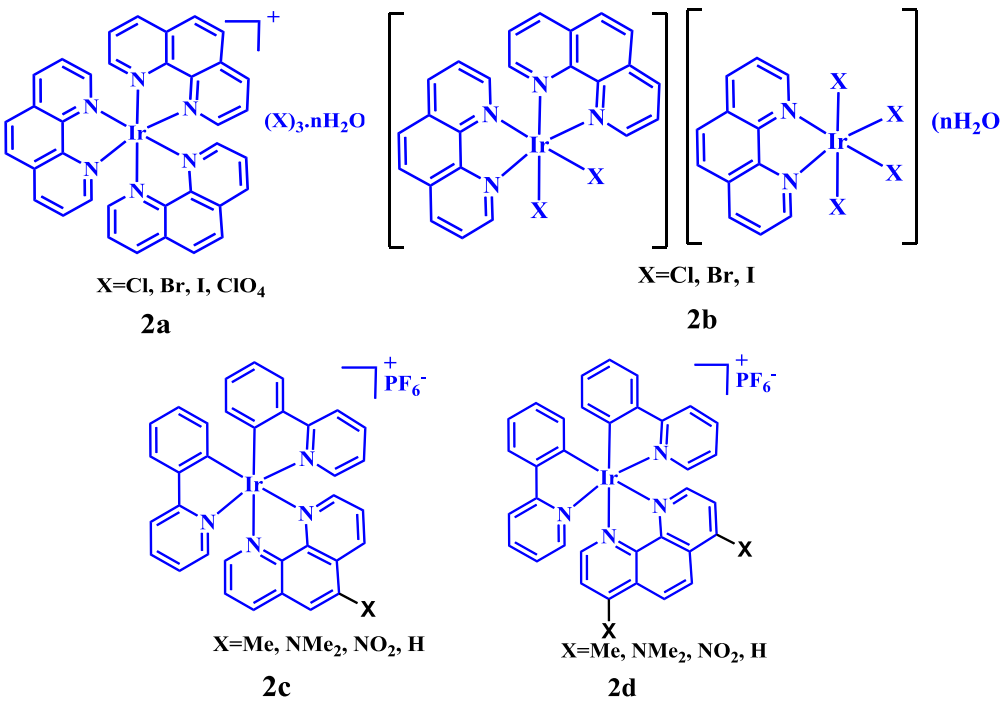

Figure 4.1.2 Structures of 1, 10 phenanthroline complexes of iridium(III).

4.1.2 Use of 2,2'-bipyridine in iridium(III) complexes

2,2'-Bipyridine (bipy) is one of the most widely used ligands in organometallic chemistry. $[Ir(bipy)_3](NO_3)_3$ (**2e**) and $Ir(bipy)_3](ClO_4)_3$ (**2f**) were the first *tris*-2,2′-bipyridyl complexes of iridium reported [15] by Flynn and Demas in 1974. The coordination mode of bipyridine in these complexes was observed in bidentated fashion (Figure 4.1.3).

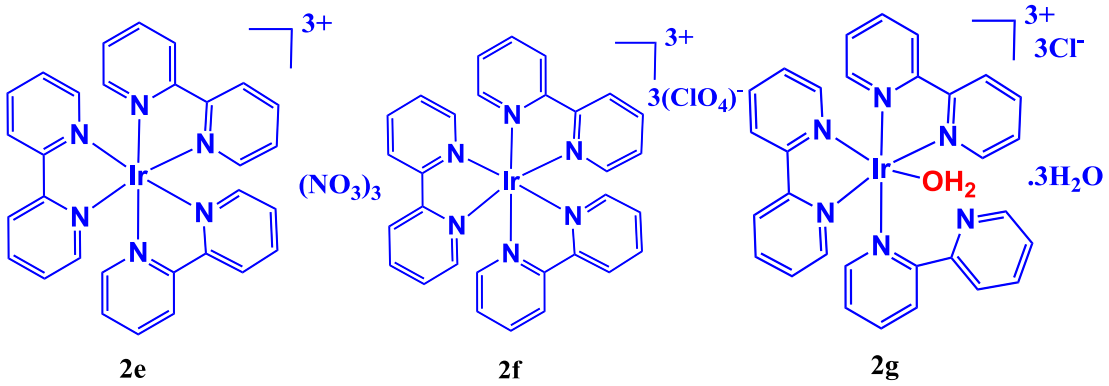

Figure 4.1.3 Structures of 2, 2'bipyridine complexes of iridium(III).

In 1977, a controversial iridium(III) complex of bipy [16] *i.e* $[Ir(bipy)_2(H_2O)(bipy)]Cl_3.3H_2O$ (**2g**) came in to picture. In this complex, the two bipyridine units were coordinated in bidented fashion while the coordination of the third unit was a mystery (Figure 4.1.3).

Just after the crystal structure of perchlorate salt of $[Ir(bipy)_2(H_2O)(bipy)]_3$ was reported [17] by Wickramasinghe, Bird and Serpone in 1981, suggested that one of the bipy ligand was rotated around the centre bond and coordinated in C^N fashion (**2i**).

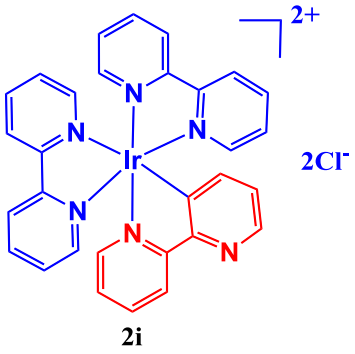

Figure 4.1.4 Structures of 2, 2′-bipyridine rollover complexes of iridium(III).

Later, this fascinating and controversial structure $[Ir(bipy)_2(bipy - H)]^{3+}$ was fully characterized by NMR and single crystal X-ray structure by Spellane, Watts and

Curtis which was the first evidence of C^N coordination [18] of bipy through C-H activation (Figure 4.1.4).

The abnormal coordination κ^2- N, C rather than normal κ^2- N, N is known as rollover [19] species (Figure 4.1.5). Till now, only a few metals, such as Pd(II) [20], Au(III) [21], Rh(III) [22], Ir(III) [23], Pt(II) [24], and Cu(II) [25] are, to be known for showing this behaviour; out of them iridium(III) is still rare. The successful utilization of uncoordinated nitrogen in the field of catalysis, C−C and C−H bond formation has been reported [26]. The emission color tuning of cyclometallated iridium(III) complexes can be done by introducing donor and acceptor groups in the ligand part [27]. The pyridine being an electron rich species, which possibly be transformed into electron deficient with immediate protonation. The photophysical property of the iridium(III) complex with free pyridine ring could be tuned by simply protonation because of electron distribution will change.

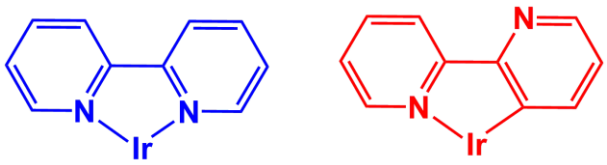

κ^2- N, N κ^2- N, C

Figure 4.1.5 Co-ordination mode of 2, 2′-bipyridine for iridium(III).

The Smart solid state luminescent materials responsive to external stimuli such as shearing, grinding, rubbing, solvent exposure, or temperature changes, have been receiving considerable attention in recent times, both in the scientific as well as in the applied research scenarios [28]. The principal interest in these materials stems from their ability to change their emission color as a response to the external perturbation that triggers changes in the weak non-covalent interactions such as π-π stacking, or hydrogen bonds between the individual molecules in molecular aggregates [29]. These materials have an immense potentiality in various applications such as optical data recorders, mechanical sensors, security paper, deformation detectors or storage devices [30]. In order to enhance the existing capabilities and guide to design of new advanced materials, it is however, necessary to develop a deep understanding of the physical nature of the mechanisms involved in their response to external perturbations.

For the ultimate application of these iridium(III) compounds in optoelectronic devices, it is evident that an enhanced emission in the solid state would be highly

desirable, so that increasingly improved solid state quantum efficiencies could be obtained. In recent years, the aggregation induced emission (AIE) [31, 32] as well as the enhanced phosphorescence emission in the solid state (EPESS terms have been coined to describe this enhancement of the emission in crystalline or aggregated forms as compared to in dilute solutions).

4.2 Part A: 1,10 phenanthroline iridium(III) complexes as Vapor-responsive luminescent materials

4.2.1 Results and discussion

The synthetic strategy of one unit of diimine complex with iridium(III) was originated from our previous report where we had synthesized monocyclometaleted iridium(III) complex in an one-pot reaction. On addition of 1, 10-phenanthroline to the reaction mixture (in place of 2-phenylpyridine in the same reaction protocol), two very close spots on TLC plate were found. These complexes were difficult to separate using traditional purification techniques, *e.g.*, column chromatography, re-crystallization. Therefore, these impure products were mixed with potassium hexafluorophosphate in methanol and the reaction mixture was treated with microwave irradiation leading to exchange of counter ions, where Cl^- was replaced by PF_6^-. A solid residue was separated out which corresponds to complex **4**. Thus, this process facilitates the separation and subsequent purification of the complexes **3** and **4**.

In this case, the diimineiridium(III) complex resulted into dihydride, **3** and chlorohydride, **4** complexes in contrast to cyclometalated ligand where chlorohydride was solely obtained (**D**) (Scheme 4.1.1). The formation of dihydride complex for cyclometalated ligand was restricted, probably to avoid the presence of strong *trans* influencing substituents (hydride and C of cyclometalated ligand) *trans* to each other. These complexes were characterized by ^1H, ^{13}C and ^{31}P NMR spectroscope. ^{31}P NMR spectra showed a single resonance peak for both complexes **3** and **4** which were observed at δ 20.88 ppm and δ 29.49, respectively. ^1H NMR peaks for hydrides were observed at δ -19.24 ppm and δ -17.56 ppm for complexes **3** and **4**, respectively.

The hydride ^1H NMR peaks were found triplet in nature because of P-H coupling ($J_{(P-H)}$ ~15Hz). The J-coupling value of J_{P-H} supports that hydride is *cis* to phosphorous in both complexes. It is clearly seen that ^1H NMR spectrum of **3** has seven sets of protons – (i)

four generated from resonances of 1,10-phenanthroline, (ii) two from triphenylphosphines and (iii) one from single hydride peak. These observations along with a single hydride NMR peak substantiate the symmetrical geometry of **3**. In case of **4**, more than four sets of protons were observed from 1, 10-phenanthroline which clearly indicates the unsymmetrical geometry of **4**. The presence of Ir-H bond in **3** and **4** were confirmed from their respective stretching frequency at 2179 and 2152 cm^{-1}, respectively.

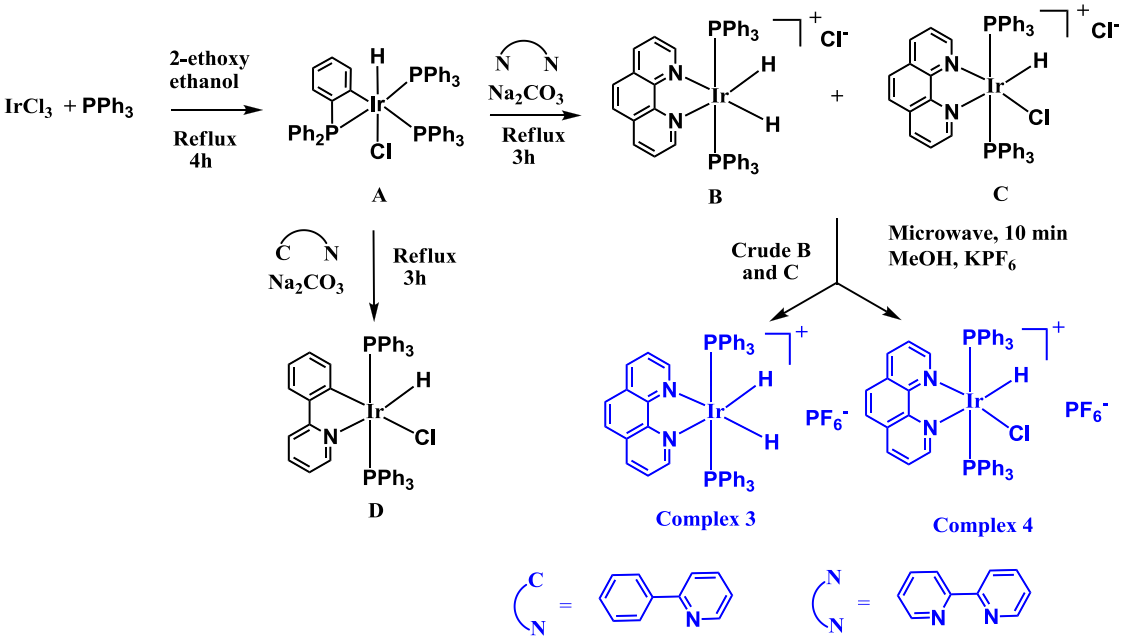

Scheme 4.2.1 Syntheses of complexes **3** and **4**

4.2.2 Structural characterization based on X-ray crystallography

The structure of the complexes **3** and **4** were established by X-ray single crystal diffraction study at 100K. The ORTEP diagrams (Figures 4.2.1) demonstrate the structure of the complex as distorted octahedral. The selected bond lengths and bond angles are shown. The packing diagram of both complexes (Figures 4.2.2) have shown that each of these contain eight dichloromethane (DCM) molecules per unit cell (both complexes were re-crystallized from DCM). The calculated void space for **3** was 980.1$Å^3$ against the cell volume of 4837.5$Å^{3.}$ For **4**, void space and cell volume values are 906.2 $Å^3$ and 4964.8 $Å^3$ respectively.

The ratios of total cell volume to the volume occupied by the solvent molecules were 4.9 and 5.3 for complexes **3** and **4,** respectively. As these ratios were similar in **3** and **4**, similar occupancy values of DCM molecules are suggested, eight DCM molecules per unit cell in **3** and **4** (Figure 4.2.2). These bound DCM molecules in their crystal lattices presumably substitute other volatile solvent molecules upon exposure.

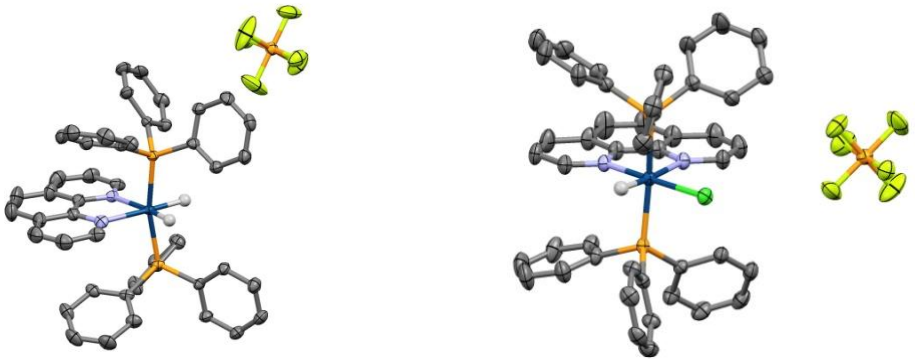

3 **4**

Figure 4.2.1 ORTEPs of **3** and **4** were drawn with 50% probability ellipsoid. All the H atoms (except hydrides), solvent molecules and the counter ion have been omitted for clarity.

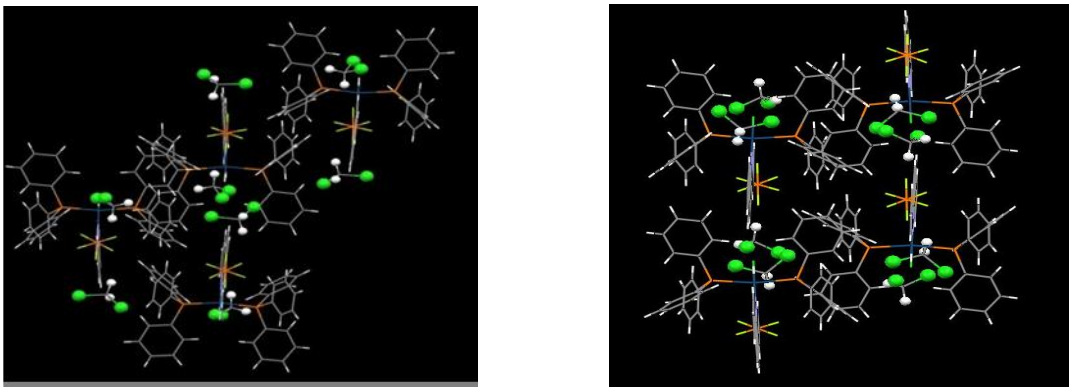

Figure 4.2.2 Unit cell packing diagram of **3** and **4** showing the locations of the CH_2Cl_2 solvent molecules.

4.2.3 Photophysical property

The complexes, **3** and **4** exhibit intense absorption bands in the range of 240 – 320 nm at 10^{-5}M DCM solution. The molar extinction co-efficient (ε, DCM) values

corresponding to the absorption maxima were found to higher than $4.5x10^4$ $M^{-1}cm^{-1}$ (Table 4.2.1). Thus, this transition can be attributed as ligand centered transitions. The observed long absorption tail which starts at 320 nm and extends upto 450 nm (λ_{max} are 364 and 410 nm for **3**; 358 and 400 nm for **4**) (Figure 4.2.3). On closer scrutiny, this long tail seems to be two partly resolved broad absorption bands.

Table 4.2.1 Photophysical properties of **3** and **4**

Complex	UV-Vis absorbance (nm) (ε x10^4) (M^{-1} cm^{-1})	PL (nm)	
		Solid	Solution
3	269 (5.0), 364 (0.50), 410 (0.40)	518	538
4	269 (5.2), 358 (0.40), 400 (0.20)	513	531

Spectra were recorded in degassed dichloromethane (DCM) at room temperature with [$c=10^{-5}$ M] .

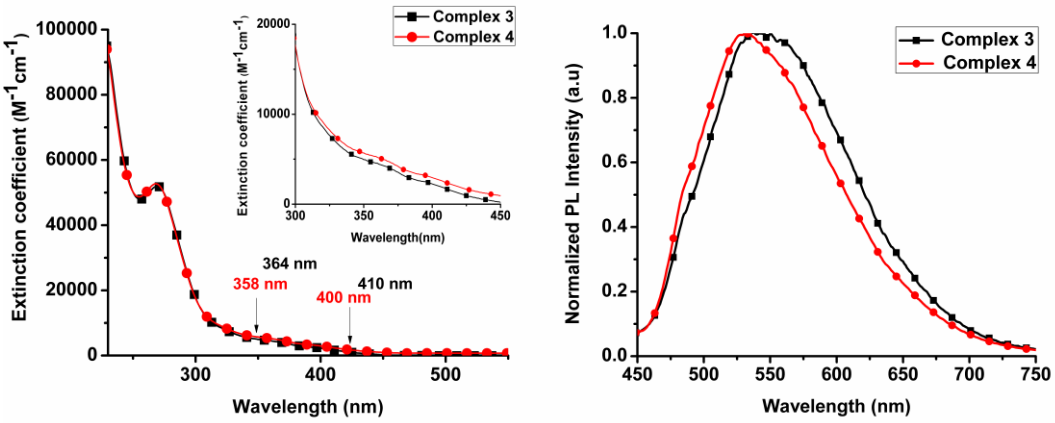

(a) (b)

Figure 4.2.3 Solution absorption spectra for **3** and **4** at a concentration of 10^{-5} M in DCM (Inset: enlarged absorption spectra in the region 290-450 nm). The calculated wavelengths are given in spectra (365 and 410 nm for **3** and 358 and 400 nm for **4**).

4.2.4 Results from TDDFT calculations

The molecular orbitals those have a significant participation in low-lying excitation for complexes **3** and **4** are shown in Figure 4.2.4. All pertinent energy gaps and corresponding assignments of each transition are listed in Table 4.2.2. The calculated energy gaps between S_0 and S_1 states were 379 nm and 386 nm for the complexes **3** and **4**, respectively.

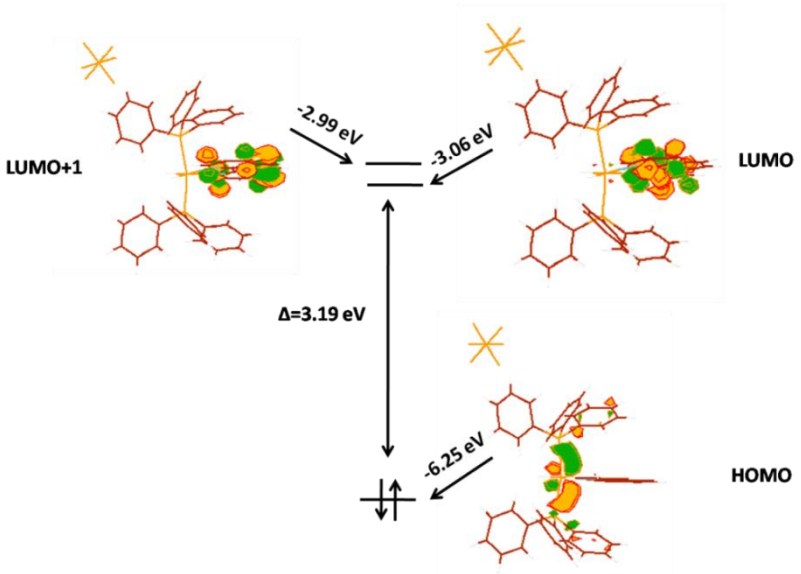

(a)

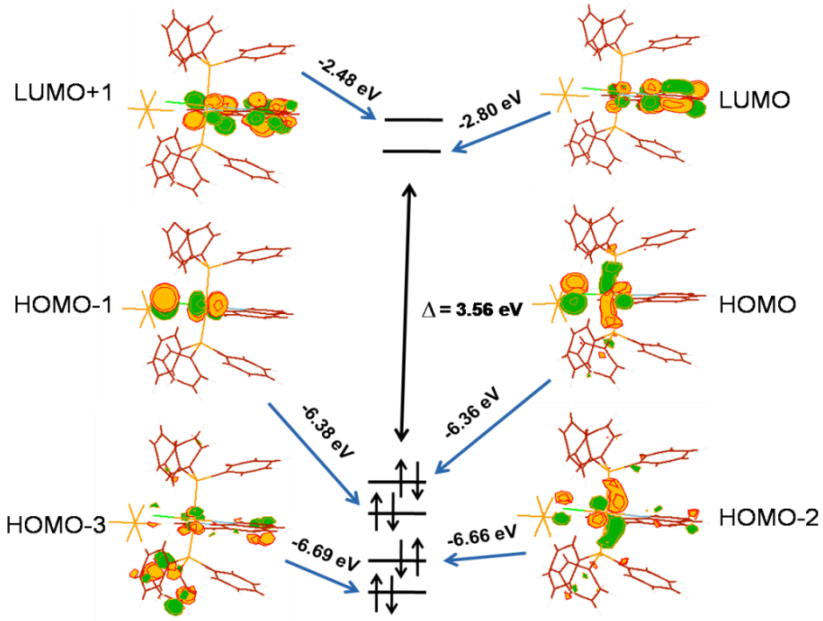

(b)

Figure 4.2.4 Selected frontier molecular orbitals (a) for **3** and (b) **4**.

Table 4.2.2 Calculated excitation wavelength (λ_{cal}), oscillator strength (f), MLCT (%) and transition energies (E) (TDDFT/B3LYP calculation in DCM solvent) for few transitions. All the excitations reported here initiate from singlet ground state, S_o. Corresponding experimental wavelengths (λ_{expt}) are shown in separate column (**3** in above and **4** in below).

States	λ_{cal} (nm)	λ_{expt} (nm)	E (ev)	f	Assignments	MLCT (%)
S_1	386	400	3.21	0.000023	HOMO-1→LUMO (81%) HOMO→LUMO+1(15%)	38.5 2.25
S_2	374	-	3.31	0.00004	HOMO→LUMO (79%) HOMO-1→LUMO (15%)	11.58 7.12
S_3	358	358	3.46	0.03600	HOMO-2→LUMO (75.5%) HOMO→LUMO+1(16%)	18.0 2.4
T_1	528	531	2.35	0	HOMO-3→LUMO+1(20%) HOMO-2→LUMO+1(17%) HOMO-2→LUMO (13%) HOMO-1→LUMO (4%)	1.0 4.0 3.1 0.6

States	λ_{cal} (nm)	λ_{expt} (nm)	E (ev)	f	Assignments	MLCT (%)
S_1	379	410	3.27	0.06	HOMO→LUMO (97%)	33.17
S_2	369	-	3.36	0.0003	HOMO-1→LUMO (98.5%)	90.6
S_3	361	364	3.43	0.02	HOMO→LUMO+1(95%)	32.3
T_1	524	542	2.36	0	HOMO→LUMO+1 (25.3%) HOMO-3→LUMO+1 (25%)	8.65 5.58

These near UV transition energies are consistent with the experimental absorption wavelengths (Table 4.2.1). Similarly, S_0 to T_1 transition energies for complexes **3** (524 nm) and **4** (528 nm) are consistent with the experimental emission spectra at blue edge (Table 4.1.1).

This consistency between the experimental and calculated transition frequencies prove the accuracy of the molecular orbital pictures. Complexes **3** and **4** differ in their metal to ligand charge transfer (MLCT) transition characters due to different extent of orbital contributions from different ligands

Redox potentials were measured by cyclic voltametry relative to an internal ferrocene reference (Cp_2Fe/Cp_2Fe^+ = 0.62 V versus SCE in dichloromethane solvent). The complexes **3** and **4** have shown that the metal-centered irreversible oxidation potentials are 1.331 and 1.329V, respectively. The reduction potentials observed for **3** and 4 at -0.700 and -0.740V, respectively correspond to the phenanthroline ligand [13, 33] LUMO state in both the complexes.

4.2.5 Aggregation Induced Emission Activity

Number of controlled experiments was performed to investigate the cause of strong solid state emission behavior exhibited by **3** and **4** with yellow and green luminescence at λ_{max} 518 and 513 nm, respectively (Table 4.2.1). The PL emission intensity of both **3** and **4** were found almost non-emissive after dissolving these in THF. However, the intensity of emission was remarkably increased in case of 90% of water in THF (Figure 4.2.5). As these complexes are insoluble in water, the observed rising PL intensity with increasing concentration of water (visible as suspended particles) proves that these complexes are 'Aggregation Induced Emission (AIE)' active. The emission intensity of **3** and **4** in solution with 90% water (by volume) was found 30 and 74 times higher, respectively than the PL intensity to their respective THF counterparts. It is to be noted that unlike the analogous complexes with cyclometalated ligands to iridium(III) published by our group, the PL intensity for these diimine complexes remains unchanged upto 60% water factions (Figure 4.2.5). This disparity is evident from the ionic character of these species (**3** and **4**) resulting more solubility as compared to the neutral cyclometalated analogues (Scheme 4.2.1, **D**).

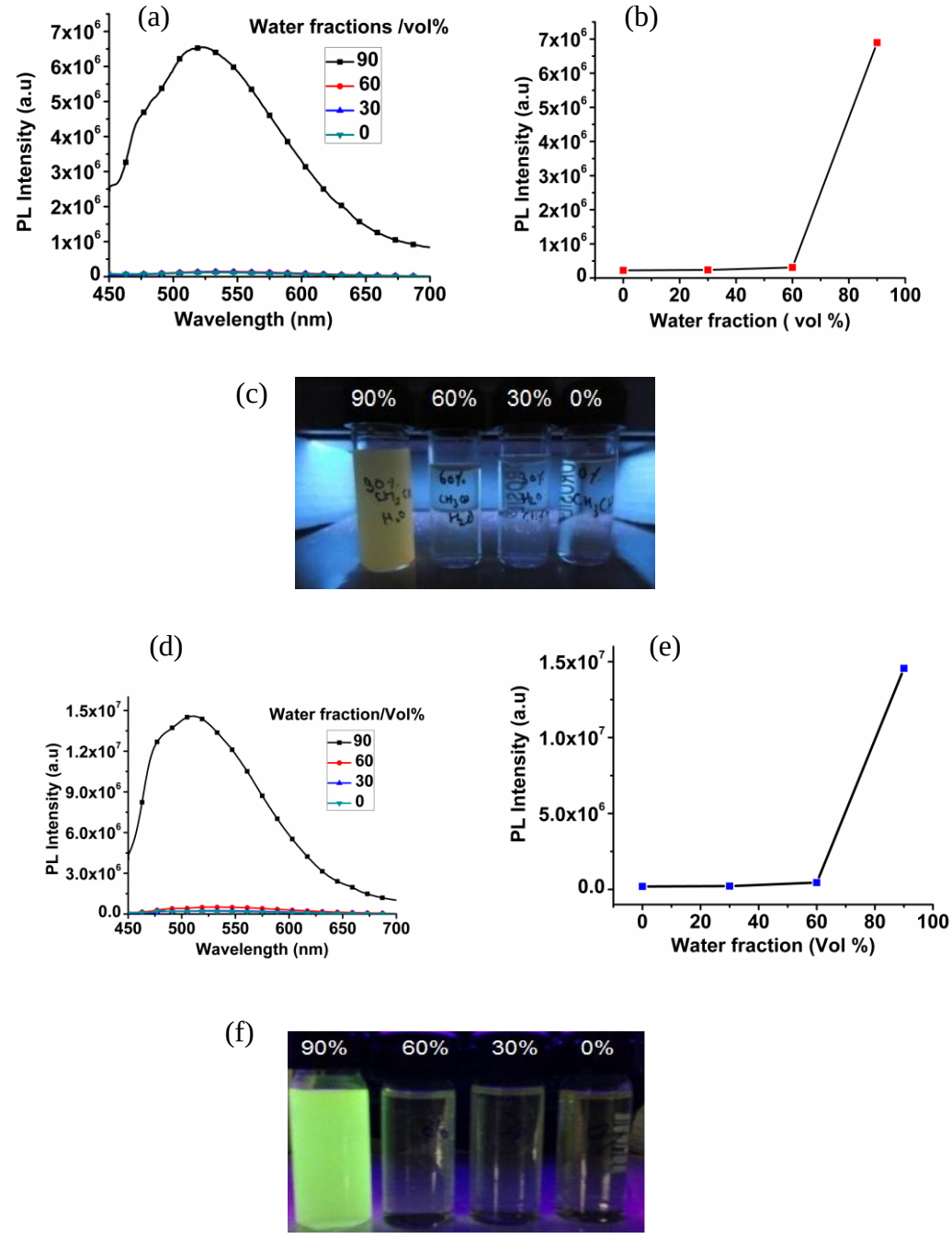

Figure 4.2.5 (a, d) Emission spectra of **3** and **4** in different fraction of water (0-90%); (b, e) PL Intensity of 3 and 4 with increasing water concentration; (c, f) Image of **3** and **4** in presence of different water fraction (0-90%) under 365 nm UV lamp. In another experiment, a slow enhancement of PL emission intensity is observed with gradual increasing concentration of viscous polyethylene glycol (PEG) at a fixed concentration of **3** (or **4**) in THF solution.

In another experiment, a slow enhancement of PL emission intensity is observed with gradual increasing concentration of viscous polyethylene glycol (PEG) at a fixed concentration of **3** (or **4**) in THF solution.

The luminescence intensity is improved to 2.7 and 2.9 times for **3** and **4**, respectively with adding 90% PEG to the solutions of the complexes in THF.

This experiment hints that the complexes possess some rotationally active part. The hindrance of the rotationally active part with increasing viscosity of the solution may be responsible for increasing luminescence intensity. Based on these experiments, it is proposed that the rotation of the rotationally active part is restricted in the solid state. The particle size of the aggregated form obtained in 90% water-THF of **3** and **4** determined by dynamic light scattering experiment was found to 146 and 186 nm, respectively (Figure 4.2.6).

Thus, the rotation of the phenyl in triphenylphosphine ring is hindered in solid state due to these interactions. This hindered rotation of phenyl rotors will block the non-radiative channels which lose energy and opens up new radiative pathways leading to improvement of solid state quantum efficiency significantly [32, 34, 35].

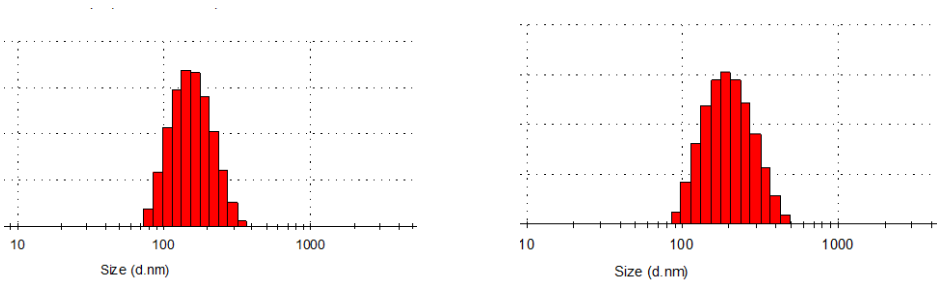

(a) (b)

Figure 4.2.6 (a, b**)** : Particle size distribution of nano-aggregate of complexes **3** and **4** formed in THF/ water mixture with 90% water fraction.

The calculated absolute efficiency was found to be 3.0% and 3.5% for **3** and **4**, respectively. Time-resolved photoluminescence spectra for **3** and **4** were measured in pure THF and the life-time obtained was 1.25 ns and 6.3 ns, respectively. The life-time for the complexes **3** and **4** in water / THF (90/10 v/v) % was raised to 2.95 µs and 1.63 µs, respectively. This increased life-time in water/THF system (90/10, v/v) (in both

cases) evidence the improved luminescence yield aggregated as compared to their respective solution in pure THF [36, 37]. The solution quantum efficiencies (in pure THF) of **3** and **4** were measured to 0.75% and 0.93%, respectively.

4.2.6 Vapoluminescent

The complex **3** was recrystallised from DCM. This complex emits greenish yellow light on exposure to UV radiation (shown in thin film; Figure 4.2.8a). The emission color of this complex in thin film changes from greenish-yellow to yellow upon exposure to the solvents with higher polarity than DCM [dielectric constant (d.c., 8.93))], like acetone (d.c., 20.7), acetonitrile (d.c., 37.5) etc.

Upon exposure to solvents with lower polarity than DCM, like, chloroform (d.c., 4.81), benzene (d.c., 2.27) / or 1,4-dioxane (d.c., 2.25), the solid thin films (recrystallised from DCM) emit yellowish green and bluish green light, respectively (Figure 4.2.8a).

The complex **4** recrystallised from DCM emits green light. The thin-film of **4**, in an analogues way emits blue emission upon exposure to non-polar solvents (benzene, 1,4-dioxane etc) and green light in polar solvents (chloroform, acetone, acetonitrile etc) (Figure 4.2.8c).

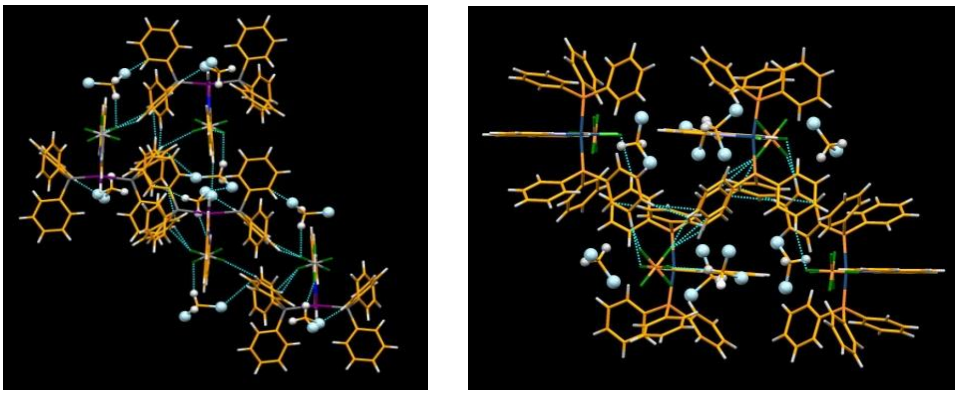

Figure 4.2.7 Packing diagram (a) for complex **3**, and (b) for **4**, showing several short contacts which was responsible for restricted intramolecular rotation (RIR).

A distinct difference in emission spectra was observed for the cases of thin-film in polar *vs* non-polar solvents. The thin-films exposed to non-polar solvents showed structured emission, while broad emission observed from the thin films exposed to polar solvents (Figure 4.2.8b & d).The complex **4** recrystallised from DCM emits green

light. The thin-film of **4**, in an analogues way emits blue emission upon exposure to non-polar solvents (benzene, 1,4-dioxane etc) and green light in polar solvents (chloroform, acetone, acetonitrile etc) (Figure 4.2.8c).

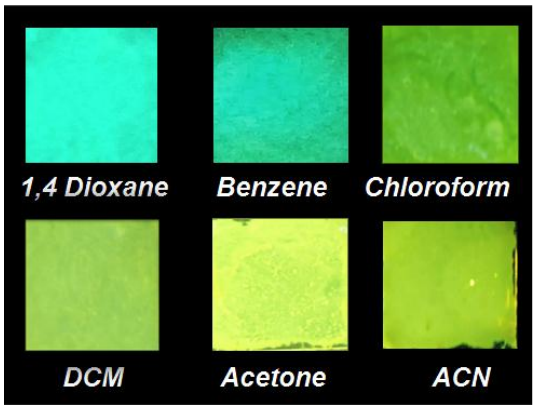

(a)

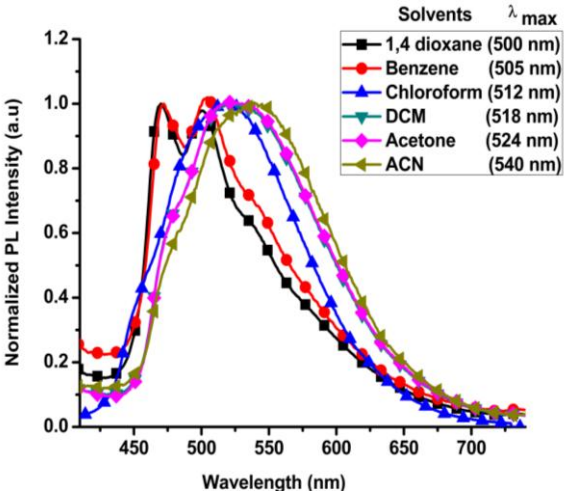

(b)

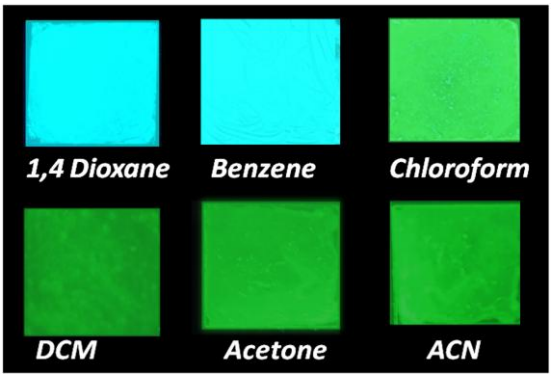

(c)

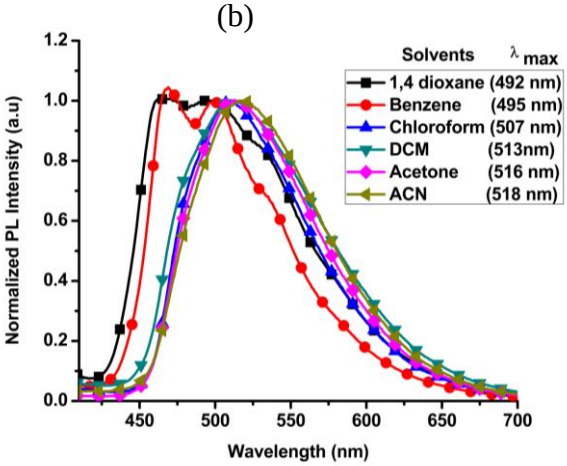

(d)

Figure 4.2.8 (a) Observed thin-film emission color of **3** (bluish-green to yellow) with systematic increasing the solvent polarities (polarity increases: 1, 4-Dioxane, Benzene, Chloroform, DCM, Acetone, Acetonitrile) on exposure to UV radiation (λ_{max} = 365 nm); (b) thin-film emissions of the corresponding thin-films moistened with the solvents. (c) Observed thin-film emission color of **4** (blue to green) with systematic increasing the solvent polarities (polarity increases: 1,4-Dioxane, Benzene, Chloroform, DCM, Acetone, Acetonitrile) on exposure to UV radiation (λ_{max} = 365 nm); (d) thin-film emissions of the corresponding thin-films moistened with the solvent.

There are two peaks are approximately separated by 1408 cm^{-1} observed in the structured emission spectra taken in non-polar solvents (1,4-doxane/benzene, Figure 4.2.8b & d) which corresponds to the stretching of the double bonds of aromatic ligands [38] .The maximum emission wavelength gradually changes towards longer wavelength with increasing polarity of the solvents (Figure 4.2.8b & d). In absorption spectra, the different band-edge absorption has been observed for thin-film of **3** exposed to polar and non-polar solvents. In case of non-polar solvents, the observed absorption wavelength was less than 350 nm and that for polar solvents was greater than 400 nm (Figure 4.2.9a). In addition, a long tail followed by band edge absorption is observed for the latter case only (Figure 4.2.9b). These spectroscopic observations suggest that the nature of the lowest excited states of the thin-film samples exposed to non-polar solvents is predominantly consisted of ligand-centered states.

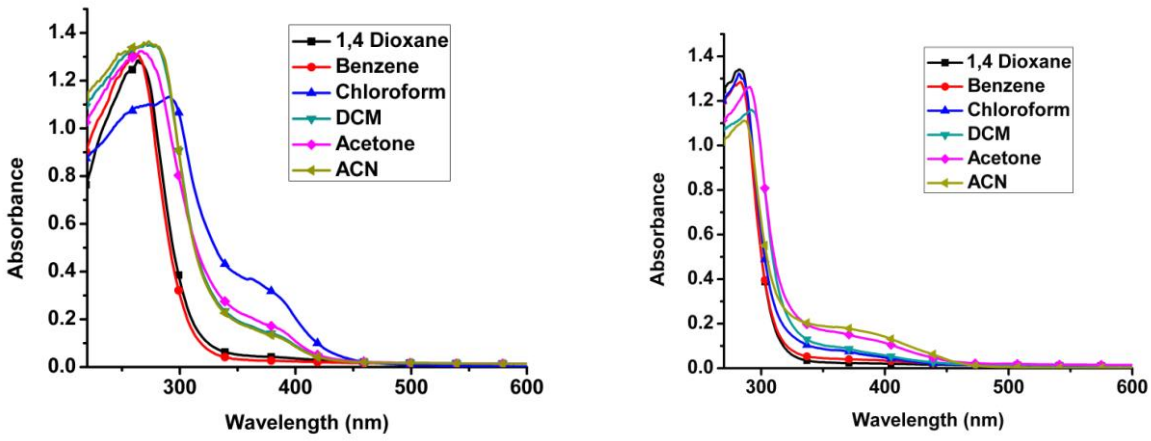

Figure 4.2.9 Thin-film absorption spectrum (a) for complex **3**, (b) complex **4**.

$$\Delta\mu = \mu_e - \mu_g = \sqrt{\frac{m\times 81}{\left(\frac{6.2}{a}\right)^3 \times 11307.6}}$$

ε = relative permittivity; n= refractive index; λ_a = absorption maximum; λ_{em} = emission maximum; Δν = Stokes shifts and E^N_T = molecular-microscopic solvent polarity parameter; where μ_e is excited state dipole moment, μ_g is ground state dipole

moment, 'a' is Onsager's cavity radii and m is the slope of the linear plot of E_T^N vs Stokes shift.

The nature of the lowest excited states changes to MLCT states on exposing the thin-films to polar solvents. In other words, switching of the excited state results due to change in the dielectric medium around the thin-film samples (Figure 4.2.9).

Table 4.2.3 Parametric values required for calculation of excited state dipole moment of **3**

Solvent	**ε**	**n**	**λ_a (nm)**	**λ_{em} (nm)**	**Δν (cm^{-1})**	**E_T^N**
Dioxane	2.3	1.4214	270	505	17235.10	0.164
Benzene	2.3	1.501	270	505	17235.10	0.111
Chloroform	4.81	1.446	270	514	17581.77	0.285
DCM	9.1	1.424	270	518	17732.01	0.321
Acetone	21.0	1.36	270	524	17953.06	0.355
ACN	37.5	1.342	270	540	18518.51	0.460

Table 4.2.4 Parametric values required for calculation of excited state dipole moment of **4**

Solvent	**ε**	**n**	**λ_a (nm)**	**λ_{em} (nm)**	**Δν (cm^{-1})**	**E_T^N**
Dioxane	2.3	1.4214	282	496	15299.70	0.164
Benzene	2.3	1.501	282	496	15299.70	0.111
Chloroform	4.81	1.446	282	507	15810.99	0.285
DCM	9.1	1.424	282	510	15853.99	0. 321
Acetone	21.0	1.36	282	513	15967.81	0.355
ACN	37.5	1.342	282	516	16081.14	0.460

The ground state dipole moments for both **3** and **4** were calculated from DFT calculations. The excited state dipole moments for both complexes were calculated with the help of following equation [39, 40] .

The calculated excited state dipole moment (DM) showed higher value as compared to its ground state (DM for **3**, G.S.: 45.9 D; E.S.: 60.7 D; DM for **4**, G.S.: 31.0 D; E.S.: 36.4 D) (Tables 4.2.3, 4.2.4). Higher DM values in excited state supports the lowering of MLCT with increasing polarity of solvents.

This fact in combination with the spectroscopic observations in thin film as described earlier support the switching of MLCT state to ligand centered (LC) state (Figure 4.2.10). In this case, the nature of the excited state is predominantly of MLCT character. The observed maximum emission wavelength in chloroform (λ_{max}, 512 nm) changes to longer wavelength when exposed the thin film to relatively higher polar solvents. The λ_{max} values are observed to 518, 524 and 540nm to the thin films of **3** exposed to DCM, acetone and acetonitrile, respectively.

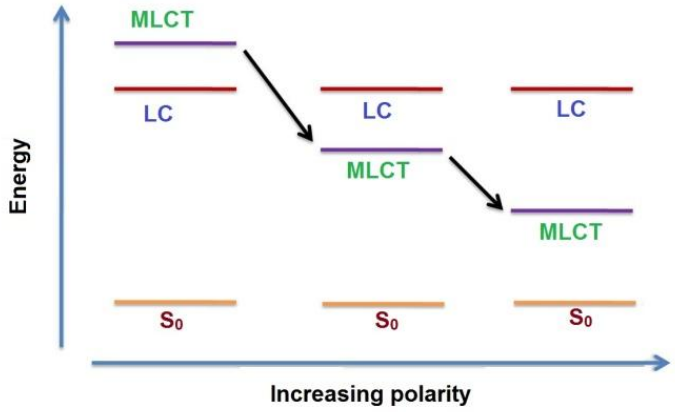

Figure 4.2.10 Solvent polarity dependent tuning of metal to ligand charge transfer (MLCT) states led to different emission color of **3** and **4** in solid state (DCM, acetone etc stabilizes the charge transfer states MLCT more as compared to 1,4-dioxane, benzene etc) [41] .

Similarly, thin film of **4** recrystallised from DCM emit blue color when it was exposed to relatively low polar solvents (1,4-dioxane and benzene) and the emission color changes to green in relatively high polar solvents, [chloroform (λ_{max} = 507nm) / DCM (λ_{max} = 513 nm) / acetone (λ_{max} = 516 nm) and acetonitrile (λ_{max} = 518 nm)]. The original green emission of **4** in DCM changes to blue on exposure the film to 1, 4-

dioxane. This thin film re-emits green light after heating it at 70°C for fifteen minutes followed by exposure to DCM vapour (Figure 4.2.11A).

It is observed that the emission color of thin-film of **4** turns to green with exposure to DCM and on the other way, the blue emission reappears when the thin-film expose to 1,4-dioxane. These observations support the switching of emission color of **4** with changing volatile organic solvents reversibly. Similar switching of emission color for **3** is also observed (Figure 4.2.12).

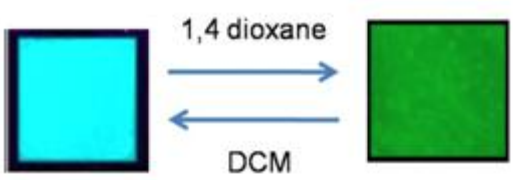

(A)

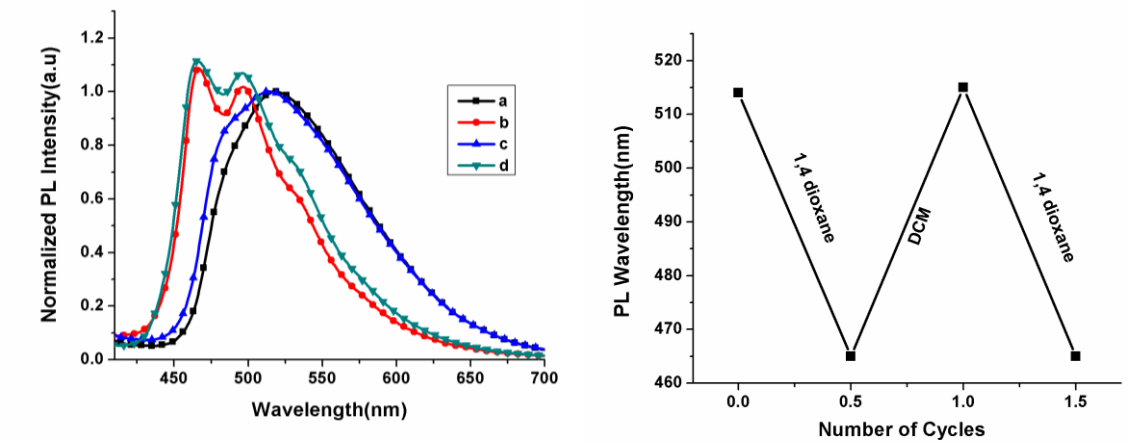

(1) (2)

(B)

Figure 4.2.11 (A) Solid-state reversal of emission color of **4** from blue to green (on exposure to DCM) and green to blue (on exposure to 1, 4-dioxane) (the photograph was taken under excitation of 365 nm); (B) (1). Reversibility of solid-state emission spectrum of **4** with repeated VOC exposure (a, 4 recrystallised from DCM; b, on exposure to 1,4-dioxane; c, on exposure to DCM after heating the film at 70°C for 15 min and d, on exposure to 1, 4-dioxane); (2). Switching of emission wavelength (~515 nm to ~465 nm and vice versa) on exposure to DCM and 1, 4-dioxane repeatedly, respectively.

We recrystallised molecular formula for the complex 3·2DCM from 1,4-dioxane and the resulting **3** showed the same VOC property as was observed in the thin film of molecular formula for the complex 1·2 DCM on exposure to 1, 4 dioxane after heating. We have recorded the ^{1}H NMR spectrum of the resulting complex. The presence of proton peak of 1,4-dioxane at ~3.7 ppm is clearly observed in the NMR spectrum, whereas there has no proton peak of dichloromethane (~5.3 ppm) observed.

(A)

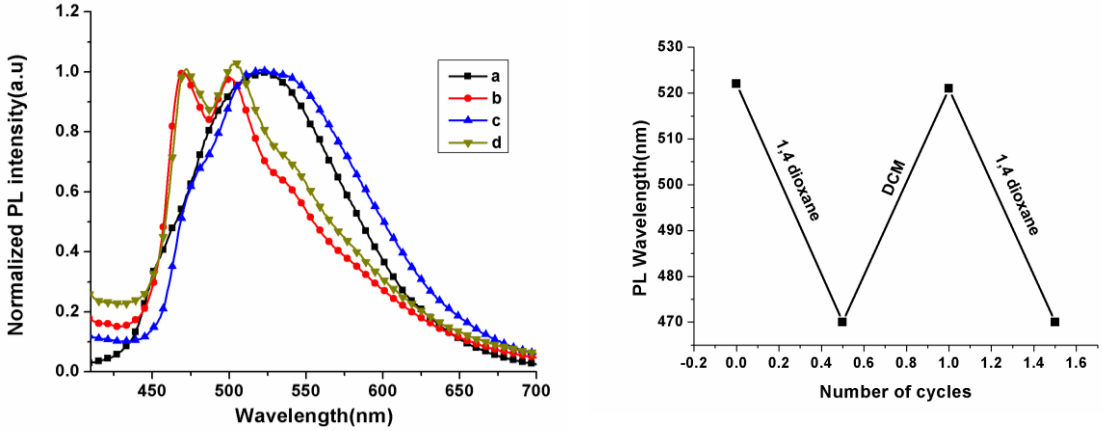

(1) (2)

(B)

Figure 4.2.12 (A) Solid-state reversal of emission color of **3** from yellowish green to bluish green (on exposure to DCM) and bluish green to yellowish green (on exposure to 1,4-dioxane) (the photograph was taken under excitation of 365 nm); (B) (1). Reversibility of solid-state emission of **3** with repeated VOC exposure (a, on exposure to DCM; b, on exposure to 1,4-dioxane; c, on exposure to DCM after heating the film at 70°C for 15 min and d, on exposure to 1, 4-dioxane); (2). Switching of emission wavelength (~520 nm to ~465 nm and vice versa) on exposure to DCM and 1, 4-dioxane, respectively.

This observation of proton peak of 1,4 dioxane support the replacement of DCM molecules with 1,4-dioxane prior to occupying the crystal sites by DCM molecules.

As described above the void space available for potentially occupying solvent molecules in **3** and **4** are 980.1 and 906.2Å^3, respectively per unit cell of crystal lattice (*vide infra*). The crystal packing diagrams for **3** and **4** (crystals recrystallised from DCM) demonstrate that the interstitial positions are occupied by the DCM molecules (eight DCM molecules per unit cell of the crystals in each case) (Figure 4.2.2).

Powder X-ray diffraction pattern of thin-film samples of **3** exposed to DCM, which is exactly matches with the structure analyzed through X-ray single crystal diffractometer. The above experiment is performed with **4** and found similar result as above (Figure 4.2.13).

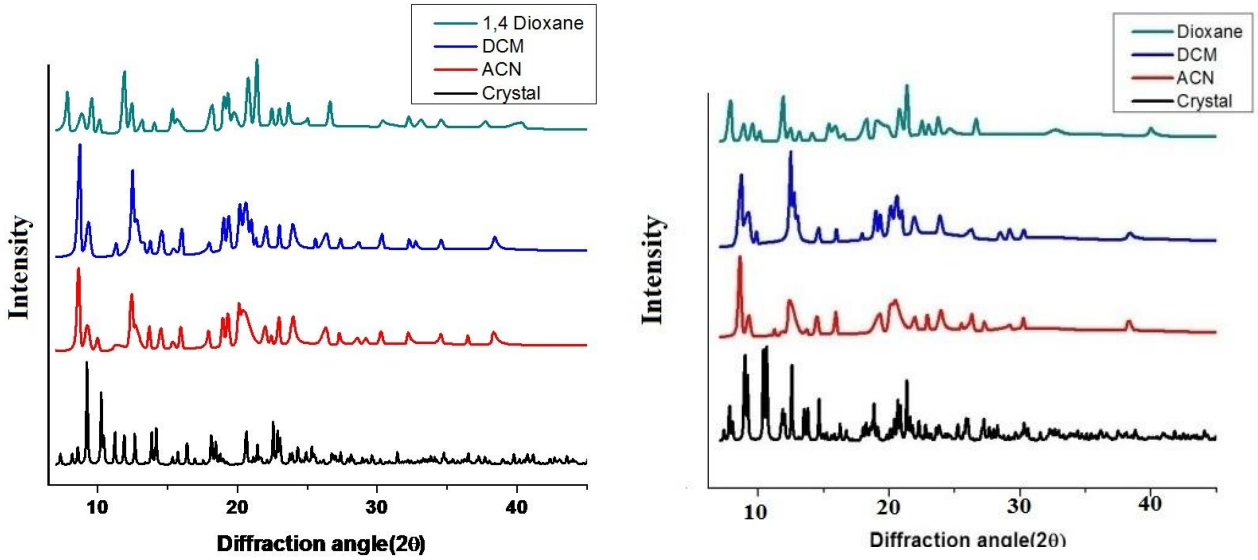

(a) (b)

Figure 4.2.13 Powder XRD patterns measured after exposure of selected solvent vapors and their comparison with the pattern obtained from X-ray single crystal structure (a) for **3** and (b) for **4**.

It is to be noted that **3** (or **4**) exhibit broad and featureless emission spectrum (with faint yellow emission color) after dissolving it in DCM. This observation remains true irrespective of polarity of the solvents. Based on this similarity, the thin film structure is identified as $1{\cdot}2CH_2Cl_2$ (Figure 4.2.13). The X-ray powder pattern for the

thin-films of 3 in other solvents (1@1,4-dioxane; the solution absorption spectra of **3** and **4** in different solvents hardly show any difference as observed solvent polarity dependent disparity in case of solid thin films (Figure 4.2.13).

Similar report [41] was found for 4,4´-tert-butyl(2,2´-bipyridine) p-dimesitylboryl) phenylacetylene Platinum(II) complex where vapoluminescent properties in solid thin film depend on the polarity of the solvents, but the same was not observed in solution. This anomalous observation could be presumably explained from localized dipole-dipole interactions operative in thin film with guest solvents occupied in the void space as compared to the interactions between **3** (or **4**) with continuously changing dipoles in bulk solution.

4.3 Part B: 2,2′-bipyridine complexes of iridium(III)

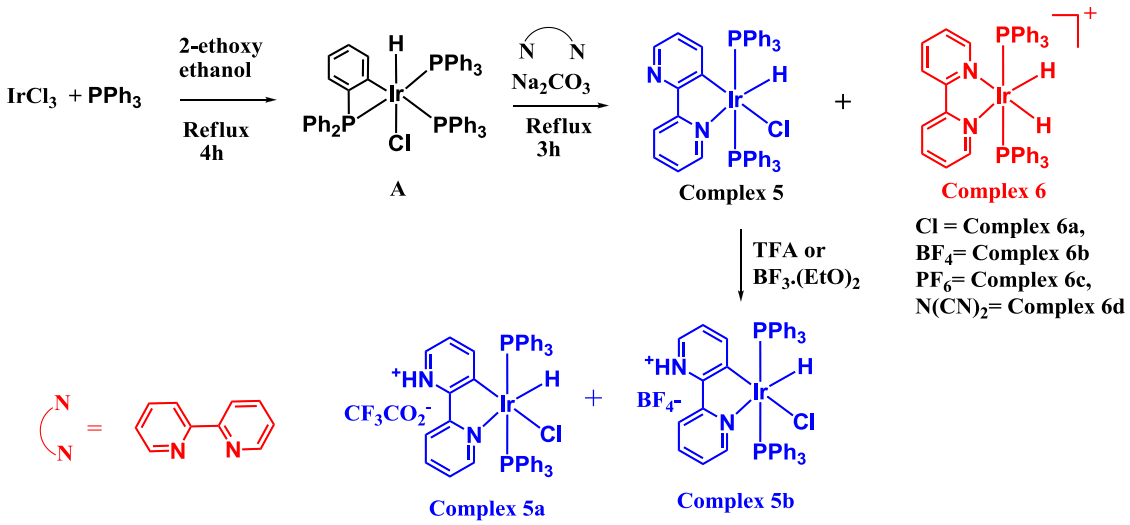

Scheme 4.3.1 Synthesis of 2,2' bipyridine complexes of iridium(III)

4.3.1 Results and discussion

Herein, the iridum(III) complex has been synthesized by using 2, 2'-bipyridine as a chromophoric ligand. On pursuing intriguing features with varying chromophoric ligands retaining the same AIE framework, the one pot synthesis of iridium(III) chloride and triphenyl phosphine mixture with 2, 2 '-bipyridine has resulted two emissive products. According to the thin layer chromatographic (TLC) study, it was observed that one of the products was nonpolar in nature with 0.5 R_f using ethyl acetate-hexane mixture (2:3) while the other one giving 0.2 R_f in methanol-DCM mixture (1:9). The ^{1}H NMR spectra of non polar complex (based on TLC study) are giving eight different signals while the polar spot is giving five different signals. The greater number of ^{1}H NMR signals in case of complex with nonpolar nature (on TLC plate) giving hints about its asymmetrical structure (Figure 4.3.1). While the ^{31}P NMR spectra with one signal at δ = 7.92 ppm is not giving any support in favour of structure of this unknown complex.

The hydride ^{1}H NMR peaks were found triplet in nature because of P-H coupling ($J_{(P-H)}$ ~16.4Hz). The J-coupling value of J_{P-H} supports that hydride is *cis* to phosphorous in the complex. Anyway, these NMR studies is unable to enlighten the true structure of this unknown complex obtained with 2,2'-bipyridine. Further, the

comparative structural study of the iridium(III) complex with 1,10 phenonthroline (N^N) is not giving any satisfactory clue to reveal the structure [where the complex with 1,10 phenanthroline has given two complexes with compositions, $[Ir(PPh_3)_2(1,10\text{-}phen)(Cl)(H)]$ and $[Ir(PPh_3)_2(1,10\text{-}phen)(H)(H)]$. After several worth full efforts, a single crystal of the unknown complex with trifluoroacetic acid (TFA) adduct was obtained.

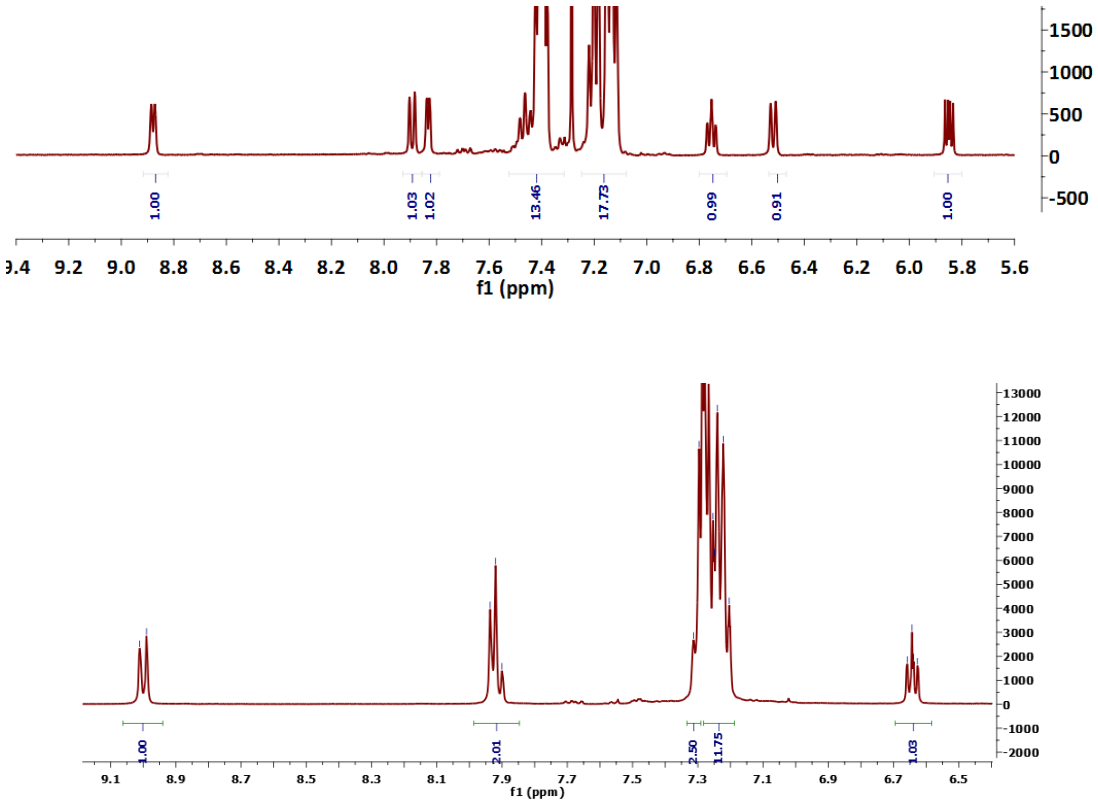

Figure 4.3.1 ^{1}H NMR spectra of nonpolar (top) and polar spot (bottom) on the TLC plate.

The single-crystal X-ray solution has revealed the first “AIE Rollover", where the displacement of one of the nitrogen atoms of bipyridine ligand followed by rotation of the pyridine ring is taking place, promoting the activation of the C−H bond (Figure 4.3.2) to give a five-membered cyclometalated complex, or “Rollover” complex [Ir(bipy-H)] (**5**) (Scheme 4.3.1).

However, the X-ray structure of the polar complex (based on the TLC plate study) confirms the normal mode of binding with 2, 2'-bipyridine *i.e.*,

$[Ir(N\hat{}N)(PPh_3)(H_2)]Cl$ (**6**) (Figure 4.3.3). In case of $[Ir(bipy)H_2(PPh_3)_2]A$, the ^1H NMR signal of the metal-hydride peak appeared in the range of -19.55-(-19.46) ppm as a triplet with a spin-spin coupling constant value, $J_{(P-H)}$ ~16.7 Hz, which was in accordance with each of the hydrides lying *cis* to two phosphorus atoms. There were no significant differences found in the m/z values of the HRMS spectra for complexes $[Ir(bipy)H_2(PPh_3)_2]A$ (**6a-d**), where A= Cl, BF_4, PF_6 and $N(CN)_2$, showing that in all four cases the same cationic species is present.

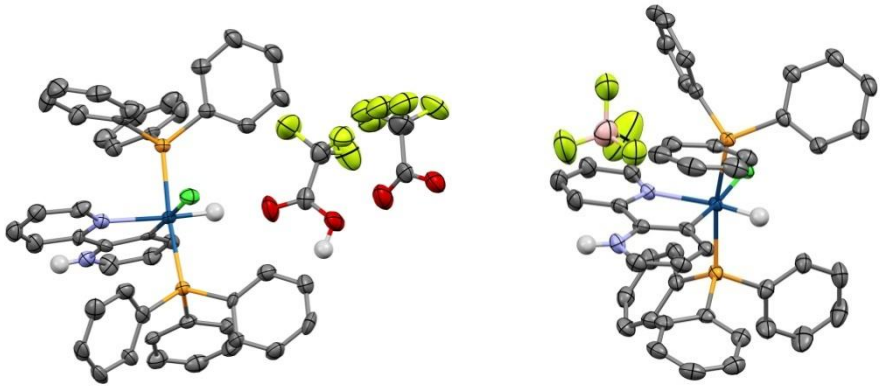

(a) (b)

Figure 4.3.2 ORTEP diagram for complexes, (a) [Ir(bipy-H)] $CF_3CO_2^-$ H^+ and (b) [(bipy-H)] BH_4^- H^+ ,showing distorted octahedral geometry at the Ir site.

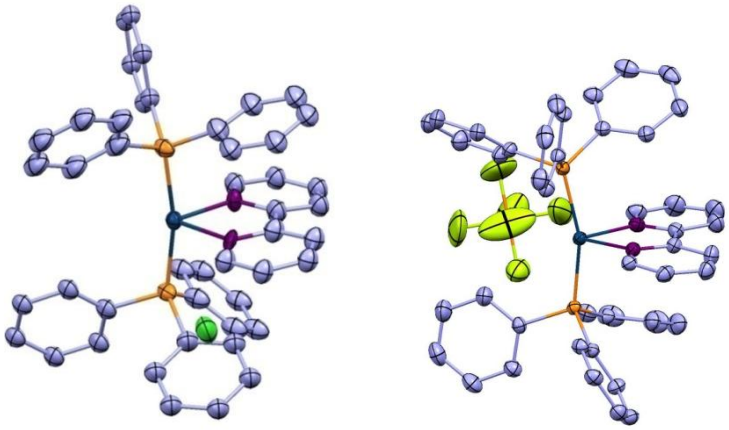

(a) (b)

Figure 4.3.3 ORTEP diagram for complexes, (a) [Ir(bipy)] Cl and (b) [(bipy-H)] PF_6 , showing distorted octahedral geometry at the Ir site.

The presence of counter ions was confirmed by measuring FTIR stretching frequencies. The complex containing the PF_6^- counterion showed a strong peak at 840

cm^{-1} (υ_{P-F}); [42] the BF_4^- containing complex a stretching frequency at 1058 cm^{-1} (υ_{B-F}); [43] while the complex with a $N(CN)_2^-$ counter ion showed peaks at 2128 and 2184 cm^{-1}(CN) [44], respectively.

The plausible mechanism for the formation of these two different species could be explained, the mixture of $IrCl_3 \cdot xH_2O$ and triphenylphosphine will generate the four-membered cyclic complex with HCl as a side product. The addition of acid scavenger and 2,2' -bipyridine in the reaction mixture will lead to the single protonation of pyridine ring in bipy and thus the protonated bipy ring will rotate and coordinate with iridium by κ^2-N,C mode. In other way, the maximum amount of acid scavenger (~10 equivalent) was resulting the chelate $[Ir(bipy)H_2(PPh_3)_2]A$ complex.

4.3.1.1 Molecular and crystal structure [Ir(bipy)]Cl and PF_6

In case of [Ir(bipy)]A , the principal building block in the synthesized molecular crystals is a cationic iridium(III) complex **6** with a distorted octahedral coordination sphere (Figure 4.3.4), as confirmed by the SC-XRD analysis obtained for the $[Ir(bipy)H_2(PPh_3)_2]Cl$ and $[Ir(bipy)H_2(PPh_3)_2]PF_6$ crystals. A bipyridine ligand along with two hydride ligands lie on the equatorial plane while the axial positions are occupied by two triphenylphosphine ligands. The chiral propeller-like arrangement of the phenyl rings in the triphenylphosphine ligand allows the possibility of having enantiomeric molecules. Indeed, the two possible enantiomers are present in the two studied crystal structures.

Table 4.3.1 contains the principal geometrical parameters of the Ir coordination sphere for the two experimental X-ray diffraction structures. Close examination of this structural data reveals that the two $[Ir(bipy)H_2(PPh_3)_2]^+$ molecular geometries are rather similar and present a distorted octahedral coordination of the iridium atom. The main departure from a perfect octahedral environment corresponds to the off-axis distortion of the two phosphorous atoms, with P-Ir-P angles on the side of the two hydride ligands about 15º smaller than in a perfect octahedron (180º).

Bond distances between the central metal atom and the coordinating atoms on the ligands are very similar in the two crystal structures, except for one of the Ir-N bond lengths, which is approximately 0.05 Å larger in the $[Ir(bipy)H_2(PPh_3)_2]PF_6$ crystal. This is because the bipyridine ligand in both structures has some differences in the

adopted geometry, probably due to intramolecular forces induced by the bulky phenylphosphine ligands.

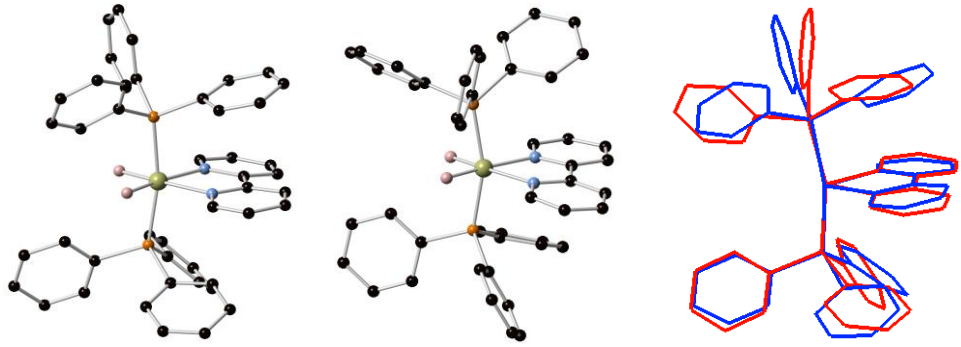

Figure 4.3.4 Structures of $[Ir(bipy)H_2(PPh_3)_2]A$ in the $[Ir(bipy)H_2(PPh_3)_2]Cl$ (left) and $[Ir(bipy)H_2(PPh_3)_2]$ PF_6 (center) crystals with the optimized hydride ligands and the superposition of their most overlapping enantiomers (right). Hydrogen atoms have been eliminated for seeking of clarity.

Table 4.3.1 Principal geometrical parameters for the coordination environment of Ir in $[Ir(bipy)H_2(PPh_3)_2]^+$, distances in Å, angles in degrees.

Bond angle/length	Cl^-	PF_6^-
Ir-P1	2.310	2.298
Ir-P2	2.297	2.291
P1-Ir-P2	168.0	162.0
Ir-N1	2.136	2.130
Ir-N2	2.119	2.164
N1-Ir-N2	77.4	76.6
Ir-H1	1.591	1.601
Ir-H2	1.599	1.584
H1-Ir-H2	86.2	86.3
C-P-P-C*	48.0	18.7

*Average value of the three smallest C-P-P-C dihedral angles.

Nevertheless, these differences do not have a great impact on the electronic structure of both cations, as suggested by our calculations discussed below. The major differences between the two geometries essentially correspond to the relative disposition of the phosphine ligands (Figure 4.3.4).

In the $[Ir(bipy)H_2(PPh_3)_2]PF_6$ crystal, the two sets of phenyl rings of the two phosphine groups in trans disposition are closer to an eclipsed conformation than in the $[Ir(bipy)H_2(PPh_3)_2]Cl$ case, as indicated by their C-P-P-C dihedral angles (Table 4.3.1). In close relation to this distortion we notice that the molecular geometries for the two crystals exhibit different degrees of rotation for some of the phenyl rings.

4.3.1.2 Photophysical property

4.3.1.2.1 Photophysical property of [Ir(bipy-H)] and $[Ir(bipy\text{-}H)]H^+$

The emission and absorption spectra of [Ir(bipy-H)] were recorded with variation of different polarity of solvents, where there was not observed any change of emission/absorption with respect to polarity. The UV-Vis absorption of [Ir(bipy-H)] and $[Ir(bipy\text{-}H)]H^+$ in dichloromethane (DCM) shows higher energy bands at 270 (sh 290 nm) and 270 (sh 310 nm), respectively which can be identified as π-π^* transitions [45]. The other set of bands were obtained for [Ir(bipy-H)] at 360 and 410 nm (Figure 4.3.5) identified as metal-to-ligand charge transfer (^{1}MLCT and ^{3}MLCT) transitions [45].

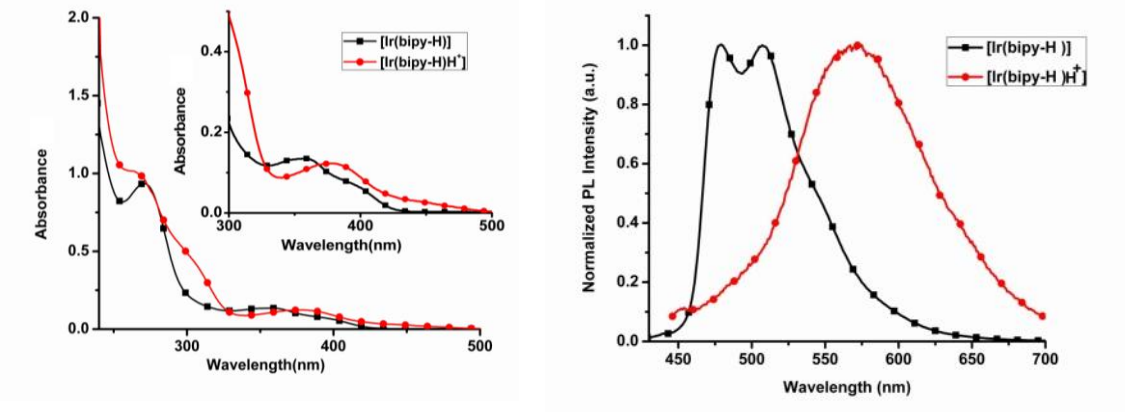

(a) (b)

Figure 4.3.5 (a) UV-Vis spectra of [Ir(bipy-H)] (1x 10^{-5} M) in degassed DCM at room temperature before ([Ir(bipy-H)]) and after the addition of TFA (inset: the same absorption spectrum is shown in shorter range); (b) Emission spectra of [Ir(bipy-H)] and $[Ir(bipy\text{-}H)]H^+$ in DCM solution.

After addition of trifluoroacetic acid (TFA) into the complex solution of [Ir(bipy-H)], the broad MLCT transition band shifted from 360 nm and 410 nm to 380 nm and 437 nm, respectively [46] (Figure 4.3.5). During such process, the visible colour of the solution was changed from colourless to yellow after addition of TFA. After protonation, the structured emission, where the low lying emissive states can be proposed of the closely spaced ^{3}LC and ^{3}MLCT emissive states, changed into the featureless and broad emission spectra (Figure 4.3.5), a pure charge transfer (CT) states. After protonation, the contribution of ^{3}LC state from lowest emitting states either has been completely lost or gets reduced. However, these facts are supported by DFT calculation which shows the LUMO orbitals of $[Ir(bipy\text{-}H)]H^+$, is mainly localized on $(bipy\text{-}H)H^+$. The computational calculations (discussed later) along with the UV-Vis absorbance differences at lower energy (Figure 4.3.5a) corroborate the facts that the formation of a new lower lying MLCT transition state in $[Ir(bipy\text{-}H)]H^+$ which arise from the electronic transition from metal d orbitals to π^* lying on $(bipy\text{-}H)H^+$ along with a ligand-to-ligand charge transfer transition (LLCT) from the p-orbitals of chloro to π^* of $(bipy\text{-}H)H^+$ leading to a red shift in UV-Vis absorption spectra.

4.3.1.2.2 Photophysical property of $[Ir(bipy)H_2(PPh_3)_2]A$

In case of chelate bipyridine complexes $[Ir(bipy)H_2(PPh_3)_2]A$, the absorption and emission spectra for all the complexes were recorded in dichloromethane solution at room temperature (Figure 4.3.6).

The higher energy bands in the UV-Vis absorption spectra for all four compounds were found between 250-300 nm and are assigned to spin-allowed ligand-centered (LC) $^1\pi$–π^* transitions.

The lower energy bands appearing in the 350 - 425 nm range were assigned to metal-to-ligand charge transfer (^{1}MLCT and ^{3}MLCT) transitions. As expected, the absorbance and emission profile of all four compounds in dichloromethane solution showed a similar pattern (Figure 4.3.6) supporting the assumption of frontier MOs mainly centered on the cationic species (emission λ_{max} values are shown in Table 4.3.2).

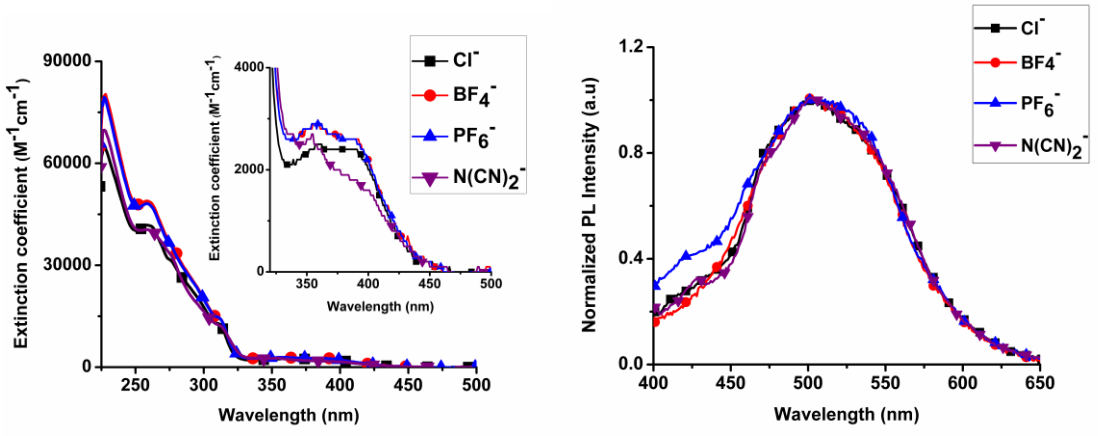

(a) (b)

Figure 4.3.6 Absorption (a) and emission (b), (λ_{exc} 385 nm) spectra for $[Ir(bipy)H_2(PPh_3)_2]A$ [A^- = Cl^-, BF_4^-, PF_6^-, $N(CN)_2^-$] compounds in dichloromethane solution.

Absorption and emission spectra of $[Ir(bipy)H_2(PPh_3)_2]A$ crystals with different counterions are shown in Figure 4.3.7. The absorption spectra are similar to those in dichloromethane solution, but the emission ones have a much more structured profile.

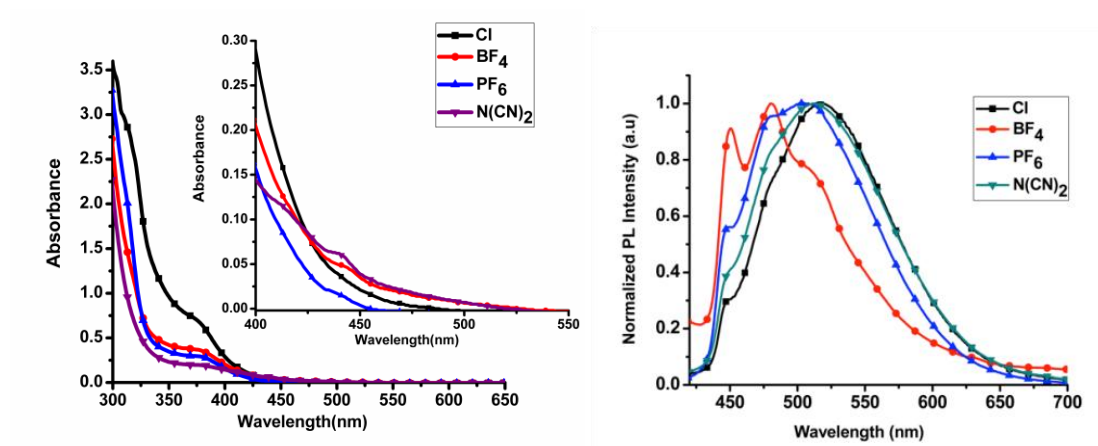

(a) (b)

If we consider the *z* axis along the P-Ir-P direction, in a perfect octahedral environment the Ir centered molecular orbitals (MOs) with t_{2g} character will be d_{xy}, d_{xz} and d_{yz}, while $d_{x^2-y^2}$ and d_{z^2} will be those with e_g character. Due to the loss of octahedral symmetry and the distortion caused by the ligands, the metal centered t_{2g}- and e_g-type orbitals, shown in red in the diagram, mix significantly with themselves as well as with other ligand centered orbitals.

Although the symmetry of the coordination environment for the iridium atom is not perfectly octahedral, we have decided to use the usual t_{2g}/e_g labels corresponding to the irreducible representation of the O_h group, to identify the d-block MOsin order to clarify the discussion.

Since the P-Ir-P angle is less than 180º, we expect the interaction with the phosphine lone pairs to cause a splitting of the t_{2g} orbitals in which the d_{xz} orbital rises significantly in energy over the remaining two, which exhibit a small energy splitting between them. As a result, the HOMO in the present compounds is mainly an iridium d_{xz} orbital as shown in the diagram, while the other two t_{2g} orbitals lie well below in energy, with several π*-type orbitals of the phenyl rings of the phosphines lying in between the highest occupied molecular orbital (HOMO) and the other two t_{2g} orbitals. Due to their M-L antibonding character, the e_g orbitals are strongly destabilized and appear rather high in energy.

Table 4.3.2 Wavelengths corresponding to the maximum emission intensity along with the vibronic progressions of the crystals with different counterions in the solid state and in dichloromethane solution. Wavelength corresponding to the maximum emission peak is indicated in bold face.

Counter ion	Wavelength / nm		Quantum yield		Life time	
	Solution (DCM)	Solid State	Solution (DCM)	Solid State	Solution (DCM) (ns)	Aggregate State (μs)
Cl^-	506	448 (sh) 512	0.018%	19.85%	0.95	1.6
PF_6^-	508	446 (sh) 479, 508	0.019%	33.64%	0.92	1.8
$N(CN)_2^-$	506	446 (sh), 513	0.011%	6.75%	0.93	1.6
BF_4^-	505	448, 479, 514	0.024%	26.76%	0.94	1.9

These two e_g orbitals also mix very significantly with orbitals from the ligands. In this case we find a large number of ligand centered π*-type MOs either from the phenyl rings of the phosphine ligands or from the bipyridine ligand between the completely filled t_{2g} orbitals and the empty e_g ones. The most important consequence of

this is that the lowest unoccupied molecular orbital (LUMO) is a π*-type orbital centered on the bipyridine ligand, with negligible participation of the iridium atom (Figure 4.3.9). The molecular orbital diagram for the cation in the $[Ir(bipy)H_2(PPh_3)_2]PF_6$ crystal is qualitatively very similar, with minor differences in the relative energies as well as the ordering of the orbitals and the degree of mixing between metal and ligand orbitals (Figure 4.3.10).

The electron density distribution associated with the HOMO and the LUMO are virtually identical for the cation in the two crystal structures.

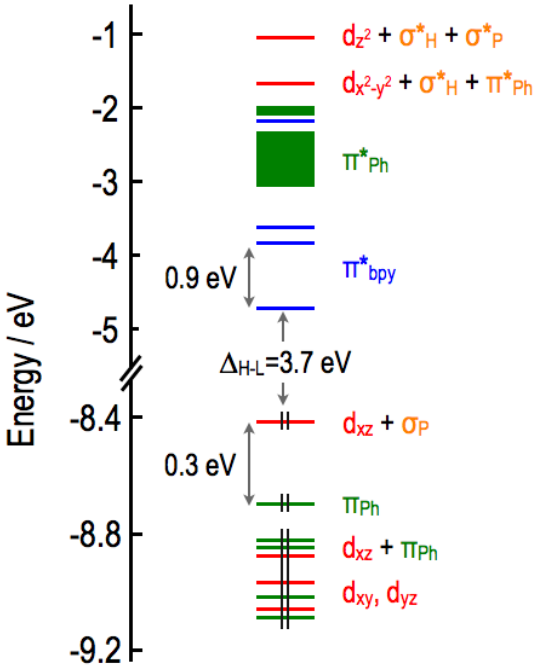

Figure 4.3.8 Molecular orbital energy diagram of **6a** in the $[Ir(bipy)H_2(PPh_3)_2]Cl$ crystal's geometry. Color code: red for d-block orbitals of the iridium atom; green for π and π* type orbitals of the phenyl rings of the phosphine ligands; blue for π*-type orbitals of the bipyridine ligand and orange for σ-type orbitals of the phosphorous'slone pairs and the hydrogen atoms bonded directly to iridium.

The computed energy for the cation's LUMO is very similar in the two compounds for which we were able to solve their crystal structure, *i.e.* $[Ir(bipy)H_2(PPh_3)_2]Cl$ and $[Ir(bipy)H_2(PPh_3)_2]PF_6$, while the HOMO is 0.15 eV lower in energy in the $[Ir(bipy)H_2(PPh_3)_2]PF_6$ crystal , leading to a 0.1 eV smaller HOMO-LUMO gap for the $[Ir(bipy)H_2(PPh_3)_2]$ cation for the crystals with PF_6^-.

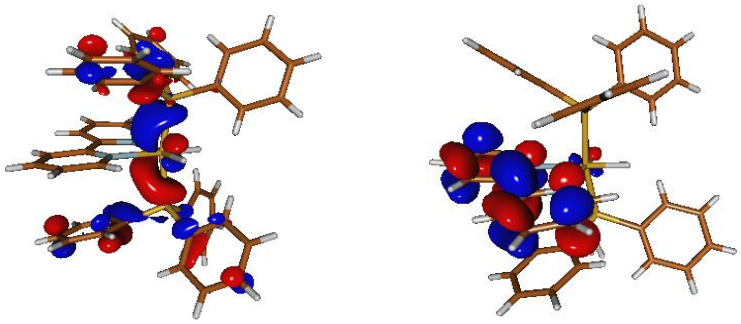

Figure 4.3.9 HOMO (left) and LUMO (right) of the [Ir(bipy)$H_2(PPh_3)_2$]Cl crystals.

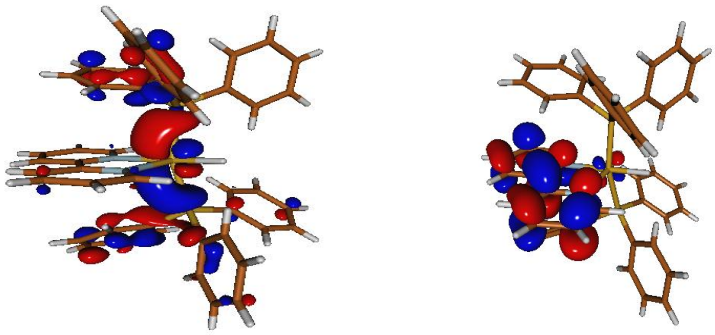

Figure 4.3.10 HOMO (left) and LUMO (right) of the [Ir(bipy)$H_2(PPh_3)_2$]PF_6 crystal.

This is indeed the difference between the calculated excitation energies to the lowest excited triplet state of the cation, which are computed at 454 nm and 433 nm for[Ir(bipy)$H_2(PPh_3)_2$]PF_6 and [Ir(bipy)$H_2(PPh_3)_2$]Cl, respectively.

The lowest singlet and triplet excited states have a predominant HOMO to LUMO contribution (>80%), except for the lowest triplet state of the cation in the [Ir(bipy)$H_2(PPh_3)_2$]PF_6 crystal, for which the HOMO to LUMO contribution accounts just for 60% of the transition. The remaining contributions are quite small and they basically belong to excitations to the LUMO from a d-type orbital of the iridium atom (~15%) or a π-type orbital of the bipyridine ligand (10%). Nevertheless, we can assign a strong metal to bipyridine charge transfer (MLCT) character to both transitions.

The vertical transition energies to the lowest singlet state are computed at 405 nm and 419 nm for the cation in the [Ir(bipy)$H_2(PPh_3)_2$]Cl and [Ir(bipy)$H_2(PPh_3)_2$]PF_6 crystals respectively, matching quite satisfactorily with the observed band just around 400 nm in the absorption spectra. It is worth to stress that the computed vertical energies to the lowest triplet state (T_1) cannot be directly compared to the

phosphorescence emission spectra (Figure 4.3.7) since the present calculations neither account for geometry relaxation of the triplet state, nor take into consideration vibronic coupling effects. The latter will be discussed below. Nevertheless, our results obtained for the atomic and electronic structure of the molecular species lead us to rule out intramolecular effects as responsible for the different phosphorescent emission properties observed for the $[Ir(bipy)H_2(PPh_3)_2]Cl$ and $[Ir(bipy)H_2(PPh_3)_2]PF_6$ crystals.

4.3.1.3 Reversible protonation and deprotonation of [Ir(bipy-H)]

The yellowish-orange emitting complex (λ_{max} = 569 nm), $[Ir(bipy\text{-}H)]H^+$ reverts to the bluish-green emitting [Ir(bipy-H)] (λ_{max} =475, 505 nm) after addition of base (triethylamine) into the solution which substantiates the reversibility of this transition. The same experiment has been performed by using thin film of [Ir(bipy-H)]. The thin film of [Ir(bipy-H)] after exposure to TFA vapour results λ_{max} at 569 nm a yellowish orange emission colour (Figure 4.3.11). When a base Et_3N vapour was exposed to yellowish-orange emitting thin film of $[Ir(bipy\text{-}H)]CF_3CO_2^-H^+$, the bluish-green colour with λ_{max} at 475 nm, 505 nm was obtained. The repeated addition of acid or base to the complex, giving similar results which was proving, the reversible nature of protonation and deprotonation (Figure 4.3.11).

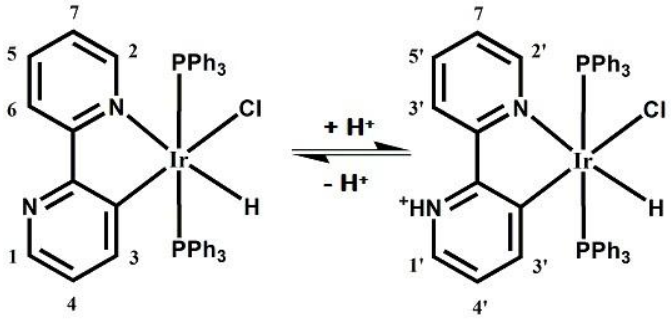

Scheme 4.3.2 Reversible protonation and deprotonation between [Ir(bipy-H)] and $[Ir(bipy\text{-}H)]H^+$.

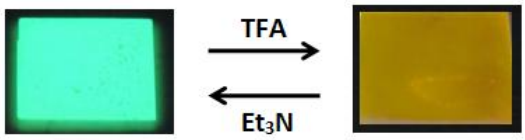

(a)

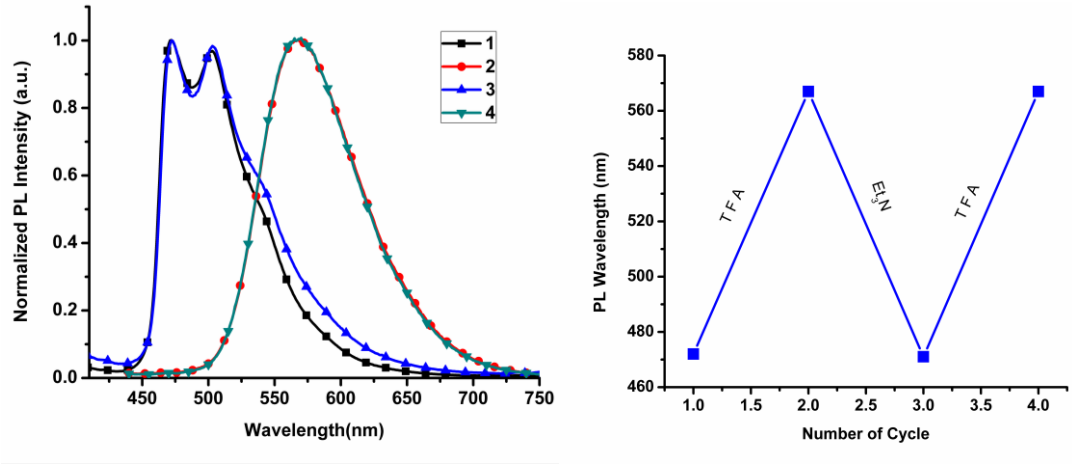

(i) (ii)

(b)

Figure 4.3.11 (a) Solid-state reversal of emission color of [Ir(bipy-H)] from blue-green to yellow-orange (on exposure to TFA) and the vice-versa (on exposure to Et_3N) (the photograph was taken under excitation of 365nm); (b) (i) Reversibility of solid-state emission spectrum of repeated protonation and deprotonation by TFA and Et_3N exposure, respectively; (ii) Switching of emission wavelength (~569 nm to ~475 nm and vice versa) on exposure to TFA and Et_3N repeatedly, respectively.

The protonation and deprotonation (Scheme 4.3.2) was also confirmed by ^1H NMR spectra. The ^1H NMR spectra of $[Ir(bipy\text{-}H)]H^+$ is recorded in $CDCl_3$, resulting more deshielded aromatic protons of pyridyl [δ= 9.01 ppm (1), 8.41 ppm (2), 8.07 ppm (3), 7.77 ppm (4)] as compare to the protons of [Ir(bipy-H)], because the pyridyl ring of $[Ir(bipy\text{-}H)]H^+$ is positively charged (Figure 4.3.12). After addition of Et_3N into $[Ir(bipy\text{-}H)]H^+$ and ^1H NMR of the resulting complex in $CDCl_3$ showed hardly any change of peak positions in comparison with the original complex, [Ir(bipy-H)] (Figure 4.3.12). The ^1H NMR spectra unequivocally supports the transformation of [Ir(bipy-H)] into $[Ir(bipy\text{-}H)]H^+$ which is completely reversible in nature.

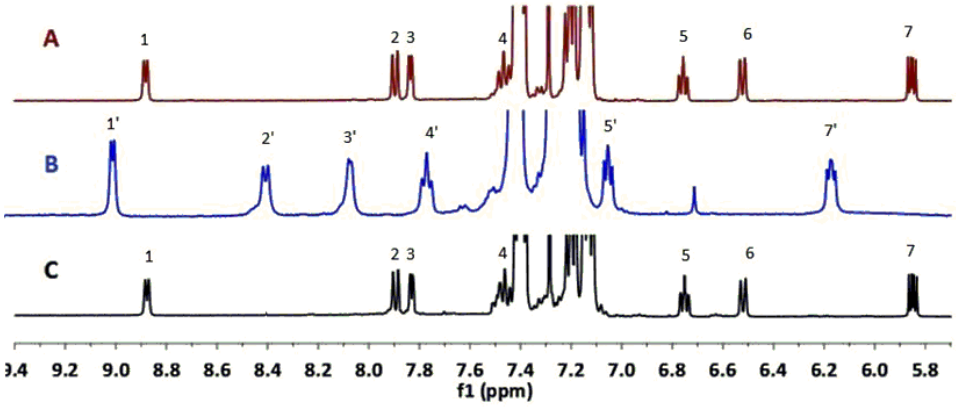

Figure 4.3.12 ^{1}H NMR spectra of [Ir(bipy-H)] in $CDCl_3$ containing (A) 0 µL trifluoroacetic acid (TFA) and (B) 100 µL of TFA and (C) was obtained by adding 300 µL of triethylamine (Et_3N) into (B).

4.3.1.4 Use of [Ir(bipy-H)]H^+ as Solvatochromic Probe

After protonation of [Ir(bipy-H)], the tendency to accept electrons / or –vely charged atoms of the pyridinium unit of [Ir(bipy-H)]H^+ has been multiplied. The pyridinium group shows affinity towards oxygen containing solvents. Taking advantage of this property, the complex, [Ir(bipy-H)]H^+ can be used as a solvatochromic probes for detection of hydrogen-bond-accepting solvents (HBAS).

The UV-Vis absorbance (Figure 4.3.13) and florescence spectroscopy studies have been performed to see the effect of HBAS on [Ir(bipy-H)]H^+. As HBAS solvents, we have randomly chosen 1, 4-dioxane, diethyl ether, dimethylformamide (DMF), dimethylsulfoxide (DMSO), tetrahydrofuran (THF), methanol (CH_3OH) - which is capable of accepting H-bonds and DCM and chloroform ($CHCl_3$) are chosen as non-HBAS solvents.

The emission spectra of [Ir(bipy-H)]H^+ is recorded using 1, 4-dioxane, diethyl ether, DMF, DMSO, THF, CH_3OH, $CHCl_3$ and DCM as shown in Figure 4.3.13b. The emission spectrum in non HBAS solvents (DCM and $CHCl_3$) was observed as a featureless and broad emission with λ_{max} at 569 nm (Figure 4.3.13b) which is similar to the emission of [Ir(bipy-H)]H^+, but the emission pattern was dramatically changed into the structured emission with λ_{max} at 475 nm and 505 nm with using HBAS solvents.

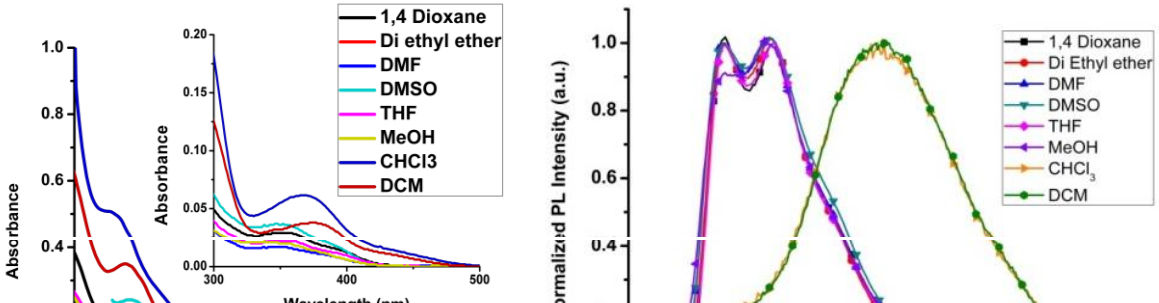

(a) (b)

Figure 4.3.13 Normalized absorption (a) and emission spectra (b) of $[Ir(bipy\text{-}H)]H^+$ in different hydrogen bond donating solvents.

In this case, the observed structured emission was found similar with the emission spectra of [Ir(bipy-H)]. As the similar variation of emission spectra was observed in presence of non-polar solvents like, 1, 4-dioxane and diethyl ether along with the polar solvents (methanol, DMSO etc), the nature of interaction of the solvent molecules with pyridinium protons become independent of polarity of the solvents (Figure 4.3.13b).

The effective change in the emission spectra can be proposed to arise from the hydrogen bonding interactions between protonated form of pyridine ring, $[Ir(bipy\text{-}H)]H^+$ with oxygen containing (H-bond acceptor) HBAS solvents. Due to hydrogen bonding interaction, HBAS pulls hydrogen from the pyridinium ring of $[Ir(bipy\text{-}H)]H^+$ which results a large emission shift exactly matching with the emission spectra of [Ir(bipy-H)].

The emission spectra of $[Ir(bipy\text{-}H)]H^+$ was recorded in DCM ($1x10^{-4}$ M) with gradual increasing amount of THF (0- 200µl) which clearly showing the fluorescence quenching with a hypsochromic emission shift (Figure 4.3.14) and that is similar with the original emission of $[Ir(bipy\text{-}H)]H^+$ (Figure 4.3.5). This experiment clearly supports the abstraction of proton from $[Ir(bipy\text{-}H)]H^+$ which is transformed into [Ir(bipy-H)] with increasing concentration of THF.

Further, ^1H NMR study was performed to investigate the hydrogen bond interaction with oxygenated solvents. The ^1H NMR of $[Ir(bipy\text{-}H)]H^+$ was recorded in $CDCl_3$ which showed the pyridinium NH^+ signal to, $\delta = 6.70$ ppm and the same signal was shielded to $\delta = 6.55$ ppm in DMSO-d_6.

The other proton signals 1' (δ = 9.01 ppm), 2' (δ = 8.41 ppm) and 3'(δ = 8.07 ppm) in $CDCl_3$ were shielded and shifted to 1'' (δ = 8.88 ppm), 2'' (δ = 8.11 ppm) and 3'' (δ = 8.00 ppm) in DMSO-d_6 (1', 2' and 3' protons are marked in Scheme 4.3.2; (Figure 4.3.15). In this case, DMSO having oxygen donor atom playing the role of a base which can interact with pyridinium NH^+ of $[Ir(bipy\text{-}H)]H^+$ *i.e.*, Bronsted acid-base interaction. In another case, ^1H NMR has been recorded for the complex of [Ir(bipy-H)] BF_4^- H^+ in $CDCl_3$ and DMSO-d_6, separately. ^1H NMR spectra was recorded in $CDCl_3$ of [[Ir(bipy-H)] BF_4^- H^+ and found the chemical shift of NH proton of bipy appears at δ = 9.00 ppm which in DMSO-d_6 changes to up-field (δ = 8.79 ppm).

These results clearly indicating of the hydrogen bond interaction playing between the NH^+ proton of $[Ir(bipy\text{-}H)]H^+$ with HBAS which is Bronsted acid-base type interaction. Further, in support of this observation, we have optimized the geometry of $[Ir(bipy\text{-}H)]H^+$ in presence of one molecule of methanol and in other case, with the presence of one molecule of dichloromethane (DCM).

The HOMO-LUMO energy gap of $[Ir(bipy\text{-}H)]H^+\cdot$MeOH (2.92 eV) was found to have higher energy value than the HOMO-LUMO energy gap of $[Ir(bipy\text{-}H)]H^+\cdot$DCM (2.84 eV) which is close to the HOMO-LUMO energy separation using the solvent DCM (HOMO-LUMO in DCM solvent = 2.76eV. This fact, further supports that the greater interaction is played between methanol with the proton of $[Ir(bipy\text{-}H)]H^+$ as compared to interaction acting on dichloromethane.

The solid state thin film of $[Ir(bipy\text{-}H)]H^+$ has been studied under exposure of volatile organic solvents (VOC's) like DMF, DMSO and other Hydrogen bond accepter solvent (HBAS). The thin-film of $[Ir(bipy\text{-}H)]H^+$ after exposing towards the solvents DMF, DMSO and other HBAS, the emission colour changes, yellowish-orange (λ_{max} = 569 nm) to yellow (λ_{max} = 555 nm) (Figure 4.3.16).

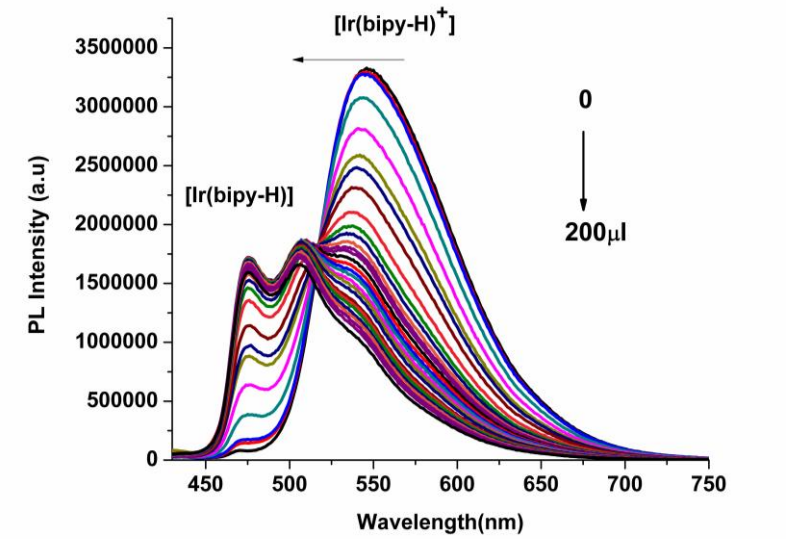

Figure 4.3.14 Emission of $[Ir(bipy\text{-}H)H^+]$ ($1x10^{-4}$ in 2mL CH_2Cl_2) with increasing amount of THF (0 -200µl) was recorded, showing the transformation from $[Ir(bipy\text{-}H)H^+]$ to [Ir(bipy-H)].

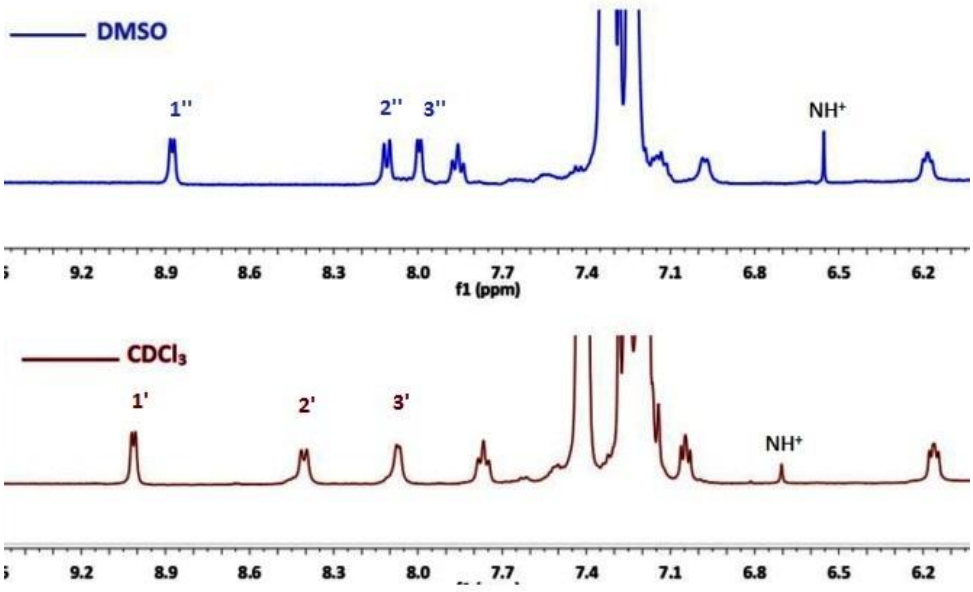

Figure 4.3.15 ^1H NMR spectra of $[Ir(bipy\text{-}H)]H^+$ in $CDCl_3$ (top) and in DMSO (bottom) showing Hydrogen bond interaction between $Ir(bipy\text{-}H)]H^+$ and DMSO.

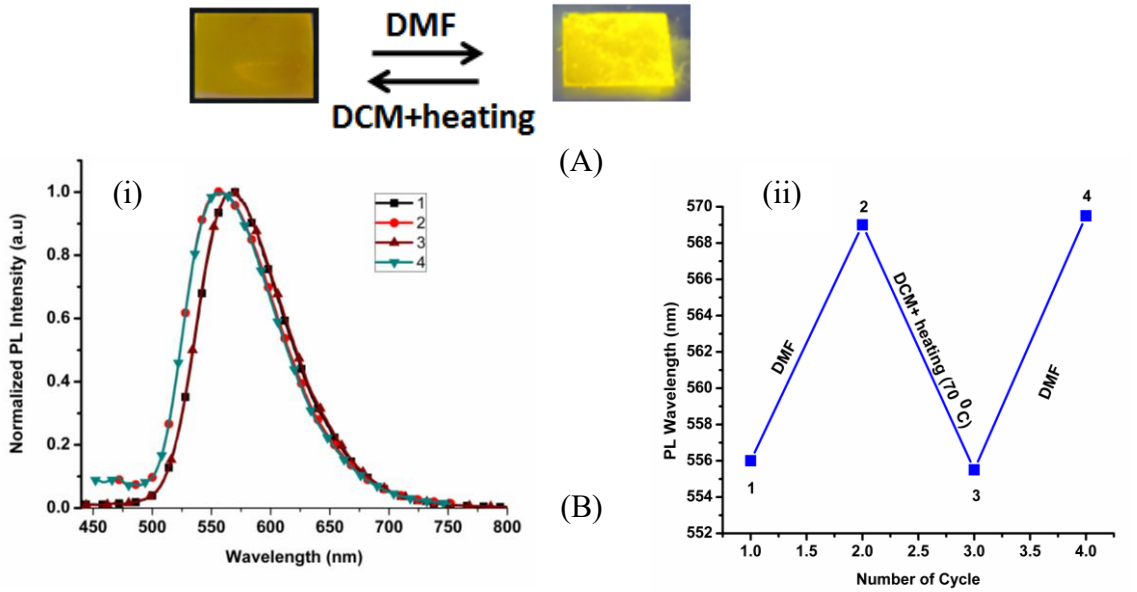

Figure 4.3.16 (A) Solid-state reversal of emission color of [Ir(bipy-H)H^+] from orangish yellow to yellow (on exposure to DMF) and orangish yellow to yellow (on exposure to DCM with 50 ^{0}C heating) (the photograph was taken under excitation of 365 nm); (B) (i) Reversibility of solid-state emission spectrum of [Ir(bipy-H)H^+] with repeated VOC exposure (2), on exposure to DMF; (3), on exposure to DCM after heating the film at 70°C for 10 min and (4, on exposure to DMF); (ii) Switching of emission wavelength (~569 nm to ~555 nm and vice versa) on exposure to DMF and DCM, respectively.

This transition is totally reversible under exposure the yellow emitting film to DCM at 70^{0}C. The same reaction on carrying out in liquid phase, the original yellowish-orange colour of the solution turns into green (*vide infra*). In the present case, the different change of colour in solid-vapour phase reaction can be demonstrated by the incomplete deprotonation of [Ir(bipy-H)]H^+. This property can be utilized for the detection of volatile organic compounds (VOCs).

The thin-layer chromatography (TLC) plate, a solid support has conveniently been used to see the effect of acid and base. The spot of the complex, [Ir(bipy-H)] on TLC plate shows bright bluish-green emission colour which was stable in presence of weakly acidic silica gel, but transformed into yellowish-orange colour in presence of

TFA vapor. However, the yellowish-orange colour reverts to the original colour (bluish green) by abstraction of proton from $[Ir(bipy\text{-}H)]H^+$ under exposure to triethylamine vapor (Figure 4.3.17).

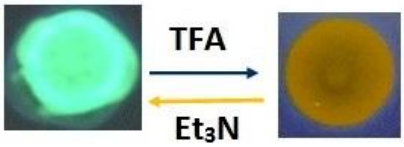

Figure 4.3.17 The TLC plate Image of [Ir(bipy-H)], the greenish blue emission color of the complex is converted into yellowish orange color after the exposure of TFA and convert back to greenish blue after exposure of Et_3N (fully reversible in nature).

4.3.1.5 Ground state optimisation

The Geometry optimization for all complexes shows slightly distorted octahedral geometries where, the position of chloro ligand is *trans* to the carbon of bipyrine ring (Figure 4.3.18).

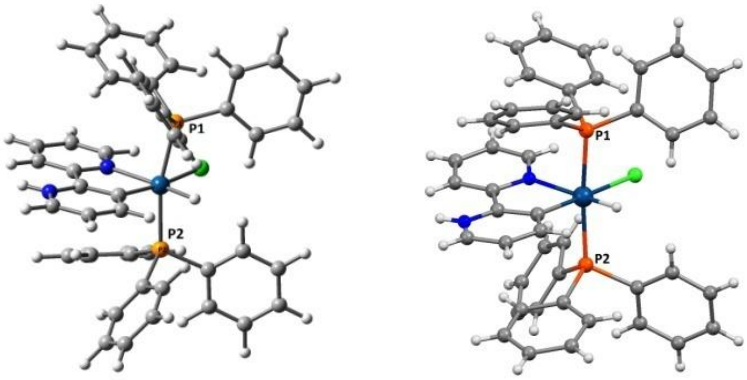

Figure 4.3.18 The optimized Ground state molecular structure of $[Ir(bipy\text{-}H)]H^+$ (Left) and single-crystal structure of $[Ir(bipy\text{-}H)]H^+$ (right), optimization has been done at the B3LYP/cc-pVDZ level.

The crystal data of $[Ir(bipy\text{-}H)]H^+$ are in good agreement with the optimized geometry of $[Ir(bipy\text{-}H)]H^+$ in DCM. For comparison, the value computed for the bond length of Ir-P1 and Ir-C (2.40 and 2.02Å, respectively) is quite in agreement with the values obtained from X-ray values (2.34 and 1.99Å, respectively). Similarly, the

computed bond angle between P1IrP2 and P1IrN (168.02˚ and 94.92˚, respectively) has been found to be in well matching with the X-ray values (174.20˚ and 95.15˚, respectively).

The frontier molecular orbitals of [Ir(bipy-H)] are shown in (Figure 4.3.19). The HOMO of this complex are located on Ir-d orbitals, chloro, the carbon bonded and little contribution on nitrogen bonded ring of bipyridine ligand (bipy-H). LUMO is mainly located on both pyridyl rings of bipyridine. These results support the existence of the metal-to-ligand charge-transfer (MLCT), ligand-centered (LC) transitions [45].

The existence of HOMO on chlorine also supports the contribution of LLCT state to the lowest excited state. The HOMO orbitals of protonated complex [Ir(bipy-H)]H^+ is quite different from [Ir(bipy-H)], is located on Ir-d orbitals, chloro and very small contribution on the carbon bonded ring of bipyridine ligand (bipy-H). While LUMO is exclusively lying over pyridyl and pyridinium ring of [Ir(bipy-H)]H^+. It shows the existence of a new lower-lying excited state in [Ir(bipy-H)]H^+ (Figure 4.3.19b), which is consisting of MLCT transition from the d orbitals of iridium(III) to the pyridinium ring of bipyridine ligand (bipy-H), interligand charge-transfer (LLCT) transition between the choloro ligand and bipyridine ligand (bipy-H) [46].

The change in emission pattern, structured to broad and structureless upon protonation is caused by the significant reduction of contribution from the LC transition. The new low lying excited state results a visible and significant red shift in UV-Vis spectra (*vide infra*). The HOMO energies of both complexes having good agreement with oxidation potential measured using cyclic voltammetric study. The computed HOMO-LUMO gap for the complexes [Ir(bipy-H)] and [Ir(bipy-H)]H^+ is approximately 4.0 eV and 3.3 eV (Table 4.3.3), respectively, which support the observed red shift in the emission spectra after protonation.

The TD-DFT calculation results were examined in detail, to gain more insight into the nature of the electronic transitions observed in the experimental absorption spectra. The calculated first excitation energies for [Ir(bipy-H)] and [Ir(bipy-H)]H^+ are found to be 3.42 eV (362 nm) and 2.76 eV (449 nm), respectively (Table 4.3.3). These values correlate satisfactorily to the observed red shift in absorption spectra (Figure 4.3.5).

This electronic transition can be seen as a promotion of an electron from the HOMO to the LUMO, with a significant MLCT character from the d orbitals of the

iridium to the π system of the bipyridine ligand together with ligand to ligand charge transfer from the p -orbital of the chlorine atom to the bipyridine ligand and a significant π to π* transition within bipyridine ligand.

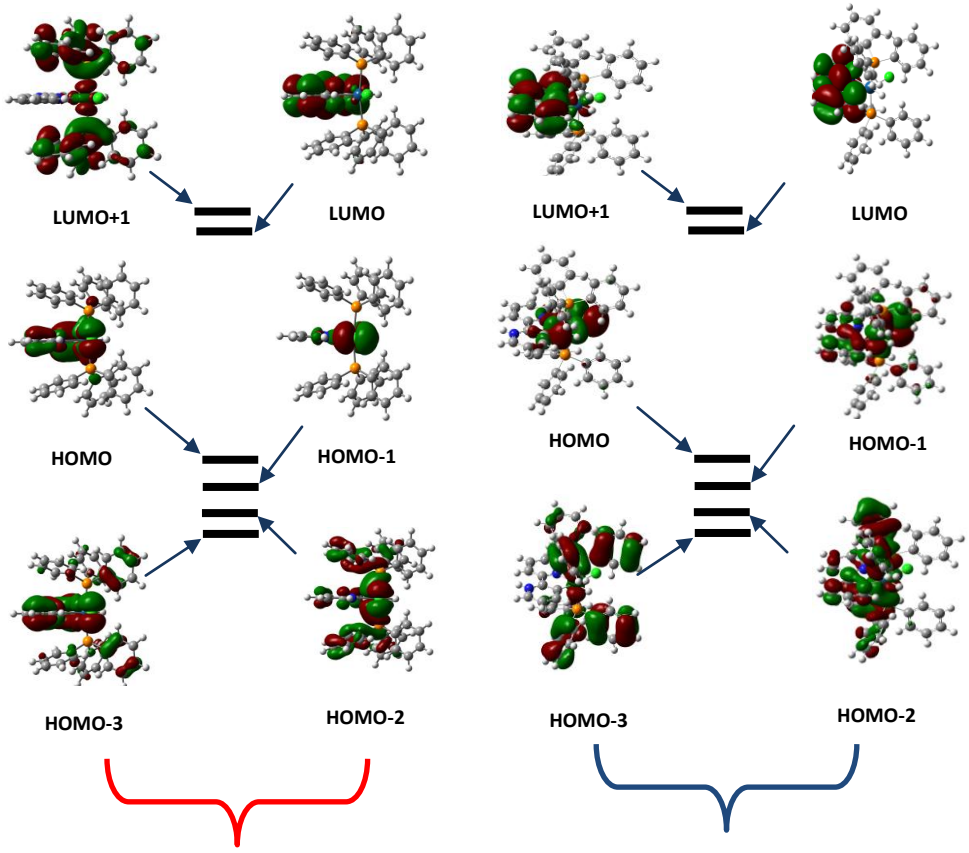

(a) (b)

Figure 4.3.19 Highest and lowest occupied molecular orbitals of [Ir(bipy-H)] (a) and $[Ir(bipy-H)]H^+$ (b).

The intense absorption band observed in the experimental spectra for [Ir(bipy-H)] at 300-370 nm corresponds mainly to the electronic transition (MLCT and LC) to the second excited singlet state (S_2) [360 nm (3.43 eV)]. The major contribution to this second singlet state is from HOMO to LUMO, with significant MLCT character. While a band 340-440 nm found for $[Ir(bipy-H)]H^+$ represents the similar types of transition with [420 nm (2.95 eV)].

The electrochemical behaviors of both complexes were measured by cyclic voltammetry (CV) in degassed acetonitrile containing 0.1 M $LiClO_4$ with a 0.05 V scan

rate. Ferrocene/Ferocenium ion^{+} (Fc/Fc^{+}) has been used as an internal standard (F_c/F_c^{+} = 3.8V in acetonitrile). Both the complexes show irreversible oxidation as well as reduction waves (Figure 4.3.20).

Table 4.3.3 Ground State energy and electrochemical data for both the complexes

Complex	**DFT**				
	ΔE, eV (nm)	Osc. Str.	%HOMO-LUMO	E_{HOMO}, eV	E_{LUMO}, eV
[Ir(bipy-H)]	3.42	0.0001	98	-5.73	-1.62
[Ir(bipy-H)H^{+}]	2.76	0.0140	95	-6.45	-3.12

Complex	**Experimental**				
		$^{a}E_{ox}$	$^{a}E_{red}$	$^{a}E_{HOMO}$,eV	$^{a}E_{LUMO}$, eV
[Ir(bipy-H)]	3.42	1.37	-1.23	-5.63	-2.7
[Ir(bipy-H)H^{+}]	2.76	1.34	-0.82	-5.60	-3.0

The anodic scan for both complexes was showing irreversible oxidation at 1.37V and 1.34V, respectively. The irreversibility in oxidation represents the redox couple of Ir(III)/Ir(IV) along with significant contribution of 'Ir-C' bonding in oxidation [47]. However, the cathodic scan shows irreversible reduction waves at -1.20V and -0.82V for [Ir(bipy-H)] and [Ir(bipy-H)]H^{+} complexes, respectively (Figure 4.3.20). The observed anodic shifts of [Ir(bipy-H)] and [Ir(bipy-H)]H^{+} from -1.20V to -

0.82V supports the increased electron withdrawing nature of pyridinium ion in [Ir(bipy-H)]H^+[47].

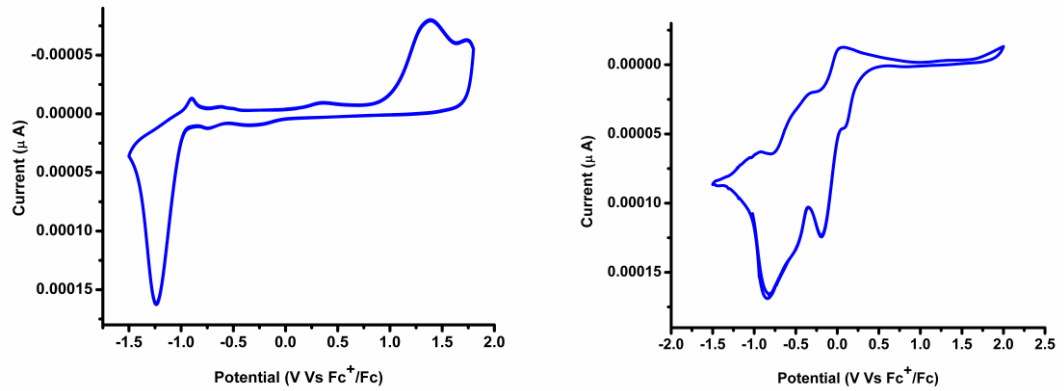

(a) (b)

Figure 4.3.20 Cyclic voltammogram of [Ir(bipy-H)] (a) and of [Ir(bipy-H)H^+] (b) respectively, recorded in ACN at a scan rate of 0.05 Vs^{-1}.

4.3.1.6 Aggregation Induced Emission

4.3.1.6.1 Aggregation Induced Emission of [Ir(bipy-H)] and [Ir(bipy-H)]H^+

The AIE property of both complexes has been investigated. [Ir(bipy-H)] is showing very faint emission in dichloromethane (DCM), chloroform ($CHCl_3$), tetrahydrofuran (THF), dimethyl sulfoxide (DMSO), 1,4 dioxane and dimethyl formamide (DMF) but showing very strong emission (λ_{max} at 475 and 505 nm) in solid state (under illumination with a 365 nm UV lamp) (Figure 4.3.21). The complex, [Ir(bipy-H)] is not soluble in water. The photoluminescent (PL) spectra of complex [Ir(bipy-H)] was studied in THF–water mixtures with different water fractions (f_w).

The different amount of the water fraction, f_w = 0-95% are added to the solution of [Ir(bipy-H)] keeping the concentration same ($1x10^{-4}$ M in THF). The PL intensity was gradually rising with increasing f_w. The maximum PL intensity was observed at f_w=90% which was showing approximately 14.5 times enhancement (Figure 4.3.21). As water was used as a non solvent, with increasing f_w in mixed solvent the complex may lead to formation of aggregated particle which was dispersed in THF. At higher f_w, the molecules come closer to form nano-aggregates and producing aggregation induced

emission in the system.

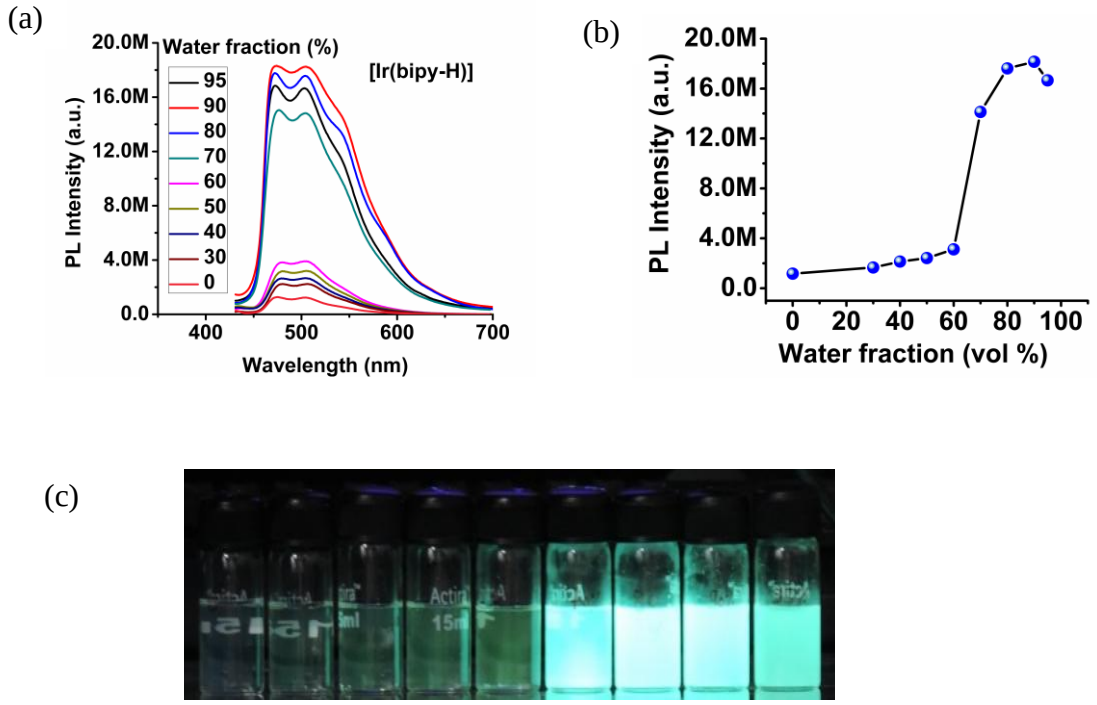

Figure 4.3.21 (a) Emission spectra of [Ir(bipy-H)] in THF/water mixtures; (b) intensity plot of intensity*(I)* values of [Ir(bipy-H)] versus the compositions of increasing water percentage in THF/water mixture, Concentration: $1x10^{-4}$ M; (c) Photographs of [Ir(bipy-H)] in THF/water mixtures with different water volume fractions (f_w) taken under UV illumination. Excitation wavelength: 365 nm.

A control viscosity experiment has been performed using THF-Polyethylene glycol (PEG) mixture. The PL spectra of the complex have been recorded with increasing PEG fraction (f_{PEG}). The maximum PL intensity was observed in case of f_{PEG} = 90% which was 14.2 times higher than pure THF solution (Figure 4.3.22). The PEG is producing viscous medium which block the rotation of phenyl rotors in triphenylphosphine ligand in the solution, resulting the emission enhancement. The absolute quantum yield of [Ir(bipy-H)] in DCM solution and solid state were estimated and found to be 0.03% and 27.95%, respectively, which is about 931 times higher.

Additionally, the photoluminescence lifetime of [Ir(bipy-H)] in THF and in

90% THF-Water was measured to be 3.33 and 12650 ns, respectively.

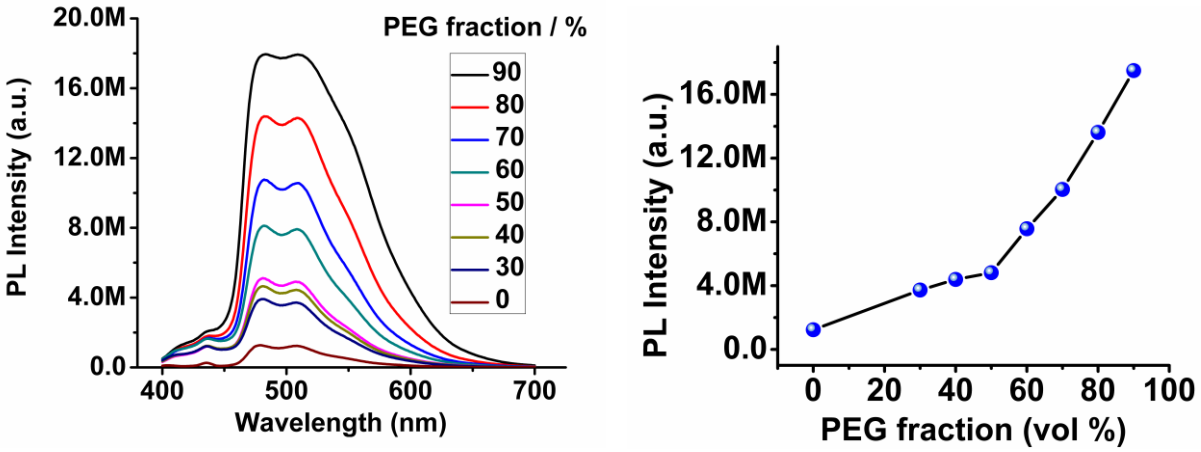

(a) (b)

Figure 4.3.22 (a) PL spectra of [Ir(bipy-H)] with [M] =10^{-5} mol L^{-1} in THF–PEG mixtures, PEG fraction (f_{PEG}); (b) intensity plot of intensity*(I)* values of [Ir(bipy-H)] versus the compositions of increasing PEG percentage in THF/PEG mixture.

Complex [Ir(bipy-H)] shows a very weak emission which is almost non luminescent in THF solvent. It happens due to rapid rotation of the triphenyl phosphine (rotor) which triggers a nonradiative transition in the system with a lowering of life-time as compared to its aggregated state. These facts prove its AIE character.

On the other hand, the emission behaviour of [Ir(bipy-H)] is totally different from [Ir(bipy-H)]H^+. After exposure to triflouroacetic acid (TFA), the maximum emission wavelength (λ_{max} = 475, 505 nm) of [Ir(bipy-H)] was red-shifted (λ_{max} = 569 nm for [Ir(bipy-H)]H^+. The absorption band at 360 nm was shifted to 388 nm and a long tail was appeared in visible region. The oxygen containing solvents such as, MeOH, THF, DMSO etc. abstract protons from [Ir(bipy-H)]H^+ and it reverts to its original form. Whenever [Ir(bipy-H)]H^+ was dissolved in THF or MeOH solvents to investigate AIE property (THF/Water, MeOH/Water or THF/ PEG, MeOH/Water), [Ir(bipy-H)]H^+ was converted into [Ir(bipy-H)] and finally at f_w =90% or f_{PEG} =90% results the same emission spectra as [Ir(bipy-H)]. This fact creates a problem to study AIP property of the protonated complex in THF-water.

The protonation was achieved after acidifying THF. The emission colour of [Ir(bipy-H)] is changed to greenish-blue to bright yellow colour after using f_w=90% in acidic THF (Figure 4.3.23). [Ir(bipy-H)]H^+ produces green emission (under 365 nm UV lamp) at lower f_w which may be the mixture of both complexes.

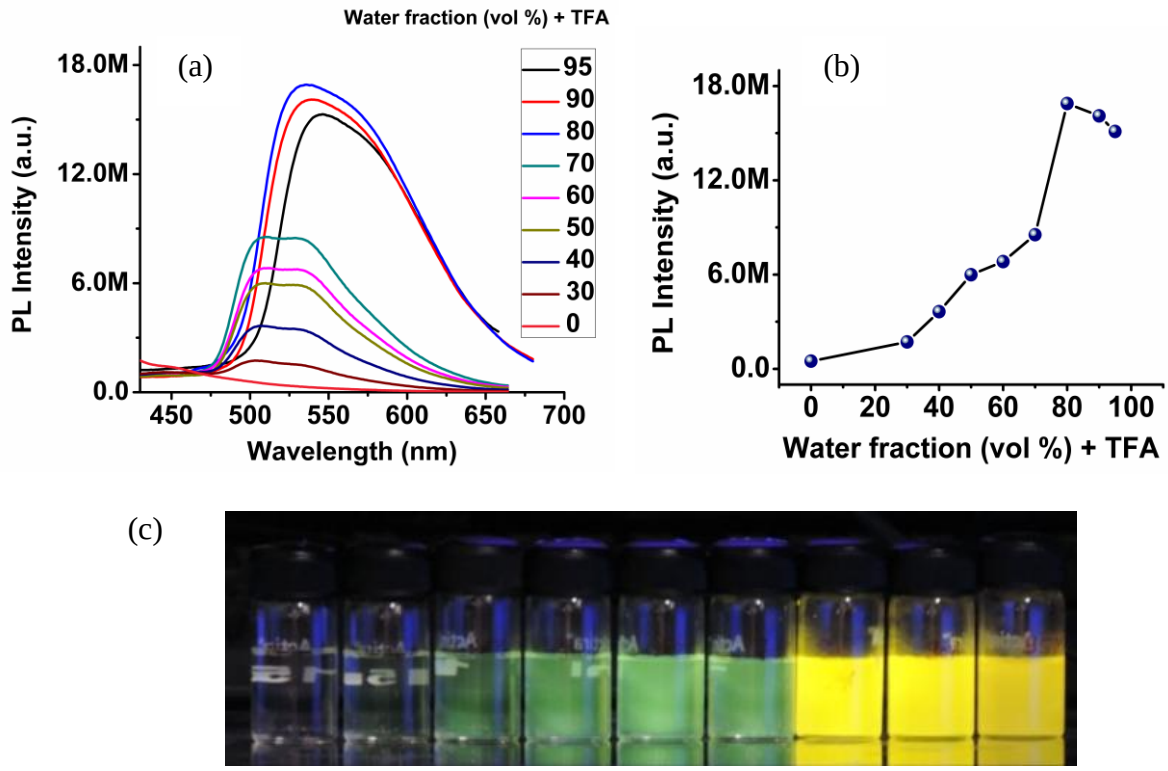

Figure 4.3.23 (a) Emission spectra of [Ir(bipy-H] in (THF/water)+TFA mixtures; (b) plot of PL intensity (I) versus the compositions of increasing water percentage in THF/water mixture + TFA (60µl in each solution)]; concentration of each solution mixture is maintained to: $1x10^{-4}$ M; (c) Photographs of the corresponding [Ir(bipy-H)] in (THF/water)+TFA mixtures taken under UV illumination (excitation wavelength: 365 nm).

We have performed a controlled experiment where 5 equivalents of TFA was added to the AIE system of [Ir(bipy-H)] (TFA was added into 0-95% THF/water mixture of [Ir(bipy-H)]). The PL spectra have been recorded, showing the gradual emission enhancement with red shifting. The λ_{max} at 475nm and 505nm of [Ir(bipy-H)] is shifted to λ_{max} at 507 nm and 532 nm with gradual increasing water fraction, f_w = 0-

70%, respectively. The following water fractions, f_w = 80, 90 and 95%, shows the maximum emission wavelengths (λ_{max}) at 534 nm, 538 nm and 545 nm, respectively (Figure 4.3.23). The PL intensity of f_w = 90% with TFA is 41 times higher than its f_w = 0% with TFA.

The viscosity experiment used to perform in THF-PEG mixture but in this case DCM-PEG mixture has been taken (as DCM is non oxygenated solvent). The PL intensity was recorded with increasing $f_{PEG.}$ There is an enhancement in PL intensity with increasing $f_{PEG.}$ The PL intensity of f_{PEG} = 90% having 17 times enhancement with respect to f_{PEG} = 0%. The emission spectra without PEG is giving λ_{max} at 569 nm, but $f_{PEG} \geq$ 30% is giving λ_{max} at 480 and 508 nm which supports the formation of [Ir(bipy-H)] (as PEG is capable of forming H-bond) (Figure 4.3.24).

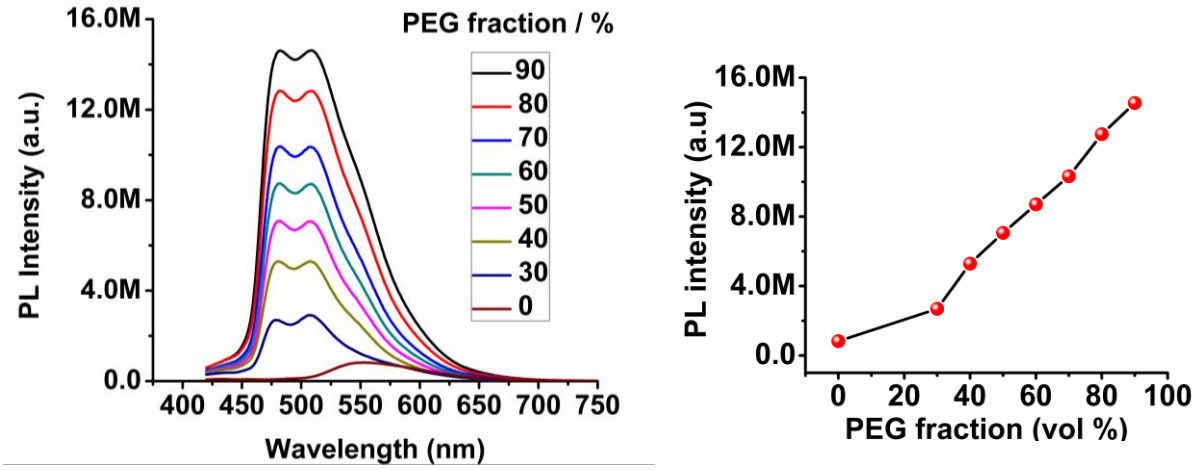

(a) (b)

Figure 4.3.24 (a) PL spectra of [Ir(bipy-H)H^+] with [M] =10^{-5} mol L^{-1} in THF–PEG mixtures , PEG fraction (f_{PEG}); (b) plot of PL intensity (I) versus the compositions of increasing PEG percentage in DCM/PEG.

Two single crystals of [Ir(bipy-H)]· $CF_3CO_2^-H^+$ and Ir(bipy-H)$H^+BF_4^-$] were obtained from slow evaporation of DCM and Hexane mixture. The structures of both the complexes have several short contact interactions (C–H···O, C–H···F and N^+–H^-···O in [Ir(bipy-H)]·$CF_3CO_2^-H^+$ and C–H···π in [Ir(bipy-H)H^+ BF_4^-.

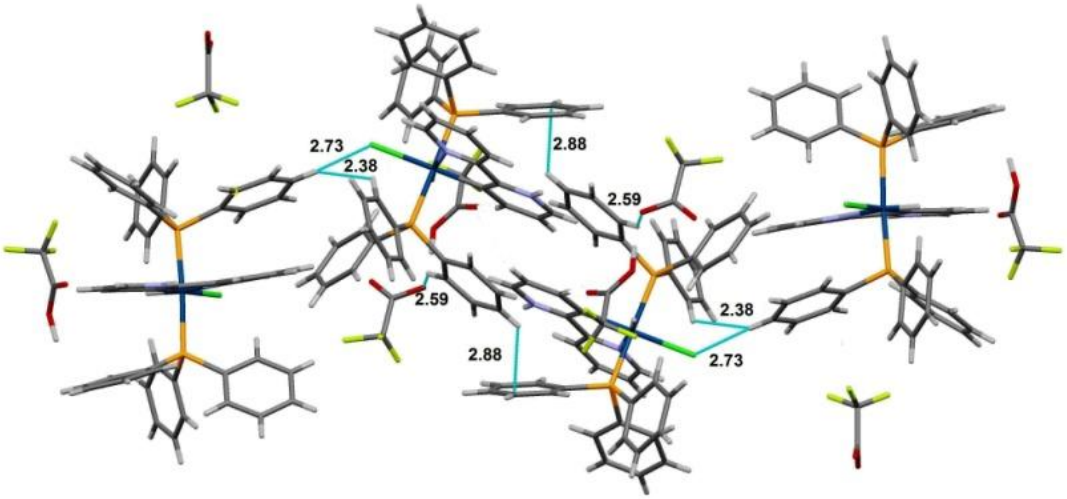

(a)

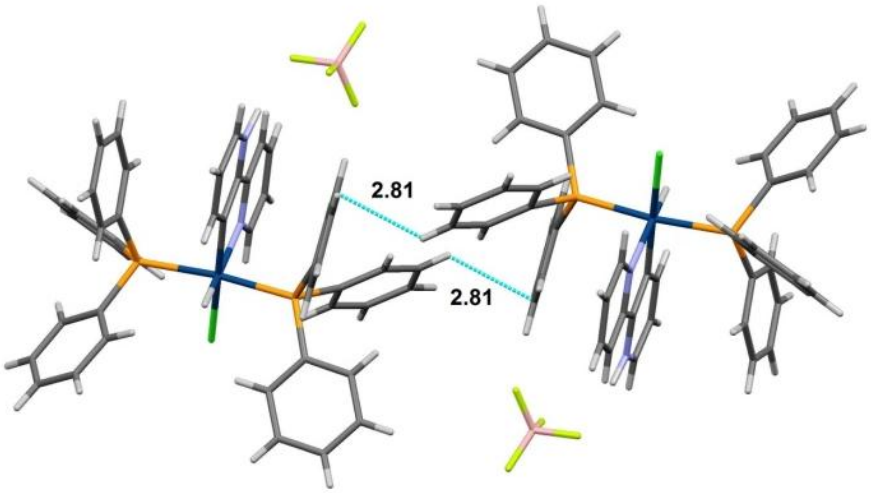

(b)

Figure 4.3.25 Packing diagram for (a) [Ir(bipy-H). $CF_3CO_2^-H^+$ and (b) [Ir(bipy-H)]$BF_4^-H^+$, shows several interactions as shown in dashed lines. The unit cell of [Ir(bipy-H)]$CF_3CO_2^-H^+$ and [Ir(bipy-H)]BF_4^- H^+, contains four and two molecules, respectively.

In the case of [Ir(bipy-H)]·$CF_3CO_2^-H^+$, the short contact distances are within 2.34-2.90 Å, while the same for [Ir(bipy-H)]BF_4^- H^+ is 2.81 Å. The phenyl rings of triphenyl phosphine moiety were involved in all these short contacts (Figure 4.3.25).

Due to these intermolecular interactions involving the -PPh_3 group, the molecular motion of the phenyl rings of this group are restricted in the solid state. Under such circumstances, the molecular motion of these groups will be restricted in solid state which will lead to close the non radiative path ways and subsequently open up several new radiative path ways. It has introduced the AIE property of both the complexes. Further studies using a particle size analyzer also put evidence the formation of nano aggregates, with diameters in the range of 0.17–2.0 mm (Figure 4.3.26). Hence, this experiment clearly showing the increasing PL intensity arise due the aggregate formation, in other words, both complexes will be AIE-active.

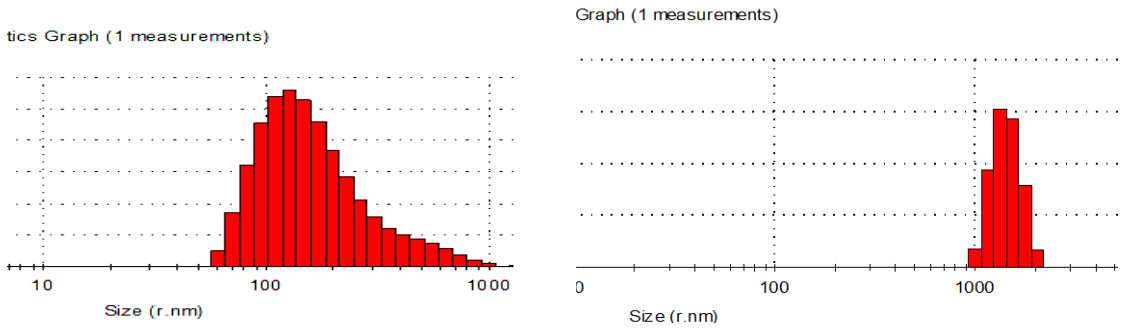

(a) (b)

Figure 4.3.26 Particle size distribution of nano-aggregates of complexes)] in a THF/ water mixture with a 90% water fraction (a) [Ir(bipy-H)] (b) [Ir(bipy-H)H^+].

4.3.1.6.1.1 Tunable AIE Property of [Ir(bipy-H)]

The reversible protonation and deprotonation effect provide us an opportunity to observe the effect of pH on emission color. Unfortunately, the buffer solution with pH~1 is not able to result full protonation of [Ir(bipy-H)] (Figure 4.3.27). The tunable AIE property of [Ir(bipy-H)] has been observed with variation of acids. The color tuning of [Ir(bipy-H)] in the aggregate form has been observed simply by changing the pK_a of the acids. As we have already discussed about the AIE property in [Ir(bipy-H)]H^+ (*vide infra*), the TFA has been used in different water fraction of [Ir(bipy-H)] (in THF), showing AIE with maximum emission wavelength (λ_{max}) at 545 nm with f_w = 95% (Figure 4.3.23). In contrast, the solution of [Ir(bipy-H)]H^+ (10^{-4}M) in THF with f_w = 95% resulted the maximum emission wavelengths at 475 nm and 505 nm (λ_{max})

while in the same solvent mixtures with addition of TFA (5 equivalent), the λ_{max} was changed to 545 nm) (Figure 4.3.23).

The emission spectra of [Ir(bipy-H)] was recorded in DCM (instead of THF) and after complete acidification with TFA (used excess of TFA to saturate), the maximum emission wavelength was further red-shifted to 569 nm (Figure 4.3.5b). The difference of emission spectra in THF and DCM in presence of TFA, indicates that the incomplete protonation of [Ir(bypy-H)] occurs in THF (which is capable of accepting protons) irrespective of the amount of a particular acid being used. This fact help us to understand that the extent of protonation to [Ir(bipy-H)] can be changed proportionately with the acids strength in mixture of solvents THF and water.

(a)

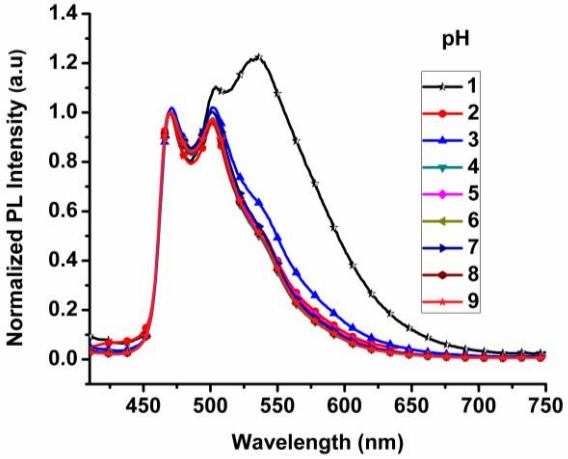

(b)

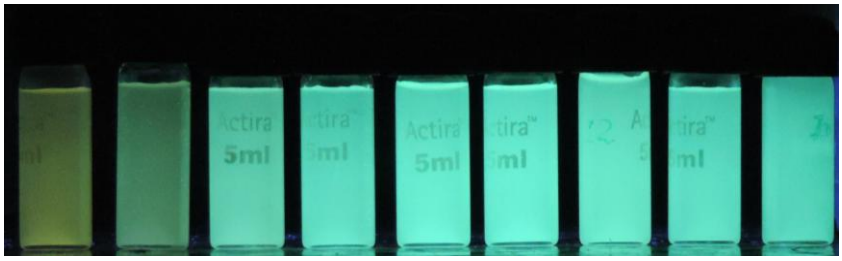

Figure 4.3.27 Emission spectra of [Ir(bipy-H)] in THF buffer mixture with different pH (1-9) (b) photo of the buffer solutions with THF, f_w =90% (pH= 1-9) under 365 nm UV lamp.

The addition of acids with different pK_a values in aggregated form of [Ir(bipy-H)] (in f_w = 95% in the mixture of THF and water) resulted a fine color tuning. After addition of acetic acid, the maximum emission wavelength remains unaltered, but with

gradual increasing strength of acid [with pK_a, 0-(-12)] resulting a red shifted emission wavelength (Figure 4.3.28 & 4.3.29).

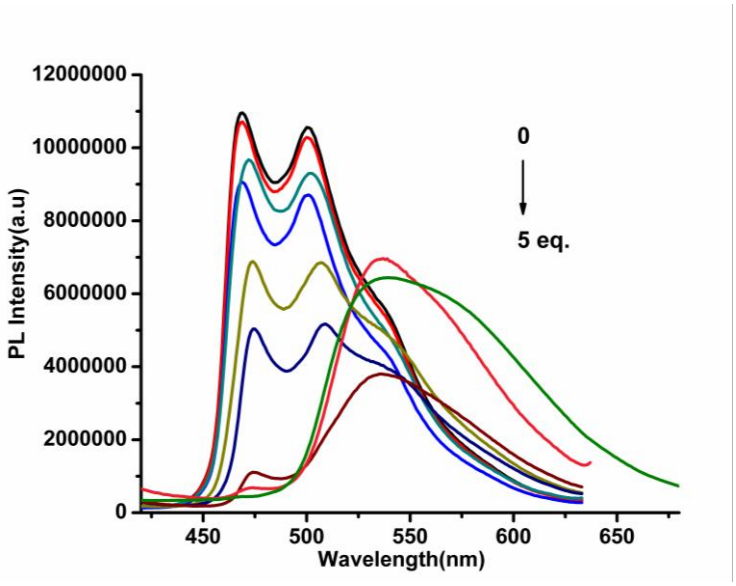

(a)

(b)

Figure 4.3.28 (a) The PL spectra of [Ir(bipy-H)] after successive addition of acid (TFA) [0-5 equivalent] in the solution of [Ir(bipy-H)] in the mixture of THF and water with f_w = 90 % concentration (10^{-4}M) and (b) the corresponding emission color under 365 UV lamp.

The emission spectra of [Ir(bipy-H)] are red shifted progressively with increasing acid concentration (TFA concentration). The structured peak at 470 and 505 nm was disappeared and the appearance of new broad peak at 545 nm, suggesting increasing extent of protonation occurs at higher concentration of acid (Figure 4.3.28).

The fine color tuning from 470 nm to 553 nm is totally dependent upon the population of both [Ir(bipy-H)] and [Ir(bipy-H)]H^+ species in the aggregate forms. In case of acetic acid, the population of [Ir(bipy-H)]H^+ is negligible which increased with

increasing the pK_a of acids, so that the progressive increase of $[Ir(bipy\text{-}H)]H^+$ in the aggregate state is responsible for tuning of emission of the aggregated solution.

(a)

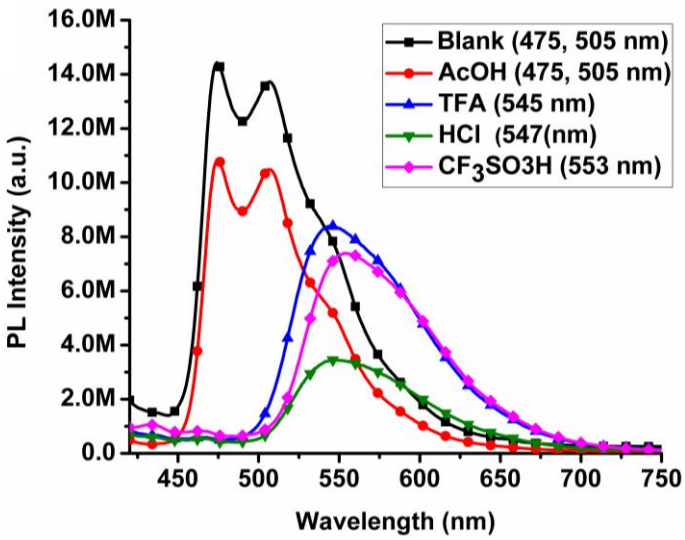

(b)

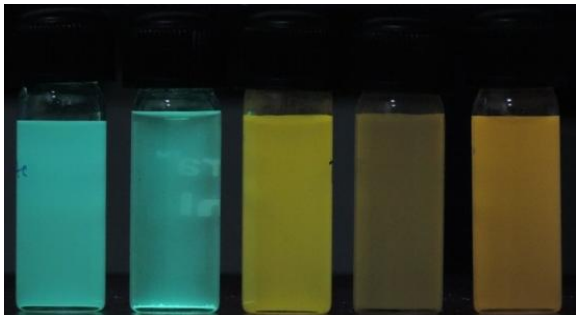

Figure 4.3.29 (a) The PL spectra of [Ir(bipy-H)] with f_w = 90 % concentration, (10^{-4}M) in the mixture of THF and water in presence of acids (5 eq.) with different p$K_{a,}$ (Blank, Acetic acid, TFA, HCl and Triflic acid (left to right), respectively); (b) the emission color under 365 UV lamp.

4.3.1.6.2 Aggregation Induced Emission of $[Ir(bipy)H_2(PPh_3)_2]A$

In the following we focus our attention on the AIE properties in the $[Ir(bipy)H_2(PPh_3)_2]A$ crystals. All four investigated compounds present quite weak emission intensities when dissolved in common organic solvents, such asdichloromethane, trichloromethane and tetrahydrofuran, while in the solid state, their phosphorescence emission becomes much more intense. To investigate and characterize the observed AIE effect, the four ionic complexes were dissolved in ethyl acetate and

then a gradually increasing amount of hexane was added (fraction of hexane (f_H) 0-90%, concentration=$1x10^{-4}$ $molL^{-1}$). Since the complexes are not soluble in hexane, the extent of aggregation should increase with higher hexane fractions. If the complexes have AIE activity, the PL intensity is expected to be enhanced with an increasing degree of aggregation of the complex. As shown in Figure 4.3.30 & 4.3.31, the PL intensity of [Ir(bipy)]BF_4 increases steadily with the fraction of hexane (f_H, 0-70%) in the mixture, while a sharp enhancement of the PL intensity was observed when increasing the hexane fraction from 70% to 90%. The PL intensity at f_H=90% was found to be about 25.6 times higher than for the solution in pure ethyl acetate. In the same way, the PL intensity of compounds [Ir(bipy)] PF_6 and [Ir(bipy)]Cl was found to increase at f_H = 90% to 27.9 and 116 times higher than in their ethyl acetate solutions, respectively. In case of [Ir(bipy)] $N(CN)_2$, the PL intensity increased slowly upto $f_{H,}$ = 70%, but at $f_{H,}$ = 90% a decrease of the intensity was observed. The PL intensity of [Ir(bipy)] $N(CN)_2$ at $f_{H,}$ = 70% and $f_{H,}$ =90% is about 7.8 and 6.9 times larger, respectively as compared to the intensity for the parent solution in pure ethyl acetate.

To further investigate the decrease of the PL intensity of [Ir(bipy)] $N(CN)_2$ for hexane fractions above 70%, we have taken TEM images with electron diffraction (ED) for samples of this complex. The TEM image clearly showed the existence of nanowire-like aggregates (90-230 nm range) at f_H=90% (Figure 4.3.32). The absence of a clear bright ring in electron diffraction supported the formation of amorphous molecular aggregates (Figure 4.3.32).The absolute quantum yields for [Ir(bipy)H_2(PPh_3)$_2$]A [A=Cl, PF_6, BF_4 and $N(CN)_2$] were estimated in powder form and found to be 19.85% (Cl), 33.64% (PF_6), 26.76 % (BF_4) and 6.75 % [$N(CN)_2$], respectively, while the relative quantum efficiencies in solution (in dichloromethane, with respect to coumarin 153 dissolved in degassed ethanol, QE = 0.38)were observed to be very low *i.e.*, 0.018 % (Cl), 0.019% (PF_6), 0.024% (BF_4), and 0.011% $N(CN)_2$. These facts support that all four compounds have an enhanced emission in the solid state.

In both crystals, there are relevant interactions between some hydrogen atoms on the bipyridine ligand or the phenyl rings and the counterions. In the [Ir(bipy)H_2(PPh_3)$_2$]Cl crystal there are short C−H···Cl contacts that range from 2.5 to 3.0 Å (Figure 4.3.33)., while in the [Ir(bipy)H_2(PPh_3)$_2$]PF_6 crystal there are C−H···F interactions that lie in the range of 2.4 to 2.9 Å (Figure 4.3.34). In this sense, the RIM

mechanism seems to offer a satisfactory explanation for the enhanced emission in the solid state observed for these complexes. Note that in this case there are two clearly different sources for the restriction of the mobility of the phenyl rings in the crystals.

On one hand, in the two crystals the rings of neighboring molecules are interlocked and their movement hindered by repulsive steric congestion. In the case of the [Ir(bipy)]PF_6 crystal, however, we have a different mechanism restricting the free rotation of the phenyl rings since they are effectively kept in place by the attractive C-H···π interaction to the rigid bipyridine ligand of a neighboring molecule.

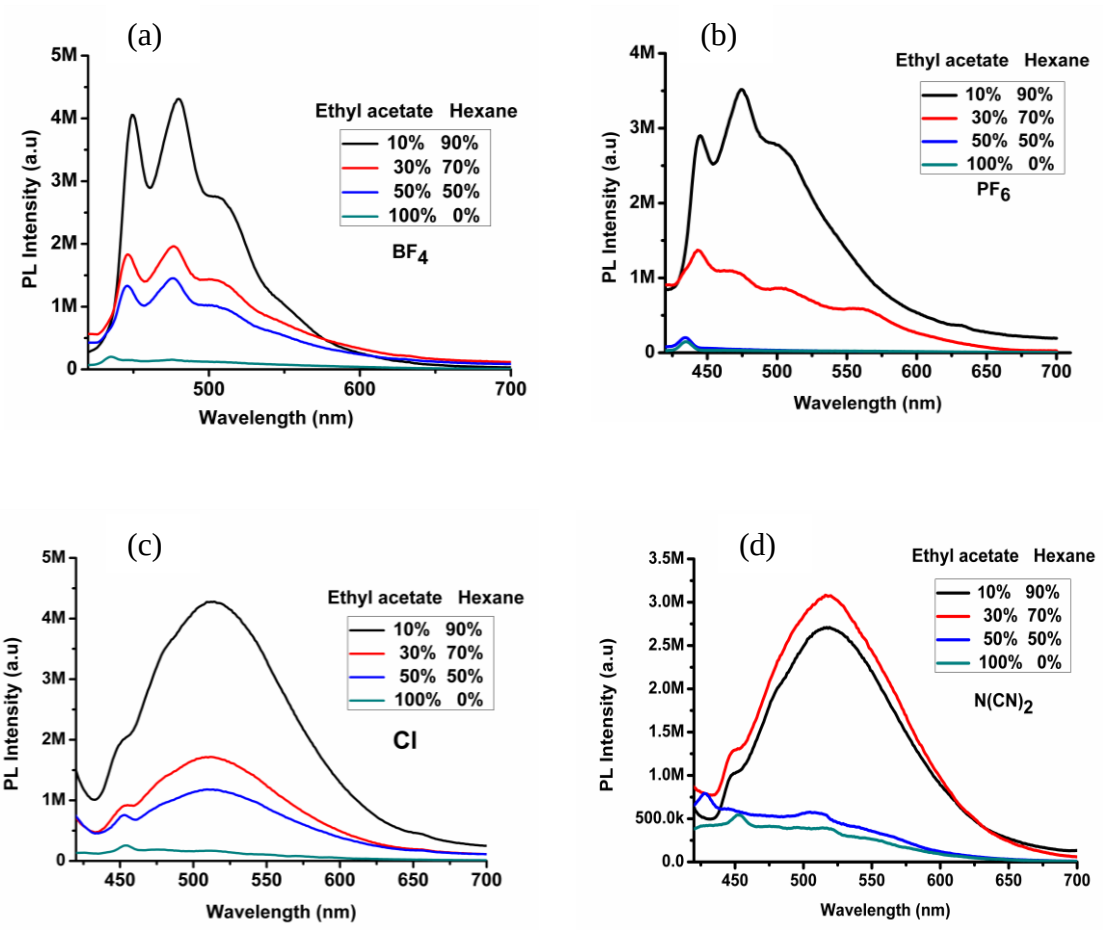

$N(CN)_2$.

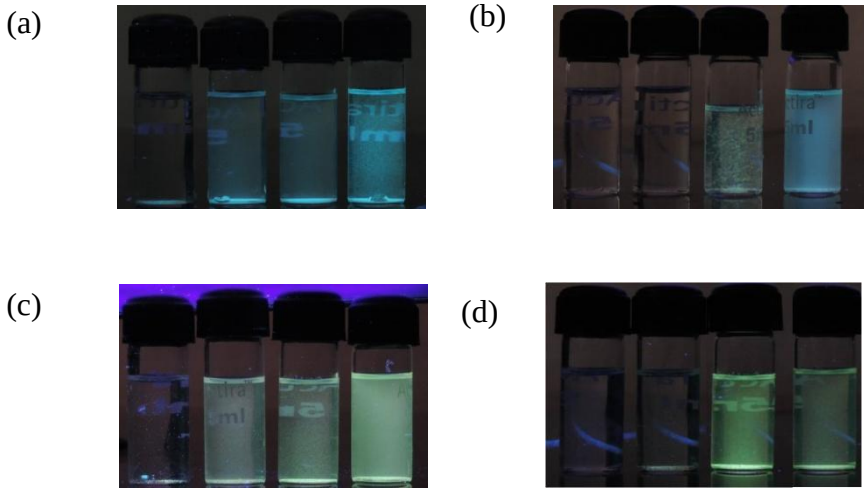

Figure 4.3.31 Luminescent images of $[Ir(bipy)H_2(PPh_3)_2]A$ under UV light with λ_{exc}365 nm. . (a) BF_4, (b) PF_6, (c), Cl (d) $N(CN)_2$ in ethyl acetate-hexane (1:9, v/v) mixed solvents keeping the concentration of the solution to 1x 10^{-4}M.

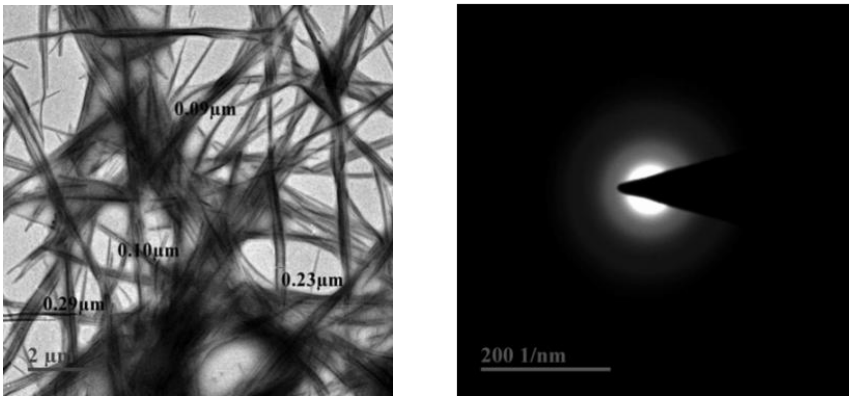

(a) (b)

Figure 4.3.32 (a) TEM image of nanoaggregates of $[Ir(bipy)H_2(PPh_3)_2]A$ (A= $N(CN)_2$) formed in ethyl acetate-hexane mixtures with 90% hexane fraction; (b) Electron diffraction (ED) pattern of the nanoaggregates showing amorphous nature of the aggregate (right).

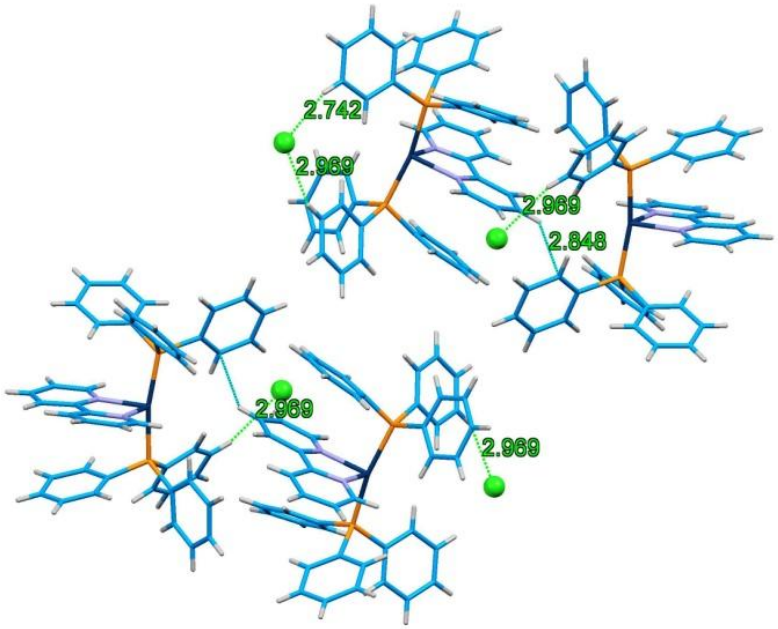

Figure 4.3.33 The crystal packing diagram of [Ir(bipy)]Cl showing short contacts in the range of 2.7-3.0 Å

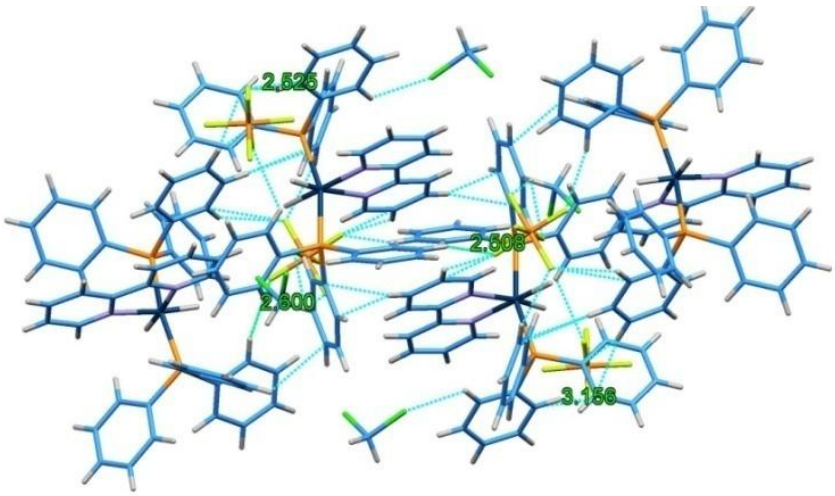

Figure 4.3.34 The crystal packing diagram of [Ir(bipy)]PF_6 showing short contacts in the range of 2.5-3.1 Å.

4.3.1.7 Mechanochromic and vapochromic phosphorescence of [Ir(bipy)]Cl

In a further investigation of the luminescent properties of the [Ir(bipy)]A compounds, [Ir(bipy)]Cl was found to exhibit the unusual mechanochromic and vapochromic behavior.

With the exposure of the green emitting solid complex, [Ir(bipy)]Cl (λ_{max} = 519 nm) to DCM or chloroform, it was transformed into a faint yellow emitting complex (λ_{max} = 548 nm). To simplify the following discussion, the yellow emitting complex will be labeled as 'Y' and the green emissive form as 'G'. Meanwhile, Y was reverted back to G after grinding with the following solvent (acetone, ethyl acetate, benzene) fuming.
In a different experiment, a 10 ton pressure was applied to the Y form of the complex using a hydraulic press, but in this case its colour remained unchanged. These facts led us to conclude that the mechanochromic behavior resulted probably from the application of a shearing force applied during the grinding process [48].

In another experiment, the Y form was coated on a filter paper and the word "BITS" was written on it with the help of a capillary tube with acetone (Figure 4.3.35). Interestingly, the observed transformation of Y into G only in the zone where the word 'BITS' was written hints to the potentiality of this compound for applications in the fields of optical recording and pressure-sensing. This drastic change in the emission behavior may attribute to the solvent/vapor induced recrystallization upon exposure to acetone which can be observed in Figure 4.3.36 where a drop of acetone solvent produced a drastic change in the emission behavior of [Ir(bipy)]Cl. The presence of DCM solvent in the Y form was revealed by thermogravimetric analysis (TGA), which showed a weight loss in the range of 50^0C-150^0C compatible with the loss of one molecule of DCM (Figure 4.3.37).

From these experiences it may be deduced that the G form, which possesses a crystalline nature, was converted into the Y form with an amorphous nature upon exposure to DCM or choloroform vapors. In this sense, these two solvents, DCM and choloroform, seem to be responsible of the formation of amorphous aggregates by intermolecular interactions with the complex.

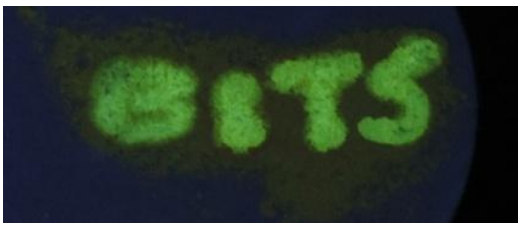

Figure 4.3.35 A filter paper coated by complex [Ir(bipy)]Cl where the word 'BITS' was written by using a capillary tube loaded with acetone.

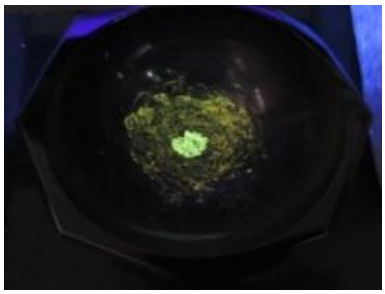

Figure 4.3.36 The effect of one drop of acetone on the ground [Ir(bipy)]Cl, showing solvent induced recrystallization.

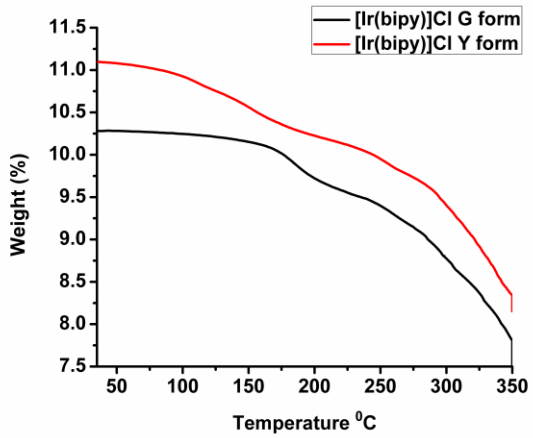

Figure 4.3.37 Thermogravimetric analysis curves of Y form and G form of [Ir(bipy)]Cl

To further investigate this hypothesis, powder X-ray diffraction (PXRD) measurements for the two different samples were performed (Figure 4.3.38). The PXRD of the G form showed sharp and intense peaks, which were in good agreement with the simulated PXRD, indicating that G corresponds to a well-ordered and crystalline material. For the Y form, the appearance of less intense and broader peaks suggests an amorphous nature for the aggregate. It is needless to say that the position of the peaks (2θ) of the G and Y forms remains the same.

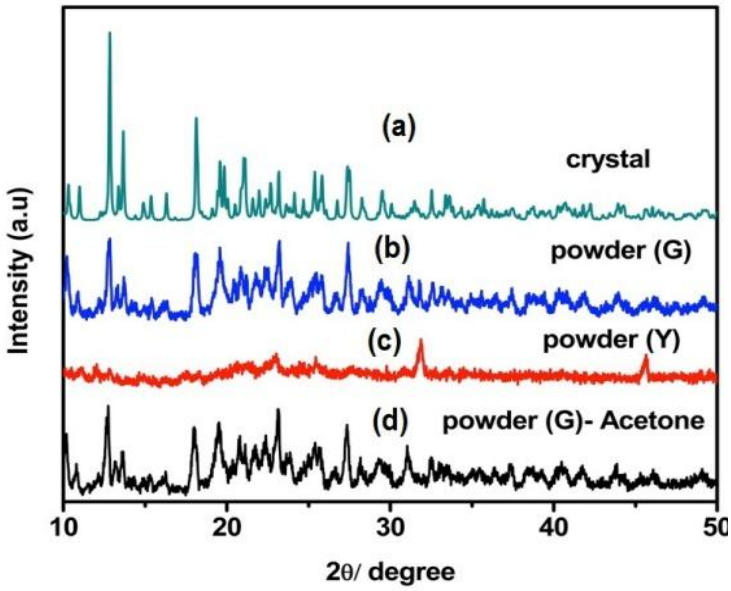

Figure 4.3.38 Power X-ray diffraction pattern of [Ir(bipy)]Cl recorded for various states (a) collected from crystal data (b) from the green powder G (c) the yellow powder Y and (d) grinding the G powder lightly followed by exposure to acetone.

Thus, the mechanochromic behavior of [Ir(bipy)]Cl can be ascribed to changes in the amorphous/crystalline nature obtained by fuming (DCM/chloroform) and grinding followed by fuming (acetone, ethyl acetate or benzene).

In a further investigation, the differential scanning calorimetry (DSC) thermograms of the Y form show exothermic peaks (recrystallization temperatures) at ~90 ^{0}C while the melting temperature was found to be ~ 240 ^{0}C (Figure 4.3.39).This results indicate that the yellow emitting complex is in a meta-stable amorphous aggregation state which undergoes crystallization upon heating. The green emitting samples obtained after grinding followed by fuming do not show any recrystallization peak in DSC (Figure 4.3.39), suggesting that the amorphous yellow emitting samples revert back to the original G form. These observations are useful to shed some light on the observed mechanochromic behavior for the chloro-complex, showing that the changes in the emission colour are due to modifications in the molecular packing upon grinding/fuming.

To further complement the information on these issues, the IR spectrum was recorded to investigate possible interaction between different solvent molecules with Ir(bipy)]Cl (Figure 4.3.40).

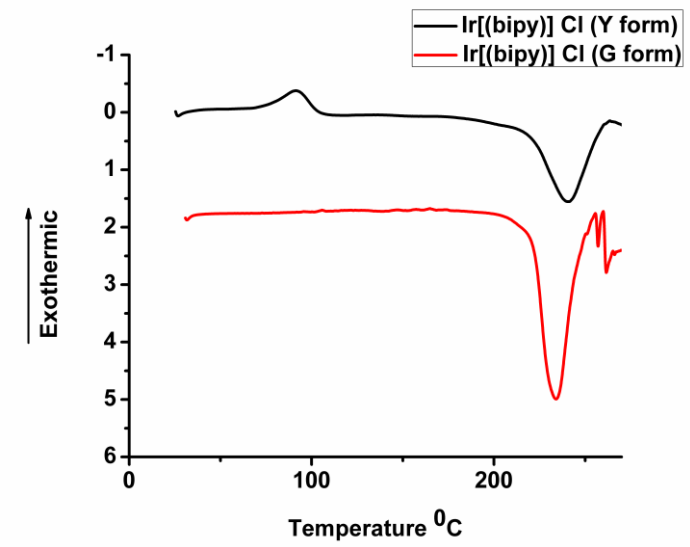

Figure 4.3.39 DSC curves of Y form and G form of [Ir(bipy)]Cl.

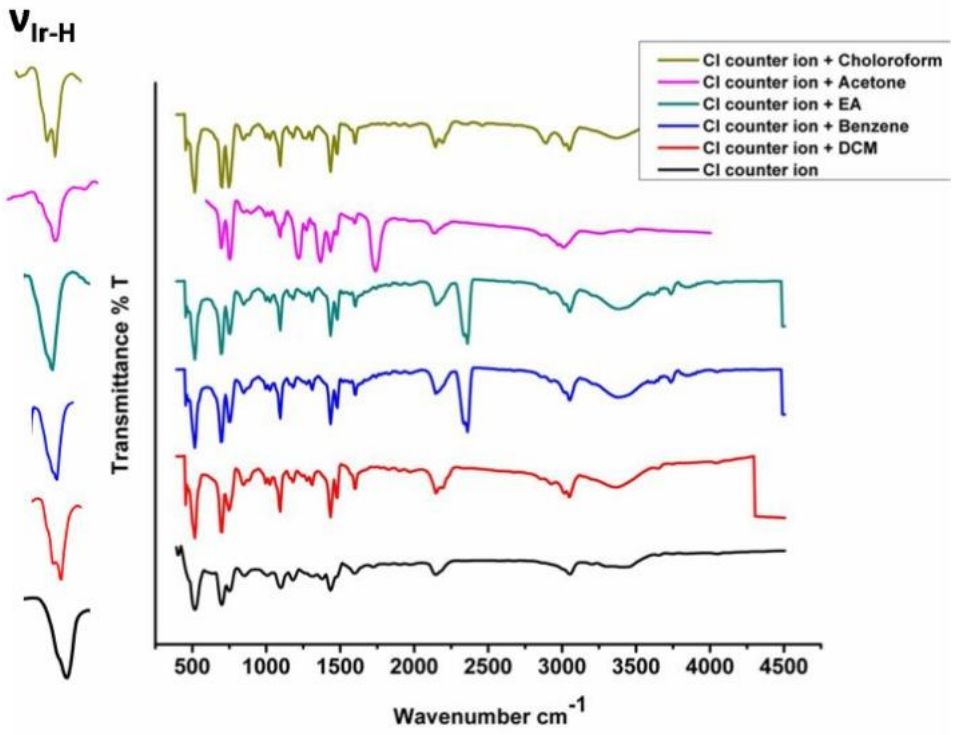

Figure 4.3.40 IR spectrum of the complex was recorded after exposure of different solvents; showing the interaction of solvents with [Ir(bipy)]Cl.

The IR spectra for the green emitting complex showed a broad signal at 2142 cm^{-1}, attributed to the Ir-H stretching frequency, that is splitted into two peaks (2145 and 2186 cm^{-1}). This splitting of the Ir-H stretching frequency can be attributed to the

interaction of DCM molecule with hydride of the complex. This result encouraged us to try to study the interaction of the cation with other solvents by analyzing the spectral features of this peak.

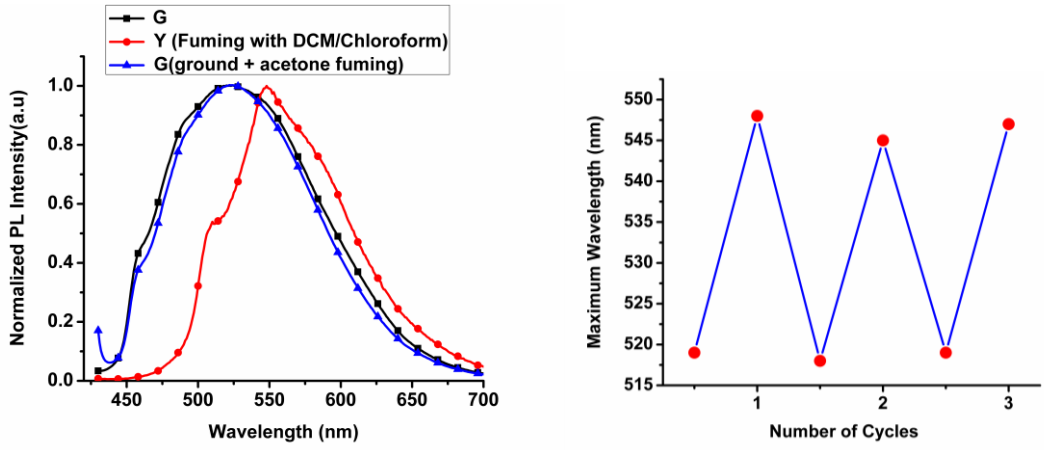

(a) (b)

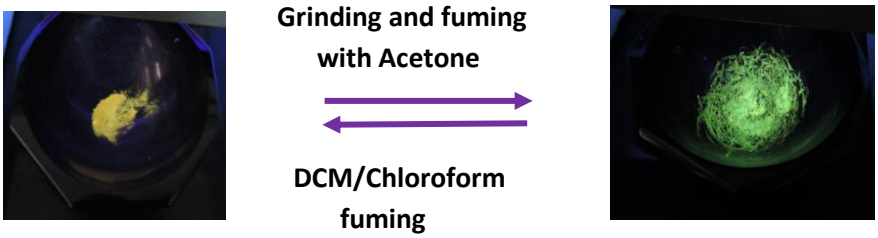

(c)

Figure 4.3.41 (a) Solid state emission spectra of [Ir(bipy)]Cl, representing the change in the emission maxima after exposure to DCM/chloroform and after grinding followed by fuming (acetone); (b) Reversibility response of [Ir(bipy)]Cl after sequential exposure to DCM/chloroform and grinding followed by fuming (acetone); (c) colour change after mechanochromic and vapochromic response.

The Ir-H stretching mode was found to give raise to a broad peak at 2143 cm^{-1}, 2145 cm^{-1} and 2142 cm^{-1} in presence of benzene, ethyl acetate, and acetone, respectively, while in presence of choloroform, two splitted peaks (2143 and 2192 cm^{-1}) were observed (Figure 4.3.40). Taking these observations into account, the changes in the hydride peak in the FTIR spectra for the Y and G forms of Ir(bipy)]Cl leads us to

propose the involvement of an interaction between the hydride of the complex and the chloro-containing solvent (DCM/chloroform). After applying external stimuli (grinding followed by fuming), these weak hydrogen-bond interactions might be broken with the resulting change of the emission colour from yellow to green. These interactions can be rebuilt after recrystallizing the complex in DCM (Figure 4.3.41),[2] which allow the process to be reversed.

4.4 Syntheses and characterizations

4.4.1 Synthesis of 3 and 4

Triphenylphosphine (622 mg, 2.348 mmol) was added to iridium(III) chloride (200 mg, 0.6711 mmol) in 2-ethoxyethanol (15 ml) and the reaction mixture was refluxed at 135°C for 4h. Then, 1, 10-phenanthroline (241 mg, 1.342 mmol) and sodium carbonate (211mg, 2.013 mmol) were added to the resulting reaction mixture and it was further refluxed for 3h. The resulting reaction mass was cooled to room temperature. The crude product was dried under reduced pressure in rota evaporator. The potassium hexafluorophosphate (KPF_6) (100 mg) was mixed with the crude product in methanol (4 ml) and the solution was heated in a microwave oven (MW) for 10 min at 60^oC (pressure, 100 psi; power, 100 W). The reaction mass was cooled to room temperature. A solid compound was separated out from the reaction mixture. The solid residue was collected through filtration and washed it with cold methanol for several times to obtain pure complex 2. Then, the mother liquor was evaporated under reduced pressure to dryness and the other complex 1 was collected (mixing with a little impurity of 2). It was purified by column chromatography eluting with a mixture of methanol and DCM (1:10) (R_f value = 0.55) (Scheme 4.2.1). Single crystals suitable for X-ray diffraction for both complexes were grown from the mixture of DCM and hexane (1 : 1) at room temperature.

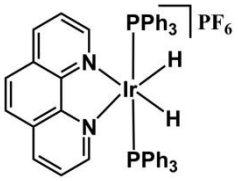

^{1}H NMR (400 MHz, $CDCl_3$) δ 8.46 (d, J = 5.1 Hz, 2H), 8.30 (d, J = 8.1 Hz, 2H), 7.91 (s, 2H), 7.27 –7.17 (m, 19H), 7.13 (m,10H), 7.05 – 6.92 (m, 3H), - 19.24 (t, J = 16.4 Hz, 2H). ^{13}C NMR (101 MHz, $CDCl_3$) δ 133.00, 132.14, 132.04, 131.98, 131.96, 128.58, 128.46. ^{31}P NMR (162 MHz, $CDCl_3$) δ 20.88 for 3; Anal. calcd for $C_{48}H_{40}F_6IrN_2P_3$: C, 55.22; H, 3.86; N, 2.68. Found: C, 55.28; H, 3.77; N, 2.75. IR (KBr, cm^{-1}): 2179 (m, ν_{Ir-H}) for 3; Yellow solid; Yield 35.77%.

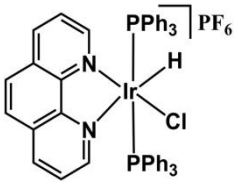

^{1}H NMR (400 MHz, $CDCl_3$) δ 9.14 (d, J = 5.0 Hz, 1H), 8.49 (d,= 7.7 Hz, 1H), 8.35 (d, J = 8.2 Hz, 1H), 8.13 (q, J = 8.9 Hz, 2H),7.71 – 7.53 (m, 2H), 7.39 – 7.26 (m, 6H), 7.27 – 7.04 (m, 24H), 6.61 (dd, J = 8.2, 5.5 Hz, 1H), -17.56 (t, J = 14.3 Hz, 1H). ^{13}C NMR (101 MHz, $CDCl_3$) δ 133.03, 132.13, 132.04, 131.99, 131.97, 128.57, 128.45.^{31}P NMR (162 MHz, $CDCl_3$) δ 29.49 for 4. Anal. calcd for $C_{48}H_{39}F_6ClIrN_2P_3$: C, 53.46; H, 3.62; N, 2.60. Found: C, 53.43; H, 3.60; N, 2.65 for 2. IR (KBr, cm^{-1}): 2152 (m, ν_{Ir-H}); Pale green solid; Yield, 11.06%.

4.4.2 Syntheses of Complexes 5 and 6: To a stirred solution of $IrCl_3{\cdot}3H_2O$ (0.5025 mmol) in 2-ethoxyethanol (6 mL), triphenyl phosphine, (1.507 mmol) were added and the reaction mixture refluxed at 130°C for 4h. Then, 2, 2'-bipyridine (1.252 mmol) was added along with Na_2CO_3 (1.507 mmol) to the reaction mixture which was further refluxed for 3h. The reaction mass was brought to room temperature. The resulting solid mass was contained two products, [Ir(bipy-H)(PPh_3)(H)(Cl)] and [Ir(N^N)(PPh_3)(H_2)]Cl which was purified by column chromatography and both products further recrystallized using a mixture of DCM and hexane (1:1). The salt formation of rollover complex of [Ir(bipy-H)(PPh_3)(H)(Cl)] was achieved with addition of trifluoroacetic acid ($CF_3CO_2^-H^+$) to the reaction mixture resulting [Ir(PPh_3)$_2$(Cl)(H)]·$CF_3CO_2^-H^+$ (similarly addition of $BF_3{\cdot}Et_2O$ results [Ir(PPh_3)$_2$ (Cl)(H)]$H^+BF_4^-$).

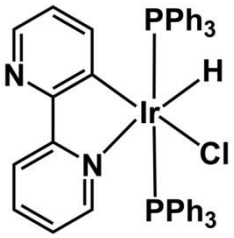

$[Ir(PPh_3)_2(bipy\text{-}H)(Cl)(H)]$ or $[Ir(bipy\text{-}H)]$ ^{1}H NMR (400 MHz, $CDCl_3$) δ 8.88 (d, *J* = 5.4 Hz, 1H), 7.89 (d, *J* = 7.8 Hz, 1H), 7.83 (d, *J* = 3.6 Hz, 1H), 7.52 – 7.36 (m, 13H), 7.17 (dt, *J*= 27.5, 7.2 Hz, 18H), 6.79 – 6.70 (m, 1H), 6.52 (d, *J* = 7.7 Hz,1H), 5.85 (dd, *J* = 7.8, 4.5 Hz, 1H), $\delta_{Ir\text{-}H}$ -17.04 (t, *J* = 16.4 Hz, 1H); ^{13}C NMR (101 MHz, $CDCl_3$) δ 163.21, 159.59, 149.37, 149.18, 140.41, 135.90, 133.99, 133.94, 133.88, 131.85, 131.59, 131.32, 129.12, 127.45, 127.40, 127.36, 124.38, 122.41, 119.77; ^{31}P NMR (162 MHz, $CDCl_3$) δ 7.92, IR (KBr, cm^{-1}): 2100 (m, $\nu_{Ir\text{-}H}$); ESI-HRMS calculated: $C_{46}H_{39}ClIrN_2P_2$ ($[M+H]^+$): m/z, 909.1906, found: $C_{46}H_{39}ClIrN_2P_2$ ($[M+H]^+$): m/z, 909.1938, Pale green solid; Yield, 60.00 % .

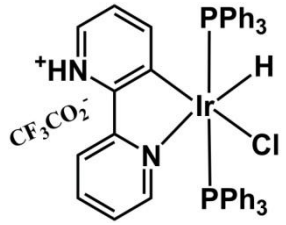

$[Ir(PPh_3)_2(bipy\text{-}H)(Cl)(H)]\cdot CF_3CO_2^-H^+$ or $[Ir(bipy\text{-}H)]\cdot CF_3CO_2^-H^+$ or $[Ir(bipy\text{-}H)]H^+$ ^{1}H NMR (400 MHz, $CDCl_3$) δ 9.01 (d, *J* = 4.9 Hz, 1H), 8.41 (d, *J* = 7.8 Hz, 1H), 8.07 (d, *J* = 4.2 Hz, 1H), 7.77 (t, *J* = 7.2 Hz, 1H),7.52 – 7.37 (m, 10H), 7.33 – 7.11 (m, 17H), 7.10 –6.98 (m, 1H), 6.70 (s, 1H), 6.16 (dd, *J* = 7.5, 5.3 Hz, 1H), $\delta_{Ir\text{-}H}$ -17.08 (t, *J* = 15.7 Hz, 1H); ^{13}C NMR (101 MHz, $CDCl_3$) δ 157.70, 137.67, 133.69, 133.64, 133.58, 130.88, 130.61, 130.34, 129.91, 127.97, 127.92, 127.87, 125.48, 124.41, 121.71; ^{31}P NMR (162 MHz, $CDCl_3$) δ 4.79, KBr, cm^{-1}): 2156 (m, $\nu_{Ir\text{-}H}$); yellow solid; Yield, 96.00 % (Fig. S2). $[Ir(PPh_3)_2(bipy\text{-}H)(Cl)(H)]\cdot CF_3CO_2^-H^+$ Or $[Ir(bipy\text{-}H)]\cdot CF_3CO_2^-H^+$ or $[Ir(bipy\text{-}H)]H^+$ ^{1}H NMR (400 MHz, DMSO) δ 8.88 (d, *J* = 5.1 Hz, 1H), 8.11 (d, *J* = 7.9 Hz, 1H), 8.00 (d, *J* = 4.8 Hz, 1H), 7.86 (t, *J* = 7.7 Hz, 1H), 7.49 – 7.11 (m, 33H), 6.98 (s, 1H), 6.55 (s, 1H), 6.18 (s, 1H), $\delta_{Ir\text{-}H}$ -17.18 (t, *J* = 15.9 Hz, 1H). ^{31}P NMR (162 MHz, DMSO) δ 6.18.

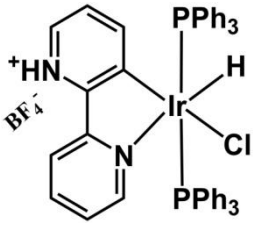

$[Ir(PPh_3)_2(bipy\text{-}H)\}(Cl)(H)]H^+BF_4^-$ or $[Ir(bipy\text{-}H)]H^+BF_4^-$ ^{1}H NMR (400 MHz, $CDCl_3$) δ 900 (d, *J* = 5.3 Hz, 1H), 8.59 (d, *J* = 7.7 Hz, 1H), 8.24 (d, *J* = 5.3 Hz, 1H), 7.75 (t, *J* = 7.4 Hz, 1H), 7.41 (dt, *J* = 10.7, 5.3 Hz, 9H), 7.30 – 7.15 (m, 20H), 7.09 (d, *J* = 7.9 Hz, 1H), 7.01 (dd, *J* = 8.1, 4.9 Hz, 1H), 6.13 (dd, *J* = 7.8, 5.3 Hz, 1H), $\delta_{Ir\text{-}H}$ -17.06 (t, *J* = 15.8 Hz, 1H). ^{31}P NMR (162 MHz, $CDCl_3$) δ 4.83. ^{1}H NMR (400 MHz, DMSO) δ

8.79 (d, *J* = 5.5 Hz, 1H), 7.97 (d, *J* = 7.5 Hz, 1H), 7.85 (d, *J* = 3.7 Hz, 1H), 7.72 (t, *J* = 8.2 Hz, 1H), 7.42 – 7.11 (m, 38H), 7.05 (t, *J* = 8.9 Hz, 1H), 6.67 (d, *J* = 4.3 Hz, 1H), 5.97 (d, *J* = 2.6 Hz, 1H), $\delta_{Ir\text{-}H}$ -17.19 (t, *J* = 16.1 Hz, 1H). ^{31}P NMR (162 MHz, DMSO) δ 7.06.

4.4.3 Synthesis of $[Ir(PPh_3)_2(bipy)(H_2)]Cl$

To a stirred solution of $IrCl_3 \cdot 3H_2O$ (0.5025 mmol) in 2-ethoxyethanol (6 mL), triphenyl phosphine, (1.507 mmol) was added and the reaction mixture refluxed at 130°C for 4h. Then, the reaction mixture was basified with excess Na_2CO_3(~10 mmol) Then, 2, 2'-bipyridine (1.252 mmol) was added to the reaction mixture which was refluxed for 3h. The reaction mass was cooled to room temperature. The resulting solid mass contained two products, $[Ir(bipy\text{-}H)(PPh_3)(H)(Cl)]$ (minor) and $[Ir(N\text{^}N)(PPh_3)(H_2)]^+Cl^-$ (major); it was purified by column chromatography Both products were further recrystallized with using a mixture of dichloromethane and hexane (1:1). The ion exchange reaction was carried out with using micro wave reactor (MW) and it was completed within a very short period of time. The methanolic solution (2ml) of $[Ir(N\text{^}N)(PPh_3)(H_2)]Cl^-$ were placed in a microwave tube along with $NaBF_4/KPF_6/Na[N(CN)_2]$ and 2 mL metanol. The whole reaction mixture was heated at 80^0C for 5 minutes. After cooling, the solid product was separated out from the reaction mixure and purified it by recrystalization with the mixture of MeOH/Hexane (~70-80%).

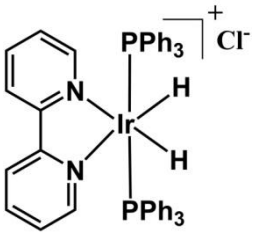

$[Ir(N\text{^}N)(PPh_3)(H_2)]Cl^-$: ^{1}H NMR (400 MHz, $CDCl_3$) δ 9.00 (d, *J* = 8.5 Hz, 2H), 7.92 (t, *J* = 7.3 Hz, 4H), 7.30 (d, *J* = 6.8 Hz, 5H), 7.28 – 7.19 (m, 23H), 6.64 (dd, *J* = 7.2, 5.1 Hz, 2H), -19.55 (t, *J* = 16.9 Hz, 2H); ^{31}P NMR (162 MHz, $CDCl_3$) δ 19.16; ^{13}C NMR (101 MHz, $CDCl_3$) δ 156.02, 154.19, 137.92, 133.13, 133.07, 133.01, 131.64, 131.37, 131.10, 130.21, 128.35, 128.30, 128.25, 126.24, 125.72.IR (KBr, cm^{-1}): 2141, 2168 (m, $\nu_{Ir\text{-}H}$); ESI-HRMS, calculated: ($[M]^+$), m/z 875.2296, found: ($[M]^+$), m/z 875.23

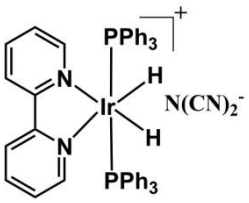

[Ir(N^N)(PPh_3)(H_2)]$N(CN)^-_2$: ^{1}H NMR (400 MHz,$CDCl_3$) δ 8.33 (d, *J* = 8.2 Hz, 1H), 8.03 (d, *J* = 5.3 Hz, 1H), 7.87 (t, *J* = 7.8 Hz, 1H), 7.40 – 7.17 (m,14H), 6.75 – 6.67 (m, 1H), -19.51 (t, *J* = 16.7 Hz,1H); ^{31}P NMR (162 MHz, $CDCl_3$) δ 20.52; ^{13}C NMR (101 MHz, $CDCl_3$) δ 155.76, 154.52, 137.57, 133.11, 133.05, 132.99, 131.51, 131.24, 130.97, 130.33, 128.43, 128.38, 128.33, 126.45, 124.28, 120.31. IR (KBr, cm^{-1}): 2221, 2190 (m, ν_{Ir-H}), 2128 (s, ν_{CN}), 2184(m, ν_{CN}); ESI-HRMS, calculated: ($[M]^+$), m/z 875.2296, found: ($[M]^+$), m/z 875.2355.

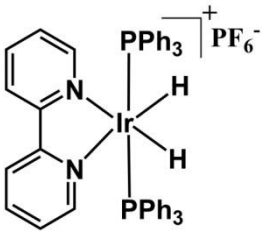

[Ir(N^N)(PPh_3)(H_2)]PF^-_6: ^{1}H NMR (400 MHz, DMSO) δ 8.33 (d, *J* = 5.3 Hz, 1H), 8.22 (d, *J* = 8.2 Hz, 1H), 7.83 (t, *J* = 7.4 Hz, 1H), 7.47 – 7.21 (m, 15H), 7.01 – 6.84 (m, 1H), -19.46 (t, *J* = 16.7 Hz, 1H); ^{31}P NMR (162 MHz, DMSO) δ 19.17. IR (KBr, cm^{-1}): 2136, 2160 (m, ν_{Ir-H}) 840 (s, ν_{P-F}); ESI-HRMS, calculated: ($[M]^+$), m/z 875.2296, found: ($[M]^+$), m/z 875.2356.

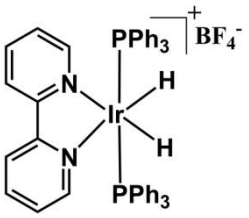

(N^N)(PPh_3)(H_2)]BF_4: ^{1}H NMR (400 MHz, DMSO) δ 8.33 (d, *J* = 5.3 Hz, 1H), 8.22 (d, *J* = 8.2 Hz, 1H), 7.84 (t, *J* = 7.4 Hz, 1H), 7.42 –7.20 (m, 14H), 6.98 – 6.89 (m,1H), -19.46 (t, *J* = 16.7 Hz, 1H), ^{31}P NMR (162 MHz, DMSO) δ 19.64. IR (KBr, cm^{-1}): 2220, 2150 (m, ν_{Ir-H}), 1058(m, ν_{B-F}); ESI-HRMS, calculated: ($[M]^+$), m/z 875.2296, found: ($[M]^+$), m/z 875.2374.

4.5 Conclusions

The synthesized 1,10 phenanthroline complexes emit very strong light in the solid state for their 'aggregation induced emission (AIE)' activity. This approach allow to introduce improved solid state light emission properties to diimine iridium(III) system. These complexes are useful as vapor-responsive luminescent materials. To the best of our knowledge, this is the first example of iridium complex where AIE active molecules sense to VOCs.

Two different varities of iridum(III) complexes [Ir(bipy-H)] and [Ir(bipy)] have been synthesized by using 2, 2'-bipyridine as a chromophoric ligand. The synthesized 'AIP

Rollover' complex, [Ir(bipy-H)] of iridium(III) showed reversible switching of emission simply by protonation and deprotonation of [Ir(bipy-H)] and [Ir(bipy-H)H^+], respectively. Furthermore, the thin film of [Ir(bipy-H)] has, successfully been employed for detection volatile organic compounds (VOCs) with acidic and basic characters. The protonated form of [Ir(bipy-H)] has been convincingly proved to be used as H-bonding probes for the solvents capable of forming H-bond. The $[Ir(bipy)]^+$ cation with the Cl^-, $N(CN)_2^-$, BF_4^- and PF_6^- counteranions were synthesized, all of them exhibiting an enhancement of the phosphorescence emission upon aggregation. The most plausible origin of the AIE effect in the studied compounds appears to be the restriction of internal motion. The larger phosphorescence quantum yield observed for the crystals with PF_6^- seems to hint at a larger RIM in this case, perhaps due to the additional C-H$\cdots\pi$ interactions found in the crystal. Interestingly, it was found that the chloro complex showed mechanochromism in presence of chlorinated solvents and the exploration of the mechanism for this phenomenon using IR spectroscopy reveals that the formation/destruction of non-covalent interactions between chlorinated solvents and the hydride ligand of the complex seem to be involved in the observed reversible color changes.

4.6 References

[1] M. Grätzel, J. Photochem. Photobiol., C, 4 (2003) 145-153.

[2] H. Sun, S. Liu, W. Lin, K.Y. Zhang, W. Lv, X. Huang, F. Huo, H. Yang, G. Jenkins, Q. Zhao, W. Huang, Nat. Commun., 5 (2014).

[3] K.-Y. Liu, C.-L. Hsu, J.-S. Ni, K.-C. Ho, K.-F. Lin, Colloid Interface Sci. 372 (2012) 73-79.

[4] E. Baranoff, J.-P. Collin, L. Flamigni, J.-P. Sauvage, Chem. Soc. Rev., 33 (2004) 147-155.

[5] J.V. Caspar, T.J. Meyer, J. Am. Chem. Soc., 105 (1983) 5583-5590.

[6] I.M. Dixon, J.-P. Collin, J.-P. Sauvage, L. Flamigni, S. Encinas, F. Barigelletti, Chem. Soc. Rev., 29 (2000) 385-391.

[7] Q. Zhao, F. Li, C. Huang, Chem. Soc. Rev., 39 (2010) 3007-3030.

[8] I.M. Dixon, E. Lebon, P. Sutra, A. Igau, Chem. Soc. Rev., 38 (2009) 1621-1634.

[9] S.C. Rasmussen, M.M. Richter, E. Yi, H. Place, K.J. Brewer, Inorg. Chem., 29 (1990) 3926-3932.

[10] B. Chiswell, S.E. Livingstone, J. Inorg. Nucl.Chem., 26 (1964) 47-51.

[11] R. Kumar, P. Bhargava, A. Dvivedi, Proce. Mater. Sci., 10 (2015) 37-43.

[12] S. Fantacci, F. De Angelis, Coord. Chem. Rev., 255 (2011) 2704-2726.

[13] C. Dragonetti, L. Falciola, P. Mussini, S. Righetto, D. Roberto, R. Ugo, A. Valore, F. De Angelis, S. Fantacci, A. Sgamellotti, M. Ramon, M. Muccini, Inorg. Chem., 46 (2007) 8533-8547.

[14] E. Margapoti, V. Shukla, A. Valore, A. Sharma, C. Dragonetti, C.C. Kitts, D. Roberto, M. Murgia, R. Ugo, M. Muccini, J. Phys. Chem. C, 113 (2009) 12517-12522.

[15] C.M. Flynn, J.N. Demas, J. Am. Chem. Soc., 96 (1974) 1959-1960.

[16] R.J. Watts, J.S. Harrington, J. Van Houten, J. Am. Chem. Soc., 99 (1977) 2179-2187.

[17] W.A. Wickramasinghe, P.H. Bird, N. Serpone, J. Chem. Soc. Chem. Commun., (1981) 1284-1286.

[18] P.J. Spellane, R.J. Watts, C.J. Curtis, Inorg. Chem., 22 (1983) 4060-4062.

[19] B. Butschke, H. Schwarz, Chem. Sci., 3 (2012) 308-326.

[20] G.L. Petretto, J.P. Rourke, L. Maidich, S. Stoccoro, M.A. Cinellu, G. Minghetti, G.J. Clarkson, A. Zucca, Organometallics, 31 (2012) 2971-2977.

[21] F. Cocco, M.A. Cinellu, G. Minghetti, A. Zucca, S. Stoccoro, L. Maiore, M. Manassero, Organometallics, 29 (2010) 1064-1066.

[22] M. Zuber, F.P. Pruchnik, Polyhedron, 25 (2006) 2773-2777.

[23] F.O. Garces, R.J. Watts, Inorg. Chem., 29 (1990) 582-584.

[24] G. Minghetti, S. Stoccoro, M.A. Cinellu, B. Soro, A. Zucca, Organometallics, 22 (2003) 4770-4777.

[25] J.-W. Zhao, C.-M. Wang, J. Zhang, S.-T. Zheng, G.-Y. Yang, Chem. Eur. J., 14 (2008) 9223-9239.

[26] B. Butschke, H. Schwarz, Organometallics, 29 (2010) 6002-6011.

[27] Y. Chi, P.-T. Chou, Chem. Soc. Rev., 39 (2010) 638-655.

[28] X. Zhang, Z. Chi, Y. Zhang, S. Liu, J. Xu, J. Mater. Chem. C, 1 (2013) 3376-3390.

[29] X. Luo, J. Li, C. Li, L. Heng, Y.Q. Dong, Z. Liu, Z. Bo, B.Z. Tang, Adv. Mater., 23 (2011) 3261-3265.

[30] J. Ni, X. Zhang, N. Qiu, Y.-H. Wu, L.-Y. Zhang, J. Zhang, Z.-N. Chen, Inorg. Chem., 50 (2011) 9090-9096.

[31] J.W. Chung, Y. You, H.S. Huh, B.-K. An, S.-J. Yoon, S.H. Kim, S.W. Lee, S.Y. Park, J. Am. Chem. Soc., 131 (2009) 8163-8172.

[32] H. Wu, T. Yang, Q. Zhao, J. Zhou, C. Li, F. Li, Dalton Trans., 40 (2011) 1969-1976.

[33] R.V. Kiran, C.F. Hogan, B.D. James, D.J.D. Wilson, Eur. J. Inorg. Chem., 2011 (2011) 4816-4825.

[34] Y. Dong, J.W.Y. Lam, A. Qin, Z. Li, J. Sun, H.H.Y. Sung, I.D. Williams, B.Z. Tang, Chem. Commun., (2007) 40-42.

[35] S. Dong, Z. Li, J. Qin, J. Phys. Chem. B, 113 (2009) 434-441.

[36] Y. Chen, L. Qiao, B. Yu, G. Li, C. Liu, L. Ji, H. Chao, Chem. Commun., 49 (2013) 11095-11097.

[37] N. Zhao, Y.-H. Wu, J. Luo, L.-X. Shi, Z.-N. Chen, Analyst, 138 (2013) 894-900.

[38] S. Obara, M. Itabashi, F. Okuda, S. Tamaki, Y. Tanabe, Y. Ishii, K. Nozaki, M.-a. Haga, Inorg. Chem., 45 (2006) 8907-8921.

[39] M. Ravi, T. Soujanya, A. Samanta, T.P. Radhakrishnan, J. Chem. Soc. Faraday Trans. 91 (1995) 2739-2742.

[40] C. Reichardt, Front Matter, in: Solvents and Solvent Effects in Organic Chemistry, Wiley-VCH Verlag GmbH & Co. KGaA, 2004, pp. i-xxvi.

[41] Z.M. Hudson, C. Sun, K.J. Harris, B.E.G. Lucier, R.W. Schurko, S. Wang, Inorg. Chem., 50 (2011) 3447-3457.

[42] T. Kizaki, T. Matsumoto, S. Ogo, Dalton Trans., 39 (2010) 1339-1344.

[43] Y. Cabon, H. Kleijn, M.A. Siegler, A.L. Spek, R.J.M.K. Gebbink, B.-J. Deelman, Dalton Trans., 39 (2010) 2423-2427.

[44] Y. Gong, L. Andrews, B.K. Liebov, Z. Fang, I.I.I.E.B. Garner, D.A. Dixon, Chem. Commun., 51 (2015) 3899-3902.

[45] M.V. Werrett, S. Muzzioli, P.J. Wright, A. Palazzi, P. Raiteri, S. Zacchini, M. Massi, S. Stagni, Inorg. Chem., 53 (2014) 229-243.

[46] A. Nakagawa, Y. Hisamatsu, S. Moromizato, M. Kohno, S. Aoki, Inorg. Chem., 53 (2014) 409-422.

[47] D.L. Davies, F. Lelj, M.P. Lowe, K.S. Ryder, K. Singh, S. Singh, Dalton Trans., 43 (2014) 4026-4039.

[48] J. Wang, J. Mei, R. Hu, J.Z. Sun, A. Qin, B.Z. Tang, J. Am. Chem. Soc., 134 (2012) 9956-9966.

Chapter V

Aggregation Induced Emission (AIE)' Active Iridium(III) Complexes with Chromophoric Schiff Base Ligands: Tunable Emission, Multi-stimuly and CO_2 Detection

5.1 Introduction

Till date the cyclometalated aromatics (C^C, C^N, N^N, C^P chelates) are a commonly used system for luminescent iridium(III) metal complexes (Figure 5.1) [1-3]. These aromatics cyclometalation is resulted a very strong covalent interaction between metal and aromatic carbon/nitrogen which helps in many aspects, *e.g* color tuning, thermal stability etc.

(1) C^N Cyclometalates

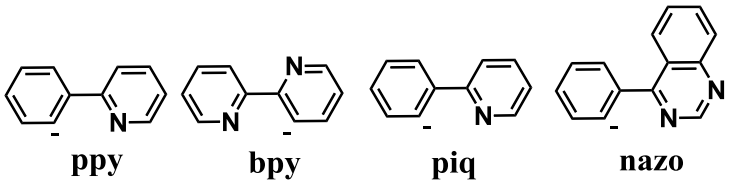

(2) N^N Cyclometalates

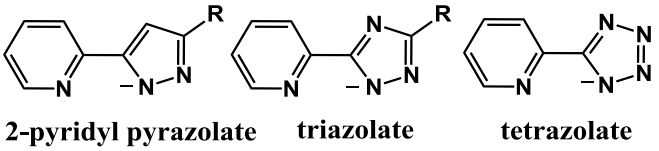

(3) C^C Cyclometalates

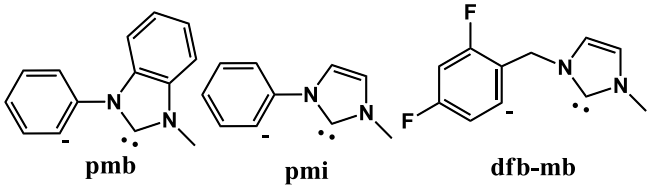

(4) C^P Cyclometalates

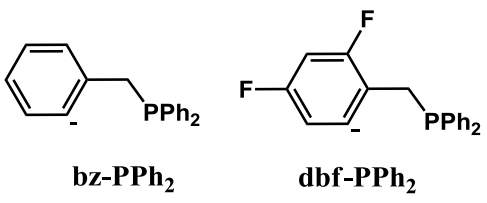

Figure 5.1 Structures of C^C, C^N, N^N and C^P Cyclometalates ligands

In 2004 and 2005 C.-H.Cheng and co-workers reported the first iridium(III) complex with olefin-tethered ligands *via* vinylic C-H activation (Figure 5.2) [4, 5]. Recently, a similar types of C-H activation has been done by Dongdong Wang and co-worker using Pt(II) metal salt [6]. These reports indicate that the C-H activation is possible not only to an aromatic compounds, but to other conjugated ligands for the formation of luminescent iridium(III) and platinum(II) complexes [7].

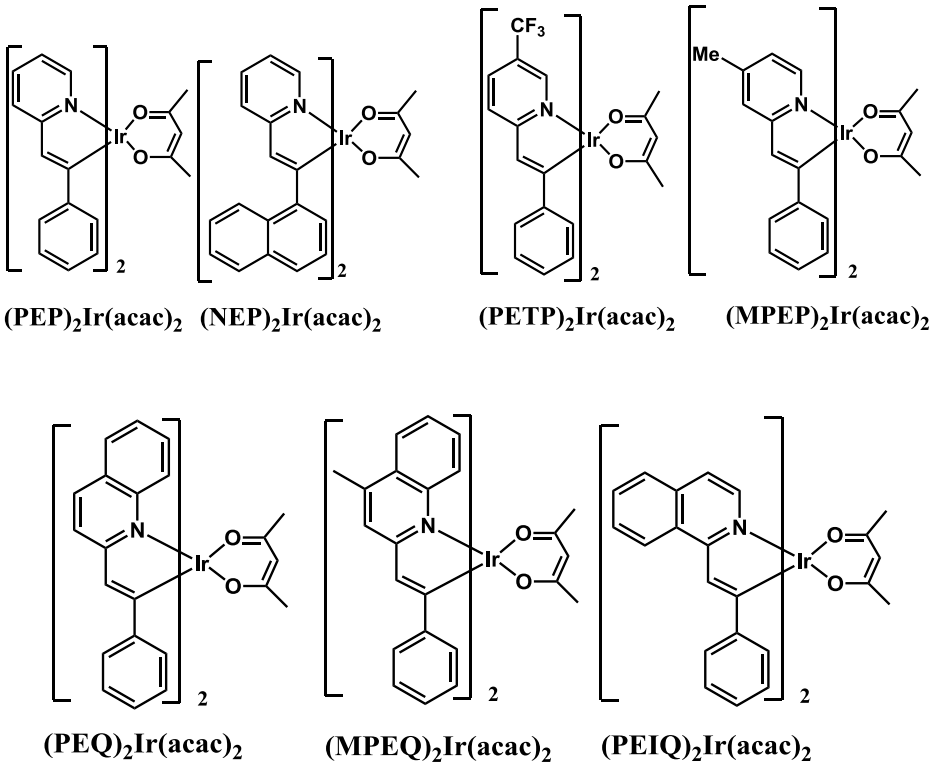

Figure 5.2 Structures of cyclometalation of olefin-tethered ligands

The emission wavelength of emissive complexes could be changed with varying solvent polarity which is termed as solvatochromism [8-12]. This property arises with the donor- accepter (D-A) system where the intramolecular rotation results a promising change in molecular conformation. This intramolecular rotation reduces the orbital overlap between donor and acceptor moiety which generated a new state known as

twisted intramolecular charge transfer (TICT) [13-16]. The molecules with TICT property are highly sensitive towards solvent polarity. Generally, the TICT probe molecules resulted bathochromic shift in the polar solvents because the excited state molecules are getting stabilized in this polar medium [17-21].

The detection of CO_2, a most promising energy source on the earth is highly desirable [22-25]. However, it is responsible for global warming. The higher concentration of CO_2 in the mines, wells, submarines are deadly for human beings.
The detection techniques, *e.g.* electrochemical (EC), infrared (IR), GC-MS methods, Field effect transistors etc are quite costly. It is required for scientific community to develop an easy and sensitive technique for detection of CO_2 gas [26-29].

In this section, we have first time used the Schiff base as a chromophoric ligand in iridium(III) complexes which are found to AIE active. The structure of all the complexes were characterized by ^{1}H, ^{13}C, ^{31}P, HRMS, IR and finally single crystal X-ray diffraction (SRXD) study. These complexes were successfully utilized for acid base sensing. However, one of the complexes having a donor-acceptor type structure that resulted in solvatochromism because of TICT and the same complex was used for CO_2 detection.

5.2 Results and discussion

5.2.1 Syntheses and Characterization

Herein, four iridium(III) complexes was readily obtained from the reaction of iridium chloride, triphenyl phosphine and Schiff-Base ligands, respectively. The Schiff-Base ligands were synthesized by reported procedure. The one-pot reaction of iridium(III) chloride and triphenyl phosphine mixture with Schiff-Bases was resulted a compound which interestingly was formed through the activation of the acyclic imine C-H by iridium(III) (Figure 5.3). The single crystals of **2** was grown from a CH_3CN–Hexane mixture and analysed by single crystal X-ray diffractometer (SCXRD). The crystal structure revealed that the imine C-H was activated by iridium(III) (Figure 5.4).

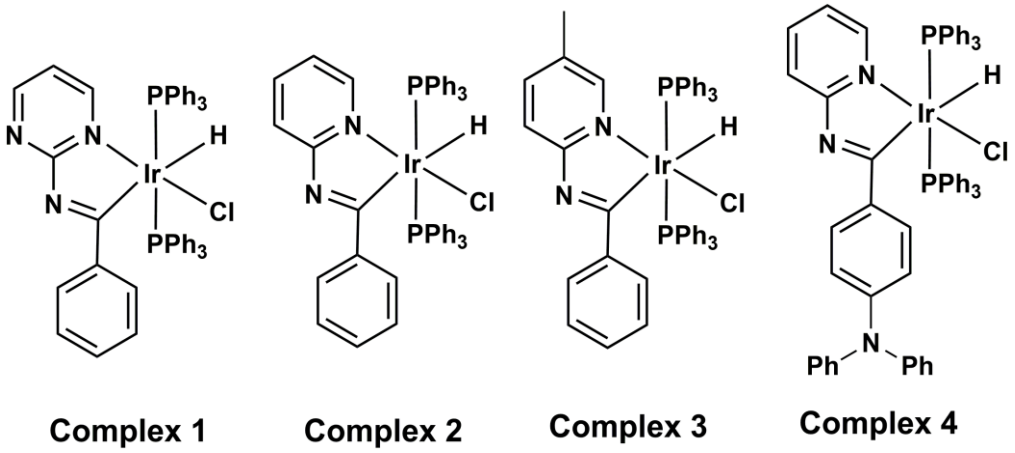

Figure 5.3 Structures of synthesized complexes.

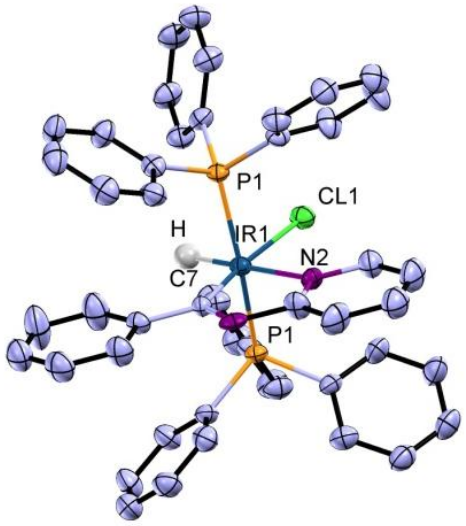

Figure 5.4 ORTEP diagram for **2**, showing distorted octahedral geometry at the Ir site .

Furthermore, these complexes were fully characterized by ^{1}H, ^{13}C, ^{31}P NMR, IR and HRMS. The highly shielded ^{1}HNMR signal in the range of -14.39-(-14.53 ppm) was indicating the presence of hydride (Ir-H) in the complexes. It was further supported with stretching frequency at 2128–2176 cm^{-1} recorded by FTIR [30]. The IR stretching frequency of C═N in schiff base ligands was found in the range of 1579-1610 cm^{-1}[31].

The ^{31}P NMR signal was observed in the range of 4.34-6.39 ppm. From HRMS data, the major fragmented peak appeared as $[M+H]^+$ at m/z in the range of 936.2476-1102.2661.

5.2.2 Photophysical property

The solution UV-Vis absorption spectra (DCM, 10^{-5} M) for **1-4** showed an intense bands below 350 nm which could be attributed to ligand-centered (LC), $^1\pi$–π^* transitions. The absorption bands in the lower energy region which were followed by weaker bands in the range of 350-450 nm was assigned to metal-to-ligand charge transfer (^{1}MLCT and ^{3}MLCT) transitions (Figure 5.5a) [32].

The emission spectra of these complexes were observed to the structured emission in the range of 490-575 nm (bluish green to orange) (Figure 5.5b). The emission and absorbance spectra of **1-3** was recorded by varying solvent polarity (non polar-polar) and found to remain unchanged irrespective of the polarity of the solvents. These results suggested that the ligand centered (LC) states are predominated into the lowest exited states [33]. The solid state emission and absorbance spectra of **1-4** were recorded. The emission spectra in solid thin films complexes were found to be structured in nature.

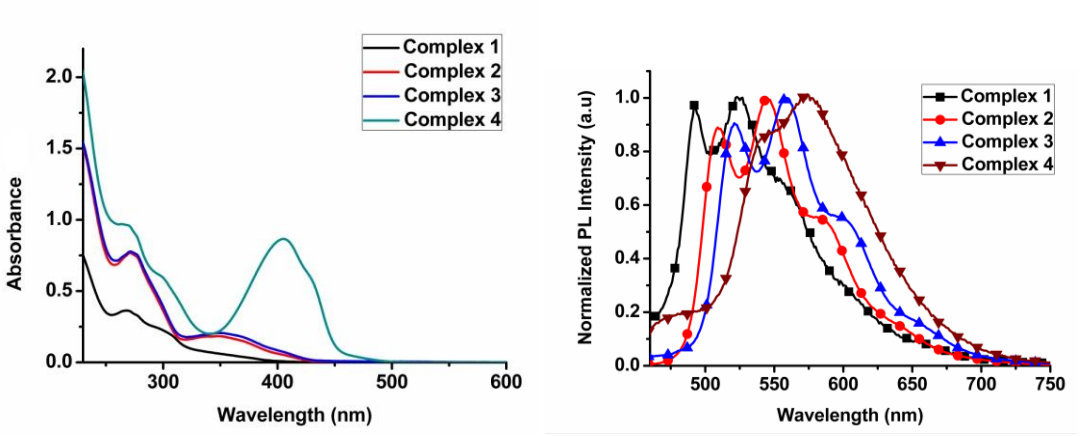

(a) (b)

Figure 5.5 (a) UV-Vis spectra of **1-4** (1x 10^{-5} M) and (b) Normalized emission spectra of **1-4,** in degassed DCM at room temperature, [c]=10^{-6} M.

The emission maxima were successfully tuned from 487 nm to 575 nm out of these complexes with a simple modification in the chromophoric ligand (Figure 5.6).

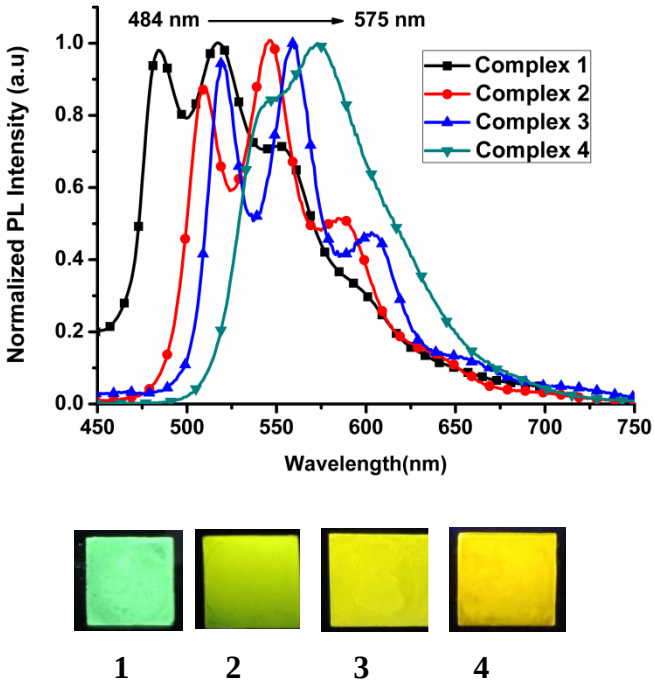

Figure 5.6 (a) Normalized thin film emission spectra of **1-4** and their respective thin film emission color under 365 nm UV lamp.

5.2.2.1 Solvent Effect

The optical property of **4** was studied using different solvents with varying polarities. Complex **4** emitted blue emission in very low polar solvents (benzene, 1,4 dioxane), whereas in relatively higher polar solvents (ethyl acetate, chloroform and DCM) the emission turned into green; in solvents with high polarity such as DMSO, DMF etc a yellow emission was observed (Figure 5.7).

The absorbance spectra were found identical with varying the solvent polarity suggesting that the ground state electronic structures was independent of solvent

polarity. The emission behaviour was observed to abrupt changes with solvent polarity. The benzene solution of **4** was exhibited an intense emission band (λ_{max} = 459 nm) along with two additional weaker bands with maximum emission wavelengths, 536 and 577 nm, respectively **(**Figure 5.7).

With increasing polarity (1,4-dioxane to DMSO), the maximum emission peak of **4** (459 nm) was shifted to 485 nm accompanied by a large decrease in the peak intensity. Such solvatochromic behaviour of luminophore could be explained by various existing hypotheses e.g., twisted intramolecular charge transfer (TICT), planer intramolecular charge transfer (PICT) or rehybridization of acceptor or donor.

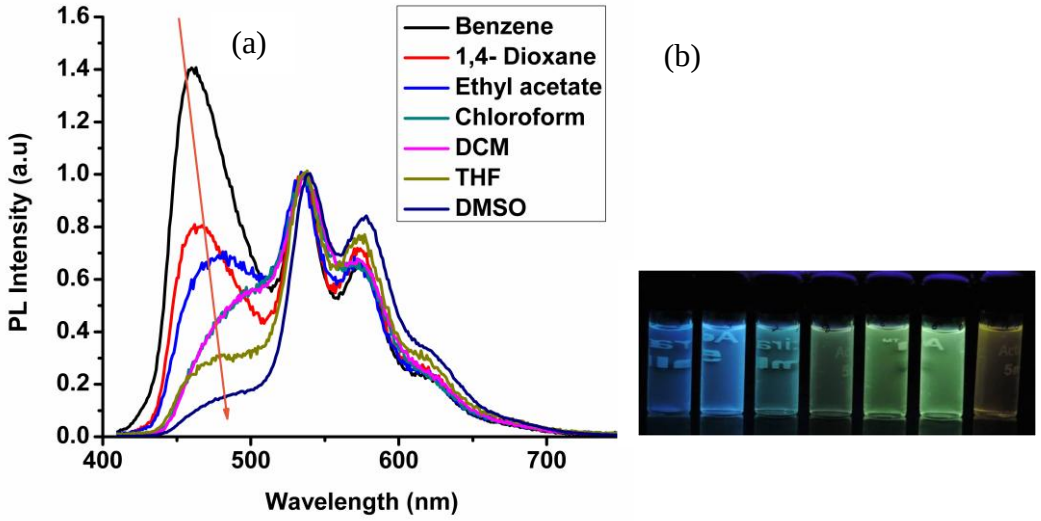

Figure 5.7 (a) Emission spectra of **4** in different solvents (b) Photographs showing the emission colors of 4 in different solvents benzene, 1, 4-dioxane , ethyl acetate, chloroform, dichloromethane, tetrahydrofuron and dimethylsulphoxide) (taken under UV light, from left to right. Concentration of **4** in all cases: 1x 10^{-5} M).

However, the TICT model was well accepted hypotheses (*vide supra*) (Figure 5.8) [34]. Such change in the emission property by changing the solvent polarity can be explained based on TICT model. This dual emission behaviour of **4** was appeared from

the locally excited (LE) and TICT states. The emission of TICT state at 459 nm (in benzene) is shifted to 485 nm (in DMSO) (Figure 5.7 a).

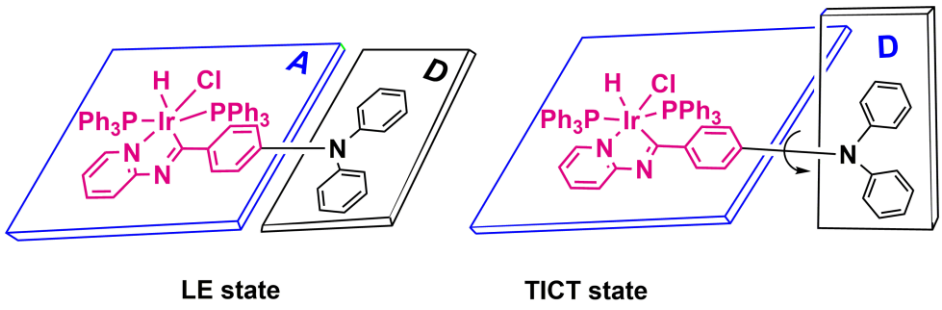

Figure 5.8 Schematic representation of the TICT state in polar solvents.

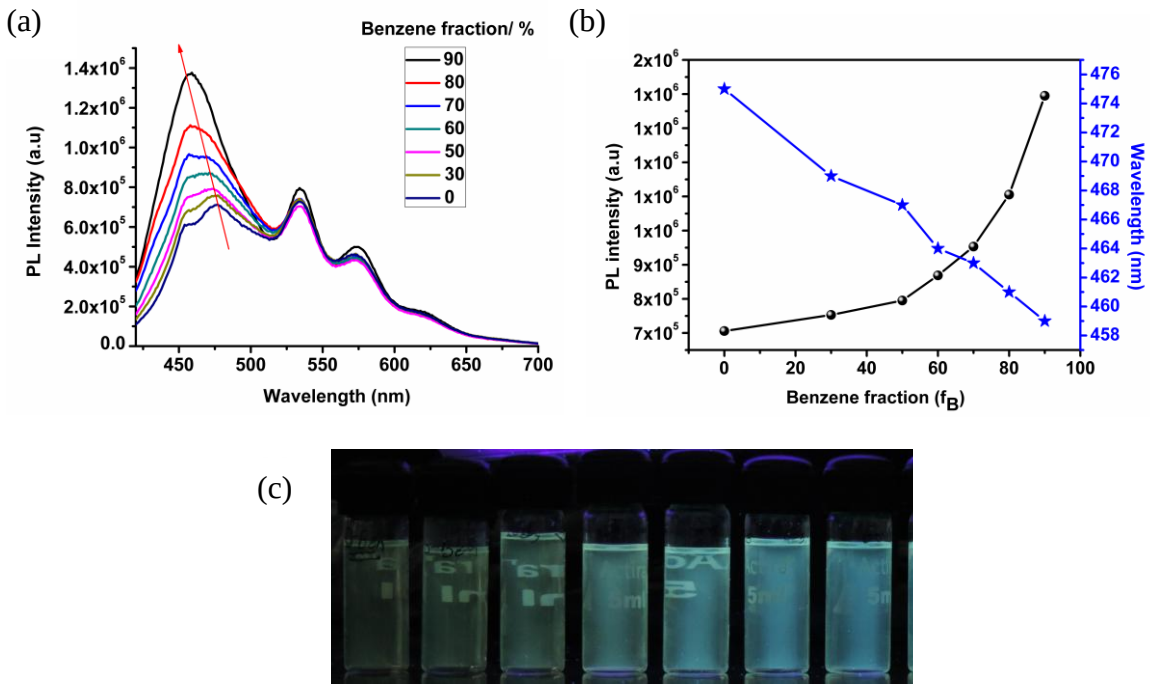

Figure 5.9 (a) Emission spectra of **4** in different THF/Benzene fraction (0-90%). (b) Plots of maximum emission intensity (I) and wavelength (λ_{max}) of **4** versus benzene fraction (f_B) in the THF/Benzene mixture. Solution concentration: $1x10^{-5}$ µM. (c) Photographs of **4** in THF/benzene mixtures with different fractions of benzene (f_B) taken under 365 nm UV illumination.

The coplanar conformation of **4** is retained in non polar medium, whereas the excited state molecules are stabilized by electronic conjugation and the LE state will be in equilibrium with the TICT state. However in polar medium, the coplanar conformation is transformed into the twisted conformation which results a total charge separation between the donor and acceptor units.

Thus, in the polar medium the equilibrium shifts to the TICT state which reduced the HOMO-LUMO energy gap resulted a bathochromic emission shift (485 nm, in DMSO) accompanied by reduced TICT intensity [35].

To investigate more about this TICT process, the emission spectra of **4** was recorded with different fraction (0-90%) of benzene (f_B) in THF. The gradual addition of benzene to the THF solution is resulted a blue shifted emission with increasing PL intensity. The spectral data revealed that with the addition of benzene increases the intensity of the original TICT peak which was less intense in THF solution (Figure 5.9).

The nature of the excited state is attributed to the effective TICT-LE transition [36]. Furthermore, the TICT was confirmed by temperature effect where the frozen sample of 4 in benzene (-80 ^{0}C) and 1,4- dioxane (-80 ^{0}C) showed yellow emission under excitation of 365 nm. The addition of TFA to the solution of **4** in different solvents resulted analmost a similar broad emission with peak maxima at~ 610 nm. The addition of TFA into the system blocks the lone pair of triphenyl amine and hampers TICT process because the system loses D-A property [37].

5.2.3 Aggregation Induced Emission

The synthesized complexes have been found to weakly emissive in common organic solvents such as, dicholorometane (DCM), tetrahydrofuron (THF), methanol, chloroform($CHCl_3$), acetonitrile (ACN), dimethylsulfoxide (DMSO) etc but highly emissive in solid state. The observation of strong solid state emission encouraged us to study the AIE property of these complexes. The aggregate formation of these complexes (**1-3**) is performed in various THF-water ratio. The complexes, **1-3** are highly soluble in THF but not soluble in water. The PL intensity is observed to be intensified after

increasing water fraction (f_w).

(a)

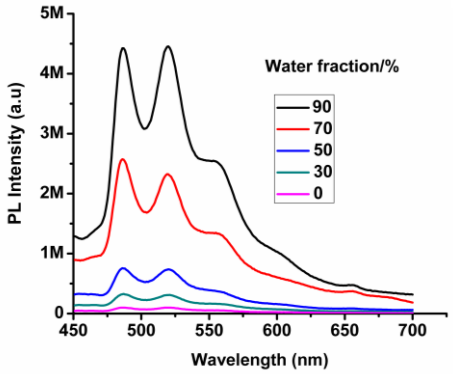

(b)

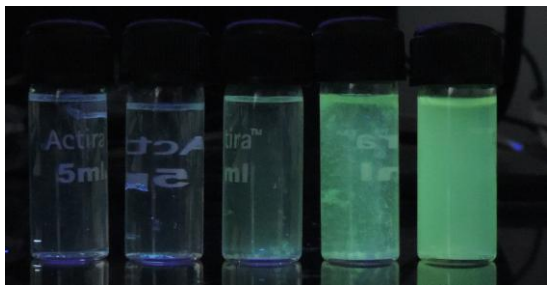

(c)

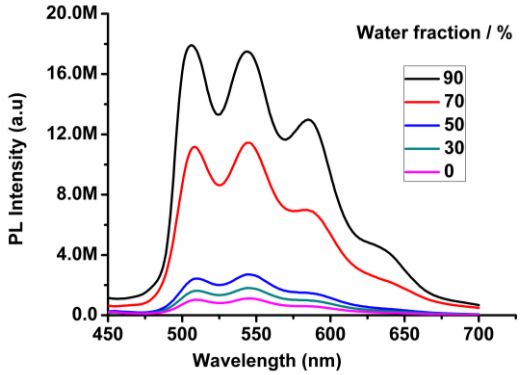

(d)

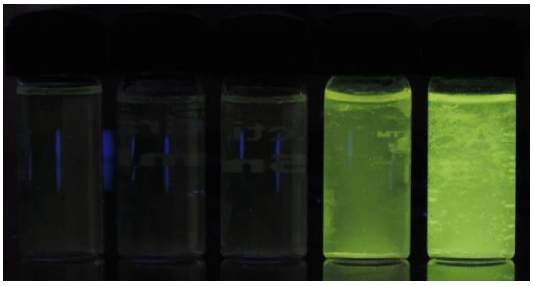

(e)

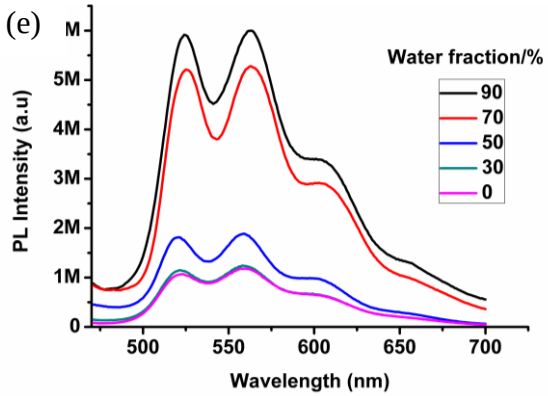

(f)

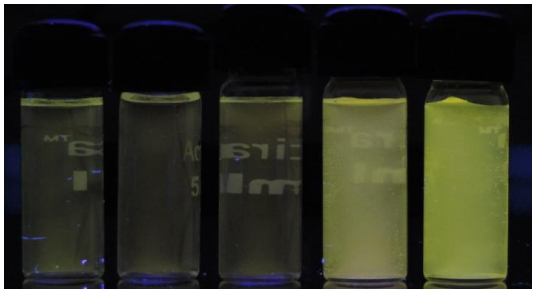

Figure 5.10 (a, c, and e) Emission spectra of **1-3** in THF/water mixtures (0-90%), Concentration: $1x10^{-5}$ M; respectively. (b, d and f) Photographs of **1-3** in THF/water taken under UV illumination (excitation wavelength: 365 nm), respectively.

The THF solution of **1-3** showed very weak emission intensity but with the gradual addition of different water fraction resulted the emission enhancement. The emission intensity of **1**, **2** and **3** was significantly increased at f_w=90% which was approximately, 45 times, 18 times and 5.5 times higher PL intensity as compared to its THF solution (Figure 5.10).

The gradual addition of water fraction in THF solution of **1-3** led to aggregate formation which may restricted intramolecular rotation (RIR) and enhanced the PL intensity and restricted intramolecular rotation (RIR) results in emission enhancement.

The aggregate formation is further studies using a particle size analyzer which also supported the formation of nano aggregates and found diameters in the range of 124–674 nm (Figure 5.11).

The RIR was further confirmed by crystal packing of **2** which showed short interactions (C−H···π and C−H···Cl) in the range of 2.80-2.83 Å (Figure 5.12).
It was observed that the phenyl rings of triphenyl phosphine moiety were involved in these short contacts. Due to these short contacts, the molecular motion of the phenyl rings is restricted in the solid state and resulted the emission enhancement by blocking the non radiative channels. The above result supports the AIE nature of complex **1-3**. However, it is interesting to investigate, AIE property of **4** being a TICT probe molecule. The AIE property of **4** is studied in each of the different solvents THF, Acetonitrile and DMSO with gradual addition of non-solvent water.

The dilute solution of THF is emitting faint green emission which was found to be intensified and red shifted (535 nm to 578 nm) at f_w=10%. The addition of little more fraction of water, (f_w=20%), the emission maxima again red shifted (from 578 nm to 610 nm) and the emission intensity is increased at f_w=20%.

However, the additional water increment (up to 70%) is not showing any abrupt change in the emission maxima. This spectral change (red shifted emission) is attributed to the TICT effect because of increasing polarity of the solvent (Figure 5.13). Meanwhile, a sudden blue shifted emission (516 nm and 557 nm) enhancement is observed at f_w=80% which is again shifted (535 nm and 574 nm) to maximum PL

intensity at f_w= 90%.

The emission intensity of **4** at f_w = 90% is found to approximately 21.6 times higher than that in pure THF (Figure 5.13b). This emission enhancement at higher water content is resulted due to aggregate formation; additionally these closely spaced aggregates are responsible to create a less polar environment which imparts relatively more hydrophobic interaction and hence the blue shifted emission is observed.

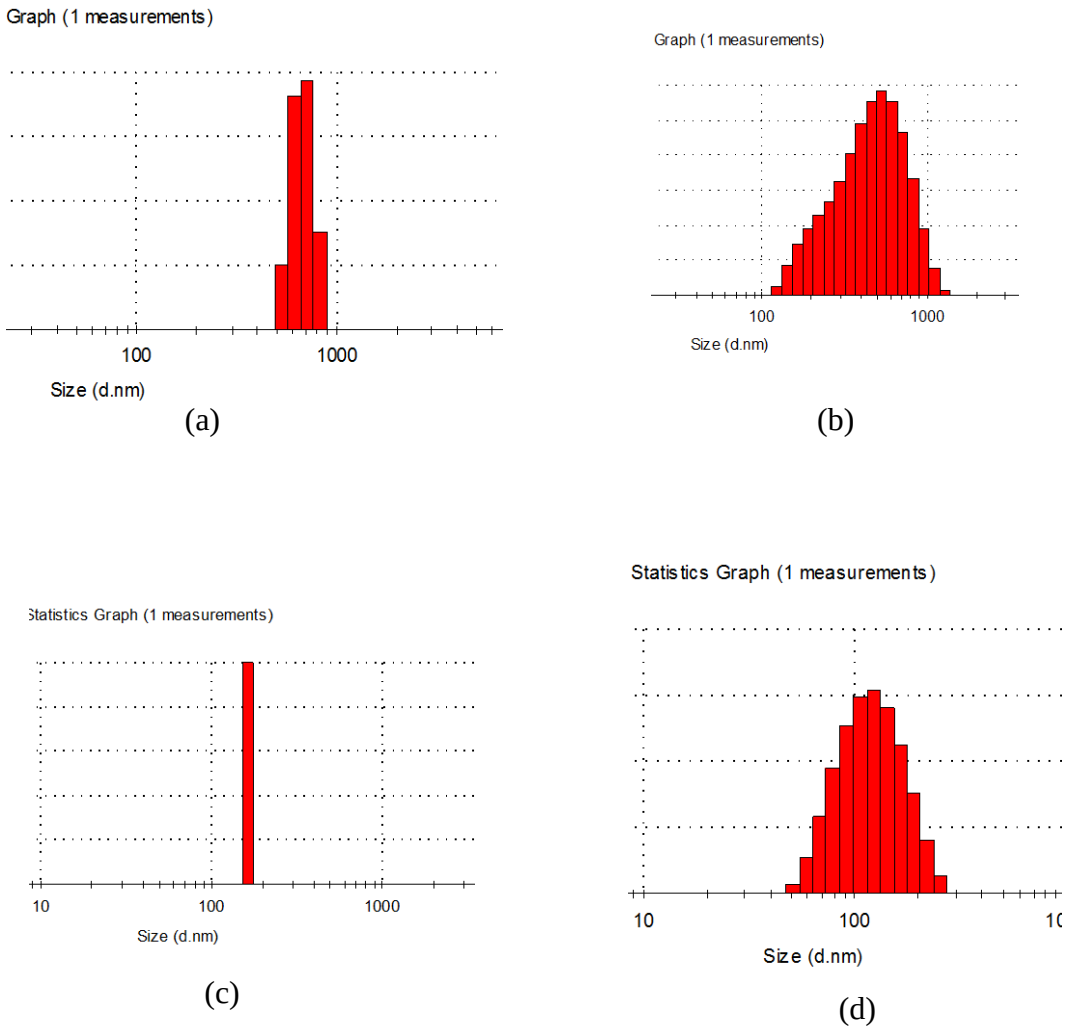

Figure 5.11 DLS measurements for (a) 1, (b) 2, (c) 3 and (d) 4.

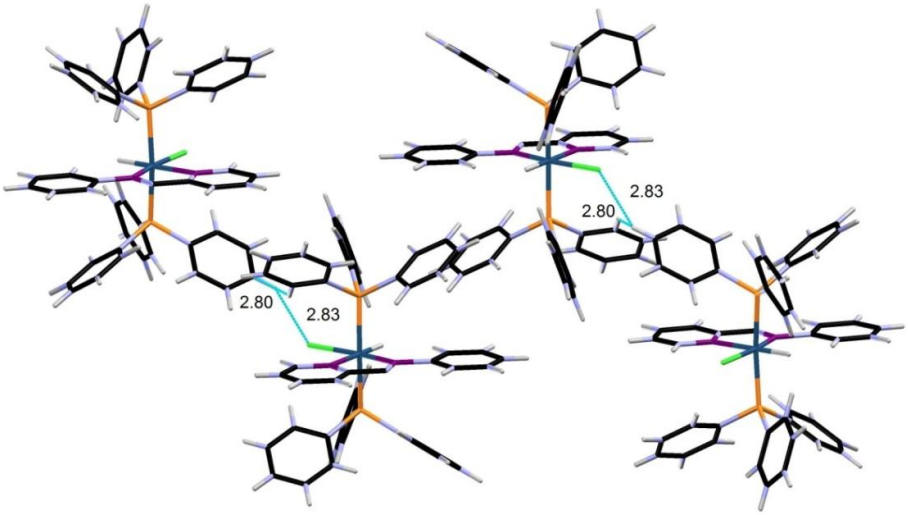

Figure 5.12 Packing diagram of complex **2**.

Furthermore, the emission behaviour of 4 was studied with different fraction of ACN- water mixture. The emission intensity of **4** is increased by 2 times at f_w= 30% in comparison to pure ACN with the emission maxima at 510 nm. However, the PL intensity is increased by 4.6 times with respect to pure ACN solution of the complex at f_w=50% with red shifted emission maxima at 523 nm. The emission intensity further intensifies at f_w=70%, and increased to 5 times with respect to pure acetonitrile with maximum emission at 517 nm. At f_w =90%, the PL intensity weakened dramatically with 3 times PL intensity as compared to pure ACN solution (Figure 5.14).

This emission change could be attributed to ICT process which commonly observed in D-A molecules [38]. The emission spectra in DMSO- water mixture does not show any change in emission maxima but the PL intensity is intensified by 32 times as compared to pure DMSO solution of the complex (Figure 5.15).

A comparison between RIR and TICT at higher water fraction revealed that the RIR is playing a dominating effect at higher fraction of water. At higher water fraction, the formation of TICT state is probably inhibited by RIR process or in other word RIR is dominated the TICT effect.

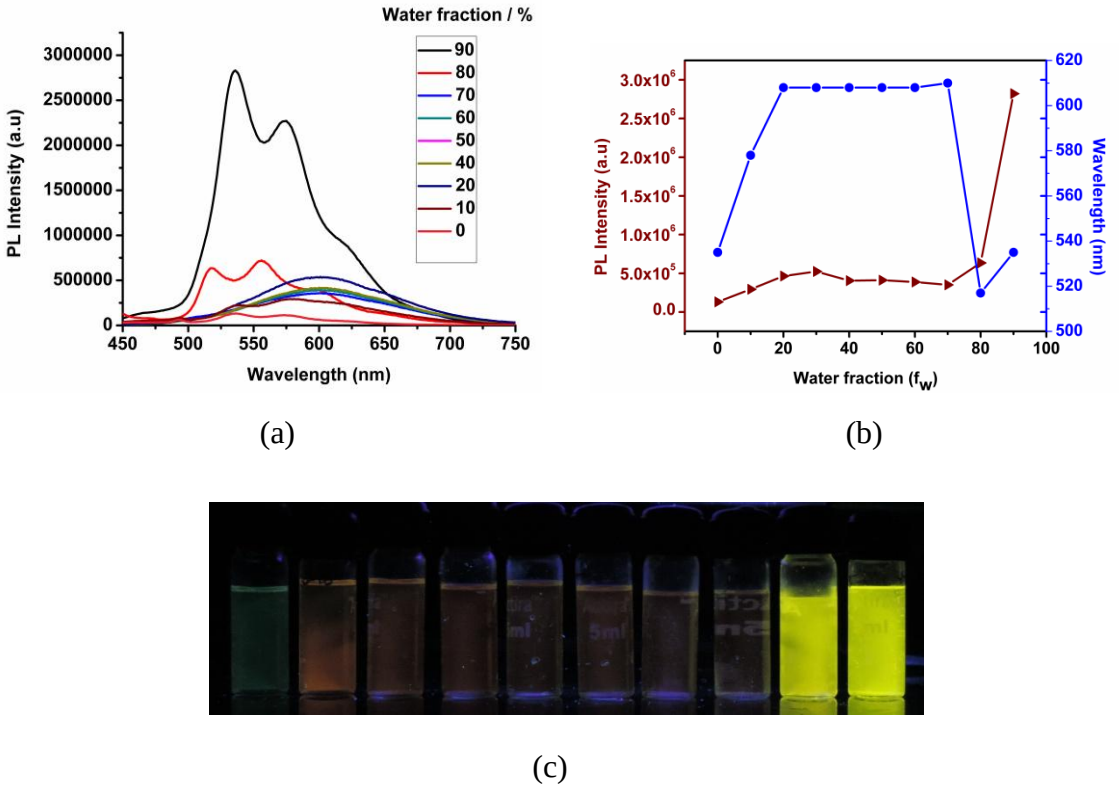

(a) (b)

(c)

Figure 5.13 (a) Emission spectra of **4** in a THF/ water mixture (0-90%). (b) Plot of maximum emission intensity (I) and wavelength (λ_{max}) of **4** versus water fraction. Concentration of **4**: $1x10^{-5}$ M. (c) Photographs of **4** in THF / water mixtures taken under UV illumination.

The remarkable AIE property of these complexes is further supported by the absolute quantum yield of solid state as compare to their relative solution state quantum yield (in DCM). The solution state quantum yield of these complexes are found in the range 0.01-0.07 % while the absolute solid state quantum yield is achieved in the range of 3.01-8.66 % which are about more than 100 times higher. It supports the remarkable AIE property of the complexes.

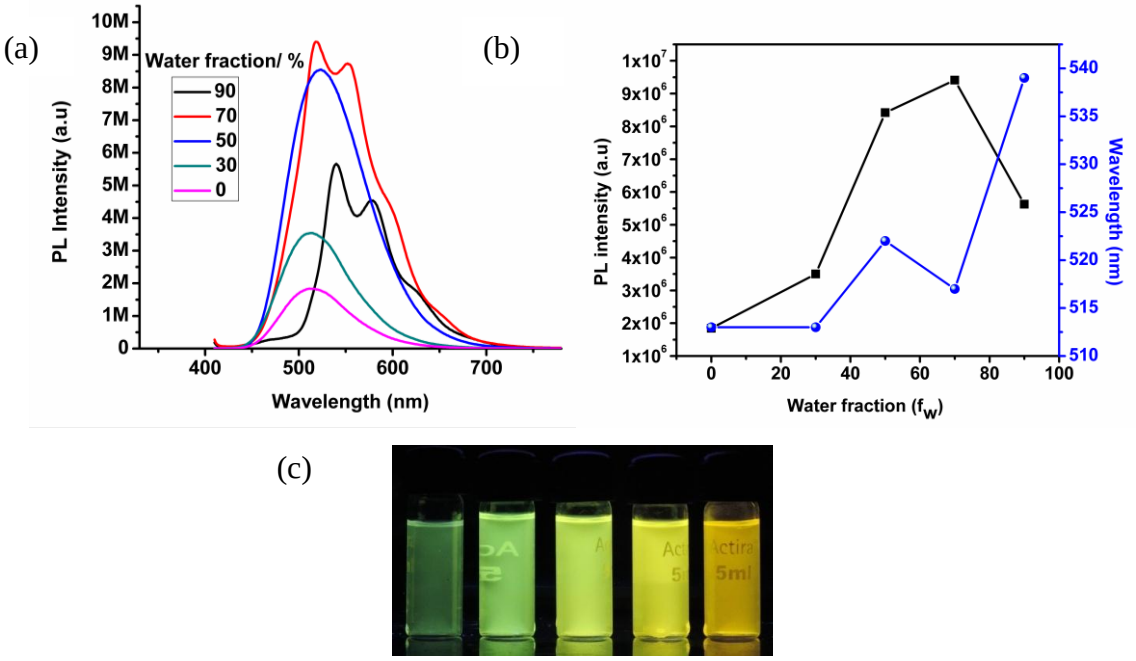

Figure 5.14 (a) Emission spectra of **4** in an Acetonitrile/ water mixture (0-90%); (b) plot of maximum emission intensity (I) and wavelength (λ_{max}) of **4** versus water fraction, concentration of **4**: $1x10^{-5}$ M; (c) Photographs of **4** in Acetonitrile/ water mixtures taken under UV illumination.

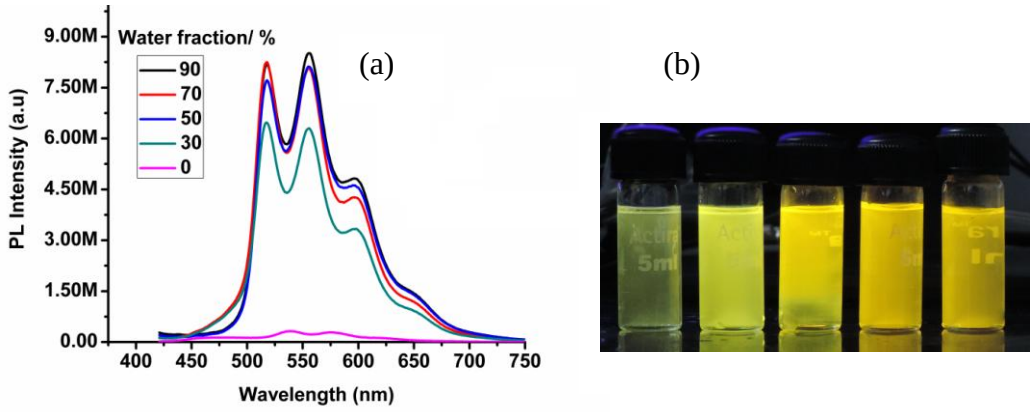

Figure 5.15 (a) Emission spectra of **4** in a DMSO/ water mixture (0-90%), Concentration of **4**: $1x10^{-5}$ M. (b) Photographs of **4** in DMSO/ water mixtures taken under UV illumination.

5.2.4 Reversible protonation- deprotonation

The photophysical studies of the complexes (**1-4**) have been performed in presence TFA/Et_3N. A green emission is observed on the thin film of **1**, showing a structured emission with maxima at 485 nm and 517 nm, as well as the thin film emission of **2** is exhibiting structured yellowish- green emission with maxima at 509 nm and 546 nm.

A similar types of structured emission was recorded for **3** with emission maxima at 521 nm and 560 nm with yellow emission while the thin film of **4** was exhibited a deep yellow emission with maxima at 542 nm and 571 nm.

The thin film emission maxima of **1** and **4** are resulted a proton- triggered bathochromic shift in the emission spectra. The exposure of TFA to thin film of **1** was resulted a yellow emission with broad maxima at 539 nm which was highly reversible and revert to its original green emission with maxima at 484 nm and 517 nm after exposure to Et_3N (Figure 5.16).

However, the yellow emitting thin film of **4** is converted to red emissive complex with maxima at 517 nm and after Et_3N exposure leads to return to its original yellow emission. While the thin films of **2** and **3** are exhibited a bathochromicshift after TFA exposure (Figure 5.16).

The reversibility of these complexes was studied by ^1H NMR spectra and obtained results support their reversible nature. The ^1HNMR spectra of protonated complexes (**1-4**) are recorded in $CDCl_3$, **1** shows a downfield ^1H NMR signal at δ= 10.01 ppm which is absent in the ^1H NMR of **1**. Similarly **2**, **3** and **4** are showing more downfield signal at δ = 13.56 ppm, 13.33 ppm and 12.99 ppm, respectively. These downfield ^1H signal may attribute to the protonation of the nitrogen atom in the imine ligand unit (Figure 5.17).

These ^1H NMR spectra unequivocally supports the transformation of these complexes into protonated form which is completely reversible in nature. Thus, the protonation can disrupt the electronic property of these complexes which results a abrupt change in photophysical behaviour. The above results are indicating that these materials

re potential candidate for H^+ detection.

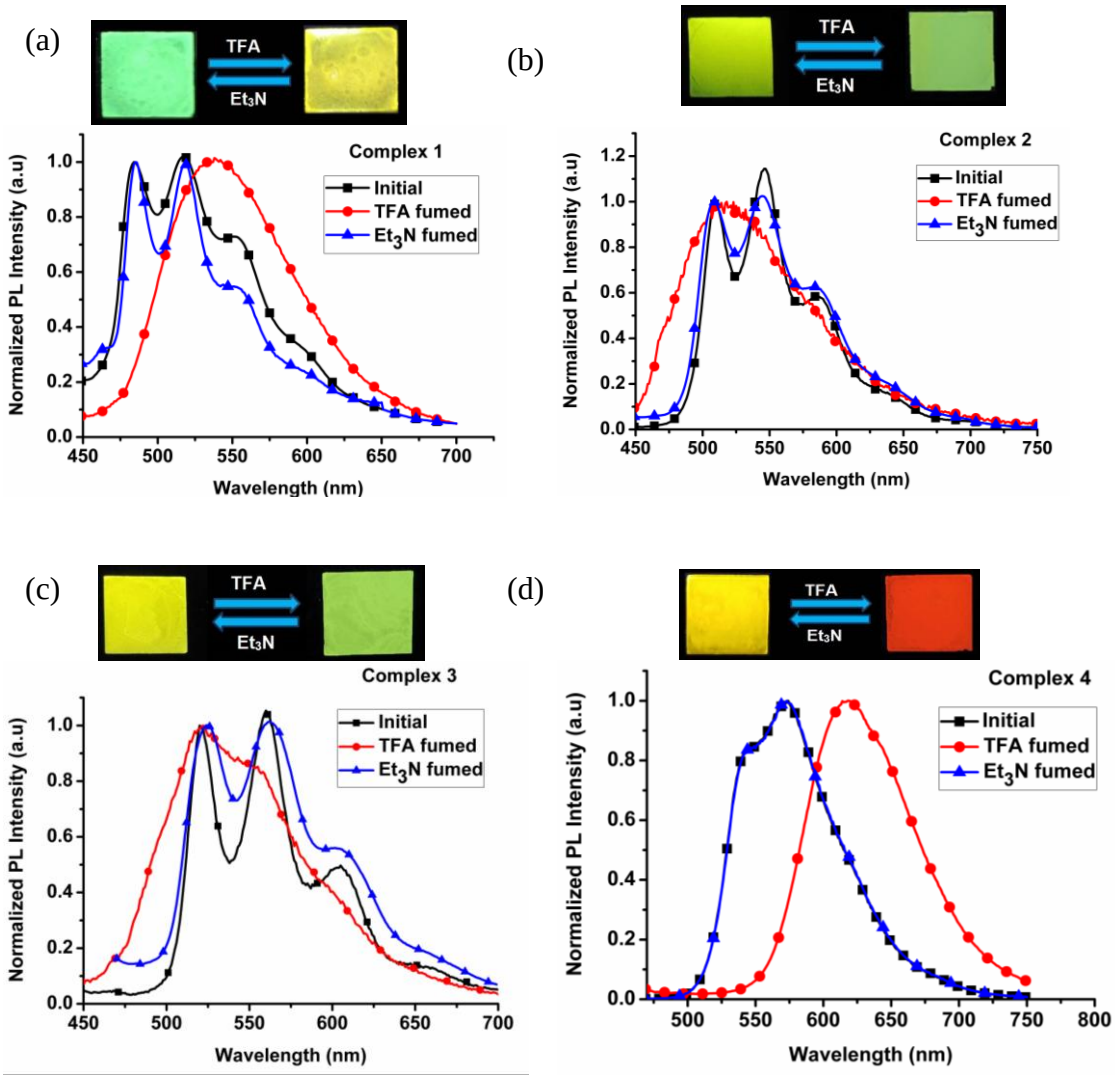

Figure 5.16 (a and c) Solid-state reversal of emission color from green to yellow (for **1**) and yellow to red (for **4**) (on exposure to TFA) and the vice-versa (on exposure to Et_3N) (the photograph was taken under excitation of 365nm); (b and d) Emission spectra showing the switching of maximum emission wavelength on exposure to TFA and Et_3N repeatedly, respectively.

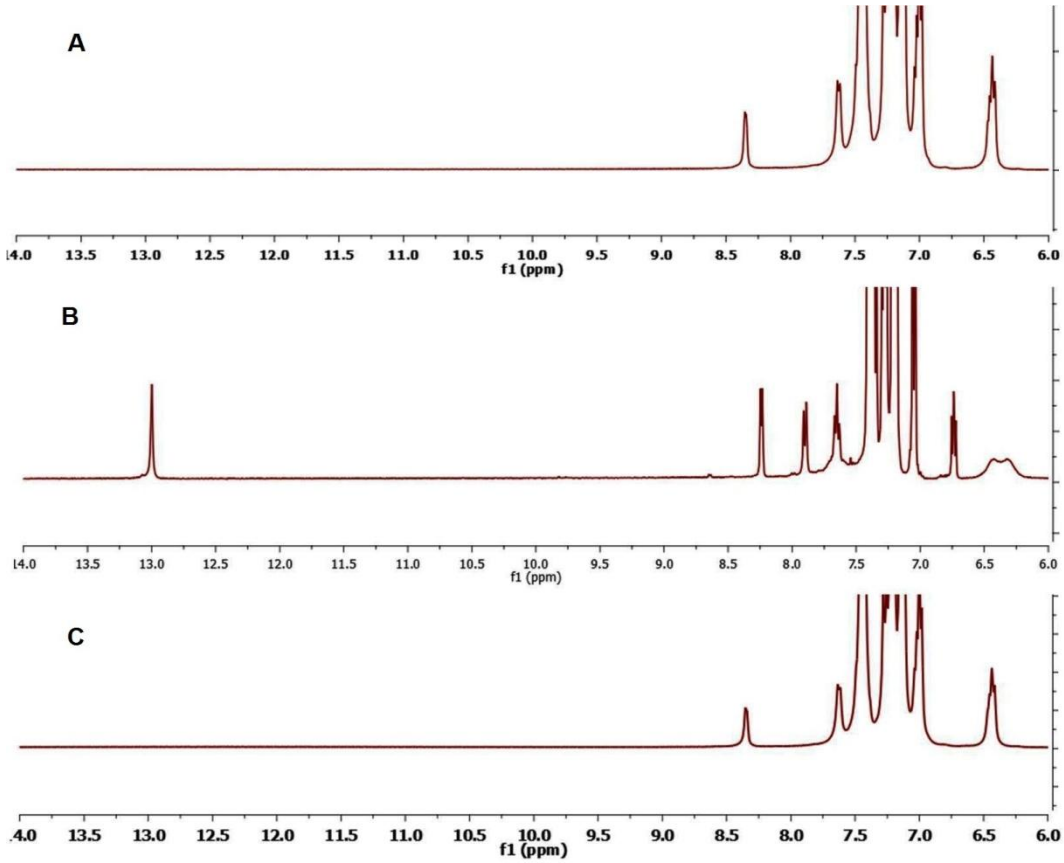

Figure 5.17 ^{1}H NMR spectra of **4** in $CDCl_3$ containing (A) 0 µL trifluoroacetic acid (TFA) and (B) 100 µL of TFA and (C) was obtained by adding 250 µL of triethylamine (Et_3N) into (B).

5.2.5 CO_2 detection

The reaction between diethyl amine, **4** and CO_2 yields a viscous carbamate ionic liquid (CIL) [39-41]. The increased viscosity will restrict the intramolecular rotation of the rotaring units. The solubility of **4** is screened with different amines e.g., pyridine,

1,8-diazabi-cyclo-[5,4,0]-undec-7-ene (DBU), piperidine and diethyl amine (DEA). The complex **4** was found completely soluble in DEA. A CIL was synthesized by a simple reaction condition where the DEA solution was purged by a large excess of CO_2 gas for 10 minutes. The synthesized CIL is characterized by ^{1}H NMR and ^{13}C NMR spectroscopy and results are well matched with the earlier reports [22].

The non emissive solution of **4** in DEA got intensified after purging of CO_2 bubbles. A linear relationship is obtained after gradual addition of CIL into the solution of **4** in DEA which makes it easy to monitor the amount of CO_2 in a quantitative manner. At f_{CIL} = 90%, the PL intensity is increased by 2.4 times as compare to its DEA solution (Figure 5.18). From the above results, it is obvious that the PL intensity is got intensified by the presence of CO_2. This emission change may be attributed to the increasing viscosity of the medium. The increasing CIL content is increasing the viscosity of the medium where the triphenyl rotor of triphenyl phosphine is getting restricted. The restriction of this phenyl ring in the viscous medium blocks the nonradiative channels followed by emission enhancement. Further, to see the response of CO_2, the different fraction of CO_2 is purged through solution of **4** into DEA at a fixed rate and time.

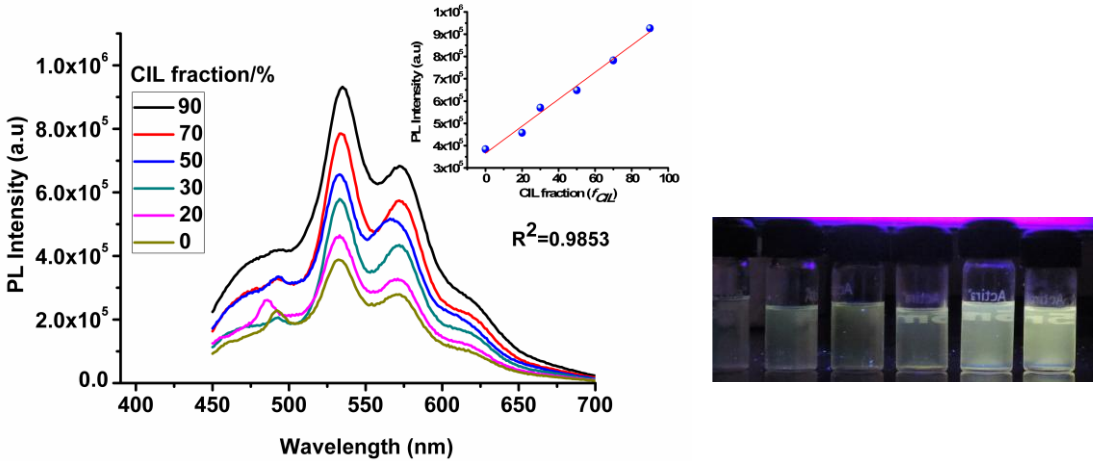

(a) (b)

Figure 5.18 (a) Emission spectra of **4** in DPA with different fraction of CIL (0-90%) (b) Photographs of **4** in DPA/ CIL mixtures taken under UV illumination.

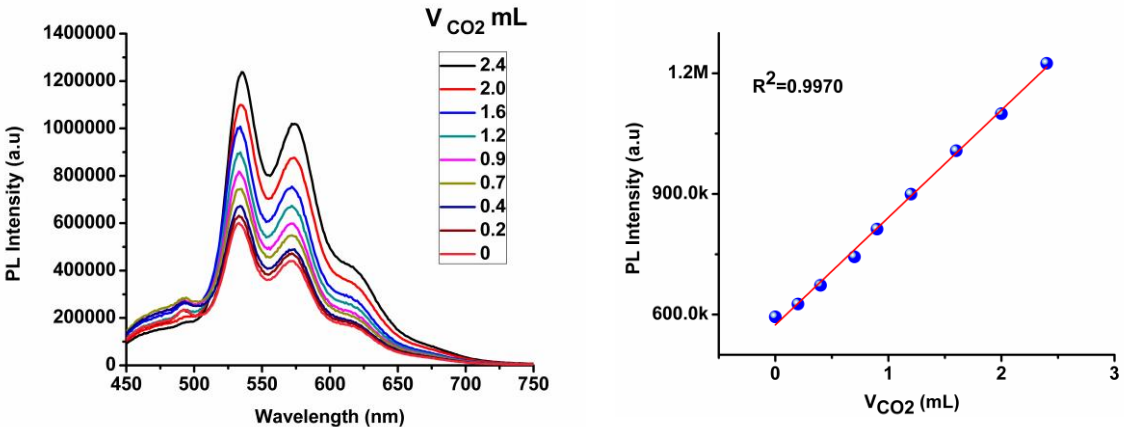

(a) (b)

Figure 5.19 (a) The PL spectra of **4** in DPA with different volumes of CO_2 showing the gradual PL intensity enhancement (b) The increasing volume of CO_2 the maximum PL intensity of the **4** was showing a linearity with (R^2 = 0.9970).

The emission of **4** is enhanced by gradual addition of CO_2 in the system which results a linear plot with the whole concentration range. This linear plot is indicating the easy way to quantify of CO_2 absorption (Figure 5.19).

5.3 Conclusions

In summary, we have demonstrated a very convenient reaction route for the syntheses of new series of 'aggregation induced emission (AIE)' active iridium(III) schiff base complexes with a facile color tuning. The presence of D-A unit in 4 exhibited a positive solvetochromic property with a facile color tuning from blue to yellow by varying the solvent polarity (benzene to DMSO). Additionally, 4 was found as a TICT probe molecule whose TICT emission was gradually increased with increasing content of nonpolar solvent (benzene) into the polar media (THF). We have developed an easy

method to detect the CO_2 gas using fluorescence technique. Finally, the thin films of these complexes have, successfully been employed for a reversible detection acidic and basic vapours. These properties was made them a multi-responsive luminescent materials.

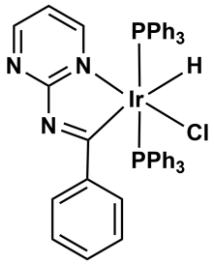

^{1}H NMR (400 MHz, $CDCl_3$) δ 8.61 – 8.27 (m, 1H), 7.84 (d, *J* = 7.6 Hz, 1H), 7.44 (dt, *J* = 10.9, 5.4 Hz, 4H), 7.12 (dt, *J* = 26.6, 7.2 Hz, 6H), 6.97 (t, *J* = 7.2 Hz, 1H), 6.72 (t, *J* = 7.4 Hz, 1H), 6.46 – 6.26 (m, 1H), -14.47 (t, *J* = 16.0 Hz, 1H); ^{31}P NMR (162 MHz, $CDCl_3$) δ 5.69; ^{13}C NMR (101 MHz, $CDCl_3$) δ 176.13, 158.13, 158.13, 155.44, 144.27, 134.09, 134.04, 133.99, 130.95, 130.68, 130.40, 130.09, 129.59, 128.68, 128.57, 128.45, 127.54, 127.49, 127.44, 126.11, 113.19; IR (KBr, cm^{-1}): 2151 (m, ν_{Ir-H}) and 1580 and 1542 (m, $\nu_{C=N}$); ESI-HRMS, calculated: ($[M+H]^+$), m/z 936.4581, found ($[M+H]^+$): m/z 936.2476 (**1**).

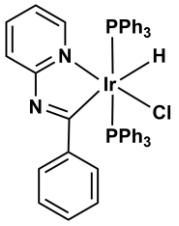

^{1}H NMR (400 MHz, $CDCl_3$) δ 8.18 (d, *J* = 5.5 Hz, 1H), 7.51(dd, *J* = 19.6, 7.7 Hz, 4H), 7.37 (ddd, *J* = 8.2, 6.7, 3.3 Hz, 12H), 7.06 (tt, *J* = 8.1, 4.1 Hz, 18H), 6.89 (t, *J* = 7.3 Hz, 2H), 6.66 (dd, *J* = 17.8, 9.8 Hz, 2H), 6.52 – 6.22 (m, 1H), - 14.49 (t, *J* = 16.1 Hz, 1H); ^{31}P NMR (162 MHz, $CDCl_3$) δ 4.34; ^{13}C NMR (101 MHz, $CDCl_3$) δ 171.22, 147.18, 145.22, 137.16, 134.15, 134.10, 134.04, 131.51, 131.24, 130.97, 129.34, 128.89, 127.37, 127.32, 127.28, 126.21, 117.81, 117.58; IR (KBr, cm^{-1}): 2128 (m, ν_{Ir-H}), 1603 (m, $\nu_{C=N}$); ESI-HRMS, calculated: ($[M+H]^+$), m/z 935.2063, found ($[M+H]^+$): m/z 935.3567 (**2**).

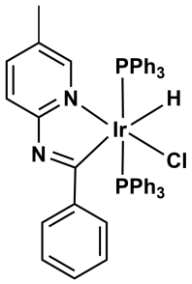

^{1}H NMR (400 MHz, $CDCl_3$) δ 7.81 (s, 1H), 7.54 (d, *J* = 7.5 Hz, 2H), 7.48 – 7.36 (m, 12H), 7.21 – 7.1 (m, 7H), 7.12 – 7.04 (m, 11H), 6.98 – 6.88 (m, 1H), 6.73 (dd, *J* = 8.2, 7.4 Hz, 2H), 1.89 (s, 3H), -14.48 (t, *J* = 15.8 Hz, 1H); ^{31}P NMR (162 MHz, $CDCl_3$) δ 5.69; ^{13}C NMR (101 MHz, $CDCl_3$) δ 169.12, 146.62, 145.41, 137.79, 134.14, 134.09, 134.03, 131.45, 131.18, 130.92, 129.22, 128.65, 127.28, 127.23, 127.18, 126.20, 117.41, 18.40.

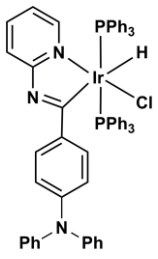

^{1}H NMR (400 MHz, $CDCl_3$) δ 8.34 (d, *J* = 4.9 Hz, 1H), 7.62 (d, *J* = 8.2 Hz, 2H), 7.51 – 7.35 (m, 14H), 7.33 – 7.07 (m, 22H), 7.01 (dd, *J* = 15.9, 7.7 Hz, 6H), 6.44 (dd, *J* = 15.3, 7.6 Hz, 3H), -14.43 (t, *J* = 16.2 Hz, 1H); ^{31}P NMR (162 MHz, $CDCl_3$) δ 4.53; ^{13}C NMR (101 MHz, $CDCl_3$) δ 171.39, 148.62, 147.48, 147.27, 139.47, 137.14, 134.31, 134.25, 134.20, 131.59, 131.32, 131.05, 129.36, 128.96, 127.40, 127.35, 127.30, 124.20, 122.69, 121.40, 117.49, 117.12; IR (KBr, cm^{-1}): 2176 (m, ν_{Ir-H}), 1580 (m, $\nu_{C=N}$); ESI-HRMS, calculated: ($[M+H]^+$), m/z 1102.2798, found ($[M+H]^+$): m/z 1102.2661.

DEA: ^{1}H NMR (400 MHz, $CDCl_3$) δ 2.53 (q, *J* = 7.2 Hz, 1H), 0.98 (t, *J* = 7.2 Hz, 2H). ^{13}C NMR (101 MHz, $CDCl_3$) δ 44.36, 15.17.

DEA CO_2 (a CIL): ^{1}H NMR (400 MHz, $CDCl_3$) δ 3.16 (s, 1H), 2.69 (s, 2H), 1.10 (s, 3H), 0.98 (s, 1H). ^{13}C NMR (101 MHz, $CDCl_3$) δ 42.17, 40.63, 13.98, 12.67.

Complex 1 **+ TFA**: 1H NMR (400 MHz, CDCl3) δ 10.02 (s, 1H), 8.63 (d, J = 5.4 Hz, 5H), 8.26 (d, J = 5.5 Hz, 4H), 7.94 (dd, J = 8.3, 1.4 Hz, 2H), 7.79 – 7.48 (m, 13H), 7.38 (td, J = 6.9, 3.4 Hz, 43H), 7.32 – 7.22 (m, 27H), 7.18 (t, J = 7.4 Hz, 33H), 7.07 – 6.90 (m, 8H), 6.75 (s, 5H).

Complex 2 + TFA : ^{1}H NMR (400 MHz, $CDCl_3$) δ 13.56 (s, 1H), 8.12 (d, *J* = 5.5 Hz, 1H), 8.00 (d, *J* = 8.2 Hz, 1H), 7.76 – 7.66 (m, 1H), 7.46 – 7.32 (m, 16H), 7.23 (t, *J* = 7.4 Hz, 8H), 7.19 – 7.12 (m, 10H), 6.89 (dd, *J* = 8.3, 7.6 Hz, 2H), 6.78 (dd, *J* = 9.6, 3.4 Hz, 1H), -14.93 (t, *J* = 14.3 Hz, 1H).

Complex 3 + TFA : ^{1}H NMR (400 MHz, $CDCl_3$) δ 13.34 (s, 1H), 7.84 (d, *J* = 8.3 Hz, 1H), 7.71 (s, 1H), 7.47 (dd, *J* = 8.3, 1.5 Hz, 2H), 7.38 (dt, *J* = 11.1, 5.5 Hz, 14H), 7.23 (t, *J* = 7.3 Hz, 7H), 7.15 (t, *J* = 7.4 Hz, 12H), 6.89 (t, *J* = 7.9 Hz, 2H), 2.11(s, 3H) -14.95 (t, *J* = 14.0 Hz, 1H).

Complex 4 + TFA : ^{1}H NMR (400 MHz, $CDCl_3$) δ 13.00 (s, 1H), 8.24 (d, *J* = 5.4 Hz, 1H), 7.90 (d, *J* = 8.2 Hz, 1H), 7.65 (t, *J* = 7.4 Hz, 1H), 7.38 (ddd, *J* = 11.5, 8.5, 6.9 Hz, 2H), 7.31 – 7.24 (m, 15H), 7.20 (t, *J* = 7.4 Hz, 21H), 7.05 (d, *J* = 7.6 Hz, 4H), 6.79 – 6.68 (t, *J*=12.9 Hz,1H), 6.37 (d, *J* = 42.1 Hz, 2H), -15.04 (t, *J* = 14.6 Hz, 1H).

5.4 References

[1] Y. Chi, P.-T. Chou, Chem. Soc. Rev., 39 (2010) 638-655.

[2] E. Baranoff, J.-P. Collin, L. Flamigni, J.-P. Sauvage, Chem. Soc. Rev., 33 (2004) 147-155.

[3] C.-H. Yang, Y.-M. Cheng, Y. Chi, C.-J. Hsu, F.-C. Fang, K.-T. Wong, P.-T. Chou, C.-H. Chang, M.-H. Tsai, C.-C. Wu, Angew. Chemie. Ger. Edit, 119 (2007) 2470-2473.

[4] B.M.J.S. Paulose, D.K. Rayabarapu, J.P. Duan, C.H. Cheng, Adv. Mater., 16 (2004) 2003-2007.

[5] D.K. Rayabarapu, B.M.J.S. Paulose, J.P. Duan, C.H. Cheng, Adv. Mater., 17 (2005) 349-353.

[6] X. Yang, X. Xu, J. Zhao, J.-s. Dang, Z. Huang, X. Yan, G. Zhou, D. Wang, Inorg. Chem., 53 (2014) 12986-13000.

[7] F. Lorenzini, P. Marcazzan, B.O. Patrick, B.R. James, Can. J. Chemistry, 86 (2008) 253-260.

[8] Y. You, S.Y. Park, J. Am. Chem. Soc., 127 (2005) 12438-12439.

[9] C.-C. Ko, J.W.-K. Siu, A.W.-Y. Cheung, S.-M. Yiu, Organometallics, 30 (2011) 2701-2711.

[10] N.M. Ali, V.L. MacLeod, P. Jennison, I.V. Sazanovich, C.A. Hunter, J.A. Weinstein, M.D. Ward, Dalton Trans., 41 (2012) 2408-2419.

[11] Y. Li, N. Dandu, R. Liu, S. Kilina, W. Sun, Dalton Trans., 43 (2014) 1724-1735.

[12] A. Beeby, S. Bettington, I.D.W. Samuel, Z. Wang, J. Mater. Chem., 13 (2003) 80-83.

[13] M. Subat, K. Woinaroschy, C. Gerstl, B. Sarkar, W. Kaim, B. König, Inorg. Chem., 47 (2008) 4661-4668.

[14] L. Flamigni, B. Ventura, F. Barigelletti, E. Baranoff, J.-P. Collin, J.-P. Sauvage, Eur. J. Inorg. Chem., 2005 (2005) 1312-1318.

[15] J. Catalán, C. Díaz, V. López, P. Pérez, R.M. Claramunt, Eur. J. Org. Chem., 1998 (1998) 1697-1704.

[16] W. Rettig, J. Phys. Chem., 86 (1982) 1970-1976.

[17] M. Vedamalai, D. Kedaria, R. Vasita, S. Mori, I. Gupta, Dalton Trans., (2016).

[18] B. Chen, X. Sun, X. Li, H. Ågren, Y. Xie, Sens. Actuators, B, 199 (2014) 93-100.

[19] Z. Xie, C. Chen, S. Xu, J. Li, Y. Zhang, S. Liu, J. Xu, Z. Chi, Angew. Chem., Int. Ed., 54 (2015) 7181-7184.

[20] B.-R. Gao, H.-Y. Wang, Y.-W. Hao, L.-M. Fu, H.-H. Fang, Y. Jiang, L. Wang, Q.-D. Chen, H. Xia, L.-Y. Pan, Y.-G. Ma, H.-B. Sun, J. Phys. Chem. B, 114 (2010) 128-134.

[21] P. Mazumdar, D. Das, G.P. Sahoo, G. Salgado-Moran, A. Misra, Phys. Chem. Chem. Phys., 17 (2015) 3343-3354.

[22] Y. Liu, Y. Tang, N.N. Barashkov, I.S. Irgibaeva, J.W.Y. Lam, R. Hu, D. Birimzhanova, Y. Yu, B.Z. Tang, J. Am. Chem. Soc., 132 (2010) 13951-13953.

[23] Y. Ma, Y. Zeng, H. Liang, C.-L. Ho, Q. Zhao, W. Huang, W.-Y. Wong, J. Mater. Chem. C, 3 (2015) 11850-11856.

[24] Y. Ma, H. Xu, Y. Zeng, C.-L. Ho, C.-H. Chui, Q. Zhao, W. Huang, W.-Y. Wong, J. Mater. Chem. C, 3 (2015) 66-72.

[25] T. Tian, X. Chen, H. Li, Y. Wang, L. Guo, L. Jiang, Analyst, 138 (2013) 991-994.

[26] R.N. Dansby-Sparks, J. Jin, S.J. Mechery, U. Sampathkumaran, T.W. Owen, B.D. Yu, K. Goswami, K. Hong, J. Grant, Z.-L. Xue, Anal. Chem., 82 (2010) 593-600.

[27] S. Neethirajan, D.S. Jayas, S. Sadistap, Food Bioprocess Tech., 2 (2008) 115-121.

[28] D.G. Khandare, H. Joshi, M. Banerjee, M.S. Majik, A. Chatterjee, Anal. Chem., 87 (2015) 10871-10877.

[29] A. Star, T.R. Han, V. Joshi, J.C.P. Gabriel, G. Grüner, Adv. Mater., 16 (2004) 2049-2052.

[30] T.M. Gilbert, R.G. Bergman, J. Am. Chem. Soc., 107 (1985) 3502-3507.

[31] L. Marin, B. Simionescu, M. Barboiu, Chem. Commun., 48 (2012) 8778-8780.

[32] D. Maggioni, M. Galli, L. D'Alfonso, D. Inverso, M.V. Dozzi, L. Sironi, M. Iannacone, M. Collini, P. Ferruti, E. Ranucci, G. D'Alfonso, Inorg. Chem., 54 (2015) 544-553.

[33] V. Guerchais, J.-L. Fillaut, Coord. Chem. Rev., 255 (2011) 2448-2457.

[34] M. Schmittel, H. Lin, Inorg. Chem., 46 (2007) 9139-9145.

[35] X.Y. Shen, W.Z. Yuan, Y. Liu, Q. Zhao, P. Lu, Y. Ma, I.D. Williams, A. Qin, J.Z. Sun, B.Z. Tang, J. Phys. Chem. C, 116 (2012) 10541-10547.

[36] E. Wang, J.W.Y. Lam, R. Hu, C. Zhang, Y.S. Zhao, B.Z. Tang, J. Mater. Chem. C, 2 (2014) 1801-1807.

[37] Y. Qian, M. Cai, X. Zhou, Z. Gao, X. Wang, Y. Zhao, X. Yan, W. Wei, L. Xie, W. Huang, J. Phys. Chem. C, 116 (2012) 12187-12195.

[38] J. Liang, Z. Chen, L. Xu, J. Wang, J. Yin, G.-A. Yu, Z.-N. Chen, S.H. Liu, J. Mater. Chem. C, 2 (2014) 2243-2250.

[39] P.G. Jessop, D.J. Heldebrant, X. Li, C.A. Eckert, C.L. Liotta, Nature, 436 (2005) 1102-1102.

[40] P.G. Jessop, L. Phan, A. Carrier, S. Robinson, C.J. Durr, J.R. Harjani, Green Chem., 12 (2010) 809-814.

[41] Z. Guo, Y. Feng, Y. Wang, J. Wang, Y. Wu, Y. Zhang, Chem. Commun., 47 (2011) 9348-9350.

Chapter VI

Syntheses of Bis cyclometalated Iridium(III) Complexes with Diphosphines: Sensitive and Selective Detection of Mercury(II)

6.1 Introduction

Last decades, the syntheses of different class of homoleptic and heteroleptic cyclometallated iridium(III) complexes have received a considerable attention because of their numerous and extraordinary properties e.g., room temperature phosphorescence, high quantum yield and fine tuning etc (Figure 6.1.1) [1-5].

Till date many cationic and anionic iridium(III) complexes were synthesized with two units of cyclometalated ligands (2-phenyl pyridine, 2-(2,4-difluorophenyl)pyridine etc) and one unit of diamine ligand (e.g., bipyridine, phenanthroline, 2,2'-bipyrimidine etc) [6, 7]. The fine tuning of the emission color can be easily achieved by changing the chromophoric ligands (**1**-**6**), putting electron withdrawing or electron donating groups at appropriate places because the electron-withdrawing substituents such as F or CF_3 in the metallated aryl ring, which lowers the HOMO and the electron donating groups Me, or ^{t}Bu in the metallated pyridine ring, which raise the LUMO (Figure 6.1.1) [8].

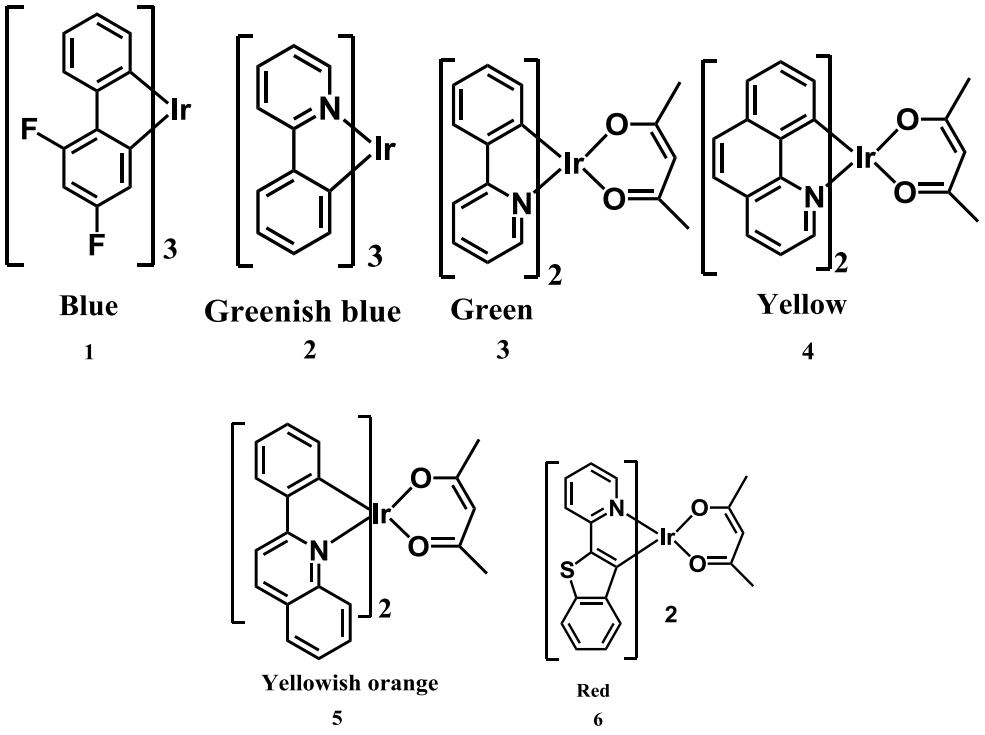

Figure 6.1.1 Structures of iridium(III) complexes were used for fine tuning.

In contrast to homoleptic complexes that usually give mixtures of *fac*- and *mer*-isomers which are tedious to separate out, heteroleptic complexes with a particular ancillary ligand always produce only one isomer. Furthermore, heteroleptic complexes introduce the possibility of facile and versatile derivatizations, so that easy color tuning is possible while the ancillary ligand hardly interferes in the phosphorescent color. For the realization of efficient full color RGB display systems, it is essential to obtain high efficiency and color purity for three primary blue, green and red emitting materials. While there have been many reports of efficient pure green and red light-emitting complexes, the search for true blue emitters is more difficult (**7**) (Figure 6.1.2) [9-11].

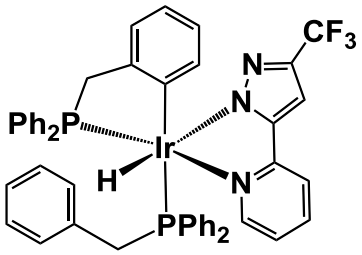

7

Figure 6.1.2 Structure of Blue emitting iridium(III) complexes.

Mercury is one of the lethal weapons for human health as well as for environment even at very low concentrations [12, 13]. Therefore, the development of different types of sensing systems for monitoring the presence of mercury in environmental samples is drawing a prime attention to the scientific community in recent years. In this context, strong emitting cyclometalated complexes of iridium(III) would be attractive candidates for sensing purposes.

In a recent literature survey, several reports [14-24] were found where the detection of mercury ions was carried out taking advantage of the photophysical properties of emissive cyclometalated iridium(III) complexes. The detection limit of mercury ions using these types of complexes can be further improved if the system used as probe molecules showing 'aggregation induced emission (AIE)' activity.

The incorporation of a strongly π-accepting PPh_2 unit in the coordination sphere of an iridium(III) complex, increases the HOMO-LUMO separation [25], opening the

way to the synthesis of new blue-emitting complexes. Furthermore, the strong bonding of a P-donor ligand to iridium(III) increases the energy of d-d* excitations on metal ion, minimizing their interference with the radiative transition from lower lying excited states. These two properties of P-donating ligands motivated the search of new blue-emitting iridium(III) complexes using $Ph_2P\text{^}PPh_2$ type ancillary ligands.

In this chapter, we present the design and syntheses of new cyclometalated iridium(III) complexes where phenyl-substituted diphosphines (as ancillary ligands) are co-ordinated as mono and chelate forms. The synthesized mono phosphine coordinated complexes were potentially utilized for selective sensing of Hg^{+2} metal ions. In addition, the excited state properties of these complexes were studied using DFT-based quantum chemical calculations.

6.1.1 Part A: Facile and Clean Microwave-Assisted Syntheses of Cyclometalated Iridium(III) Complexes

In this section, we describe the synthesis of three greenish-blue emitting complexes with three different P-coordinated chelating ligands (dppel, 1,2-Bis(diphenylphosphino)ethylene; dppp, 1,3-Bis(diphenylphosphino)propane; dppe, 1,2-Bis(diphenylphosphino)ethane) retaining the same chromophoric 2-phenylpyridine ligand in each case. We also studied their photophysical properties and modeled these complexes using quantum chemistry methods to get a deeper understanding of their excited state properties. In an initial phase, the new complexes were obtained adopting a traditional, lengthy two step process, analogous to that reported for other heteroleptic cyclometalated iridium(III) compounds [26]. Alternatively, the synthesis of these complexes has been performed using a newly developed microwave irradiation technique (MW) which reduces the time drastically as compared to the conventional route. In addition, this new efficient synthetic route has been shown to be extensible to other iridium(III) complexes with varying ancillary ligands such as, N^N, N^O, O^O type of bidentate chelating ligands and monodentate ligand opening the way to a facile route to obtain new luminescent materials for OLED applications.

6.1.1.1 Results and Discussion

The cyclometalated dinuclear iridium(III) precursor, **8,** and the phosphorous-coordinating mononuclear iridium(III) complexes, **9-11,** were synthesized through an established conventional route (Scheme 6.1.1). The iridium(III)chloride hydrate and phenylpyridine were mixed in 2-ethoxyethanol and refluxed for ~24h which resulted a dichloro bridged iridium(III) complex, **9**. Subsequently, the bridging dichlorides from complex **8** were replaced by the ancillary phosphorous coordinated chelating ligands (dppel, dppp, dppe) (Scheme 6.1.1) by refluxing the mixture for ~12h in presence of sodium carbonate. Then, the cationic cyclometalated iridium(III) complexes were formed. The counter monochloride ion in the cationic complex was exchanged with one equivalent hexafluoro phosphate in dichloromethane through microwave irradiation which resulted in the desired complexes, **9-11**. These complexes (**9-11**) were characterized by elemental analyses and (^{1}H, ^{13}C, ^{31}P) NMR spectra.

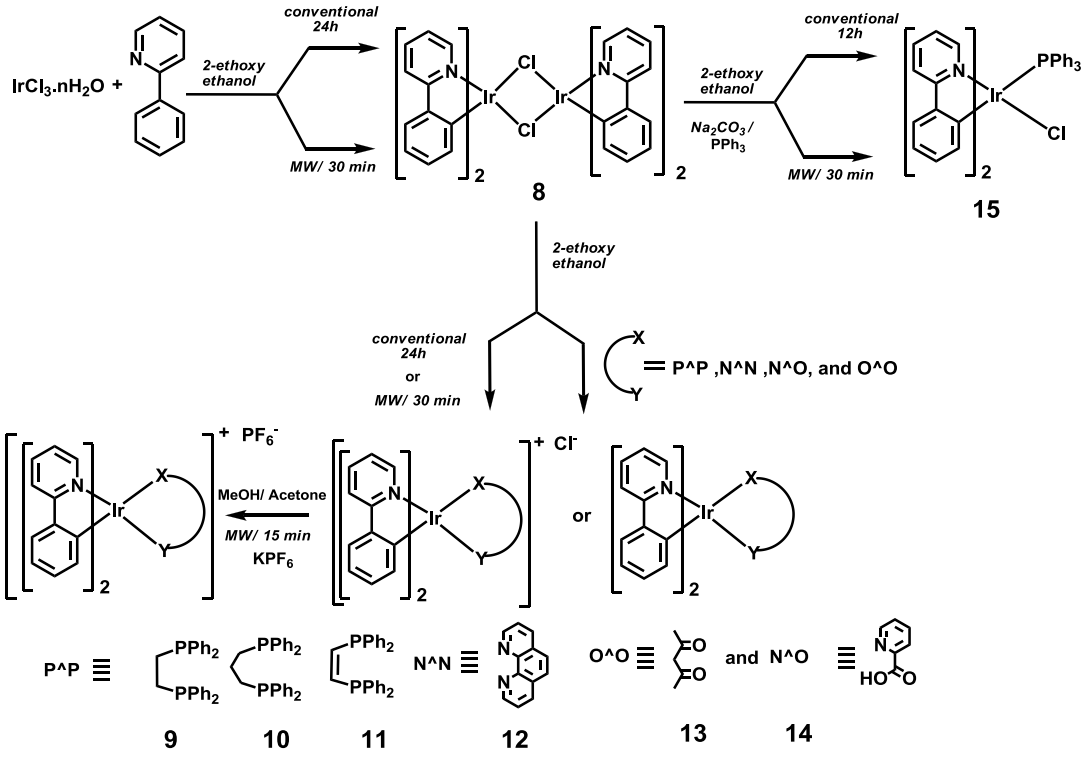

Scheme 6.1.1 Syntheses of iridium(III) complexes by Microwave technique.

6.1.1.2 X-ray crystal structure

The structure of $[Ir(ppy)_2(dppe)](PF_6)$, **9** was determined by X-ray single crystal structure analysis. The ORTEP diagram of **9** is presented in (Figure 6.1.3).

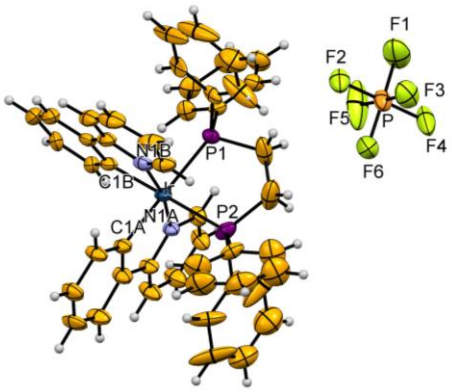

Figure 6.1.3 ORTEP diagram for complex **9** showing the octahedral geometry around iridium(III) (using 50% probability ellipsoid).

The molecule possesses a distorted octahedral geometry with a *cis*-C, C-*trans*-N,N configuration. The Ir-P bond distances found for **10** are somewhat larger than those reported for similar complexes of iridium(III) [27], an elongation that can be rationalized considering the strong *trans*-effect exerted by the 'C' positioning *trans* to the 'P' atom.

6.1.1.3 Photophysical Property

The solution UV-VIS and photoluminescence spectra (in DCM, 10^{-4}M) of these complexes have been measured. Their UV-VIS absorption spectra show intense bands appearing in the range, 270-340 nm (Figure 6.4a).

These bands can be assigned to spin-allowed $^1\pi$-π^* transitions, within the ligands. These ligand-centred bands are accompanied by weaker transitions at lower energies, extending to the visible region upto 400 nm. Based on previous reports on cyclometalated complexes of iridium(III), these can be assigned to intraligand $^3\pi$-π^* and spin-allowed ^{1}MLCT transitions. In addition, spectra of all these complexes exhibit weaker absorptions that extend upto 460 nm which can be assigned to ^{3}MLCT transitions. The band-edge of ^{3}MLCT transitions for these complexes has been observed

to be blue-shifted in comparison to what is found for the well-known acetylacetonate/picolinate analogues (Figure 6.1.4b). This observation can be explained from the coordination of strongly π-accepting phosphorous atoms to iridium(III) in **9-11** which result in an increase of the HOMO-LUMO separation in these compounds.

This behaviour in combination with the observed structured emission spectra supports the supposition that the nature of the lowest excitations consists basically of $^{3}\pi$-π^* transitions with a significant admixture of ^{3}MLCT transitions. This hypothesis is also supported through the quantum chemical modeling of these complexes as described below.

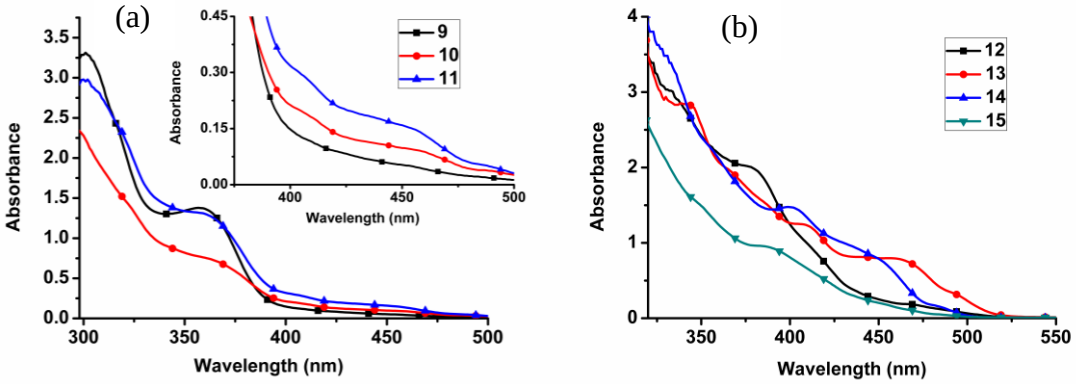

Figure 6.1.4 Solution absorbance spectra for the complexes (DCM, 10^{-4}M) showing the blue-shifted ^{3}MLCT band for the complexes, (a) **9-11 as** compared to (b) **14** and **15**.

This fact is also at the origin of the blue-shifted emission spectra of complexes **9-11** relative to their acetylacetonate/picolinate analogues (Figure 6.1.4b). Complexes **9-11** do not exhibit a solvatochromic effect (Figure 6.1.5).

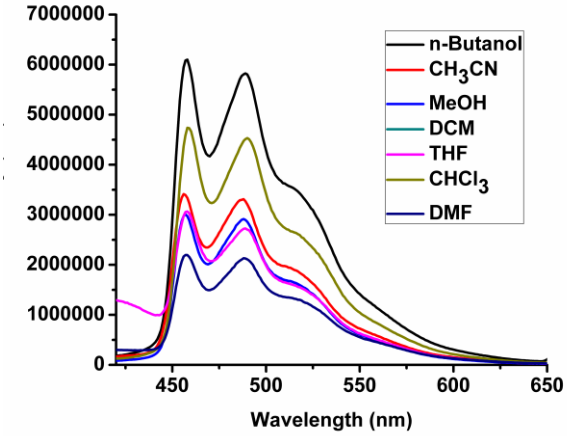

Figure 6.1.5 Emission spectra of **9** in presence of different solvents.

The conventional synthesis of mononuclear iridium(III) complexes (**9-11**) involves a lengthy route (32h-36h) (Table 6.1.1). In an alternative approach, these complexes were prepared using a microwave irradiation based technique (MW) that reduces the total reaction time drastically (Table 6.1.1).

Further, the syntheses of these complexes through the MW procedure were observed to be much cleaner with a similar yield in comparison to their respective compounds obtained *via* the conventional route. This new MW mediated synthetic technique has been extended to other iridium(III) complexes (Scheme 6.1.1). In these cases, the ancillary chelating ligands were varied to N^N, N^O and O^O types (Scheme 6.1.1 & Figure 6.1.6) and the observed total reaction time was also found to be drastically reduced in comparison with the syntheses *via* conventional routes (Table 6.1.1). The same complex, obtained following the two alternative routes, was characterized by NMR spectra (^{1}H, ^{31}P) (Figure 6.7).

The NMR peaks [^{1}H, ^{13}C and ^{31}P (in some cases)] for each pair of complexes (obtained through the conventional and MW routes) match well with each other, supporting the hypothesis that the same compound is being formed in the two alternative routes. The six-coordinated cyclometalated iridium(III) complex with monodenate triphenylphosphine as coordinating ligand was also synthesized *via* the conventional and MW routes (Scheme 6.1.1).

Figure 6.1.6 A wide range of emission color can be observed from iridium(III) complexes synthesized through the new microwave-based procedure.

The absorption and emission properties were recorded for the products synthesized following the two different routes (Figure 6.1.8). The same emission color and the spectral pattern obtained for both cases support the identity of the two compounds. The wide ranges of emission color that can be obtained for complexes synthesized *via* the MW shown in (Figure 6.1.9) nicely illustrate that this alternative synthetic procedure can be employed for a large variety of emitting materials for OLED applications in a cleaner and more efficient way.

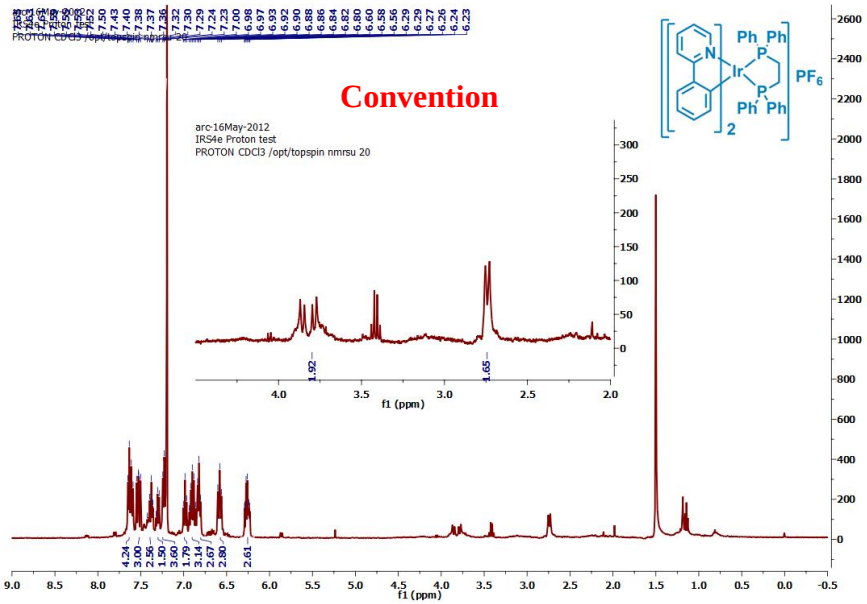

(a)

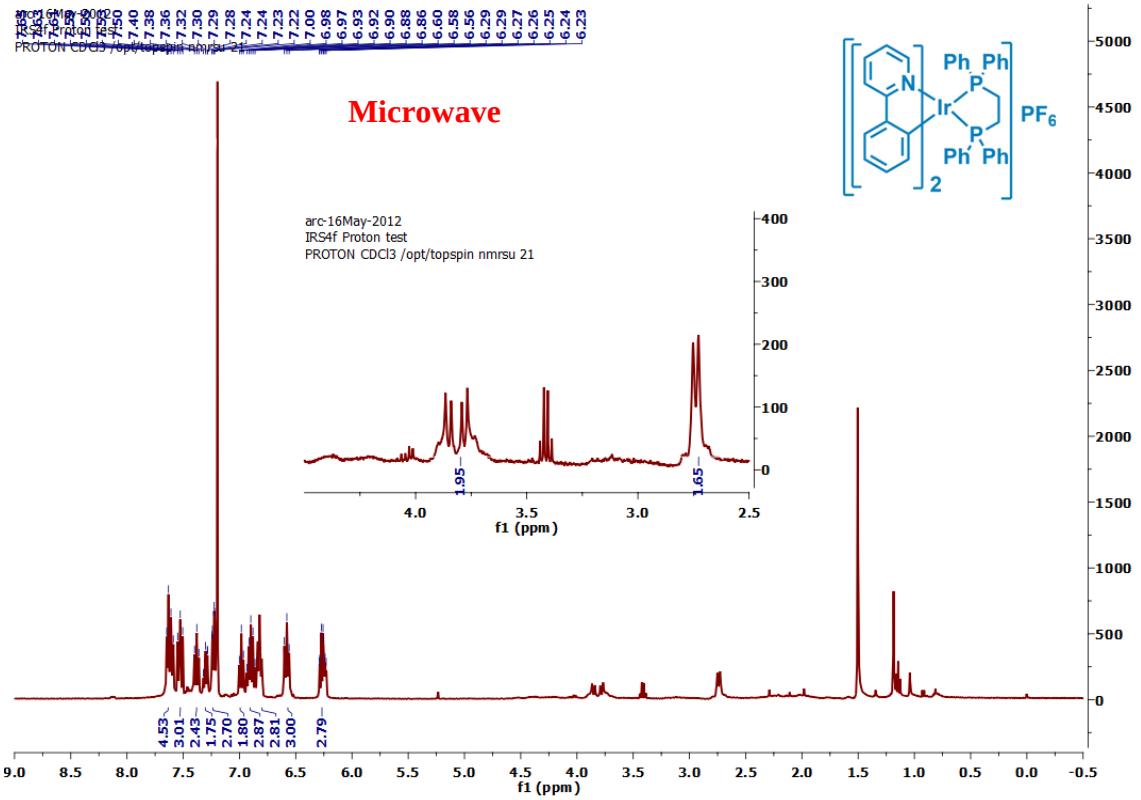
Microwave
arc-16May-2012
IRS4f Proton test
PROTON CDCl3 /opt/topspin nmrsu 21
f1 (ppm)
4.53
3.01
2.43
1.75
2.70
1.80
2.87
2.81
3.00
2.79
1.95
1.65
Ph Ph
P
Ir
N
PF6
2

(b)

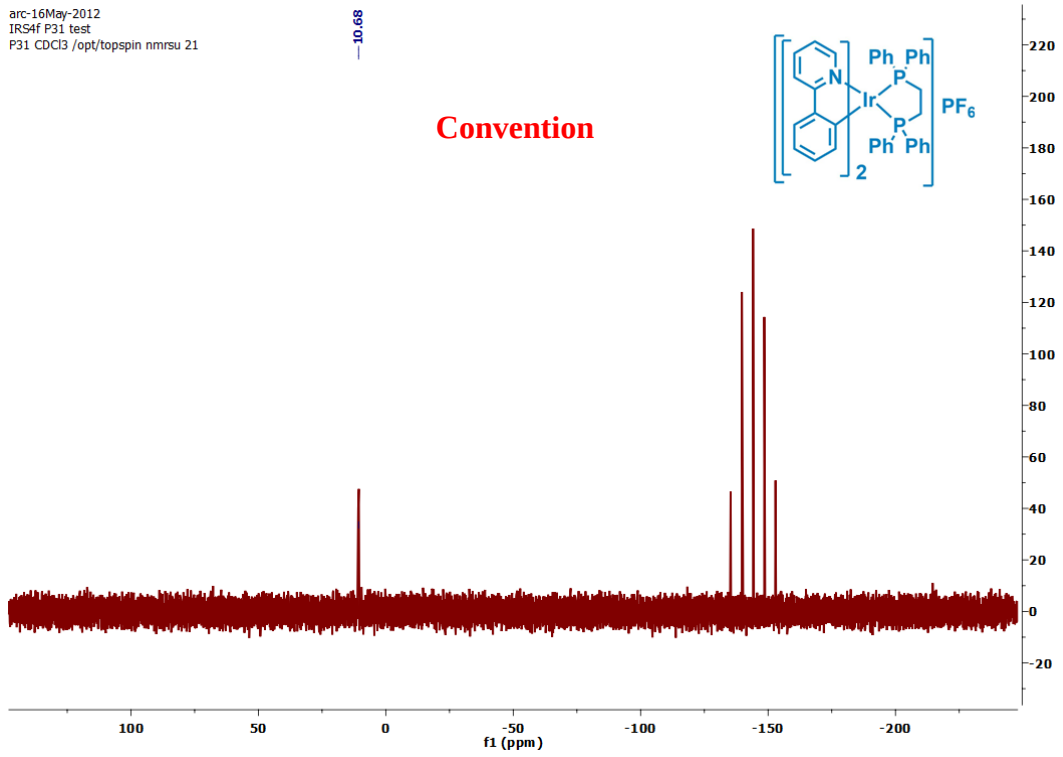
arc-16May-2012
IRS4f P31 test
P31 CDCl3 /opt/topspin nmrsu 21
10.68
Convention
f1 (ppm)
Ph Ph
P
Ir
N
PF6
2

(c)

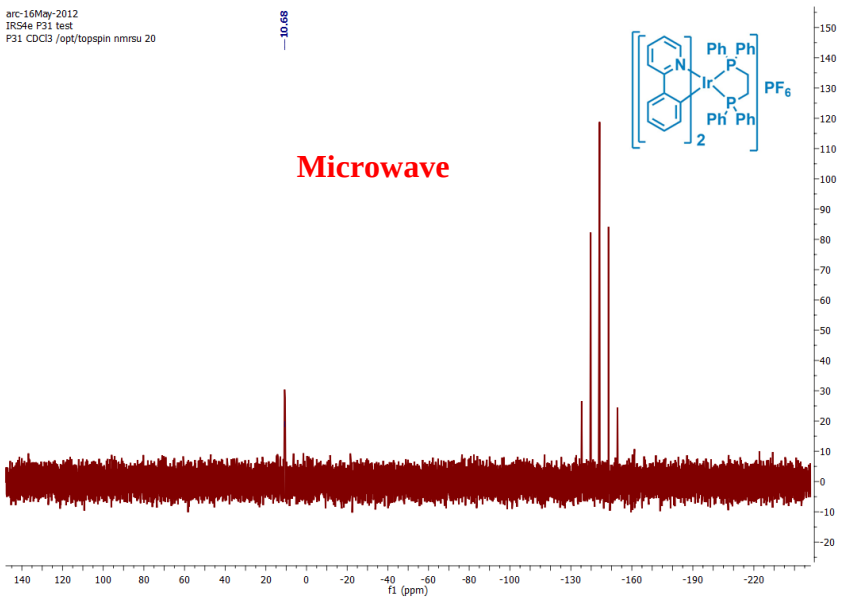

(d)

Figure 6.1.7 (a, c) ^{1}H and ^{31}P of **9** synthesized by conventional method; (b, d) ^{1}H and ^{31}P of 10 synthesized by microwave method.

Table 6.1.1 Comparative study of the time and the yield of the complexes synthesized in two different routes

Complex	Time (min.) MW *vs* Conv.	Yield (%) MW Vs Conv.
8	30.0/1440.0	36.0/35.0
9	15.0/720.0	82.0/85.0
10	15.0/720.0	74.0/75.0
11	15.0/720.0	72.0/78.0
12	15.0/720.0	85.0/78.0
13	15.0/720.0	84.0/86.0
14	15.0/720.0	93.0/79.0
15	15.0/720.0	53.0/83

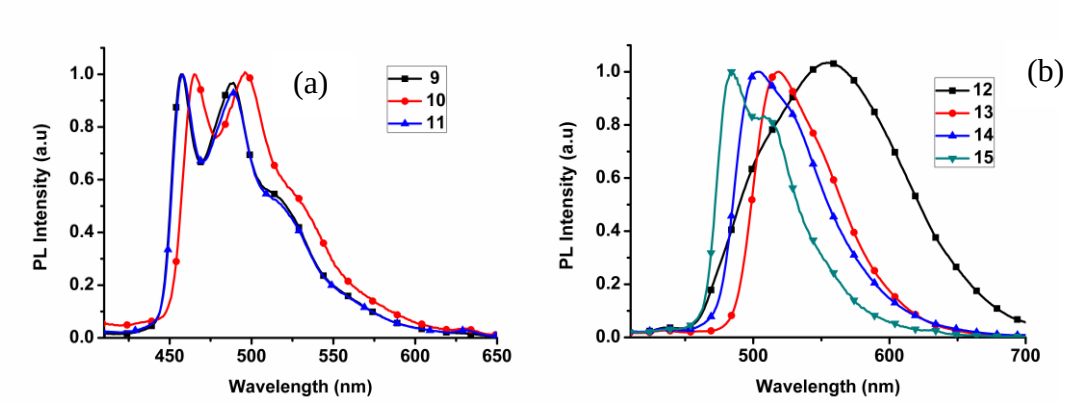

Figure 6.1.8 Emission spectra for the complexes (DCM, 10^{-4}M) showing the blue-shifted emission in case of complexes, (a) **9-11** as compared to (b) **12** and **14**.

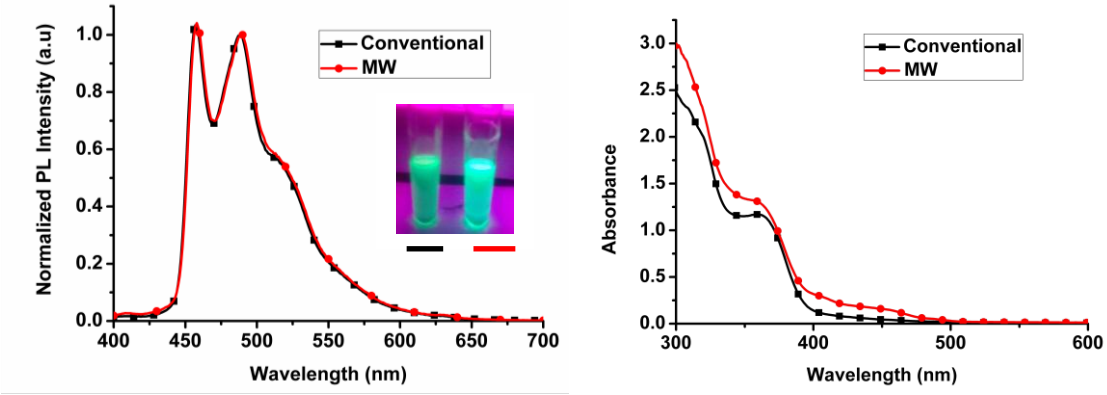

Figure 6.1.9 Absorbance (left) and emission (right) spectra for complex **9** synthesized following the two alternative synthetic procedures; the same emission color (right, inset) has been observed on exciting the two solutions at 365 nm.

6.1.1.4 Computational modeling of the photophysical properties of complexes 9-11

6.1.1.4.1 Ground State Geometries

Optimizations of the ground-state molecular structure of the three iridium(III) complexes **9-11** in dichloromethane solution yield very similar coordination environments for the iridium atom (Figure 6.1.10) in all three cases.

The optimized values for the Ir-X distances are in good agreement with those obtained for similar compounds [28] both from X-ray diffraction and theoretical calculations (Table 6.1.2).

As expected, the only significant difference in the geometry of the coordination environment of iridium in the three compounds is the simultaneous opening of the P-Ir-P angle and closing of the C-Ir-C angle in **10** in order to fit the larger propane bridge between the two phosphorus atoms.

9 **10** **11**

Figure 6.1.10 Molecular structures obtained for the ground state of the three studied iridium(III) compounds in dichloromethane solution (Hydrogen atoms are not displayed for the sake of clarity).

This leads also to a slightly larger Ir-P distance for this case. There is, however, practically no difference between the other two cases with two-carbon ethane or ethene bridges. Of these two observed changes, the most important one is the opening of almost 6º for the P-Ir-P angle.

Table 6.1.2 Geometrical parameters for the coordination environment of iridium(III) in the three optimized ground-state structures in dichloromethane solution.

	Bond distances[(a)], Å			Angles (º)		
molecule	Ir-N	Ir-P	Ir-C	N-Ir-N	P-Ir-P	C-Ir-C
9	2.109	2.479	2.059	168.6	82.9	86.2
10	2.110	2.539	2.061	169.6	88.9	82.8
11	2.106	2.499	2.059	168.7	83.0	84.8

6.1.1.4.2 Frontier Molecular Orbitals

In (Figure 6.1.11) we show an isovalue representation of the molecular orbitals that have a significant participation in the low-lying excitations for compound **9**. The calculated HOMO – LUMO gap is approximately 4.1eV for all three compounds. As it is evident from this picture, while there is a significant participation of iridium d orbitals together with π-type orbitals of the phenyl rings of the 2-phenylpyridyl ligands in the HOMO, the LUMO is on the contrary dominated by π*-type orbitals of the pyridine rings of the 2-phenylpyridyl ligands. There is no significative participation of the phosphine ligands to any of the orbitals involved in the low-lying excitations for any of the three compounds.

6.1.1.4.3 Excited States

If we consider the excitation from the ground state to the first excited singlet state S_1 our results (Table 6.1.3) indicate that for all three compounds **9-11** the electronic transition can be considered basically as a simple HOMO to LUMO electron promotion. According to this finding and considering the representation of the molecular orbitals involved in the transition (Figure 6.1.11).

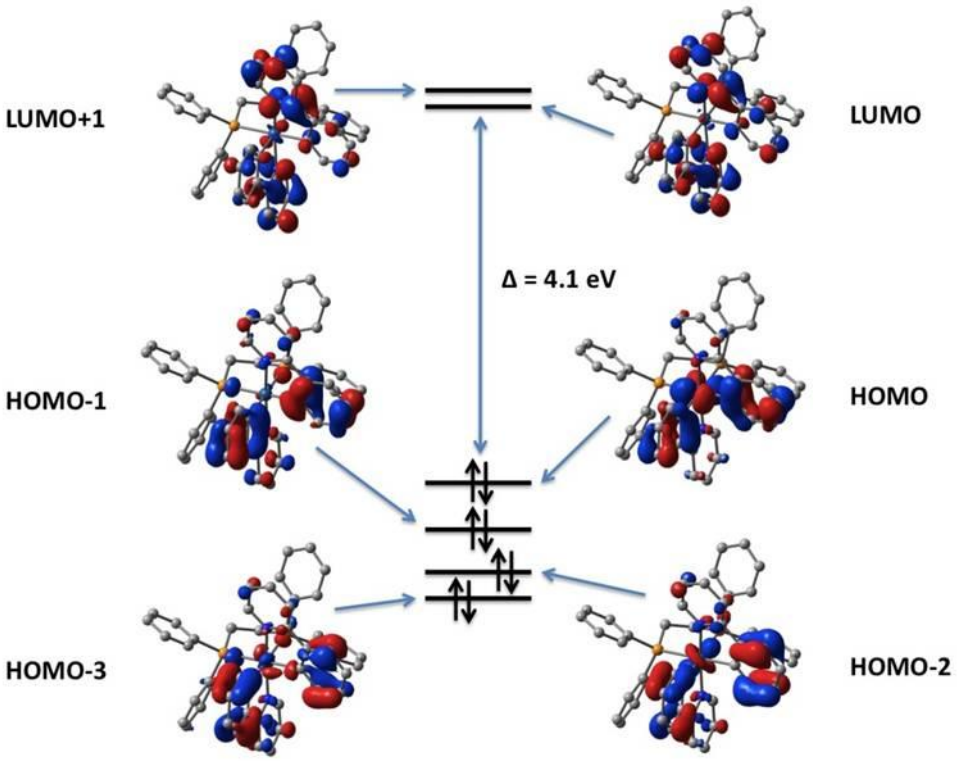

Figure 6.1.11 Molecular orbital diagram showing the highest occupied and lowest unoccupied molecular orbitals for **9**.

It can be deduced that this transition has a significant MLCT character from the *d* orbitals of the iridium atom to the π system of the coordinated 2-phenylpyridyl ligands, mainly to π* orbitals of the C_5N pyridine rings. It is also worth noting the existence of some amount of π to π* transition in these ligands with electronic charge being transferred from the π orbitals of the C_6 phenyl rings of the 2-phenylpyridyl ligands to π* orbitals of the C_5N pyridine rings.

Table 6.1.3 Vertical excitation energies calculated for the lowest lying singlet and triplet states for the three studied compounds (**9**-**11**)

molecule	states	ΔE, eV (nm)	Assignaments
9	T_1	2.85 (434)	HOMO-3 → LUMO+1 (6%)
			HOMO-2 → LUMO (12%)
			HOMO-1 → LUMO+1 (22%)
			HOMO-1 → LUMO+3 (2%)
			HOMO → LUMO (44%)
	T_2	2.86 (433)	HOMO-3 → LUMO (9%)
			HOMO-2 → LUMO+1(10%)
			HOMO-1 → LUMO (29%)
			HOMO → LUMO+1 (36%)
	S_1	3.39 (366)	HOMO → LUMO (97%)
10	T_1	2.84 (437)	HOMO-3 → LUMO+1 (6%)
			HOMO-2 → LUMO (10%)
			HOMO-2 → LUMO+1 (3%)
			HOMO-1 → LUMO (4%)
			HOMO-1 → LUMO+1 (15%)
			HOMO → LUMO (35%)
			HOMO → LUMO+1 (10%)
	T_2	2.85 (435)	HOMO-3 → LUMO (9%)
			HOMO-3 → LUMO+1 (3%)
			HOMO-2 → LUMO+1 (6%)
			HOMO-1 → LUMO (22%)

			HOMO-1 → LUMO+1 (7%)
			HOMO → LUMO (7%)
			HOMO → LUMO+1 (28%)
	S_1	3.39 (365)	HOMO → LUMO (97%)
11	T_1	2.85 (435)	HOMO-3 → LUMO+1 (7%)
			HOMO-2 → LUMO (12%)
			HOMO-1 → LUMO+1 (21%)
			HOMO-1 → LUMO+3 (2%)
			HOMO → LUMO (42%)
	T_2	2.86 (434)	HOMO-3 → LUMO (10%)
			HOMO-2 → LUMO+1 (9%)
			HOMO-1 → LUMO (27%)
			HOMO → LUMO+1 (35%)
	S_1	3.39 (366)	HOMO → LUMO (97%)

6.2 Part B: New 'Aggregation Induced Emission (AIE)' Active Cyclometalated Iridium(III) Based Phosphorescence Sensors: High Sensitivity for Mercury(II) Ions

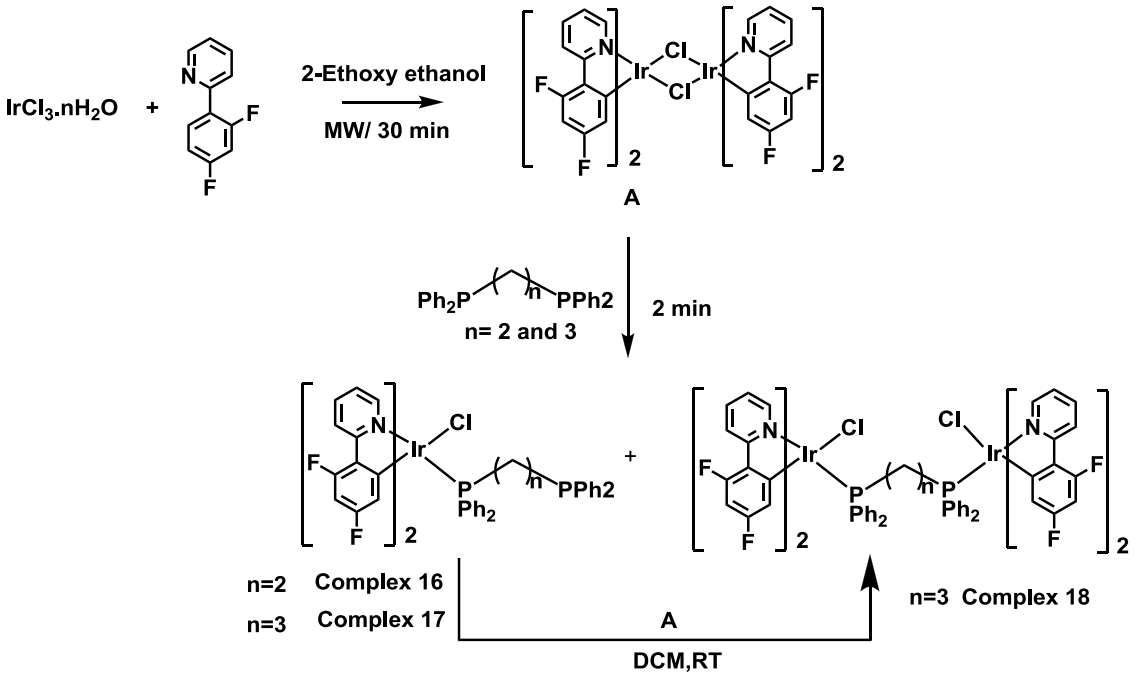

Scheme 6.2.1 Syntheses of blue emitting iridium(III) complexes.

6.2.1 Results and Discussion

Blue emitting phosphorescent transition metal complexes are usually being synthesized by employing a wide energy-gap cyclometalated ligand, such as 4,6-difluorophenyl pyridine (dfppyH), 3-trifluoromethyl-5-(2-pyridyl) pyrazole and many other functionalized cyclometalates [10, 29]. The electron withdrawing fluoro substituents which are located at the meta-positions with respect to the central metal atom, stabilize the metal d_{π} orbitals [30], while strong-field ligands such as cyanide or phosphines directly bonded to metal are found to be capable of increasing the band gap.

6.2.1.1 Syntheses

Several new blue-emitting complexes were synthesized (Scheme 6.2.1) using a strong-field ligand with phosphorous-donating diphosphine ligands. In these cases, diphosphines are coordinated to bis-cyclometalated iridium(III) complex in a monodentated mode while the other donating phosphines remain as appended with the possibility of coordinating to another metal. This idea was originated from our previous report where $[(ppy)_2Ir(\mu\text{-}Cl)_2Ir(ppy)_2]$ (ppy = 2-phenyl pyridine) was reacted with diphosphine ligands (L_1/L_2), resulting a chelate complex of diphosphine $[Ir(ppy)_2(PPh_2CH_2CH_2PPh_2)]PF_6$. This was obtained as the absolute product even lowering the temperature to room temperature. For the syntheses of the compounds described in this report, the chloro-bridged dinuclear iridium(III) complex, $[(F_2ppy)_2Ir(\mu\text{-}Cl)_2Ir(F_2ppy)_2]$($F_2$ppy=2-(2′,4′-difluoro)phenylpyridine) and diphosphine ligands (L_1/L_2) were reacted in dichloromethane at room temperature for very short periods (2 minutes). The synthesized complexes exhibit an intense blue emission under excitation by UV ray with a fascinating structure where the diphosphine coordinate as monodentate to the central metal atom. Probably, the presence of strong electronegative fluorine atoms in phenyl of 2-phenylpyridine restricts the formation of chelating complex of diphosphine to iridium(III) in these cases. With using bis(diphenylphosphino)propane (L_2) as diphosphine, the crude reaction mass contains two products that were isolated by column chromatography (**17** and **18**). The complex **16** corresponds to the appended diphosphine in bis-2-(2′,4′-difluoro)phenylpyridine iridium(III) complex (Scheme 6.2.1). The complex **18** was characterized which corresponds to $[(F_2ppy)_2Ir(\mu\text{-}L_2)Ir(F_2ppy)_2]$. On the other hand, for the case of 2-bis(diphenylphosphino)ethane (L_1), the exclusive formation of the complex which corresponds to bis-2-(2′,4′-difluoro)phenylpyridineiridium(III) where diphosphine remains as appended (mono coordinated) (**16**) at room temperature (Scheme 6.2.1). It is to be noted that there has no formation of chelating diphosphine iridium(III) complex even upon allowing the reaction to continue for 72h. The chelating diphosphine mixture was isolated when the reaction mixture was refluxed in methanol for 15 min. This observation depicts the occurrence of chelating / or non-chelating belongs to temperature dependent. We have isolated and characterized the chelating complex by ^{1}H NMR and HRMS.

The ^{1}H, ^{31}P and ^{19}F NMR spectra of these complexes support that the structure of complexes **16** and **17** contains a free terminal phosphine group whereas **18** is a bimetallic iridium complex with the diphosphine ligand acting as a bridge between the two iridium(III) centers. The isolation of **18** from the reaction mixture indirectly supports the monodentate rather than chelating coordination mode of diphosphines to iridium in **16** and **17** (Scheme 6.2.1). The synthesized complexes have C1 symmetry, and as a consequence, the results show a ^{1}H NMR spectrum where the total number of proton resonances equals the total number of aromatic protons present in the complex. The ^{1}H NMR data of **16** and **17** show 12 distinct sets of aromatic protons which correspond to the total number of protons present in the complexes.

In the ^{31}P-NMR spectrum of **16** and **17**, the presence of two clearly non-equivalent P atom peaks supports the fact that one of the phosphorous atoms remains without coordination in the complex. The ^{31}P signal of the coordinated phosphorous atom appears as a double triplet (dt) at δ -9.2 ppm with J_{P-F} = 8.1 Hz, whereas the non-coordinated phosphorous atom shows a peak corresponding to a double singlet signal at δ -12.2 ppm with J_{P-P}= 31.5 Hz which matches well with previous reports [31-33] (Figure 6.2.1) for free PPh_2. Each phosphorous signal will split into a doublet [34] and signal "a" (db signal) will split further into a triplet by P-F coupling while signal "b" will not split further because of weak long range coupling. Similarly, for the case of **17**, the ^{31}P-NMR spectrum shows two different signals: the one labelled as "a", a triplet at δ -12.9 ppm with J_{P-F} =7.7 Hz and a signal "b" appearing as a singlet. In this case, since there should be no splitting between two P atoms (because of the long range coupling), they should appear both as singlets, but signal "a" will be further split by interaction with the F atom into a triplet with $J_{P-F} \sim 8$ Hz. The ^{31}P-NMR of complex **18** is showing again two different signals "a" and "b", as a double triplet at δ -11.96 ppm and δ -12.46 ppm with J_{P-F} = 8 Hz.

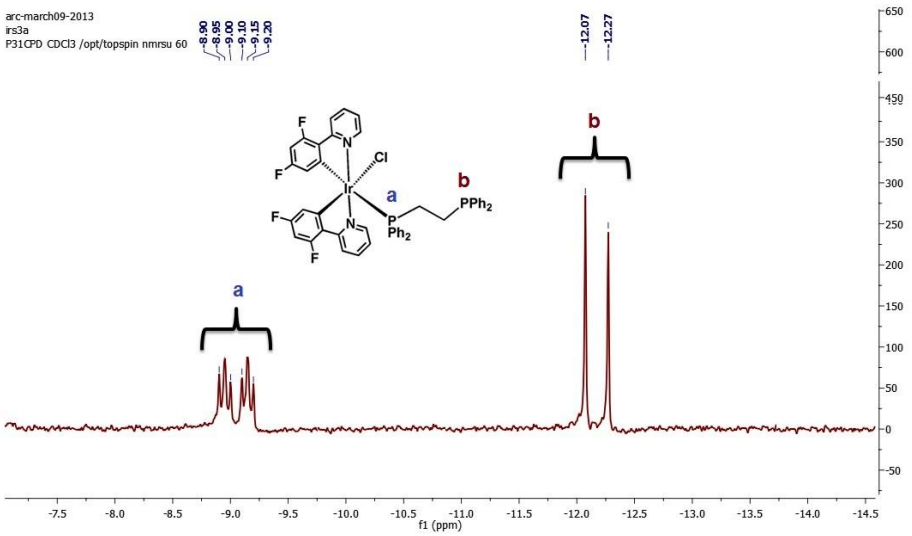

Figure 6.2.1 ^{31}P NMR spectra of complex **16** showing two different signals appearing as a doublet of triplets (a) and a doublet (b).

6.2.2.2 Aggregation-Induced Enhanced Emission Property

The 'aggregation induced emission (AIE)' property of the blue phosphorescence at λ_{max} 461 and 488 nm for both (Table 6.2.1) complexes, respectively, is investigated. Both compounds are highly soluble in common organic solvents such as dichloromethane (DCM), chloroform ($CHCl_3$), tetrahydrofuran (THF), dimethyl sulfoxide (DMSO) or dimethyl formamide (DMF) but they are not soluble in water.

These complexes show a very weak emission only in DMF, but they are both strongly emissive in the solid state (under illumination with a 365 nm UV lamp). A different amount of water (f_w in the range 0-99%) is gradually added to a set of solutions of complexes **16** and **17,** keeping the overall concentration of the solution to 10^{-5} M. The measured photoluminescence (PL) intensity of complex **16** diminishes up to a water concentration about $f_w \leq 50\%$ [$\leq$60% for **17**], then starting to increase for water fractions up to f_w= 70% (Figure 6.2.2).

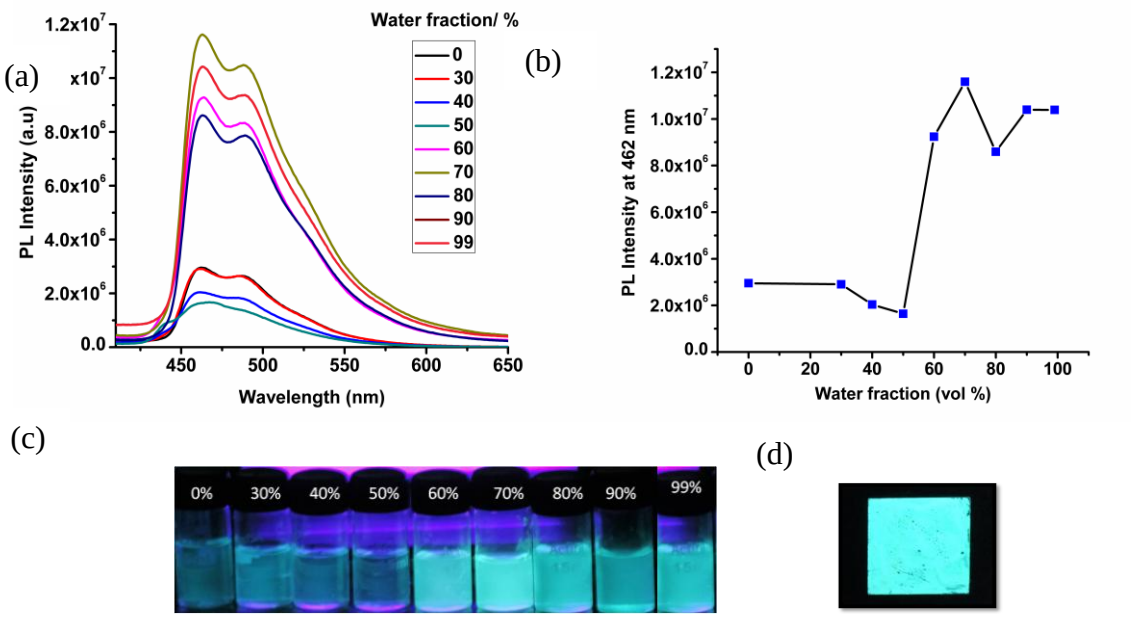

Figure 6.2.2 (**a**) PL spectra of complex **16** with [M] =10^{-5} mol L^{-1} in DMF–water mixtures water fractions (f_w). (**b**) The PL Intensity at λ_{max}=462 nm with different fraction of water. (c) Fluorescent photos of the aqueous mixtures radiated with an ultraviolet light at 365 nm. (**d**) Solid state emission of complex **16**.

At this condition, the PL intensity is about 4 times (3.5 times for **17**) higher than the PL intensity measured in pure DMF solution (Figure 6.2.2 & 6.2.3). After reaching a maximum intensity at f_w = 70%, the PL intensity decreases along with increasing water content. In the case of **16**, the PL intensity again decreases after reaching maximum at 70%. This abnormal variation of the AIE property for both complexes may be due to two reasons only those molecules which are present on the surface of nano particles emit light and contribute to the fluorescent intensity upon excitation, leading to a decrease in the fluorescence intensity after aggregation.

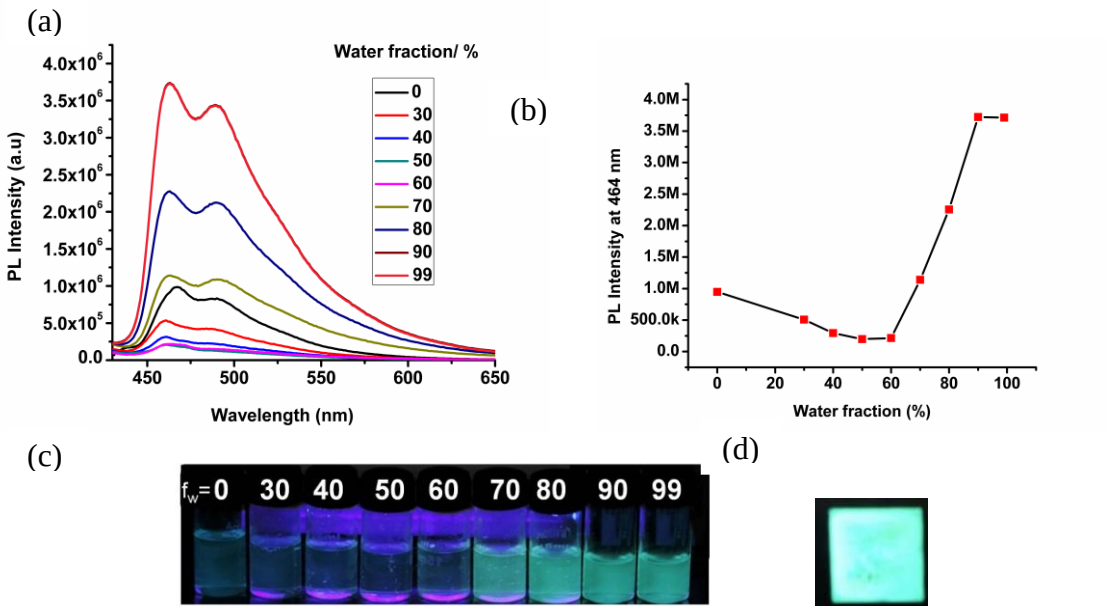

Figure 6.2.3 (**a**) PL spectra of complex **17** with [M] =10^{-5} mol L^{-1} in DMF–water mixtures water fractions (f_w). (**b**) The PL Intensity at λ_{max}=462 nm with different fraction of water. (c) Fluorescent photos of the aqueous mixtures radiated with an ultraviolet light at 365 nm. (**d**) Solid state emission of complex **17**.

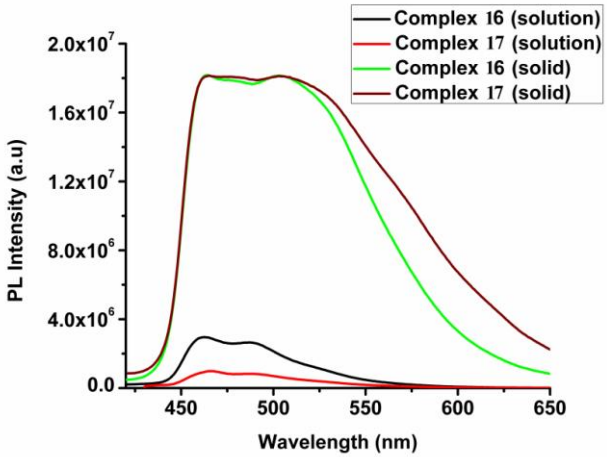

Figure 6.2.4 Comparative solid state and solution (10^{-4} M, DCM) photoluminescence spectra for complexes **16** and **17** [peaks in solution: (461 and 488 nm), peaks in solid: (468 and 503 nm) respectively].

Table 6.2.1 Photophysical property of complexes

Complex	UV-Vis absorption[a] nm, (ε,$M^{-1}cm^{-1}$)	PL[b] (λ_{emi}) (nm)	PL[c] (λ_{emi}) (nm)	τ (ns)[d]	τ (μs)[e]	QY[f] (%) (ϕ_{sol})	QY[g] (%) (ϕ_{solid})
16	254 (60190), 307(17333), 370(4333), 469(103)	461,488	463,504	19.3	2.0	0.067	7.3
17	253(68571), 302(25857), 371(6714), 450(247),	461,488	468,504	55.2	3.4	0.020	6.2
18	253(67450), 302(24350), 371(6580), 450(197),	461,488					

[a] Spectra were recorded in degassed dichloromethane (DMF) at room temperature with ε x10^{-5} $M^{-1}cm^{-1}$; [b] recorded in DMF ; [c]thin film emission, [d] life time was measured in DMF, [e]aggregated form of the complexes resulted in water-DMF mixtures (9:1) f_w= 70% for complex **16** and 99 % for complex **17** [f]quantum yields for the two complexes were measured in degassed DMF against quinine sulfate in 1.0 N sulfuric acid as reference (QY = 0.546). [g]Solid state phosphorescence QE (ϕ_{solid}) has been recorded using integrating sphere.

The RIR (restriction of intermolecular rotations) of phenyl rings around the single bonds in the aggregated state will enhance light emission. The emission intensity of aggregate species will depend on which of both phenomena is going to dominate and affect the fluorescent behaviour of the aggregated molecules after addition of water; the other reason, the solute molecules can aggregate into two kinds of nanoparticle suspensions: crystalline and amorphous particles..

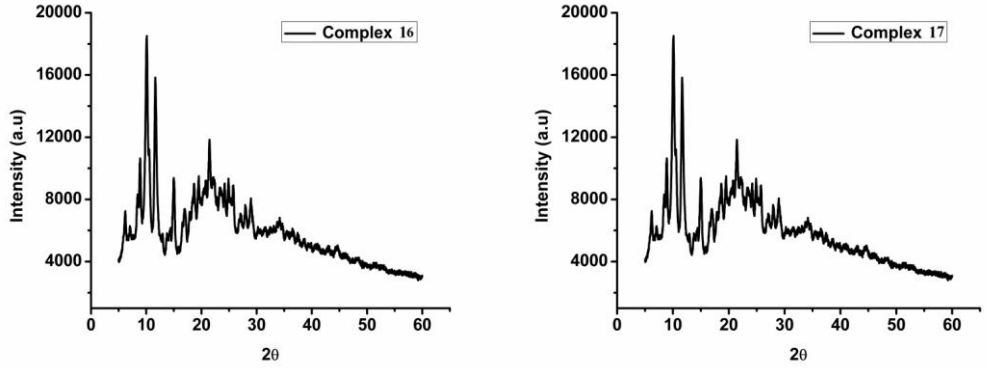

(a) (b)

Figure 6.2.5 PXRD data for complexes **16** and **17** showing the partial crystaline and amorphous nature of the complexes, respectively.

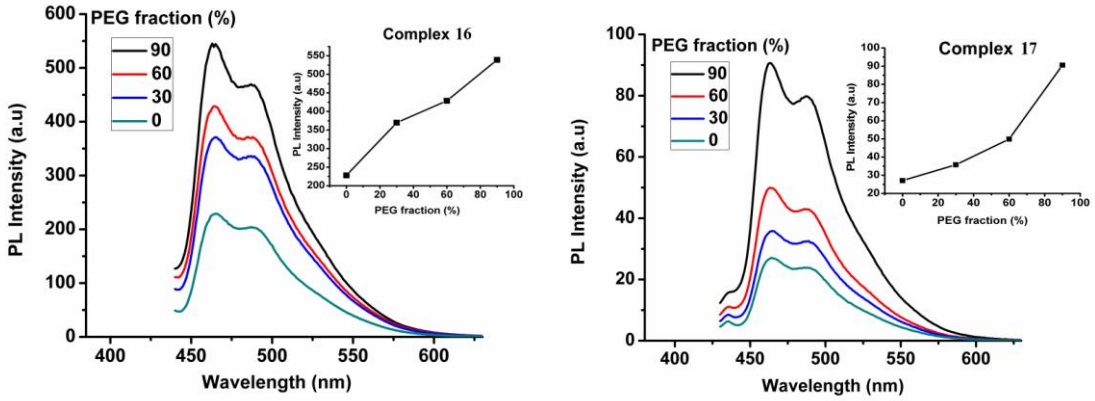

(a) (b)

Figure 6.2.6 (a) PL spectra of complex **16** with [M] =10^{-5} mol L^{-1} in DMF–PEG mixtures, PEG fraction (f_{PEG}) (b) PL spectra of complex **17** with [M] =10^{-5} mol L^{-1} in DMF–PEG mixtures, PEG fraction (f_{PEG}).

Crystalline particles would enhance the PL intensity, while amorphous ones lead to a reduction in the intensity [36, 37]. The aqueous mixtures with higher f_w for which the formation of precipitate is not observed, suggests that the size of the aggregates are in the nano-scale dimension.

The solution quantum efficiencies of the complexes **16** and **17** have been measured to 0.067 % and 0.020 %, respectively [reference is used quinine sulphate in

0.1M sulphuric acid, quantum yield (QE) = 0.55]. The absolute solid state QE for the complexes **16** and **17** has been measured using integrating sphere and the values obtained 7.252% and 6.165 %, respectively.

So, these QEs are 107 and 295 times higher as compared to their solution quantum efficiencies, respectively in agreement with the strong emission observed in the solid state with respect to their respective solutions showing the remarkable AIE property of the complexes. Life time data for complexes in solution and solid state were found to be 19.30 ns and 2 μs for **16,** and 55.19 ns and 3.382 μs for **17** (Table 6.2.1), respectively.

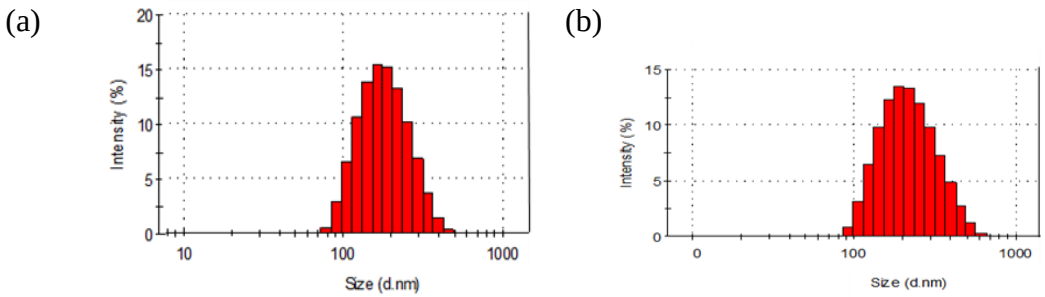

Figure 6.2.7 (a, b) . Particle size distribution of nano-aggregates of complexes **16** and **17** formed in a DMF / water mixture with a 90% water fraction.

Studies using a particle size analyzer also reveal the formation of nanoaggregates (in 90% water fraction) with diameters in the range of 170–200 nm (Figure 6.2.7). Clearly, aggregate formation has enhanced the PL of both complexes, in other words, both complexes are AIE-active.

.

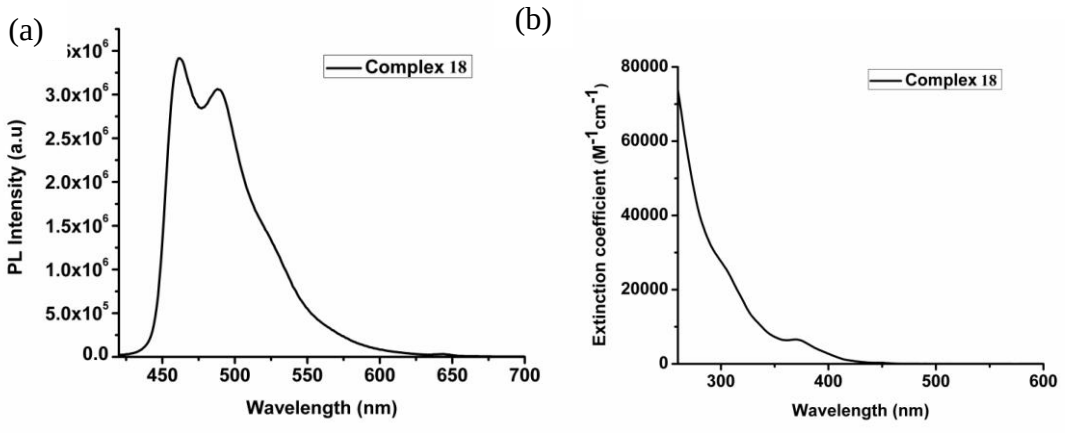

Figure 6.2.8 (a,b) Emission and absorption spectra for complex **18** in DMF (10^{-5}M)

The photophysical properties of complex **18** have been studied and found similar emission and absorption bands as those observed for complexes **16** and **17** (Figure 6.2.8, Table 6.2.1).

6.2.2.3 Ground State Geometries

The optimization of the molecular structure for the ground state suggests slightly distorted octahedral coordination geometries for the two Iridium(III) complexes **16** and **17** (Figure 6.2.10). As shown in Table 6.2.2, there has no major difference neither in the Ir-X distances nor in the X-Ir-X angles between **16** and **17** except for the Ir-P distance and the Cl-Ir-P angle, whose values increase slightly as the bridge between the two diphenylphoshines becomes larger.

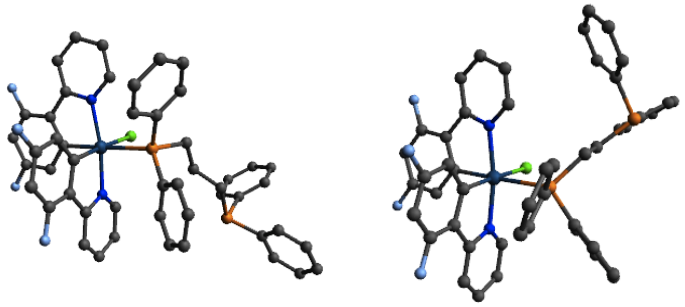

Complex 16 Complex 17

Figure 6.2.9 Ground state molecular structures calculated in dichloromethane solution. Hydrogen atoms are not displayed for the sake of clarity.

In the two structures shown (Figure 6.2.10), It is evident that only one of the two phosphorus atoms of the diphosphine belongs to the coordination environment of the iridium atom, while the other one remains free to coordinate with other metal atoms present in the solution.

Table 6.2.2 Geometrical parameters for the coordination environment of Iridium in the optimized ground state structures of compounds **16** and **17** in dichloromethane solution.

	Bond distances[(a)], Å				Angles (º)		
Complex	Ir-N	Ir-C	Ir-Cl	Ir-P	N-Ir-N	C-Ir-C	Cl-Ir-P
16	2.091	2.025	2.589	2.582	170.0	89.9	90.2
17	2.094	2.026	2.571	2.608	169.9	88.2	89.5

6.2.2.3.1 Frontier Molecular Orbitals

The frontier molecular orbitals of complex **16** are shown (Figure 6.2.10). While the HOMO-3, HOMO-2 and HOMO have a remarkable d contribution from the Iridium(III) center, along with a p orbital from the Cl atom and π character from the two 2-phenylpyridine ligands, the HOMO-1 consists on a π type orbital located on one of the diphenylphoshines. The latter one is the only frontier molecular orbital which has participation from the ancillary ligand. The LUMO and LUMO+1 are quasi-degenerate orbitals composed of π* type orbitals located on the 2-phenylpyridine ligands, with no significant metal participation.

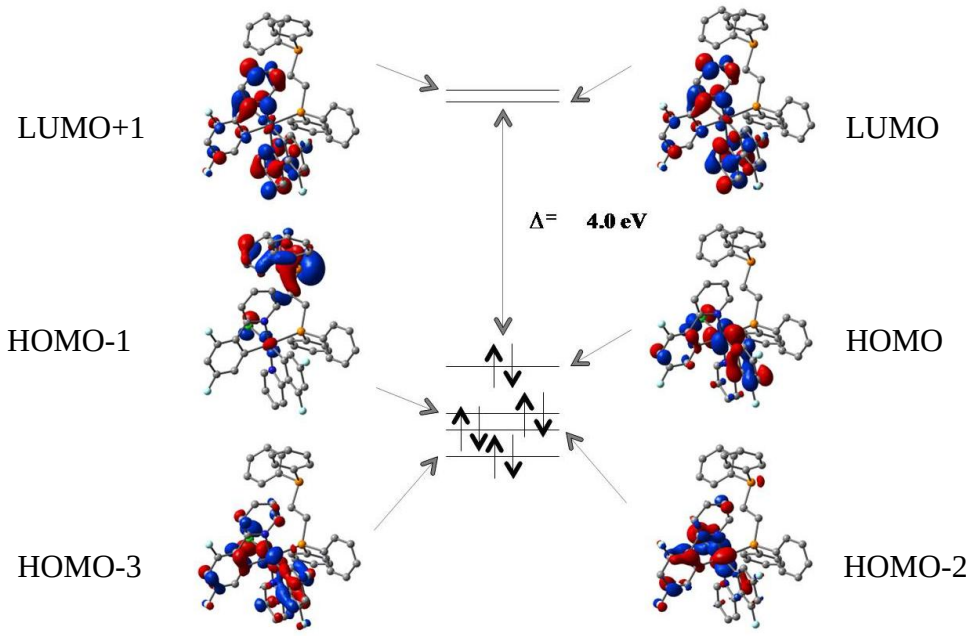

Figure 6.2.10 Highest occupied and lowest unoccupied molecular orbitals for complex **16**.

Except for the HOMO-1 and HOMO-3, all the other mentioned orbitals have a notable participation in the low-lying electronic states. The relevant molecular orbitals related to the electronic transitions and the HOMO-LUMO gap of approximately 4.0 eV are quite similar for the two studied complexes.

6.2.2.3.2 Excited States

The calculated excitation energies (Table 6.2.3) corresponding to the electronic transition from the ground state to the first excited singlet state S_1 are 3.26 and 3.19 eV, respectively. This electronic transition can be seen as a promotion of an electron from the HOMO to the LUMO, with an important MLCT character from the d orbitals of the iridium atom to the π system of the two 2-phenylpyridine ligands, together with some charge transfer from the p orbital of the Cl atom to the two 2-phenylpiridines and a significant π to π* transition within these ligands. The slightly smaller HOMO-LUMO gap obtained for complex **17** (3.95 vs. 4.04 eV) is responsible for the lower excitation energy calculated for this complex. This information correlates satisfactorily with the

experimental absorption spectra. The associated computed oscillator strengths predict similar absorption intensities for the two complexes, in good agreement with the experimental observations.

Table 6.2.3 Vertical excitation energies, oscillator strengths, and orbital contributions (≥5 %) to the electronic transitions calculated for the transition to lowest excited states of the studied complexes.

Complex	states	ΔE, eV (nm)	f	Assignaments
16	T_1	2.87 (432)		HOMO-4 → LUMO (10%)
				HOMO-3→ LUMO+1 (8%)
				HOMO-2 → LUMO+1 (14%)
				HOMO → LUMO (48%)
	T_2	2.89 (430)		HOMO-4 → LUMO+1 (8%)
				HOMO-3 → LUMO (8%)
				HOMO-2 → LUMO (21%)
				HOMO -2→ LUMO+1 (5%)
				HOMO → LUMO+1 (39%)
	S_1	3.26 (380)	0.037	HOMO → LUMO (95%)
	S_2	3.32 (373)	0.004	HOMO → LUMO+1 (95%)
	S_4	3.72 (333)	0.049	HOMO-2 → LUMO (26%)
				HOMO-2 → LUMO+1 (47%)
				HOMO-1 → LUMO (5%)
				HOMO-1 → LUMO+1 (9%)
17	T_1	2.84 (436)		HOMO-4 → LUMO (15%)
				HOMO → LUMO (60%)

T_2	2.89 (428)		HOMO-3 → LUMO (6%)
			HOMO-3 → LUMO+1 (13%)
			HOMO-2 → LUMO (7%)
			HOMO -2→ LUMO+1 (18%)
			HOMO → LUMO+1 (38%)
S_1	3.19 (389)	0.032	HOMO → LUMO (97%)
S_2	3.33 (373)	0.004	HOMO → LUMO+1 (96%)
S_4	3.75 (331)	0.043	HOMO-2 → LUMO+1 (85%)
			HOMO-3 → LUMO+1 (5%)

In order to gain more insight into the nature of the electronic transitions observed in the experimental absorption spectra, excitations to other low-lying singlet and triplet states were calculated. This information is summarized in Table 6.2.3. The excitation from the ground state to the second excited singlet state, S_2, is mainly an HOMO to LUMO+1 transition. The nature of this second excited singlet state is quite similar to that of the first excited singlet state because of the resemblance between the LUMO and LUMO+1, although the corresponding oscillator strength for this transition is almost negligible for the two complexes. The intense absorption band observed in the experimental spectra at 300-330 nm (Figure 6.2.11) corresponds mainly to the electronic transition to the fourth excited singlet state (with contributions from other high-lying singlet states). The major contribution to this fourth singlet state is an excitation from the HOMO-2 to the LUMO or LUMO+1, with an important MLCT character as it is found for the first singlet state. In the low energy region of the absorption spectra (400-450nm) (Figure 6.2.11), a band of low intensity is observed which can be attributed to the partially allowed transitions to low-lying triplet states due to the spin-orbit coupling induced by the presence of the metal centre.

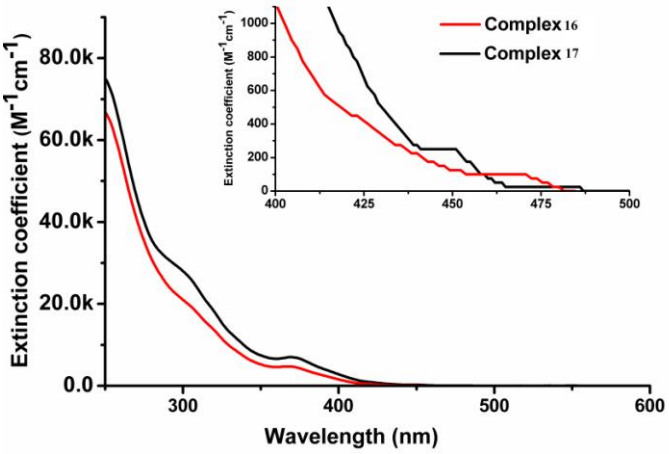

Figure 6.2.11 Solution absorption spectra for **16** and **17** at a concentration of 10^{-5}M in DCM (Inset: enlarged absorption spectra in the region 400-500 nm).

The calculated excitation energies to the first and second triplet states are in excellent agreement with those found for the experimental absorption bands (Table 6.2.1). The character of the transitions from the ground state (S_0) to the first and fourth excited singlet (S_1,S_4) and the first triplet states (T_1) has been analyzed comparing the atomic Mulliken populations for each fragment in the molecule. The results shown in Table 6.2.4 indicate very similar MLCT character for the two complexes for the excitations to S_1 and S_4, while the MLCT character play a minor role in the transition to the first excited triplet state T_1.

The nature of the MLCT character of these transitions can be further visualized by plotting the difference between the charge densities of the two states involved in the transition. Figure 6.2.12 shows these difference plots for complex **16**.

Table 6.2.4 MLCT character for the transitions from the ground state (S_0) to the first and fourth excited singlet (S_1, S_4) and triplet states (T_1).

Complex	$S_0 \rightarrow S_1$	$S_0 \rightarrow S_4$	$S_0 \rightarrow T_1$
16	43%	46%	14%
17	45%	48%	20%

From this representation it can be easily seen that the most important charge transfer in the $S_0 \rightarrow S_1$ and $S_0 \rightarrow S_4$ transitions, responsible for the absorption process, is between the Iridium atom and one of the two 2-phenylpyridine rings. Very similar plots can be obtained for complex **17**.

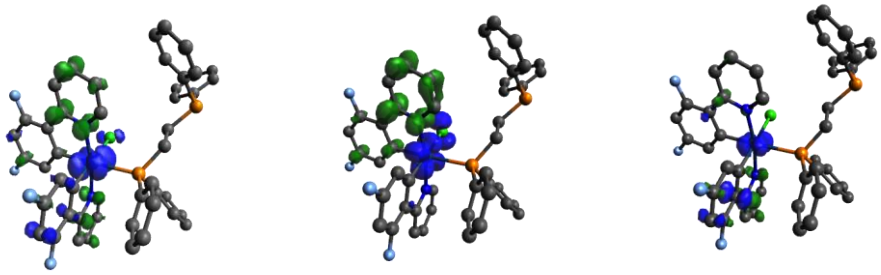

$S_0 \rightarrow S_1$ $S_0 \rightarrow S_4$ $S_0 \rightarrow T_1$

Figure 6.2.12 Electron density differences between the S_1 and the S_0 states (left), S_4 and S_0 states (middle), and T_1 and S_0 states (right) for complex **16**. Blue corresponds to negative values (higher electron density in the ground state) while green corresponds to positive ones (higher electron density in the corresponding excited state).

6.2.2.4 Selective optical response to various metal ions along with Hg^{+2}

AIE active complexes with appended phosphorous donating atoms such as **16** and **17** have a great potentiality in sensing applications. The emission spectra of **16** in presence of individually different metal ions such as Mg^{2+}, K^{+}, Ni^{2+}, Al^{3+}, Cd^{2+}, Co^{2+}, Pb^{2+}, Bi^{2+}, Fe^{2+}, Ag^{+1}, Cu^{2+}, Au^{+3}, Zn^{+2} with Hg^{+2} were recorded (the solution giving AIE property is prepared **16** in DMF/H_2O = 3/7) (Figure 6.2.13 a). As it can be seen in (Figure 6.2.13 a-c), the emission intensity was ~80 % quenched in the presence of Hg^{+2} ions. The specificity of the probe molecules towards Hg^{+2} ions has been studied in competitive experiments in the presence of other metal ions (Figure 6.2.13 b). The grey bars represent the intensity of the emitted radiation in presence of Hg^{+2} ions in solution together with individual metal ions such as Mg^{2+}, K^{+}, Ni^{2+}, Al^{3+}, Cd^{2+}, Co^{2+}, Pb^{2+}, Bi^{2+}, Hg^{+2}, Fe^{2+}, Ag^{+}, Cu^{2+}, Au^{+3}, and Zn^{+2} showing the high impact on the emission intensity when compared to the black bars which correspond to the emission intensity of a solution of the same metal ion in absence of Hg^{+2}.

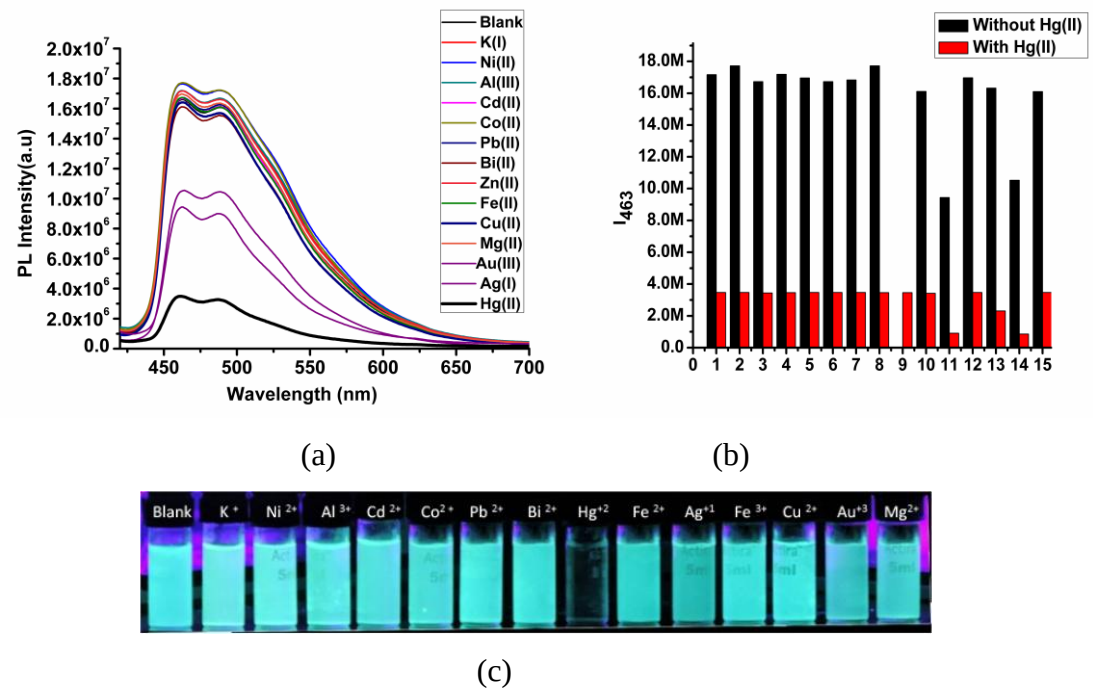

Figure 6.2.13 (a) Fluorescence spectra of complex 16 with [M] =10^{-5} mol L^{-1} at f_w = 70 % upon the addition of 4 equivalent of metal ions. (b) Column diagrams of the fluorescence intensity of complex 16 + M^{n+} at 463 nm. Black bars represent the addition of various metal ion to the blank solution and gray bars represents the subsequently addition of Hg^{+2} (4 equivalent) to the above solutions (complex 16+ M^{n+}+ Hg^{+2}) (**c**) photo of complex 16 when dispersed at f_w = 70 % with [M] =10^{-5} mol L^{-1}, by adding 4 equivalent of metal ions. From left to right: 1,blank ; 2, K^{+}; 3, Ni^{+2}; 4,Al^{+3}; 5,Cd^{+2} ; 6, Co^{+2}; 7, Pb^{+2}; 8,Bi^{+2}; 9, Hg^{+2};10, Fe^{+2}; 11,Ag^{+}; 12,Cu^{2+}; 13, Fe^{+3};14, Au; and 15, Mg^{+} radiated with an ultraviolet light at 365 nm.

The quenching effect on the emission intensity of **16** in presence of Hg^{+2} shows that it is a highly selective ratiometric luminescent molecular probe for the detection of Hg^{+2} ions in solution. The experiment performed with **17**, showed similar results. The absorption spectra of **16** were also recorded in presence of different cations, showing a gradual variation of the absorption spectra (Figure 6.2.14).

The effect of Hg^{+2} on solutions containing complex **16** was also studied very carefully by UV-Vis absorption and PL spectroscopy. Some changes in the UV-Vis absorption spectrum have been observed after titrating **16** with Hg^{+2}: the band at 372

nm which is assigned to the spin-allowed metal-to-ligand charge-transfer (^{1}MLCT) (dπ(Ir) → π*(C^N) transition is slowly shifted to 356 nm resulting in two isosbestic points at 322 and 360 nm, indicating strong interactions between **16** and the Hg^{2+} ions. A continuous decrease in the absorption intensity at 340 nm for the addition of up to 15μM of Hg^{2+} is observed, while further addition of Hg^{2+} induces only very minor changes in A_{340}, indicating that **16** has a 1:1 interaction [38] with the Hg^{+2} ions (Figure 6.2.15).

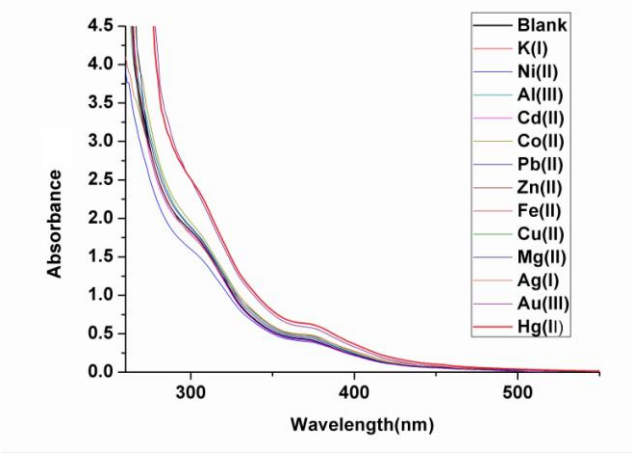

Figure 6.2.14 Absorption response of complex **16** in the presence of various metal cations (4 eq.) in a (7:3)v/v Water : DMF mixture.

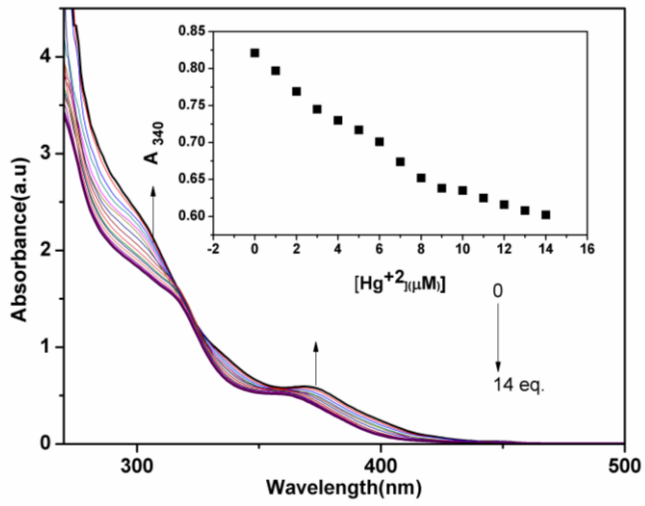

Figure 6.2.15 Changes in the UV–Vis absorption spectrum of **16** with a gradual variation of the Hg^{+2} concentration (0 -14 μM).

The titration experiment was also performed with the help of photoluminescence spectroscopy. In this case, the emission spectra of **16** are gradually decreasing after addition of Hg^{+2} to the solution (Figure 6.2.16).

A linear relationship was obtained between I_{463} and the concentration of Hg^{+2} ions between 0 to 6μM, indicating the sensitivity of **16** towards Hg^{+2}.

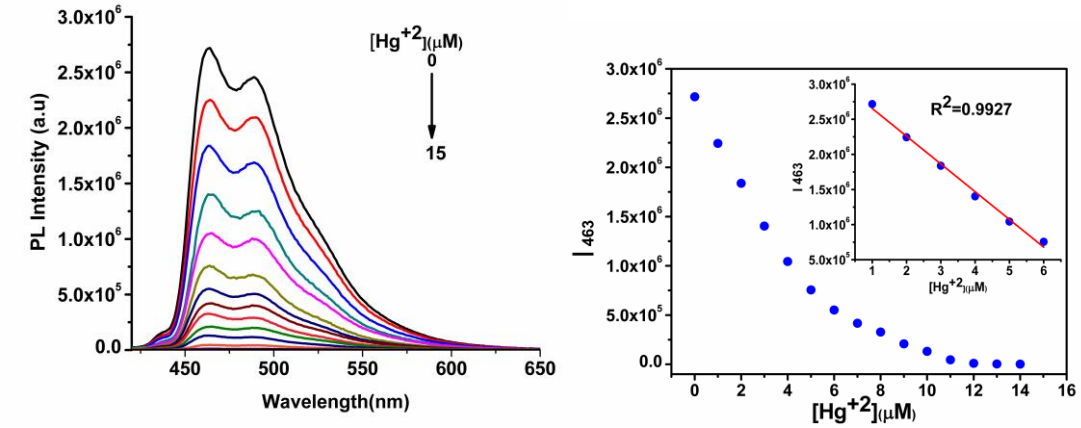

(a) (b)

Figure 6.2.16 (a) The luminescent spectral changes of complex **16** (f_w = 70 % with [M] =10^{-5} mol L^{-1}) upon the increasing addition of Hg^{+2} ions (from 0.0 to 14.0 μM) (nitrate salt). DMF–H_2O (3:7 v/v). λ_{ex} = 380 nm. (b) The plot of I_{463} vs. the concentration of Hg^{+2}; inset, the linear relation of I_{463} vs the concentration of Hg^{+2} in the range of 0.0–6.0 μM.

The limit of detection was calculated [39, 40] to be 170 nM, based on 3σ /m, where σ corresponds to the standard deviation of the blank measurements, and m is the slope in the plot of the intensity versus the sample concentration. This value is reasonably good in comparison to many other iridium(III) based Hg^{+2} chemodosimeter [36].

6.2.2.4.1 The Sensing of the Mechanism of Hg^{+2} by complex 16

According to Pearson's hard-soft acid-base theory, Hg^{+2} is a soft ion (soft acid) that will interact preferentially with a soft base. A glimpse at previous reports shows that the most widely used soft base is sulphur, whose lone pair can interact with Hg^{+2}

ions very easily. According to Hui Zeng *et al.* lone pairs on nitrogen can also interact with Hg^{+2} forming soft acid base complexes [41]. Herein, we report the first iridium(III) phosphine complex that can be used as a chemodosimeter for low level detection of Hg^{+2}. The synthesized iridium(III) complexes have a free lone pair on the non-coordinated phosphorous atom that can easily interact with Hg^{+2} ions. The interaction of **16** with Hg^{+2} was studied by NMR using different nuclei such as ^{1}H, ^{31}P and ^{19}F (Figure 6.2.17-6.2.19).

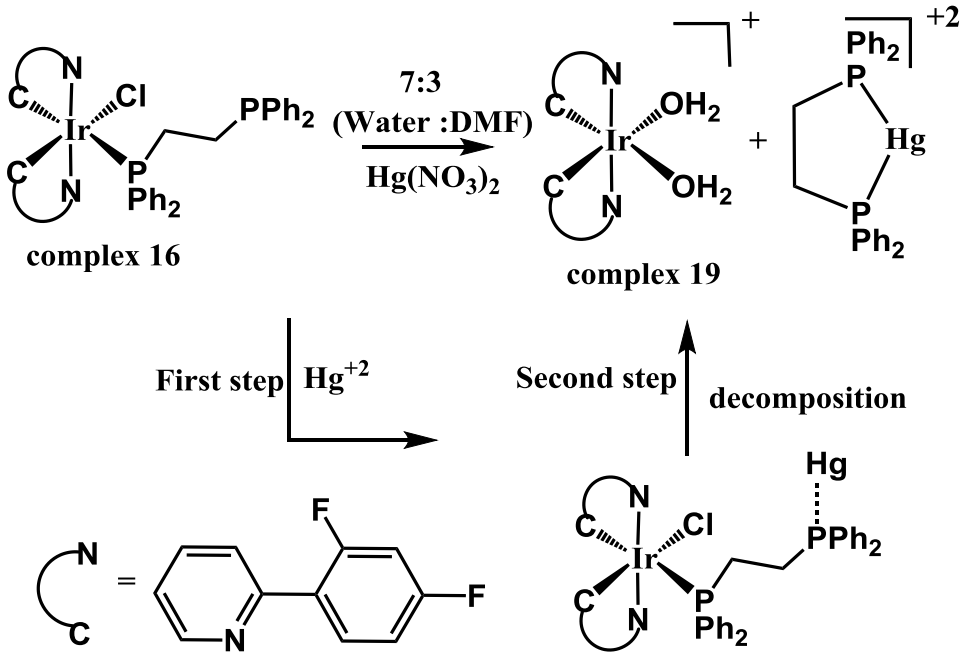

Scheme 6.2.2 Sensing mechanism of Hg^{+2}

The Hg-probing mechanism the interaction of dppe ligand (PPh_2 ligand) with Hg^{+2} has been investigated. The ^{1}H and ^{31}P spectra of the PPh_2 ligand with 2 equivalent and without Hg^{+2} has been recorded which was showing deshielded proton signal (the signal 7.29 ppm is shifted to 7.64 ppm).The downfield signals are suggesting the interaction between PPh_2 ligand and Hg^{+2}. One ^{31}P signal suggesting the symmetrical nature of PPh_2-Hg (1:1) complex. The ^{1}H NMR spectra of **16** with 2 equivalent of Hg^{+2} is giving new signal between 7.52 ppm and 7.79 ppm and these peaks can be found in ^{1}H NMR spectra of PPh_2 ligand (with 2 equivalent) (Figure 6.2.17). The chemical shift

for ^{31}P signal after addition of 2 equivalent Hg^{+2} is moved to more deshielded region (-14.59 ppm to 38.80 ppm) and the chemical shift at 31.80 ppm was appears in the ^{31}P NMR spectra of **16** after addition of Hg^{+2} (Figure 6.2.17b). These ^{31}P NMR spectra of complex and ligand also revealed about the interaction between Hg^{+2} and PPh_2 ligand. Therefore we tentatively suggest the sensing mechanism where Hg^{+2} can be easily interact with **16** and formed an intermediate complex [(Ir(F_2ppy)$_2$(PPh2(CH_2)$_2$PPh2Hg Cl] with Hg^{+2} (Scheme 6.2.2). The experimental HRMS data (mass fragments) are supporting the formation of intermediate complex (Figure 6.2.17c). Further, after addition of four equivalents of Hg^{+2} salt in **16**, the luminescent intensity was quenched and a new complex was isolated from the solution by extraction using DCM and water and characterized by NMR. The ^{1}HNMR spectra of the isolated complex are shown less number of signals as the parent compound **16** (Figure 6.2.18). The signal of the diphenyl substituents in the chelated diphosphine ligand disappear (^{1}H NMR signal between δ=6.2-7.3 ppm) indicating the possibility of the interaction of the phosphine ligand with Hg^{+2} ions. This interaction of Hg^{+2} with the phosphorous atom leads to the detachment of a phosphine ligated mercury complex and the [Ir(F_2ppy)$_2$]$^+$ fragment that further reacts with water giving a new bis-aqua iridium complex[25] [Ir(F_2ppy)$H_2O)_2$]$^+$, **19** (Scheme 6.2.2). To confirm the absence of phosphorus in **19,** it was further studied by ^{31}P NMR spectroscopy which clearly supports the absence of phosphorous in this complex [no P peak at δ=-8.90 ppm-(-12.60 ppm)] (Figure 6.2.19). In addition, the IR spectrum of **19** clearly indicates the presence water molecules (Figure 6.2.19b). This mechanism was further supported by ESI-HRMS measurements on a mixture of complex 16 and 4.0 equiv of Hg^{+2}, the original peak at m/z 1006.1608 assigned complex 16 disappeared and a new signals were observed at m/z 573.0561 and 614.0826 attribute to [Ir(F_2ppy)$_2$]$^+$ and [Ir(F_2ppy)$_2$(ACN)]$^+$ respectively (Figure 6.2.19c) From the above analysis it can be concluded that the *cis*-bis-aquo complex [Ir (F_2ppy) ($H_2O)_2$]$^+$ is formed. The ^{1}H NMR spectrum of 19 in $CDCl_3$ shows six proton signals that match well with [(F_2ppy)$_2$Ir($H_2O)_2$]$^+$ and the ^{19}F proton peak at δ= -107.07 ppm and δ= -109.72 ppm (Figure 6.2.19d) reveal its facial geometry.

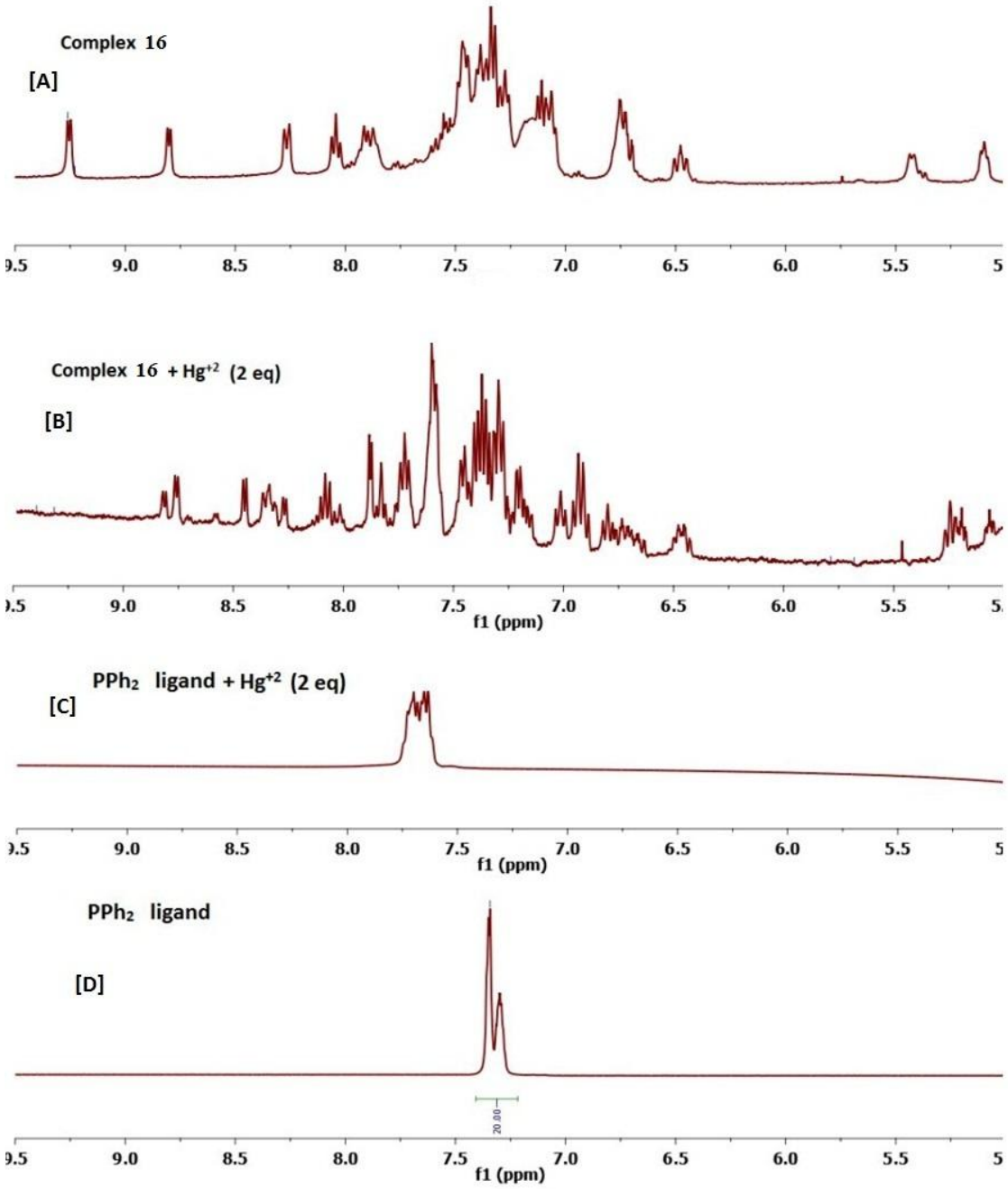
Complex 16
[A]
9.5 9.0 8.5 8.0 7.5 7.0 6.5 6.0 5.5 5
Complex 16 + Hg+2 (2 eq)
[B]
9.0 8.5 8.0 7.5 7.0 6.5 6.0 5.5
f1 (ppm)
PPh2 ligand + Hg+2 (2 eq)
[C]
9.0 8.5 8.0 7.5 7.0 6.5 6.0 5.5
f1 (ppm)
PPh2 ligand
[D]
20.00
9.5 9.0 8.5 8.0 7.5 7.0 6.5 6.0 5.5 5
f1 (ppm)

(a)

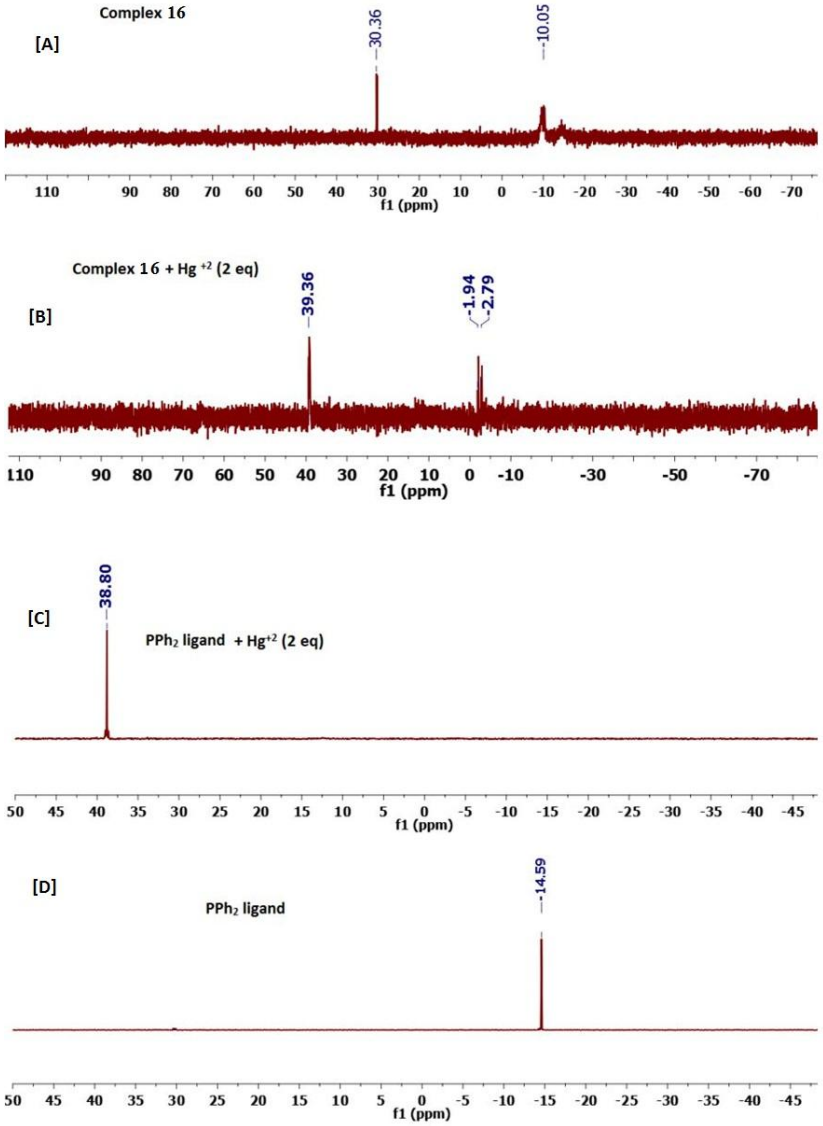
Complex 16
[A]
30.36
-10.05
f1 (ppm)
Complex 16 + Hg +2 (2 eq)
[B]
39.36
-1.94
-2.79
f1 (ppm)
[C]
38.80
PPh2 ligand + Hg+2 (2 eq)
f1 (ppm)
[D]
PPh2 ligand
-14.59
f1 (ppm)

(b)

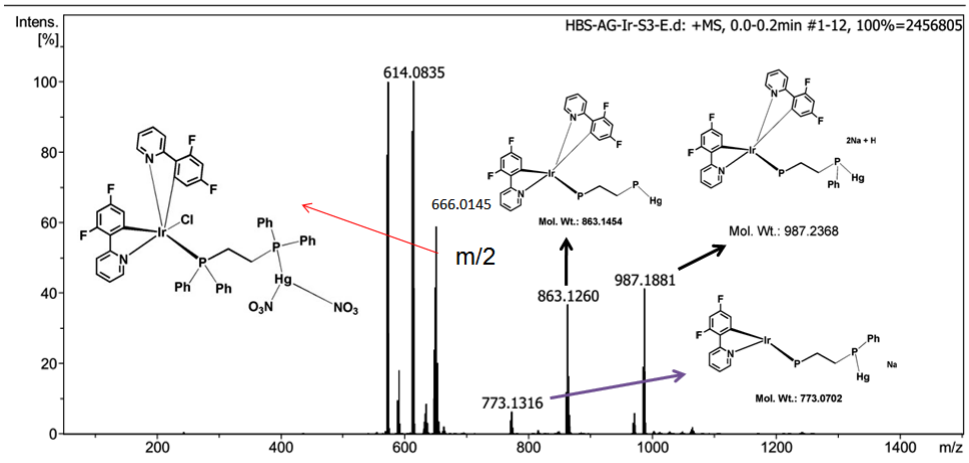
Intens. [%]
HBS-AG-Ir-S3-E.d: +MS, 0.0-0.2min #1-12, 100%=2456805
614.0835
666.0145
m/2
863.1260
773.1316
987.1881
Mol. Wt.: 863.1454
Mol. Wt.: 987.2368
Mol. Wt.: 773.0702
m/z

(c)

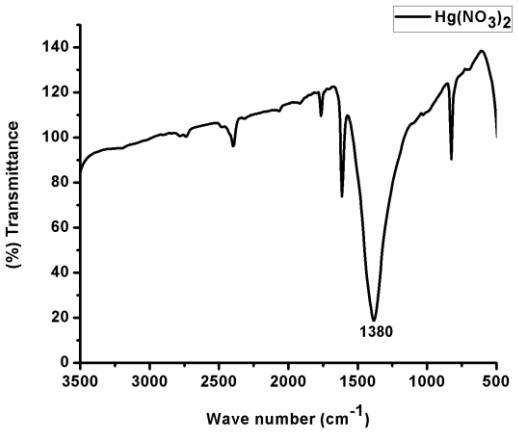

(i)

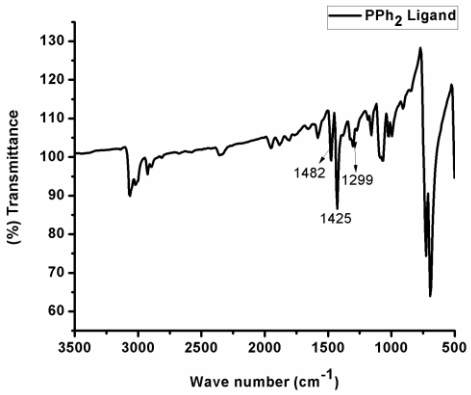

(ii)

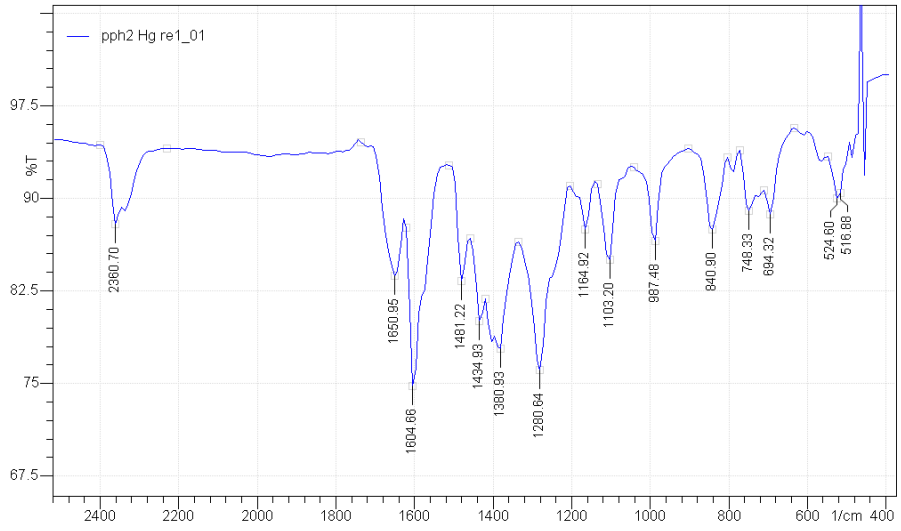

(iii)

(d)

Figure 6.2.17 (a) ^{1}H NMR spectra of PPh_2 ligand and complex **16** with Hg^{+2} in d_6 DMSO. (A) only complex 16; (B) complex **16** + Hg^{+2} (2.0eq) ; (C) PPh_2 ligand+ Hg^{+2} (2.0eq) (D) PPh_2 ligand, (b) ^{31}P NMR spectra of PPh_2 ligand and complex 16 with Hg^{+2} in d_6 DMSO. (A) only complex 16; (B) complex **16** + Hg^{+2} (2.0eq) ; (C) PPh_2 ligand + Hg^{+2} (2.0eq) (D) PPh_2 ligand. (c) HRMS spectra of **16** after using 2 equivalent of Hg^{+2} (d) (i) only $Hg(NO_3)_2$, 1380 cm^{-1} (ii) PPh_2 ligand, 1482, 1299 and 1225 cm^{-1} (iii) PPh_2 + 2 equivalents of Hg^{+2}, 1481, 1434, 1380, and 1280 cm^{-1}

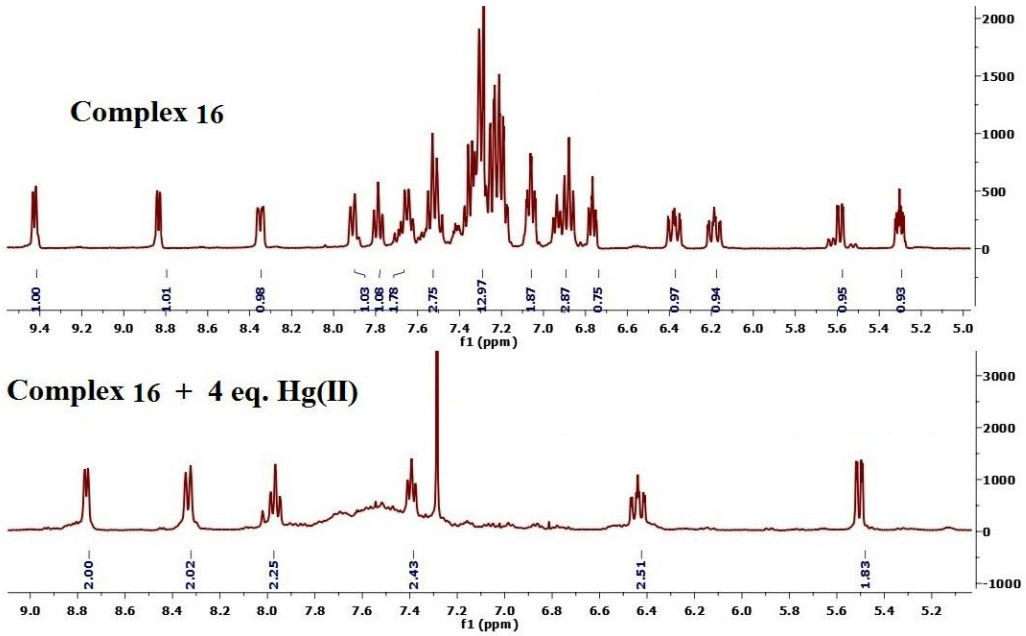

Figure 6.2.18 ^{1}**H** NMR spectra of **16** (Top) and after addition of 4 eq. of Hg^{+2} to **16** (below).

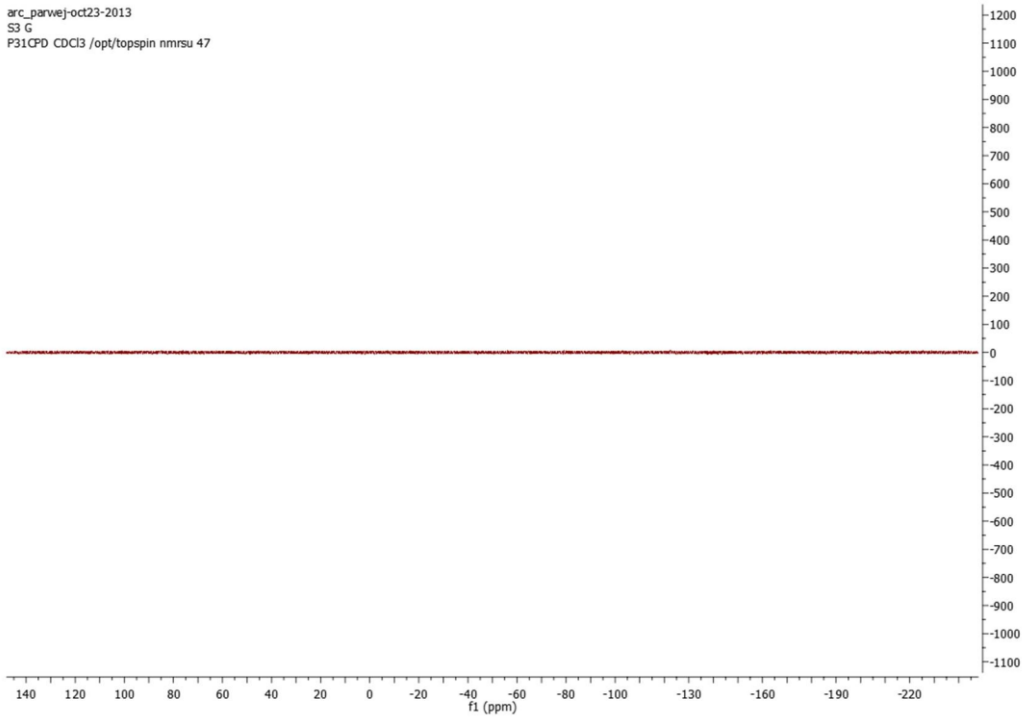

(a)

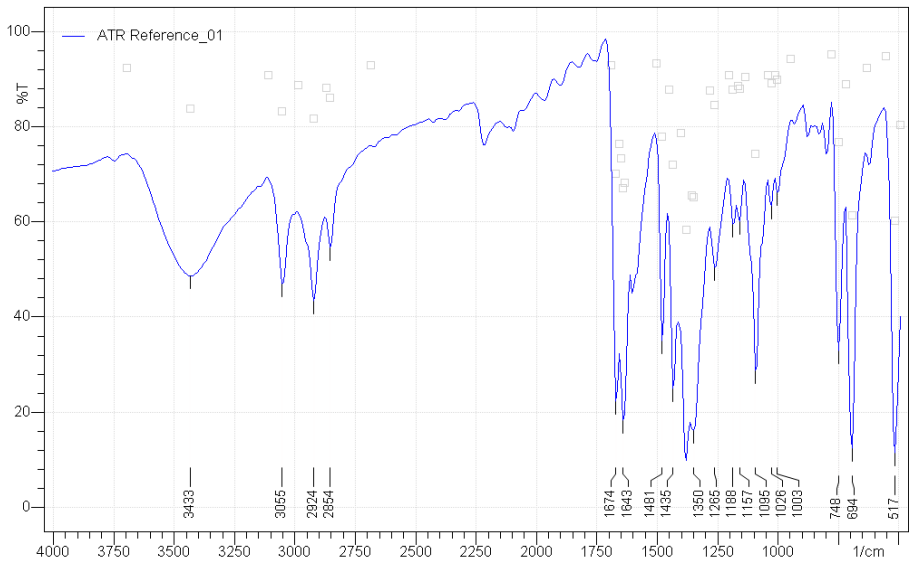
ATR Reference_01
%T
100
80
60
40
20
0
3433
3055
2924
2854
1674
1643
1481
1435
1350
1265
1188
1157
1095
1026
1003
748
694
517
4000
3750
3500
3250
3000
2750
2500
2250
2000
1750
1500
1250
1000
1/cm

(b)

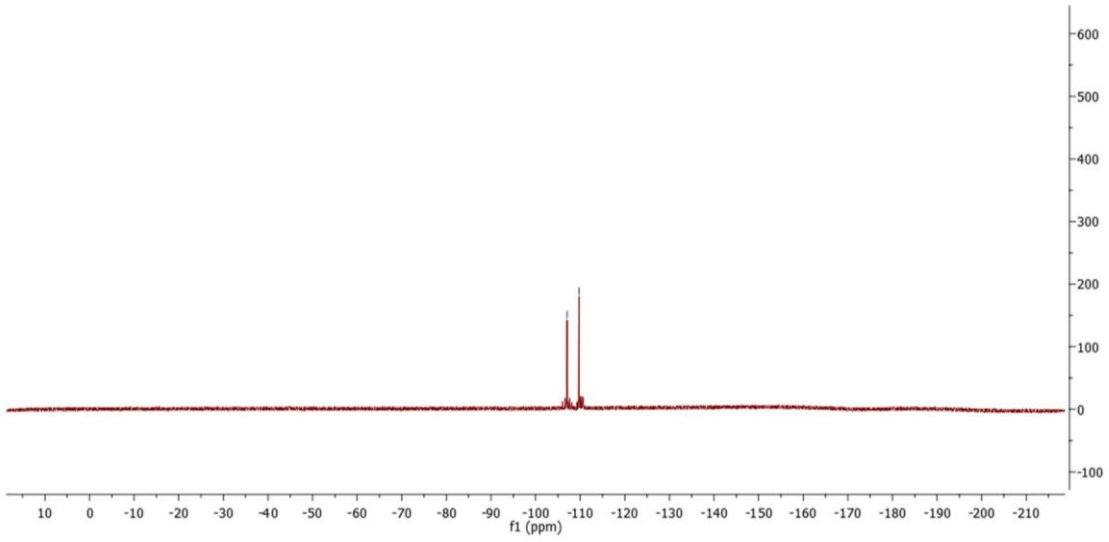
600
500
400
300
200
100
0
-100
10
0
-10
-20
-30
-40
-50
-60
-70
-80
-90
-100
-110
-120
-130
-140
-150
-160
-170
-180
-190
-200
-210
f1 (ppm)

(c)

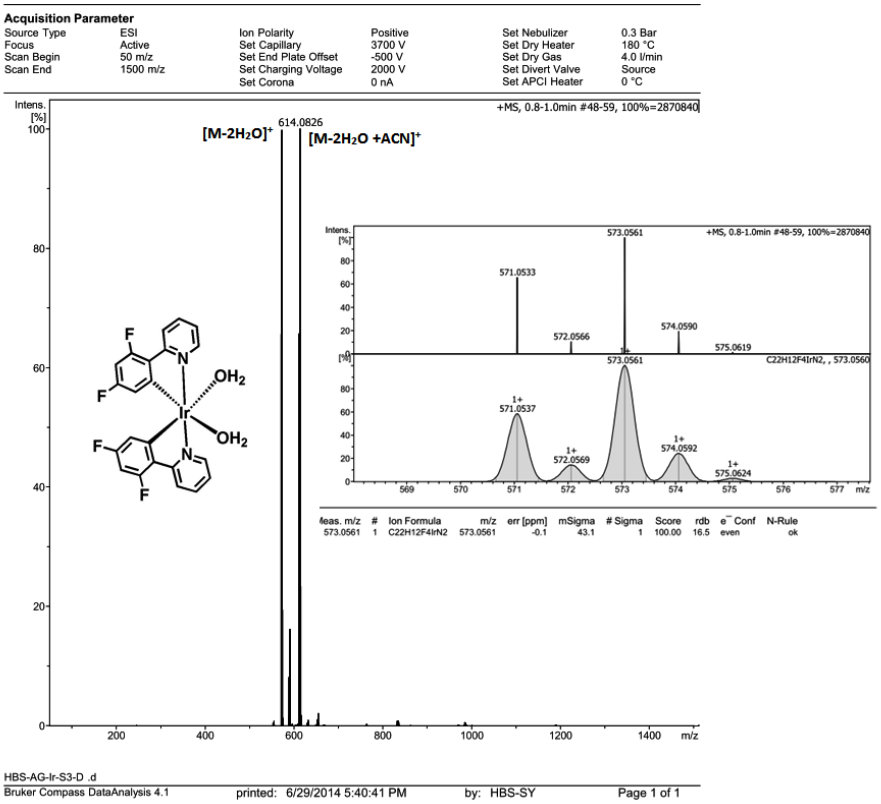

(d)

Figure 6.2.19 (a, b, c and d); ^{31}P, IR, HRMS and ^{19}F NMR spectra of **19**, respectively.

6.3 Syntheses and Characterisations

6.3.1 Syntheses of complexes 8-15

The dichloro-bridged iridium(III) complex, $[(ppy)_2Ir(\mu\text{-}Cl)_2Ir(ppy)_2]$, **8** and the mononuclear iridium(III) complexes (**9-12**, **13-14**, **15**) were synthesized following the conventional routes as described in the literature. Alternatively, these complexes have, also been synthesized, as described below, by an alternative microwave irradiation technique (MW) developed in our laboratory.

6.3.1.1 Synthesis of $[(ppy)_2Ir(\mu\text{-}Cl)_2Ir(ppy)_2]$, 8: Iridium(III)chloride hydrate (0.17 mmol) and 2-phenyl pyridine (0.33 mmol) were dissolved in 2-ethoxyethanol and water (3:1) in a vial which was afterwards placed in a microwave reactor for 30 min at 135^{0}C. The yellow precipitate that was obtained after half an hour was separated and washed with ethylacetate, hexane and ethanol, successively for several times. Yield, 36%.

6.3.1.2 Synthesis of $[Ir(ppy)_2(dppel/dppp/dppe/phnan)](PF_6)$, (9-12) and **$[Ir(ppy)_2(acac/pic)]$,** (**13-14**): 0.09 mmol of **8**, 0.18 mmol ancillary ligands and ~85-90 mg of sodium carbonate were mixed in 2-ethoxyethanol in a vial and placed into a microwave reactor (MW) for 15 min maintaining the temperature at 135^0C. Then, the solvent was evaporated under reduced pressure and the crude product collected. This crude product and KPF_6 were dissolved into (1:1) MeOH/acetone and put again into the MW for further 15 min for ion-exchange. Afterwards, the crude product was purified by column chromatography (100-200 mess of silica gel). Yield, 72-82%. The counter ion, chlorides from the ionic complexes were exchanged with PF_6^-. In a vial, 1eq. of chloride complex and 2eq. of KPF_6 were dissolved in the mixture of methanol and acetone (1:1) and the reaction mixture was placed in a microwave reactor at 65^0C for 15 min. Then, the solvent was evaporated under reduced pressure and the product purified by column chromatography. Yield, 70-95%.

6.3.1.3 Synthesis of $[Ir(ppy)_2(Cl)PPh_3]$, 15: In a vial, 0.09 mmol **8**, 0.18 mmol triphenylphosphine and ~85-90 mg sodium carbonate were mixed in 2-ethoxyethanol and the mixture introduced in the MW at135^0C for 15 min. Then, the solvent was evaporated under reduced pressure and the crude product was collected and purified by column chromatography. Yield, 53%.

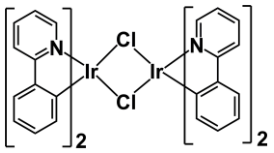

^{1}H and ^{13}C NMR spectra of the complex **8** (above, MW and below, conventional); ^{1}H NMR (400 MHz, $CDCl_3$) δ 9.17 (d, J = 4.9 Hz, 1H), 7.80 (d, J = 7.9 Hz, 1H), 7.72 – 7.59 (m, 1H), 7.41 (dd, J = 7.8, 1.1 Hz, 1H), 6.76 – 6.59 (m, 2H), 6.55 – 6.39 (m, 1H), 5.86 (dd, J = 7.8, 0.8 Hz, 1H), for MW route; ^{13}C NMR (101 MHz, $CDCl_3$) 13C NMR (101 MHz, $CDCl_3$) δ 168.72, 151.69, 145.22, 143.70, 136.17, 130.59, 129.10, 123.66, 122.13, 121.32, 118.41. ^{1}H NMR (400 MHz, $CDCl_3$) δ 9.16 (d, J = 5.7 Hz, 1H), 8.94 (s, 1H), 8.30 (s, 1H), 8.13 (s, 1H), 8.01 (s, 1H), 7.80 (d, J = 7.9 Hz, 1H), 7.67 (dd, J = 11.3, 4.1 Hz, 1H), 7.58 (s, 1H), 7.42 (t, J = 9.0 Hz, 1H), 6.67 (dd, J = 13.3, 6.4 Hz, 2H), 6.52 – 6.37 (m, 1H), 5.85 (d, J = 7.2 Hz, 1H). ; ^{13}C NMR (101 MHz, $CDCl_3$) δ 168.39, 151.68, 143.68, 136.18, 130.69, 129.93, 129.06, 128.46, 123.66, 122.03, 121.37, 121.35, 118.41, for conventional route.

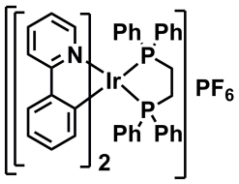

^{1}H NMR and ^{31}P NMR spectra of the complex **9** (above, MW and below, conventional); ^{1}H NMR (400 MHz, $CDCl_3$) (400 MHz, $CDCl_3$) δ 8.48 (m, J = 56.4 Hz, 2H), 7.68 (t, J = 8.5 Hz, 4H), 7.48 – 7.23 (m, 14H), 6.99 – 6.89 (m, 2H), 6.93 – 6.83 (m, 4H), 6.75 (t, J = 6.7 Hz, 4H), 6.46 (t, J = 8.8 Hz, 4H), 6.21 (dd, J = 9.6, 3.6 Hz, 4H), and ^{31}P NMR (MHz) δ 20.51 for MW route. ^{1}H NMR (400 MHz, $CDCl_3$) δ 8.50 (m, J = 56.4 Hz, 2H), 7.70 (t, J = 8.3 Hz, 4H), 7.51 – 7.23 (m, 14H), 6.98 (m, J = 16.2, 9.0 Hz, 2H), 6.96 – 6.84 (m, 4H), 6.77 (t, J = 6.8 Hz, 4H), 6.48 (t, J = 8.7 Hz, 4H), 6.22 (t, J = 5.8 Hz, 4H). ^{31}P NMR (MHz) δ 20.51 for conventional route.

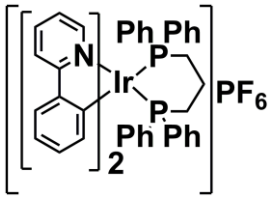

^{1}H and ^{31}P NMR spectra of the complex **10** (above, MW and below, conventional); ^{1}H NMR (400 MHz, $CDCl_3$) δ 8.68 (d, J = 5.8 Hz, 1H), 8.18 (d, J = 5.4 Hz, 1H), 8.01 (dd, J = 13.0, 8.4 Hz, 1H), 7.63 (t, J = 8.3 Hz, 3H), 7.44 (dt, J = 14.6, 6.1 Hz, 13H), 7.38 – 7.21 (m, 4H), 7.10 – 6.94 (m, 6H), 6.94 – 6.68 (m, 3H), 6.61 (dt, J = 12.0, 6.2 Hz, 2H), 6.26 – 6.21 (m, 1H), 5.97 (d, J = 6.2 Hz, 1H), 2.92 (dd, J = 114.3, 35.6 Hz, 4H), 2.03 (m, 2H). ^{31}P NMR (162 MHz, $CDCl_3$) δ -31.61, for MW route; ^{1}H NMR (400 MHz, $CDCl_3$) δ 8.67 (d, 1H), δ 8.18 (d, J = 5.5 Hz, 1H), 8.01 (dd, J = 12.1, 7.6 Hz, 1H), 7.62 (t, J = 8.0 Hz, 2H), 7.44 (dt, J = 15.2, 7.3 Hz, 5H), 7.38 – 7.21 (m, 8H), 7.02 (m, 7H), 6.93 – 6.69 (m, 5H), 6.60 (dt, J = 13.4, 6.4 Hz, 2H), 6.53 – 6.43 (m, 1H), 6.29 (t, J = 8.3 Hz, 1H), 6.24 (s, 1H), 5.96 (d, J = 6.6 Hz, 1H), 2.91 (dd, J = 109.4, 37.0 Hz, 4H), 2.13 – 1.72 (m, 2H). ^{31}P NMR (162 MHz, $CDCl_3$) δ -31.10, for conventional route.

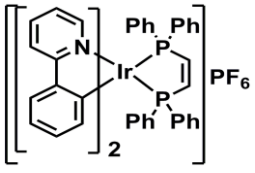

^{1}H and ^{31}P NMR spectra of the complex **11** (conventional); ^{1}H NMR (400 MHz, $CDCl_3$) δ 7.62 (m, 5H), 7.53 (m, 4H), 7.37 (m, 3H), 7.33 – 7.28 (m, 2H), 7.24 (t, J = 6.2 Hz, 4H), 6.98 (m, 2H), 6.90 (m, 4H), 6.82 (t, J = 6.8 Hz, 4H), 6.58 (t, J = 8.5 Hz, 4H), 6.31 – 6.21 (m, 4H), 3.82 (m, 2H), 2.74 (d, J = 9.9 Hz, 2H), and ^{31}P NMR (MHz) δ 10.68 for MW route. ^{1}H NMR (400 MHz, $CDCl_3$) δ 7.62 (dd, J = 16.1, 7.3 Hz, 5H), 7.55 – 7.48 (m, 4H), 7.38 (t, J = 7.8 Hz, 3H), 7.30 (t, J = 10.5, 4.2 Hz, 2H), 7.23 (m, 6H), 6.98 (t, J = 7.2 Hz, 2H), 6.90 (m, 4H), 6.82 (dd, J = 7.6, 5.8 Hz, 4H), 6.58 (t, J = 8.5 Hz, 3H), 6.26 (m, 3H), 3.82

(m, J = 29.2, 9.9 Hz, 2H), 2.74 (d, J = 9.9 Hz, 2H). ^{31}P NMR (MHz) δ 10.68 for conventional route.

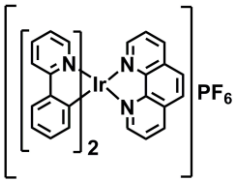

^{1}H NMR spectra of the complex **12** (MW in above and conventional in below); ^{1}H NMR (400 MHz, $CDCl_3$) δ 8.94 (d, J = 4.8 Hz, 1H), 8.61 (d, J = 7.9 Hz, 1H), 8.38 – 8.27 (m, 1H), 8.22 – 8.14 (m, 1H), 8.14 – 8.04 (m, 2H), 7.96 (d, J = 8.9 Hz, 1H), 7.88 – 7.48 (m, 9H), 7.36 – 7.24 (m, 2H), 7.18 – 7.10 (m, 2H), 7.08 – 6.96 (m, 1H), 6.96 – 6.87 (m, 1H), 6.84 (m, 1H), 6.34 (t, J = 7.3 Hz, 1H). (for MW route; ^{1}H NMR (400 MHz, $CDCl_3$) δ 8.94 (d, J = 4.8 Hz, 1H), 8.64 – 8.53 (m, 1H), 8.34 (m, 2H), 8.20 (m, J = 3.8 Hz, 1H), 8.13 – 8.03 (m, 2H), 7.96 (d, J = 8.9 Hz, 1H), 7.88 – 7.46 (m, 9H), 7.38 – 7.23 (m, 2H), 7.19 – 7.05 (m, 1H), 7.11 – 6.99 (m, 1H), 6.89 (s, 1H), 6.84 (s, 1H), 6.34 (d, J = 6.6 Hz, 1H). for conventional route.

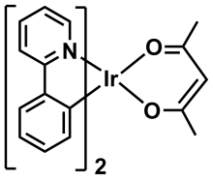

^{1}H and ^{13}C NMR spectra of the complex **13** (MW in above and conventional in below); ^{1}H NMR (400 MHz, $CDCl_3$) δ 8.77 – 8.64 (d, 1H), 8.26 (d, J = 7.3 Hz, 1H), 7.85 –7.74 (m, 3H), 7.73 – 7.68 (m, 1H), 7.68 – 7.61 (m, 2H), 7.53 (m, 2H), 7.40 (dd, J = 5.8, 0.8 Hz, 1H), 7.26 (m, 1H), 7.07 (m, 1H), 6.92 – 6.62 (m, 5H), 6.34 (d, J = 7.6, 0.8 Hz, 1H), 6.12 (d, J = 7.6, 0.8 Hz, 1H). and ^{13}C NMR (101 MHz, $CDCl_3$) δ 148.89, 148.30, 147.94, 137.57, 132.37, 129.87, 129.45, 128.26, 127.81, 124.36, 124.00, 122.30, 121.93, 121.51, 121.05, 119.08, 118.43 for MW route; ^{1}H NMR (400 MHz, $CDCl_3$) δ 8.77 – 8.64 (d, 1H), 8.26 (d, J = 7.3 Hz, 1H), 7.85 – 7.74 (m, 3H), 7.73 – 7.68 (m, 1H), 7.68 – 7.61 (m, 2H), 7.53 (m, 2H), 7.40 (dd, J = 5.8, 0.8 Hz, 1H), 7.26 (m, J = 7.5, 5.3, 1.4 Hz, 1H), 7.07 (m, J = 7.3, 5.8, 1.4 Hz, 1H), 6.92 – 6.62 (m, 5H), 6.34 (d, J = 7.6, 0.8 Hz, 1H), 6.12 (d, J = 7.6, 0.8 Hz, 1H) ; ^{13}C NMR (101 MHz, $CDCl_3$) δ 148.89, 148.30, 147.94, 137.57, 132.37, 129.87, 129.45, 128.26, 127.81, 124.36, 124.00, 122.30, 121.93, 121.51, 121.05, 119.08, 118.43 for conventional route.

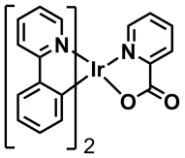

^{1}H and ^{13}C NMR spectra of the complex **14** (MW in above and conventional in below); ^{1}H NMR (400 MHz, $CDCl_3$) δ 8.44 (d, *J* = 5.6 Hz, 2H), 7.77 (d, *J* = 8.1 Hz, 2H), 7.69 – 7.60 (m, 2H), 7.47 (d, *J* = 7.7 Hz, 2H), 7.11 – 6.97 (m, 2H), 6.78 – 6.67 (m, 2H), 6.61 (m, *J* = 7.5, 1.2 Hz, 2H), 6.19 (d, *J* = 7.5 Hz, 2H), 5.14 (s, 1H), 1.71 (s, 6H). and ^{13}C NMR (101 MHz, $CDCl_3$) δ 184.60, 168.61, 148.18, 147.60, 144.73, 136.80, 133.05, 129.11, 123.81, 121.43, 120.72, 118.39, 100.39, 28.78 for MW route; ^{1}H NMR (400 MHz, $CDCl_3$) δ 8.41 (d, J = 5.6 Hz, 2H), 7.74 (d, J = 8.1 Hz, 2H), 7.66 – 7.56 (m, 2H), 7.47 – 7.42 (m, 2H), 7.08 – 6.96 (m, 2H), 6.75 – 6.64 (m, 2H), 6.59 (m, 1H), 6.17 (d, *J* = 7.5 Hz, 2H), 5.18 (d, *J* = 32.3 Hz, 1H), 1.69 (s, 6H) and ^{13}C NMR (101 MHz, $CDCl_3$) δ 184.61, 168.60, 148.18, 147.59, 144.73, 136.81, 133.05, 129.11, 123.81, 121.43, 120.72, 118.40, 100.41, 28.78.

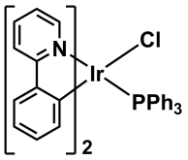

^{1}H and ^{31}PNMR spectra of the complex **15** (MW in above and conventional in below); 1H NMR (400 MHz, $CDCl_3$) δ 9.25 (d, J = 5.9 Hz, 1H), 8.81 (d, J = 5.4 Hz, 1H), 7.83 (dd, J = 13.0, 4.8 Hz, 1H), 7.69 – 7.59 (m, 1H), 7.56 – 7.44 (m, 2H), 7.45 – 7.35 (m, 3H), 7.17 (m, 9H), 7.05 (m, 6H), 6.86 – 6.60 (m, 4H), 6.54 – 6.43 (m, 1H), 5.88 – 5.68 (m, 2H). ^{31}P NMR (MHz) δ -2.01. for MW route; ^{1}H NMR (400 MHz, $CDCl_3$) δ 9.24 (d, J = 5.4 Hz, 1H), 8.81 (d, J = 5.7 Hz, 1H), 7.90 – 7.78 (m, 1H), 7.69 – 7.59 (m, 1H), 7.55 – 7.45 (m, 3H), 7.45 – 7.34 (m, 3H), 7.27 – 7.12 (m, 9H), 7.05 (m, J = 7.7, 1.8 Hz, 6H), 6.83 – 6.58 (m, 4H), 6.53 – 6.42 (m, 1H), 5.89 – 5.72 (m, 2H).

6.3.1.4 General Synthesis Syntheses of **16 and 17**

In a two-necked round bottom flask (50 ml), diphosphine ligands [L_1/L_2] (0.087 mmol) and ([dfppy)$_2$Ir(μ-Cl)]$_2$ (0.087 mmol) were dissolved in 20 mL DCM. The mixture was stirred at room temperature for 2 minutes under an atmosphere of N_2 gas. The solution mixture was evaporated to dryness and the residue purified by column chromatography using DCM-Hexane (30:70) as the as the eluent, getting a green solid product (**Scheme 6.2.1**).

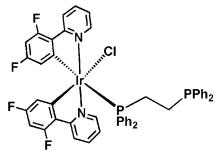

^{1}H NMR (400 MHz, $CDCl_3$) δ 9.43 (d, *J* = 5.9 Hz, 1H), 8.83 (d, *J* = 4.8 Hz, 1H), 8.35 (dd, *J* = 8.2, 2.4 Hz, 1H), 7.90 (t, *J* = 8.2 Hz, 1H), 7.79 (t, *J* = 8.0 Hz, 1H), 7.73 – 7.58 (m, 2H), 7.60 – 7.45 (m, 3H), 7.45 – 7.13 (m, 13H), 7.06 (td, *J* = 7.9, 2.1 Hz, 2H), 6.98 – 6.82 (m, 3H), 6.80 – 6.71 (m, 1H), 6.38 (ddd, *J* = 12.7, 9.0, 2.3 Hz, 1H), 6.25 – 6.13 (m, 1H), 5.59 (dd, *J* = 9.0, 2.0 Hz, 1H), 5.30 (ddd, *J* = 8.2, 5.6, 2.4 Hz, 1H), 2.78 – 1.91 (m, 2H), 1.89 – 1.66 (m, 2H). ^{19}F NMR (376 MHz, $CDCl_3$) δ -107.36, -107.38, -107.39, -107.41, -107.51, -107.53, -107.54, -107.56, -108.13, -108.14, -108.15, -108.16, -109.78, -109.81, -109.83, -109.87, -109.89, -109.92, -110.01, -110.04, -110.13, -110.16. ^{31}P NMR (162 MHz, $CDCl_3$) δ -8.90, -8.95, -9.00, -9.10, -9.15, -9.20, -12.07, -12.27, -12.67. Anal. calcd for $C_{48}H_{36}ClF_4IrN_2P_2$: C, 57.28; H, 3.61; N, 2.78; Found: C, 57.10; H, 3.57; N, 2.75; HRMS calculated: ($[M\text{-}Cl]^+$): m/z 971.1919 found: ($[M\text{-}Cl]^+$), m/z 971.1892; Green solid; Yield 68.49% for **16**.

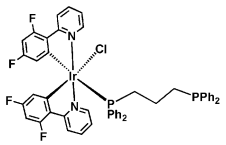

^{1}H NMR (400 MHz, $CDCl_3$) δ 9.45 (d, *J* = 5.5 Hz, 1H), 8.74 (d, *J* = 5.6 Hz, 1H), 8.33 (dd, *J* = 7.7, 3.2 Hz, 1H), 7.96 (dd, *J* = 32.1, 8.5 Hz, 1H), 7.82 – 7.57 (m, 3H), 7.57 – 7.39 (m, 4H), 7.39 – 7.19 (m, 10H), 7.05 (m, 7H), 6.66 (dt, *J* = 12.1, 6.4 Hz, 1H), 6.38 (ddd, *J* = 12.7, 9.1, 2.2 Hz, 1H), 6.31 – 6.10 (m, 1H), 5.61 (ddd, *J* = 14.8, 8.9, 1.9 Hz, 1H), 5.40 – 5.23 (m, 1H), 2.68 (m, 2H), 2.31 – 2.05 (m, 2H), 2.03 – 1.77 (m, 2H) . ^{19}F NMR (376 MHz, $CDCl_3$) δ -107.46, -107.48, -107.48, -107.50, -107.53, -107.54, -107.55, -107.57, -107.59, -108.22, -108.25, -108.35, -108.38, -109.83, -109.85, -109.88, -109.91, -109.93, -109.97, -110.00, -110.13, -110.15. ^{31}P NMR (162 MHz, $CDCl_3$) δ -12.43, -12.94, -12.99, -13.04, -17.56, -18.27. Anal. calcd for $C_{49}H_{38}ClF_4IrN_2P_2$: C, 57.67; H, 3.75; N, 2.75; Found: C, 57.50; H, 3.70; N, 2.68, HRMS calculated: ($[M\text{-}Cl]^+$): m/z 985.2076 found: ($[M\text{-}Cl]^+$), m/z 985.2066; Green solid; Yield 54.79% for **17**.

6.3.1.5 Synthesis of Synthesis of 18

Complex **17** (equimolar) and $[dfppy_2Ir(\mu\text{-}Cl)]_2$ were added in stirred solution of DCM at room temperature for 5 minutes. The product was purified using 60-120 mesh silica gel, DCM as eluent, getting a green product (Scheme 6.2.1).

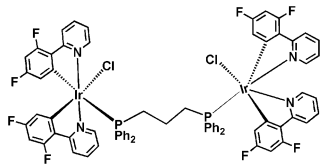

^{1}H NMR (400 MHz, $CDCl_3$) δ 9.43 (d, *J* = 6.0 Hz, 1H), 9.30 (d, *J* = 5.8 Hz, 1H), 8.56 (d, *J* = 5.8 Hz, 2H), 8.31 (dd, *J* = 7.9, 4.2 Hz, 2H), 7.96 (d, *J* = 8.6 Hz, 1H), 7.88 (d, *J* = 8.6 Hz, 1H), 7.76 – 7.60 (m, 5H), 7.31 (d, *J* = 8.3 Hz, 6H), 7.19 (ddd, *J* = 18.4, 15.3, 8.1 Hz, 5H), 7.10 – 6.99 (m, 3H), 6.99 – 6.84 (m, 1H), 6.80 (t, *J* = 8.3 Hz, 3H), 6.49 (t, *J* = 6.1 Hz, 1H), 6.37 (ddd, *J* = 13.6, 5.5, 2.2 Hz, 3H), 6.28 – 6.14 (m, 1H), 5.59 (dd, *J* = 8.9, 2.0 Hz, 1H), 5.52 (dd, *J* = 8.8, 1.9 Hz, 1H), 5.27 (tdd, *J* = 8.2, 5.7, 2.3 Hz, 2H), 2.61 – 2.28 (m, 4H), 1.78 (d, *J* = 6.0 Hz, 2H), ^{31}P NMR (162 MHz, $CDCl_3$) δ -11.96, -12.46. HRMS calculated: ($[M\text{-}C_{22}F_4N_2ClIr]^+$): m/z 1021.1842 found: ($[M\text{-}C_{22}F_4N_2ClIr]^+$ m/z 1021.1831 .

6.3.1.6 Synthesis of Synthesis of 19

$Hg(NO_3)_2$ (4 moles) was added to a stirred solution of **16** (1 mole) dissolved in a mixture of water and DMF (7 : 3). The reaction was completed in very short period of time (~1 minute). The reaction mixture was washed by cold water and extracted by DCM. The organic layer was dried over Na_2SO_4 and evaporated under reduced pressure resulting in a light yellow product (Scheme 6.2.2).

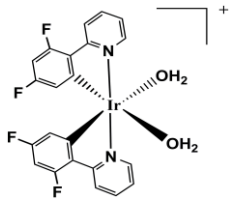

^{1}H NMR (400 MHz, $CDCl_3$) δ 8.76 (d, *J* = 5.6 Hz, 2H), 8.33 (d, *J* = 8.4 Hz, 2H), 7.97 (t, *J* = 7.7 Hz, 2H), 7.41 – 7.37 (m, 2H), 6.44 (ddd, *J* = 11.8, 9.2, 2.3 Hz, 2H), 5.51 (dd, *J* = 8.7, 2.2 Hz, 2H), 1.67 (s, 6H). ^{19}F NMR (376 MHz, $CDCl_3$) δ -107.07, -109.72. Anal. calcd for $C_{22}H_{16}ClF_4IrN_2O_2$: C, 41.03; H, 2.50; N, 4.35; Found: C, 40.51; H, 2.79; N, 4.32, HRMS calculated: ($[M\text{-}2H_2O]^+$), m/z 573.0566 and ($[M\text{-}2H_2O+ACN]^+$): m/z 614.0831 found: ($[M\text{-}2H_2O]^+$), ($[M\text{-}2H_2O+ACN]^+$) : m/z 614.0826, Light yellow solid; Yield 16.00% for **19**.

6.4 Conclusions

The inclusion of a strong π-acceptor chelating ligand (PPh_2) in iridium(III) 2-phenylpyridyl complexes induces wide shifts of the maximum emission wavelength (λ_{max}) towards the blue-region of the spectrum, although λ_{max} remains almost unchanged on changing the ring size / conjugation in the ancillary ligand. Both

photoluminescence experiments and computational calculations support the nature of the lowest excited state which arises from the admixture of ^{3}MLCT and $^3\pi$-π^* excitations with major contribution from the latter. We have shown in this report that these types of complexes may be synthesized, in a more facile, greener way through a MW irradiation technique. This alternative MW-based synthetic technique has also been shown to be suitable for the synthesis of other iridium(III) complexes with different ancillary ligands. This fact hints that the new technique proposed here can be tested to obtain the other cyclometalated iridium(III) complexes potentially useful in OLED devices in a much faster and clean process.

We have demonstrated a strategic design of a new blue emitting AIE active iridium(III) complexes with appended free phosphorous atoms that selectively interact with Hg^{+2} ions and has been used in the efficient detection of mercury(II) ion from environmental samples. The detection limit of mercury(II) from solution went to 170 nM which demonstrates the efficiency of the probe molecules as mercury(II) sensors. Hence, these types iridium based probe molecules can be considered as an efficient chemodosimeter for Hg^{+2}.

6.5 References

[1] H.-Y. Li, L. Zhou, M.-Y. Teng, Q.-L. Xu, C. Lin, Y.-X. Zheng, J.-L. Zuo, H.-J. Zhang, X.-Z. You, J. Mater. Chem. C, 1 (2013) 560-565.

[2] G. Li, T. Fleetham, E. Turner, X.-C. Hang, J. Li, Adv. Opt. Materials, 3 (2015) 390-397.

[3] D. Kourkoulos, C. Karakus, D. Hertel, R. Alle, S. Schmeding, J. Hummel, N. Risch, E. Holder, K. Meerholz, Dalton Trans., 42 (2013) 13612-13621.

[4] F. Kessler, Y. Watanabe, H. Sasabe, H. Katagiri, M.K. Nazeeruddin, M. Gratzel, J. Kido, J. Mater. Chem. C, 1 (2013) 1070-1075.

[5] J.A. Gareth Williams, S. Develay, D.L. Rochester, L. Murphy, Coord. Chem. Rev., 252 (2008) 2596-2611.

[6] A.B. Tamayo, B.D. Alleyne, P.I. Djurovich, S. Lamansky, I. Tsyba, N.N. Ho, R. Bau, M.E. Thompson, J. Am. Chem. Soc., 125 (2003) 7377-7387.

[7] A. Tsuboyama, H. Iwawaki, M. Furugori, T. Mukaide, J. Kamatani, S. Igawa, T. Moriyama, S. Miura, T. Takiguchi, S. Okada, M. Hoshino, K. Ueno, J. Am. Chem. Soc., 125 (2003) 12971-12979.

[8] Y. You, W. Nam, Chem. Soc. Rev., 41 (2012) 7061-7084.

[9] L. Chen, H. You, C. Yang, D. Ma, J. Qin, Chem. Commun., (2007) 1352-1354.

[10] S.J. Lee, K.-M. Park, K. Yang, Y. Kang, Inorg. Chem., 48 (2009) 1030-1037.

[11] S.J. Yeh, M.F. Wu, C.T. Chen, Y.H. Song, Y. Chi, M.H. Ho, S.F. Hsu, C.H. Chen, Adv. Mater., 17 (2005) 285-289.

[12] H.H. Harris, I.J. Pickering, G.N. George, Science, 301 (2003) 1203-1203.

[13] D.W. Boening, Chemosphere, 40 (2000) 1335-1351.

[14] C. Wang, K.M.-C. Wong, Inorg. Chem., 50 (2011) 5333-5335.

[15] A. Pucci, F. Di Cuia, F. Signori, G. Ruggeri, J. Mater. Chem., 17 (2007) 783-790.

[16] Q. Zhao, S. Liu, F. Li, T. Yi, C. Huang, Dalton Trans., (2008) 3836-3840.

[17] Y. Wu, H. Jing, Z. Dong, Q. Zhao, H. Wu, F. Li, Inorg. Chem., 50 (2011) 7412-7420.

[18] H.-F. Shi, S.-J. Liu, H.-B. Sun, W.-J. Xu, Z.-F. An, J. Chen, S. Sun, X.-M. Lu, Q. Zhao, W. Huang, Chem. Eur. J., 16 (2010) 12158-12167.

[19] Q. Zhao, T. Cao, F. Li, X. Li, H. Jing, T. Yi, C. Huang, Organometallics, 26 (2007) 2077-2081.

[20] H. Yang, J. Qian, L. Li, Z. Zhou, D. Li, H. Wu, S. Yang, Inorg. Chim. Acta, 363 (2010) 1755-1759.

[21] F. Lu, M. Yamamura, T. Nabeshima, Dalton Trans., 42 (2013) 12093-12100.

[22] F. Yan, Q. Mei, L. Wang, B. Tong, Z. Xu, J. Weng, L. Wang, W. Huang, Inorg. Chem. Commun., 22 (2012) 178-181.

[23] B. Tong, Y. Zhang, Z. Han, D. Chen, Q.-F. Zhang, Inorg. Chem. Commun., 28 (2013) 31-36.

[24] Y. Liu, M. Li, Q. Zhao, H. Wu, K. Huang, F. Li, Inorg. Chem., 50 (2011) 5969-5977.

[25] Y. Chi, P.-T. Chou, Chem. Soc. Rev., 39 (2010) 638-655.

[26] S. Lamansky, P. Djurovich, D. Murphy, F. Abdel-Razzaq, H.-E. Lee, C. Adachi, P.E. Burrows, S.R. Forrest, M.E. Thompson, J. Am. Chem. Soc., 123 (2001) 4304-4312.

[27] B.-S. Du, C.-H. Lin, Y. Chi, J.-Y. Hung, M.-W. Chung, T.-Y. Lin, G.-H. Lee, K.-T. Wong, P.-T. Chou, W.-Y. Hung, H.-C. Chiu, Inorg. Chem., 49 (2010) 8713-8723.

[28] C.-H. Lin, Y. Chi, M.-W. Chung, Y.-J. Chen, K.-W. Wang, G.-H. Lee, P.-T. Chou, W.-Y. Hung, H.-C. Chiu, Dalton Trans., 40 (2011) 1132-1143.

[29] C.-H. Yang, M. Mauro, F. Polo, S. Watanabe, I. Muenster, R. Fröhlich, L. De Cola, Chem. Mater., 24 (2012) 3684-3695.

[30] Y.-C. Chiu, C.-H. Lin, J.-Y. Hung, Y. Chi, Y.-M. Cheng, K.-W. Wang, M.-W. Chung, G.-H. Lee, P.-T. Chou, Inorg. Chem., 48 (2009) 8164-8172.

[31] C. Jiang, Y.-S. Wen, L.-K. Liu, T.S.A. Hor, Y.K. Yan, J. Orgmetal. Chem., 590 (1999) 138-148.

[32] K.A. Giffin, D.J. Harrison, I. Korobkov, R.T. Baker, Organometallics, 32 (2013) 7424-7430.

[33] F. Zhang, L. Wang, S.-H. Chang, K.-L. Huang, Y. Chi, W.-Y. Hung, C.-M. Chen, G.-H. Lee, P.-T. Chou, Dalton Trans., 42 (2013) 7111-7119.

[34] M.G. Haghighi, M. Rashidi, S.M. Nabavizadeh, S. Jamali, R.J. Puddephatt, Dalton Trans., 39 (2010) 11396-11402.

[35] P. Alam, P. Das, C. Climent, M. Karanam, D. Casanova, A.R. Choudhury, P. Alemany, N.R. Jana, I.R. Laskar, J. Mater. Chem. C, 2 (2014) 5615-5628.

[36] X. Zhang, Z. Chi, X. Zhou, S. Liu, Y. Zhang, J. Xu, J. Phys. Chem. C, 116 (2012) 23629-23638.

[37] X. Zhang, Z. Chi, B. Xu, H. Li, Z. Yang, X. Li, S. Liu, Y. Zhang, J. Xu, Dyes Pigm., 89 (2011) 56-62.

[38] L. Zhang, S. Dong, L. Zhu, Chem. Commun., (2007) 1891-1893.

[39] M.-H. Yang, P. Thirupathi, K.-H. Lee, Org. Lett., 13 (2011) 5028-5031.

[40] L.N. Neupane, J.M. Kim, C.R. Lohani, K.-H. Lee, J. Mater. Chem., 22 (2012) 4003-4008.

[41] H. Zeng, F. Yu, J. Dai, H. Sun, Z. Lu, M. Li, Q. Jiang, Y. Huang, Dalton Trans., 41 (2012) 4878-4883.

Chapter VII

Highly Selective Detection of H^+ and OH^- with a Single Emissive Iridium(III) Complex: A Mild Approach to Conversion of Non-AIEE to AIEE Complex

7.1 Introduction

For the detection and estimation of analytes from the environment, different analytical techniques have been used such as, Raman spectroscopy, cyclic voltammetry, gas chromatography, mass spectrometry, electrochemical sensing, photoluminescence (PL) spectroscopy etc [1, 2]. Among the various analytical techniques, fluorescence based detection methods have shown a great deal of interest because of its' higher sensitivity, low response time, portability etc [3-5]. The fluorescence based sensors often suffer from small Stoke shifts and photo-bleaching effect. On this context, development of sensitive phosphorescence cyclometalated complexes of iridium(III) would be a major breakthrough in the field of sensing application.

The hydroxide ion has a great importance in chemical, biological, environmental and atmospheric processes [6]. Worldwide many chemical industries are using hydroxide in several industrial processes [7]. Furthermore, the detection of hydroxides is highly desirable for quality control. A sensitive technique need to develop for sensing hydroxide ions because it is harmful for pH electrodes. It is used to corrode the pH electrodes and make it less sensitive and unstable at high concentrations [8, 9]. A small change in the environmental pH can be a big cause to destroy animal and plant life. The environmental pollution caused by human activities leads to ecological and natural disaster. The prevention and preservation of our living environment become easier by monitoring the pH level [10, 11]. Hence, it is desirable to design an AIE active molecule which can be used in multi-responsive materials.

In the continuous searching of noble AIE active materials at our endeavor, the current work is the extension of our recent work, where the incorporation of a pendent phosphine group has resulted AIE property. In the present work, we have designed and synthesized a cyclometalated iridium(III) complex with incorporating a bulky rotating unit in non-coordinating site of ethane-1, 2-diamine, with anticipating to originate AIE activity. The synthesized complex was found to be AIE inactive, but exposing it to 1M NaOH, a new Ir-hydroxy complex was isolated which exhibited the 'Aggregation Induced Enhanced Emission (AIEE)' activity. Furthermore, the complex was used for highly sensitive detection of OH^- as well as H^+ ions. Additionally, the synthesized complex has been successfully utilized for monitoring the pH of a solution. DFT and

TD-DFT based calculations were performed to investigate the excited state properties and validate certain experimental facts.

7.2 Results and discussion

The introduction of bulky rotating units in a chromophoric entity can be attributed to a strong emission in the solid state because of restricted intramolecular rotation (RIR) of the rotating unit. This phenomenon is termed as AIE or AIEE activity. To keep up this mechanistic pathway active, we have successfully synthesized a bulky group (trityl-) substituted ethylenediamine '(en-trityl)' ligand (L1) where the trityl can be operated as propel-shaped rotor (Scheme 7.1) [12]. The ligand was characterized by ^{1}H NMR and HRMS. The bulky group was incorporated in **1** by the reaction of $Ir_2(F_2ppy)_4Cl_2$ and trityl-substituted ethylenediamine ligand (en-trityl) that produced a *bis*-iridium(III) complex, $[Ir(F_2ppy)_2(en\text{-}trityl)Cl]$ within a short period (3h).

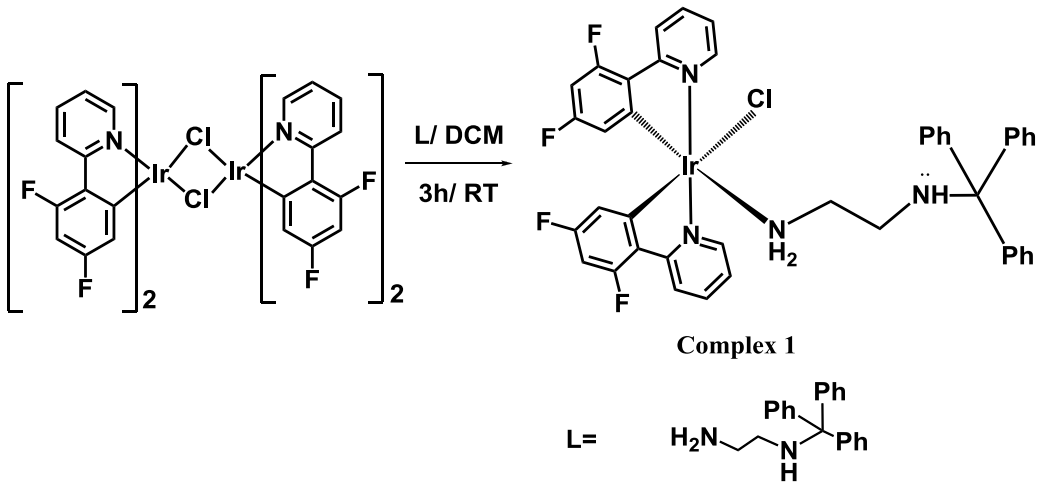

Scheme 7.1 Illustrating the synthetic procedure of **1**

The structure of the complex was characterized by (^{1}H, ^{19}F) NMR, HRMS and finally it was authenticated by single crystal X-ray diffractometer (SCXRD). The ^{1}H NMR spectra of **1** resulted ten different ^{1}H signals in the aromatic region (δ = 9.9 -5.73 ppm) (Figure 7.1) which confirmed the unsymmetrical nature of the complex. The ^{19}F NMR spectra showed triplet of doublet (td) peaks which appeared because of N-F coupling (Figure 7.2). From HRMS data, the major fragmented peak appeared as $[M\text{-}Cl]^{+}$ at m/z 875.2033 which was in favour of the proposed structure (Figure 7.3). The SCXRD analysis confirmed a distorted octahedral geometry where the supporting en-

trityl and Cl ligands having the *cis* configuration with a bond angle ∠Cl1Ir1N1 = 87.2^0 (Figure 7.4, Table 7.1).

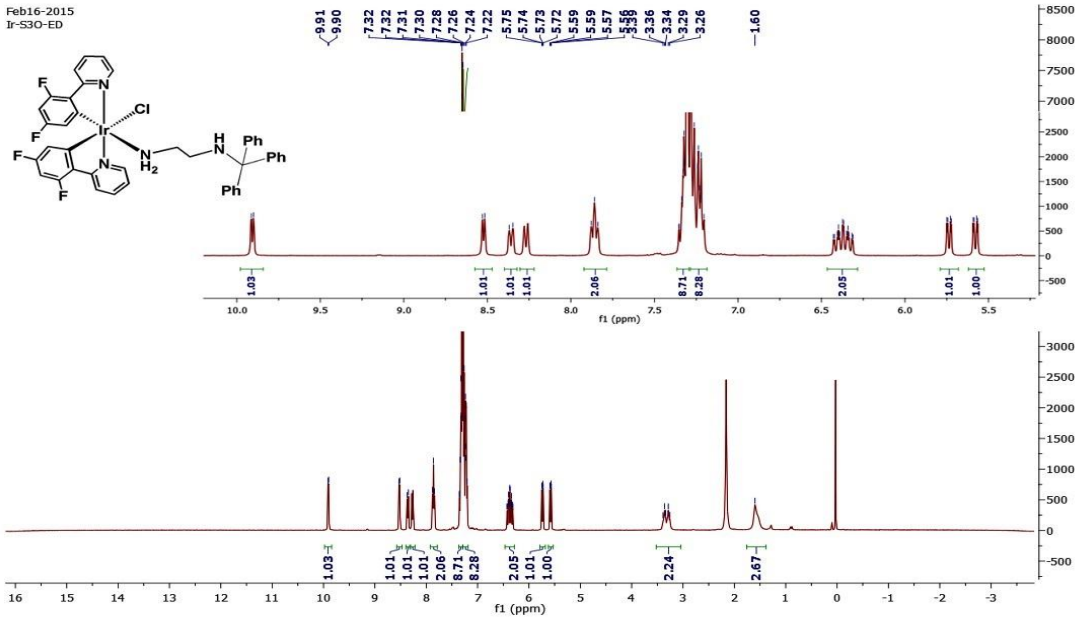

Figure 7.1 ^{1}H NMR spectra of complex **1** in $CDCl_3$

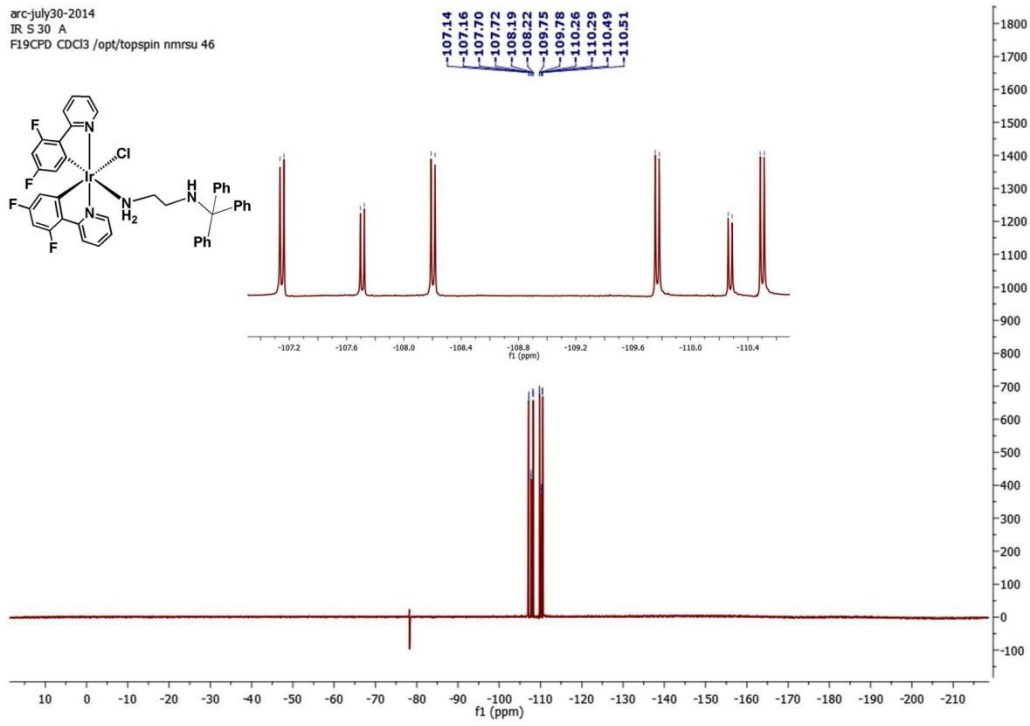

Figure 7.2 ^{19}F NMR spectra of complex **1** in $CDCl_3$

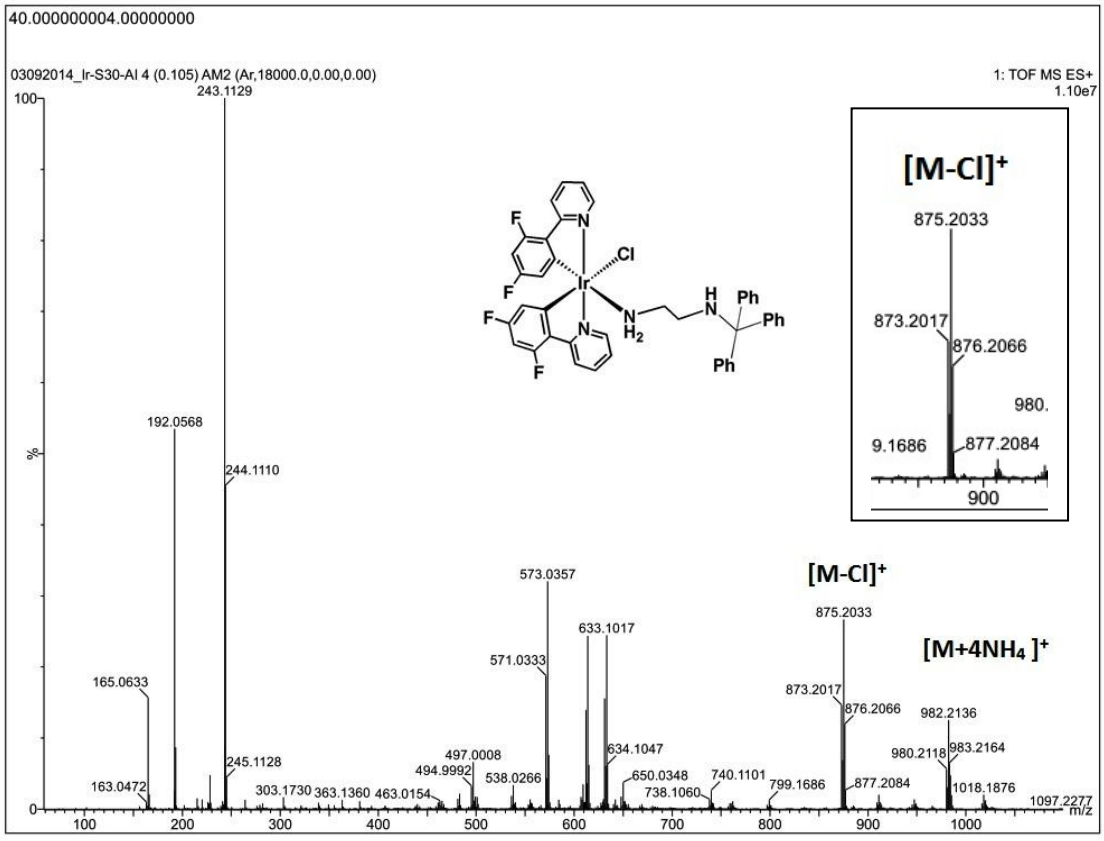

Figure 7.3 HRMS of complex **1**

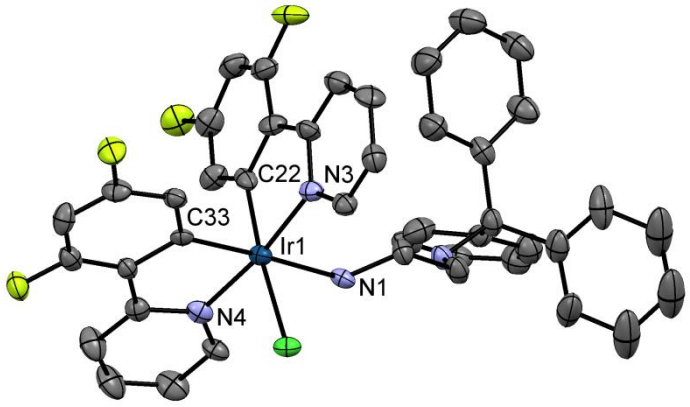

Figure 7.4 ORETP of structure of **1** drawn using 50% probability ellipsoid, showing the octahedral geometry of iridium(III). H atoms are eliminated for clarity.

Table 7.1 Selected Bond lengths [Å] and angles [°] for **1**

Bonddistances (Å)	**Complex 1**
Ir1- C33	2.020 (8)
Ir1- C22	2.019 (9)
Ir1-Cl1	2.485 (2)
Ir1-N3	2.052 (7)
Ir1-N4	2.049 (7)
Ir1-N1	2.193 (7)
Bond angles (°)	
N4 Ir1 Cl1	87.8 (2)
N3 Ir1 Cl1	96.5 (2)
N1 Ir1 Cl1	87.2 (2)
N3 Ir1 C22	80.4 (3)
N4 Ir 1N3	172.4 (2)
N1 Ir1 C33	176.8 (2)

7.2.1 Photophysical study

The absorption and emission spectra of **1** was recorded in degassed DCM at room temperature. **1** displayed intense absorption bands at *ca.* 270–310 nm, moderate bands at 310-400 nm and less intense tailing nature band beyond 400 nm, which was attributed to spin-allowed ^{1}IL ($\pi \rightarrow \pi^*$) (N^C), ^{1}MLCT ($d\pi(Ir) \rightarrow \pi^*$(N^C)) and spin-forbidden ^{3}MLCT ($d\pi(Ir) \rightarrow \pi^*$(N^C)) transitions, respectively (Figure 7.5) [13-17]. The complex exhibited intense greenish blue emission (under excitation at 365 nm) in fluid solutions at ambient temperature. The emission spectra of **1** in degassed DCM showed a structured emission [(λ_{max} = 485 nm, 512 nm (sh)] at 298 K (Figure 7.5, Table 7.2). Further, the emission spectra of **1** remains insensitive with varying the solvents (Figure 7.6). This observation along with the nature of the emission spectrum

suggesting that the lowest excited states of **1** have predominantly ligand-center character (Figure 7.6).

Table 7.2 Photophysical properties of **1, 2** and **3**

Complex	UV-Vis [a](nm), (ε x 10^4,$M^{-1}cm^{-1}$)	PL[a] (λ_{emi}) (nm)	τ (μs)[b]	QY[c]	QY[d]
Complex **1** [C43H34ClF4IrN4] (solution)	262 (5.0), 331(1.2) 388(0.52), 436(0.32),468(0.10)	485	1.3	3.0	
Complex **1** [$C_{43}H_{34}ClF_4IrN_4$] (Solid)		497			3.08
Complex **2** [$C_{43}H_{35}OF_4IrN_4$] (solution)	256(4.42), 383(0.64), 433(0.28),464(0.14)	507		2.5	
Complex **2** [$C_{43}H_{35}OF_4IrN_4$] (solid)		522			3.40
Complex **3** [$C_{24}H_{20}F_4IrN_4$] (solution)	262(3.50), 329(0.50), 435(0.16), 468(0.08)	507		0	
Complex **3** [$C_{24}H_{20}F_4IrN_4$] (Solid)		510			0

[a] Spectra were recorded in degassed dichloromethane (DCM) at room temperature with ε x 10^4, $M^{-1}cm^{-1}$; [b] Life time data recorded in DCM with [c]=1 x 10^{-4} M ; [c]solid state quantum yield for **1-3** were calculated using integerating sphere. [d]quantum yields for the two complexes were measured in degassed DCM against quinine sulfate in 1.0 N sulfuric acid as reference (QY = 0.546).

Cyclic voltammetry (CV) was used to investigate the electrochemical behavior of **1**. This complex was exhibited a single electron irreversible oxidation process with the peaks lying at, +1.10V which was attributable to a metal-centered Ir(IV/III) oxidation process (Figure 7.7) [18-20]. The highest occupied molecular orbital (HOMO) was found to be -5.91eV by using the following equation: HOMO (eV) = $-(4.83 + E_{onset})$ [21-24]. The experimentally obtained band gap, ΔE_g was observed to be 2.56 eV.

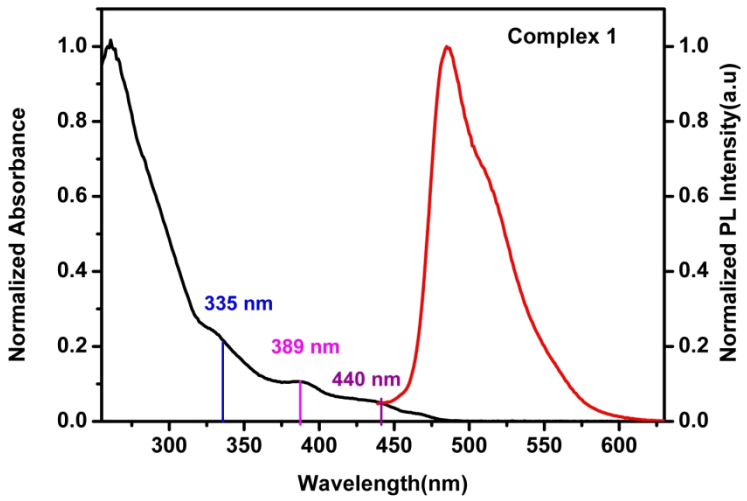

Figure 7.5 UV–Vis absorbance and photoluminescence spectra of **1** [1x 10^{-5} M, in DCM] (the TD-DFT based calculated wavelengths are shown in the spectra).

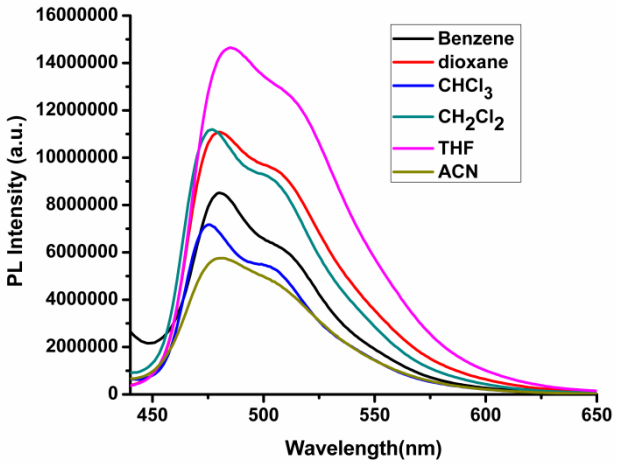

Figure 7.6 Emission spectra of **1** in different solvents keeping concentration same, [c]=1x10^{-5}

This band gap (E_g) of the complex was evaluated from the long-wavelength absorption edge using the equation $\Delta E_g = h\upsilon = hc / \lambda = 1241 / \lambda$, where, h is Planck's constant; c is the speed of light and λ is the wavelength in nm [25-27].

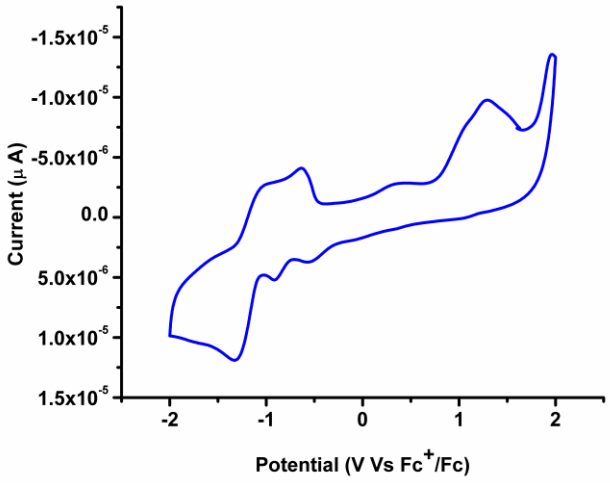

Figure 7.7 Cyclic voltammogram of **1**, recorded in ACN at a scan rate of 0.05 V s^{-1}

7.2.2 Density Functional Theory (DFT) based approach to understand the photophysical Correlation between ground state optimized geometry and the X-ray structure

The ground state optimized structure of **1** in DCM solvent is presented in Figure 7.8. The corresponding geometrical parameters along with the X-ray data are reported in Table 7.1. It is obvious from the comparison of the parameters that the structures generated by these two different ways are very similar. The calculated Ir-Cl bond distance is found to be 2.53 Å which is quite close to the experimentally determined bond length value of 2.49 (2) Å. Similarly, the observed experimental (Figure 7.8) bond distances for Ir-N1, Ir-N4 and Ir-N3 are 2.19 Å (7), 2.05 Å (5) and 2.05 Å (7), respectively and the corresponding theoretically calculated values are 2.23 Å, 2.04 Å and 2.04 Å, respectively. Computed bond angle values for the complex are also in good agreement with the experimental data. Earlier reported theoretical studies on similar complexes provide excellent agreement to our present DFT based findings on different structural parameters of the iridium(III) complex [28, 29] [30].

Table 7.3 Comparison of some selected structural parameters (*i.e.*, bond distances and bond angles) for the complex 1 obtained from experiment (*i.e.*, X-ray study) and theoretical calculation.

Structural parameters	Specific bond/angle	Experimental value (Å)	Theoretical (Å)
Bond angle	Ir-Cl	2.485 (2)	2.53
	Ir-N1	2.193 (7)	2.23
	Ir-N3	2.054 (7)	2.04
	Ir-C33	2.020 (8)	1.99
	Ir-C22	2.019 (9)	1.99
Bond angle	∠NC33Ir	80.9^{o} (3)	80.63^{o}
	∠C22IrN3	80.4^{o} (3)	80.62^{o}
	∠C22IrN4	95.6^{o} (3)	96.05^{o}
	∠N1IrN3	90.5^{o} (3)	90.50^{o}
	∠N1IrCl	87.2^{o} (2)	87.08^{o}
	∠C22IrC33	90.7^{o} (3)	87.40^{o}
	∠N3IrC33	92.7^{o} (3)	94.03^{o}
	∠N3IrCl	96.5^{o} (2)	96.03^{o}
	∠C33IrCl	92.7^{o} (2)	94.33^{o}
	∠N4IrN1	95.9^{o} (3)	94.96^{o}
	∠N1IrC22	89.7^{o} (3)	91.04^{o}

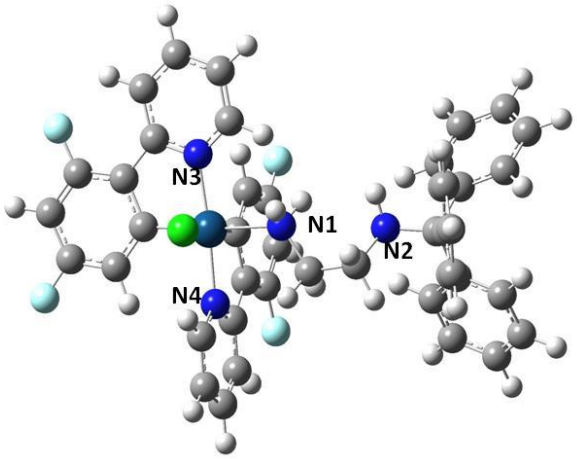

Figure 7.8 Optimized structure of **1**, (using Gaussian 09 program suite) in DCM solvent.

However, some minor deviations in theoretical calculation is observed for the two angles (∠N3IrC33 = 94.03^{o} and ∠C33IrCl = 94.33^{o}) from the X-ray data (*i.e.*, ∠N3IrC33 = 92.70^{o} (3) and ∠C33IrCl = 92.70^{o} (2)). In the optimized structure, these two particular angles are found to be slightly open-up from the original X-ray structure. Except this small conflict, the optimized structural parameters are reasonably consistent with the X-ray data (Table 7.3).

7.2.2.1 Frontier Molecular Orbital Analysis

The pictorial representations of the theoretically generated HOMO and LUMO for the ground state geometry of **1** are displayed in Figure 7.8. The HOMO consists of the metal d(Ir) orbital and π orbitals of the ligand (which mainly localizes on phenyl part of 2, 4-difluoro phenyl pyridine). However, the LUMO of the complex is mainly lying on the 2-phenylpyridine ring of the ligand (*i.e.*, 2,4-difluoro phenylpyridine) leaving a very small part on the metal. It is worth mentioning here that, the N^{1}-tritylethane-1, 2-diamine [L1] of the complex does not have any noticeable contribution in FMOs. The approximate calculated value for HOMO-LUMO gap in this particular complex is found to be 3.85 eV. The corresponding experimental value obtained from long-wavelength absorption band edge study is 2.59 eV.

7.2.2.2 TD-DFT calculation to study the excited state photophysical properties of the complex

The time dependent DFT calculation is a sophisticated theoretical tool to model the photophysical properties of a chemical system and the values generated from these calculations can be correlated to the UV-Vis spectroscopic data. The TD-DFT based vertical excitation energies and corresponding oscillator strength (OS) values for the complex is reported in Table 7.4. On the basis of the OS values, it will be more logical to conclude that transition from ground state (S_0) to first singlet excited state (S_1) (*i.e.*, $S_0 \rightarrow S_1$) is the more dominant one.

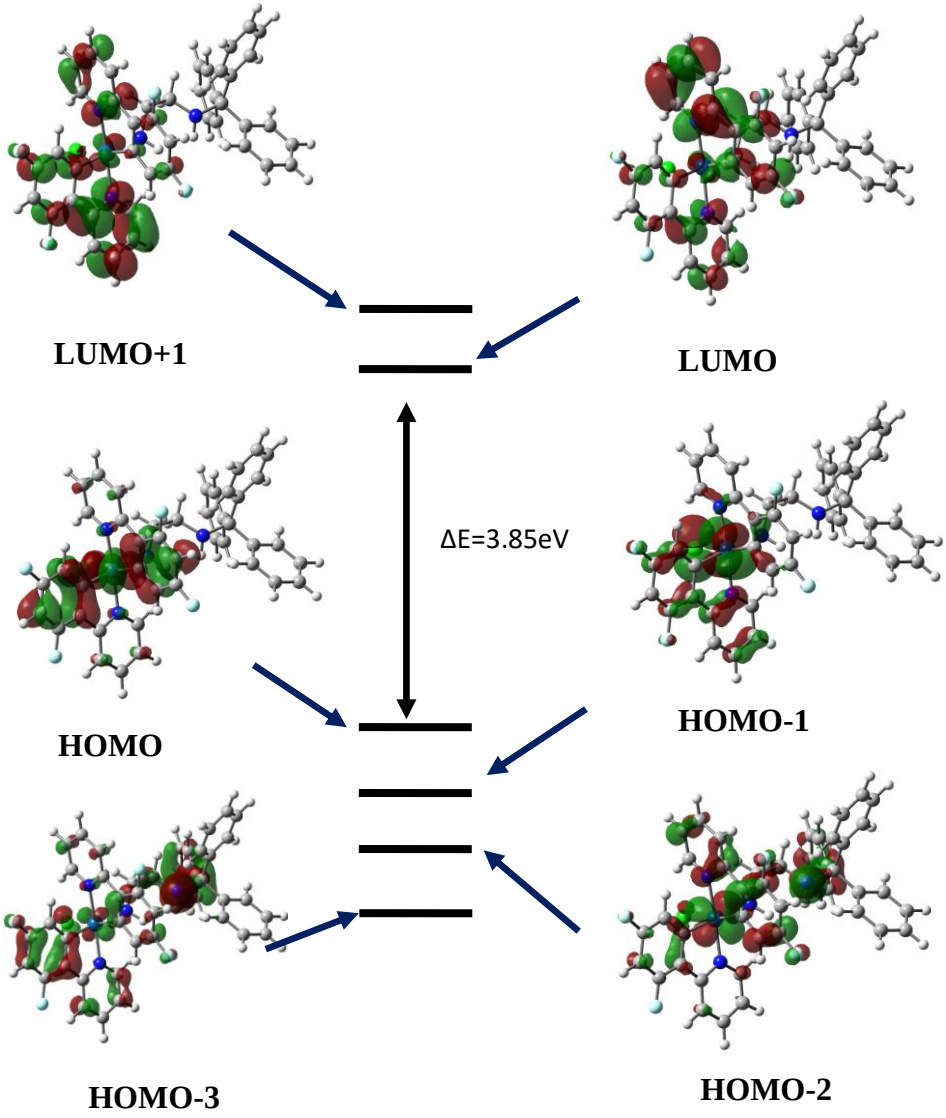

Figure 7.9 Molecular orbital diagram showing the highest occupied and lowest unoccupied molecular orbitals for **1**.

Various possible transitions between different frontier molecular orbitals (FMOs) in the complex are investigated and an exclusively higher HOMO→LUMO transition probability is evident from the calculation (as evident from the oscillator strength values).

Calculated transition probability values (in %) for different excitations from ground to singlet and triplet states are reported in Table 7.4. The FMO analysis emphasizes the favourable MLCT character in the complex, indicating the transfer of electron density from the d-orbital of iridium to the π*-orbital of the ligand (mainly to the phenyl and pyridine moieties of the ligand).

Analysis of the FMOs and computed excitation energy values also indicates the occurrence of some amount of π→π* type of electronic transition in the complex (Figure 7.9). These computational calculations in combining with the experimental facts (*vide infra*) suggest that the lowest excited states is an admixture of ligand-centered with MLCT states.

Table 7.4 Vertical excitation energies and corresponding orbital contributions

State	ΔE, eV (nm)	Osc. Str.	Orbital contribution
T_1	2.77 (447.8)		HOMO→LUMO (66%)
T_2	2.82 (440.2)		HOMO→LUMO+1 (53.65%)
S_1	3.07 (403.4)	0.042	HOMO→LUMO (96.42%)
S_2	3.18 (389.0)	0.002	HOMO→LUMO+1 (95.71%)
S_3	3.56 (348.0)	0.003	HOMO-1→LUMO (83.26%)
			HOMO-1→LUMO+1 (10.35%)
S_4	3.70 (335.0)	0.005	HOMO-1→LUMO (78.40%)

7.2.3 Acid-Base sensing

The presence of secondary amine (-NH-) functionality in 1 directed it to response in acidic as well as basic media. Such functionality further made it to be responsible as pH

responsive. We studied the photophysical property of 1 under acidic and basic conditions which was resulted some interesting observations. The original emission intensity of **1** gets quenched to ~63 times in presence of trifluoroacetic acid (TFA) (15μM). The effect of TFA to **1** was investigated very carefully by UV-VIS absorption and PL spectroscopes.

UV-Vis spectrum showing some changes after titrating **1** with TFA - a continuous decrease at the band position 382 nm, 426 nm and 463 nm was observed (Figure 7.10). The titration experiment was also performed with the help of photoluminescence spectroscopy. The gradual addition of TFA (up to 15μM) to **1** gradually weakens the PL intensity and eventually quenched completely the emission spectrum (Figure 7.11a). A linear relationship was found between I_{485} against the concentration of TFA in the range of 0 - 4 μM, indicating the sensitivity of **1** towards TFA (Figure 7.11b). The limit of detection was calculated to 252 nM, based on 3σ/m, where σ corresponds to the standard deviation of the blank measurements, and m is the slope in the plot of the intensity versus the sample concentration.

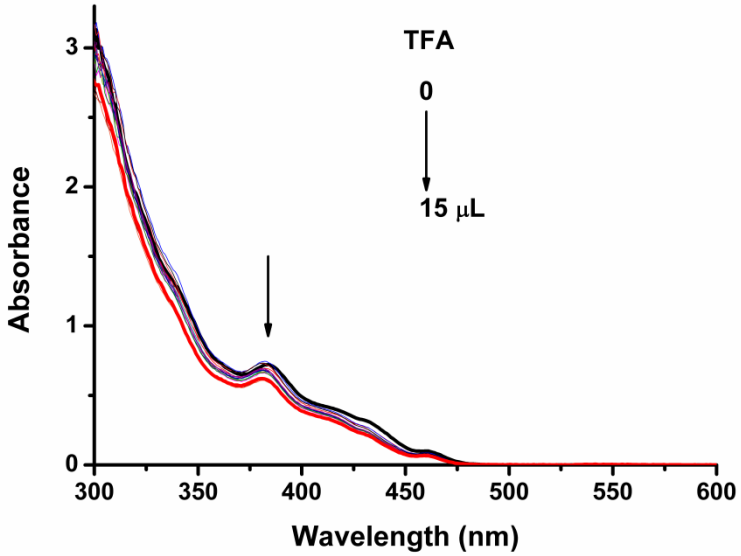

Figure 7.10 Absorbance spectra of **1** with increasing concentration of TFA (0-15 μL) with [c] =$1x10^{-5}$

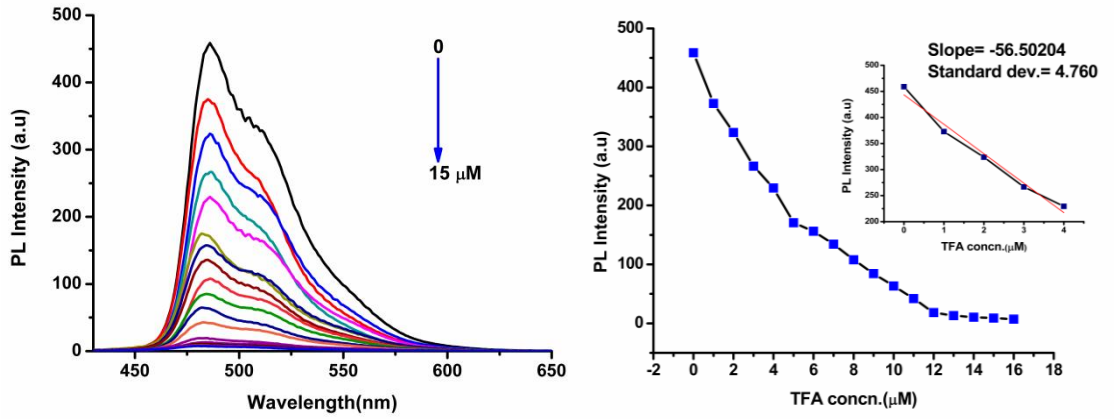

(a) (b)

Figure 7.11 (a) The luminescent spectral changes of **1** ([M] =1x10^{-5} mol L^{-1}) upon the gradual addition of TFA (from 0.0 to 15.0 μM, λ_{ex} = 380 nm). (b) The plot of PL intensity (I_{485} vs. the concentration of TFA); inset, the linear relation of I_{485} vs. concentration of TFA in the range of 0.0–4.0 μM.

Further, the emission spectra of 1 in presence of anions such as F^-, Br^-, Cl^-, I^-, ClO_4^- , $S_2O_3^{-2}$, NO_3^-, $H_2PO_4^-$ and OH^- were recorded (the solution prepared of 1 in THF–H_2O = 1:9, v/v with c=1x10^{-4} M) (Figure 7.12). The addition of 1M NaOH to the solution of **1** shifted the maximum emission by 60 nm, *i.e.* from 485 nm to 545 nm as well as the emission intensity was dramatically enhanced by ~8 times. The selectivity of **1** towards OH^- ion was studied and the emission of this solution was recorded in the presence of other anions (Figure 7.12).

The presence of OH^- in the solution resulting a drastic turn-on red shift while the other anions not having much influence on the PL emission intensity (Figure 7.12c). The selectivity toward OH^- was explained by change in the ratiometric analysis of the PL intensity ratio at I_{545}/I_{485} [(I_{545} implies PL intensity of **1** + OH^- (in case of both black and red bars); I_{485} implies PL intensity of 1 + anions (in case of red bar) and **1** + anions + OH^- (in case of black bar)]. There has higher ratio is observed in case of black bar, while red bar shows the lower ratio. This fact indicating that the presence of other anions has the negligible influence on the signal response as shown by OH^- ion. These results reveal the selectivity of **1** towards OH^-. The calculated detection limit was foundto be 126 nM based on 3σ/m calculations (Figure 7.13).

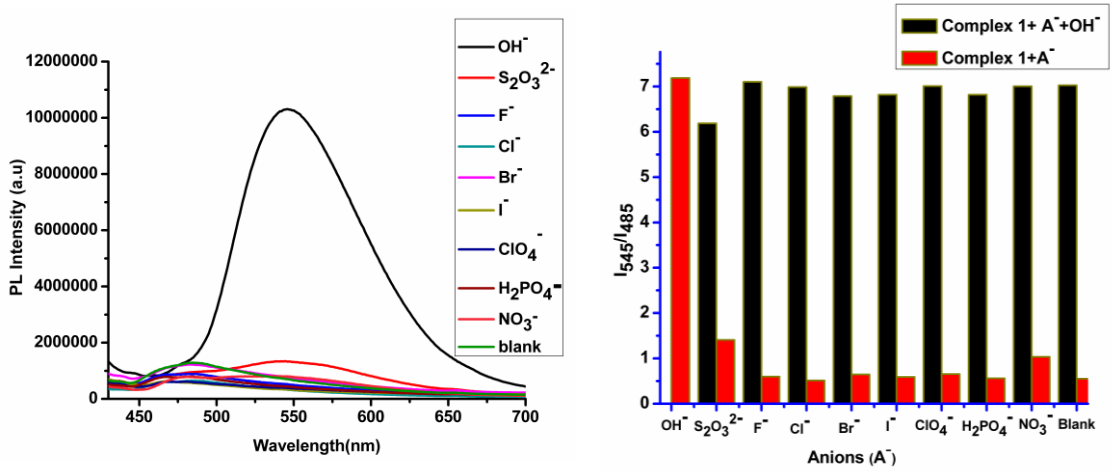

(a) (b)

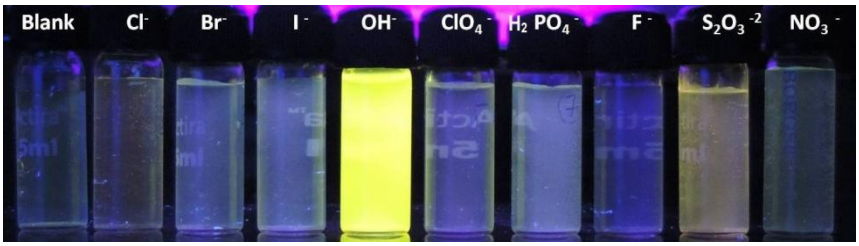

(c)

Figure 7.12 (a) Fluorescence spectra of **1** with [c] = 10^{-4} molL^{-1} at f_w = 90 % upon the addition of 4 equivalents of anionic species; (b) Column diagrams of the fluorescence intensity of **1** + A^{n-} at I_{545}/I_{485} nm. Red bars represent the addition of various anionic species to the blank solution and black bar represents the subsequent addition of NaOH (4 equivalent) to the above solutions (1 + A^{n-} + NaOH); (**c**) photo of **1** when dispersed at f_w = 90 % with [c] =10^{-4} mol L^{-1}, by adding 4 equivalents of different anions. From left to right: blank ; Cl^-; Br^-; I^-; OH^-; ClO_4^-; $H_2PO_4^-$; F^-; $S_2O_3^{2-}$; NO_3^-; irradiated with an ultraviolet light at 365 nm.

7.2.3.1 The sensing mechanism of 1 to OH^- and TFA

According to acid–base theory, amine functionality is basic in nature, so it has a natural tendency to interact with acids.

Herein, we reported **1** that can be used as a chemodosimeter for low level detection of TFA. The lone pair of NH-group in en-trityl ligand in **1** could easily be

interacted with TFA. The interaction of 1 with TFA was studied by (^{1}H, ^{19}F) NMR and HRMS. A comparative ^{19}F NMR study was done between **1** and **1** with 4 equivalents of TFA (Figure 7.14). After addition of TFA to **1**, the obtained NMR spectra have proved a symmetrical geometry of the complex. The proposed structure of **3** which was formed after addition of TFA could be an ethylenediamine chelating complex which was supported by ^{1}H NMR spectra (Figure 7.15) (Scheme 7.2).

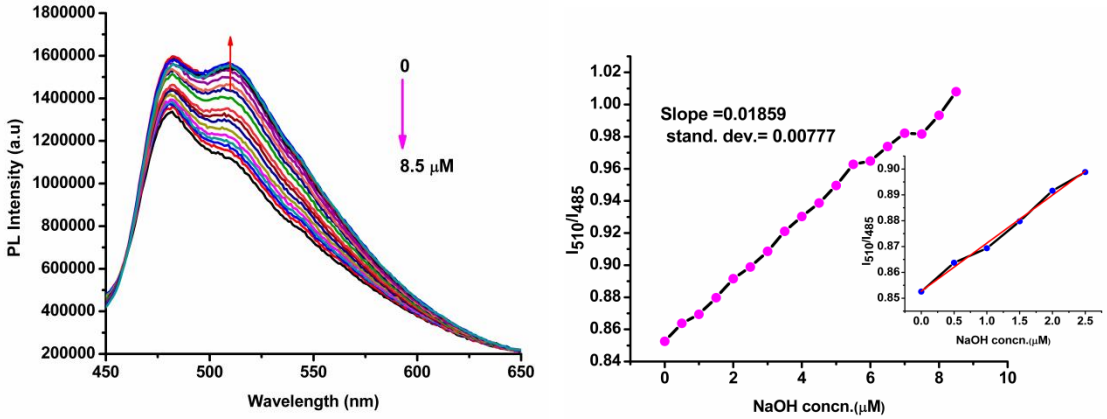

(a) (b)

Figure 7.13 (a) The luminescent spectral changes of **1** (f_w = 90 % with [M] =10^{-4} mol L^{-1}) upon the increasing addition of NaOH (from 0.0 to 8.5 μM) [THF–H_2O (1:9 v/v), λ_{ex} = 380 nm]. (b) The plot of I_{510}/I_{485} vs. the concentration of NaOH; inset, the linear relation of I_{510}/I_{485} vs. the concentration of NaOH in the range of 0.0–2.5 μM.

Further, the following structure was supported by ESI-HRMS data. The ESI-HRMS spectra was recorded after addition of TFA in **1** which showed three major fragments at m/z 573.0650, 614.0894 and 669.1082 and these can be attributed to $[Ir(F_2ppy)]^+$, $[Ir(F_2ppy) + K + 2H]^+$ and $[Ir(F_2ppy)en + 4NH_4 + H]^+$, respectively.

The obtained peak at m/z 669.1082 (which was missing in **1)** confirmed the formation of chelating entylenediamine complex, **3** after de-protecting trityl substitutent from **1**.The more clear picture of formation of ethylenediamine chelating product was confirmed by m/z 633.1316 and 650.0657 which corresponds to $[Ir(F_2ppy)en]^+$ and $[Ir(F_2ppy)en + NH_4]^+$, respectively.

All these experimental results tentatively proposed the sensing mechanism with TFA, where H^+ could easily be interacted with the free lone pair of nitrogen in the

complex at the initial stage. Then, they might form an intermediate complex, $[Ir(F_2ppy)_2(NH_2CH_2\ CH_2NH_2{}^+CPh_3)]$ in which the trityl functionality gets deprotected from the ethylenediamine ligand that resulted NH_2 terminal free iridium(III) complex. This complex subsequently, formed the chelating with iridium(III) centre.

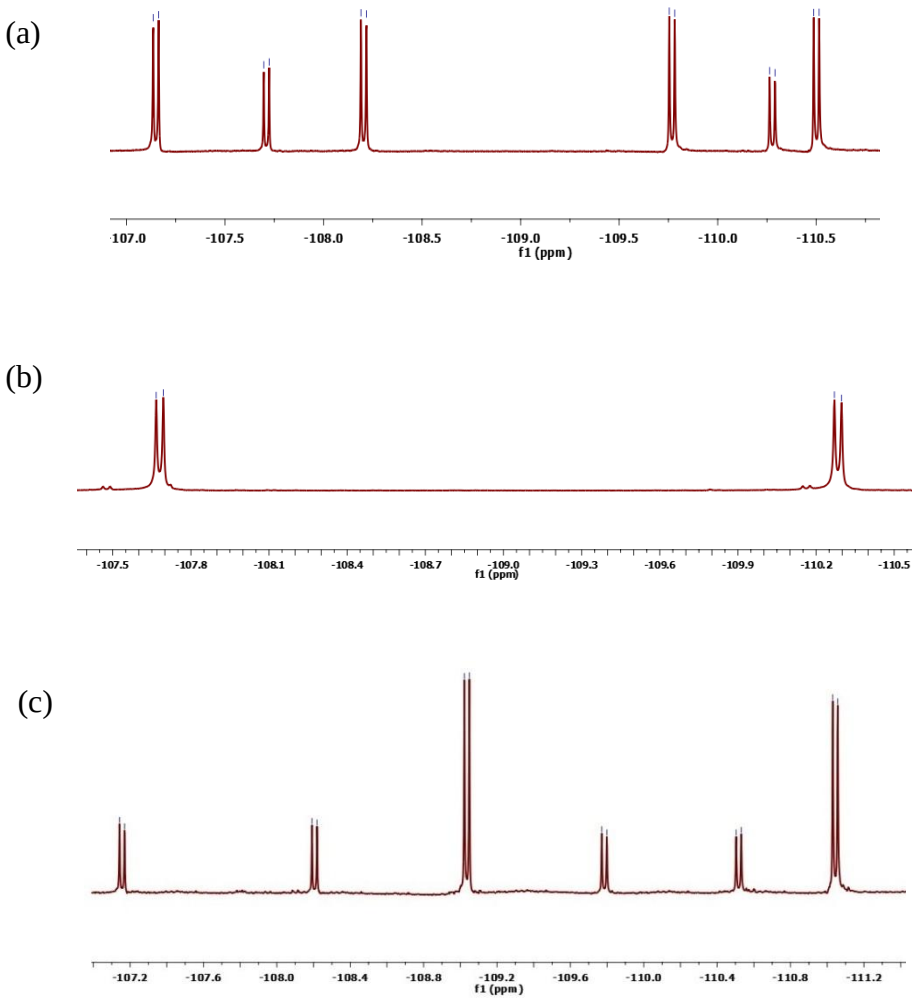

Figure 7.14 ^{19}F NMR spectra of (a) **1**; (b) after addition of 4eq. of TFA to **1**; (c) **2**.

The emission spectra of **1** has been recorded in presence of 1M NaOH solution (in THF), resulted the shifting of emission wavelength from greenish-blue to bright yellow (λ_{max} 485 nm to 545 nm) (Figure 7.16).

The mechanistic point of this conversion was explored by ^{1}H NMR, HRMS and IR spectra. The yellow emitting **2** was synthesized (Scheme 7.2), purified and characterised by ^{1}H NMR spectra which showed quite different resonance signal as compared to **1**. The ^{1}H and ^{19}F NMR spectra were recorded after addition of 1M NaOH to **1** which clearly supporting the gradual conversion of **1** into **2** (Figure 7.17 and 7.14c). ^{19}F NMR of **2** resulted six signals and found similar splitting pattern with **1**, but only two signals out of these were observed to move downfield as compared to the ^{19}F NMR peaks in **1** [-110.28 (d, *J* = 10.3 Hz) and -111.04 (d, *J* = 10.2 Hz) peaks obtained for **2** (Figure 7.14c) were observed at -107.71 (d, *J* = 10.3 Hz) and -109.04 (d, *J* = 10.2 Hz) for the case of **1**].

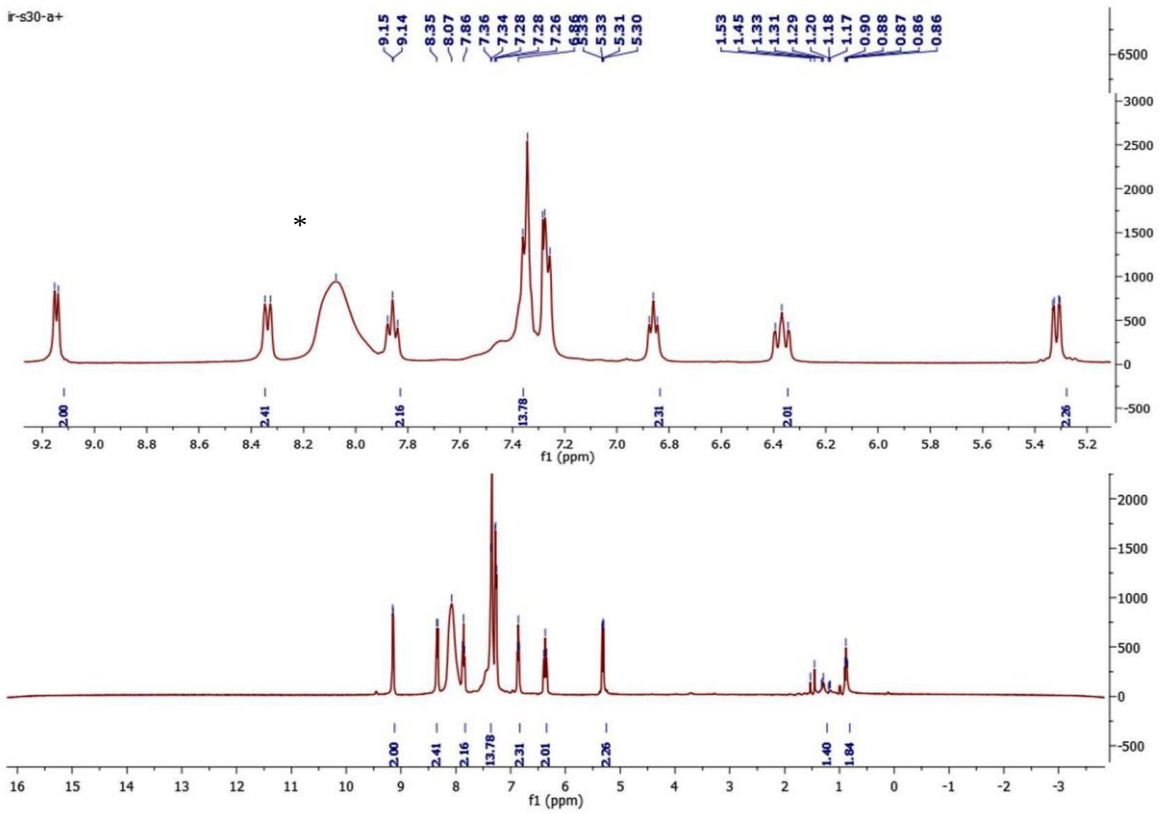

Figure 7.15 ^{1}H NMR spectra of **3** in $CDCl_3$ (* TFA, acid proton signal in ^{1}H NMR).

The ESI-HRMS data showed two major fragments at m/z 573.0650 and 614.0894 like previous results, which attributed to $[Ir(F_2ppy)]^+$ and $[Ir(F_2ppy)+K+2H]^+$,

respectively. The another two peaks at m/z 875.2410 and 921.2466 representing the important fragments of $[M–OH]^+$ and [M–OH+2Na], respectively [31].

These data supporting the replacement of chloro group by hydroxyl group in **1**. Further, the presence of coordinated hydroxyl group in complex **2** was supported by FTIR that resulted O-H stretching frequency at 3421 cm^{-1}.

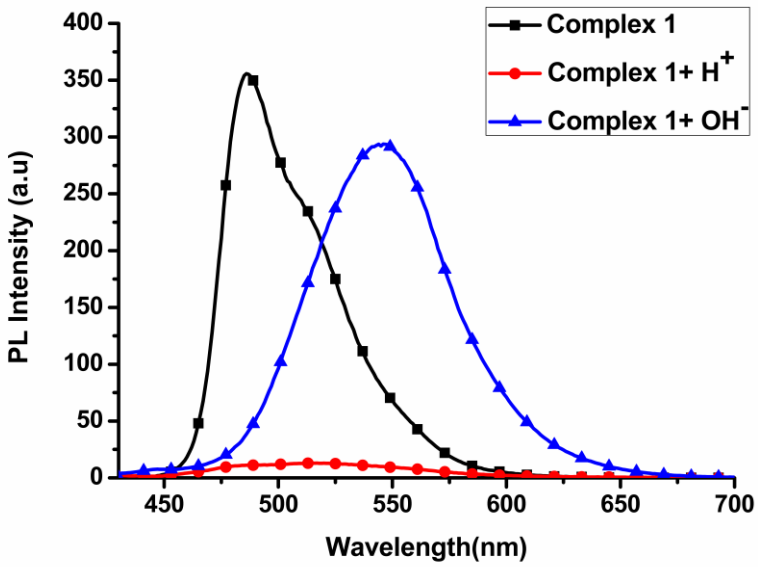

Figure 7.16 Emission spectra of **1** in DCM , DCM + TFA and THF + 1M NaOH in water (1:9, v/v).

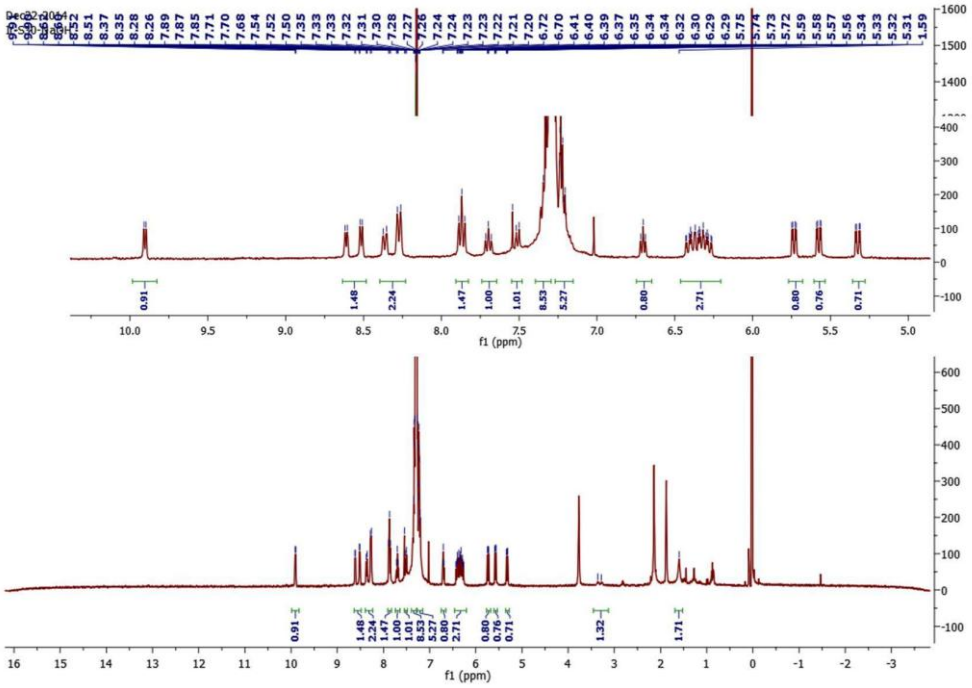

Figure 7.17 (a) ^{1}H NMR spectra of **2** in $CDCl_3$.

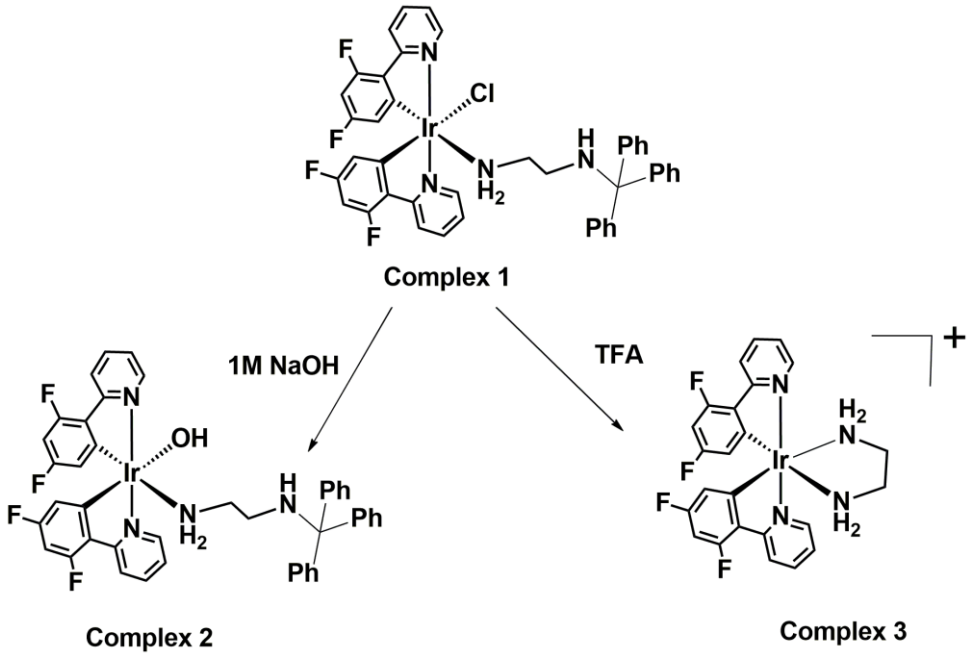

Scheme 7.2 Chemical structures of the resulting complexes (**2** & **3**) after treating of **1** with base and acid.

7.2.4 pH Sensing

It is envisioned that the emission spectra of **1** will be affected by pH of the medium and could be considered as sensitive probe for pH monitoring. This thought encouraged us to check its applicability as a fluorescent pH sensor. The PL spectrum of **1** in THF-buffer mixture [32] (1:9, v/v), at lower pH (1-8) showing weak emission, but at pH > 8 the emission intensity was increased gradually (Figure 7.18). The quenching in the emission spectra at lower pH value attributed to de-protection of the trityl protected NH group. In a controlled experiment, ^{1}H and ^{19}F NMR spectra of the **1** in presence of acetic acid has been recorded.

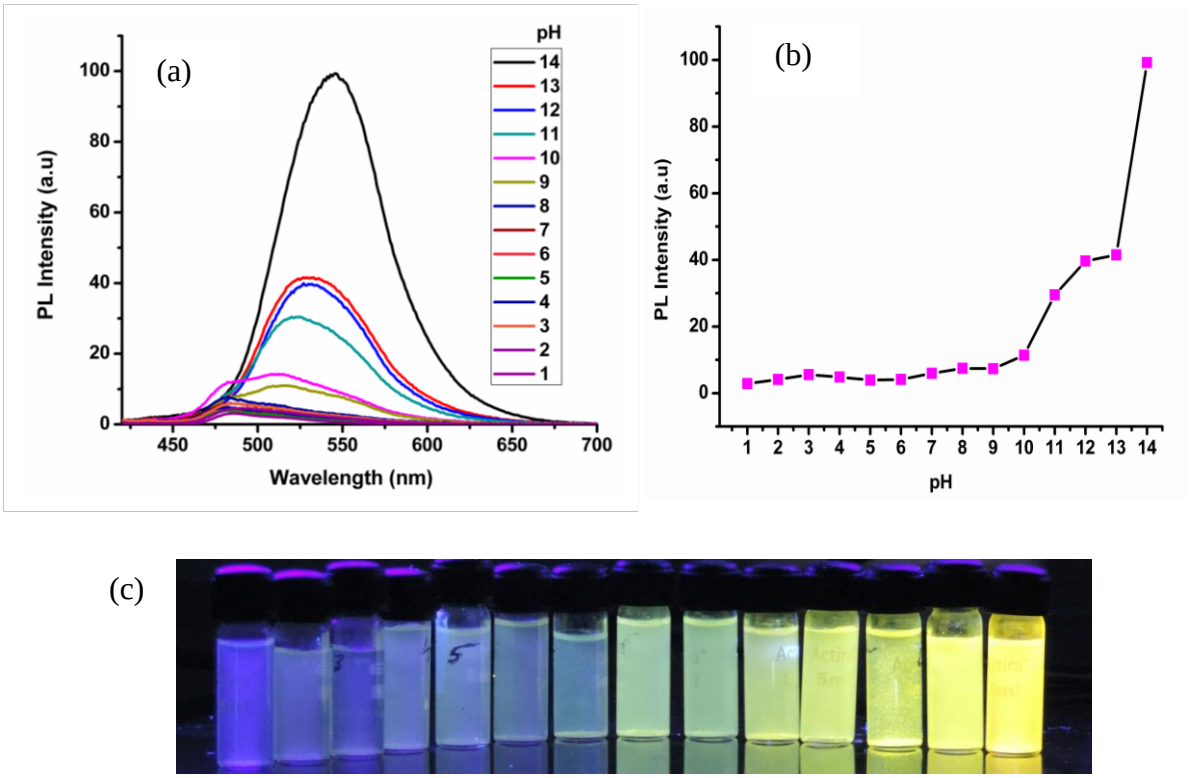

Figure 7.18 (a) pH dependent PL spectra of **1** with [M] =1x10^{-4} mol L^{-1} in different buffer solution (THF/buffer, 1:9) (b) pH dependent intensity plot in different pH. (c) Fluorescent photos of the **1** in different pH at 365 nm.

The ^{1}H NMR spectra after addition of AcOH (4 equivalents) showing six different signals ranging, 5.27 - 9.12 ppm (Figure 7.19a) and two different NMR signals for ^{19}F, ─107.79-(─110.41) ppm (Figure 7.19b).

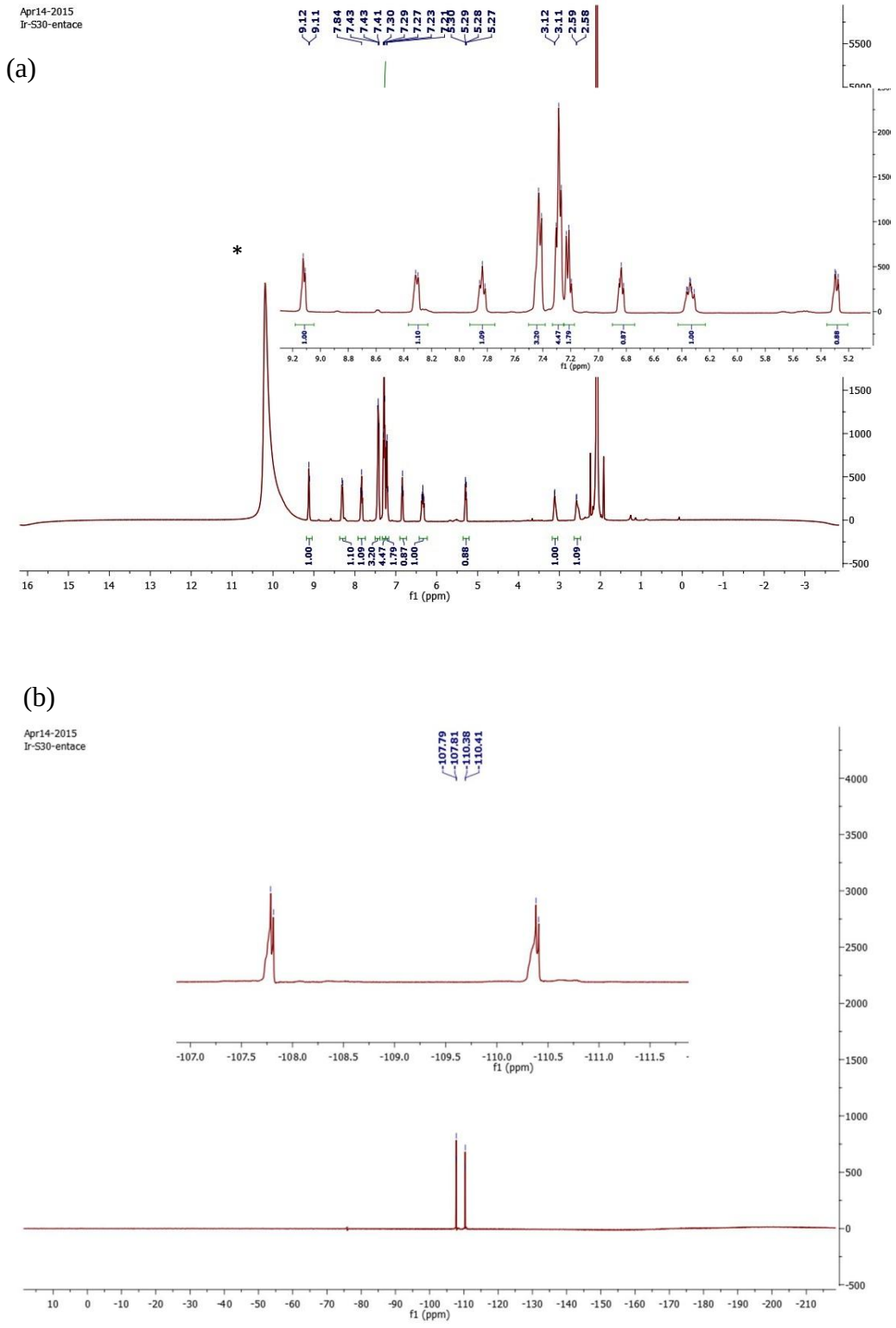

Figure 7.19 (a) ^{1}H NMR spectra of **1** in $CDCl_3$ after addition of AcOH (*AcOH, acid proton signal in ^{1}H NMR); (b) ^{19}F NMR spectra of **1** in $CDCl_3$ after addition of AcOH.

These NMR results are indicating the symmetrical nature of the complex which can be obtained after de-protection of trityl group from ethylenediamine ligand. At basic pH (≥ 8), the emission intensity was gradually increasing with red shifted emission spectra because at basic pH the **1** could be changed to **2**.

7.2.5 Aggregation Induced Enhanced Emission (AIEE)

In the present case, the incorporation of trityl-en in iridium(III) complex is the continuation of the previous attempts. But the synthesized iridium(III) complex weren't turned-up in AIE activity [33-36] rather exhibited 'aggregation caused quenching (ACQ)' effect [37-39]. The **1** resulted twenty eight times less emissive photoluminescence (PL) intensity at higher water fraction (water fraction, f_w=90% in THF) as compared to its' pure THF solution (Figure 7.20).

In the other case, **1** results a bright yellow emission after addition of 1M NaOH in THF (9:1, v/v) (Figure 7.21). This property made it to use as a chemosensor for detection of OH^-. To investigate this property, we have added different amount of 1M NaOH solution in **1** (keeping the overall concentration of the solution to 10^{-4} M). The photoluminescence (PL) intensity of **1** was slowly diminished up to 40% $f_{(NaOH)\ (1M)}$ in THF, but a sudden increase in PL intensity was observed at $f_{(NaOH)\ (1M)} > 50\%$.

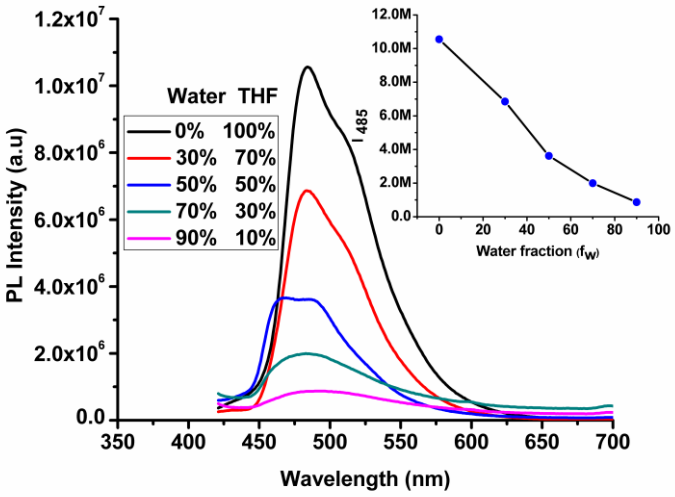

Figure 7.20 Emission spectra of **1** in presence of different water fraction (0 - 90%).

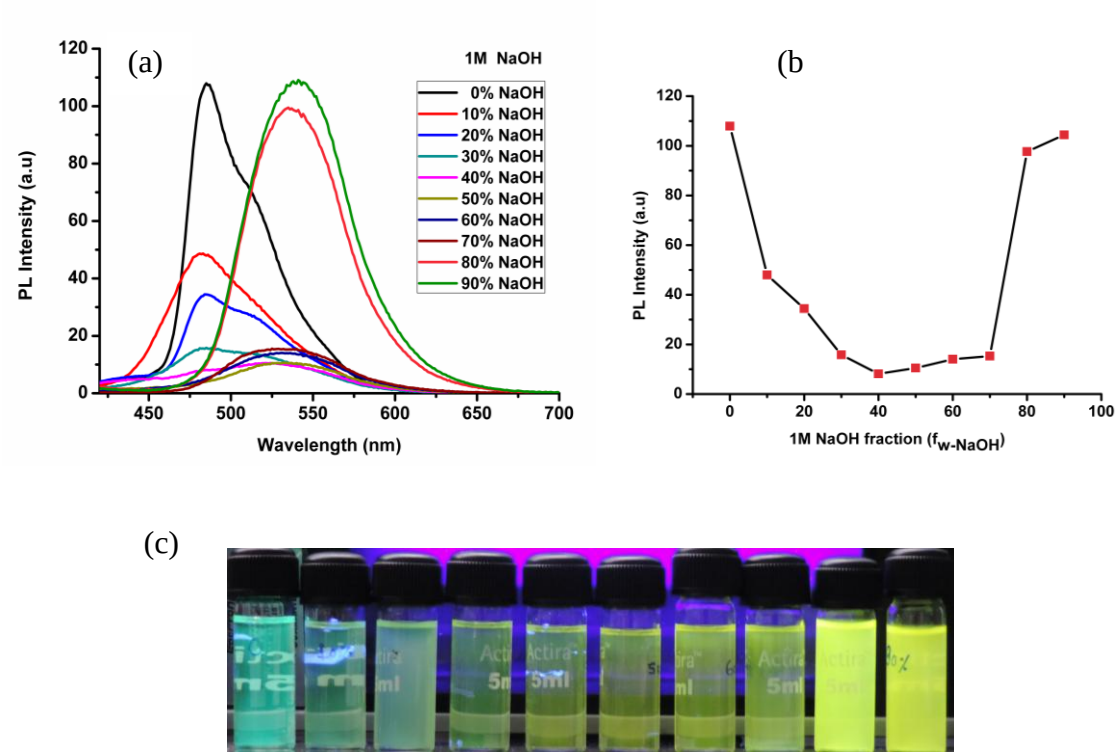

Figure 7.21 (**a**) PL spectra of **1** with [M] =10^{-5} $molL^{-1}$ in different THF–1M NaOH mixtures (v/v, 0-90%) NaOH [$f_{w(\ NaOH)(1M)}$]; (**b**) The PL intensity of **1** after addition of different 1M NaOH fraction [$f_{w(\ NaOH)}$]; (c) Fluorescence photographs recorded under 365nm UV irradiation for **1** in THF/1M NaOH mixture with $f_{w(1M)(NaOH)}$ ranging from 0-90%.

At $f_{(NaOH)(1M)}$ = 90%, the PL intensity of the solution showed almost more or less same to the PL intensity measured in pure THF solution (Figure 7.21b). The emission spectra of **1** in lower fraction of NaOH, the reaction mixture contain predominantly **1** in comparison to the product, **2**. Hence, the ACQ property is dominated because **1** shows ACQ effect in presence of water (sodium hydroxide is dissolved in water). The amount of **2** is gradually enhanced with the increasing concentration of NaOH. As **2** is found to be AIEE active, the PL intensity is expected to be increased and matches with the result which is observed from 40% and above concentration of NaOH. Red-shifted emission is observed with increasing concentration of NaOH because the solid form of **2** exhibits red-shifted emission in comparison to complex **1**. The transformation of **1** into **2**, after

addition of 1M NaOH was confirmed by ^{1}H and ^{19}F NMR analysis (*vide infra*, Figure 7.17 and 7.14c).

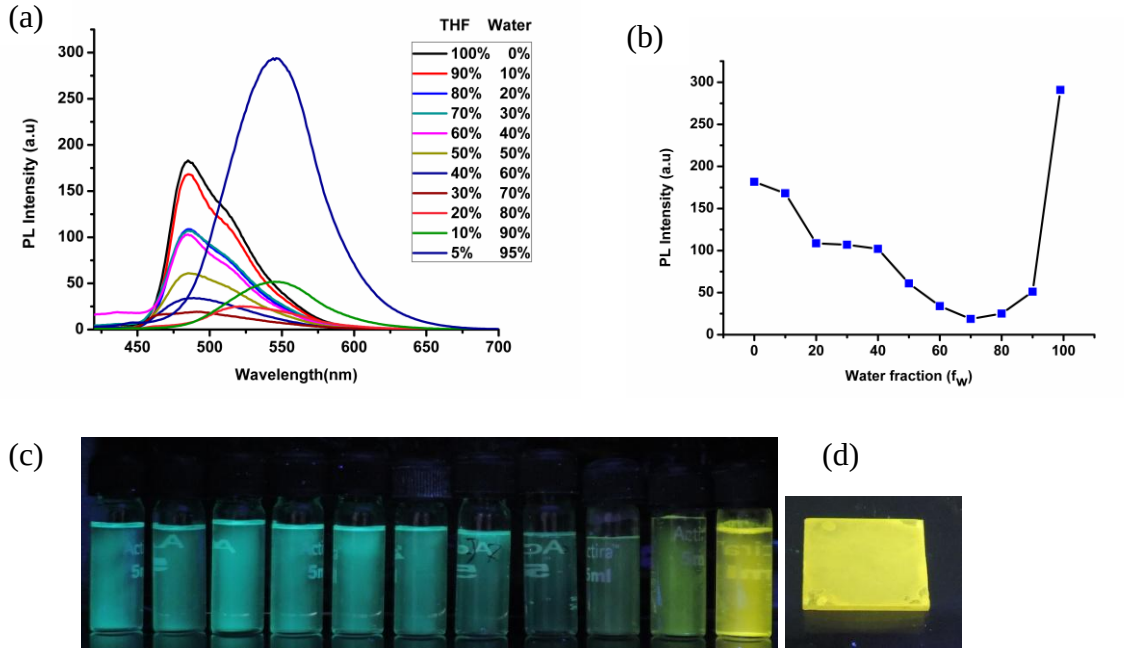

Figure 7.22 (**a**) PL spectra of **2** with [M] =1x10^{-5} molL^{-1} in different THF–water mixtures (v/v, 0-90%) [f_w]; (**b**) The PL intensity of **2** after addition of different water fraction [f_w]; (c) Fluorescence photographs recorded under 365-nm UV irradiation for **2** in THF/water mixture with f_w ranging from 0-95%; (d) Thin film emission of **2** under 365-nm UV irradiation.

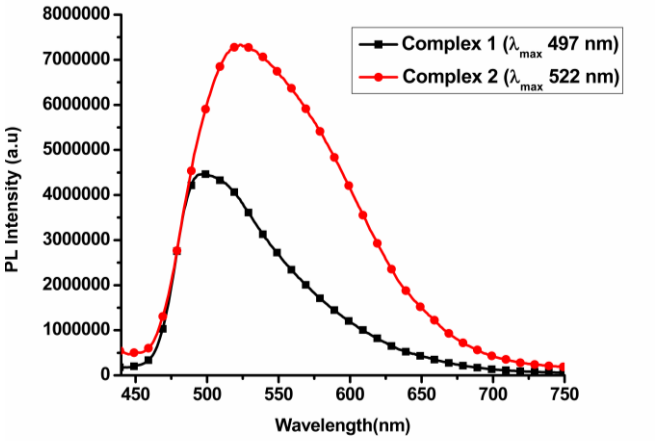

Figure 7.23 Thin film emission of **1** and **2**.

The AIEE property of the **2** was investigated. The solution of **2** was dissolved in THF and gradually increased the water concentration (keeping the overall concentration of the solution to 10^{-4} M). The PL intensity was diminished upto a water concentration of about $f_w \leq 70\%$, after this point the intensity starts increasing upto f_w = 95%. The PL intensity at f_w= 95% is 1.6 times higher than its solution in pure THF (Figure 7.22). The recorded solid state emission spectrum of **2** is, also found to 1.6 times higher than **1** (Figure 7.23). The absolute quantum efficiency for the sloid powder samples, **1-3** have been calculated and found that 3.08 %, 3.40% and 0% respectively.

The lowering of PL intensity seems to be the formation of amorphous aggregates, while the observation of increasing PL intensity is resulted because of the formation of crystalline nature of the aggregated form which is supported by TEM and ED. The TEM image of **2** was recorded with 40% and 90% of water fraction. The ED patterns of the aggregates formed at 40% water fraction showed a very faded diffraction ring indicating the formation of amorphous nanoaggregates while at 90% water fraction, a series of diffraction spots was clearly observed around the diffraction ring, indicating the formation of crystalline nanoaggregates (Figure 7.24) [40-44]. Further, the maximum emission is gradually red-shifted with increasing concentration of water content (Figure 7.22) because the particle size gradually approaches towards the solid state that lead to the solid state emission of **2** which may be resulted of π-π stacking between the fused aromatic rings [45].

Furthermore, studies using a particle size analyzer in different 1M NaOH solution has been recorded and that the average sizes of **1** at 50 % and 90% was found in the range of 320-416 nm and 270-408 nm, respectively (Figure 7.25) while for **2,** at the same concentration results 300-494 nm and 150-206 nm, respectively (Figure 7.26).

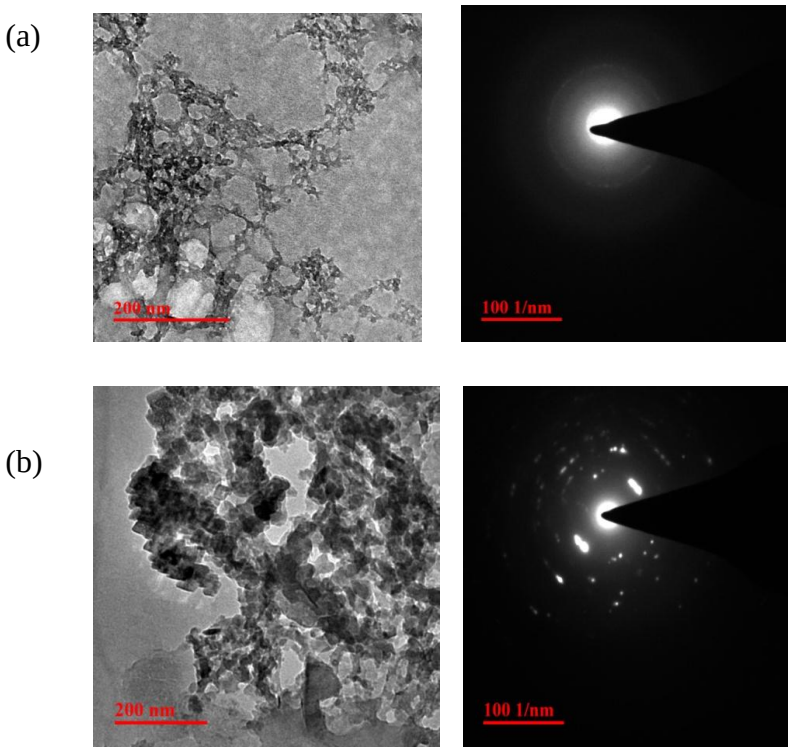

Figure 7.24 TEM images and ED patterns of **2** (a) amorphous nano aggregates at f_w= 40% and (b) crystalline aggregate at f_w= 90%

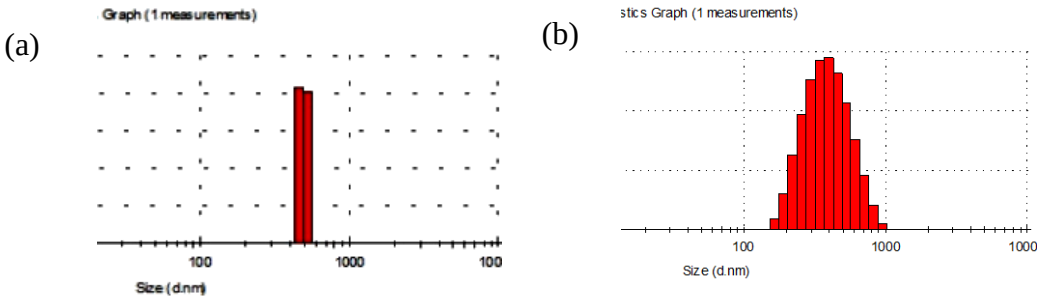

Figure 7.25 (a, b) Size distribution graph for **1** in presence of different 1M NaOH fractions (a) at 50%, (b) at 90%.

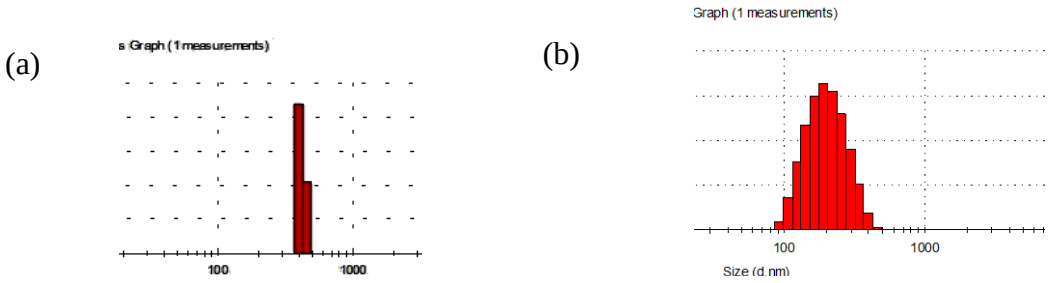

Figure 7.26 Size distribution graph for **1** in presence of different water fractions (a) at 50%, (b) at 90%

7.3 Syntheses of complexes

7.3.1 Synthesis of N^1-tritylethane-1,2-diamine [L_1]

In a two-necked round bottom flask (50 mL), trityl chloride (100 mg, 0.359 mmol), Et_3N (50 µL, 0.359 mmol) and ethylenediamine (27.0 µL, 0.359 mmol) were dissolved in 30 mL THF. The reaction mixture was maintained at room temperature for 24h under an atmosphere of N_2 gas. The solution mixture was evaporated to dryness and the residue was purified by recrystallization resulting a white powder (yield, 50%); ^{1}H NMR (400 MHz, $CDCl_3$) δ 7.55 – 7.48 (m, 5H), 7.35 – 7.27 (m, 7H), 7.25 – 7.17 (m, 3H), 2.83 (t, *J* = 6.0 Hz, 2H), 2.23 (t, *J* = 6.0 Hz, 2H), 1.63 (s, 3H).; ESI-HRMS calculated: ($[M+H]^+$): m/z, 302.1783, found: ($[M+Na]^+$): m/z, 325.1764, ($[M+TFA+H+Na]^+$): m/z, 423.1753.; White solid; Yield, 85.00 %.

7.3.2 Synthesis of 1

In a two-necked round bottom flask (50 mL), N^1-tritylethane-1, 2-diamine [L_1] (0.259 mmol) and $[Ir(F_2ppy)_2Cl]_2$ (0.259 mmol) were dissolved in 20 mL DCM. The mixture was stirred at room temperature for 10 minutes under an atmosphere of N_2 gas. The solution mixture was evaporated to dryness and the residue purified by column chromatography using Ethyl acetate-Hexane (4:6) as the eluent, getting a green solid product (yield, 70-80%) (Scheme 7.1).

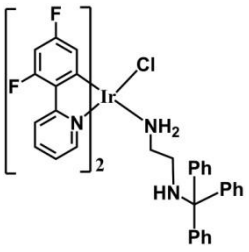

^{1}H NMR (400 MHz, $CDCl_3$) δ 9.91 (d, *J* = 5.0 Hz, 1H), 8.52 (d, *J* = 5.4 Hz, 1H), 8.36 (d, *J* = 8.8 Hz, 1H), 8.27 (d, *J* = 8.4 Hz, 1H), 7.86 (t, *J* = 12.7, 6.7 Hz, 2H), 7.43 – 7.08 (m, 17H), 6.48-6.25 (m, 2H), 5.74 (dd, *J* = 8.7, 2.3 Hz, 1H), 5.58 (dd, *J* = 8.9, 2.2 Hz, 1H), 3.13 (m, 2H), 1.60 (s, 2H).; ^{19}F NMR (376 MHz, $CDCl_3$) δ -107.15 (d, *J* = 10.4 Hz), -107.71 (d, *J* = 10.3 Hz), -108.20 (d, *J* = 10.5 Hz), -109.77 (d, *J* = 10.4 Hz), -110.28 (d, *J* = 10.3 Hz), -110.50 (d, *J* = 10.5 Hz).; ESI-HRMS calculated: ($[M-Cl]^+$): m/z, 875.2349, found: m/z, 975.2033, calculated: ($[M+4NH_4]^+$): m/z, 982.3412, found: m/z, 982.2136.; green solid; Yield, 60.00 %.

7.3.3 Synthesis of 2

1 (50 mg, 0.055 mmol) was dissolved in THF-1M NaOH mixture (1:9, v/v) resulting a yellow precipitate immediately. After 10 minutes, the yellow precipitate was dried under vacuum which yielded a yellow solid powder.

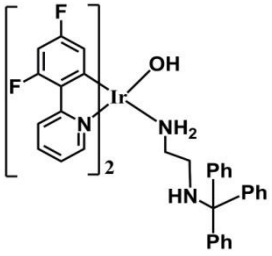

^{1}H NMR (400 MHz, $CDCl_3$) δ 9.90 (d, J = 4.9 Hz, 1H), 8.61 (d, J = 5.9 Hz, 1H), 8.51 (d, J = 5.6 Hz, 1H), 8.36 (d, J = 8.7 Hz, 1H), 8.27 (d, J = 8.7 Hz, 2H), 7.87 (t, J = 7.7 Hz, 2H), 7.70 (t, J = 7.1 Hz, 1H), 7.51 (d, J = 7.3 Hz, 2H), 7.32 (ddd, J = 12.2, 7.9, 4.8 Hz, 9H), 7.27 – 7.17 (m, 6H), 6.70 (t, J = 6.0 Hz,1H), 6.48 – 6.20 (m, 3H), 5.73 (dd, J = 8.7, 2.4 Hz, 1H), 5.58 (dd, J = 8.9, 2.3 Hz, 1H), 5.32 (dd, J = 9.3, 2.3 Hz, 1H), 3.32 (d, J = 30.3 Hz, 2H), 2.14 (s, 3H), 1.27 (t, J = 11.7 Hz, 2H).; ^{19}F NMR (376 MHz, $CDCl_3$) δ -107.16 (d, *J* = 10.4 Hz), -108.21 (d, *J* = 10.4 Hz), -109.04 (d, *J* = 10.2 Hz), -109.78 (d, *J* = 10.4 Hz), -110.52 (d, *J* = 10.4 Hz), -111.04 (d, *J* = 10.2 Hz).; (KBr, cm^{-1}): 3432 (br, $\nu_{Ir\text{-}OH}$).; ESI-HRMS calculated: ($[M\text{-}OH]^+$): m/z, 875.2349, found: ($[M\text{-}OH]^+$): m/z, 875.2410.; calculated: ($[M\text{-}OH+2Na]^+$): m/z, 921.2144, found: ($[M\text{-}OH+2Na]^+$): m/z, 921.2466, yellow solid; Yield, 40.00 % .

7.3.4 Synthesis of 3

1 (50 mg, 0.055 mmol) was dissolved in DCM followed by addition of ~10 µL TFA (or ~7 µL AcOH) (0.110 mmol). After 1 minute of stirring, the solution mixture was evaporated to dryness which results the 3.

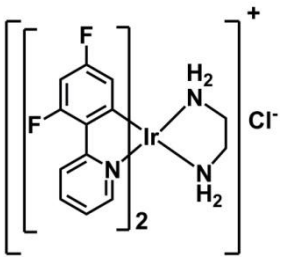

^{1}H NMR (400 MHz, $CDCl_3$) in presence of TFA, δ 9.15 (d, *J* = 5.4 Hz, 2H), 8.34 (d, *J* = 8.3 Hz, 2H), 7.86 (t, *J* = 7.6 Hz, 2H), 7.66 – 7.06 (m, 15H), 6.86 (t, *J* = 6.3 Hz, 2H), 6.37 (t, *J* = 9.8 Hz, 2H), 5.32 (dd, *J* = 9.0, 1.9 Hz, 2H), 1.41 – 1.04 (m, 2H), 0.95 – 0.68 (m, 2H), ^{19}F NMR (376 MHz, $CDCl_3$) δ -107.68 (d, *J* = 10.3 Hz), -110.28 (d, *J* = 10.3 Hz). ESI-HRMS calculated: ($[M]^+$): m/z, 633.1253, found: ([M]+): m/z, 633.1316, ($[M+NH_4]$+): m/z, 650.0657. 1H NMR (400 MHz, $CDCl_3$) in presence of AcOH, ^{1}H NMR (400 MHz, $CDCl_3$) δ 9.12 (d, *J* = 5.5 Hz, 2H), 8.31 (d, *J* = 7.0 Hz, 2H), 7.84 (t, *J* = 7.6 Hz, 2H), 7.49 – 7.34 (m, 6H), 7.29 (t, *J* = 7.2

Hz, 9H), 7.21 (t, *J* = 7.2 Hz, 4H), 6.84 (t, *J* = 6.0 Hz, 2H), 6.46 – 6.21 (m, 2H), 5.28 (dd, *J* = 8.9, 2.1 Hz, 2H), 3.12 (d, *J* = 4.4 Hz, 2H), 2.58 (d, *J* = 3.9 Hz, 2H) .

7.4 Conclusions

We have reported the synthesis and characterization of bluish-green emitting iridium(III) complex by a straightforward synthetic protocol. The synthesized **1** was tested successfully in using of acid (H^+), base (OH^-) and pH sensing multi-responsive probe molecule. The emission intensity of 1 gets quenched sharply in presence of acid. The **1** sensed to OH^- and transformed it into a yellow emitting complex. The isolated complex was characterized and identified as AIEE active. The mechanistic pathway for the sensing mechanism was explored. The acid induced chelation and base induced substitution reaction, made **1** as an efficient chemodosimeter for H^+ and OH^-, respectively.

7.5 References

[1] S.J. Toal, W.C. Trogler, J. Mater. Chem., 16 (2006) 2871-2883.

[2] I.A. Popov, H. Chen, O.N. Kharybin, E.N. Nikolaev, R.G. Cooks, Chem. Commun., (2005) 1953-1955.

[3] L. Li, S. Zhang, L. Xu, L. Han, Z.-N. Chen, J. Luo, Inorg. Chem., 52 (2013) 12323-12325.

[4] T.K. Kim, J.H. Lee, D. Moon, H.R. Moon, Inorg. Chem., 52 (2013) 589-595.

[5] Y. Bai, G.-j. He, Y.-g. Zhao, C.-y. Duan, D.-b. Dang, Q.-j. Meng, Chem. Commun., (2006) 1530-1532.

[6] J. Du, M. Hu, J. Fan, X. Peng, Chem. Soc. Rev., 41 (2012) 4511-4535.

[7] H. Xu, O.A. Sadik, Analyst, 125 (2000) 1783-1786.

[8] R.J. Berman, G.D. Christian, L.W. Burgess, Anal. Chem., 62 (1990) 2066-2071.

[9] L.R. Allain, Z. Xue, Anal. Chem., 72 (2000) 1078-1083.

[10] A.P. de Silva, H.Q.N. Gunaratne, T. Gunnlaugsson, A.J.M. Huxley, C.P. McCoy, J.T. Rademacher, T.E. Rice, Chem. Rev., 97 (1997) 1515-1566.

[11] W.P. Ambrose, P.M. Goodwin, J.H. Jett, A. Van Orden, J.H. Werner, R.A. Keller, Chem. Rev., 99 (1999) 2929-2956.

[12] J.J. Marugan, W. Huang, O. Motabar, W. Zheng, J. Xiao, S. Patnaik, N. Southall, W. Westbroek, W.A. Lea, A. Simeonov, E. Goldin, M.A. DeBernardi, E. Sidransky, Med.Chem.Comm., 3 (2012) 56-60.

[13] S. Lamansky, P. Djurovich, D. Murphy, F. Abdel-Razzaq, H.-E. Lee, C. Adachi, P.E. Burrows, S.R. Forrest, M.E. Thompson, J. Am. Chem. Soc., 123 (2001) 4304-4312.

[14] S. Lamansky, P. Djurovich, D. Murphy, F. Abdel-Razzaq, R. Kwong, I. Tsyba, M. Bortz, B. Mui, R. Bau, M.E. Thompson, Inorg. Chem., 40 (2001) 1704-1711.

[15] S. Sprouse, K.A. King, P.J. Spellane, R.J. Watts, J. Am. Chem. Soc., 106 (1984) 6647-6653.

[16] K.-C. Tang, K.L. Liu, I.C. Chen, Chem. Phys. Lett., 386 (2004) 437-441.

[17] W.-S. Huang, J.T. Lin, C.-H. Chien, Y.-T. Tao, S.-S. Sun, Y.-S. Wen, Chem. Mater., 16 (2004) 2480-2488.

[18] K.K.-W. Lo, J.S.-W. Chan, L.-H. Lui, C.-K. Chung, Organometallics, 23 (2004) 3108-3116.

[19] Y.-Y. Chang, J.-Y. Hung, Y. Chi, J.-P. Chyn, M.-W. Chung, C.-L. Lin, P.-T. Chou, G.-H. Lee, C.-H. Chang, W.-C. Lin, Inorg. Chem., 50 (2011) 5075-5084.

[20] L.M. Vogler, B. Scott, K.J. Brewer, Inorg. Chem., 32 (1993) 898-903.

[21] G. Zhang, H. Zhang, Y. Gao, R. Tao, L. Xin, J. Yi, F. Li, W. Liu, J. Qiao, Organometallics, 33 (2014) 61-68.

[22] W. Jiang, Y. Gao, Y. Sun, F. Ding, Y. Xu, Z. Bian, F. Li, J. Bian, C. Huang, Inorg. Chem., 49 (2010) 3252-3260.

[23] L. He, Y. Li, C.-P. Tan, R.-R. Ye, M.-H. Chen, J.-J. Cao, L.-N. Ji, Z.-W. Mao, Chem. Sci., 6 (2015) 5409-5418.

[24] P.E. Burrows, Z. Shen, V. Bulovic, D.M. McCarty, S.R. Forrest, J.A. Cronin, M.E. Thompson, J. Appl. Phy., 79 (1996) 7991-8006.

[25] V. Srikant, D.R. Clarke, J.Appl.Phy., 83 (1998) 5447-5451.

[26] X. Wang, K. Maeda, A. Thomas, K. Takanabe, G. Xin, J.M. Carlsson, K. Domen, M. Antonietti, Nat Mater, 8 (2009) 76-80.

[27] S. Monticone, R. Tufeu, Kanaev, J. Phys. Chem. B, 102 (1998) 2854-2862.

[28] F. Monti, F. Kessler, M. Delgado, J. Frey, F. Bazzanini, G. Accorsi, N. Armaroli, H.J. Bolink, E. Ortí, R. Scopelliti, M.K. Nazeeruddin, E. Baranoff, Inorg. Chem., 52 (2013) 10292-10305.

[29] K. Dedeian, J. Shi, E. Forsythe, D.C. Morton, P.Y. Zavalij, Inorg. Chem., 46 (2007) 1603-1611.

[30] C.-H. Yang, S.-W. Li, Y. Chi, Y.-M. Cheng, Y.-S. Yeh, P.-T. Chou, G.-H. Lee, C.-H. Wang, C.-F. Shu, Inorg. Chem., 44 (2005) 7770-7780.

[31] K.A. McGee, K.R. Mann, Inorg. Chem., 46 (2007) 7800-7809.

[32] Z. Yang, W. Qin, J.W.Y. Lam, S. Chen, H.H.Y. Sung, I.D. Williams, B.Z. Tang, Chem. Sci., 4 (2013) 3725-3730.

[33] X. Zhang, Z. Chi, B. Xu, H. Li, Z. Yang, X. Li, S. Liu, Y. Zhang, J. Xu, Dyes Pigm., 89 (2011) 56-62.

[34] Z. Yang, Z. Chi, T. Yu, X. Zhang, M. Chen, B. Xu, S. Liu, Y. Zhang, J. Xu, J. Mater. Chem., 19 (2009) 5541-5546.

[35] N. Zhao, Z. Yang, J.W.Y. Lam, H.H.Y. Sung, N. Xie, S. Chen, H. Su, M. Gao, I.D. Williams, K.S. Wong, B.Z. Tang, Chem. Commun., 48 (2012) 8637-8639.

[36] H. Li, Z. Chi, B. Xu, X. Zhang, Z. Yang, X. Li, S. Liu, Y. Zhang, J. Xu, J. Mater. Chem., 20 (2010) 6103-6110.

[37] S.A. Jenekhe, J.A. Osaheni, Science, 265 (1994) 765-768.

[38] T.P.I. Saragi, T. Spehr, A. Siebert, T. Fuhrmann-Lieker, J. Salbeck, Chem. Rev., 107 (2007) 1011-1065.

[39] K.-Y. Pu, B. Liu, Adv.Funct. Mater., 19 (2009) 277-284.

[40] Y. Dong, J.W.Y. Lam, A. Qin, J. Liu, Z. Li, B.Z. Tang, J. Sun, H.S. Kwok, Appl. Phy. Lett., 91 (2007) 011111.

[41] Z. Zhao, S. Chen, X. Shen, F. Mahtab, Y. Yu, P. Lu, J.W.Y. Lam, H.S. Kwok, B.Z. Tang, Chem. Commun., 46 (2010) 686-688.

[42] H. Tong, Y. Dong, Hau, J.W.Y. Lam, H.H.Y. Sung, I.D. Williams, J. Sun, B.Z. Tang, Chem. Commun., (2006) 1133-1135.

[43] X. Zhang, Z. Chi, H. Li, B. Xu, X. Li, W. Zhou, S. Liu, Y. Zhang, J. Xu, Chem. Asian J., 6 (2011) 808-811.

[44] Y. Dong, J.W.Y. Lam, A. Qin, Z. Li, J. Sun, H.H.Y. Sung, I.D. Williams, B.Z. Tang, Chem. Commun., (2007) 40-42.

[45] K.S. Bejoymohandas, T.M. George, S. Bhattacharya, S. Natarajan, M.L.P. Reddy, J. Mater. Chem. C, 2 (2014) 515-523.

Design and synthesis of new 'Aggregation Induced Emission (AIE)' active metal complex

Recently, we developed one pot methodology to synthesis of mono cyclometalated strong solid state luminescent iridium complex by using iridium(III) chloride, different triphenylphosphine derivatives along with chelated chromophoric ligands (cyclometalted/diimine) in 2-ethoxy ethanol. We did a facile tuning of emission color using a common framework and used many synthesized complexes in different applications such as bio-imaging and sensors.

1. The incorporation of bulky rotor groups

A further opportunity to improve quantum efficiency by introducing rigidity into the synthesized AIE molecules such as,

The efficiency may be increased by replacing the triphenyl phosphine with more bulky substituted triphenyl phosphine derivatives (L1 and L2).

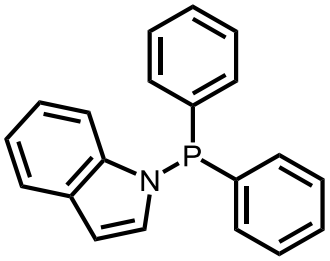

L1

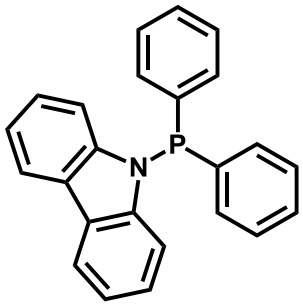

L2

Scheme 1 Chemical structure of modified triphenyl phosphine derivatives.

2. Modification on cyclometaleted ligands

It provides the opportunity to explore the new AIE molecules through incorporation of rotating units in the chromophoric ligands (e.g. L3 and L4). Restricted rotation (due to bulkiness) will minimize the nonradiative energy loss and efficiency would increase in the solid state.

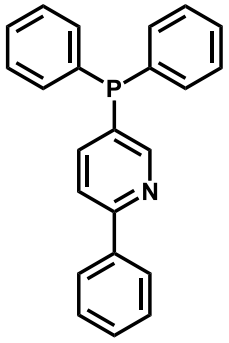

L3

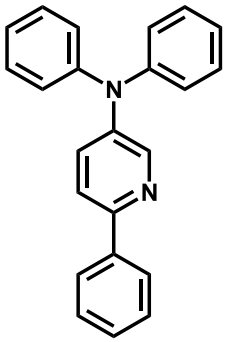

L4

3. Design and syntheses of new AIE active iridium(III) based complexes for targeted sensingof different analytes

The selective and sensitive detection of different ions can be done by using signaling unit approach.

Syntheses of following complexes (**1** and **2**) may lead to very good results in the field of sensors for different analytes.

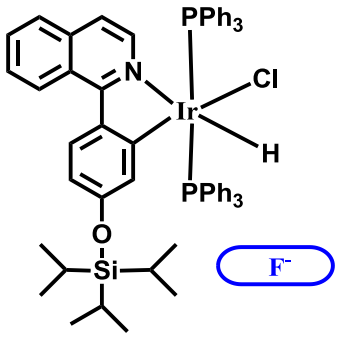

1

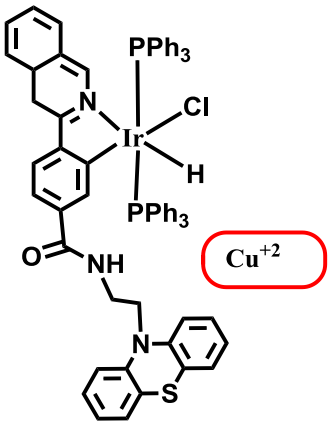

2

In a similar way the specific imaging of different cell organelle can be achieved by modification of functional groups in the complex.

4. Introduce biocompatibility into the parent AIE active iridium(III) complexes for bioimaging applications

The synthesized AIE complexes can be modified to biocompatibility for using as promising candidates in bioimaging (**3-5**), AIE active cationic complexes are the most demanding complex in bioimaging due to water solubility as well as dispersibility nature. Further, the

strategic functionalized these AIE complexes can selectively targeted to biomolecules e.g., DNA, Protein etc.

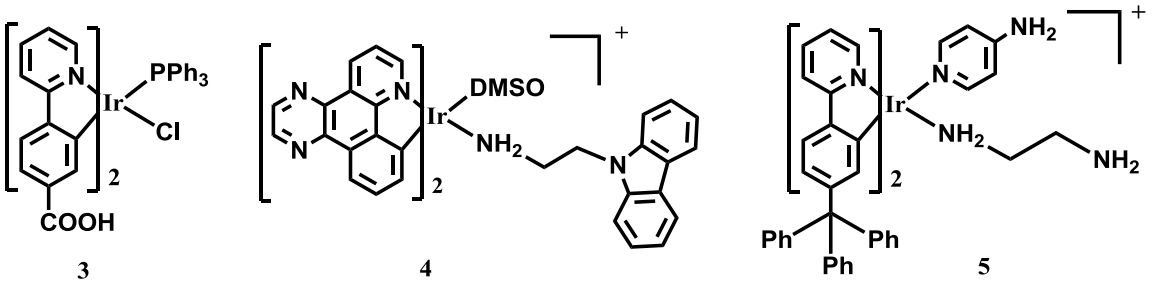

3 4 5

5. Mesoporous silica embedded AIE molecules for early detection of cancerous cells

High internal surface area and pore volume, tunable pore sizes, colloidal stability, and the possibility to functionalize the inner pore system with specific functional groups made the mesoporous silica nanoparticles as a promising candidate for different biomedical applications such as bioimaging, biosensing, biocatalysis and drug delivery. The incorporation of AIE iridium(III) complexes into the pore of the mesoporous silica can provide promising biomaterials which may utilize for bioimaging as well as the DNA aptamor functionalized nanoparticles may specifically target the tumor tissue among the healthy tissues. These approaches will be auspicious for early age detection of cancerous cells.

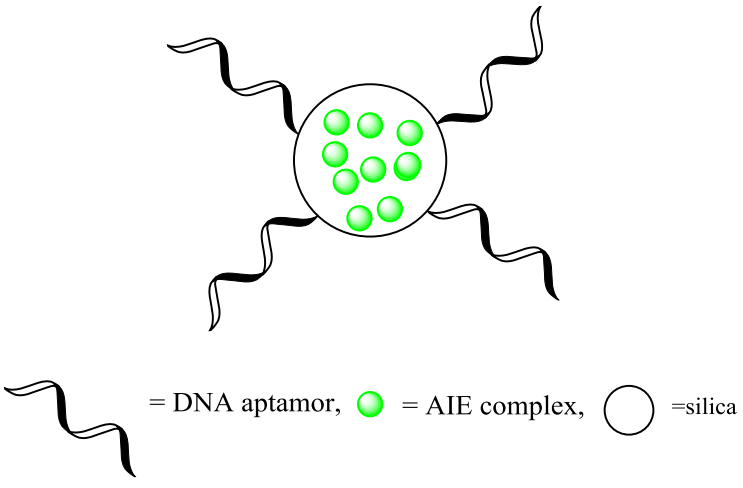

6. AIE complexes for Organic Light-Emitting Diodes (OLEDs)

OLEDs a future display technology system was recognized as most economical and superior system as compared to the existing display systems. Fabrication of OLED devices can be

performed by incorporating AIE iridium(III) complexes (**6**-**7**) into the emitting layers and using other appropriate electronic layers may lead to superior device performances.

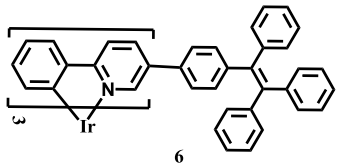

6

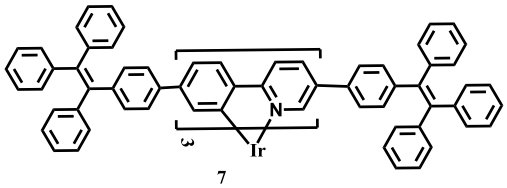

7

7. AIE Stimuli Responsive systems

Mechanochromic luminogens (MCL) or piezochromic luminogens (PCL) are smart materials which change their emission properties by experience of external stimuli such as pressure, grinding, stress, shearing, rubbing, milling and crushing. The MCL were fall in the category of fourth generation of materials after natural materials, synthetic polymer materials and artificial design materials. These materials have been achieved a considerable attention by the scientific community because of their potential applications in mechanosensors, security papers, and optical storage. It is obvious that the development of such kind of materials will lead the world to the next generation technologies. These AIEgens have a propeller types twisted geometry (**8**) which resulted a weak interaction in the crystal packing. Such inherent structural characteristics of these AIEgens make potentially useful as MCL as well as smart materials.

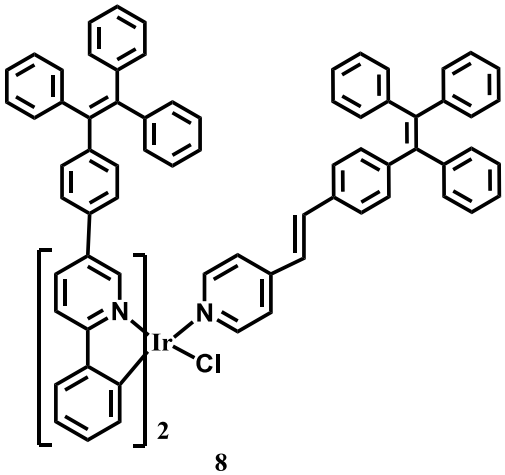

8

Design and synthesis of new 'Aggregation Induced Emission (AIE)' active metal complex

Recently, we developed one pot methodology to synthesis of mono cyclometalated strong solid state luminescent iridium complex by using iridium(III) chloride, different triphenylphosphine derivatives along with chelated chromophoric ligands (cyclometalted/diimine) in 2-ethoxy ethanol. We did a facile tuning of emission color using a common framework and used many synthesized complexes in different applications such as bio-imaging and sensors.

1. The incorporation of bulky rotor groups

A further opportunity to improve quantum efficiency by introducing rigidity into the synthesized AIE molecules such as,

The efficiency may be increased by replacing the triphenyl phosphine with more bulky substituted triphenyl phosphine derivatives (L1 and L2).

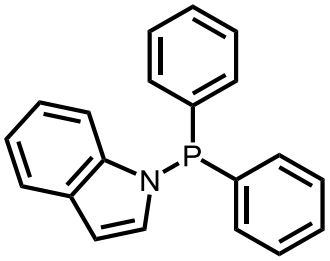

L1

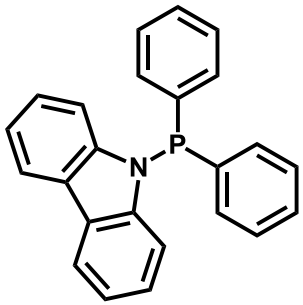

L2

Scheme 1 Chemical structure of modified triphenyl phosphine derivatives.

2. Modification on cyclometaleted ligands

It provides the opportunity to explore the new AIE molecules through incorporation of rotating units in the chromophoric ligands (e.g. L3 and L4). Restricted rotation (due to bulkiness) will minimize the nonradiative energy loss and efficiency would increase in the solid state.

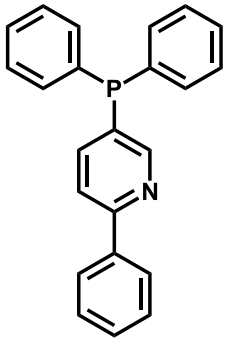

L3

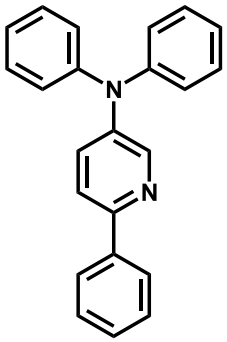

L4

3. Design and syntheses of new AIE active iridium(III) based complexes for targeted sensingof different analytes

The selective and sensitive detection of different ions can be done by using signaling unit approach.

Syntheses of following complexes (**1** and **2**) may lead to very good results in the field of sensors for different analytes.

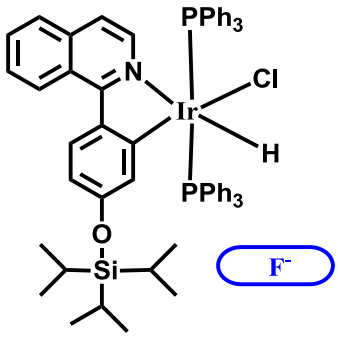

1

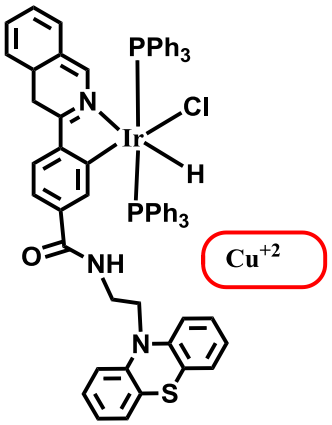

2

In a similar way the specific imaging of different cell organelle can be achieved by modification of functional groups in the complex.

4. Introduce biocompatibility into the parent AIE active iridium(III) complexes for bioimaging applications

The synthesized AIE complexes can be modified to biocompatibility for using as promising candidates in bioimaging (**3-5**), AIE active cationic complexes are the most demanding complex in bioimaging due to water solubility as well as dispersibility nature. Further, the

strategic functionalized these AIE complexes can selectively targeted to biomolecules e.g., DNA, Protein etc.

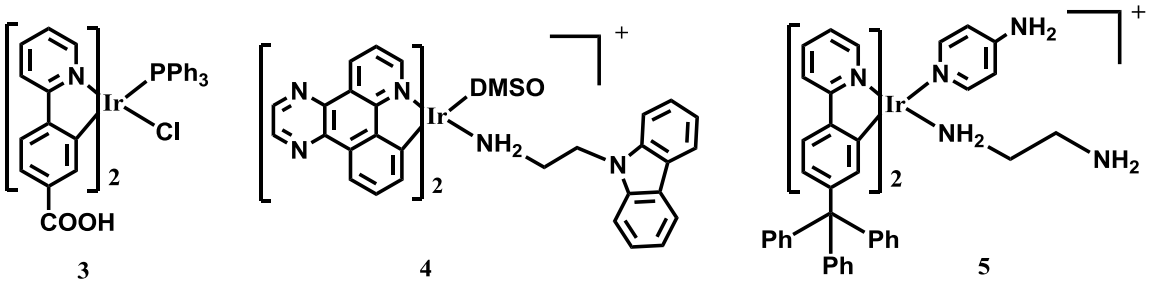

3 4 5

5. Mesoporous silica embedded AIE molecules for early detection of cancerous cells

High internal surface area and pore volume, tunable pore sizes, colloidal stability, and the possibility to functionalize the inner pore system with specific functional groups made the mesoporous silica nanoparticles as a promising candidate for different biomedical applications such as bioimaging, biosensing, biocatalysis and drug delivery. The incorporation of AIE iridium(III) complexes into the pore of the mesoporous silica can provide promising biomaterials which may utilize for bioimaging as well as the DNA aptamor functionalized nanoparticles may specifically target the tumor tissue among the healthy tissues. These approaches will be auspicious for early age detection of cancerous cells.

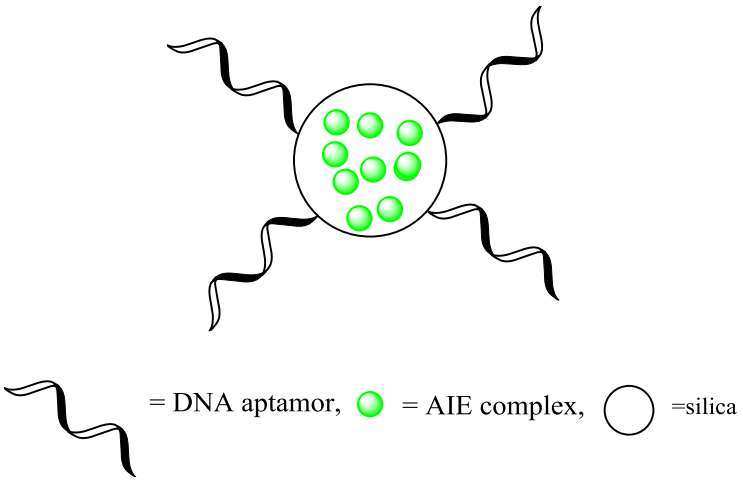

6. AIE complexes for Organic Light-Emitting Diodes (OLEDs)

OLEDs a future display technology system was recognized as most economical and superior system as compared to the existing display systems. Fabrication of OLED devices can be

performed by incorporating AIE iridium(III) complexes (**6**-**7**) into the emitting layers and using other appropriate electronic layers may lead to superior device performances.

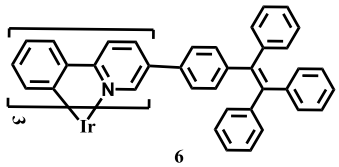

6

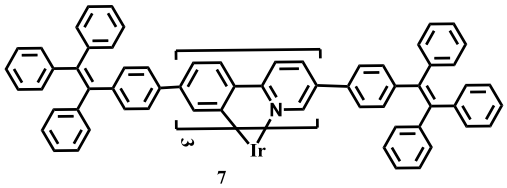

7

7. AIE Stimuli Responsive systems

Mechanochromic luminogens (MCL) or piezochromic luminogens (PCL) are smart materials which change their emission properties by experience of external stimuli such as pressure, grinding, stress, shearing, rubbing, milling and crushing. The MCL were fall in the category of fourth generation of materials after natural materials, synthetic polymer materials and artificial design materials. These materials have been achieved a considerable attention by the scientific community because of their potential applications in mechanosensors, security papers, and optical storage. It is obvious that the development of such kind of materials will lead the world to the next generation technologies. These AIEgens have a propeller types twisted geometry (**8**) which resulted a weak interaction in the crystal packing. Such inherent structural characteristics of these AIEgens make potentially useful as MCL as well as smart materials.

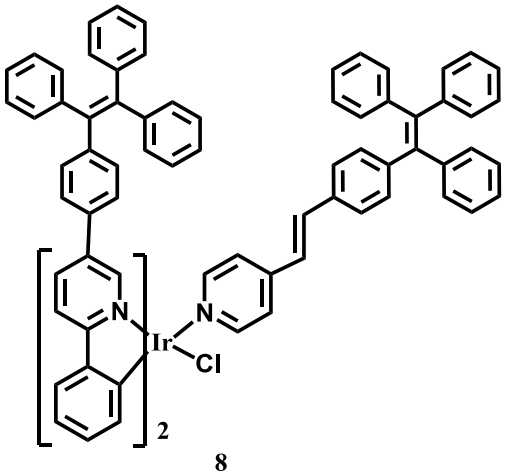

8

Appendices

List of Publications ***[A-1]***

---

1. **Parvej Alam**, Vishal Kachwal and Inamur Rahaman Laskar, A Multi-stimuli Responsive "AIE" Active Salicylaldehyde-based Schiff Base for Sensitive Detection of Fluoride, *Sensor and Actuator B,* 2016, 228, 539.

2. **Parvej Alam,** Gurpreet Kaur, Amrit Sarmah, Ram Kinkar Roy, Angshuman Roy Choudhury, and Inamur Rahaman Laskar, Highly Selective Detection of H^+ and OH^- with a Single Emissive Iridium(III) Complex: A Mild Approach to Conversion of Non-AIEE to AIEE Complex (AIEE = Aggregation Induced Enhanced Emission, *Organometallics*, 2015, 34, 4480.

3. Navin Jain, **Parvej Alam**, Inamur Rahman Laskar and Jitendra Panwar, Aggregation Induced Phosphorescence' Active Iridium(III) Complexes for Integrated Sensing and Inhibition of Bacteria in Aqueous Solution, *RCS advances*, 2015, 61983.

4. **Parvej Alam**, Gurpreet Kaur, Vishal Kachwal, Asish Gupta, Angshuman Roy and Inamur Rahaman Laskar, Highly Sensitive Explosive Sensing by "Aggregation Induced Phosphorescence" Active Cyclometalated Iridium(III) complexes, *Journal of Materials Chemistry C*, 2015, 3, 5450.

5. **Parvej Alam**, Gurpreet Kaur, Shamik Chakraborty, Angshuman Roy Choudhury, and Inamur Rahaman Laskar, Aggregation Induced Phosphorescence' Active 'Rollover' Iridium(III) Complex as Multi-Stimuli-Responsive Luminescence Material, *Dalton Trans*., 2015, 44, 6581.

6. Sheik Saleem Pasha, **Parvej Alam**, Subhra Dash, Gurpreet Kaur, Debashree Banerjee, Rajdeep Chowdhury, Nigam Rath, Angshuman Roy Choudhury and Inamur Rahaman Laskar, Rare Observation of 'Aggregation Induced Emission' in Cyclometalated Platinum(II) Complexes and their Biological Activities, *RSC Advances*, 2014, 50549.

7. **Parvej Alam**, Gurpreet Kaur, Clàudia Climent, Saleem Pasha, David Casanova, Pere Alemany, Angshuman Roy Choudhury and Inamur Rahaman Laskar, 'Aggregation Induced Emission (AIE)' Active Cyclometalated Iridium(III) Based Fluorescent Sensors: High Sensitivity for Mercury(II) Ions, *Dalton Trans*., 2014, 43, 16431.

8. **Parvej Alam**, Pradip Das, Clàudia Climent, Maheswararao Karanam, David Casanova, Pere Alemany, Angshuman Roy Choudhury, Nikhil Ranjan Jana and Inamur Rahaman Laskar, Facile Tuning of the Aggregation Induced Emission Wavelength in a Common Framework of a Cyclometalated Iridium(III) Complex : Micellar Encapsulated Probe in Celluler Imaging, *Journal of Materials Chemistry C*, 2014, 2, 5615.

9. **Parvej Alam**, Maheswararao Karanam, Debashree Bandyopadhyay, Angshuman Roy Choudhury and Inamur Rahaman Laskar, Aggregation Induced Emission Activity in Iridium(III)-Diimine Complexes: Investigations of Their Vapochromic Properties, *Eur. J. Inorg. Chem*., 2014, 23, 3710.

10. **Parvej Alam**, Inamur Rahaman Laskar, Clàudia Climent, David Casanova, Pere Alemany, Maheswararao Karanam, Angshuman Roy Choudhury and J. Raymond Butcher, Microwave Assisted Facile and Expeditive Syntheses of Phosphorescent Cyc lometalated Iridium(III) Complexe, *Polyhedron*, 2013, 286.

11. **Parvej Alam**, Maheswararao Karanam, Angshuman Roy Choudhury and Inamur Rahaman Laskar, One-Pot Synthesis of Strong Solid State Emitting Mono-cyclometalated Iridium(III) Complexes: Study of their Aggregation Induced Enhanced Phosphorescence, *Dalton Trans*., 2012, 9276.

Research articles under review

1. **Parvej Alam**, Gurpreet Kaur, Clàudia Climent, Saleem Pasha, David Casanova, Pere Alemany, Angshuman Roy Choudhury and Inamur Rahaman Laskar, Tuning of Aggregation Induced Emission Wavelength of Organometallic Iridium(III) Cationic Complexes and Mechanochromic Effect: by Influence of Counterions (Under review).

2. **Parvej Alam,** Gurpreet Kaur, Clàudia Climent, David Casanova, Pere Alemany, Angshuman Roy Choudhury and Inamur Rahaman Laskar, An Aggregation Induced Phosphorescence (AIP) Iridium(III) Complexes with chromophoric Schiff base ligand: Tunable emission, multi-stimuly and CO_2 detection (Under review).

3. **Parvej Alam**, Pere Alemany and Inamur Rahaman Laskar, Aggregation Induced Emission (AIE): Insights into the Metal Complexes and Organoboron Complexes (Review article, Communicated).

4. **Parvej Alam**, Rajdeep Choudhury, Angshuman Roy Choudhury and Inamur Rahaman Laskar, "An Aggregation Induced Emission "AIE" active Iridium(III) complex and mitochondrial staining" (Under review).

List of Oral/poster presented in conferences ***[A-2]***

---

1. **Parvej Alam** Gurpreet Kaur, Clàudia Climent, Saleem Pasha, David Casanova, Pere Alemany, Angshuman Roy Choudhury and Inamur Rahaman Laskar, Tuning of Aggregation Induced Emission Wavelength of Organometallic Iridium(III) Cationic Complexes and Mechanochromic Effect: by Influence of Counter ions, New Frontiers in Chemistry-from Fundamentals to Applications (NFCFA2015) held at BITS Pilani KK Birla Goa Campus during Dec 18^{th}-19^{th} 2015 **(poster)**.

2. **Parvej Alam,** Gurpreet Kaur, Amrit Sarmah, Ram Kinkar Roy, Angshuman Roy Choudhury, and Inamur Rahaman Laskar, Highly Selective Detection of H^+ and OH^- with a Single Emissive Iridium(III) Complex: A Mild Approach to Conversion of Non-AIEE to AIEE Complex (AIEE =Aggregation Induced Emission enhancement, Nascent Developments in Chemical Sciences: Opportunities for Academia-Industry Collaboration NDCS International Conference (NDCS-2015) held at BITS Pilani, Pilani Campus during October 16^{th}-18^{th}, 2015, (**Best poster award**).

3. **Parvej Alam**, Gurpreet Kaur, Shamik Chakraborty, Angshuman Roy Choudhury and Inamur Rahaman Laskar, Aggregation Induced Phosphorescence' Active 'Rollover' Iridium(III) Complex as Multi-Stimuli-Responsive Luminescence Material, 21^{st} ISCB International Conference (ISCBC-2015) on "Current Trends in Drug Discovery and Developments" held at Central Drug Research Institute, Lucknow during 25^{th} - 28^{th} February, 2015 (**Best poster award**).

4. **Parvej Alam,** Gurpreet Kaur, Vishal Kachwal, Asish Gupta, Angshuman Roy Chaudhury and Inamur Rahaman Laskar, Highly sensitive explosive sensing by "aggregation induced phosphorescence" active cyclometalated iridium(III) complexes, National Conference on Nano- and Functional Materials (NFM-2014), organized by Department of Chemistry, BITS Pilani, Pilani Campus, Rajasthan, 7^{th}-8^{th} November 2014 (**poster**).

5. **Parvej Alam**, Gurpreet Kaur, Shamik Chakraborty, Angshuman Roy Choudhury and Inamur Rahaman Laskar, Aggregation Induced Phosphorescence' Active 'Rollover' Iridium(III) Complex as Multi-Stimuli-Responsive Luminescence Material,(Oral) National Conference on Nano- and Functional Materials (NFM-2014), organized by Department of Chemistry, BITS Pilani, Pilani Campus, Rajasthan, 7^{th}-8^{th} November 2014, **(Best oral award).**

6. **Parvej Alam** and Inamur R. Laskar, "Tuning of Aggregation Induced Emission Wavelength in a Common Framework of Cyclometalated Iridium(III) Complex: Miceller Encapsulated Prove in Bioimaging" (oral), in 5th national symposium for Materials research Scholars MR-13 held at Department of Matallurgical Engineering & Materials Science, IIT Bombay on 8^{th} May 2013, **(Best oral award).**

7. **Parvej Alam** and Inamur Rahaman Laskar "Aggregation Induced Enhanced Phosphorescent Emission and their Applications" held at University of Delhi (Department of chemistry) January 21^{st}-23^{rd}, 2013 **(poster)**.

8. **Parvej Alam** and Inamur R. Laskar, Syntheses of Highly Efficient Divalent Iridium Complexes and Study of their Aggregation Induced Enhanced Emission Properties, held at BITS, Pilani, Rajasthan (Dept. of Physics), February, 24^{th}-25^{th}, 2012 **(poster)**.

9. **Parvej Alam** and Inamur R. Laskar, Microwave-Assisted Facile and Clean Synthesis of Cyclometaleted Iridium(III) Complexes Useful for Organic Light Emitting Diodes, held at BITS, Pilani, Rajasthan (Dept. of Chem.), March, 25^{th}, 2012 **(poster)**.

10. **Parvej Alam** and Inamur Rahaman Laskar, "One-pot synthesis of strong solid state emitting mono-cyclometalated iridium(III) complexes: study of their aggregation induced enhanced phosphorescence", held at Dr. B R Ambedkar National Institute of Technology, Jalandhar (Department of chemistry) September 10^{th}-12^{th}, 2012 **(poster)**.

BRIEF BIOGRAPHY OF THE CANDIDATE ***[A-3]***

Mr. Parvej Alam, is a Ph.D student at BITS Pilani, Pilani Campus, Rajasthan, obtained his master degree from Deen Dayal Upadhyay University Gorakhpur, U.P. (India) in 2007. Then, he joined at TCG Life Sciences (Chemical Industry), Kolkata (India) and had worked there for 3.5 years. He started pursuing Ph.D at the Department of Chemistry, BITS Pilani on Dec., 2010. He has been working on the project "Chemistry of Iridium(III) based 'Aggregation Induced Emission' Active Complexes: Applications in Sensing and Bioimaging". He has published eleven research articles in peer reviewed international journals and presented papers in ten conferences/symposiums.

Currently, **Prof. Inamur Rahaman Laskar** has been employed as an Associate Professor at Department of Chemistry, Birla Institute of Technology & Science, Pilani Campus, Pilani, Rajasthan, India. He was awarded Ph. D. degree in Inorganic Chemistry from 'Indian Association for the Cultivation of Science (IACS)', Kolkata, India in 2000. He was working as a Lecturer at Ananda Mohan College (affiliated to University of Calcutta), Kolkata, India during Sept., 1999–July, 2001. He worked as a postdoctoral associate at NCTU Taiwan, during April, 2002–March, 2006 and NTHU Taiwan, during July, 2001–Feb., 2002. Further, he did his Post-doctoral (as JSPS Postdoctoral Fellow) research work at Kochi University, Japan in the period of April, 2006–March, 2008. He joined the Department of Chemistry, BITS Pilani on August, 2008. His current research interest is mainly focused on the design and syntheses of novel luminescent and AIE active luminescent materials, exploring the AIE mechanism, detailed study of luminescent behavior and targeted these materials in various applications such as applications in bio-imaging and cancer therapy, sensing (explosive/toxic analytes from solution and vapor phase), mechanofluorochromic and organic light emitting diodes etc. Modeling of the synthesized luminescent materials to explore the excited state properties and validation into the spectroscopic data of these complexes remains his further interest.